(NASA-CP-2449) RAPID FLUCTUATIONS IN SOLAR N87-21785
FLARES (NASA) 491 p CSCL 03B THRU
N87-21833
Unclas
G3/92 43054

NASA Conference Publication 2449

Rapid Fluctuations in Solar Flares

Edited by
Brian R. Dennis and Larry E. Orwig
NASA Goddard Space Flight Center
Greenbelt, Maryland

Alan L. Kiplinger
Systems Applied Sciences Corporation-Technologies
Landover, Maryland

Proceedings of a workshop held at
the Ramada Hotel
Lanham, Maryland
September 30–October 4, 1985

NASA
National Aeronautics
and Space Administration

Scientific and Technical
Information Branch

1987

TABLE OF CONTENTS

Page

PARTICIPANTS vii

PREFACE ix

RAPID FLUCTUATIONS IN SOLAR FLARES 1
Peter A. Sturrock

SECTION 1
X-RAYS

SUB-SECOND VARIATIONS OF HIGH-ENERGY (> 300 keV) HARD X-RAY EMISSION FROM SOLAR FLARES 29
Taeil Bai

INTERPRETATION OF RAPID RISES IN HARD X-RAYS AND MICROWAVES WITH THE THERMAL CONDUCTION FRONT MODEL 35
D. A. Batchelor

IMPULSIVE PHASE SOLAR FLARE X-RAY POLARIMETRY 47
Gary Chanan, A. Gordon Emslie, and Robert Novick

PERSISTENT TIME INTERVALS BETWEEN FEATURES IN SOLAR FLARE HARD X-RAY EMISSION 63
Upendra D. Desai, Chryssa Kouveliotou, C. Barat, K. Hurley, M. Niel, R. Talon, and G. Vedrenne

EVIDENCE FOR BEAMED ELECTRONS IN A LIMB X-RAY FLARE OBSERVED BY HXIS 75
Eberhard Haug and Gerhard Elwert

A STUDY OF STARTING TIME IN GREAT HARD X-RAY FLARES 79
K. L. Klein, M. Pick, and A. Magun

STATISTICAL ANALYSIS OF FAST HARD X-RAY BURSTS BY SMM OBSERVATIONS AND MICROWAVE BURSTS BY GROUND-BASED OBSERVATIONS 85
Li Chun-sheng and Jiang Shu-ying

MICROWAVE AND HARD X-RAY EMISSIONS DURING THE IMPULSIVE PHASE OF SOLAR FLARES: NONTHERMAL ELECTRON SPECTRUM AND TIME DELAY 91
Gu Ye-ming and Li Chun-sheng

HARD X-RAY IMAGING OBSERVATION OF FLUCTUATING BURSTS 111
K. Ohki and M. Harada

HARD X-RAY DELAYS 121
Richard A. Schwartz

FAST FLUCTUATIONS OF SOFT X-RAYS FROM ACTIVE REGIONS 123
G. F. Simnett and B. R. Dennis

SECTION 2
RADIO AND MICROWAVES

RADIO AND MICROWAVE GROUP SUMMARY OF DISCUSSIONS 131
Arnold O. Benz

PRECEDING PAGE BLANK NOT FILMED

TABLE OF CONTENTS (Continued)

Page

EXTREMELY RAPID RADIO SPIKES IN FLARES (Review) 133
A. O. Benz

RELATION BETWEEN SOLAR NARROW-BAND DECIMETER WAVE BURSTS AND ASSOCIATED X-RAY BURSTS 145
Shinzo Enome and Larry E. Orwig

POSITION MEASUREMENTS OF RAPIDLY FLUCTUATING MICROWAVE BURSTS 147
K. Kai and H. Nakajima

THE ROLE OF NARROWBAND DM-SPIKES IN SOLAR FLARES 155
Marian Karlicky

THE POSSIBLE IMPORTANCE OF SYNCHROTRON/INVERSE COMPTON LOSSES TO EXPLAIN FAST MM-WAVE AND HARD X-RAY EMISSION OF A SOLAR EVENT 161
E. Correia, P. Kaufmann, J. E. R. Costa, A. M. Zodi Vaz, and B. R. Dennis

RAPID SPECTRAL AND FLUX TIME VARIATIONS IN A SOLAR BURST OBSERVED AT VARIOUS DM-MM WAVELENGTHS AND AT HARD X-RAYS 171
A. M. Zodi Vaz, P. Kaufmann, E. Correia, J. E. R. Costa, E. W. Cliver, T. Takakura, and K. F. Tapping

QUASI-PERIODIC PULSATIONS IN SOLAR HARD X-RAY AND MICROWAVE FLARES 185
Takeo Kosugi and Alan L. Kiplinger

MICROWAVE MILLISECOND SPIKE EMISSION AND ITS ASSOCIATED PHENOMENA DURING THE IMPULSIVE PHASE OF LARGE FLARES 193
LI Chunsheng, JIANG Shuying, LI Hongwei, and FU Qijun

THE MICROWAVE SPECTRUM OF SOLAR MILLISECOND SPIKES 205
M. Stahli and A. Magun

SOLAR VLBI 211
H. F. Tapping and J. Kuijpers

TEMPORAL FREQUENCY OF RADIO EMISSIONS FOR THE APRIL 25, 1984 FLARE 215
G. D. Wells, B. A. Hausman, and H. W. Kroehl

SOLAR MICROWAVE MILLISECOND SPIKE AT 2.84 GHZ 237
Qi-Jun Fu, Sheng-zhen Jin, Ren-yang Zhao, Le-ping Zheng, Yu-ying Liu, Xioa-cong Li, Shu-lan Wang, Zhi-jun Chen, and Chu-min Hu

SECTION 3
THERMAL RESPONSE

THE SENSITIVITY OF Hα PROFILES TO RAPID ELECTRON BEAM FLUCTUATIONS 249
Richard C. Canfield and Kenneth G. Gayley

A SEARCH FOR FAST VARIATIONS IN THE Fe XXI EMISSION DURING SOLAR FLARES 263
Chung-Chieh Cheng

FAST TEMPORAL CORRELATION BETWEEN HARD X-RAY AND ULTRAVIOLET CONTINUUM BRIGHTENINGS 271
Marcos E. Machado and Pablo J. Mauas

TABLE OF CONTENTS (Continued)

Page

COMPARISON OF SOLAR HARD X-RAY AND UV LINE AND CONTINUUM BURSTS WITH HIGH TIME RESOLUTION 277
L. E. Orwig and B. E. Woodgate

OV AND HARD X-RAYS, OBSERVATIONS AND MODEL CALCULATIONS 279
A. I. Poland and J. T. Mariska

RAPID SOFT X-RAY FLUCTUATIONS IN SOLAR FLARES OBSERVED WITH THE X-RAY POLYCHROMATOR 289
D. M. Zarro, J. L. R. Saba, and K. T. Strong

SOFT X-RAY OSCILLATIONS DURING THE FLARE OF 7 AUGUST 1972 299
Roger J. Thomas, Werner M. Neupert, and William T. Thompson

RAPID CHANGES IN Hα-FLARES CORRELATED WITH MICROWAVES 301
J-P. Wülser and N. Kämpfer

SECTION 4
PLASMA PHYSICS

PLASMA TURBULENCE AND IMPULSIVE UV LINE EMISSION IN SOLAR FLARES 311
John C. Brown

ELECTRON-CYCLOTRON MASER AND SOLAR MICROWAVE MILLISECOND SPIKE EMISSION ... 319
Li Hong-wei, Li Chun-sheng, and Fu Qi-jun

THE EFFECT OF BEAM-DRIVEN RETURN CURRENT INSTABILITY ON SOLAR HARD X-RAY BURSTS 327
D. Cromwell, P. McQuillan, and J. C. Brown

ELECTRON-CYCLOTRON MASER EMISSION DURING FLARES: EMISSION IN VARIOUS MODES AND TEMPORAL VARIATIONS 341
R. R. Winglee and G. A. Dulk

IMPULSIVELY GENERATED FAST CORONAL PULSATIONS 347
P. M. Edwin and B. Roberts

SHOCK ACCELERATION OF ELECTRONS AND IONS IN SOLAR FLARES 359
Donald C. Ellison and Reuven Ramaty

THE GENERATION OF RAPID SOLAR FLARE HARD X-RAY AND MICROWAVE FLUCTUATIONS IN CURRENT SHEETS 361
Gordon D. Holman

THE QUASI-LINEAR RELAXATION OF THICK-TARGET ELECTRON BEAMS IN SOLAR FLARES .. 373
K. G. McClements, J. C. Brown, and A. G. Emslie

THE PROPAGATION OF SOLAR FLARE PARTICLES IN A CORONAL LOOP 383
J. M. Ryan

SIGNATURES OF CURRENT LOOP COALESCENCE IN SOLAR FLARES 393
J. Sakai, E. Zaidman, T. Tajima, H. Nakajima, T. Kosugi, and F. Brunel

TABLE OF CONTENTS (Continued)

Page

THERMAL WAVES OR BEAM HEATING IN THE 1980, NOVEMBER 5 FLARE 435
Dean F. Smith

A DOUBLE LAYER MODEL FOR SOLAR X-RAY AND MICROWAVE PULSATIONS 445
K. F. Tapping

THEORETICAL STUDIES ON RAPID FLUCTUATIONS IN SOLAR FLARES 455
Loukas Vlahos

SECTION 5
FUTURE PLANS

A JAPANESE PLAN: LARGE RADIO HELIOGRAPH IN THE SOLAR MAX #22 461
Shinzo Enome

THE HESP PROJECT 467
H. Kai

THE PROPOSED NRAO MILLIMETER ARRAY AND ITS USE FOR SOLAR STUDIES 471
Mukul R. Kundu

Collection Editors: Brian R. Dennis, Alan Kiplinger, and Larry Orwig

Scientific Organizing Committee:

John Brown	University of Glasgow, Scotland
Brian Dennis	Goddard Space Flight Center
Gordon Emslie	University of Alabama in Huntsville
Gordon Hurford	California Institute of Technology
Alan Kiplinger	Goddard Space Flight Center

Local Organizing Committee:

- Brian Dennis
- Bernie Gibson
- Steve Graham
- Shelby Kennard
- Alan Kiplinger
- Larry Orwig
- Kim Tolbert
- Gloria Wharen

PARTICIPANTS

NAME	GROUP	INSTITUTION	COUNTRY
Taeil Bai	X-rays	Stanford U., CA	USA
David Batchelor	X-rays	APL, Laurel, MD	USA
Arnold Benz	radio	ETH, Zurich	Switzerland
John C. Brown	plasma physics	U. of Glasgow	Scotland
Marilyn Bruner	thermal response	Lockheed, Palo Alto	USA
Richard Canfield	thermal response	U. of Calif. at San Diego	USA
Chung-Chieh Cheng	thermal response	NRL, Wash., DC	USA
Emilia Correia	microwaves	INPE, Sao Paulo	Brazil
Carol Crannell	X-rays	NASA/GSFC	USA
David Cromwell	plasma physics	U. of Glasgow	Scotland
Brian Dennis	X-rays	NASA/GSFC	USA
Upendra Desai	X-rays	NASA/GSFC	USA
Patricia Edwin	plasma physics	U. of St. Andrews	Scotland
Gordon Emslie	thermal response	U. of Alabama, Huntsville	USA
Shinzo Enome	microwaves	Toyokawa Observatory	Japan
Judy Fennelly	thermal response	U. of Alabama, Hunstville	USA
Fu Qui Jun	microwaves	U. of Md., College Park	USA
Dale Gary	microwaves/X-rays	CIT, Pasadena, CA	USA
Kenneth Gayley	thermal response	U. of Calif. at San Diego	USA
Tom Gergely	radio	U. of MD., College Park	USA
Eberhard Haug	X-rays	U. der Tubingen	West Germany
Gordon Holman	plasma physics	NASA/GSFC	USA
Gordon Hurford	microwaves	CIT, Pasadena, CA	USA
Keizo Kai	microwaves	Tokyo Astron. Obs.	Japan
Sharad Kane	X-rays	Berkeley, CA	USA
Pierre Kaufmann	microwaves	INPE, Sao Paulo	Brazil
Alan Kiplinger	X-rays	NASA/GSFC	USA
Ludwig Klein	X-rays	Meudon	France
Takeo Kosugi	microwaves	NASA/GSFC	USA
Chryssa Kouveliotou	X-rays/radio	NASA/GSFC	USA
Mukul Kundu	radio	U. of Md., College Park	USA
Ted LaRosa	radio	U. of Md., College Park	USA
Li Chun-sheng	microwaves	U. of Nanjing	China
Bob Lin	X-rays	Berkeley, CA	USA
Raffaella Loiacono	radio	U. of Md., College Park	USA
Marcos Machado	thermal respone	NASA/MSFC	USA
John Mariska	thermal response	NRL, Wash., DC	USA
Kenneth McClements	plasma physics	U. of Glasgow	Scotland
Robert Novick	X-rays	Columbia U. New York	USA
Larry Orwig	X-rays	NASA/GSFC	USA
Arthur Poland	thermal response	NASA/GSFC	USA
James Ryan	plasma physics	U. of NH, Durham	USA
Julia Saba	thermal response	NASA/GSFC	USA
Jun-ichi Sakai	plasma physics	Toyama University	Japan
Richard Schwartz	X-rays	JPL, Pasadena, CA	USA
Dean Smith	plasma physics	U. of CO., Boulder	USA
Dan Spicer	plasma physics	NASA/GSFC	USA
Markus Staehli	microwaves	Berne University	Switzerland

PRECEDING PAGE BLANK NOT FILMED

Keith Strong	thermal response	NASA/GSFC	USA
Peter Sturrock	review speaker	Stanford U., CA.	USA
Ken Tapping	microwaves	Herzberg Inst., Ottawa	Canada
Roger Thomas	thermal response	NASA/GSFC	USA
William Thompson	thermal response	NASA/GSFC	USA
Ana Marie Zodi Vaz	microwaves	INPE, Sao Paulo	Brazil
Loukas Vlahos	plasma physics	U. of Md., College Park	USA
Gary D. Wells	microwaves	NOAA, Boulder, CO	USA
Steven White	plasma physics	U. of Md, College Park	USA
Robert Winglee	plasma physics/ microwaves	U. of CO, Boulder	USA
Bruce Woodgate	thermal response	NASA/GSFC	USA
Jean-Pierre Wuelser	thermal response	Berne	Switzerland
Dominic M. Zarro	thermal response	NASA/GSFC	USA

PREFACE

This is a collection of papers resulting from the workshop on Rapid Fluctuations in Solar Flares held at the Ramada Hotel in Lanham, Maryland, from September 30 to October 4, 1985. This workshop was one in a series of NASA workshops that is part of the ongoing analysis of results from the Solar Maximum Mission. The first three SMM workshops took place in January and June 1983, and February 1984, and covered the full range of solar flare observations. A workshop with more limited coverage was held in April 1985 on Coronal Prominences and Plasmas. Thus, this workshop on Rapid Fluctuations in Solar Flares is the second in a series of topical SMM workshops, with more planned for the future.

The objectives of the workshop were to present observations of solar flare emissions that showed fluctuations on time scales generally shorter than ~ 10 s and to discuss the possible theoretical interpretations of these fluctuations. Over 60 people attended the workshop and the hoped for wide range of the electromagnetic spectrum was covered with observations presented at radio, microwave and mm wavelengths, in the Hα, the UV, and EUV, and in soft and hard X-rays. At least a quarter of the contributions were devoted to theoretical interpretations.

All of the original contributions to the workshop were either given orally or were on posters. The papers contained in this publication were completed, in most cases, after the workshop and contain some of the flavor of the discussions that took place. We have been able to include nearly all of the contributions; only in a few cases were "abstracts only" available and in most of those cases the material is being published elsewhere.

None of the papers were formally refereed although the authors were encouraged to have a colleague review their work. This method of publication was chosen after much discussion at the workshop. It was felt that since the field of rapid fluctations in solar flares is relatively new, the free discussion of the observations and theories should be encouraged without the possibly inhibiting worry of having to please a referee. Also, the more rapid dissemination of the material possible using this method was deemed to be important for the advancement of this field.

It is hoped that the workshop and this publication will generate new interest in the field of rapid fluctuations and will promote future publications in the regular scientific journals leading to greater insight into the fundamental questions of solar flare physics.

The participants at the workshop were divided into four groups to facilitate discussion. The groups and their leaders were as follows:

X-Rays (X) - Alan Kiplinger
Radio and Microwaves (R) - Arnold Benz and Ken Tapping
Thermal Response (T) - Gordon Emslie
Plasma Physics (P) - John Brown

This publication is organized along the same lines with four sections for the contributions from the four groups and a fifth section for the paper resulting from Peter Sturrock's introductory talk.

This workshop and collection of papers could not have been accomplished without the support of Gloria Wharen, Kim Tolbert, Steve Graham, Shelby Kennard and Bernie Gibson. We also acknowledge the contribution of Vicki Greer at Birch and Davis and the staff of the Ramada Hotel, who helped to make the workshop run as smoothly as it did.

N87
21786
UNCLAS

N87-21786

RAPID FLUCTUATIONS IN SOLAR FLARES

Peter A. Sturrock

Center for Space Science and Astrophysics
Stanford University
Stanford, California

ABSTRACT

Study of rapid fluctuations in the emission of radiation from solar flares provides a promising approach for probing the magneto-plasma structure and plasma processes that are responsible for a flare. It is proposed that "elementary flare bursts" in X-ray and microwave emission may be attributed to fine structure of the coronal magnetic field, related to the aggregation of photospheric magnetic field into "magnetic knots." Fluctuations that occur on a sub-second time-scale may be due to magnetic islands that develop in current sheets during magnetic reconnection. The impulsive phase may sometimes--or possibly always--represent the superposition of a large number of the elementary energy-release processes responsible for elementary flare bursts. If so, one faces the challenge of trying to explain the properties of the impulsive phase in terms of the properties of the elementary processes. For instance, if the impulsive phase produces a power-law energy distribution of energetic particles, this may be due to scaling laws governing the elementary processes rather than to power-law acceleration in the each elementary event. Magnetic field configurations that might produce solar flares are divided into a number of categories, depending on: whether or not there is a filament; whether there is no current sheet, a closed current sheet, or an open current sheet; and whether the filament (if present) erupts into the corona, or is ejected completely from the sun's atmosphere. Analysis of the properties of these possible configurations is compared with different types of flare, and to Bai's subdivision of gamma-ray/proton events. The article ends with a number of theoretical questions related to the study of rapid fluctuations in solar flares.

I. Selected Observational Data.

This introduction will present a brief review of some of the forms of rapidly fluctuating output produced by solar flares, and a brief discussion of some of the relevant aspects of the flare problem.

One of the earliest studies of rapidly fluctuating X-rays was carried out by van Beek and his collaborators (van Beek et al. 1974). They found indications that the fairly brief hard X-ray flares that they investigated could all be decomposed into a number of smaller bursts with rise and decay times of the order of a few seconds. These spikes were called "elementary flare bursts." They estimated the energy involved in such a burst, on the basis of a thick-target model, assuming that the electron beam is impinging on the chromosphere, and found the energy to lie within the range 10^{27} to 10^{28} erg.

Although the early analysis was carried out by eye, de Jager and de Jonge (1978) later made a more systematic study involving a procedure similar to the CLEAN algorithm used in radio astronomy. They found that it was possible to represent a typical record as a sequence of standard pulses with a selected triangular profile. See Figure 1.

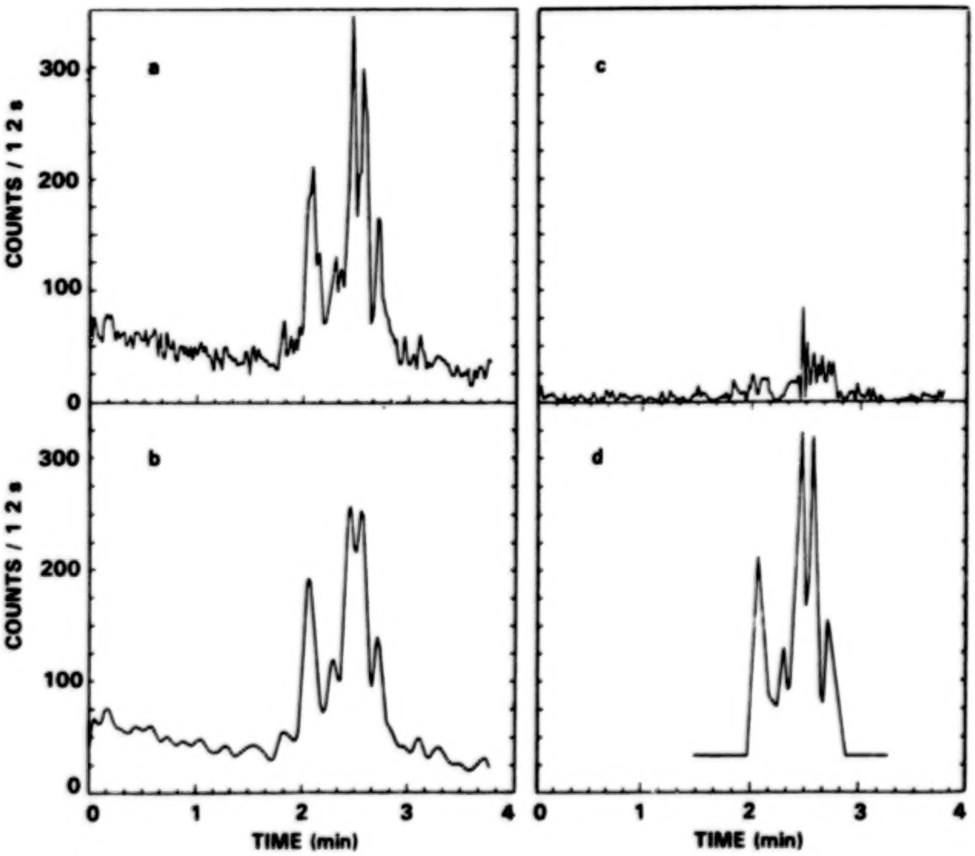

Fig. 1. *Filtering the noise, and decomposition into EFB's. (a) The X-ray flare of 1972, August 2, 18:39 UT as observed. (b) Filtered flare profile. (c) Residual noise after subtraction of the EFB's and continuous background. (d) Analytic flare profile, composed of the EFB's (de Jager and de Jonge 1978).*

Tremendous advances were made as a result of the Solar Maximum Mission. The HXRBS experiment provided data recorded in two modes, the normal mode having a time resolution of 128 ms, and a rapid mode having a resolution of about 10 ms. Only about 10 percent of flares were found to show fine structure. But, of that 10 percent, fine structure was detected on a time scale down to about 30 ms. An example of such a record, taken from Kiplinger et al. (1983), is shown in Figure 2.

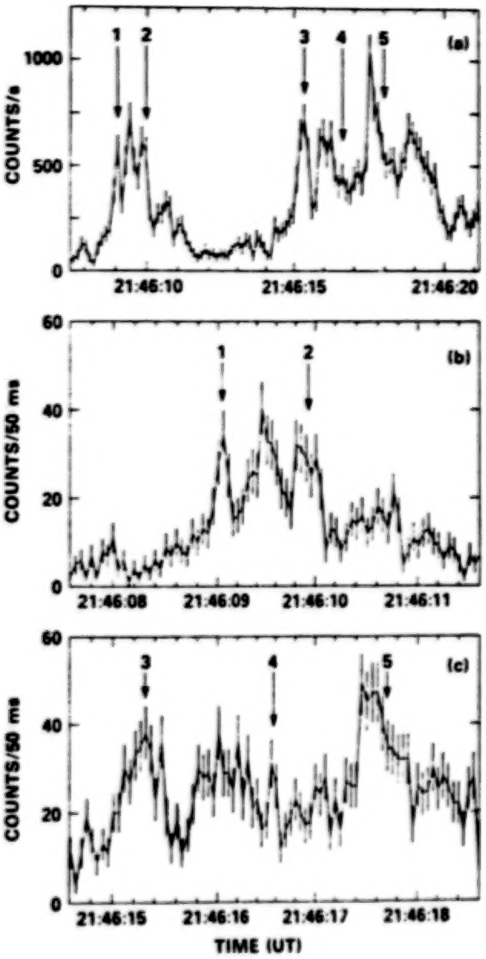

Fig. 2. *Hard X-ray time profiles (29-183 keV) of a solar flare which occurred on 1980 October 18. The curve in (a) shows PHS data at 128 ms per point, while curves in (b) and (c) show memory data at 50 ms per point. The numbered features indicate varying morphologies that are present within a single 9 s interval (Kiplinger et al. 1983).*

It is possible to make observations with an even finer time resolution in the radio part of the spectrum. Kaufmann and his collaborators have been carrying out such observations for several years with equipment at the Itapetinga Observatory, normally operating at 22 gHz and 44 gHz. Figure 3 is an example of a radio impulse (Kaufmann et al. 1984). The figure also includes data from Owen's Valley Radio Observatory that operates at 10.6 gHz. This burst is a few seconds in duration leading one to suspect that it is produced by basically the same process as produces the "elementary flare bursts" discovered by the Dutch solar X-ray astronomy team.

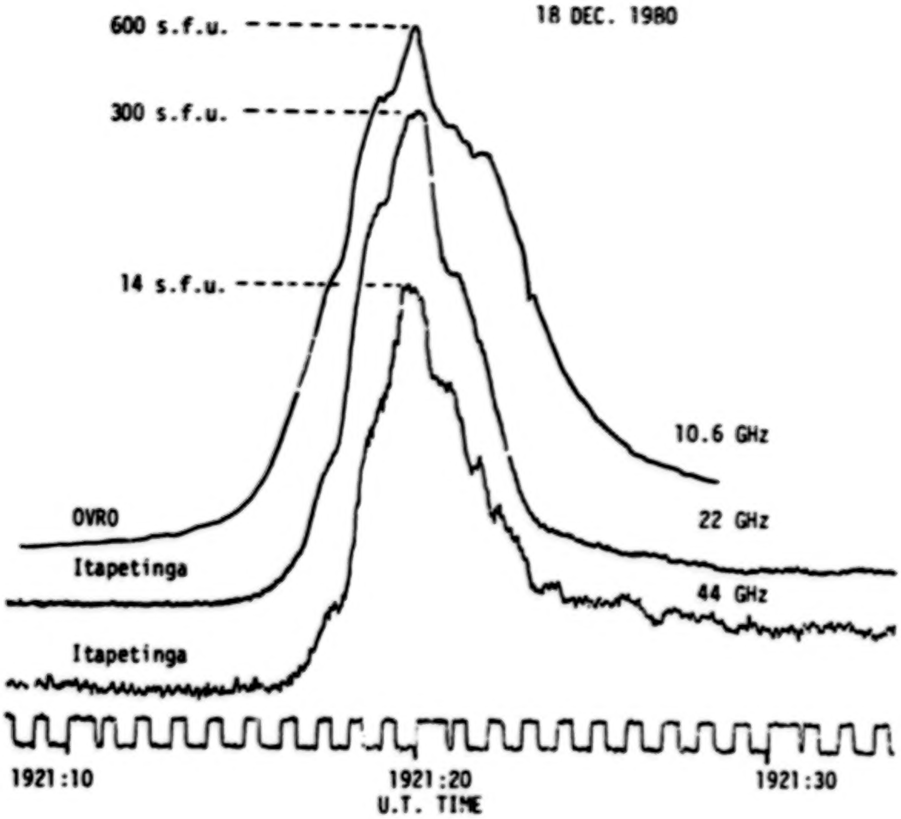

Fig. 3. The 18 December 1980, 19:21:20 UT spike-like burst, as observed at 44 GHz, 22 GHz, and 10.6 GHz. Slower time structures are evident, especially at 44 GHz (Kaufmann et al. 1984).

However, the radio observations offer much higher time resolution than the early X-ray observations. It is found that there is clearly good correspondence between the records obtained at 22 gHz and 44 gHz, so that the fluctuations are real and probably represent fluctuations of the process producing the high-energy electrons responsible for the radio emission.

Kaufmann et al. (1985) have more recently published data concerning a very interesting burst that is clearly evident at 90 gHz, but is barely detectable at lower frequencies. This is a very surprising event and a real challenge for theorists.

Another very exciting development has been Lin's balloon-borne experiment. This experiment is much more sensitive than the instruments on board SMM, and we see from Figure 4 (Lin 1984) that very low-level bursts are continually present on the sun. There are reasons to believe that these bursts are due to active regions that were present on the sun at that time.

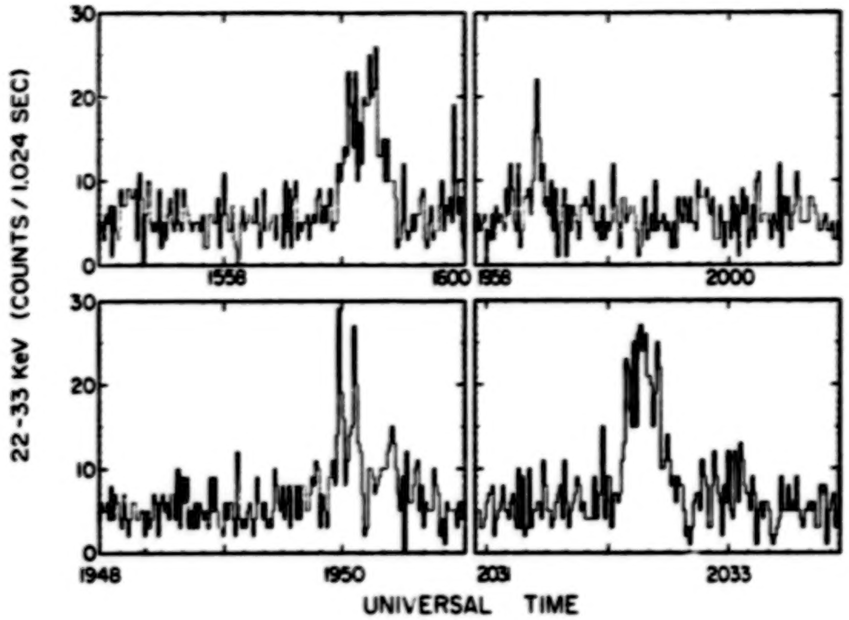

Fig. 4. ***The four largest hard X-ray microflares are shown here at 1.024 s resolution (Lin et al. 1984).***

We need to ask whether these low-level fluctuations are related to solar flares. Figure 5, taken from Lin et al. (1984),

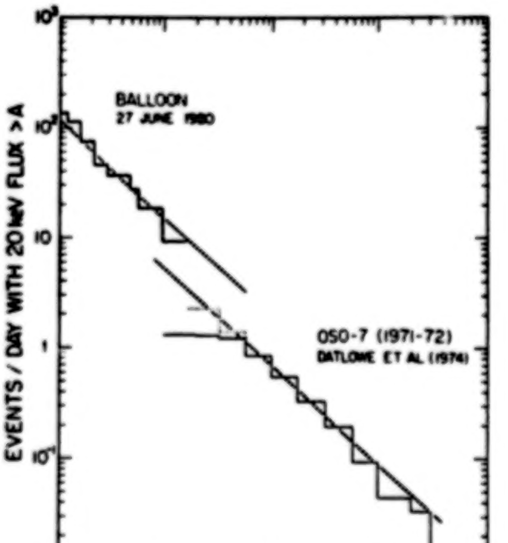

Fig. 5. ***The distribution of the integral rate of occurrence of events vs. peak 20 keV photon flux for the solar hard X-ray microflares observed in this balloon flight. Also shown for comparison is the distribution of solar flare hard X-ray bursts reported by Datlowe, Elcan, and Hudson (1974) (Lin et al. 1984).***

presents a histogram of the number of events per day as a function of photon flux, for photons of energy 20 keV or more. In the same diagram, Lin has reproduced comparable data derived by Datlowe et al. (1974) from analysis of OSO-7 data. We see that each experiment produces a well defined power-law histogram, and one can well imagine that if instrumental differences and/or variations in time were taken into account, the two histograms would be found to form one continuous curve. It certainly appears from this work that the same process is operative in both ranges of photon flux, suggesting that flares do not cut off at any particular level but continue down to a much lower level than we had previously thought. Lin has indeed introduced the term "microflares" to describe these low-level fluctuations.

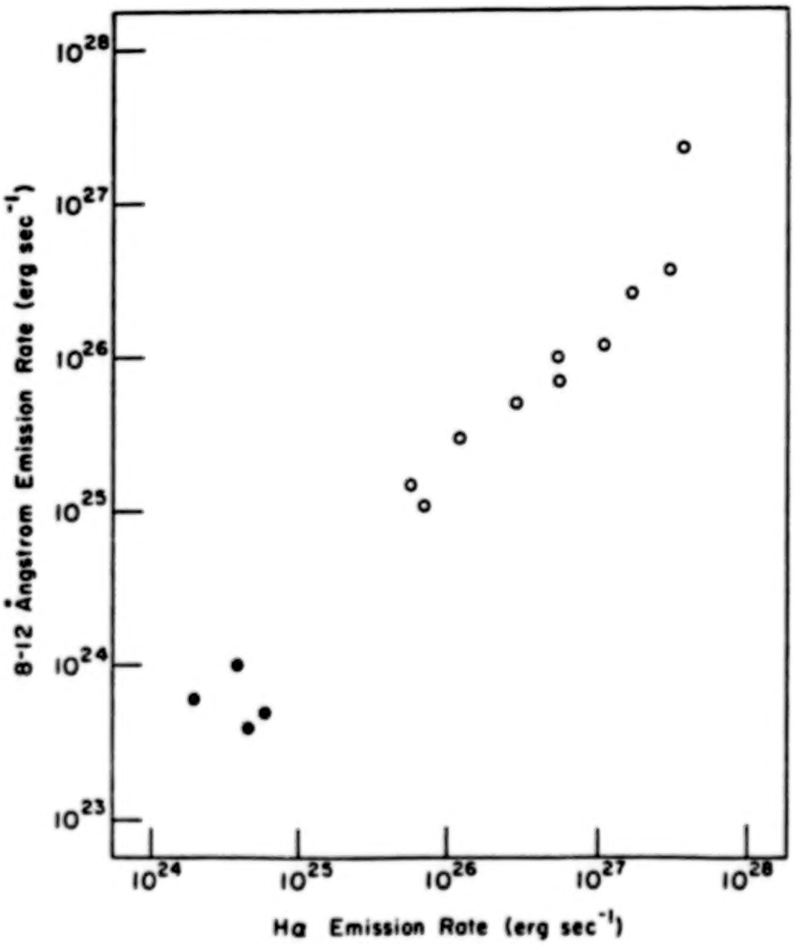

Fig. 6. *Relationship of mean peak emission rates in H-alpha and in soft X-rays for flares (open circle) and for spike events (filled circles). Flare data have been taken from Thomas and Teske (1971) (Teske 1971).*

A very important question to be addressed is the relationship between X-ray bursts and radio bursts. Kaufmann and his collaborators (Takakura et al. 1983) have indeed analyzed a few bursts in terms of both X-ray and microwave data. For the events they analyzed, there appeared to be little correspondence on the one-second time scale, but some correspondence on a finer time scale. A significant study was carried out about 15 years ago by Teske (1971) using soft X-ray data obtained from the instrument on board OSO-3. Teske searched for a correlation between soft X-ray fluctuations and Type III bursts and found that about ten percent of the X-ray bursts were in fact correlated with Type III bursts. Teske was concerned also to search for corresponding H-alpha events. He selected periods when active regions were on the limb of the sun, and then examined the X-ray data for small isolated bursts. He found that there was a very high correlation between H-alpha events on the limb and X-ray bursts. The H-alpha events could be classified into several types, but the one which showed the strongest correlation with small X-ray bursts of a few seconds duration were small surge-like or spike-like ejections (large spicules or small surges) reaching heights of between 10,000 and 40,000 km. Teske compared the ratio of mean peak emission rates in H-alpha and in soft X-rays for these spike events and for flares (Figure 6) and found that the ratio for spike events was indistinguishable from the ratio for flares. This again suggests that the flare process continues to a lower energy level than that for which events are usually recognized as "flares."

It is unfortunate that the time resolution of the H-alpha data was only about 15 or 20 seconds (as is typical of flare patrols). There is a need for this work to be repeated using H-alpha observations that have as high a time resolution as the radio and X-ray data. Teske's analysis indicates that the X-ray event tends to occur shortly before the Type III event. This is a curious result, and it would be interesting to see if further investigations confirm it and also to determine the relative timing of the X-ray and radio events with respect to the optical event.

II. Selected Theoretical Concepts.

In order to see how the flare problem has progressed, it is interesting to look back at flare theories that were advanced more than 20 years ago. At that time, a theorists considered that he had only two facts to explain. One is that a large flare involves an energy release of order 10^{32} ergs, and the other is that the time scale for energy release is (or was at that time thought to be) about two minutes. Although the first fact needs little modification, the second fact requires a great deal of elaboration in both directions. We now believe there is energy release on a much longer time scale than two minutes, and--as is the focus of this workshop--we also believe that there is energy release on a very much shorter time scale.

Early models were already based on the idea that the stored energy is magnetic and that a flare releases the free energy associated with the coronal current system. In order to achieve sufficiently rapid energy release, theorists were soon lead to the concept of current sheets. The first explicit current-sheet model (Figure 7) was that of Peter Sweet (1958) who considered that approaching sunspots would develop a current sheet that would persist for some time, then suddenly disappear as the result of magnetic reconnection.

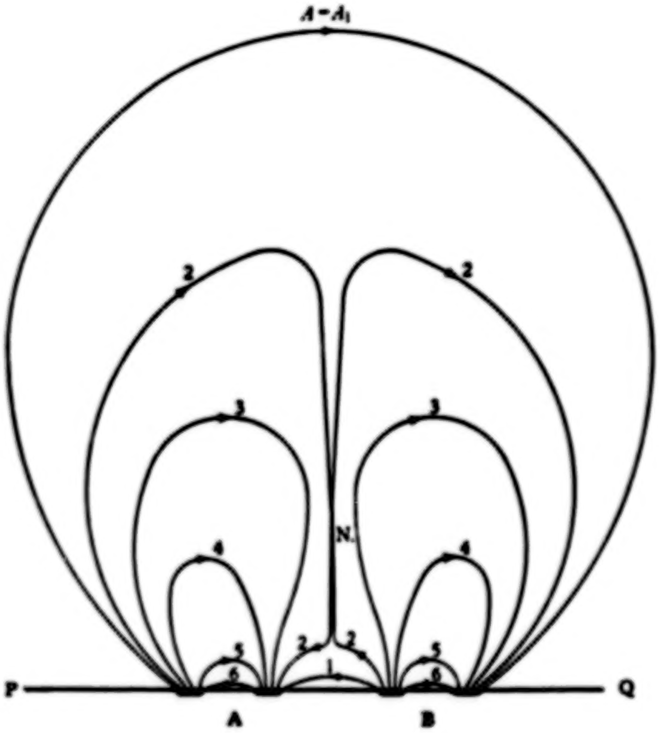

Fig. 7. *Sweet model. Movement towards each other of magnetic dipoles A and B produces a current sheet with "neuteral line" N in an atmosphere assumed to be perfectly conducting (Sweet 1958).*

In one form or another, this idea still persists. One of the flare models that is still very much alive and well is the flux-emergence model of Heyvaerts et al. (1977) and others (Figure 8), in which it is imagined that a new flux region emerges into an old pre-existing flux region, and that the interface comprises a current sheet. In an early stage, there may be only a "soft" instability that is considered to be responsible for "preheating." At a later stage, if the sheet becomes sufficiently thin, there may be a "hard" instability that produces an impulsive energy release, considered to be responsible for the impulsive phase of a flare.

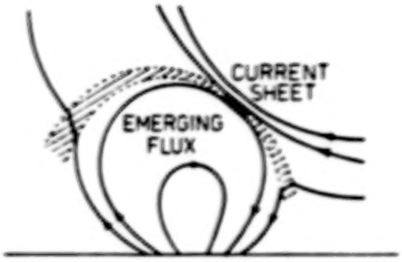
CURRENT SHEET
EMERGING FLUX

(a) Preflare Heating

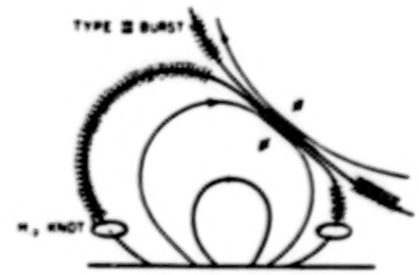
TYPE III BURST
H$_\alpha$ KNOT

(b) Impulsive Phase

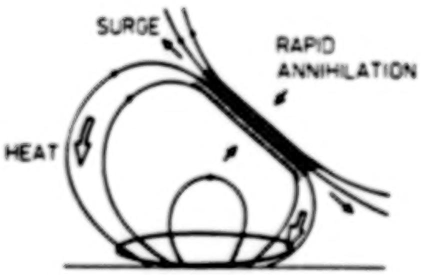
SURGE
RAPID ANNIHILATION
HEAT

(c) Main Phase

Fig. 8. *Emerging-flux model. (a) During the "preflare phase" ("onset phase"), the emerging flux begins to reconnect with the overlying field. (b) During the impulsive phase, the onset of turbulence in the current sheet causes a rapid expansion with rapid energy release. (c) During the "main phase" ("late phase"), the current sheet reaches a new steady state, with reconnection based on a marginally turbulent resistivity (Heyvaerts et al. 1977).*

The instability that leads to magnetic reconnection is named the "tearing-mode instability." The linear theory was first developed by Furth, Killeen and Rosenbluth (1963), but numerical studies by Carreras et al. (1980) and others have shown that nonlinear effects have the important effect of speeding up the reconnection rate.

Within the solar physics community, Dan Spicer was the first to draw attention to the importance of mode interaction in speeding up the energy-release process. One mode tends to interact with another and develop small-scale structure including current sheets and "magnetic islands" (Kahler et al. 1980) (Figures 9, 10). It seems to me that if we are to understand energy release on a time scale of milliseconds, we need to understand more fully the development and implications of this small-scale island structure.

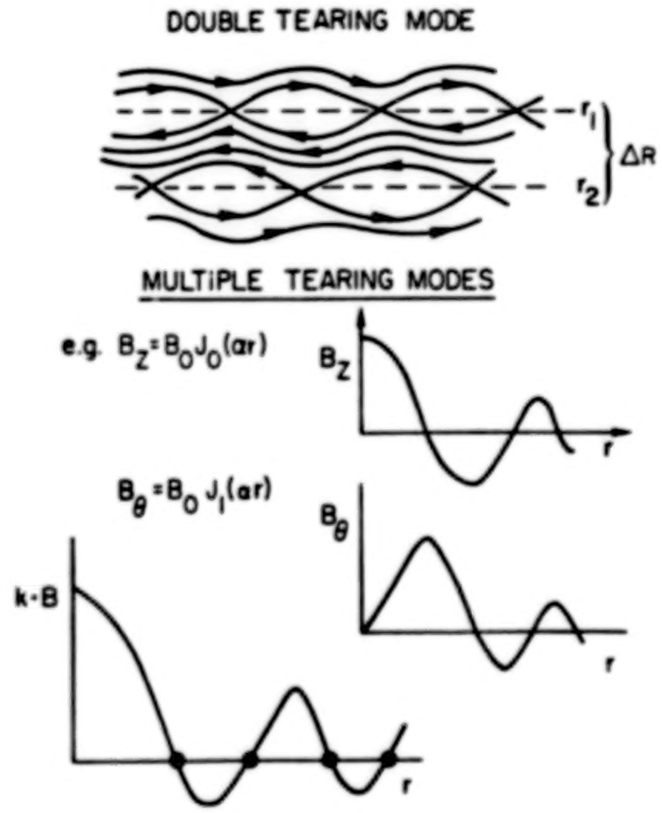

Fig. 9. *Top: The simplest example of multiple tearing modes, the double tearing mode, in which* $k.B_o = 0$ *occurs at two different radii from the center of the loop. Bottom: The Lunquisst field in which multiple tearing modes can occur (Kahler et al. 1980).*

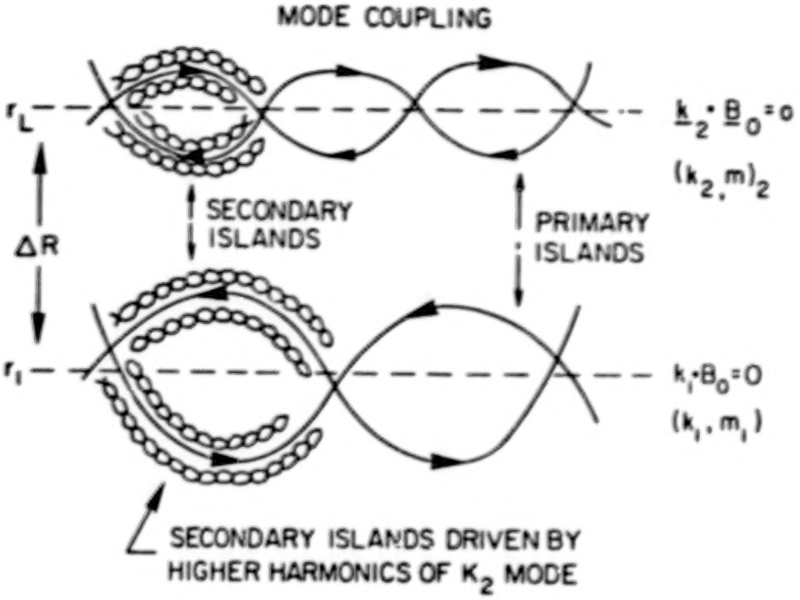
MODE COUPLING
r_L
$\underline{k}_2 \cdot \underline{B}_0 = 0$
$(k_2, m)_2$
SECONDARY ISLANDS
PRIMARY ISLANDS
ΔR
r_1
$k_1 \cdot B_0 = 0$
(k_1, m_1)
SECONDARY ISLANDS DRIVEN BY HIGHER HARMONICS OF K_2 MODE

Fig. 10. *The phenomenon of mode coupling. Primary islands are generated when* k.B_o=0 *for different wave number vectors* k. *The coupling between these primary islands results in the generation of secondary islands of shorter wavelength* k^{-1} (Kahler et al. 1980).

Recent computer modeling, such as that of Carreras et al. (1980), is providing more information on this topic. Since their work is directed at Tokomaks, they use a toroidal geometry. Figure 11 shows the growth in time of the radial size of various

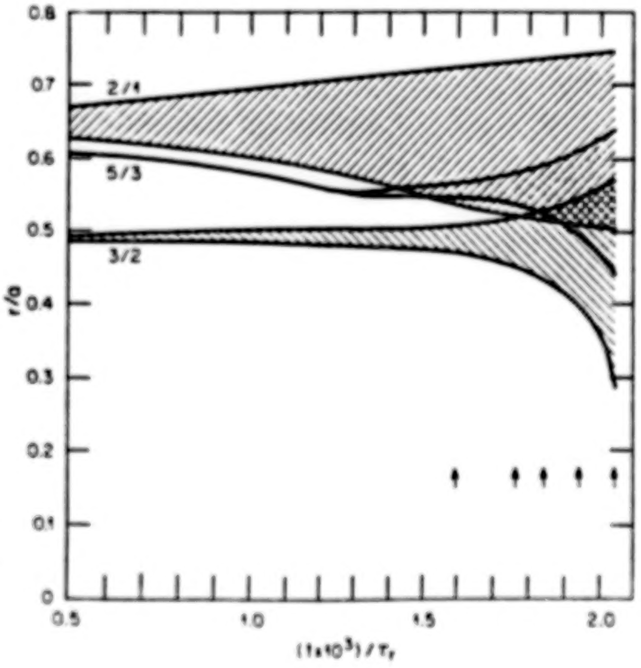

Fig. 11. *Time evolution of the magnetic island width for the* (*m*=2; *n*=1), (*m*=3; *n*=2), *and* (*m*=5; *n*=3) *modes in a multiple-helicity calculation (Carreras et al. 1980).*

modes. Different modes develop at different locations in the minor radius. Initially they are well separated and develop according to single-mode theory. However, at a certain time they may be sufficiently large that the modes begin to overlap. At this stage, the behavior is changed drastically. For instance, Figure 12 shows a plot of the growth rate of two modes (the 2-1 mode and the 3-2 mode), and we see that when the modes begin to interact, the growth rate increases rapidly. The growth rate can increase by at least an order of magnitude.

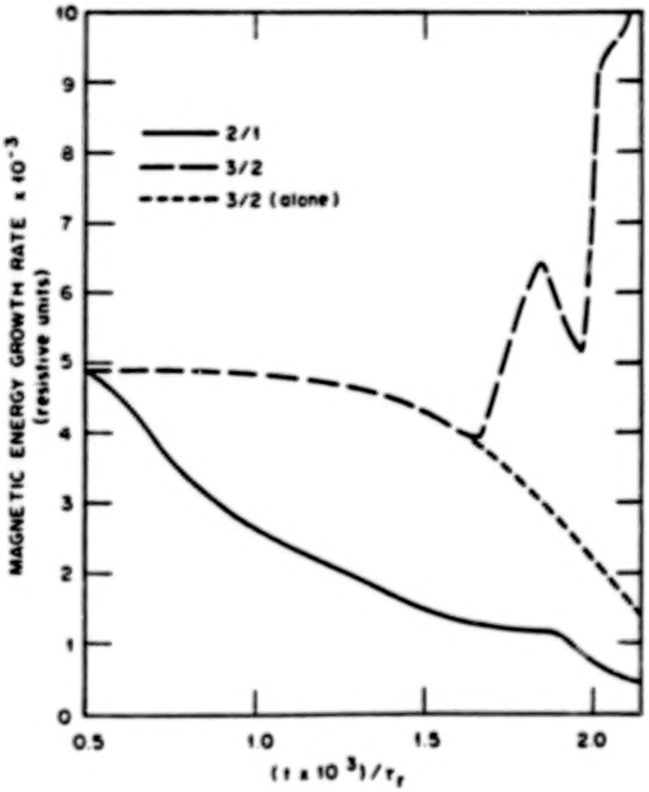

Fig. 12. *Nonlinear magnetic energy growth rate of the (m=2; n=1) mode (continuous line) and (m=3; n=2) mode (broken line). The (m=3; n=2) growth rate is compared with its value in the single 3/2 helicity evolution (Carreras et al. 1980).*

If more modes are included (Figure 13), mode interaction gives rise to an even more rapid increase in the growth rate. Another important aspect of these results is the following: In the early stage, the growth is fairly smooth and follows closely the linear FKR theory. However, when the modes begin to interact, leading to an increase in the growth rate, the current pattern becomes stochastic. The electric field also will become stochastic, and I think that an important topic to investigate is the process of particle acceleration in the stochastic electromagnetic fields that will develop in a reconnecting region when mode interaction takes place.

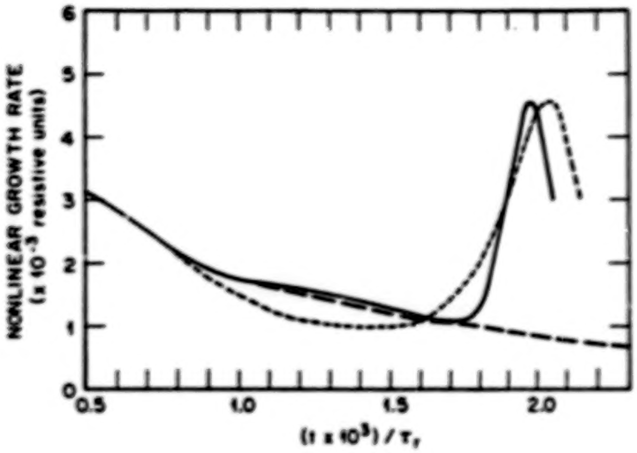

Fig. 13. *Nonlinear growth rate of the (m=3; n=2) mode for a calculation in which 5 modes were included (----) compared with the same case with 29 modes included (______). It is also compared with the case in which only the 3/2 helicity is included in the calculation (-- -- --) (Carreras et al. 1980).*

Spicer also pointed out some time ago that reconnection may not be spontaneous, but may instead be "driven." This certainly occurs in laboratory experiments such as that of Baum and Bratenahl (1985). The more recent experiments of Stenzel and his collaborators (Stenzel and Gekelman 1985) show similar effects. Large currents are suddenly driven through two plane conductors in such a way as to develop a field reversal region between them. The development of the magnetic field depends very much on the aspect ratio. If the width of the current sheet is no more than the separation between the conductors, an X-type point develops. However, if the width of the current-carrying conductors is larger than the separation, then there develops a series of magnetic islands (O-type points) separated by X-type points. The number of islands is approximately the same as the ratio of the width to the separation.

Leboeuf et al. (1982) have set up a numerical code to study the Stenzel-type experiment, and confirm that when the width to the separation is larger than unity, a sequence of X-points and O-points develops. However, these do not survive in the form in which they are created. Their numerical studies show that there is a strong tendency for adjacent magnetic islands to coalesce, as shown in Figure 14.

Leboeuf et al. find that the current densities, and therefore the electric fields, are very much stronger in the coalescence phase than they are during the tearing phase. Tajima et al. (1985) argue that this process is significant for solar flares. It is certainly conceivable that,if the process occurs, it might be responsible for the fine structure in X-ray emission.

ORIGINAL PAGE IS
OF POOR QUALITY

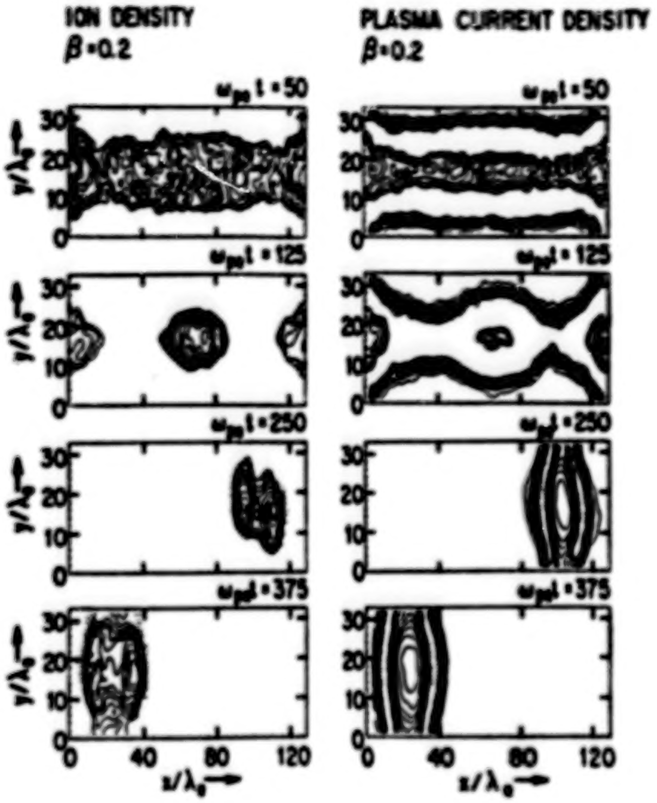

Fig. 14. 127x32 island coalescence run. The ion density is displayed on the left at, from top to bottom, $\omega_{pe}t=50$, 125, 250, and 375. The dotted contours represent levels below the average density at a particular time, full contours levels above. The plasma current density in the z direction is shown on the right at equivalent times. Dotted coutours indicate regions of highest return current (Leboeuf et al. 1982).

It must be emphasized, however, that one must be cautious in carrying over results from laboratory experiments to solar situations, since the parameters differ enormously. One must similarly be careful in carrying over the results obtained from numerical experiments. For instance, Leboeuf et al. (1982) adopt a "particle in a box" model, and there are on the average only four particles per box, which is not very many, and the ion-to-electron mass ratio is taken to be 10 rather than 2,000. Furthermore, laboratory and numerical experiments typically have magnetic Reynolds numbers very much smaller than those that are relevant to solar situations. Since the coalescence instability depends upon the magnetic attraction of two current filaments, it clearly depends sensitively on whether or not the field can adopt a vacuum configuration on a small scale, hence on the plasma density.

The fine structure of the X-ray flux or radio flux from some solar flares gives the impression that the elementary process is a very rapid process producing a spike of short time scale and that the overall development of the impulsive phase is the occurrence of a very large number of such elementary bursts. If this is so, we need to think carefully about the interpretation of the total flux from the impulsive phase of a flare. In many cases, the flux will indicate that the electron energy spectrum has the form of a power law. We then face the question: Does the power law represent the spectrum produced by an elementary energy-release process, or is it the result of the convolution of many elementary processes, each one of which produces a spectrum differing from a power law?

In this context, it is worth considering once more the radio burst detected by Kaufmann et al. (1985), that was clearly detectable at 90 gHz but barely detectable at 30 gHz. This is suggestive of a peaked electron-energy spectrum. Even for a more typical microwave burst, it is difficult to understand the energetics if each burst of electrons has the form of a power law extending down to a few keV (Sturrock et al. 1984). Hence we should consider the possibility that the elementary energy-release process produces something other than a power-law spectrum.

Let us consider, for example, that the elementary process produces a spectrum of the following form:

$$\frac{dJ}{dE} = L^{\lambda} f(L^{\varepsilon} E) \ . \qquad 1$$

In this equation L is the length scale, and we suppose that the intensity and the characteristic energy each depend in a power-law fashion on L.

Now suppose, as an example, that the length scale increases linearly with time,

$$L = Vt \qquad 2$$

and let us consider the integral flux, integrating over time. This is seen to be

$$J_T(E) = \frac{1}{V}\int dL \ L^{\lambda} f(L^{\varepsilon} E) \ . \qquad 3$$

If we now write

$$x = L^{\varepsilon} E \ , \qquad 4$$

we see that the total energy spectrum is expressible as

$$J_T(E) = \frac{1}{V}\left[\int dx \ x^{\frac{\lambda+1}{\varepsilon}-1} f(x)\right] E^{-\frac{\lambda+1}{\varepsilon}} \ . \qquad 5$$

Hence, in this example, we have obtained a power-law spectrum even though the elementary process need not have a power-law spectrum.

My purpose here is not to argue that this is an accurate representation of what occurs in a solar flare, but simply to point out that the spectrum of the entire impulsive phase may differ significantly from that of each elementary burst.

III. Phases of Solar Flares.

So far I have been referring to bursts that proceed either in isolation or as part of the impulsive phase of a flare. However, there are more phases of energy release than simply the impulsive phase, as is exemplified by Figure 15 that is taken from Kane (1969). This flare shows a sharp impulsive phase, but it also shows a steady growth of soft X-ray emission before the impulsive phase, and extended soft X-ray emission after the impulsive phase. Some time ago, it was tempting to consider that the extended soft X-ray emission simply represents the decay of energy released during the impulsive phase. However, Moore et al. (1980) and others have shown conclusively that during many flares such extended emission must be the result of extended energy release.

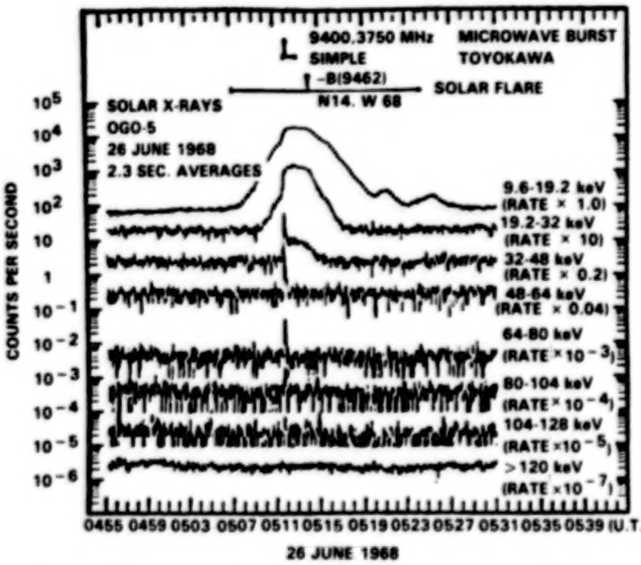

Fig. 15. *Example of an X-ray burst with the impulsive hard component occurring 4 min after the onset of the soft X-ray burst (Kane 1969).*

Similar conclusions can be drawn from study of the H-alpha maps of two-ribbon flares. As the two ribbons separate, the energy-release region excites different regions of the chromosphere, indicating that energy is being drawn from different regions of the corona. Hence it is clear that the separation phase of two-ribbon flares, that corresponds to the extended phase of soft X-ray emission, must be ascribed to continuous energy release, not simply to the decay of energy released during the impulsive phase.

Another significant development is the analysis by Bai (1986) of the properties of flares that produce gamma rays and particle events. Bai subdivides gamma-ray/proton events into two classes: those that are impulsive, with a spike duration of less than 90 seconds and total duration of less than 10 minutes, and those that are gradual, with spikes longer than 90 seconds and durations longer than 10 minutes. These two classes have certain properties in common, as we see in Table 1, but the two classes have more points on which they differ, as we see in Table 2.

Table 1.
COMMON PROPERTIES OF
IMPULSIVE AND GRADUAL GAMMA-RAY/PROTON FLARES
(These properties are in general not found from ordinary flares)

	CATEGORIES	IMPULSIVE FLARES	GRADUAL FLARES
1	H.X.R. SPECTRUM	HARD (average index 3.5)	HARD (average index 3.5)
2	H.X.R. SPECTRAL HARDENING	SOME (6 out of 13)	YES (22 out of 23)
3	ASSOCIATION WITH TYPE II OR IV	GOOD (9 out of 13)	GOOD (20 out of 23)

The first four points of Table 2 concern the temporal development, that are clearly a reflection of the definition of the two classes. However, the last seven items (excepting perhaps item 8) are not so obviously related to the selection process. The overall impression is that gradual flares involve something that is ejected from the sun, and that this ejection process facilitates the escape of high-energy particles. Item 7, the "microwave richness index," may give some clue as to the difference in conditions in the flare site in the two classes of flares. It seems that the gradual flares involve something that is ejected from the sun, and that during the ejection process it is possible for particles (electrons and protons) to escape from whatever kind of trap they were formed in.

These considerations of the various stages of a flare and the various types of flares suggest that it would be worthwhile to draw up a category of conditions in which flares can occur. Since we believe that the magnetic field is the main context in which a flare occurs, we face the following question: What are the possible categories of magnetic-field configurations that

Table 2.
DIFFERENCES BETWEEN
IMPULSIVE AND GRADUAL GAMMA-RAY/PROTON FLARES

	CATEGORIES	IMPULSIVE FLARES	IMPULSIVE FLARES
1	HIGH-ENERGY H.X.R.DELAY	SHORT (< 4 s)	LONG (> 8 s)
2	H.X.R. SPIKE DURATION	< 90 s (<30 s)	> 90 s
3	H.X.R. TOTAL DURATION	< 10 min	> 10 min
4	SOFT X-RAY DURATION	< 1 hr	> 1 hr
5	H-alpha AREA	SMALL	LARGE
6	LOOP HEIGHT	LOW (<10^9 cm)	HIGH (>10^9 cm)
7	MRI	< 1.0	> 1.0
8	AVG. TYPE II DUR.	14 min	25 min
9	$\frac{\text{I.P. PROTONS}}{\text{ON SITE PROTONS}}$	SMALL (<<1)	LARGE (>1)
10	INTERPLANETARY SHOCK	NO	YES
11	CORONAL MASS EJECTION	SOME	YES
12	[e/p] RATIO	LARGE	NORMAL
13	I.P PROTON FLUX DECAY	RAPID (2)	SLOW

could give rise to flares and might have some bearing on the different phases (and other aspects of the time structure) of those flares?

I think we should begin with the fact that magnetic flux at the photosphere is not spread uniformly over the photosphere. We know from the work of Harvey, Sheeley, Title, and others (see, for instance, Tarbell and Title 1977) that the magnetic flux at the photosphere tends to be aggregated into knots of less than one arc second in size, with field strengths of 1,000 to 1,500 gauss. This is bound to have an important influence on the magnetic-field structure in the corona, where we believe the main energy-release of a flare occurs. Rather than think of a distributed field pattern in the corona, this flux concentration at the photosphere leads one to consider that the field in the corona is really made up of individual flux loops, each loop ending in one of these knots, although there may be two or three elementary flux tubes arising from the same knot (Figure 16).

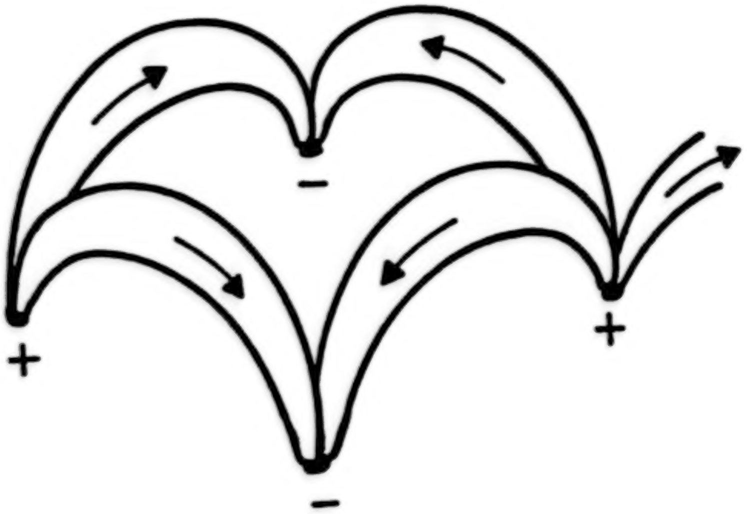

Fig 16. *Schematic representation of possible coronal magnetic field structure, determined by the aggregation of photospheric magnetic field into discrete knots (Sturrock et al. 1984).*

If one pursues this idea and inquires into the typical length of such an elementary flux tube in an active region, and how much energy can be stored in such a tube due to twisting of the foot points, we find that the time scale for energy release should be a few seconds and the energy released should be in the range 10^{27} to 10^{28} ergs (Sturrock et al. 1984). Hence energy release from such elementary flux tubes may well be the explanation of the elementary X-ray bursts identified by van Beek and his collaborators. The "microbursts" with time scales of 10 to 100 milliseconds, that are found in both X-ray and microwave data, may be attributed to energy release in "magnetic islands" that develop during reconnection in such flux tubes.

In what follows, I depart from the earlier idea that a flare is simply the manifestation of magnetic-field reconnection, and that the only requirement for a flare is a pre-existing current sheet. In a talk given 22 years ago at Goddard Space Flight Center during a symposium on the "Physics of Solar Flares" organized by Bill Hess, the great solar astronomer K.O. Kiepenheuer made the following remarks (Kiepenheuer 1963):

> "Those who have seen in an accelerated movie the brightening of a flare out of a dark filament, and the almost chaotic interaction of bright and dark structures, will not doubt the existence of a causal relation between the activation of a dark filament and the formation of a flare."

All large two-ribbon flares involve the disruption--maybe eruption--of a filament. It is not the case that the filament is disrupted because of the flare, but rather the other way round. Some time ago, Sara Martin and Harry Ramsey (Smith and Ramsey 1964) studied the behavior of filaments near the time of occurrence of flares and found that there are definite signs of disturbance in the filament long before the flare occurs. These "precursors" may occur many minutes or even hours before the flare. The fluctuations become larger and larger until the onset of the flare. This suggests either that an instability of the filament creates the conditions that lead to the flare, or that a flare is simply one manifestation of a complex instability that leads to the disruption of the filament.

In order to pursue this line of inquiry, it is essential to have a clear understanding of the nature and structure of filaments. Unfortunately this understanding does not exist at this time. I suggest that a filament comprises a rope-like structure involving many intertwined magnetic flux tubes, each tube linked to the photosphere at both ends. The foot-points are close to the magnetic neutral line, so that the rope tends to run along the neutral line (Figure 17). The interplay of the different flux tubes will lead to regions of field that are concave upwards; these are the regions that support the cool gas responsible for the visible H-alpha appearance of a filament.

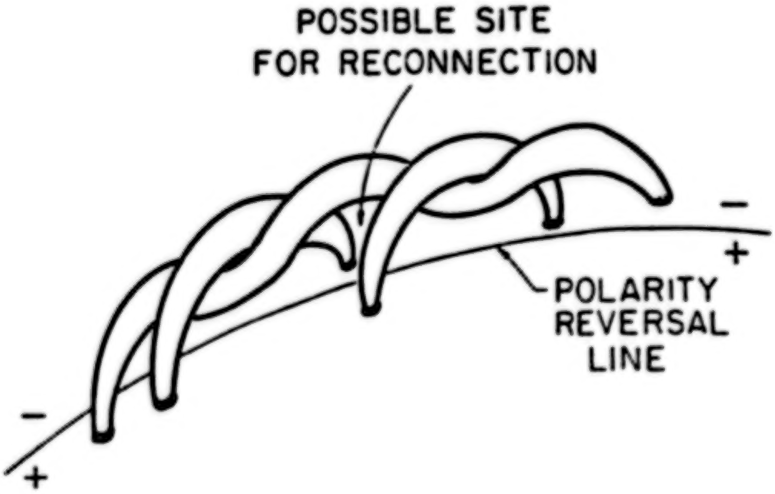

Fig. 17. *Schematic representation of possible magnetic field configuration of a filament (Sturrock et al. 1984).*

When viewed in the wings of H-alpha, a flare always begins with two bright points very close together on opposite sides of the neutral line. Moore et al. (1984) have found that the time of this initial brightening is also the time when the filament first begins to show rapid upward motion. Our interpretation (Sturrock et al. 1984) is that reconnection has begun to occur between the feet of two adjacent flux tubes, as indicated in Figure 17. This reconnection has two effects. One is that energy is released that gives rise to the two H-alpha brightenings. The other is that two strands tying the filament to the photosphere have been severed. This is rather like the severing of ropes that hold a buoyant balloon to the ground. When the strands are severed, the filament begins to rise. This change of configuration of the filament puts more strain on the remaining flux tubes connecting the filament to the photosphere. As a result, there may occur a runaway action in which similar reconnection occurs sequentially, running in both directions along the neutral line. The end effect of this process would be the formation of a large twisted flux tube rooted simply at its end points, as shown in Figure 18. The eruption of such a tube looks very much like movies of erupting prominences that are visible in H-alpha above the limb.

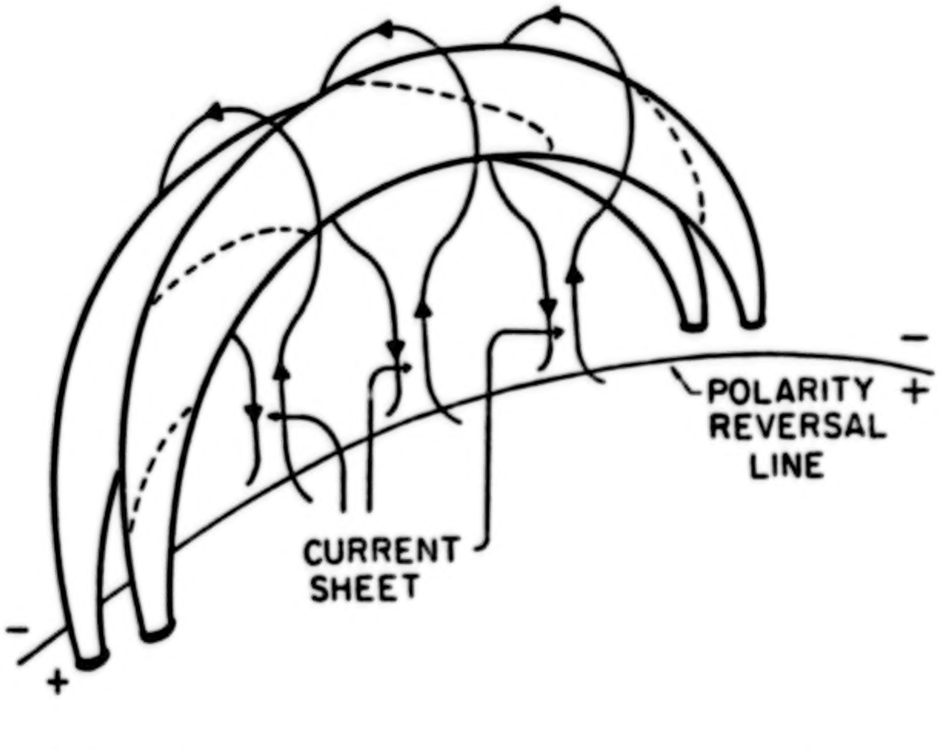

Fig. 18. Schematic representation of the development of an extended current sheet beneath an erupting filament (Sturrock et al. 1984).

The eruption of the filament may lead to the end result that the filament forms a large loop high in the corona.

Alternatively, if the stress due to twisting is sufficiently great, the filament may expand into interplanetary space by attempting to adopt an open-field configuration. Which of these two processes occurs depends partly on the initial stress in the filament and partly on the strength and topology of the surrounding magnetic field.

In either case, the eruption of the filament is going to disturb the overlying magnetic field, and the disturbance is such that it will produce a current sheet below the filament. This situation is rather like the the Stenzel experiment in which a current sheet is suddenly formed. In this situation, reconnection of the sheet is more in the nature of "driven reconnection" rather than spontaneous reconnection.

The end result of reconnection of the newly formed current sheet is that a region of magnetic field near the filament is returned to its current-free state. In addition (Sturrock 1986), a toroidal magnetic trap forms that embraces the filament (Figure 19).

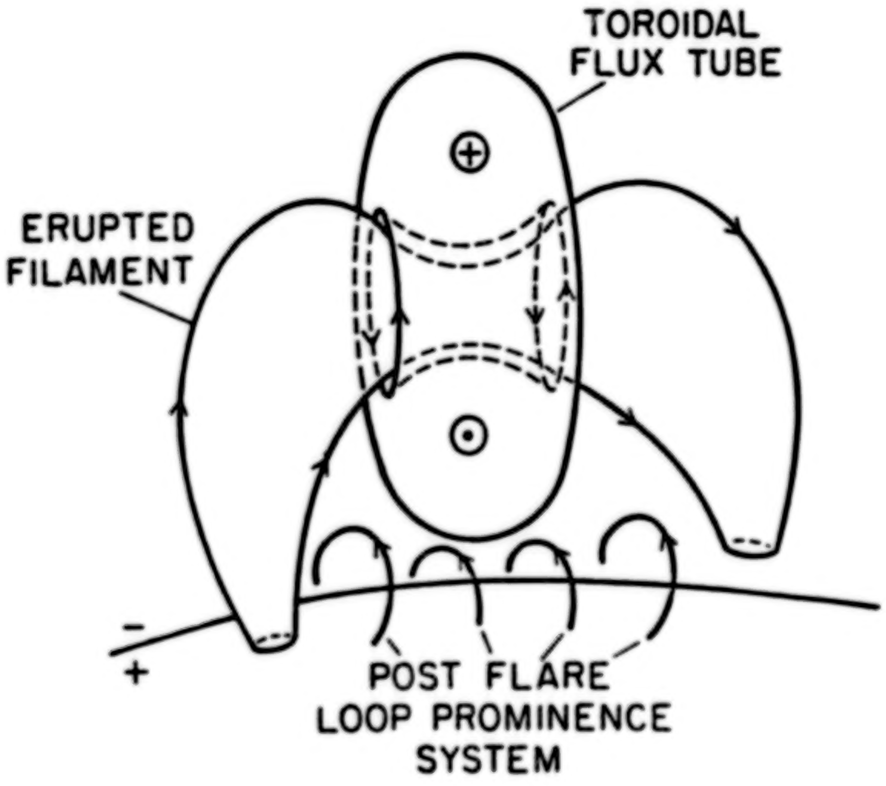

Fig. 19. *Schematic representation of a toroidal magnetic flux tube encircling an erupted prominence, as a result of the reconnection indicated in Fig.18. The toroid would be detectable as a stationary type IV radio burst (Sturrock 1986).*

The reconnection is likely to produce high-energy electrons, so that the magnetic trap when formed would already contain a population of energetic electrons; this may be the explanation of Type IV radio bursts. If the filament simply rises up into the corona, we would observe a *stationary* Type IV burst. However, if the stresses are such that the filament expands out into interplanetary space, we would observe *moving* Type IV burst. This ejection may also be the explanation of coronal transients. If the ejection is sufficiently rapid, it should produce a bow shock which could in turn produce a Type II radio burst (Figure 20).

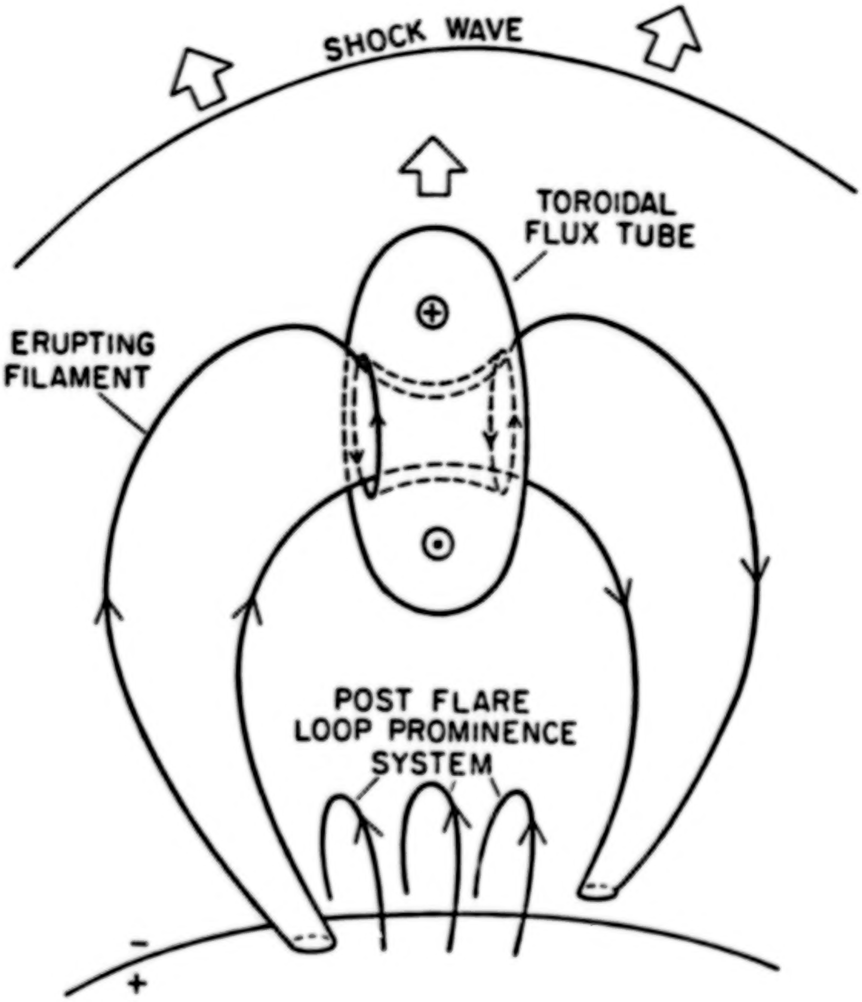

Fig. 20. *Schematic representation of situation that arises when a filament, encircled by a toroidal flux tube, is completely ejected from the sun. The toroid would be detectable as a moving type IV radio burst. The shock wave would give rise to a type II radio burst (Sturrock 1986).*

Table 3 shows another way of categorizing magnetic structures, and the properties of the resulting flares. In this table, we focus on only four properties. Does the flare produce a mass ejection? Does it produce a shock wave? Does it produce gamma-ray emission? Does it produce a particle event?

TABLE 3.
CATEGORIES OF MAGNETIC STRUCTURES AND PROPERTIES OF RESULTING FLARES

	AN	AC	AO	PCR	POR	PCJ	POJ
Mass Ejection	X	X	X	X	X	✓	✓
Shock Wave	X	X	X	✓	✓	✓	✓
Gamma-Ray Emission	X	✓	✓	✓	✓	✓	✓
Particle Event	X	X	✓	X	✓	✓	✓

A: filament absent
P: filament present
N: no current sheet
C: closed current sheet
O: open, or partially open, current sheet
R: filament eruption, but no ejection
J: filament ejection

Concerning the environment in which the flare occurs, we first notice that there may be no filament in the system, that we denote by "A" (the filament is absent). It may be that there is simply a small flux tube that becomes stressed and then reconnects releasing energy. I do not know whether this ever occurs, but Hal Zirin has expressed the opinion that any flare - no matter how small - always involves the disappearance of some dark feature, implying that any flare always involves something like a filament disruption. This viewpoint would appear to be consistent with the work of Teske referred to earlier.

Assuming that there is a configuration that does not involve a filament, we next ask whether there is a current sheet. If there is no current sheet (AN), there is no reason to expect mass ejection or a shock wave. I suggest that intense electric fields, causing strong electron acceleration, occur only in reconnection in a current sheet, not in reconnection in an extended tube. If this is the case, there should be no gamma-ray emission and no particle event if there is no current sheet.

If there is a current sheet, but the sheet is completely closed (AC), the high-energy electrons could give rise to gamma-ray emission, but there should be no particle event. On the other hand, if the current sheet is open or partly open (AO), some of the particles can escape so that there may also be a particle event.

Next we suppose that a filament is present (P), but we distinguish between eruption (R) and ejection (J). In either case, the existence of a filament necessarily requires the existence of a current sheet at the interface between the filament and the ambient magnetic field. This initial current sheet may be either closed or partly open. If the filament erupts (but is not ejected), and if the initial current sheet is closed (case PCR), there should be no mass ejection, there may be a mild shock wave (a blast wave), and there may be gamma-ray emission, but there should be no particle event. On the other hand, if the filament erupts and if the initial current sheet is partly open (case POR), some of the high-energy particles may escape and produce a particle event. Events of these two types may be responsible for the impulsive gamma-ray/proton flares in Bai's classification (Table 2).

We now consider the final possibility that a large filament is ejected from the sun into interplanetary space. This produces a mass ejection, and - if the speed is high enough - it may produce a bow shock. Such a shock would tend to maintain its strength as it propagates, whereas the strength of a blast wave tends to decrease rapidly as it propagates. In this case, the expansion of the magnetic-field system will weaken the magnetic trap, so that particles can escape into interplanetary space. If the filament is ejected from the sun, we get the same end result whether the initial current sheet was closed or open, so that cases PCJ and POJ have the same properties:- There is mass ejection, a strong shock wave, gamma-ray emission, and a particle event. However, the ejection of a filament takes longer than does its partial eruption into the corona. For this reason, it seems likely that this category of flares is responsible for the gradual flares of the gamma-ray/proton flares studied by Bai (Table 2).

IV. Looking Ahead.

Since this is the beginning of the Workshop, it is a good time to consider what one would like to see come out of it. We would surely like to get additional insight into a number of questions that face us in trying understand solar flares. I now list a few of these questions.

1. What is the pre-flare magneto-plasma configuration? I do not think it is enough to ask only about the pre-flare magnetic-field configuration. A filament or a similar structure is usually involved, and the stress of plasma contained in the filament may be significant.

2. Is the instability responsible for a flare macroscopic, microscopic, or a symbiotic combination of the two? There are good reasons to be suspicious of the earlier idea that a flare simply represents reconnection of a current sheet. As I have

indicated, it is quite possible that the basic instability involves an MHD effect that gives rise to an erupting filament. Hence we can ask whether the instability is macroscopic like an MHD eruption, whether it is microscopic like a simple tearing mode, or whether it is a combination of the two.

3. **What fine structure develops as a result of the macroscopic flow?** It is clearly possible that the macroscopic flow leads to the development of a shock wave, but it may be that the macroscopic flow is unstable and leads to some form of turbulence.

4. **What fine structure develops as a result of the microscopic flow?** As I have indicated, numerical simulations of the reconnection process indicate that very fine structure may develop. It is clearly important to pursue this line of inquiry if we are to understand the development of fine structure on the sub-second time scale.

5. **Do shocks usually occur? If so, what is their role in particle acceleration?** Any sudden change of magnetic configuration is surely likely to develop a shock wave, either as a propagating blast wave or as a convecting bow shock. Since shocks are known to be promising locations for particle acceleration, it is clearly important to have a better understanding of how and where shocks are generated during flares.

6. **Is flare energy release always composed of elementary bursts?** For some flares, the X-ray time curves show a great deal of fine structure strongly suggesting that the energy release process comprises as many elementary events. When such structure is not evident, is it because of a real difference in the energy release process, or is it simply a reflection of our imperfect observational capabilities?

7. **Is the energy release process sometimes periodic?** There has been a debate for many years as to whether apparent periodicity of X-ray emission or microwave emission is really significant. Some years ago, Lipa and Petrosian (1975) looked into this question but were unable to find a case for real periodicity. On the other hand, Roger Thomas many years ago obtained a "light curve" of X-ray emission that seemed to present a very strong case for periodicity. If periodicity does sometimes occur, it is a real challenge to the theorist to come up with an explanation that is even plausible.

8. **What is the relationship between the energy spectrum of the integrated flare emission and the energy spectrum of the elementary bursts?** This is the question that was raised earlier in this review. The first requirement is to have more detailed information of the energy spectrum of an elementary burst. If this resembles the energy spectrum of the entire impulsive phase, there is no further work to be done. If, however, the spectrum of an elementary burst usually differs significantly from that of an entire impulsive phase, we must seek to understand the

relationship between the two, perhaps along the lines suggested in Section II.

This work was supported in part by the Office of Naval Research Contract N00014-85-K-0111 and by NASA Grants NAGW-92 and NGL-05-020-272.

REFERENCES

Bai, T. 1986, *Ap.J.* (in press).

Bratenahl, A., and Baum, P.J. 1985, in M.R. Kundu and G.D. Holman (eds.), *Unstable Current Systems and Plasma Instabilities in Astrophysics*, (Dordrecht:Reidel), p. 147.

Carreras, B.A., Hicks, H.R., Homes, J.A., and Waddell, B.V. 1980, *Phys. Fluids*, 23, 1811.

Datlowe, D.W., Elcan, M.J., and Hudson, H.S. 1974, *Solar Phys.*, 39, 155.

de Jager, C., and de Jonge, G. 1978, *Solar Phys.*, 58, 127.

Dennis, B.R. 1985, *Nature*, 313, 380.

Furth, H.P., Killeen J., and Rosenbluth, M.N. 1963, *Phys. Fluids*, 6, 459.

Kahler, S., Spicer, D., Uchida, Y., and Zirin, H. 1980, in P.A. Sturrock (ed.), *Solar Flares*, (Boulder:Colorado U. Press), p. 83.

Kane, S.R. 1969, *Ap.J. (Letters)*, 157, L139.

Kaufmann, P., Correia, E., and Costa, J.E.R. 1984, *Solar Phys.*, 91, 359.

Kaufmann, P., Correia, E., Costa, J.E.R., Zodi Vaz, A.M., and Dennis, B.R. 1985, *Nature*, 313, 380.

Kiepenheuer, K.O. 1963, in W.N. Hess (ed.), *Proc. AAS- NASA Symposium on the Physics of Solar Flares*, NASA SP-50 (Washington, DC), p. 323.

Kiplinger, A.L., Dennis, B.R., Emslie, A.G., Frost, K.J., and Orwig, L.E. 1983, *Ap.J. (Letters)*, 265, L99.

Leboeuf, J.N., Tajima, T., and Dawson, J.M. 1982, *Phys.Fluids*, 25, 784.

Lin, R.P., Schwartz, R.A., and Kane, S.R. 1984, *Ap.J.*, 283, 421.

Lipa, B., and Petrosian, V. 1975, *Bull. American Astron. Soc.*, 7, 423.

Moore, R.L., et al. 1980, in P.A. Sturrock (ed.), *Solar Flares*, (Boulder:Colorado U. Press), p. 341.

Moore, R.L., Horvitz, J.L., and Green, J.L. 1984, *Planet.Space Sci.*, 32, 1439.

Orwig, L.E. 1983, *Ap.J. (Letters)*, 265, L99.

Smith, S.F., and Ramsey, H.E. 1964, *Z. Astrophys.*, 60, 1.

Stenzel, R.L., and Gekelman, W. 1985, in M.R. Kundu and G.D. Holman (eds.), *Unstable Current Systems and Plasma Instabilities in Astrophysics*, (Dordrecht:Reidel), p. 47.

Sturrock, P.A. 1986, in P. Simon (ed.), *Proc. Solar Terrestrial Prediction Workshop*, (France:Meudon Obs.), (in press).

Sturrock, P.A., Kaufmann, P., Moore, R.L., and Smith, D.F. 1984, *Solar Phys.*, 94, 341.
Sweet, P.A. 1958, *Nuovo Cimento Suppl. 8* (Ser. 10), 188.
Tajima, T., Brunel, F., Sakai, J.-I., Vlahos, L., and Kundu, M.R. 1985, in M.R. Kundu and G.D. Holman (eds.), *Unstable Current Systems and Plasma Instabilities*, (Dordrecht:Reidel), p.197.
Takakura, T., Kaufmann, P., Costa, J.E.R., Degaonkar, S.S., Ohki, K., and Nitta, N. 1983, *Nature*, 302, 317.
Tarbell, T.D., and Title, A.M. 1977, *Solar Phys.*, 52, 13.
Teske, R.G. 1971, *Solar Phys.*, 21, 146.
Thomas, R.J., and Teske, R.G. 1971, *Solar Phys.*, 16, 431.
van Beek, H.F., de Feiter, L.D., and de Jager, C. 1974, *Space Res.*, 14, 447.

N87
21787
UNCLAS

N87-21787

SUB-SECOND VARIATIONS OF HIGH-ENERGY (> 300 keV) HARD X-RAY EMISSION FROM SOLAR FLARES

Taeil Bai
Stanford University

INTRODUCTION

Sub-second variations of hard X-ray emission from solar flares was first observed with a balloon borne detector (Hurley and Duprat 1977). With the launch of SMM, it is now well known that sub-second variations of hard X-ray emission occur quite frequently (Kiplinger et al. 1983, 1984). Such rapid variations give constraints on the modeling of electron energization.

Such rapid variations reported until now, however, have been observed at relatively low energies. Fast mode data obtained by HXRBS has time resolution of ~ 1 ms but has no energy resolution (Orwig et al. 1980). Therefore, rapid fluctuations observed in the fast-mode HXRBS data are dominated by the low-energy (~ 30 keV) hard X-rays. It is of interest to know whether rapid fluctuations are observed in high-energy X-rays. The highest energy band at which sub-second variations have been observed is 223 - 1057 keV (Hurley et al. 1983). In this paper I am going to report sub-second variations observed with HXRBS at energies > 300 keV, and discuss the implications.

OBSERVATIONS

In the normal mode, the time resolution of HXRBS is 0.128 s. Therefore, one can still study sub-second variations of high-energy hard X-rays with normal mode HXRBS data. Because the hard X-ray flux decreases rapidly with increasing energy, in order to observe statistically significant sub-second fluctuations at high energies, one should study flares with high peak count rates and flat energy spectra. The flare observed at 0118 UT on 1980 June 21 meets both requirements, with the peak count rate being 141,000 counts/s and the spectral index near the X-ray peak being 2.0 (cf. Bai and Dennis 1985).

Figure 1 shows time profiles of four energy bands (28 - 55, 55 - 125, 125 - 259, 259 - 484 keV), with integration time 0.128 s. Figure 2 shows a time profile of 290 - 484 keV X-rays. The vertical bars in these figures indicate one-sigma error bars. We can see statistically significant rapid variations at several places in Figure 2, with time scales as short as 0.1 or 0.2 s.

INTERPRETATION

The energy loss rate of electrons due to Coulomb collisions is given (for E > 150 keV) by

$$(dE/dt) = -3.8 \times 10^{-10} n \text{ keV/s}, \tag{1}$$

where n is the ambient electron density in cm^{-3}. The energy loss time for 300 keV electrons is then given by

$$E\,(dE/dt)^{-1} = 79 \times (10^{10}/n) \text{ s}. \tag{2}$$

Therefore, the electrons responsible for the sub-second decreases must have interacted in a medium with density $> 10^{12}$ cm^{-3}, i.e., below the transition region. Rapid rise of high-energy X-rays indicates rapid increase of the number of high-energy electrons in the interaction region.

In interpreting the sub-second variations shown in Figure 2, I can think of the following two alternatives:

(1) High-energy electrons were accelerated with small pitch angles, and they immediately penetrate below the transition region to radiate there while losing energy. The rapid variations of the high-energy hard X-ray flux are due to rapid change in production rate of high-energy elelctrons.

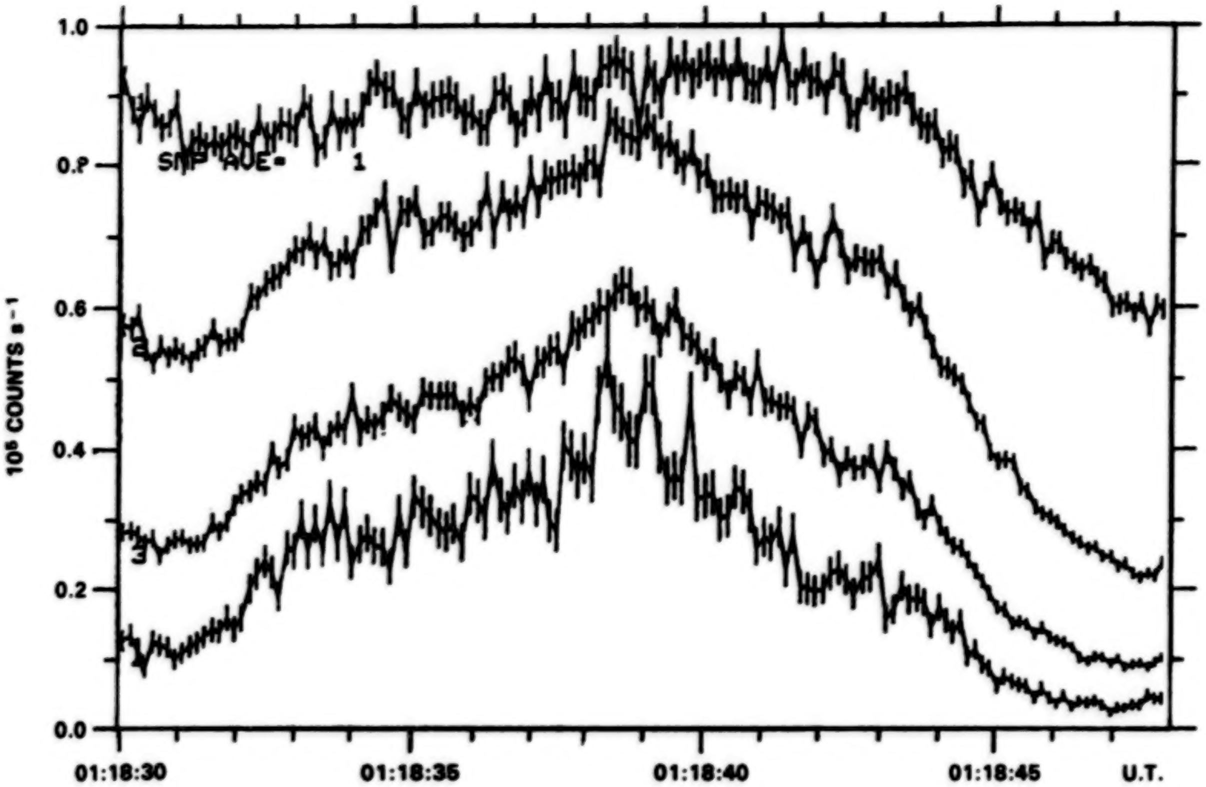

Figure 1. High resolution hard X-ray time profiles of the 1980 June 21 flare. From top to bottom, the 4 (four) curves are time profiles of X-rays in the 4 energy bands (28 – 55, 55 – 125, 125 – 259, 259 – 484 keV). Integration time is 0.128 s, and one-sigma error bars are shown.

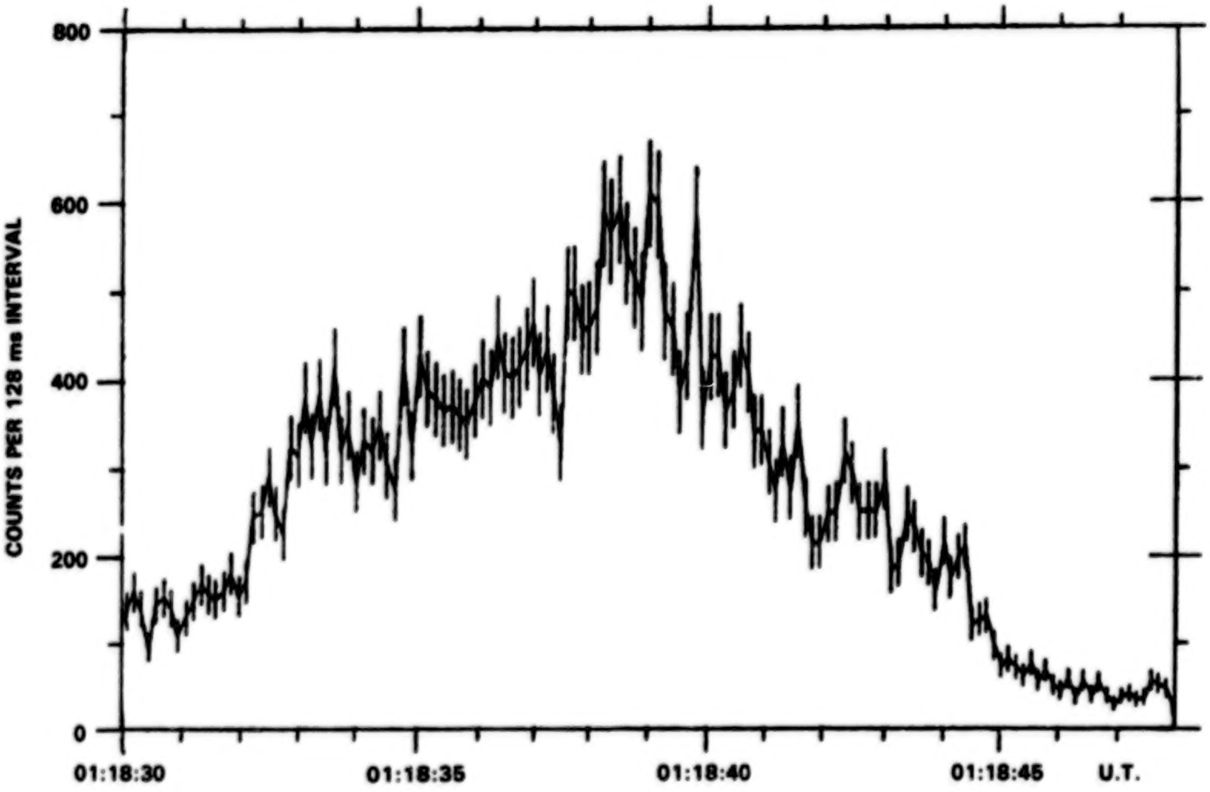

Figure 2. Same as Fig. 1, for energy band 290 – 484 keV. (Figures, courtesy of Brian Dennis)

(2) High-energy electrons are accelerated with large pitch angles, and they are initially trapped in the magnetic loop with density $< 10^{11}$ cm^{-3}. Once in a while some instability develops which rapidly scatters energetic electrons into the loss cone. The rapid variations of the high-energy hard X-rays are due to rapid scattering of high-energy electrons.

For the following reason I think the first alternative is a more likely scenario. One can estimate the efficiency of microwave emission of solar flares by comparing the microwave peak density to the hard X-ray peak flux. For this purpose, Bai (1986) defined microwave-richness index (MRI) as follows:

$$\mathrm{MRI} = \frac{\text{peak flux density of 9 GHz microwaves (sfu)}}{\text{HXRBS peak count rate (counts/s)}} \times 10. \qquad (3)$$

When defined as such, the median value of MRI for flares observed in 1980 through 1981 is about unity. Relatively speaking, flares with MRI > 1 are more efficient in prodoucing 9 GHz microwaves than flares with MRI < 1. For the 1980 June 21 flare, the MRI is 0.097 (Bai and Dennis 1985). This means that this flare was ten times less efficient in microwave emission than the average flare. This flare had flat hard X-ray spectrum with spectral index 2.0. Therefore, this flare produced large numbers of high-energy electrons, as evidenced from the large count rate of high-energy X-rays shown in Figures 1 and 2. High-energy electrons are very efficient emitters of microwaves; nevertheless this flare has a small MRI. The most plausible way of suppressing microwave emission is to accelerate high-energy electrons with small pitch angles and inject them below the transition region.

CONCLUSION

We have seen sub-second variations of high-energy (> 300 keV) X-rays in the 1980 June 21 flare. Such rapid variations are interprted to be due to rapid acceleration of high-energy electrons with small pitch angles. This flare occurred at the Western limb (N19 W90), and continuum radiation above 10 MeV was observed from this flare (Rieger et al. 1983). This continuum is mostly due to bremsstrahlung by highly relativistic electrons (Chupp 1984). The decay time of this continuum is several seconds, and from this one can deduce that these highly relativistic electrons interacted below the transition region, similarly to > 300 keV electrons.

REFERENCES

Bai, T. 1986, Astrophys. J. (to be published).

Bai, T., and Dennis, B. R. 1985, Astrphys. J. 292, 699.

Chupp, E. L. 1984, Ann. Rev. Astron. Astrophys. 22, 359.

Hurley, K., and Duprat, G. 1977, Solar Phys. 52, 107.

Hurley, K., Niel, M., Talon, R., Estulin, I. V., and Dolidze, V. Ch. 1983, Astrophys. J. 265, 1076.

Kiplinger, A. L., Dennis, B. R., Emslie, A. G., Frost, K. J., and Orwig, L. E. 1983, Astrophys. J. (Letters) 265, L99.

Kiplinger, A. L., Dennis, B. R., Frost, K. J., and Orwig, L. E. 1984, Astrophys. J. 287, L105.

Orwig, L. E., Frost, K. J., and Dennis, B. R. 1980, Solar Phys. 65, 25.

Rieger, E., Reppin, C., Kanbach, G., Forrest, D. J., Chupp, E. L., et al. 1983, 18th Int. Cosmic Ray Conf., Bangalore, India, Vol. 10, p. 338.

N87
21788
UNCLAS

N87-21788

INTERPRETATION OF RAPID RISES IN HARD X RAYS AND MICROWAVES WITH THE THERMAL CONDUCTION FRONT MODEL

D. A. Batchelor

Johns Hopkins University
Applied Physics Laboratory
Laurel, MD 20770

ABSTRACT

Impulsive hard X-ray and microwave bursts with rise times from 0.1 to 10 seconds are discussed. Source areas calculated by the method of Crannell et al. (1978) were compared with source areas determined from Hinotori and HXIS images. The agreement strongly suggests that the method is valid. If the thermal conduction front model for the hard X-ray and microwave source is adopted, then the method enables one to derive area, density, magnetic field, and rise time from hard X-ray and microwave spectral observations. This approach was used to derive these parameters for several rapid impulsive rises in the flares of 1980 July 1 and 1984 May 21. It is shown that the model provides a consistent interpretation of the observations of these impulsive increases. Indeed, the model provides a way to calculate rise times from spectra alone (to within a factor of about three) over more than two orders of magnitude.

1. INTRODUCTION

This paper has two purposes. First, we evaluate a method first applied by Crannell et al. (1978) to calculate the area of a flare source of hard X rays and microwaves from data without spatial resolution. The area calculation is made by assuming that a single thermal distribution of energetic electrons

PRECEDING PAGE BLANK NOT FILMED

emits the microwaves (thermal gyrosynchrotron radiation) and the hard X rays (thermal bremsstrahlung). We show that the method yields values in agreement with those observed with spatially resolved hard X-ray imaging instruments for the two test cases considered. With this additional support for the method, we go on to apply it to some rapid spike bursts and show that the thermal conduction-front model fits the rise times of the rapid bursts. The rapid bursts have rise times from 0.1 to 1.4 s, and allow us to extend the thermal analysis to bursts almost 10 times more rapid than heretofore. The thermal analysis of these bursts suggests that they occur in smaller coronal loops with unusually high magnetic fields, but represent part of a continuous family of impulsive bursts with rise times as long as 20 sec, studied previously (Crannell et al. 1978; Batchelor 1984; Batchelor et al. 1985). At present, nonthermal models of flare hard X-ray and microwave bursts do not make specific analogous predictions that can be compared with the results of the thermal analysis. Such predictions are sorely needed to make a meaningful comparison possible.

2. REVIEW OF AREA CALCULATION

The area of a hard X-ray and microwave burst source was calculated from the Rayleigh-Jeans law:

$$S(f) = 1.36 \times 10^{-44} f^2 A_0 T_e \qquad (1)$$

where S is the microwave flux (solar flux units -- 1 sfu = 10^{-22} W m^{-2} Hz^{-1} at a frequency f (Hz) in the optically thick portion of the microwave spectrum, A_0 is the area (cm^2), and T_e is the temperature (deg K) found by spectral fit to the hard X-ray spectrum. The units are those of Batchelor et al.; Crannell et al. expressed the temperature in keV.

Equation (1) is strictly applicable only to a homogeneous thermal source. There is evidence that variations in temperature and magnetic field sometimes affect the spectra (Matzler 1978; Schochlin and Magun 1979; Dulk and Dennis 1982). For the optically thick part of the microwave spectrum of interest here, the result of these nonuniformities is to alter the index of f in Equation (1) to a value less than 2. Considerations of a suitable model for such a nonuniform thermal source lead to the conclusion that the central, hottest part of the source is the origin of the optically thick emission of maximum frequency. The most intense X-ray emission also would originate in the hottest region of the source. Thus, if the index of the optically thick microwave emission is less than 2, then the area can be approximated by using the flux at the maximum frequency of optically thick emission in Equation (1).

3. TEST OF AREA CALCULATION

Two sources of data currently can be used to test the derivation of hard X-ray area: the Hard X-ray Imaging Spectrometer (HXIS) aboard SMM, and the two Solar X-ray Telescope (SXT) instruments aboard the Japanese Hinotori spacecraft. SXT data for one flare have been used by Wiehl et al. (1985), but no HXIS area has been compared with the area of the same flare calculated by this method. In addition, microwave observations from Bern and Sagamore Hill were available for these tests.

Test case 1: Hinotori SXT Observation

Wiehl et al. made use of the image of the 1981 August 10 flare at 0659:06 UT, published by Ohki et al. (1982). This is shown in Figure 1 (a). The area enclosed in the 40% peak contour is 1.2×10^{18} cm^2. The temperature was found by Wiehl et al. to be 3.1×10^8K, by means of a thermal bremsstrahlung function fit to the 30-500 keV spectrum from the Hard X-Ray Burst Spectrometer (HXRBS) on SMM. Microwave spectra from Bern were available. The area calculated from Equation (1), using a microwave flux of 779 sfu at 11.8 GHz, is 1.3×10^{18} cm^2.

Test case 2: HXIS Observation

In Figure 1 (b), the raw image data are shown for the 1980 May 21 flare during the sharpest, largest rise in hard X rays. If we choose the 40% contour again, for consistency, 18 pixels are at the 40% level, yielding a total area of 5.6×10^{18} cm^2. The spectrum of microwaves was observed at Sagamore Hill. Optically thick emission at 4.995 GHz was observed of approximately 1200 sfu. The temperature from the HXRBS fit was 6.6×10^8K. The calculated area is 5.4×10^{18} cm^2.

The close numerical agreement between measured and model-derived area in each case is within the uncertainties, which were estimated to be a factor of about three (Batchelor et al.).

4. THE THERMAL CONDUCTION-FRONT MODEL AND THE DERIVED AREA

A thermal model for the production of hard X rays in impulsive flares was originally proposed because the popular nonthermal models required intense beams of electrons with embarrassingly large number densities and energies to explain the observed hard X-ray fluxes from flares (e.g. Hoyng, Brown, and van Beek 1976). Whereas bremsstrahlung of a nonthermal beam in a thick target is a very inefficient process, emitting only about 10^{-5} of the electron energy as X rays, thermal bremsstrahlung from a confined, thermally relaxed electron distribution offered a much more efficient mechanism to produce the radiation,

TEST OF AREA CALCULATION

Case 1

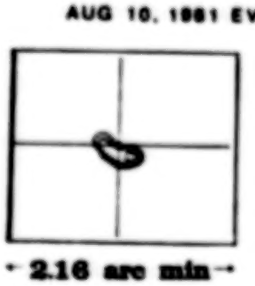

SXT1 Hard X-ray Image
Hinotori Spacecraft

From 0658:55.200 UT
To 0659: 1.876 UT
20-40 keV

Contours: 80%, 60%, 40%
(Ohki et al. 1982)

Measured area within 40% contour: 1.2 x 10^{18} cm^2

Calculated area (779 sfu @ 11.8 GHz): 1.3 x 10^{18} cm^2
(Wiehl et al. 1985)

Case 2

HXIS, SMM Spacecraft
May 21, 1980

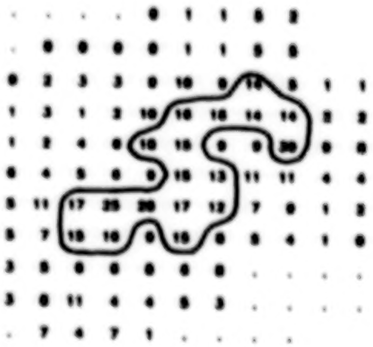

From 2055:44 UT
To 2055:54.5 UT

8 arc sec per pixel
16-30 keV

18 pixels › 40% of maximum: 5.6 x 10^{18} cm^2

Calculated area (1200 sfu @ 5 GHz): 5.4 x 10^{18} cm^2

Figure 1. Comparison between area of X-ray source within 40% contour and derived source area for two flares. Solar north is up.

if the confinement was sufficiently good. Brown, Melrose and Spicer (1979) introduced the idea that an impulsively heated electron population at the top of a coronal loop might be confined by ion-acoustic turbulence excited by electrons attempting to escape from the source. Smith and Lilliequist (1979) explored this model with fluid simulations, and this led to a number of papers by Smith and collaborators in which the model was refined. Many variations on the thermal conduction-front model have since appeared in the literature. Batchelor et al. (1985) gave arguments for the confinement of high-energy microwave-emitting electrons in the source as well. A schematic of that variation of the model appears in Figure 2.

It is assumed that heating of the electrons near the apex of a loop is continuous until the peak of the hard X-ray burst or later. This is the assumption of Smith and collaborators rather than Brown, Melrose and Spicer, who assumed impulsive heating and studied the aftermath. Observational evidence for this assumption comes from the time histories of fitted temperature during the rises of bursts, which typically indicate rising temperature. The theoretical arguments of Batchelor et al. suggest that the microwave and hard X-ray-emitting regions are cospatial up to the peak of the burst. It is justified then to use the area derivation described in Section 2 to estimate the loop length. If Equation (1) is used to derive A_0, then the half-length of the loop is proportional to $L_0 = A_0^{1/2}$.

In the continuous heating version of the model considered here, the rise time of the hard X rays is then the travel time of the conduction front from the loop apex to the chromosphere. The velocity of the conduction front is approximately $c_s = (kT_e/m_p)^{1/2}$, the ion-acoustic velocity. T_e is found from the hard X-ray thermal bremsstrahlung spectral fit. Therefore the rise time of an impulsive burst in this variation of the model is $L_0/c_s = \tau_0$. If the assumptions of the model are valid, we should find t_r, the rise time measured from the time history of a spike burst, to be linearly related to τ_0, which depends on spectral parameters only. This linear relation was found to hold by Batchelor et al. for the set of 20 impulsive rises from different flares with rise times ranging from 1.8 to 22 s.

The impulsive and continuous-heating versions of the model have been studied analytically by MacKinnon (1985). That work supports our assumption, $t_r = L_o/c_s$, given that heating continues for $t \geq t_r$ after the start of the burst.

We proceed to test this prediction of the thermal conduction-front model with data from additional rapid rises from two flares.

5. RAPID RISES IN THE 1980 JULY 1 FLARE

The flare produced a series of seven sharp peaks, superposed on a more gradual component, which we treat as background. These peaks are shown in

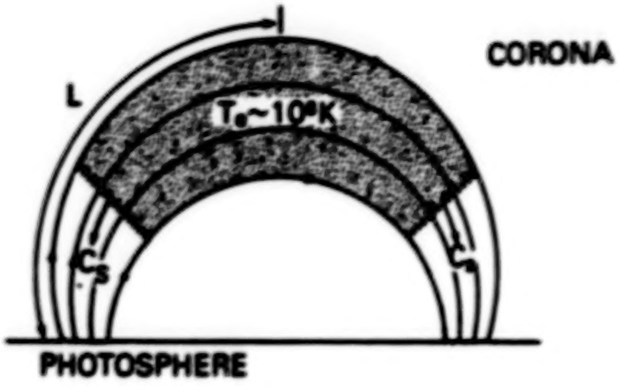
L
CORONA
$T_e \sim 10^8 K$
C_s
C_s
PHOTOSPHERE

Figure 2. Schematic of the conduction-front model for emission of impulsive hard X rays (30-500 keV) and associated microwaves.

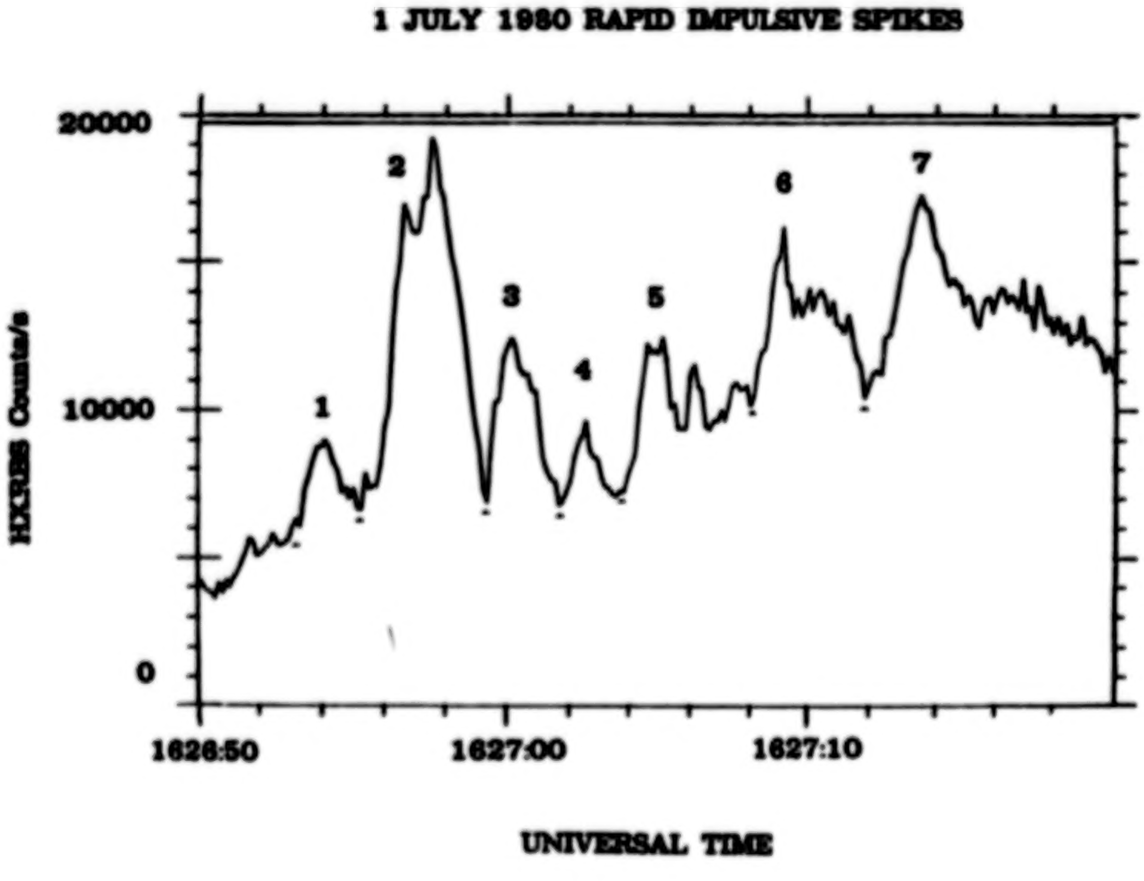

Figure 3. Time-intensity plot of the seven rapid impulsive rises in hard X rays (33-490 keV) on 1980 July 1, observed with HXRBS.

X rays in Figure 3. Microwave data were also available from Bern, courtesy of A. Magun.

Hard X-ray spectra of the seven spikes were computed by fitting a thermal bremsstrahlung function as described in Batchelor et al. Microwave fluxes were computed at the maximum optically thick frequency. The observed and derived parameters for these spikes appear in Table 1. The table includes several parameters of interest that are defined by formulae in Batchelor et al. The emission measure ($n_e{}^2 L_0{}^3$) and temperature of the fitted thermal bremsstrahlung function are listed, μ and T_e. The observed rise time, t_r, and the predicted rise time, τ_0, computed from S, f, and T_e, are in neighboring columns. The magnetic field is calculated from our estimate of the peak frequency of the microwave spectrum, f, and from S, T_e, and μ (see Equation (15) of Batchelor et al.). The formula is derived from the simplified expressions for gyrosynchrotron emission by Dulk and Marsh (1982). The electron density, n_e, and thermal energy density, w_T, are derived from μ and L_0. The standard plasma β for the electrons is also given. The < and > symbols with some values of B and β occur because f is a lower bound on the microwave peak frequency.

Table 1
Observed and Derived Parameters for 1980 July 1 Spikes

	Observed					Derived from Model					
No.	μ	T_e	S	f	t_r	τ_0	L_0	B	n_e	w_T	β
	10^{45} cm^{-3}	10^8K	sfu	GHz	s	s	10^9 cm	gauss	10^9 cm^{-3}	erg cm^{-3}	
1	.36	4.9	135	19.6	.8	1.1	.22	325	5.7	580	.14
2	1.0	6.4	750	35	.9	1.1	.26	>470	7.4	980	<.11
3	.53	5.7	39	19.6	.8	.53	.11	270	19	2200	.77
4	.22	6.5	82	35	1.0	.4	.086	>470	19	2600	<.29
5	.40	7.1	486	28	.8	1.0	.25	350	5.0	[illegible]30	.15
6	.43	7.3	894	35	1.0	1.1	.27	>440	4.5	680	<.088
7	.44	7.8	1330	35	1.4	1.3	.32	>425	3.7	600	<.083

The seven pairs of t_r and τ_0 are plotted in Figure 4, with the other pairs calculated by Batchelor et al. (Spike 2 was included in previous work; the six new values are indicated by diamond symbols.)

Noteworthy features of the parameters are the relatively high temperatures, magnetic fields and densities, as compared with the set of rises

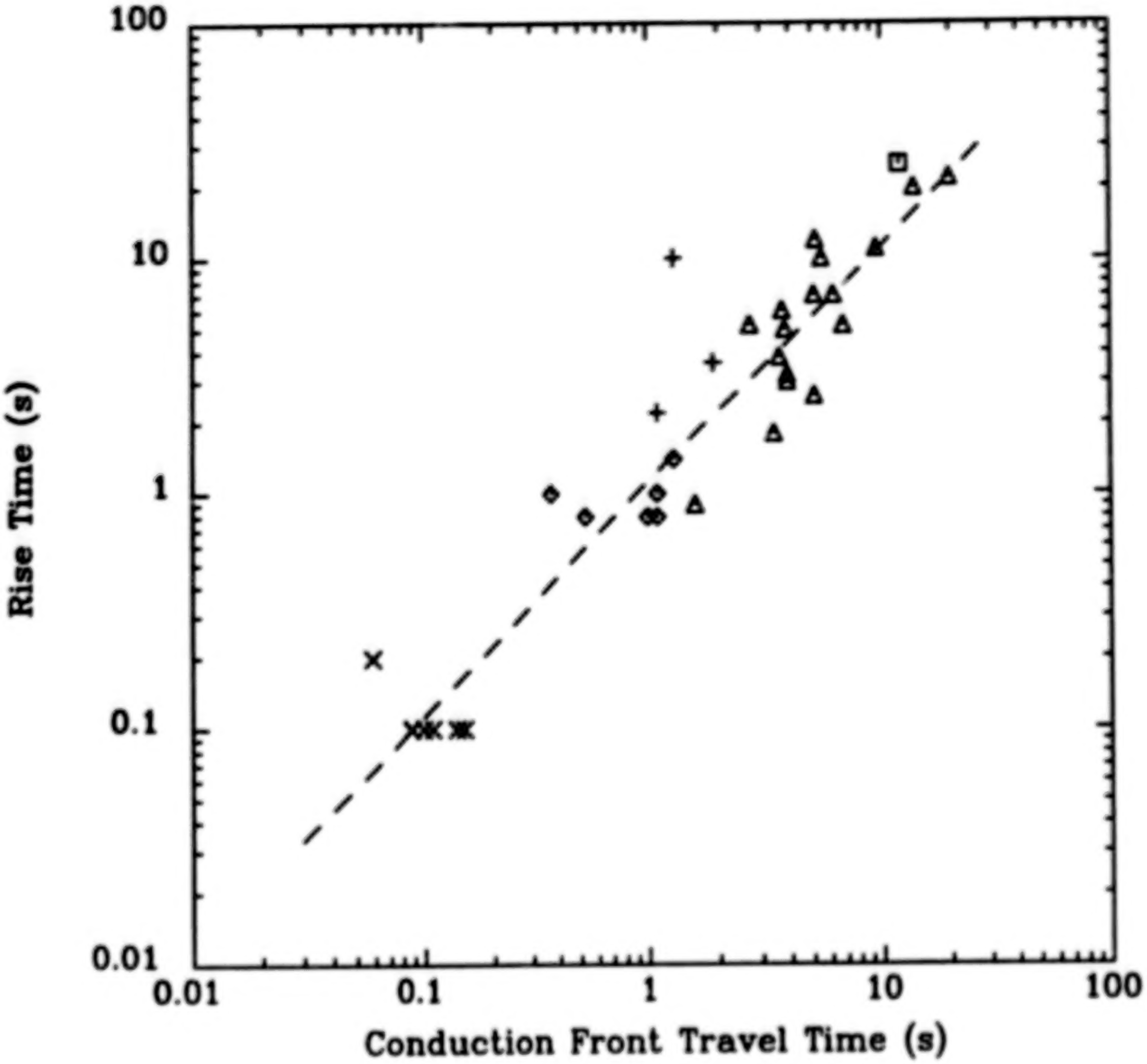

Figure 4. Correlation of measured rise times of 34 impulsive rises with rise times derived from the X-ray and microwave spectra, using the conduction front model. Triangles: rises from different flares on the disk (Batchelor et al.); pluses: rises from different flares on the limb (Batchelor et al.); square: 1980 November 5, 2232 UT; diamonds: other impulsive rises from 1980 July 1 flare; crosses: other impulsive rises from 1984 May 21 flare. The square, diamonds and crosses are presented here for the first time. The dashed line is the linear least-squares best fit to the (log t_r, log τ_o) pairs, excluding limb events because of possible occultation: $t_r = 1.12\ \tau_o^{1.00}$, correlation coefficient r = 0.96.

studied by Batchelor et al. Association of high temperatures with high fields is quite reasonable if the source of energy is magnetic reconnection. The derived loop lengths are relatively small, which is interesting because the flare was remarkably compact in Hα. The high densities might be expected in relatively small, low-lying coronal loops.

6. RAPID RISES IN THE 1984 MAY 21 FLARE

Microwave and hard X-ray data on this event were first presented by Kaufmann et al. (1985). This flare is discussed in detail by Correia et al., elsewhere in this volume. Several rapid rises in microwave flux at 90 GHz were observed, with t_r from 0.1 to 0.2 s. Seven clearly-resolved spike features from the microwave bursts labeled B, C, and E (see Correia et al.) were selected for analysis. In the simultaneous X-ray observations with HXRBS, the time resolution (128 ms) did not permit complete resolution of the spikes. The X-ray bremsstrahlung spectral fit was necessarily performed on a blend of the first three spikes in feature C and on a blend of the first three spikes in feature E. Feature B was resolved in both data sets. As in previous cases, the slow component of emission was treated as background.

The observed and derived parameters for these seven spikes are given in Table 2.

Table 2
Observed and Derived Parameters for 1984 May 21 Spikes

	Observed				Derived from Model					
Label	μ 10^{45}cm^{-3}	T_e 10^8K	S sfu	t_r s	τ_0 s	L_0 10^9cm	B gauss	n_e 10^9cm^{-3}	w_T erg cm^{-3}	β
B	0.12	7.9	20	0.2	0.059	0.015	$\gtrsim 940$	180	29000	$\lesssim 0.84$
C_1	0.13	7.5	40	0.1	0.088	0.022	$\gtrsim 990$	110	17000	$\lesssim 0.44$
C_2	0.13	7.5	55	0.1	0.10	0.026	$\gtrsim 1000$	87	14000	$\lesssim 0.34$
C_3	0.13	7.5	60	0.1	0.11	0.027	$\gtrsim 1000$	81	13000	$\lesssim 0.32$
E_1	0.32	4.5	15	0.1	0.090	0.017	$\gtrsim 1400$	250	23000	$\lesssim 0.30$
E_2	0.32	4.5	35	0.1	0.14	0.027	$\gtrsim 1400$	130	12000	$\lesssim 0.16$
E_3	0.32	4.5	40	0.1	0.15	0.028	$\gtrsim 1400$	120	11000	$\lesssim 0.14$

All derived values for this flare depend on observations at 90 GHz. Because of the positive spectral index in each case from 30 GHz to 90 GHz, it has been assumed that at 90 GHz the source is optically thick. The magnetic field computations are lower limits, depending on the assumption that the gyrosynchrotron spectral peak is > 90 GHz. More observations in this microwave spectral range would help to determine the properties of these rapid spikes more decisively. Values of t_r were found by measuring the time-intensity plots of microwaves given by Correia et al.

The pairs t_r and τ_0 corresponding to these seven spikes are plotted in Figure 4 as "x" symbols. The values of τ_0 should be regarded as uncertain by a factor of about three, due to blending of spikes in the X-ray spectral analysis. Nevertheless, agreement with the linear relation found in the other cases is the result. The best linear least-squares fit is $t_r = 1.12\ \tau_o^{1.00}$, with a correlation coefficient r = 0.96. (The three limb flares were omitted from correlation analysis, due to the possibility of occultation effects.)

Unusually high values of B, 10^3 gauss and more, are derived for these spikes. Loop sizes of a few hundred km, and densities of order 10^{11}cm^{-3} are also implied. All of these properties are consistent with an origin of the radiations in unusually low-lying magnetic loops.

Considering all of the impulsive rises analyzed here and by Batchelor et al., we find sources sizes rangeing from 150 km to 27000 km, magnetic fields ranging from 110 gauss to more than 1400 gauss, and densities ranging from 10^8cm^{-3} to 2.5 x 10^{11}cm^{-3}. In all cases, $\beta < 1$ is found, indicating confinement of the plasma by the magnetic field, and that only a fraction of the field had to be annihilated to supply the thermal energy of the plasma. This is unlikely to result by chance alone, given the large range of parameters contributing to β, and suggests that the derived parameters are physically meaningful.

7. CONCLUSIONS

The two test cases suggest that the area computation using Equation (1) is physically meaningful. The analysis of rapid rises in the 1980 July 1 and 1984 May 21 flares leads to derived physical parameters that are reasonable for a simple extension of the same thermal source confinement mechanism to smaller loops with higher magnetic fields than usual. The linear relationship of observed and model derived rise times found by Batchelor et al. is supported for short rise times.

It bears repeating here that the linear relationship displayed in Figure 4 is not due to a strong correlation with t_r of any one of the parameters S, f, and T, that are used to compute τ_o. As shown by Batchelor et al., t_r is not correlated with either S, f, or T alone; only the combination of these parameters to compute L_o or τ_o is correlated with t_r, consistent with the model.

This thermal model provides a physically meaningful way of connecting independent temporal and spectral parameters of impulsive hard X rays and microwaves. A challenge for future work is to develop comparable nonthermal mechanisms to explain the relationship of the observed parameters in the context of a nonthermal model.

This work was supported by NASA under grant NSG 7055, and by the National Science Foundation under grant ATM-8312720. Stimulating discussions and helpful suggestions from C. J. Crannell and D. M. Rust are gratefully acknowledged.

REFERENCES

Batchelor, D. A. 1984, Ph.D. Dissertation, University of North Carolina, Chapel Hill, NASA TM86102.

Batchelor, D. A., Crannell, C. J., Wiehl, H. J., and Magun, A. 1985, Astrophys. J., 295, 258.

Crannell, C. J., Frost, K. J., Matzler, C., Ohki, K., and Saba, J. L. 1978, Astrophys. J., 223, 620.

Hoyng, P., Marsh, K. A., Zirin, H., and Dennis, B. R. 1983, Astrophys. J., 268, 865.

Kaufmann, P., Correia, E., Costa, J. E. R., Zodi Vaz, A. M., and Dennis, B. R. 1985, Nature, 313, 380.

MacKinnon, A. 1985, Solar Phys., 98, 293.

Ohki, K., Nitta, N., Tsuneta, S., Takakura, T., Makishima, K., Murakami, T., Ogawara, Y., and Oda, M. 1982, Proceedings of Hinotori Symposium on Solar Flares, Tokyo, Japan, Jan. 27-29, 1982.

Wiehl, H. J., Batchelor, D. A., Crannell, C. J., Dennis, B. R., Price, P. N., and Magun, A. 1985, Solar Phys., 96, 339.

N87
21789
UNCLAS

N87-21789

IMPULSIVE PHASE SOLAR FLARE X-RAY POLARIMETRY

Gary Chanan

Department of Physics
University of California
Irvine, California 92717

A. Gordon Emslie*

Department of Physics
University of Alabama
Huntsville, Alabama 35899

Robert Novick

Columbia Astrophysics Laboratory
Columbia University
New York, New York 10027

ABSTRACT

The pioneering observational work in solar flare X-ray polarimetry was done in a series of satellite experiments by Tindo and his collaborators in the Soviet Union; initial results showed high levels of polarization in X-ray flares (up to 40%), although of rather low statistical significance, and these were generally interpreted as evidence for strong beaming of suprathermal electrons in the flare energy release process. However, the results of the polarimeter flown by the Columbia Astrophysics Laboratory as part of the STS-3 payload on the Space Shuttle by contrast showed very low levels of polarization. The largest value - observed during the impulsive phase of a single event - was 3.4% ± 2.2%. At the same time but independent of the observational work, Leach and Petrosian (1983) showed that the high levels of polarization in the Tindo results were difficult to understand theoretically, since the electron beam is isotropized on an energy loss timescale - an effect which substantially reduces the expected levels of polarization, although not to zero. A subsequent comparison by Leach, Emslie, and Petrosian (1985) of the impulsive phase STS-3 result and the above theoretical treatment shows that the former is consistent with several current models and that a factor of ~3 improvement in sensitivity is needed to distinguish properly among the possibilities. In addition, there is reason to expect stronger polarization effects at higher energies: There may have been a strong thermal component to the flare at the energies seen by the STS-3 instrument (predominantly below 10 keV), and in addition the preponderance of γ-ray ($\gtrsim$ 300 keV) events on the solar limb (Rieger et al. 1983) suggests that beaming must be important at sufficiently high energies.

---

* Presidential Young Investigator

PRECEDING PAGE BLANK NOT FILMED

Here we point out that a satellite instrument with the necessary sensitivity and high energy response to make meaningful and important measurements is well within current technological capabilities. We describe an instrument whose sensitivity for a moderate (M class) event approaches polarization levels of 1% in each of 7 energy bins spanning the 10 to 100 keV range for integration times as short as 10 seconds. Comparable results can be obtained for an X class flare in 1 second.

1. Solar Flare X-ray Polarimetry

The idea that X-ray emission from solar flares might be linearly polarized and that polarization measurements could therefore provide a strong flare diagnostic was first discussed by Korchak (1967) and Elwert (1968). Subsequent theoretical investigations (Elwert and Haug 1970, 1971; Haug 1972; Brown 1972; Henoux 1975; Langer and Petrosian 1977; Bai and Ramaty 1978; Emslie and Brown 1980) have resulted in polarization predictions for a variety of models. There are two extreme classes of models under investigation, termed "thermal" and "non-thermal", whose physical difference lies principally in whether the electrons responsible for the bremsstrahlung are part of a relaxed distribution or of a suprathermal tail. Although some form of hybrid model (e.g., Elmslie and Vlahos 1980) is probably appropriate for actual events, the basic components differ significantly in their polarization predictions: the thermal models predict polarizations of at most a few percent, due to either photospheric backscatter of primary photons (Henoux 1975), or an anistropy in the source electron velocity distribution, caused by the presence of a field-aligned thermal conductive flux (Elmslie and Brown 1980). The beamed or linear bremsstrahlung models, on the other hand, predict quite high polarizations, of the order of 10% for the spatially integrated radiation field, and even higher than this for the collisionally thin upper portions of the flare loop (Leach et al. 1985).

The two models also predict different directivities with the non-thermal models tending to give anistropic distributions (Elwert and Huag 1970, 1971), although the intrinsic effect is substantially reduced by photospheric backscattering (Bai and Ramaty 1978). Stereoscopic observations by Kane et al. (1980) put limits on the anistropy and tend to favor the thermal models, but are thus far not conclusive. Recent gamma ray observations from the Solar Maximum Mission Observatory show that above 300 keV more flares are observed at the limb of the solar disk than at the center (Rieger et al. 1983, Vestrand 1985). Dermer and Ramaty (1985) have attributed this apparent beaming to electron beaming parallel to the surface of the sun. It is important to recognize that the observations of photon beaming directly imply non-vanishing polarization. The beaming observations that have been made to date are purely statistical in nature. They require one to compare the photon fluxes from different solar flares; since no two flares are the same, this is a very suspect procedure. Polarimetric observations provide direct evidence for electron beaming within a particular flare without recourse to any data from a different flare.

The pioneering observational work in solar X-ray polarimetry was done in a series of satellite experiments by Tindo and his collaborators in the Soviet Union (Tindo et al. 1972a, 1972b; Tindo, Mandel'stam, and Shuryghin 1973; Tindo, Shuryghin, and Steffen 1976). Initial results showed high levels of polarization (up to 40%), although of rather low statistical significance, and these were generally interpreted as evidence for strong beaming of the electrons. These results are shown in Figure 1 where they are compared to the theoretical calculations of Bai and Ramaty (1978). The theoretical curve marked "thermal" in this figure is the polarization expected to arise by X-ray backscattering in the photosphere when the intrinsic flare radiation is unpolarized (and so presumably thermal in origin). The results of the polarimeter flown by the Columbia Astrophysics Laboratory as part of the OSS-1 payload on the Space Shuttle mission STS-3 by contrast showed very low levels of polarization - no more than a few percent. At the same time but independent of the observational work, Leach and Petrosian (1983) showed that the high levels of polarization in the Tindo results were difficult to understand theoretically, since the electron beam is isotropized on an energy loss timescale - an effect which substantially reduces the expected levels of polarization, although not to zero. Recently Haug, Elwert, and Rausaria (1985) also considered the effect of electron scattering on electron beaming and X-ray polarization. These workers predict higher polarization than Leach and Petrosian but it is important to note that Haug et al. consider only a straight electron path, they do not consider the curvature of the electron path in the flare, an effect which will almost certainly reduce the polarization. In Figure 2 we compare the results of Tindo et al. (1976) to the predictions of Leach and Petrosian (1983) (which do not include photospheric backscatter effects). For comparison we again show the predictions of Bai and Ramaty (1978) which do include a photospheric backscattered component, but which predict a higher intrinsic source polarization due to their approximate treatment of the beam-target interaction. In Figure 3 we compare the STS-3 results to the calculations of both Bai and Ramaty and Leach and Petrosian. These results are considerably below those of Tindo and all of the theoretical results. As noted on Figure 3 one of the STS-3 events was impulsive in nature. A subsequent comparison by Leach, Emslie, and Petrosian (1985) of the (impulsive phase) STS-3 result and the above theoretical treatment shows that the former are consistent with several current models (see Figure 4) and that a factor of ~3 improvement in sensitivity is needed to distinguish properly among the possibilities. In addition, there is reason to expect stronger polarization effects at higher energies: Although the predicted polarization curves of Leach and Petrosian (1983) are only weakly energy dependent (up to at least 100 keV), there may be a strong admixture of thermal X-rays at the energies seen by the STS-3 instrument (5-20 keV, but predominantly below 10 keV). As Leach, Emslie, and Petrosian (1985) stress, this thermal "contamination" will tend to reduce the observed polarization, but the effect should decrease sharply with increasing energy (see also Emslie and Vlahos 1980), so that the need for higher energy observations is clear. Further, in the case where the coronal component can be observed in isolation, such as in a flare whose footprints are just behind the occulting photospheric limb, the predicted polarization is much higher (Leach et al. 1985). Thus we clearly see that better polarimetric observations are needed, particularly at high energies where thermal effects are unimportant. In the next section we describe a new polarimeter that is designed to answer the outstanding questions regarding electron beaming and scattering in solar flares.

2. AN IMPROVED SOLAR FLARE POLARIMETER

The previous STS-3 instrument exploited the polarization dependence of Thomson scattering (see Figure 5). The targets (whose dimensions are set by the relevant scattering length) were 12 rectangular blocks of metallic lithium, monitored on two of the four sides by xenon-filled proportional counters; there were thus effectively six targets. The low energy threshold was set at ~5 keV by photoelectric losses in the lithium, the high energy cutoff by the transparency of the proportional counters at ~20 keV. The improved instrument uses plastic scintillator (composed mainly of carbon) in place of the lithium targets, which raises the low energy threshold to ~10 keV. The xenon counters are in turn replaced by sodium iodide detectors; this extends the high energy response upward to $\gtrsim$ 100 keV.

A fundamental improvement in background rejection results from using the carbon target in the form of plastic scintillator. A sufficiently high energy photon which interacts in the target will give rise to a Compton electron which can be detected by a photomultiplier tube which monitors the optical output of the target from below. This can then be used as a trigger for the acceptance of events in the NaI(Tl) detectors. Although the exact value of the Compton threshold (experimentally found to be ~40 keV) is somewhat uncertain, the ultimate performance of the instrument is not very sensitive to the precise value. The reason is that at energies which are low enough for the detection of the Compton electron to be difficult, the source fluxes are high enough that the background is simply not a problem [It was not a problem for example in the STS-3 polarimeter]. Conversely, at energies which are sufficiently high that good background rejection is essential (because of the low fluxes), the Compton electron will have enough energy that it will be relatively easy to detect. In fact since both target and detector events will be recorded in flight, the precise value of the Compton threshold can be chosen post-flight to optimize the polarization response.

Because the NaI(Tl) detectors are relatively compact, a large number of target/detector assemblies can be packed into a relatively small space. We further plan to adopt a hexagonal geometry (as opposed to the square geometry used on STS-3); this results in an improved modulation factor which in turn results in higher sensitivity and reduced vulnerability to systematic effects. Current plans are for an array of 37 targets each surrounded by 6 detectors (the latter shared by 2 targets, except on the periphery) (see Figures 6, 7 and 8). Such an array would be 28 in. in diameter. This result will increase the sensitivity by a factor of $\sqrt{(37/6)} = 2.5$ over the STS-3 instrument in the region where the bandwidths overlap; the high energy response will be extended upward simultaneously by a factor of 5. The entire polarimeter assembly will be rotated to avoid a large number of possible systematic effects (instrumental polarization). With a static polarimeter it is necessary to compare the counting rates in different sodium iodide detectors. Since the sensitivity and spectral responses of such detectors are difficult to monitor this procedure can lead to false indications of polarization. With a rotating polarimeter one searches for a modulation of the response of each detector. The depth of modulation and phase are simply related to the degree of polarization and the position angle of the polarization vector. By rotating the polarimeter at 20 RPM only 1.5 seconds is needed for a determination of the polarization of the incident X-rays. This is clearly desirable for solar flares which vary rapidly in intensity.

Preliminary sensitivity calculations for the instrument described above for 5 typical (moderate) flares are shown in Table I; the flare parameters were taken from actual observed events (Lemen 1981). Assumed integration times are 10 s in each case. Note that sensitivities of a few percent are routinely attained up to ~100 keV energies.

3. CONCLUSION

In this paper we have described a new solar flare X-ray polarimeter that has sufficient sensitivity so that it can be used to detect and measure the polarization that is predicted to arise from beaming in solar flares even when suitable account is taken of electron scattering. In Figure 9 we show the sensitivity of the polarimeter to an M-3 flare in 10 seconds or for an X-3 flare in 1 second; in both cases we have assumed a spectral photon index of 4.4. Note that the sensitivity is 2% or less at energies up to 50 keV. At these energies unpolarized thermal emission from the flare should be unimportant (Elmslie and Vlahos 1980). It is also important to note that the instrument has sufficient sensitivity to detect the polarization expected due to X-ray back-scattering in the photosphere. Since this phenomenon must be present the polarimeter will certainly yield a positive result. Any deviation of the observed polarization from that due to back-scattering must be attributed to intrinsic flare polarization resulting from electron beaming. (Backscatter can reduce the intrinsic source polarization if the angles are right.) This polarimeter represents a considerable improvement over the STS-3 instrument, especially at high energies where the contaminating effects of unpolarized thermal radiation are relatively unimportant. The design is based on laboratory tests of individual modules, on detailed computer simulations, and it incorporates the heritage of several successful rocket flights as well as that of the STS-3 experiment. This polarimeter is well matched to the outstanding questions about electron beaming and scattering in solar flares.

ACKNOWLEDGMENT

This work was supported by the National Aeronautics and Space Administration under NAGW-93 and NAGW-588 (GAC); NAGW-588 and NAG5-618 (RN); and NAGW-294 (AGE) and the National Science Foundation ATM-8505475 (AGE). This paper is Columbia Astrophysics Laboratory Contribution Number 311.

Table I

Polarization Sensitivities (1σ) Predicted for Five Typical Flares

(10 second observation time)

1. Photon flux at 1 keV = 1.35×10^5 photons cm^{-2} s^{-1} keV^{-1}
   Spectral index = 3.34
   Classification = M2

Energy Range	Polarization
10-20 keV	1.25%
20-30 keV	1.70%
30-40 keV	2.69%
40-50 keV	3.89%
50-60 keV	5.40%
60-150 keV	4.25%

2. Photon flux at 1 keV = 3.60×10^7 photons cm^{-2} s^{-1} keV^{-1}
   Spectral index = 4.28
   Classification = X2

Energy Range	Polarization
10-20 keV	0.27%
20-30 keV	0.46%
30-40 keV	0.87%
40-50 keV	1.41%
50-60 keV	2.15%
60-150 keV	2.01%

3. Photon flux at 1 keV = 2.61×10^7 photons cm^{-2} s^{-1} keV^{-1}
   Spectral index = 4.66
   Classification = M3

Energy Range	Polarization
10-20 keV	0.52%
20-30 keV	1.01%
30-40 keV	2.02%
40-50 keV	3.44%
50-60 keV	5.47%
60-150 keV	5.46%

Table I (continued)

Polarization Sensitivities (1σ) Predicted for Five Typical Flares

(10 second observation time)

4. Photon flux at 1 keV = 2.49×10^7 photons cm^{-2} s^{-1} keV^{-1}
Spectral index = 4.36
Classification = M3

Energy Range	Polarization
10-20 keV	0.36%
20-30 keV	0.63%
30-40 keV	1.20%
40-50 keV	1.97%
50-60 keV	3.03%
60-150 keV	2.87%

5. Photon flux at 1 keV = 2.30×10^5 photons cm^{-2} s^{-1} keV^{-1}
Spectral index = 3.0
Classification = M2

Energy Range	Polarization
10-20 keV	0.60%
20-30 keV	0.75%
30-40 keV	1.12%
40-50 keV	1.55%
50-60 keV	2.09%
60-150 keV	1.74%

REFERENCES

Bai, T., and Ramaty, R.: 1978, Ap. J., **219**, 705.

Brown, J.C.: 1972, Solar Phys., **26**, 441.

Dermer, C.D. and Ramaty, R.: 1985, preprint.

Elwert, G.: 1968, in K.O. Kiepenheuer (ed.), "Structure and Development of Solar Active Regions," IAU Symp., 35, 444.

Elwert, G., and Haug, E.: 1970, Solar Phys., **15**, 234.

Elwert, G., and Haug, E.: 1971, Solar Phys., **20**, 413.

Emslie, A.G., and Brown, J.C.: 1980, Ap. J., **237**, 1015.

Emslie, A.G., and Vlahos, L.: 1980, Ap. J., **242**, 359.

Haug, E. 1972: Solar Phys., **25**, 425.

Haug, E., Elwert, G., and Rausaria, R.R. 1985: Astron. & Astrophys., **148**, 115.

Henoux, J.C.: 1975, Solar Phys., **42**, 219.

Kane, S.R. *et al.*: 1980, Ap. J. (Letters), **239**, L85.

Korchak, A.A.: 1967, Soviet Phys. Dokl., **12**, 192.

Langer, S.H., and Petrosian, V.: 1977, Ap. J., **215**, 666.

Leach, J., and Petrosian, V.: 1983, Ap. J., **269**, 715.

Leach, J., Emslie, A.G., and Petrosian, V.: 1985, Solar Phys., **96**, 331.

Lemen, J.R.: 1981, Ph.D. Thesis, Columbia University (unpublished).

Lemen, J.R., Chanan, G.A., Hughes, J.P., Laser, M.R., Novick, R., Rochwarger, I.R., Sackson, M., and Tramiel, L.J.: 1982, Solar Phys., 80, 333.

Reiger, E., Reppin, C., Kanbach, G., Forrest, D.J., Chupp, E.L., and Share, G.H.: 1983, in 18th International Cosmic Ray Conference (Late Papers), Bangalore, **10**, 338

Tindo, I.P., Ivanov, V.D., Mandel'stam, S.L., and Shuryghin, A.I.: 1972a, Solar Phys., **24**, 429.

Tindo, I.P., Ivanov, V.D., Valnicek, B., and Livshits, M.A.: 1972b, Solar Phys., **27**, 426.

Tindo, I.P., Mandel'stam, S.L., and Shuryghin, A.I.: 1973, Solar Phys., **32**, 469.

Tindo, I.P., Shuryghin, A.I., and Steffen, W.: 1976, Solar Phys., **46**, 219.

Tramiel, L.J., Chanan, G.A., and Novick, R.: 1984, Ap. J., 280, 440.

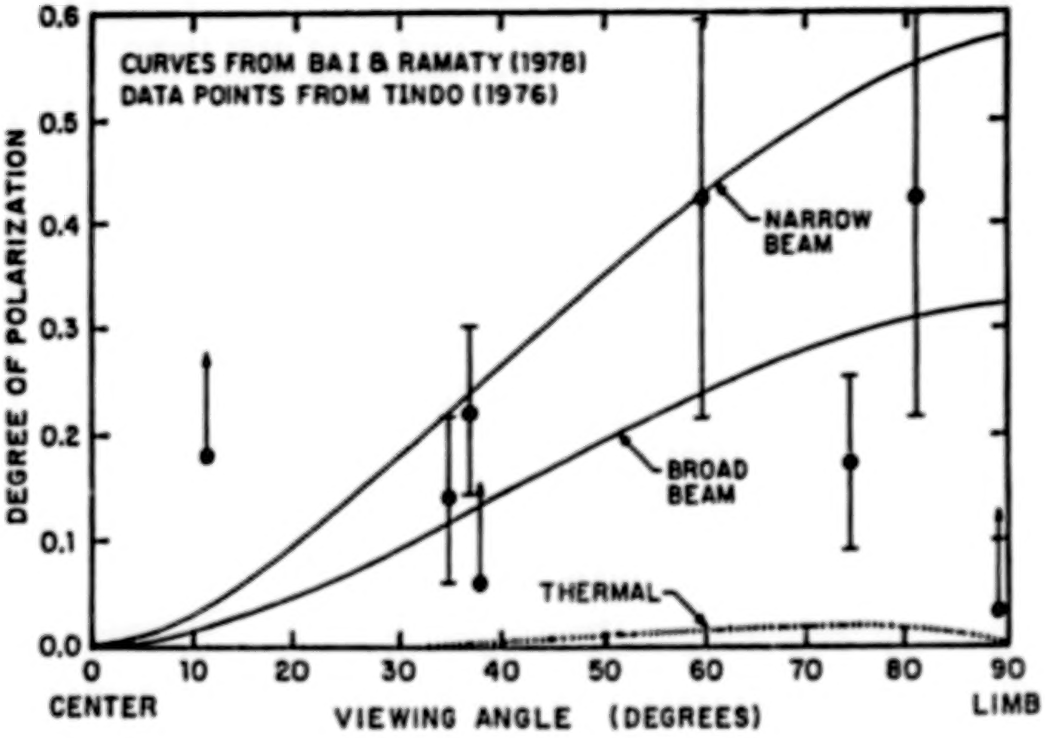

Figure 1: Comparison of the polarization results of Tindo (1976) with the theoretical results of Bai and Ramaty (1978).

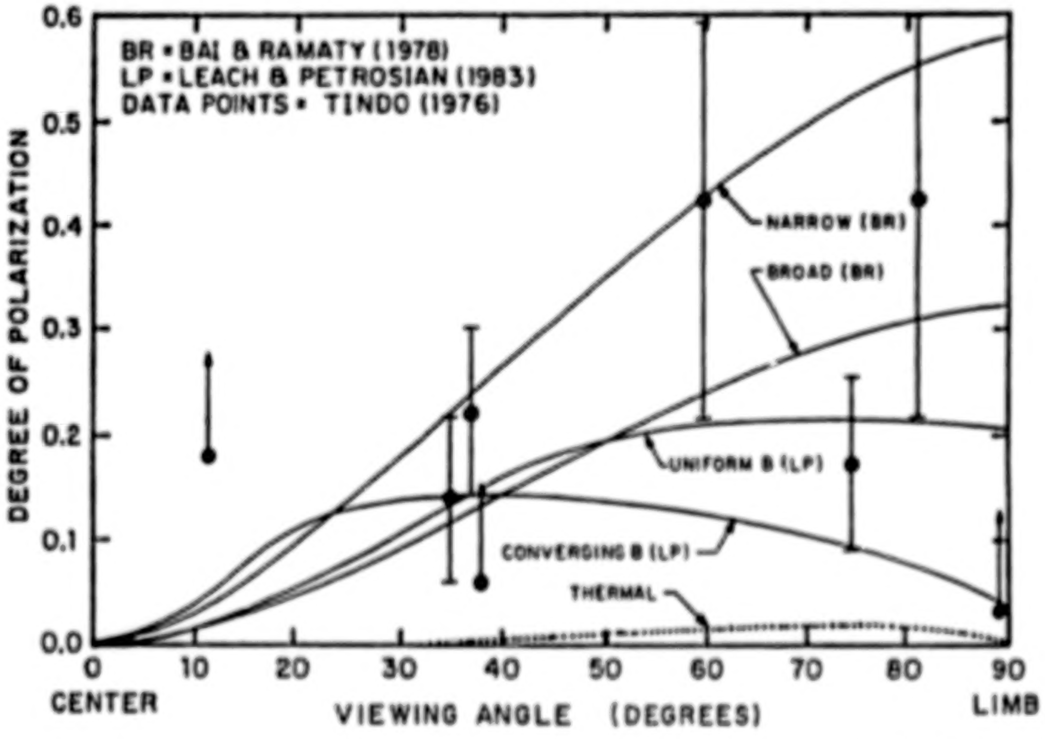

Figure 2: Comparison of the polarization results of Tindo (1976) with the theoretical results of Bai and Ramaty (1978) and of Leach and Petrosian (1983). Note that the theoretical curves of Leach and Petrosian are generally below the polarization results of Tindo.

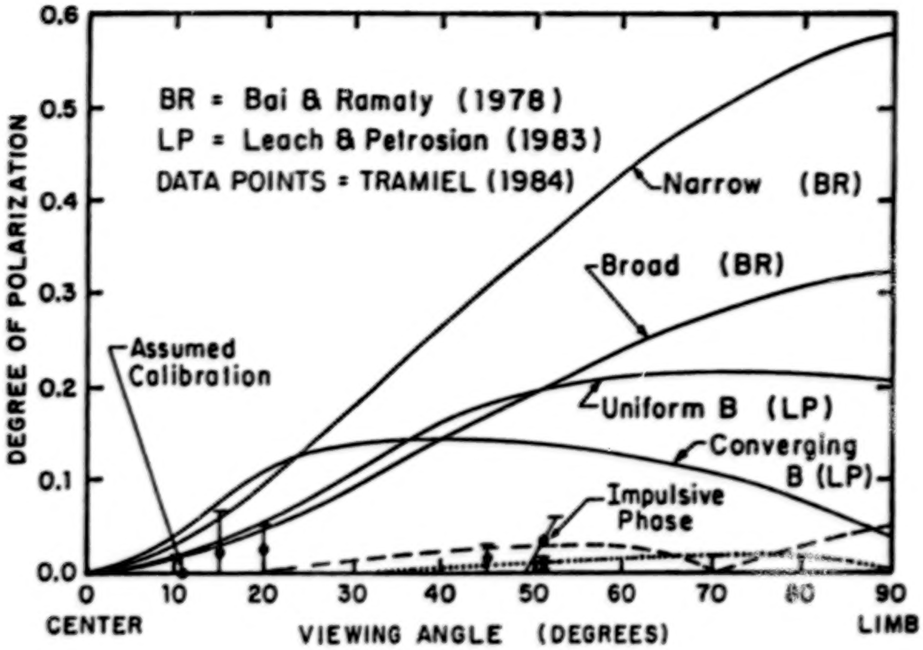

Figure 3: Comparison of the STS-3 polarization results with the calculation of Bai and Ramaty (1978) and Leach and Petrosian (1983). Note that the STS-3 results are lower than all of the theoretical predictions. The points marked "Assumed Calibration" were obtained near the center of the solar disc where the polarization is expected to be zero. This fact was exploited to determine the instrumental polarization.

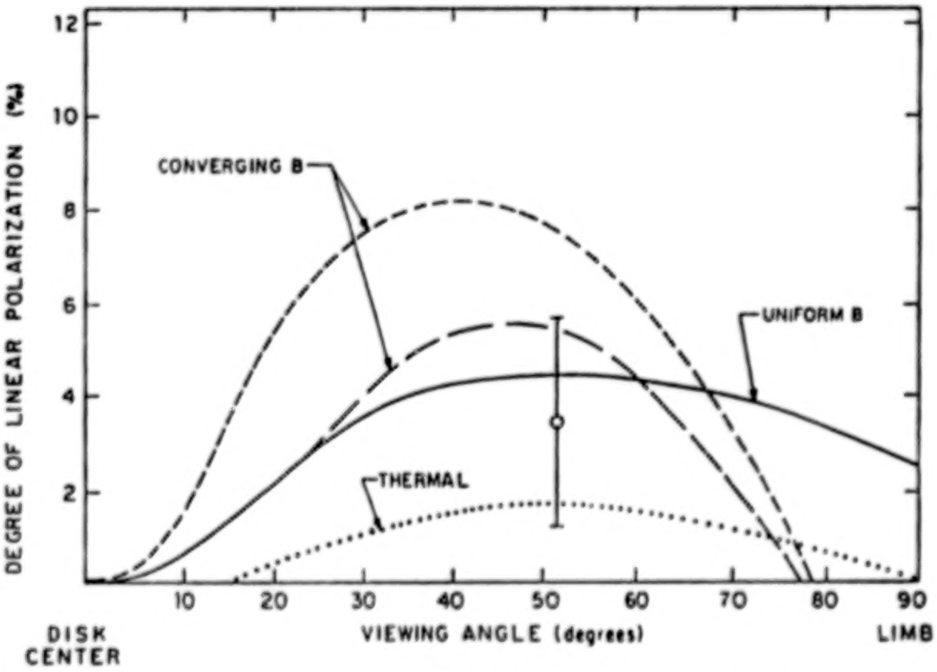

Figure 4: Comparison of the STS-3 impulsive event polarization result with theoretical predictions of Leach, Emslie, and Petrosian (1985). The reader is referred to the theoretical paper for details of the three different theoretical results that are shown in this figure.

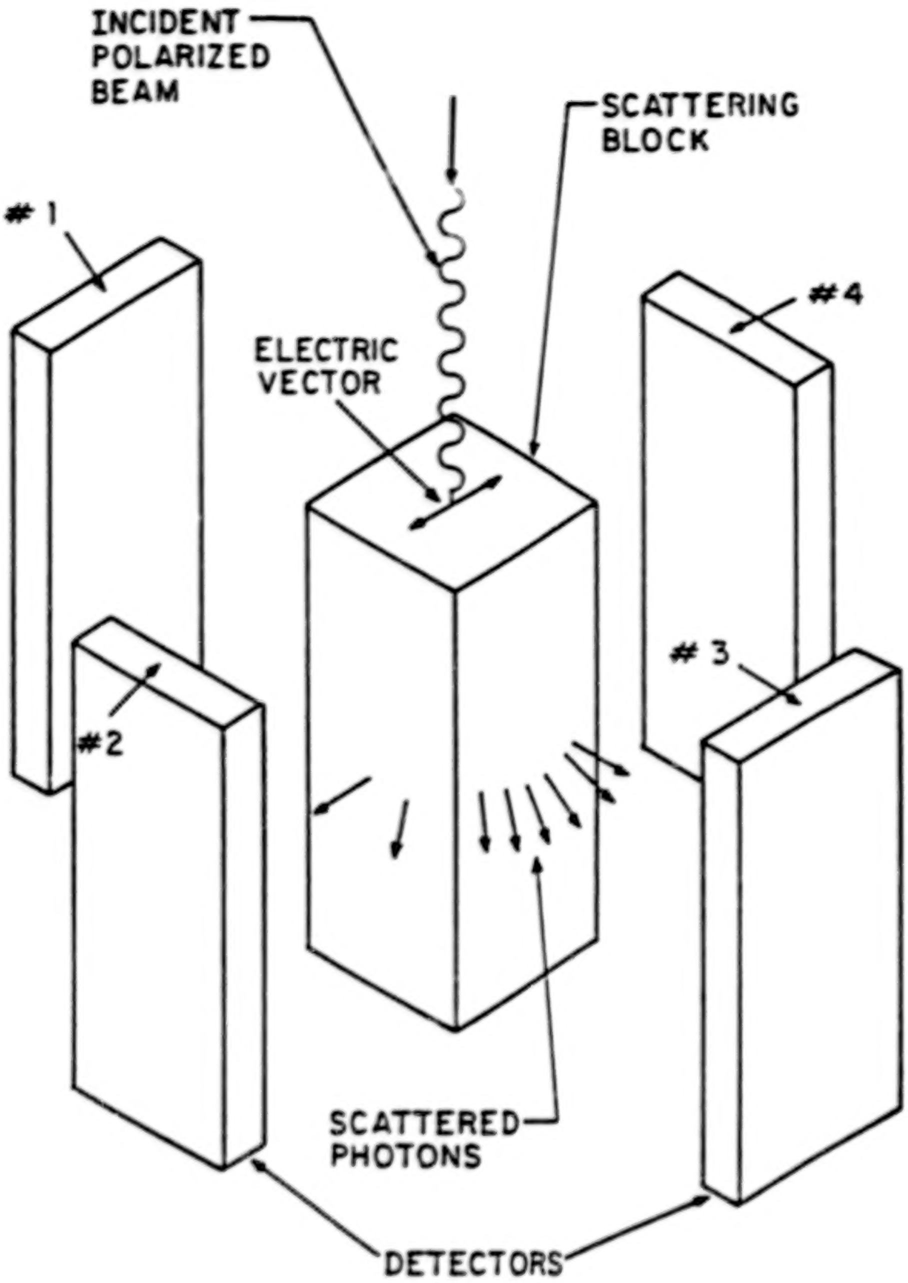
INCIDENT POLARIZED BEAM
SCATTERING BLOCK
# 1
#4
ELECTRIC VECTOR
# 3
#2
SCATTERED PHOTONS
DETECTORS

Figure 5: Scattering polarimeter concept.

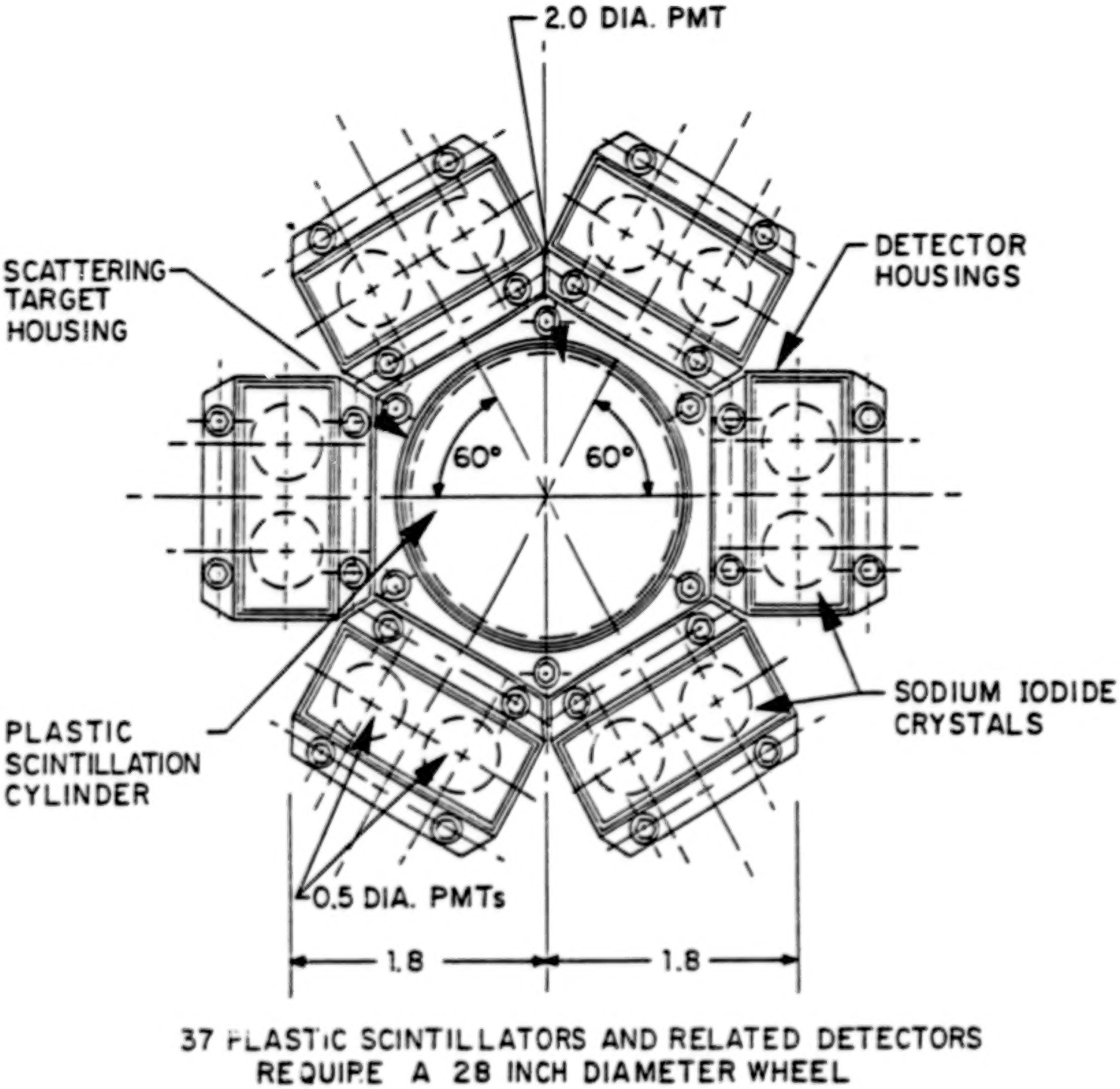
2.0 DIA. PMT
SCATTERING TARGET HOUSING
DETECTOR HOUSINGS
60°
60°
PLASTIC SCINTILLATION CYLINDER
SODIUM IODIDE CRYSTALS
0.5 DIA. PMTs
1.8
1.8
37 PLASTIC SCINTILLATORS AND RELATED DETECTORS
REQUIRE A 28 INCH DIAMETER WHEEL

Figure 6: Basic hexagonal polarimeter configuration. Note that the scattering target consists of an active scintillator which produces a light pulse when a Compton scattering event takes place in the target. The scattered photon is recorded by one of the six NaI(Tl) detectors that surround the target.

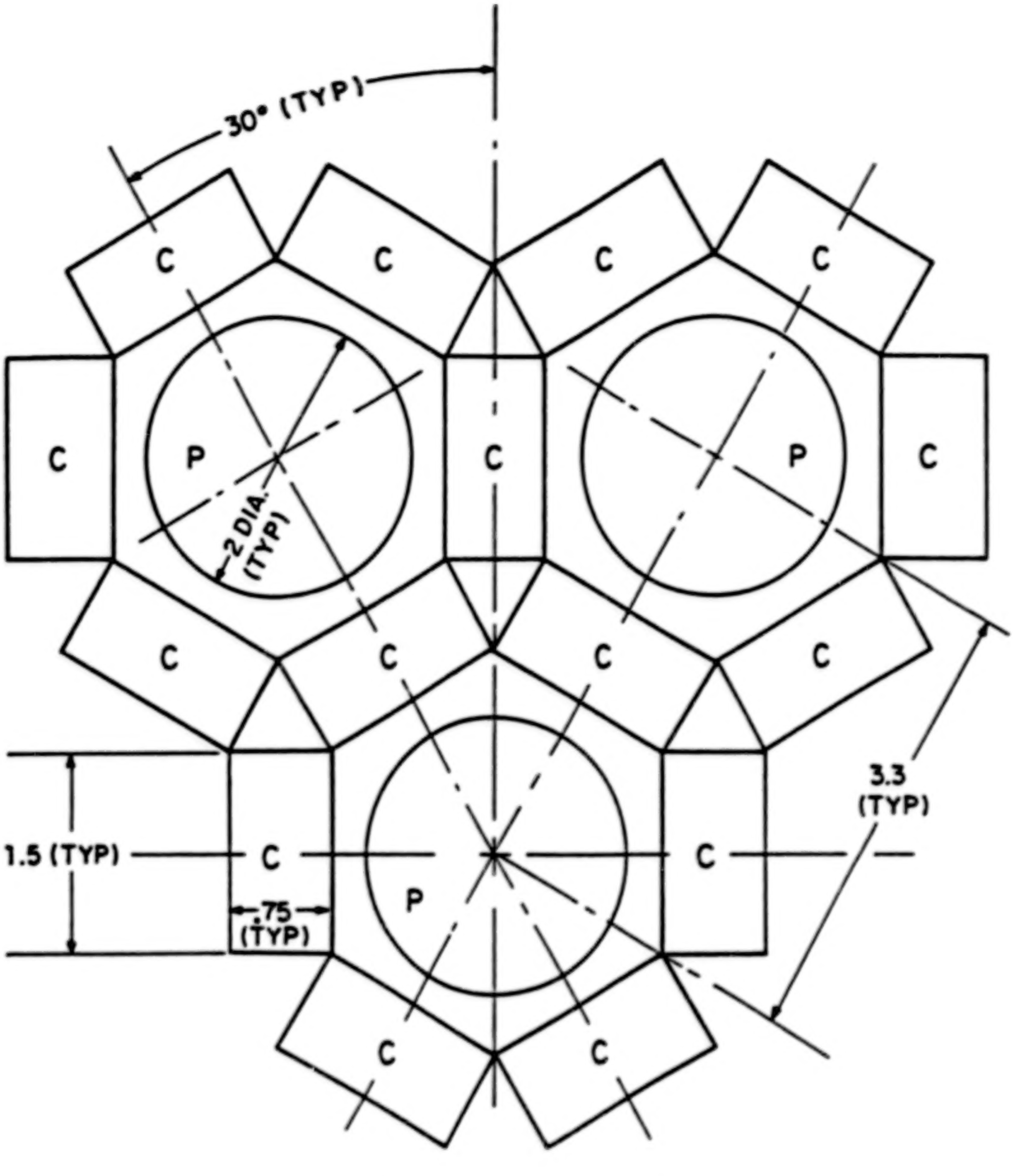
30° (TYP)
C
C
C
C
C
P
C
P
C
2 DIA. (TYP)
C
C
C
C
3.3 (TYP)
1.5 (TYP)
C
P
C
.75 (TYP)
C
C

C = SODIUM IODIDE DETECTOR
P = PLASTIC SCINTILLATOR

FULL SIZE
DIMENSIONS IN INCHES

Figure 7: Assembly of three scintillation targets and surrounding NaI(Tl) detectors.

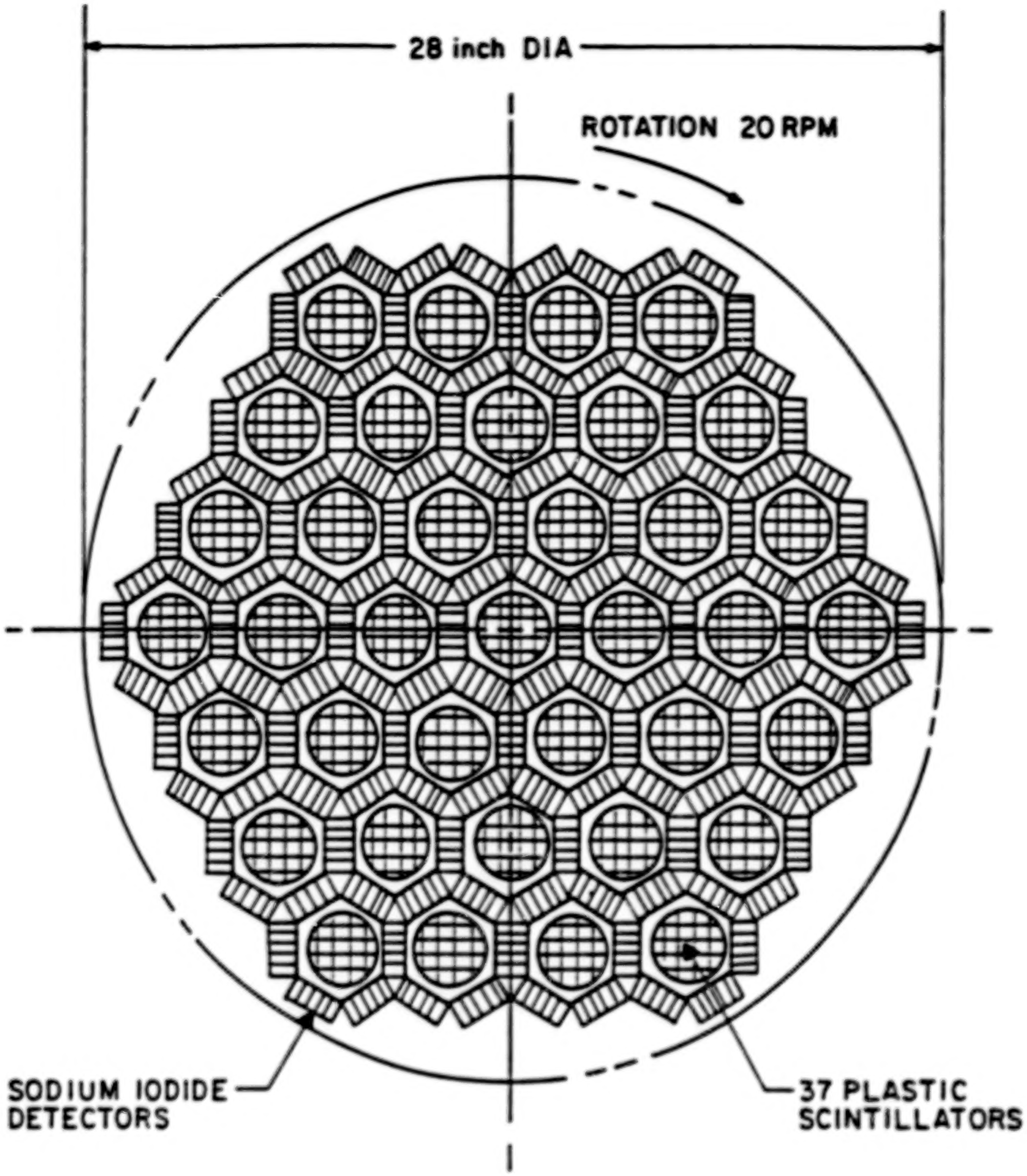
28 inch DIA
ROTATION 20 RPM
SODIUM IODIDE DETECTORS
37 PLASTIC SCINTILLATORS

Figure 8: Complete solar flare polarimeter consisting of 37 scintillator targets and surrounding NaI(Tl) detectors. The entire assembly will be rotated at 20 RPM. This avoids many possible systematic errors that could arise in a static polarimeter in which one must compare the signals in different NaI(Tl) detectors. With rotation polarization manifests itself as a modulation of the signals in each of the NaI(Tl) detectors, the amplitude of modulation is simply related to the degree of polarization and the phase of the modulation to the position angle of the polarization vector.

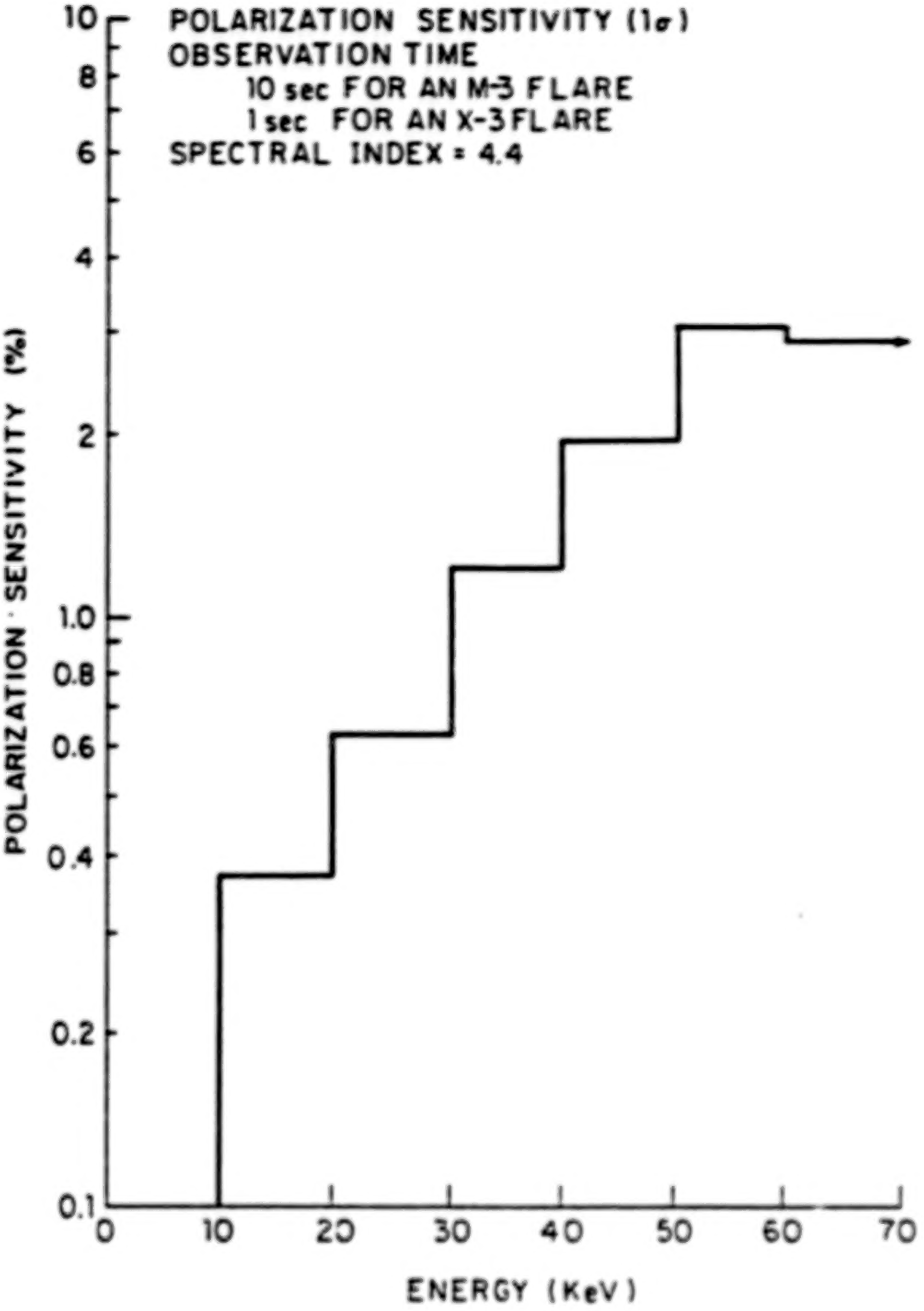

Figure 9: Sensitivity of the polarimeter to an M-3 flare in 10 seconds or an X-3 flare in 1 second. In both cases we have assumed a spectral index of 4.4. Note that the highest energy bin extends up to 150 keV.

N87
21790
UNCLAS

N87-21790

PERSISTENT TIME INTERVALS BETWEEN FEATURES IN SOLAR FLARE HARD X-RAY EMISSION

Upendra D. Desai and Chryssa Kouveliotou

Laboratory for Astronomy and Solar Physics
NASA Goddard Space Flight Center

C. Barat, K. Hurley, M. Niel, R. Talon, and G. Vedrenne

Centre d'Etudes Spatiale de Rayonnment
Toulouse, France

Abstract

Several solar hard X-ray events (> 100 keV) have been observed simultaneously with identical instruments on the Venera 11, 12, 13, 14 and Prognoz spacecraft. High time resolution (= 2 ms) data were stored in memory when a trigger occurred. We present the observations of modulation with a period of 1.6s for the event on 1978 December 3. We also present evidence for fast time fluctuations from an event on November 6, 1979, observed from Venera 12 and another on September 6, 1981, observed from the Solar Maximum Mission. We have used power spectrum analysis, epoch folding, and Monte Carlo simulation to evaluate the statistical significance of persistent time delays between features. The results are discussed in light of the MHD model proposed by Zaitsev and Stepanov (Soviet Astron. Letters, 1982, 8, 132, and Solar Physics, 1984, 92, 283).

1. Introduction

Light curves of a number of solar flare events observed in microwaves and/or X-rays with high time resolution (~ 0.1 s) show distinctive features during the rise and/or decay phases. The time histories of hard X-rays observations with time resolution of about a second on TD-1A could be resolved into "elementary flare bursts" with full width at half maximum of 4 to 25 s (van Beek 1974, de Jager and de Jonge 1978). The study of a number of such elementary flare bursts in a single event or their distribution in time was not pursued in earlier papers. Recently, Loran et al. (1985) have simulated the fast ripple structure by incorporating in their model a variable repetition rate of these elementary bursts. Sturrock et al. (1984) have tried to associate elementary event bursts with "elementary flux tubes", thus suggesting that the features are spatial in origin. However, Ohki (1985) reports from Hinotori imaging data that the small size of the sources of impulsive flares and the lack of motion indicate that spikes are temporal rather than spatial in origin, i.e. that the same flux tube flares repeatedly.

Pioneering observations of solar hard X-rays (> 20 keV) by Parks and Winckler (1969) with a balloon-borne detector revealed significant power at a period of 16 s. They also reported similar simultaneous behavior in microwaves at 15.4 GHz. Frost (1969) reported the existence of modulation in OSO-5 data with a period of 35 s. Rosenberg (1970) analysing the solar radio event of February 15, 1969 (160-320 MHz), reported modulations with a period of 1 s. He explained the modulations on the basis of magnetohydrodynamic (MHD) oscillations in a coronal magnetic flux tube. Janssens et al. (1973) also reported periodicities in radio data. In two homologous microwave events on May 29, 1980, Urpo (1983) has reported features with an average separation of 3.04 s. Recently Zodi et al. (1984) have reported 1.5 s pulsations in both 22 GHz and 44 GHz high time resolution microwave data. Wiehl and Matzler (1980) studied both hard X-ray and microwave events and reported the existence of quasi-periodic modulations with periods as short as five seconds. In their study a change of slope during the rise or fall was accepted as a modulation feature.

In the studies mentioned above emphasis has been given on results that demonstrate periodicities or quasi-periodicities. We present solar events which show the prevalence of persistent time-delays between successive or alternate features indicative of the existence of a synchronized series of features. We examine this in the light of the proposed MHD model of Zaitsev and Stepanov (1982, 1984). Various models have been proposed to explain pulsations both in hard X-rays and in radio data (Rosenberg 1970, McClean et al. 1975, Chiu 1970).

Power spectrum analysis of transient events to find out periods which are fractions of the total duration of the transients are not adequate. We have also pursued auto correlation, the epoch-folding technique, and Monte-Carlo stimulation to statistically evaluate the persistence of delay times between features. In highly dynamic turbulent phenomena like solar flares, strict periodicities may not prevail but parameter dependent characteristic times - rise, decay, and delay times - could prevail.

2. Observations

Observations reported here were made on the Venera 12 deep space probe (V_{12}) and the Earth orbiting Solar Maximum Mission (SMM) satellite. Detailed discriptions of the instrumentation have appeared in Barat et al. (1981), Chambon et al. (1979), and Orwig et al. (1980). The basic detectors on V_{12} are 4.5-cm radius, 3.7-cm thick NaI(Tℓ) scintillators with a plastic anticoincidence shield; the Hard X-Ray Burst Spectrometer (HXRBS) on SMM consists of a CsI(Na) scintillator surrounded by a CsI(Na) shield with an opening angle of ~ 40° FWHM. In both detectors, an increase in counting rate above a certain threshold initiates data storage in memory. The finest time resolution available is 2 ms for V_{12} and 1 ms for SMM. The average photon energy threshold is ~ 100 keV for V_{12} and ~ 30 keV for SMM. For the present study data with 109 ms and 15 ms integration are used for V_{12} and 128 ms for SMM data.

The Event on 1978 December 3

On 1978 December 3 at 20^h30^m UT, an Hα flare of importance SB was observed from McMath region 15694 located at S22E65. Figure 1 shows the time history of the hard X-rays observed from V_{12} with 109 ms resolution. V_{12} was closer to the Sun than Earth-orbiting spacecraft and consequently had better statistics. The total duration of the event was 16 s with the maximum counting rate occurring 9 s from the start. Significant temporal variations are seen during the rising phase. The filtered data are shown at the bottom of Figure 1 with the times of various statistically significant peaks indicated. Two series of peaks with delay times of about 1.6 s are indicated in the figure. Figure 5 shows the histograms of the delay times between alternate features. The amplitude of the pulses of the first series appears to be constant while the amplitude of the second series of pulses is growing. The average pulse profile after proper phase folding for 6 cycles is also indicated in Figure 4a. The shape of the first series of pulses is symmetrical with rise and decay times of about 300 ms. The time-varying second series of pulses is poorly defined statistically. During the decay phase after about 11 s, the pulsations are significantly attenuated.

Bogovalov et al. (1983) have analysed several solar events for quasi-periodicities and have reported for this same 1978 December 3 event pulsation frequencies of 1.22 ± 0.03 Hz and 0.50 ± 0.03 Hz with 99% confidence limits. We have also carried out the power spectrum analysis and agree with their results, but to emphasise the existence of two synchronised series of features, we have also used the epoch-folding technique and evaluated the χ^2 for various periods. We found that χ^2 peaks at a period of 1.64 s.

The light curve of this event shows a succession of ten prominent peaks. The times of occurrence of all ten peaks can be described as a periodic series of seven peaks with an "inter-pulse" which occasionally appears at a stable phase. The probability of the peaks happening with this arrangement can be calculated by a Monte Carlo simulation. Specifically, we ask what is the probability that ten peaks can be randomly scattered and yield ten "hits" to a periodic peak with interpulse. In one thousand Monte Carlo trials none demonstrated periodicity. In fact, on average, only four out of ten peaks could be fitted into a periodic pattern.

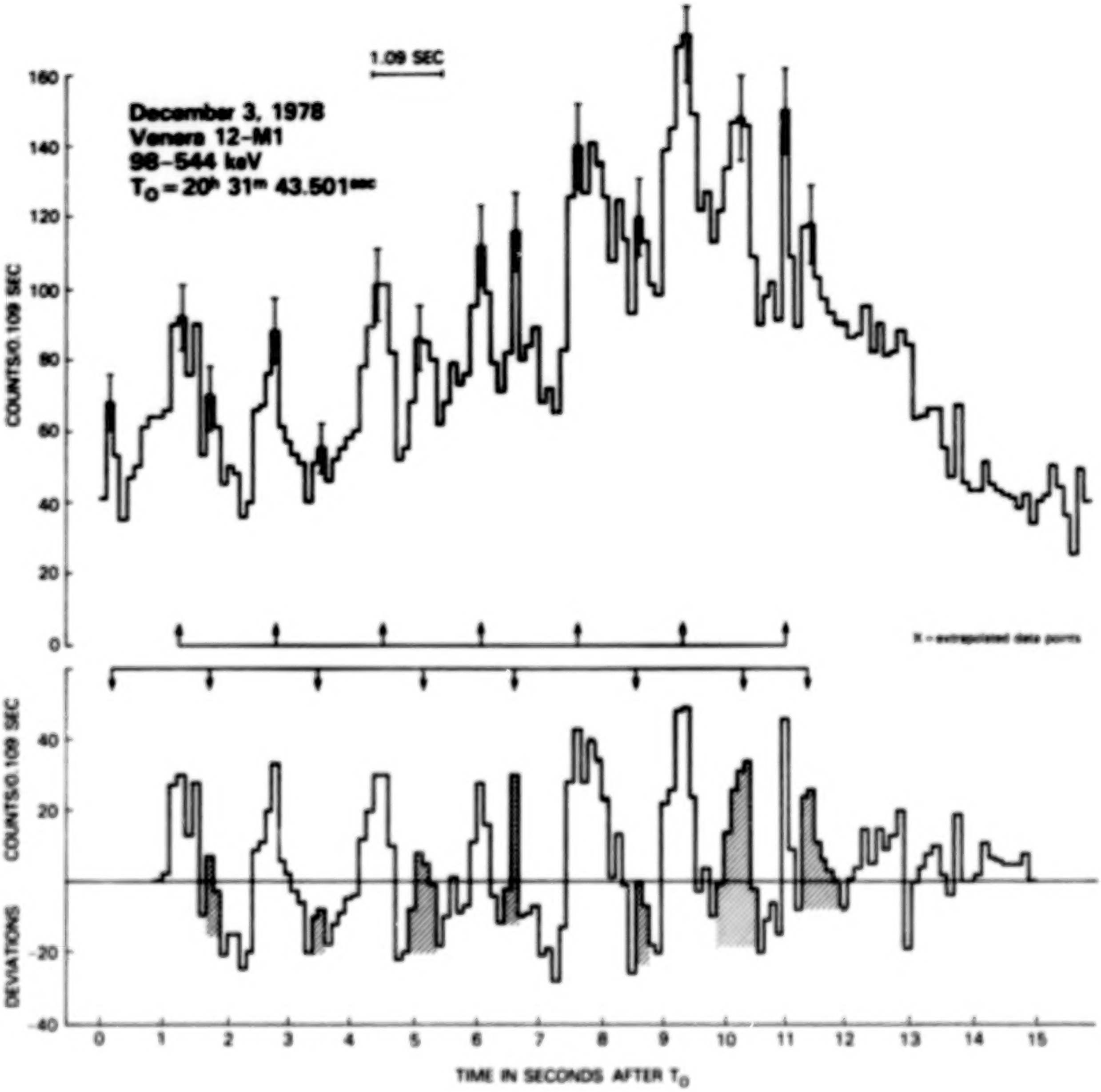

Figure 1. Time history of the December 3, 1978 event with the filtered variational part shown by the lower curve. Arrows indicate the 2 synchronized time series mentioned in the text.

The Event on 1969 November 6

A second event occurred on 1969 November 6 at 08^h38^m UT. Figure 2 shows the light curve with 109 ms resolution. The total duration of the event is about 10 s. There are three major features and three secondary features. The delay times between both series are indicated in Figure 2. The folded light curve of the pulse profiles is presented in Figure 4b with a time resolution of about 15 ms. Time variations down to 30 ms are seen in the average pulse profile. The initial rise occurs within 150 ms and the decay takes ~ 360 ms. The distribution of interval times between features is shown in Figure 5.

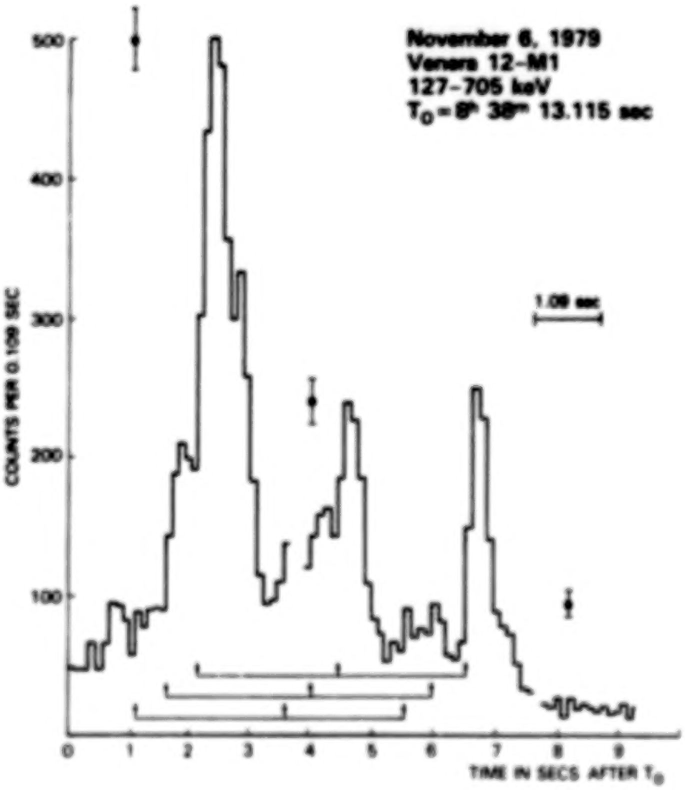

Figure 2. Time history of the November 6, 1979 event.

The Event on 1981 September 6

Another short event which shows well defined multiple pulse structure occurred on 1981 September 6 at 23^h53^m UT. Figure 3a shows the total event. A time-expanded view of both the initial low level and later high intensity multiple structures are shown in Figure 3b. There is a total of nine peaks with a characteristic time delay of ∼ 2.5 s. The light curve could also be interpreted as repetitive groups of three peaks with a time delay of about 6 s. The successive light curves of these groups are shown in Figure 4c. This pattern is revealed at energies up to 300 keV. The distribution of interval times between features is shown in Figure 5.

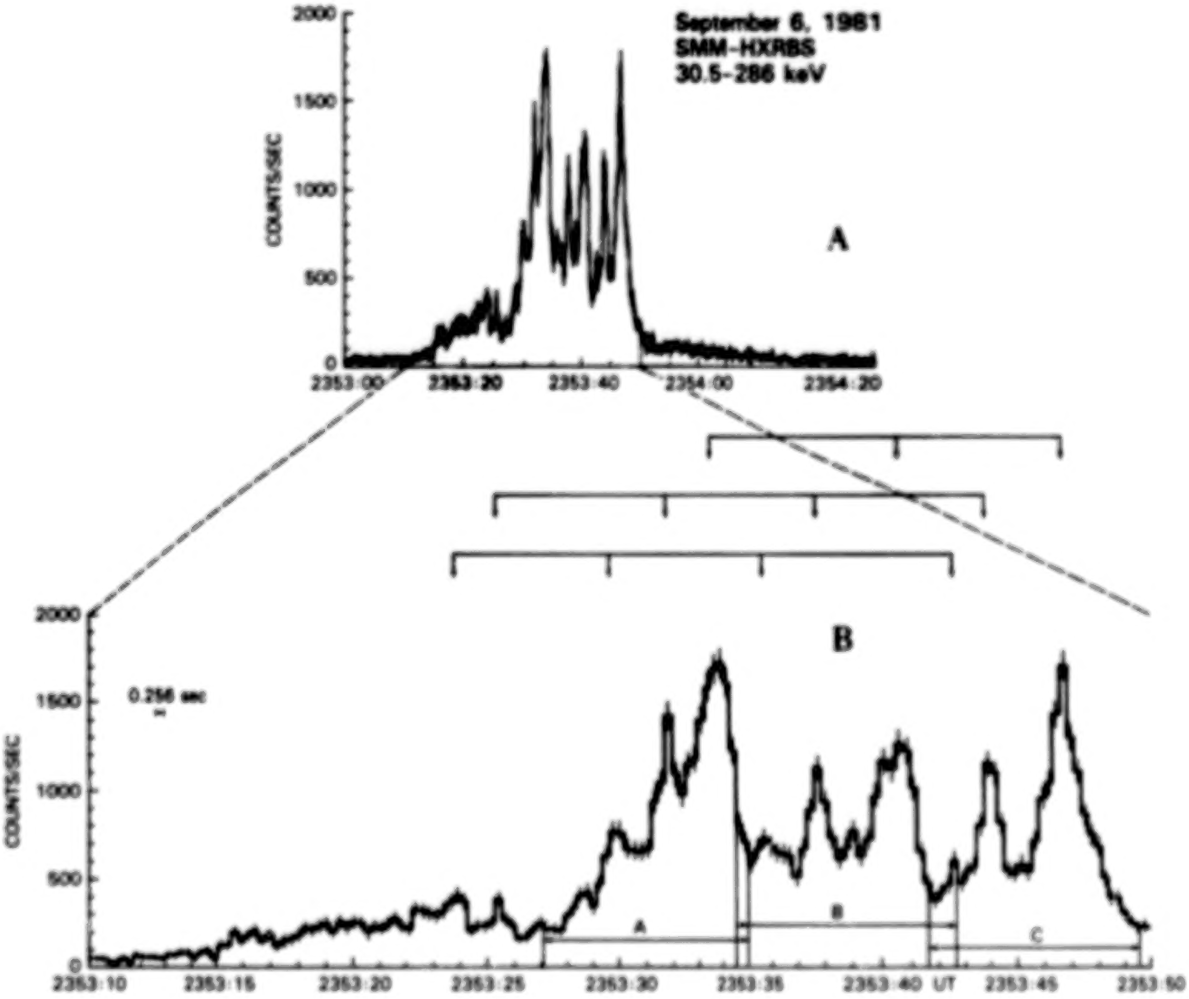

Figure 3. Time history of the September 6, 1981 event.

In order to evaluate the characteristic parameters of the repetitive features we have epoch-folded appropriate intervals of the light curves of events 1 and 2 and the results are shown in Figure 4a and 4b, respectively. The similarities of the features of the third event are revealed by the aligned profiles of Figure 4c.

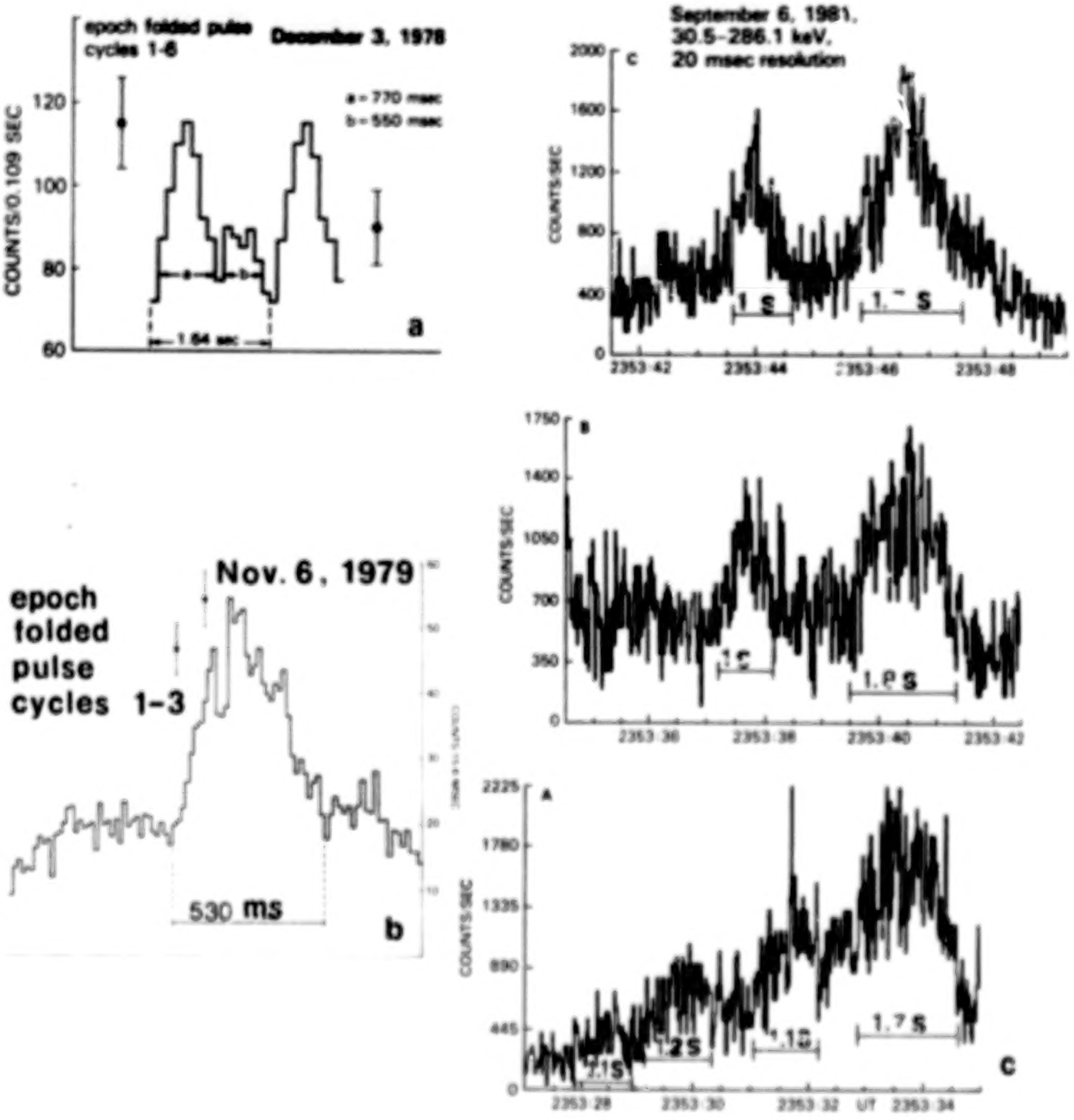

Figure 4. Common temporal aspects of the pulsed features of events 1, 2 and 3.

All of these events are short with total durations not exceeding 40 s. Significant features with widths of about a second are revealed as distinct peaks with persistant delays between them. The characteristic time delay for three events is 1.6 s, 2.3 s, and 6 s, respectively. Figure 5 shows the frequency distribution of these intervals for all 3 events.

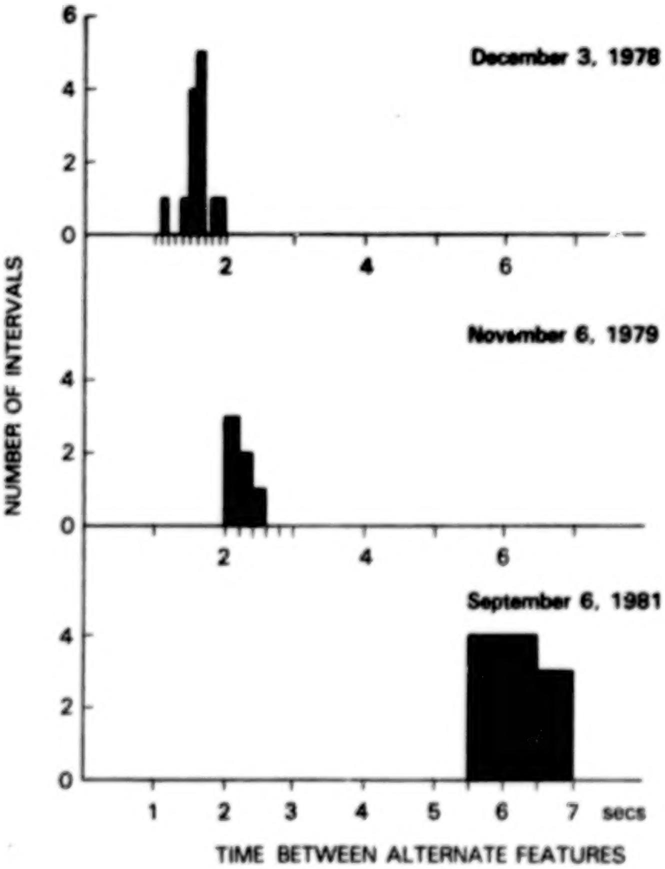

Figure 5. Frequency distribution of the alternate time intervals between significant features of the three events.

The ratio of the amplitude of the pulse ΔJ to the average intensity J is ~ 50%. The pulses occur at energies up to 360 keV. The amplitude of the successive peaks of the December 3 event are nearly constant giving a high value of the quality Q of the assumed generating oscillator, where $Q = \pi t/P$, t is the e-folding time of the decrease in the pulse amplitude, and P is the pulse period. In Figure 6a,b, and c, we show the simultaneous behavior at various energies for all events.

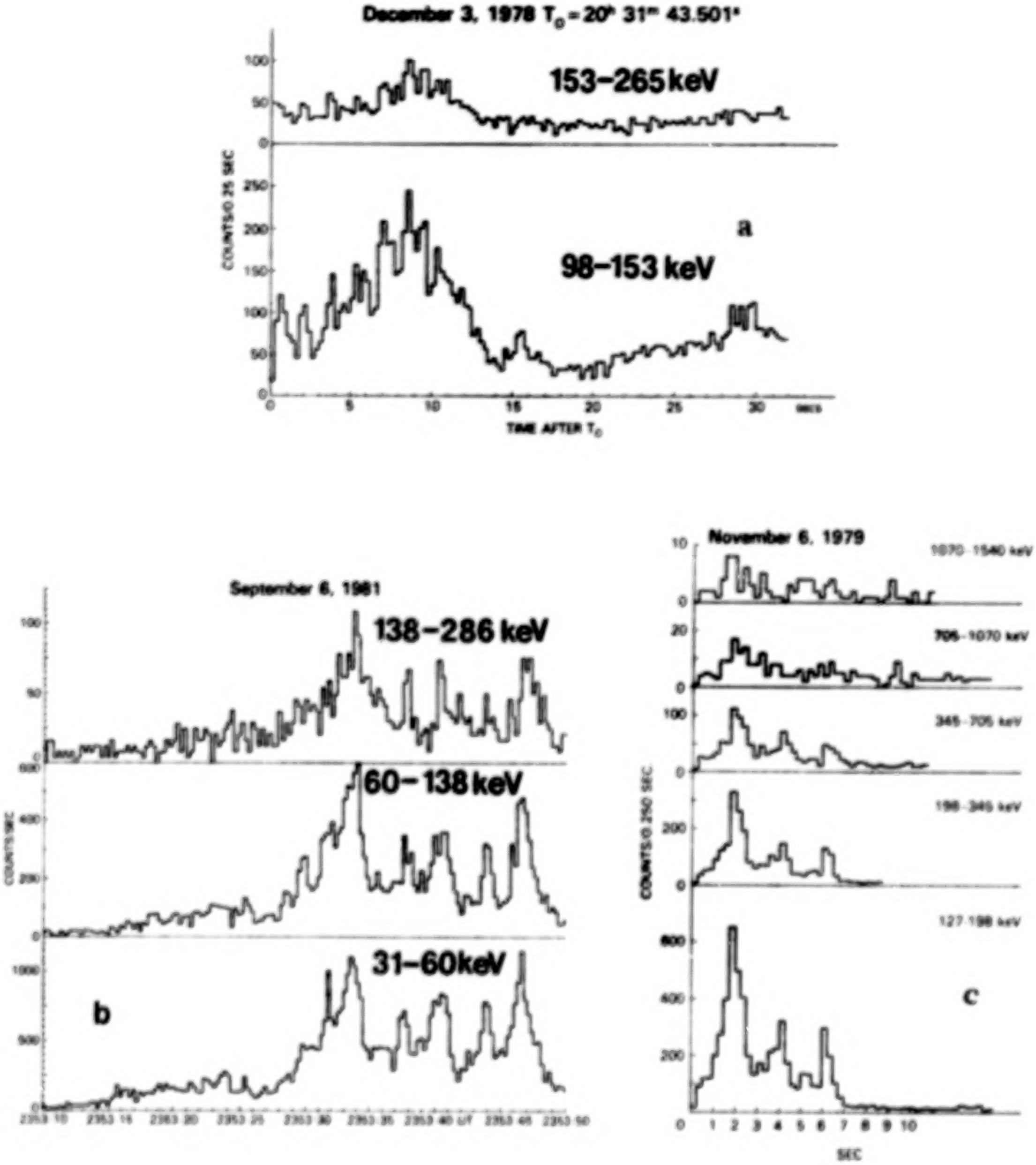

Figure 6. Time profiles at various energies for all 3 events.

We have studied the evolution of the X-ray spectrum for the event of September 6, 1981 with a time resolution of 256 ms. Figure 7 shows the spectral index A_2 of the best fitted power law along with the intensity profile of the event. At least three of the peaks are associated with lower power law index values indicating a harder spectrum than in the valleys. This type of behavior of spectral variation is also reported by Kosugi (1985) at this meeting.

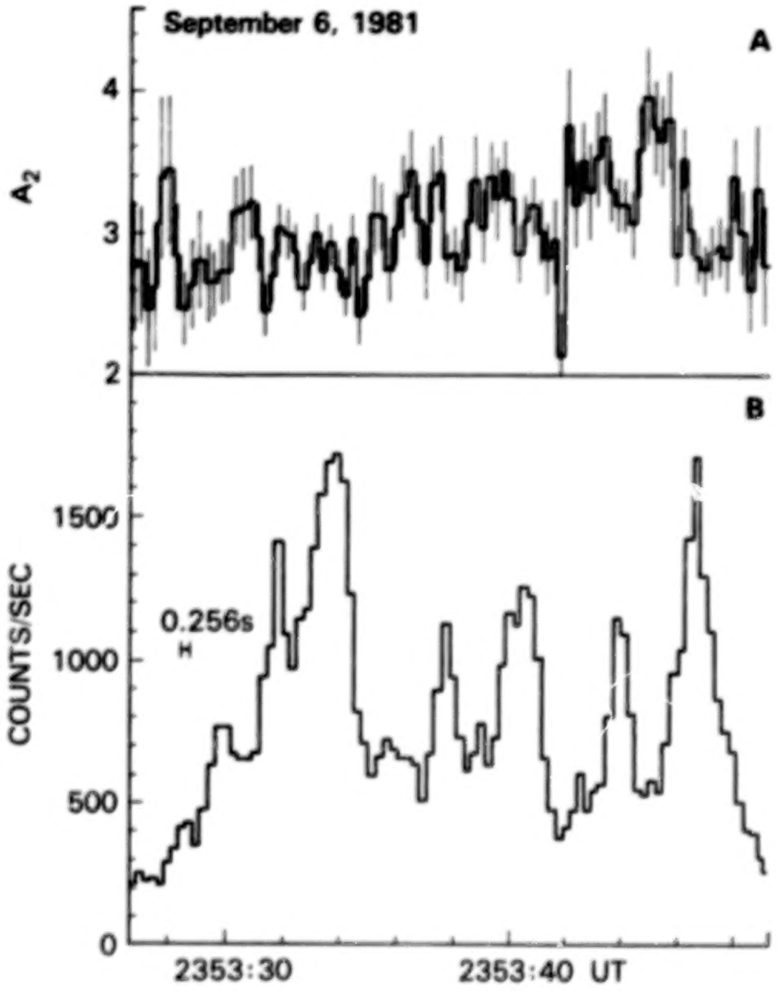

Figure 7. Temporal variation of the power law index A_2 and the HXRBS count rate for the event of September 6 in the energy range from 30 to 290 keV.

In the MHD model reported by Zaitsev and Stepanov (1982, 1984), compact ($\leq 10^{10}$ cm) magnetic loops with plasma density and electron temperature one or two orders of magnitude higher than the ambient values are considered as the resonators for fast mode MHD waves. The period P of fast magnetoacoustic oscillations in a loop with a radius r that is much smaller than the length is given by the following expression:

$$P = r(c_A^2 + c_s^2)^{-1/2}$$

where c_A is the Alfven speed and c_s is the sound speed. With r between 10^8 and 10^9cm and $(c_A^2 + c_s^2)^{1/2} \approx 10^8$cm s^{-1}, one gets P in the range of 1-10s, in good agreement with our results. Values of the period P, the degree of modulation $\Delta J/J$, and the quality of the oscillator Q obtained from the observations enable estimations to be made of the plasma density, the plasma temperature, and the magnetic field strength in the loop (Zaitsev and Stepanov, 1982).

This type of analysis for the three events presented here indicates temperatures of $\sim 10^7$ K, magnetic fields of ~ 100 Gauss and plasma densities between 10^{10} and 10^{12}cm^{-3}. These are in general agreement with values of these parameters derived from other models.

We want to thank B.R. Dennis for providing SMM-HXRBS data, for critically reviewing the text, and for suggesting valuable improvements for this final presentation.

References

Barat, C., Chambon, G., Hurley, K., Niel, M., Vedrenne, G., Estulin, I.V., Kuznetsov, A.V. Zenchenko, V.M., 1981, Sp. Sci. Inst., 5, 229.

Bogovalov, S.V., Iyudin, A.F., Kotov, Yu D., Dolidze, V.I., Estulin, I.V., Vedrenne, G., Niel, M., Barat, C., Chambon G. and Talon, M. 1983, Sov. Astron. Lett., 9, 3.

Chambon, G., Hurley, K., Niel, M., Vedrenne, G., Zenchenko, V.M., Kuznetsov, A.V., and Estulin, I.G., 1979, Sp. Sci. Instr., 5, 340

Chiu, Y., 1970, Sol Phys., 13, 420.

de Jager, C. and de Jonge, G., 1978, Solar Phys., 58, 127.

Frost, K., 1969, Ap.J., 155, L159.

Janssens, J.J., White III, K.P. and Broussard, R.M., 1973, Solar Phys., 31, 307.

Kosugi, T., 1985, these proceedings.

Loran, J.M., Brown, J.C., Correia, Emilia and Kaufmann, P., 1985, Solar Phys., 97, 363.

McLean D.I., Sheridan, K.V., Stewart R.T. and Wild, I.P. 1971, Nature, 234, 140.

Ohki, K., 1985, these proceedings

Orwig, L., Frost, K.J. and Dennis, B.R., 1980, Sol. Phys., 65, 25.

Parks and Winckler, 1969, Ap.J., 155, L117.
Rosenberg, H., 1970, Astron. & Astrophys., 9, 159.
Urpo, S., 1983, Adv. Space Res., Vol. 2, 11, 105.
van Beek, H.F., de Feiter, L.D. and de Jager, C., 1974, Space Research XIV, 447.
Wiehl H. & Matzler, C., 1980, Astron. & Astrophys., 82, 93.
Zaitsev & Stepanov, 1982, Soviet Astron. Lett., 8, 132.
Zaitsev & Stepanov, 1984, Sol. Phys., 93, 363.

N87
21791
UNCLAS

N87-21791

EVIDENCE FOR BEAMED ELECTRONS IN A LIMB X-RAY FLARE OBSERVED BY HXIS

Eberhard Haug and Gerhard Elwert

Lehrstuhl für Theoretische Astrophysik
Universität Tübingen, F.R.G.

The limb flare of 1980 November 18, 14:51 UT, was investigated on the basis of X-ray images taken by the Hard X-ray Imaging Spectrometer (HXIS) and of X-ray spectra from the Hard X-Ray Burst Spectrometer (HXRBS) aboard SMM. The impulsive burst was also recorded at microwave frequencies between 2 and 20 GHz whereas no optical flare and no radio event at frequencies below 1 GHz was reported. The flare occurred directly at the SW limb of the solar disk; this fact allows to study the height variation of the X-ray emission. During the impulsive phase several X-ray bursts of short duration (elementary flare bursts) were recorded by HXRBS at energies between 29 and ~300 keV (Fig.1) and by the high-energy bands of HXIS (16 - 30 keV).

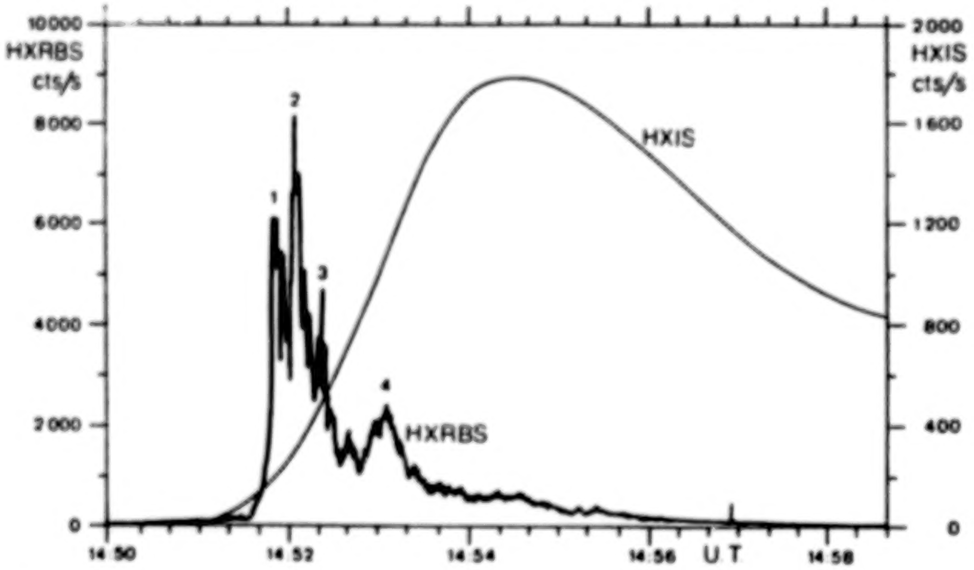

Fig. 1. Time evolution of the soft and hard X-radiation as observed by HXIS and HXRBS, respectively.

Deconvolved contour maps of the flare site (Fig.2) show that during the short-term spikes the 22 - 30 keV radiation is mainly emitted from a compact area close to the solar limb. In contrast, the source of the last major X-ray spike which has a longer duration of about 15 sec and a softer

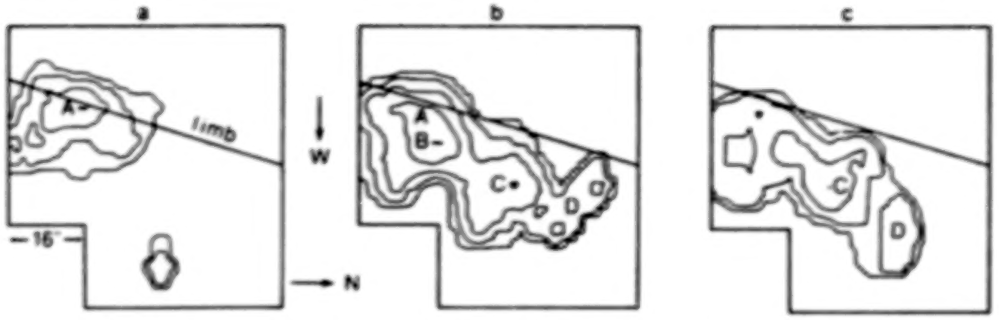

Fig. 2. 22–30 keV contour maps of the flare region for the time periods (a) 14:51:37–14:51:58, (b) 14:52:45–14:53:05, and (c) 14:53:10–14:53:33. The contour levels correspond to 100, 50, 25, 12.5, and 6.25% of the peak counting rate.

spectrum is situated at greater heights in the solar atmosphere. The hard X-ray light curves of the short-time bursts are in very good agreement with the microwave time profiles whereas the broader X-ray spike is missing in microwaves.

Taking advantage of the spatial resolution of the HXIS images (8" corresponding to ~6000 km on the Sun), the time evolution of the X-radiation originating from relatively small source regions can be studied (Fig.3). In particular, the elementary flare bursts which are observed by HXRBS without spatial resolution may be attributed to different source regions.

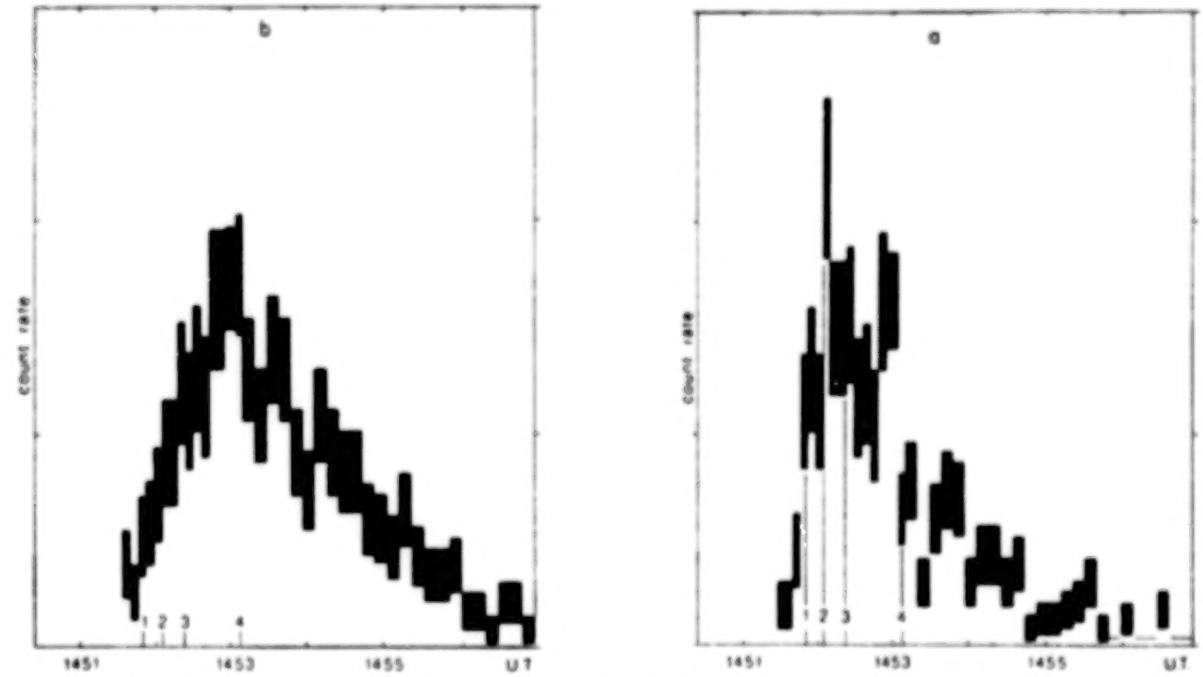

Fig. 3. Time evolution of the 22-30 keV count rates in areas A (a) and B (b). The marks on the abscissae denote the maxima of the corresponding hard X-ray spikes of Figure 1.

During the impulsive phase of the flare the hard X-ray spectra generally could be well fitted to a power law with spectral index γ (Fig.4). Using the HXIS count rates of individual pixels it is possible to determine the spectra of X-rays originating from different source regions. Particularly, in limb flares the height variation of spectra measured simultaneously can be studied. This was performed for the regions around the compact source of the short-term X-ray spikes. During these bursts the spectra are quite hard (γ = 3.2 to 4) and there is a systematic trend of the spectral index γ to increase with increasing height of the source above the solar limb.

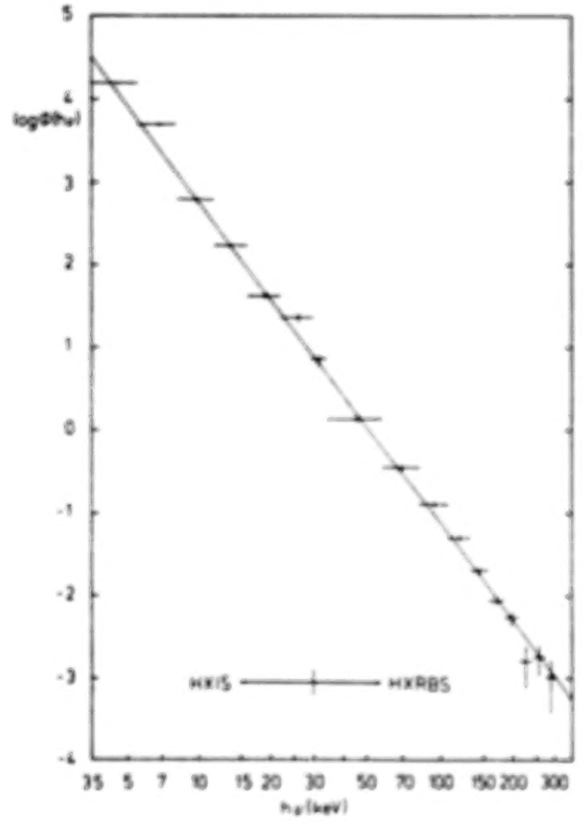

Fig. 4. Composite HXIS and HXRBS spectrum (X-ray flux Φ(hν) in units of $cm^{-2}s^{-1}keV^{-1}$) taken during the first hard X-ray spike around 14:51:56. The straight line represents the best fit to a power law with spectral index γ = 3.88.

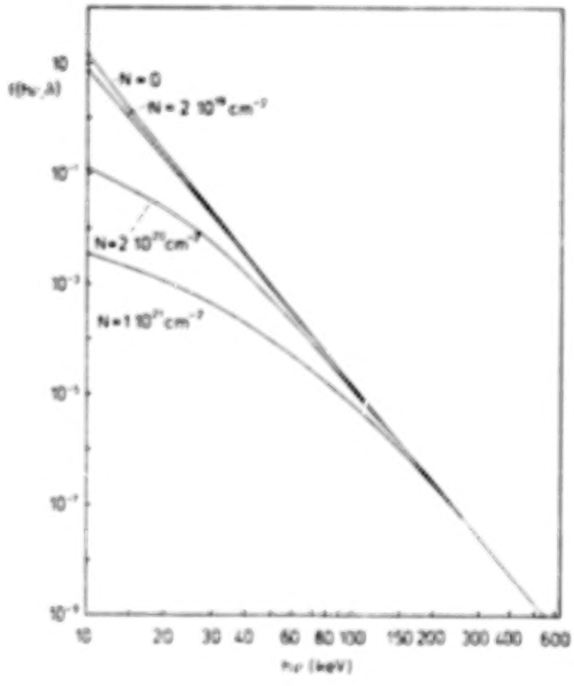

Fig. 5. Theoretical variation of X-ray spectra, produced by electrons injected with a power-law energy distribution, with increasing column density traversed, N. The electron spectral index is δ = 5, and the ordinate scale is in arbitray units.

Using Monte Carlo computations of the energy distribution of energetic electrons traversing the solar plasma, the bremsstrahlung spectra produced by these electrons have been derived (Haug et al., 1985). Under the assumption that the electrons are injected at high altitudes in the corona, e.g., at the top of a magnetic loop, with a power-law spectrum in kinetic energy, the resulting X-ray spectra are hardest at high column densities of the plasma traversed by the electrons, i.e., at low altitudes (Fig.5). This is a consequence of the more rapid slowing down of the less energetic electrons due to Coulomb collisions. The observed hardening of the X-ray spectra with decreasing altitude of the X-ray source is consistent with the existence of nonthermal electron beams precipitating from the corona toward the dense layers of the solar atmosphere. The compact X-ray source situated close to the solar surface can be interpreted as the footpoint of a flaring loop; the other footpoint is occulted by the solar disk. This interpretation is also in accordance with the fact that after the short-term spikes the differences between the γ values of regions at various altitudes have decreased considerably. Moreover, the spectra have softened. These characteristics indicate that the injection of electrons has ceased and that the energetic particles have thermalized.

A full account of this work has been given in Solar Physics 99, 219 (1985).

Reference

Haug, E., Elwert, G., and Rausaria, R.R. 1985, Astron. Astrophys. 146, 159.

N87
21792
UNCLAS

N87-21792

A STUDY OF STARTING TIME IN GREAT HARD X-RAY FLARES

K. L. Klein
M. Pick

Observatoire de Paris
Section de Meudon
92195 Meudon, France

A. Magun

Institut für Angewandte Physik
Sidlerstr. 5
3012 Bern, Switzerland

Abstract

An analysis of the starting time in ten great hard x-ray bursts observed with HXRBS is presented. It is shown that the impulsive phase of nine of them is composed of a pre-flash phase, during which the burst is observed up to an energy limit ranging from some tens of keV to 200 keV, followed ten to some tens of seconds afterwards by a flash phase, where the count rate rises simultaneously in all detector channels. For two events strong gamma-ray line emission is observed and is shown to start close to the onset of the flash phase.

1. Introduction

Hard x-ray and gamma-ray observations from SMM have shown that energetic electrons and ions are accelerated since the early stage of solar flares. There is nevertheless still controversy as to whether high energy electrons and ions are accelerated simultaneously with electrons of lower energy or whether a second, distinct step of acceleration is necessary to account for high particle energies. This controversy arose mainly from analyses of the temporal evolution of hard x-ray bursts, where in a minority of cases high energy peaks were observed to lag those at lower energies. This was ascribed to the acceleration process itself by several authors (e.g. Bai and Ramaty, 1979; Bai and Dennis, 1985), whereas others showed that the interaction of energetic electrons with the background plasma can account for such delays (Vilmer et al., 1982). In fact the interaction effects make the peak time analyses yield ambiguous results. On the other hand, as hard x-ray emission is the immediate response of a plasma to the injection of energetic electrons, the starting time of the burst is not affected by the above-mentioned ambiguities. It is clear, however, that this parameter is influenced by the energy-dependent detector threshold.

Studies of the onset phase of the radiation from energetic electrons in solar flares are still rare. Forrest and Chupp (1983) concluded for two events that the hard x-ray and gamma-ray observations were compatible, within the limits of detector sensitivity, with a simultaneous start of photon emission from 40 keV to 8 MeV. Benz et al. (1983) considered hard x-rays and radio waves at the very beginning of the impulsive phase. They found in some events evidence for two components of the impulsive phase: a weak hard x-ray emission lasting up to one minute, followed by a steep rise within some seconds to the peak count rate. They termed these phases respectively pre-flash and flash phase. Subsequently Raoult et al. (1985) showed for a series of energetic hard x-ray bursts a systematic evolution from the pre-flash phase, associated with metric type III bursts, to the more energetic flash phase with associated continua in the decimetre to metre waveband (type V burst).

In this contribution we present an analysis of the onset phase of hard x-ray bursts aiming at the precise definition of the starting time of the burst in each detector channel. The paper focusses on the observational results. Section 2 introduces the method of analysis and the selection criteria for the studied events. The results are presented in section 3 and discussed in section 4 with respect to relevant observations in other ranges of the electromagnetic spectrum.

2. Method

We have analyzed the starting time of ten hard x-ray bursts observed with the Hard X-ray Burst Spectrometer (HXRBS; Orwig et al., 1980) on the Solar Maximum Mission. These events had peak count rates above 7000 s^{-1} integrated over all detector channels (HXRBS event listing; Dennis et al., 1982). Six of them exhibit significant emission in the 4 to 8 MeV band of the Gamma-Ray Spectrometer (Chupp, pers. comm.). For some of the events ISEE 3 data were also available (courtesy S.R. Kane).

In order to define a starting time of the burst, we computed in each channel the background count rate (mean value) and the noise (standard deviation σ) in the minutes before burst onset. The starting time was defined by the instant after which for the first time three successive count rate values exceeded the background + $n\sigma$ level. We considered separately the cases $n=3$ and $n=5$ in order to have an approximate measure of the uncertainty of our results. In all channels count rates integrated during 1.024 s were used.

3. Results

Fig. 1 shows the results for the strongest event of our sample, the neutron flare of 1982 June 3. Crosses give the photon energy where the count rate exceeds the threshold value, as a function of time: horizontal error bars delimit the time interval between the 3 σ and 5 σ levels' being exceeded (if no error bars are plotted, these levels are exceeded simultaneously), vertical error bars represent

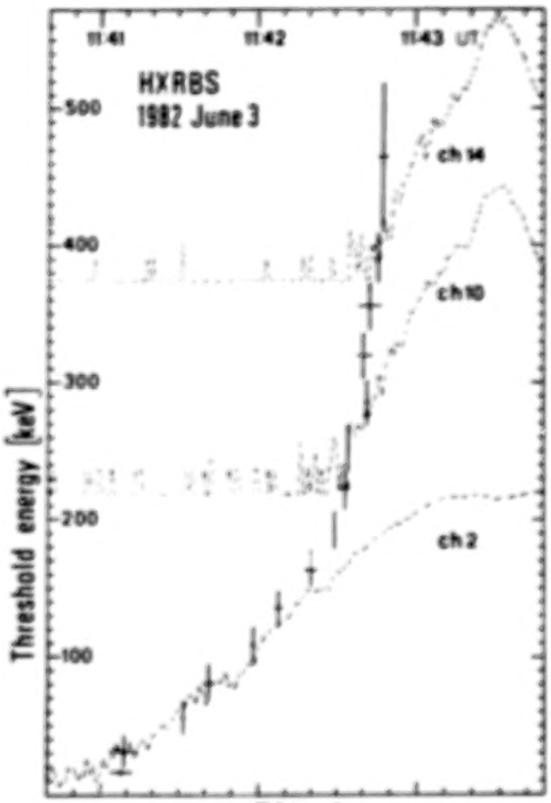

Fig. 1

the width of the detector channels. For the purpose of illustration we have also plotted – on a logarithmic scale – the count rate time histories in three HXRBS channels. At low photon energies the burst starts with apparent delays of several seconds between successive detector channels. After some tens of seconds the delays shorten and at high photon energies the emission starts nearly simultaneously in all channels. This rapid rise of the count rate, which is the first feature of the burst detected at high energies, is also discerned at lower energies, but there its start is masked by the preceding emission. The delays between successive channels, which are particularly important at low energies, are seen to be at least partly an artefact due to the energy-dependent detector threshold.

Figs. 2.a, b compare the results obtained with HXRBS and with ISEE 3 for the 1980 June 7 event and the one of fig. 1.Despite of differences introduced by the detector characteristics, the global pictures converge: Low-energy emission is detected first, with an apparent delay between adjacent channels. Some tens of

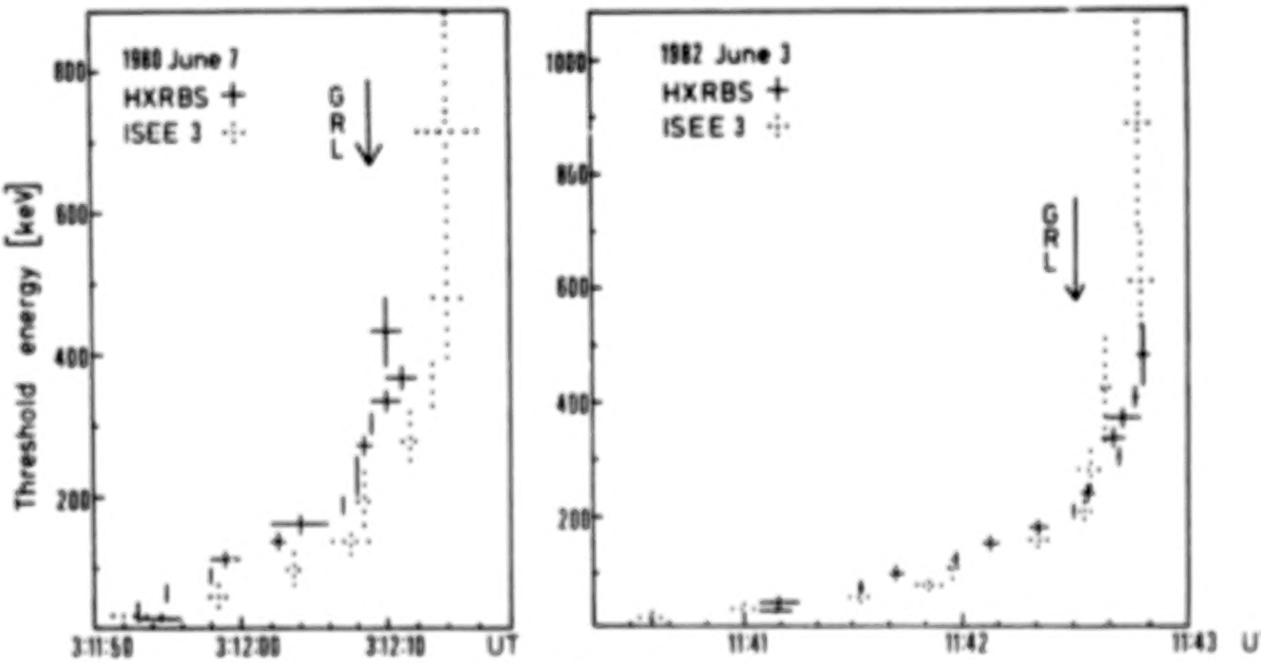

Fig. 2

2 OF 6

N87-21785 UNCLAS

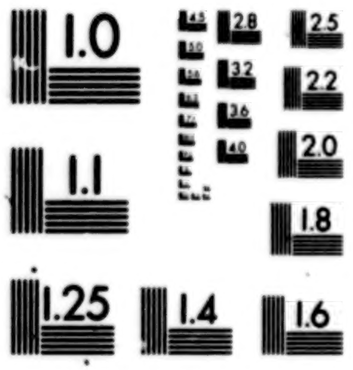
1.0
4.5
5.0
5.6
6.3
7.1
2.8
3.2
3.6
4.0
2.5
2.2
2.0
1.1
1.8
1.25
1.4
1.6

MICROCOPY RESOLUTION TEST CHART
NATIONAL BUREAU OF STANDARDS
STANDARD REFERENCE MATERIAL 1010a
(ANSI and ISO TEST CHART No. 2)

seconds after the first signature at low energies a rapid rise occurs as a distinctive feature in all channels, and during which the detection threshold is exceeded in the high energy channels nearly simultaneously. In accordance with the terminology of Benz et al. (1983), we refer to these two phases as pre-flash and flash phase, respectively. The onset times of the flash phase observed with HXRBS and ISEE 3 are seen to coincide within some seconds. Both events exhibit strong excess emission in the 4-8 MeV photon energy range. This emission (Forrest and Chupp, 1983; Chupp, pers. comm.) starts, as indicated by the arrows in figs. 2.a, b, close to the onset of the flash phase of hard x-rays.

As at low energies the start of the flash phase is masked by the pre-flash emission, it cannot be analyzed by the method of section 2. We attempted to get an indication of the starting time by extrapolating the observed rise back to zero through a straight line. This was possible for four events of our sample. The starting time of the flash phase found this way in the low energy channels agreed with that in the high energy channels obtained with the method of section 2 within an uncertainty of ±3 s, which cannot be considered as a significant difference in the frame of the method used here.

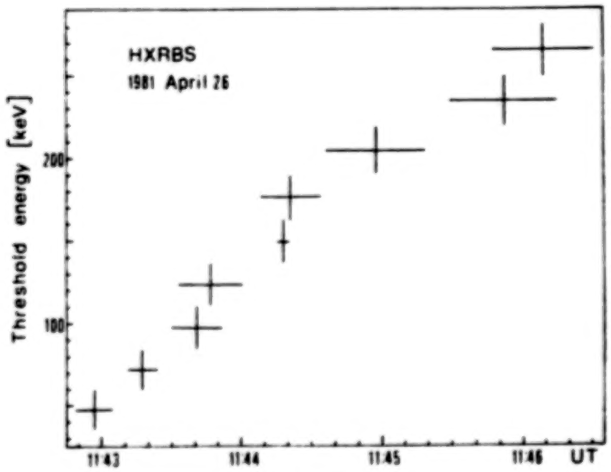

Fig. 3

The two phases have been found in nine of the ten events studied. The upper energy limit where pre-flash emission could be detected ranges between some tens of keV to 200 keV. The duration is some seconds to 80 s. No flash phase signature has been observed in the "gradual" flare of 1981 April 26 at 11:40 UT (Bai and Dennis, 1985). Fig. 3 shows the temporal evolution of its threshold energy. The emission exhibits a slow rise in all detector channels up to 250 keV. In the two highest channels there seems to be some fine structure disturbing the slow rise, but the count rate statistics is too poor to yield clear evidence for flash-phase like features.

4. Discussion

We have shown that nine out of our sample of ten hard x-ray bursts with peak count rates above 7000 s^{-1} exhibit two components of the impulsive phase:

- -a pre-flash phase restricted to lower energies up to 200 keV and lasting some seconds to 80 s,
- -a flash phase during which the emission in all detector channels rises simultaneously within an uncertainty of some seconds.

In their study of 45 events with HXRBS count rates above 1000 s^{-1} Benz et al. (1983) found evidence for these two phases in seven cases from visual inspection

C-2

of the count rate time histories integrated from 26 keV to 461 keV. Two of these events (on 1980 March 29, cf. fig. 1 of Benz et al.) belong to the sample discussed in this contribution and confirm the identification of pre-flash and flash phase with the features found in our analysis. The presence of these two phases seems to be a much more frequent phenomenon in the great hard x-ray bursts discussed here than in the smaller events of Benz et al. (1983), probably because the pre-flash emission is too weak to be detected in events with low peak count rate.

In the two events where we dispose of precise onset times measured with the gamma-ray spectrometer, the rise of emission in the 4 to 8 MeV band occurs close to the onset of the flash phase of energetic electrons. Forrest and Chupp (1983), comparing starting times of the 40 keV to 8 MeV emission in the 1980 June 7 and June 21 events, concluded on their simultaneous rise in all channels of the gama-ray spectrometer. This is, however, only valid for the flash phase, in agreement with our results. The pre-flash emission was not detected in their study. For the 1982 June 3 flare detailed observations of low-energy photons are also available. Centimetric radio observations at Bern University show a spectrum peaking at low frequencies during the pre-flash phase. With the rise of the flash phase the spectral maximum starts a rapid drift to high frequencies. In the metre waveband the pre-flash hard x-rays are accompanied by fast-drift bursts. Near the onset of the flash phase the starting frequency increases rapidly - in accordance with the observations reported by Benz et al. (1983) - and a continuum emission extending over all the band 150 MHz to 470 MHz covered by the Nançay radio spectrograph is established some seconds after the start of the flash phase in hard x-rays. Raoult et al. (1985) have shown that this is a typical evolution of radio emission associated with impulsive hard x-ray bursts.

These independent observations suggest that the pre-flash and flash phase as defined by the method of section 2 are physically significant phenomena occurring during the early stage of a flare, despite the problems introduced by the detector properties into an analysis based on low count rates. These problems affect the question of time delays between different photon energies. The reality and physical meaning of these - evolution of a single mechanism of acceleration/injection or action of different processes - can only be investigated through a thorough simulation of the detector response to model spectra.

Acknowledgements

The authors are indepted to Brian Dennis and the HXRBS team for providing the data used for this communication and to Sharad Kane for having made ISEE 3 observations available. K.-L.K. acknowledges helpful discussions with B. Dennis and D. Forrest on the subject of this paper. This research was supported by CNES and CNRS. One of the authors (K.-L.K.) acknowledges financial support by an ESA fellowship.

References

Bai, T., and Dennis, B.: 1985, Astrophys. J. 292, 699

Bai, T., and Ramaty, R.: 1979, Astrophys. J. 227, 1072

Benz, A.O., Barrow, C.H., Dennis, B.R., Pick, M., Raoult, A., and Simnett, G.: 1983, Solar Phys. 83, 267

Dennis, B.R. et al.: 1982, NASA TM 84998

Forrest, D.J., and Chupp, E.L.: 1983, Nature 305, 291

Orwig, L.E., Frost, K.J., and Dennis, B.R.: 1980, Solar Phys. 65, 25

Raoult, A., Pick, M., Dennis, B.R., and Kane, S.R.: 1985, Astrophys. J. 299, 1027

Vilmer, N., Kane, S.R., and Trottet, G.: 1982, Astron. Astrophys. 108, 306

N87
21793
UNCLAS

N87-21793

STATISTICAL ANALYSIS OF FAST HARD X-RAY BURSTS BY SMM OBSERVATIONS AND MICROWAVE BURSTS BY GROUND-BASED OBSERVATIONS

Li Chun-sheng and Jiang Shu-ying

Astronomy Department
Nanjing University
Nanjing, China

1. Data and Method of Analysis

In order to understand the relationship between fast hard X-ray bursts (HXRB) and microwave bursts (NWB), we have used the data published in the following publications.

1. NASA Technical Memorandum 84998.
   The Hard X-Ray Burst Spectrometer Event Listing 1980, 1981 and 1982.
2. Solar Geophysical Data (1980-1983). Academia Sinica
3. Monthly report of Solar Radio Emission. Toyokawa Observatory, Nagoya University (1980-1983).
4. NASA and NSF: Solar Geophysical Data (1980-1983).

We get the data of fast HXRB detected with time resolutions of 10 ms, 5 ms, and 1 ms and corresponding data of MWB observed (with a time constant of 1 s) at frequencies of 17GHz, 9.4 GHz, 2.75 GHz, and 2.8 GHz during the same flare-burst event.

For analyzing individual events, the criterion of the same event for HXRB and MWB is determined by the peak time difference.

$$T = |T_{mw} - T_{hx}| < 20 \text{ seconds}$$

The regression relation between the physical parameters of MWB and HXRB may be written as:

$$Y = A + BX$$

where X indicates the logarithm of the following parameters: peak flux density Sp, total flux density St, and duration T'mw of MWB. Y indicates the logarithm of the corresponding parameters: peak rate Cp, total counts Ct, and duration T'hx of HXRB.

B is the regression coefficient
A is the regression constant
Sp is in s.f.u.
St = $\overline{S}$.T'mw, $\overline{S}$ = the mean flux density
T'mw in seconds
Cp in counts per second
Ct in counts
Thx in seconds

2. Results and Conclusion

With the method of data analysis mentioned above, we obtain the results presented in Table 1 and Figures 1 to 4.

In Table 1, the parameters have the following meanings:

R is the correlation coefficient between X and Y for the energy range of channels 1 to 15 (i.e. 25-500 keV)
R1 is the correlation coefficient for the energy range of channels 1 to 5 (i.e. 25-140 keV)
R2 is the correlation coefficient for the energy range of channels 6 to 15 (i.e. 145-500 keV).

The statistical analysis run so far and the comparisons of correlation parameters with one another allow us to draw the following conclusions:

1. There is a good linear correlation between the physical parameters of MWB and fast HXRB.

2. Comparison of R, R1 and R2 at different frequencies for MWB show the best correlation coefficients occur at 9.4 GHz.

3. R2 is larger than R1 at any frequency. This means that the correlation between X and Y is closer in the higher energy range of 145-550 keV than that in the energy range of 25-140 keV at the same frequency.

4. Correlation coefficients between T'mw and T'hx are not as good as the others, but they increase as the frequency decreases.

Table 1. The parameters of the linear relation between X and Y.

Considered Parameters	Number of Events	Correlation Coefficient R	Correlation Coefficient R1	Correlation Coefficient R2	Regression Constant A	Regression Coefficient B
f1 = 17 GHz						
Sp and Cp	162	0.781	0.46	0.81	1.168	0.960
St and Ct	/	/	/	/	/	/
T'_{mw} and T'_{hx}	158	0.511			1.412	0.423
f2 = 9.4 GHz						
Sp and Cp	190	0.856	0.65	0.76	1.463	0.778
St and Ct	190	0.857	0.73	0.86	1.179	0.878
T'_{mw} and T'_{hx}	191	0.613			0.831	0.631
f = 3.75 GHz						
Sp and Cp	153	0.797	0.055	0.79	1.515	0.848
St and Ct	160	0.733	0.76	0.82	1.258	0.859
T'_{mw} and T'_{hx}	161	0.686			0.748	0.639
f = 2.8 GHz						
Sp and Cp	206	0.743	0.52	0.71	1.663	0.675
St and Ct	209	0.722	0.58	0.84	1.819	0.703
T'_{mw} and T'_{hx}	201	0.695			0.735	0.702

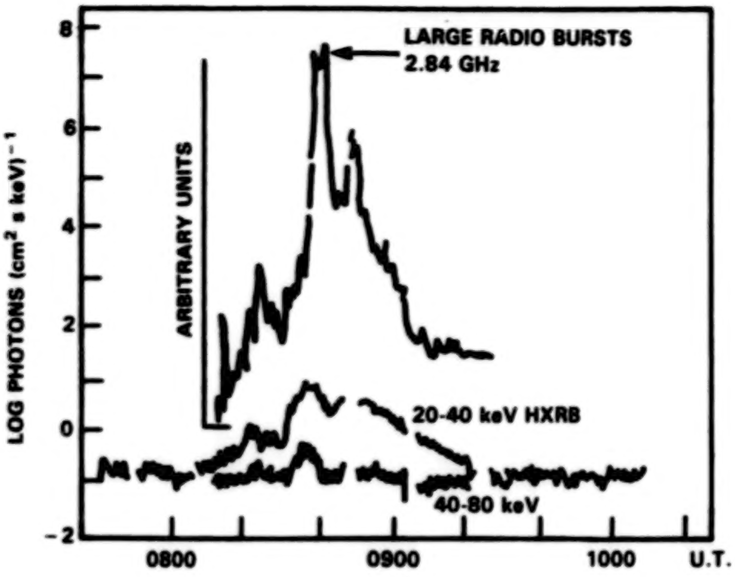

Figure 1: Time profiles of radio bursts at 2.84 GHz and hard X-ray bursts during the large solar flare of May 16, 1981.

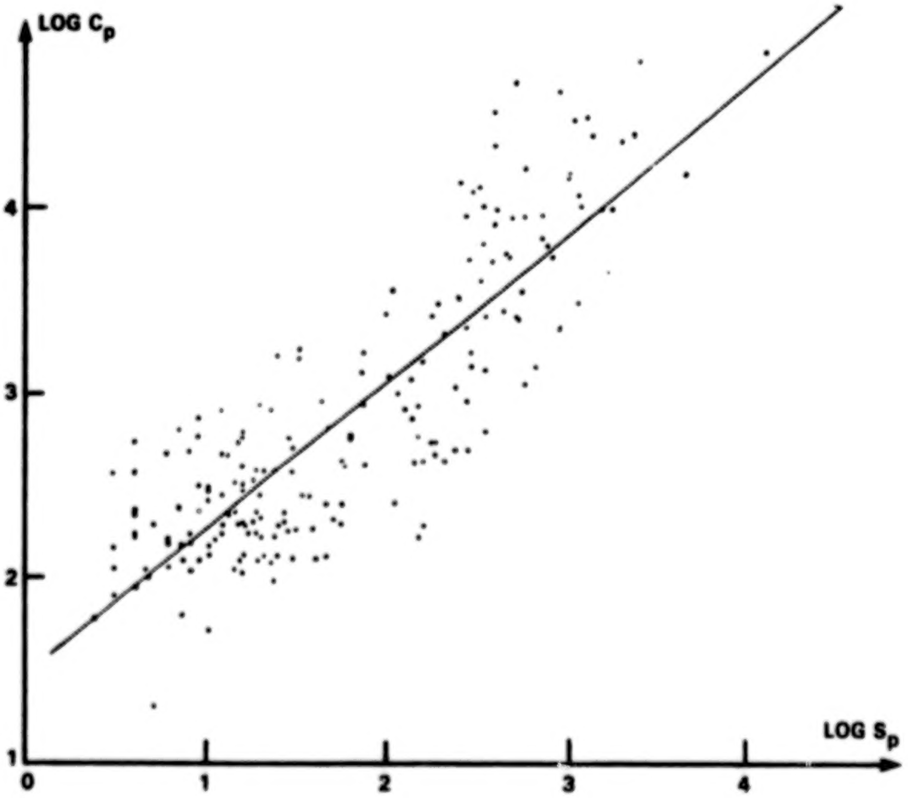

Figure 2: Correlation diagram between peak flux Sp at 9.4 GHz and hard X-ray intensity Cp (in counts/s) in the energy range of 25-500 keV.

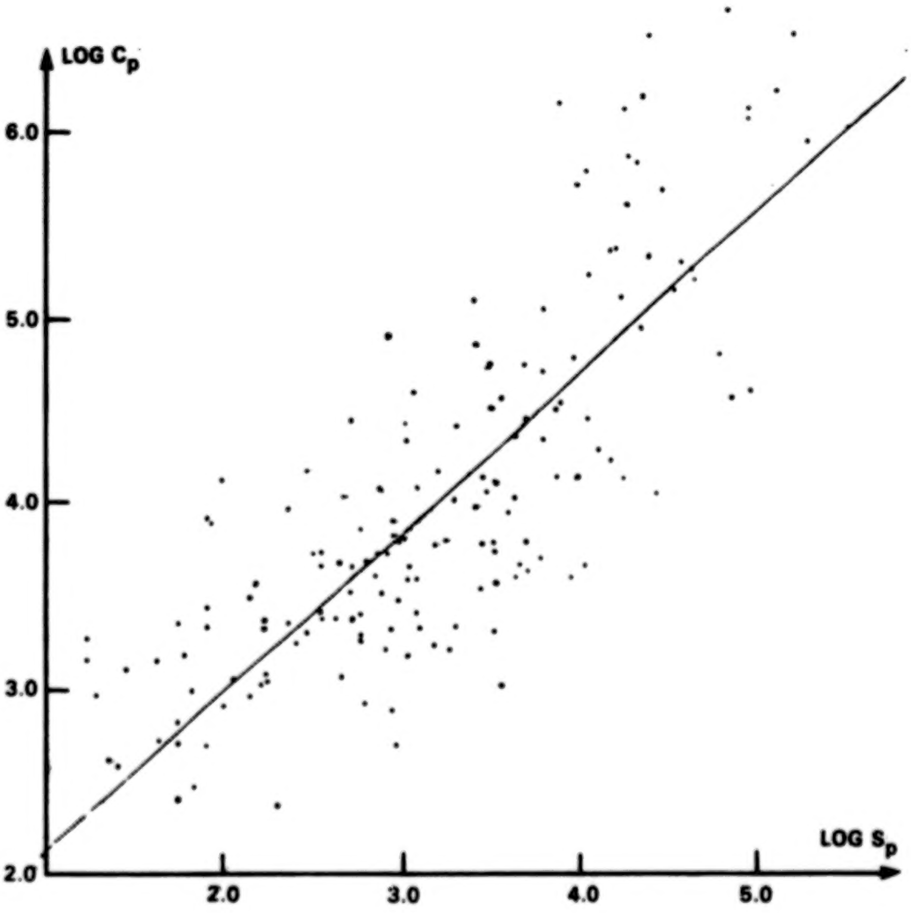

Figure 3: Correlation diagram between peak flux Sp at 3.75 GHz and hard X-ray intensity Cp (in counts/s) in the energy of 25-500 keV.

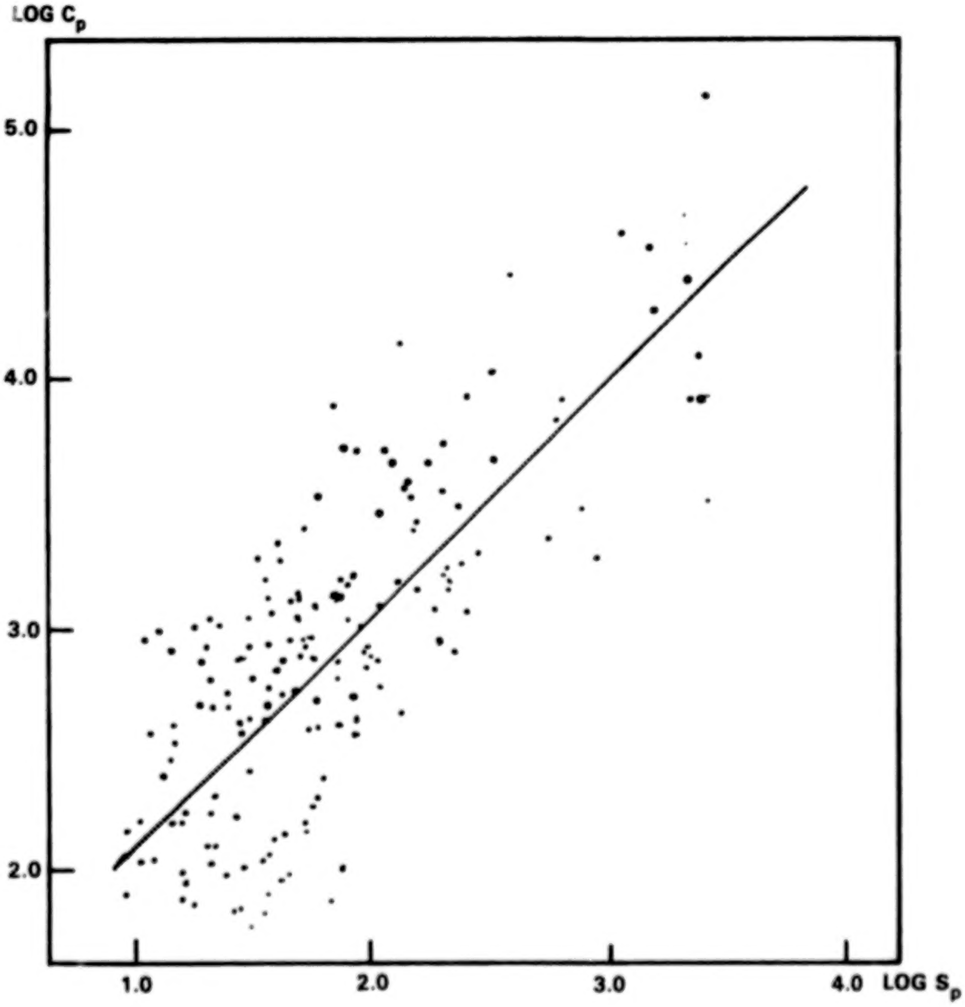

Figure 4: Correlation diagram between peak flux Sp at 17 GHz and hard X-ray intensity Cp (in counts/s) in the energy of 25-500 keV.

N87
21794
UNCLAS

N87-21794

MICROWAVE AND HARD X-RAY EMISSIONS DURING THE IMPULSIVE PHASE OF SOLAR FLARES: NONTHERMAL ELECTRON SPECTRUM AND TIME DELAY

Gu Ye-ming* and Li Chun-sheng

Department of Astronomy
Nanjing University
Nanjing, Peoples Republic of China

*Present address:
Institute of Electron Physics
Shanghai University of Science and Technology
Shanghai, Peoples Republic of China

Abstract

On the basis of the summing-up and analysis of the observations and theories about the impulsive microwave and hard X-ray bursts, we have investigated the correlations between these two kinds of emissions. It is shown that it is only possible to explain the optically-thin microwave spectrum and its relations with the hard X-ray spectrum by means of the nonthermal source model. A simple nonthermal trap model in the mildly-relativistic case can consistently explain the main characteristics of the spectrum and the relative time delays.

I. Introduction

In recent years, along with the continuous development of space observations, the investigation of solar high-energy phenomena plays a more and more important role in flare physics. The so-called high-energy phenomena include the high-energy particles produced by the flare energy release, and the electromagnetic emissions from these particles. It is believed that a significant part of the flare energy is released in the form of high-energy particles during the impulsive phase. But the properties of these particles are not clearly known. For example, what is their velocity distribution (thermal and nonthermal)? Are they produced by heating or by acceleration, etc.?

Since we can't detect these particles in the flaring region on the surface of the Sun, we can only observe their emission on the ground or in interplanetary space, or the escaped particles from the Sun. The former is the basic way to understand these particles.

The emissions most closely related to these high-energy particles are microwave, ultraviolet, hard X-ray, and γ-ray emissions. One of the fundamental problems for our theorists is to relate the observational quantities of these emissions with the high-energy particles. All these emissions are detected during the impulsive phase, so they are of impulsive characteristic, i.e. they have fast oscillating time profiles.

By analyzing the temporal, spatial, and spectral character of the microwave and hard X-ray bursts, we can get some important information about the high-energy particles and the flare energy-release region. In this paper, we have investigated the spectral correlations between these two kinds of emissions and the time delays and reached some important conclusions.

For convenience, in the following discussion we use "MW" and "HX" to represent "Microwave" and "Hard X-Ray", respectively. The units of all the quantities used in the paper are listed in Table 1.

Table 1. Quantities used in this paper

Symbols	Meaning	Units
L, S, V	linear dimension, projected area and volume of emission source respectively	10^9cm, 10^{18}cm^2 10^{27}cm^3
Fx	photon flux of HX	photons cm^{-2} s^{-1} keV^{-1}
F_μ	flux density of MW source	S.F.U.
T_b, T_{eff}	brightness and effective temperature of MW source	10^9 K
B	magnetic field in the source	10^2 Gauss
N_o	electron density of medium	10^{10}cm^{-3}
N	nonthermal electron density	10^9cm^{-3}
$\xi = N.N_o.V$	emission measure	10^{46}cm^{-3}
E, ε	electron and photon energy	keV
f	MW frequency	10^9 Hz(GHz)
A	index of power-law spectrum	10^7

II. Impulsive Microwave and Hard X-ray Bursts

To show the purpose of this work and to provide a foundation of our discussion, we give a brief review of both observational and theoretical investigations of MW and HX bursts.

1. Morphology and Time-correlation

Both MW and HX bursts have an impulsive character and have similar structures. Their morphologies are varied. The simplest one is a single-spike event. A multi-impulsive burst may have a very complex time profile. But in general we can resolve a multi-impulsive burst into many single-spike bursts, and all these resolved single-spike bursts are of similar character, with durations between a few seconds and tens of seconds. So it is convenient for us to investigate the short duration single-spike bursts and to extend the results to multiimpulsive bursts (including those with quasi-period structures). We do not consider the so-called "fine-structures" (of subsecond time scale) in this paper.

The time-correlation between MW and HX emissions was recognized as early as the HX bursts from the solar flares were first detected. Space observations have shown that MW and HX bursts are not only similar in time structures, but also reach maximum at approximately the same time and have similar time profiles (we will discuss the time-delays in Section IV). These similarities have been taken as evidence for a common source of MW and HX emissions.

Actually such close correlations show that, even if MW and HX emissions do not come from the same population of electrons in a common source, they should be emitted by the high-energy electrons from the same acceleration process.

2. Spectrum

The observed MW spectrum is composed of data at a few fixed frequencies. The statistical analysis for a large amount of events shows that most of MW bursts have a "C-Type" spectrum. A typical "C-Type" spectrum rises at frequencies of > 1 GHz, and reaches a maximum in the range of ∼ 5-15 GHz, then decays toward higher frequencies. The rise and decay before and after the maximum can be approximately described with power-law spectra (Guidice and Castelli, 1975).

There are three spectral forms used to describe HX specta: single power-law, double power-law and exponential. But the spectrum represented by them may have differences in essence: the power-law spectrum is of "nonthermal" character, and the exponential one is of "thermal" character. Because of low resolution it is difficult to distinguish between the thermal and nonthermal properties for most of the observed spectra, but generally a single-power-law fit can describe the main characters of the observed spectra. We will use this form in the following discussions.

3. Thermal and Nonthermal Models for MW and HX Emissions

There have been controversies in deciding the thermal or nonthermal origin of the energetic electrons.

In a thermal model, all the electrons in the energy-release region are bulk-heated to temperatures in excess of 10^8 K. They are trapped in a magnetic loop or an arcade of loops and limited by the ion-acoustic turbulent fronts. The thermal bremsstrahlung and gyrosynchrotron emissions from these hot electrons produce the HX and MW bursts, respectively. In a nonthermal model, a relatively small fraction of the electrons in the energy-release region are accelerated to energies of $E >$ 10-100 keV. They are distributed in an approximate power-law spectrum. There are three limiting cases for HX emission: thin-target, thick-target, and magnetic trap model. Because of the low energy efficiency of the thin-target model, we do not consider it in this paper.

4. Possible Discrimination Between Thermal and Nonthermal Models

It is feasible in principle that, there could be a simple criterion to decide which model is more suitable. But we meet difficulties in reality.

Spectra studies of both HX and MW and their modeling have been undertaken to decide the thermal or nonthermal origin of the energetic electrons. But it has been pointed out that, when the inhomogenities of the source are introduced, regardless of the spectral forms, the spectra, on their own, are not capable of distinguishing the thermal model from the nonthermal model (Brown, 1974 and Emslie, 1983). Because of the uncertainties in both observations and theories, we can not reach definite conclusions from other observational diagnostics of HX emissions, such as the directivity, prolarization and the spatial location of the emission source.

Thus, it can be seen that the only possible way to seek the criteria for distinguishing between the models is to investigate the optically-thin MW spectrum and its morphology (since the optically-thin part is not so seriously affected by the inhomogenities as the optically-thick part) and their relations with the spectrum and morphology of HX emissions.

Table 2. Data for Impulsive Flare Events

No.	Date	Maximum Time (UT)	Importance Hα/SX	Position	τ_{HX}	Delay		MW Spectrum				HX Spectrum		References
						Δt_{MX-MW}	Δt_{MW}	f_μ	F_μ	m	δ	γ		
1	69.3.25	0205.5	SF	McMath 9994	15	10	+	>17	335	(2.5)	/	(3.2)	(0.003)	(a)
2	69.3.30	0230.53	SN	McMath 10014	10	3	+	>17	211	(2.12)	/	3.6	0.097	(a)
3	70.6.14	1250.52	1N	McMath 10389	10	-5.9±2.5	?	>15.4	52	(3.05)	/	(3.0)	(0.002)	(a)
4	72.5.18	1617.35	1B/M4	S16E24	60	?	+	9.4	234	1.76	1.0			(b)
5	80.5.8	1937.15	SB/M2	S22W29	50	0.24	+	7	100	0.5	1.65			(c)
6	80.6.29	0234.33	/M3.6	S25W85	200		+	9.4	320	0.84	1.22	4.6	8.5	(d)
7	80.11.1	1919.0	1B/M1.2	N17E64	200	6±3	≈ 0	6.0	145	1.80	2.3			(e)
8	81.4.1	0146.0	2B/X2.3	S43W52	100	10	+	9.4	5200	1.30	1.27	3.2	0.07	(f)
9	81.4.4	0502.5	2B/X1.6	S44W85	80	-6	+	9.4	3050	0.8	0.5	2.55	0.06	(f)
10	81.8.11	0145.2	2B/M4.4	S13W24	100	8	+	17	1730	1.4	2.3	3.70	1.3	(f)
11	80.6.7	0312.2	SB/M7.3	N14W70	60	2	+	17	1000	1.7	1.2	3.10	0.38	(f),(g)
12	80.6.27	1617.0	SB/M6	S27W67	200	?	?	/	/	/	/	3.15	0.067	(h)
13	72.8.4	0626.11	3B/X5	N13E08	1000	?	+(u)	19	25000	(u)	0.9	3.1		(i)
14	72.8.7	1521.20	3B/X5	N14W39	1000	?	+(u)	19	27000	1	1.2	3.0		(i)
15	81.10.15	0444.1	1B/M2.0	S21W14	40	≈ 0	≈ 0	9.4	5340	1.3	2.8	4.1	3.4	(f)
									Mean	1.47	1.49	3.41		

References: (a) Crannell et al. 1978; (b) Wiehl et al. 1980; (c) Kaufmann et al. 1983; (d) Dulk and Dennis 1982; (e) Tandberg-Hanssen et al. 1984; (f) Hinotori Symposium on Solar Flares 1982; (g) Kane et al. 1983; (h) Bai et al. 1983; (i) Hoyng et al. 1976.

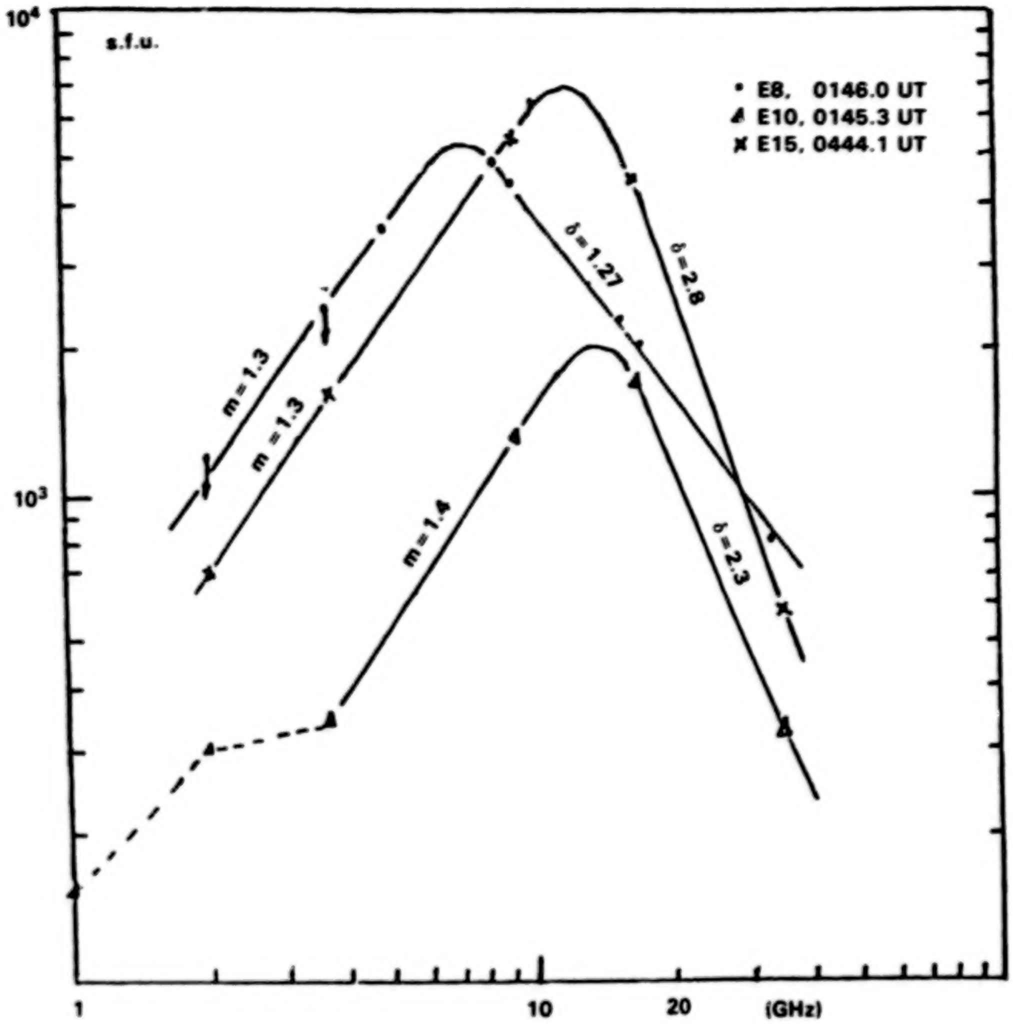

Figure 1. Three typical MW spectra from SGD data.

III. Nonthermal Models of the Emission Source

- Trap Model and Electron-stream Thick-target Model

According to the discussions in the last section, we now try to find criteria to distinguish the two models.

1. Collection of Observational Data

We list the observational data for 15 impulsive events in Table 2. Spectral data for both MW and HX bursts are given for the peak time.

For multi-impulsive (or the so-called "extended bursts") we consider the main impulsive spike. The maximum time is given for the HX burst. Two kinds of delays are given: Δt_{HX-MW} is the delay between HX and MW, a positive value for HX preceding MW; Δt_{MW} is the frequency dependent delay of MW and a positive value is for the precedence of higher frequencies. Most of the MW data are from Solar Geophysical Data (SGD). F_μ is the maximum observed flux and f_μ is the frequency at which the maximum is reached; m and δ are the power-law indices before and after the maximum (reverse frequency), respectively. All the HX spectral data are selected from the literature. γ is the single power-law index and A is the coefficient of the HX spectrum.

2. Two Nonthermal Models: Model I and Model II

It would be of great significance to explain the main characteristics of MW and HX bursts with a simple model and to make reasonable estimates of the source parameters from the observed data. Crannell et al. (1978) used a homogeneous thermal model to explain 22 simple spike bursts. In this section we will use two kinds of homogeneous nonthermal models instead.

Suppose that, in the energy-release region near the top of the magnetic loop in corona, a fraction of electrons is accelerated to a distribution which can be approximated by

$$N(E) = KE^{-\alpha}\ (\mathrm{cm}^{-3}\mathrm{keV}^{-1}) \qquad (1)$$

where $$K = (\alpha-1)E_o^{\alpha-1}N \qquad (2)$$

N is the total number density of the nonthermal electrons with energies $E>E_o$, and E_o is the low cut-off energy of the power-law spectrum. The accelerated electrons may be trapped in magnetic loops or precipitate along the magnetic lines to the denser solar atmosphere. The energy-spectrum of the freely precipitating electron stream is given by:

$$F(E) = N(E)\ \surd\ (2/m_e)\ E^{1/2}S = 1.88*10^{27}SKE^{-\alpha+1/2}(\mathrm{electrons/cm^2s}) \qquad (3)$$

where we have assumed that the magnetic loop has a uniform cross-section with area S. The observed HX spectrum is described as:

$$F_x(\varepsilon) = 10^7 A\varepsilon^{-\gamma} \qquad (4)$$

According to Brown (1974, 1976), the relations between electron spectra and HX photon spectra can be given by:

$$N(E)N_oV = 3.61*10^{11}\gamma(\gamma-1)^2B(\gamma-1/2,3/2)AE^{-\gamma+1/2} \qquad (5)$$

$$F(E) = 2.68*10^{40}\gamma^2(\gamma-1)^2B(\gamma-1/2,3/2)AE^{-\gamma-1} \qquad (6)$$

for the two cases: trap (Model I) and precipitation (Model II), respectively. B(p,q) is the Beta function. Comparing (1), (5) with (3), (6) we get the relationships between source parameters and observational quantities:

$$\text{Model I:}\quad A = 2.77*10^{-3}\xi K_1 \text{ or } \xi = 3.61*10^{2}A/K_1 \tag{7}$$

$$\text{Model II:}\quad A = 7.01*10^{2}SNK_2 \text{ or } SN = 1.43*10^{-3}A/K_2 \tag{8}$$

$$\text{where } K_1 = K/(\gamma(\gamma-1)^2\, B(\gamma-1/2,3/2));\quad K_2 = K_1/\gamma \tag{9}$$

The corresponding relationships between the spectral indices are

$$\alpha_1 = \gamma - 1/2;\qquad \alpha_2 = \gamma + 3/2 \tag{10}$$

To calculate the gyrosynchrotron emission from HX emitting electrons, we use the empirical formulae derived from the numerical method given by Dulk and Dennis (1982). It is convenient to express the peak (spectral reverse) frequency and effective temperature as:

$$f_{peak} = 35.9*10^{-0.21\alpha}\,(\sin\Theta)^{x4}(NL)^{x1}B^{x2} \tag{11}$$

$$T_{eff} = 4.16*10^{-0.26\alpha}\,(\sin\Theta)^{x5}B^{-x3}f^{x3} \tag{12}$$

The emission and absorption coefficients are given by

$$\eta_f = 1.56*10^{-12-1.02\alpha}\,(\sin\Theta)^{x6}B^{d+1}N.f^{d} \tag{13}$$

$$K_f = 2.67*10^{-3.0-0.76\alpha}\,(\sin\Theta)^{x7}B^{x5-1}N.f^{x8} \tag{14}$$

where we use the indices

$$\begin{aligned} &x1 = 0.32-0.03\alpha;\quad x2 = 0.68+0.03\alpha;\quad x3 = 0.50+0.085\alpha\\ &x4 = 0.41+0.03\alpha;\quad x5 = -0.36-0.06\alpha;\quad x6 = -0.43+0.65\alpha\\ &x7 = -0.09+0.72\alpha;\quad x8 = 1.30+0.98\alpha;\quad d = 0.90\alpha-1.22 \end{aligned} \tag{15}$$

For a source with brightness temperature T_b, the MW emision flux observed on the Earth is given by

$$F_\mu(f) = S/4\pi R^2.2kf^2/C^2.T_b \quad \text{(in c.g.s. units)}$$

where R is the distance between the Earth and the Sun. According to the solution of radiation transfer in a homogeneous source, we have

$$T_b = T_{eff}\,(1-e^{-\tau_f});\qquad \tau_f = 10^9LK_f \tag{16}$$

$$\text{and}\quad F_\mu(f) = 1.08Sf^2T_b = 1.08Sf^2T_{eff}\,(1-e^{-\tau_f}) \tag{17}$$

where τ_f is the optical depth of the source.

It is obvious that the observed spectra of HX and MW emissions are completely determined by the nonthermal electron spectrum (N, E_0, α) and the source parameters (B,L,S,V). For simplicity we take E_0=20 keV and assume

$$S = L^2,\ V = SL = L^3 \qquad (18)$$

in the following discussion.

3. Evidence for a Nonthermal Electron Spectrum

Correlation between the Indices of the Optically-thin MW and HX Spectra

In a nonthermal source, the optically-thin MW spectrum is determined only by the electron spectrum; it is independent of the inhomogenities of the source parameters. Its spectral index is the same as that of the emission coefficiency given by (13):

$$\delta = d = 0.90\gamma - 1.22 \qquad (19)$$

From (10) and (19) we can get the relations between the spectral indices of optically-thin MW and HX emissions for the two models, respectively:

$$\text{Model I:}\quad \delta = 0.90\gamma - 1.67 \quad \text{or} \quad \gamma = 1.11\delta + 1.86 \qquad (20.a)$$

$$\text{Model II:}\quad \delta = 0.90\gamma + 0.13 \quad \text{or} \quad \gamma = 1.11\delta - 0.14 \qquad (20.b)$$

which are valid for both homogeneous and inhomogeneous sources.

For comparison, let's see the behavior of the optically-thin MW spectrum in the thermal model. For a thermal source with temperatures of $>10^8$-10^9 K, both analytical derivation and numerical analysis (Matzler 1978 and Dulk et al., 1979) shows that the optically-thin thermal gyro-synchrotron spectrum produced by the mildly-relativistic thermal electrons is very steep, typically with a spectral index of ~ 7 or 8. But for a typical HX spectral index of γ = 4, the corresponding optically-thin MW spectral index is δ = 2.38 and δ = 3.74 for Model I and Model II, respectively. Observations obviously support the nonthermal models. The statistical results of Das and Das Gupta (1983) show that usually the index δ is between ~0.5 and 3 and the mean value for 20 events is 1.05. In Table 2 the mean value of δ is 1.49 for 11 events. It can be seen from the above discussion that no thermal model can explain such hard MW spectra.

We can conclude from (20) that, if both MW and HX emissions are produced by the same population of electrons or by the electrons with the same distribution in energy, there should be a definite relation between the two kinds of emissions. Benz (1977) noticed such a relation.

But instead of (19) he used the highly relativistic approximation

$$\delta = (\alpha - 1)/2 = (\gamma - 3/2)/2$$

(for the trap case) to explain the spectral correlations observed during two outstanding flares. For electrons with energies of >100 keV, the highly relativistic approximation is not suitable.

We plot a δ-γ correlation diagram in Figure 2 by using the data in Table 3. Although the observational data points are relatively few, we can see from Figure 2 that there is a relationship between δ and γ. The following conclusions can be made from Figure 2: (a) Usually the nonthermal models, especially the nonthermal trap model (Model I), can explain the relation between the two kinds of spectral index for most of the impulsive events. (b) It is not excluded that the highly relativistic electrons may make a relative contribution to the high frequency MW spectrum. Some observations of the continuous γ-ray spectrum support such a possibility. (c) MW, especially high frequency MW, emissions mainly come from energetic electrons with energies of $E > 100$-300 keV. keV.

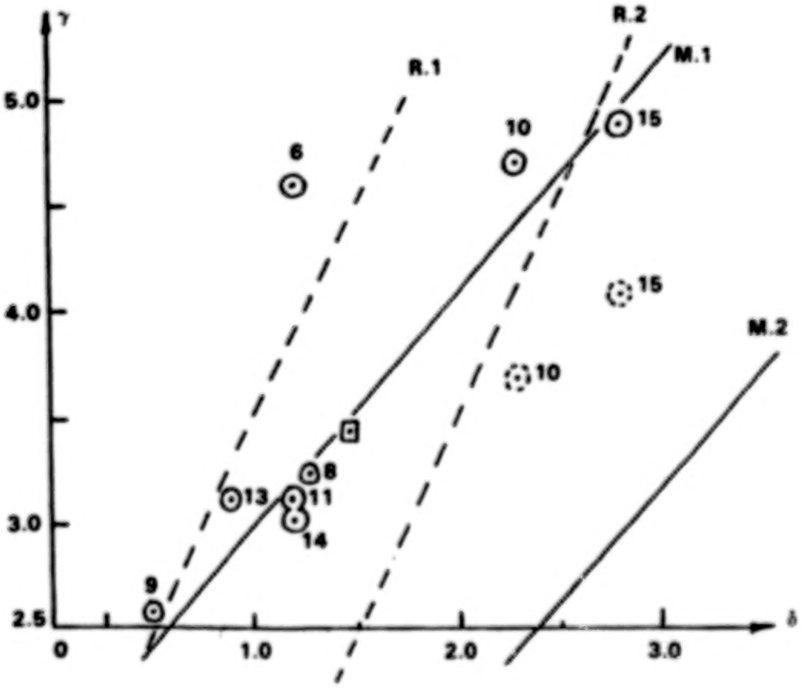

Figure 2: δ-γ correlation diagram. Dotted circles is for the HX spectral indices in the low energy range in double-powerlaw fit events. The small square is for the main values of δ and γ given in Table 2. The lines M.1 and M.2 are the theoretical correlation curves predicted by Model I and II (according to (20)), and R.1 and R.2 are for the high-relativistic approximation: $\delta = (\alpha - 1)/2$, α is given by (10).

Table 3

Table 3. Spectral indices of optically-thin MW and HX emissions. $\Delta\varepsilon$ is the energy range for observation. The double-power-law fit parameters are given when it is appropriate.

Event No.	MW Spectrum		HX Spectrum			
	f_μ	δ	γ	$\Delta\varepsilon$(keV)	γ'	$\Delta\varepsilon'$(keV)
6	9.4	1.22	4.6	20-200		
8	9.4	1.27	3.2	20-400		
9	9.4	0.5	2.55	20-350		
10	17	2.3	3.70	20-120	4.71	>120
11	17	1.2	(1.50)	(<69)	3.10	>69
13	19	0.9	3.1	>30		
14	19	1.2	3.0	>30		
15	9.4	2.8	4.1	20-300	4.9	300-600

4. Application of Nonthermal Models to HX and MW Bursts

Now we use Model I and II discussed above to estimate the parameters of flare sources. To relate the observational quantities to source parameters, we extend the optically-thick MW spectrum to $f=f_\mu$ (taking $\tau_f = \infty$ and $f = f_\mu$ in (17)) and write

$$F_\mu = F_\mu(f_\mu) = 4.49*10^{-0.26\alpha}(\sin\theta)^{x5}L^2B^{-x3}f_\mu^{\,m} \tag{21}$$

where $m = 2 + x3 = 2.5 + 0.085\alpha$ (22)

and $f_\mu = f_{peak} = 35.9*10^{-0.21\alpha}(\sin\theta)^{x4}(NL)^{x1}B^{x2}$ (23)

For an event with observed parametes (A,γ) and (f_μ,F_μ), we can solve the source parameters (N,α) and (B,L) from equations (8) (10) (21) (23) in Model II. In Model I, the emission measure is determined by the HX spectral coefficient A through (7). But since another source parameter N_0 is added in Model I, we introduce a new paremater $H = N/10N_0$, and the source parameters can be solved from equations (7) (10) (21) (23) for any given value of H.

Considering the first order of approximation in our simple models, we take $\theta = 45°$ in the following calculations. The calculated results are given in Table 4 and 5. The results show: (a) Although we used the simplest nonthermal models, we can get good estimates of the burst

Table 4

The observed quantities of the MW and HX spectra and the source parameters calculated in Model I for two H values.

No.	MW Spectrum		HX Spectrum		Source Parameters with H = 0.001				Source Parameters with H = 0.01				
	f_μ	F_μ	γ	A	B	L	N	N_o	B	L	N	N_o	ξ
1	17	335	(3.2)	(0.003)	10.67	0.87	0.013	1.26	7.27	0.76	0.049	0.49	0.011
2	17	211	3.6	0.097	8.56	0.71	0.055	5.49	5.98	0.62	0.21	2.13	0.11
3	15.4	52	(3.0)	(0.002)	7.20	0.32	0.061	6.06	4.84	0.28	0.24	2.37	0.013
6	12	360	4.6	8.5	7.79	1.90	0.028	2.77	5.79	1.67	0.106	1.06	0.526
7	7.5	6000	3.2	0.07	3.10	7.20	0.0026	0.257	2.11	6.26	0.010	0.10	0.247
8	11	3300	2.55	0.06	2.37	2.48	0.03	3.02	1.55	2.15	0.118	1.18	1.39
10	14	2500	3.70	1.3	6.10	2.88	0.021	2.13	4.29	2.52	0.083	0.83	1.08
11	17	1000	3.10	0.38	4.71	1.09	0.116	11.7	3.19	0.95	0.48	4.56	1.79
15	12	8000	4.1	3.4	7.02	7.49	0.0046	0.46	5.06	6.57	0.18	0.18	0.894
				mean	6.42	2.77	0.0037	3.66	4.45	2.42	0.14	1.4	0.67

Table 5

The observed quantities of the MW and HX spectra and the source parameters calculated in Model II.

No.	MW Spectrum		HX Spectrum		Source Parameters			
	f_μ	F_μ	γ	A	B	L	N	T_b
1	17	335	(3.2)	(0.003)	21.3	2.04	3.66×10^{-4}	0.26
2	17	211	3.6	0.097	14.4	1.52	8.30×10^{-3}	0.29
3	15.4	52	3.0	(0.002)	15.1	0.75	2.76×10^{-3}	0.36
6	12	360	4.6	8.5	12.3	4.12	8.40×10^{-3}	0.14
8	7.5	6000	3.2	0.07	7.76	18.0	1.09×10^{-4}	0.31
9	11	3300	2.55	0.06	5.94	5.72	3.61×10^{-3}	0.77
10	14	2500	3.70	1.3	10.5	6.17	5.35×10^{-3}	0.31
11	17	1000	3.10	0.38	8.28	2.25	4.71×10^{-2}	0.63
15	12	8000	4.1	3.4	12.1	16.6	7.27×10^{-4}	0.19
				mean	12.0	6.35	8.52×10^{-3}	0.35

source parameters. (b) Comparing the results in Table 4 and 5, it can be seen that the source parameters derived in the trap model (Model I) are more reasonable than those derived in the precipitation model (Model II), since it seems not possible that the magnetic field in the corona is stronger than 1000 G. This tends to support the trap model and is consistent with the conclusion from the above analyses of spectral correlation. But the strong magnetic fields of 800-2000 G calculated in Model II suggest that, in the freely precipitating thick-target model the position of MW source should be near the foot of the magnetic loop or loops, where the magnetic field is much stronger than that at the top of the loop. (c) Comparing the results for different H values in Table 4, we find that in the magnetic region where the emitting electrons are trapped, the ratio of nonthermal electrons to medium electrons, H, may have very different values for different events.

IV. Time Delays of MW and HX Bursts

Observations with high time resolution have shown that there are delays between the time structures of different kinds of emission. We will give a simple explanation for these delays

1. Characters of Time Delays

Some data about the delays was given in Table 2. It can be seen that, for most of the events HX precedes MW. The time difference is from a few hundreds of milliseconds to tens of seconds. The high frequency MW ususally precedes the low frequency MW and the low energy HX precedes the high energy HX. All these may be taken as the regular pattern of the delays. But there also exist some unusual delay patterns, such as event No. 3 and No. 9 in Table 2.

Morphologically, the time delays can be divided into three kinds; (a) "profile delay", i.e. the time profiles of the two kinds of emission show a systematic shift; (b) "peak delay", i.e. both of the emissions start to rise at nearly the same time but the times for them to reach the maximum are different; (c) "start-time delay", i.e. both of the emissions peak at the same time but with different start times. Different kinds of delays may correspond to different mechanisms in the emission source.

2. Explanation of the Time Delays

Both the frequency-dependent and energy-dependent delays are the manifestations of the temporal evolution of emission spectra (Ref. e.g., Takakura et al. 1983). In a nonthermal model the evolution of the emission spectrum corresponds to that of the electron spectrum. The usual pattern of the spectral evolution of HX emission is "soft-hard-soft" and the spectrum is hardest at the time of peak flux. But some events show continuous hardening in HX spectrum after the peak flux is reached.

Having carefully investigated the relationship between the spectral evolution and time delays, we find that: if the HX spectrum is hardest at the peak time, there is no time delay longer than a second between HX and MW; for events with long HX to MW delay (longer than a few seconds), the HX spectrum continues to harden after the peak.

According to the above discussions, we know that MW, especially the high frequency MW emissions (in the optically-thin part), are mainly contributed by the electrons with energies of E>100-300 keV. The hardening of the HX spectrum reflects the hardening of electron spectrum. Under certain conditions, there may be a case where the total number of nonthermal electrons (with $E>E_o$) is decreasing but the number of the electrons with higher energies (e.g. with E>100 keV) is increasing. This can cause the peak delay of MW relative to HX and the energy-dependent delay of HX. The continuous hardening of the HX spectrum after the maximum time of the event may correspond to the energy-dependent life time of electrons trapped in the magnetic loop (Enome 1982) or to second-step acceleration during the impulsive phase.

To see the actual relation between time delay and the evolution of electron spectrum, we use Model I to make a quantitative analysis.

We choose event No. 2 for our analysis. In Table 4 we choose the parameter values corresponding to H = 0.1% for the following calculation. Suppose that the source parameters L, N and B are constants during the lifetime of the event and the acceleration process rises and decays with exponentially according to the following expressions:

$$N(t) = N^*\exp((t-t_m)/t_{01}) \text{ for } t<t_m \qquad (24)$$

$$= N^*\exp((t_m-t)/t_{02}) \text{ for } t>t_m$$

where t_m is the maximum (peak) time of the event (when the nonthermal electron number reaches maximum) and t_{01}, t_{02} are the characteristic times for the rising and the decay phase respectively. To simplify the calculation we take $t_m = 2t_{01}$ and assume two cases for the decay phase as illustrated in Figure 4,

(a): $t_{02} = t_{01} = 4s$

(b): $t_{02} = t_{01}/2 = 4s$

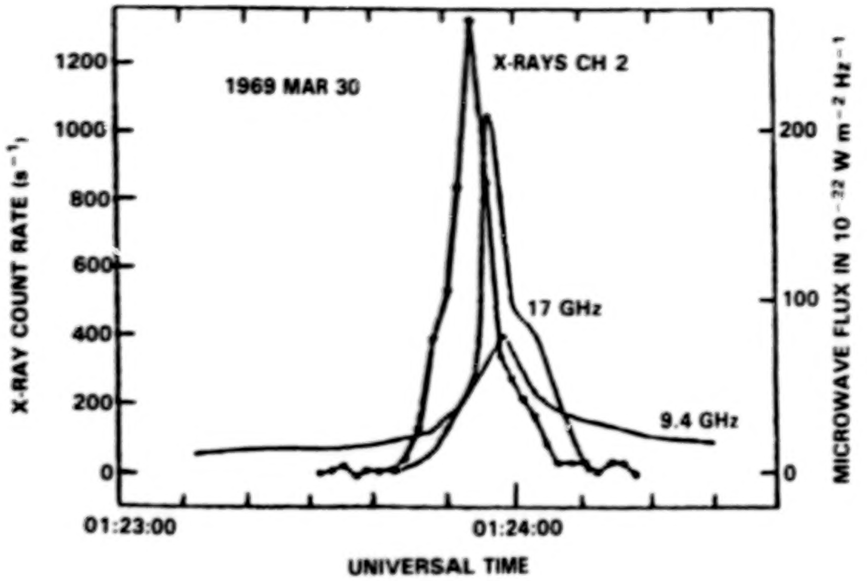

Figure 3. The time profiles of the HX flux is the energy range 28-55 keV and 9.4 and 17 GHz MW flux, copied from the Crannell et al. (1978).

The time evolution of the HX spectral index $\alpha(t)$ is plotted in Figure 4. We also assumed two cases to correpond to that of $N(t)$. In both cases the minimum time of $\alpha(t)$ is delayed from t_m by several seconds but with no softening in case (b). By introducing the time evolution of $N(t)$ and $\alpha(t)$, we can calculate the time profiles of HX and MW emissions. The calculated profiles are illustrated in Figure 5a and 5b corresponding to case (a) and (b) in Figure 4, respectively. The MW flux was calculated for two frequencies of 9.4 and 17 GHz and the HX photon flux is given for a photon energy of $\varepsilon = 41.5$ keV, which is the logarithmic middle energy of the second channel of the HX spectrometer on OSO-5 (ref. Crannell et al. 1978).

Thus, it can be seen that the HX to MW delay can be explained very well in the present model (comparing Figure 3 and Figure 5). The longer delay of low frequency MW (e.g. 9.4 GHz) emission is probably caused by the expansion of the optically-thick emission source. The energy-dependent delay of HX can also be explained in this model. It is interesting that the rare "reversed" delay (with MW preceding HX, such as event No. 3 and No. 9) could be easily explained if we reverse the time axes in Figure 4 and Figure 5. The physical meaning of this reverse may be that the second-step acceleration ceases before the maximum time of the event.

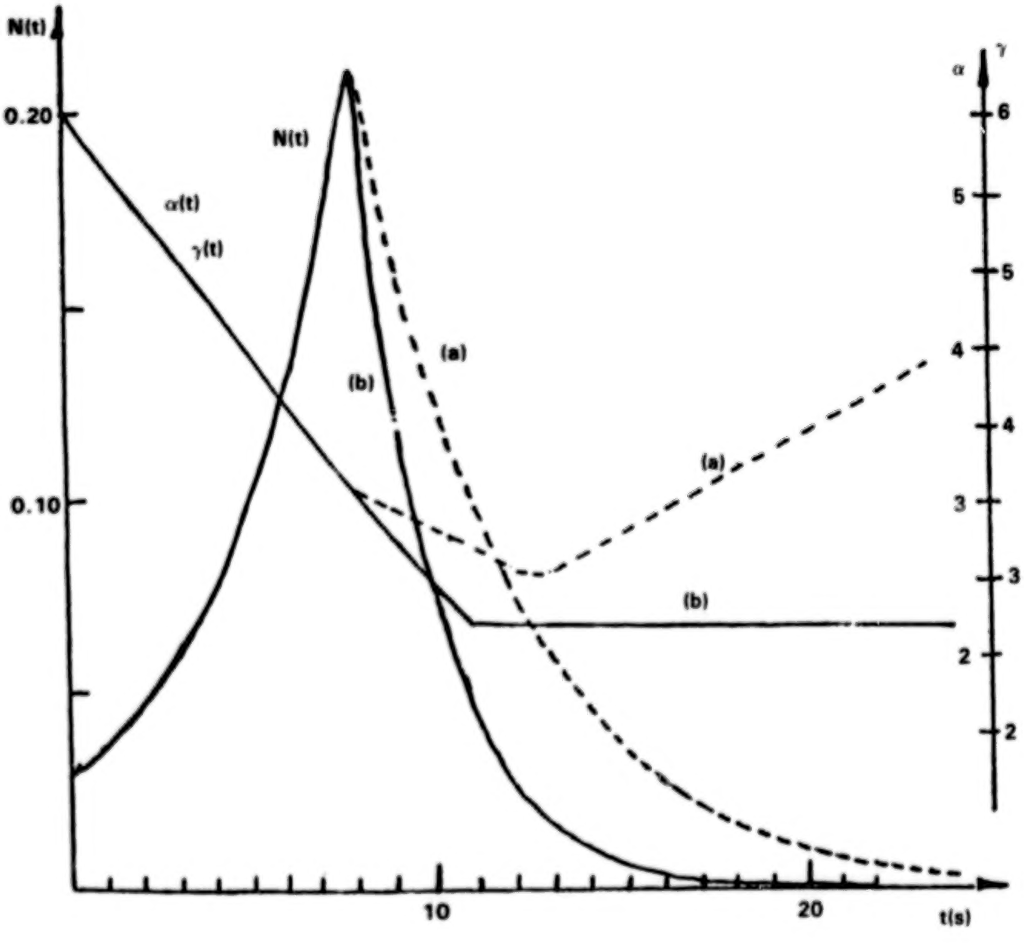

Figure 4. The supposed time evolution of the nonthermal electron spectrum in event No. 2. N(t) is determined by (24) and (25). α(t) (then γ(t)) is inferred from the data given by Crannell et al. (1978, Figure 12).

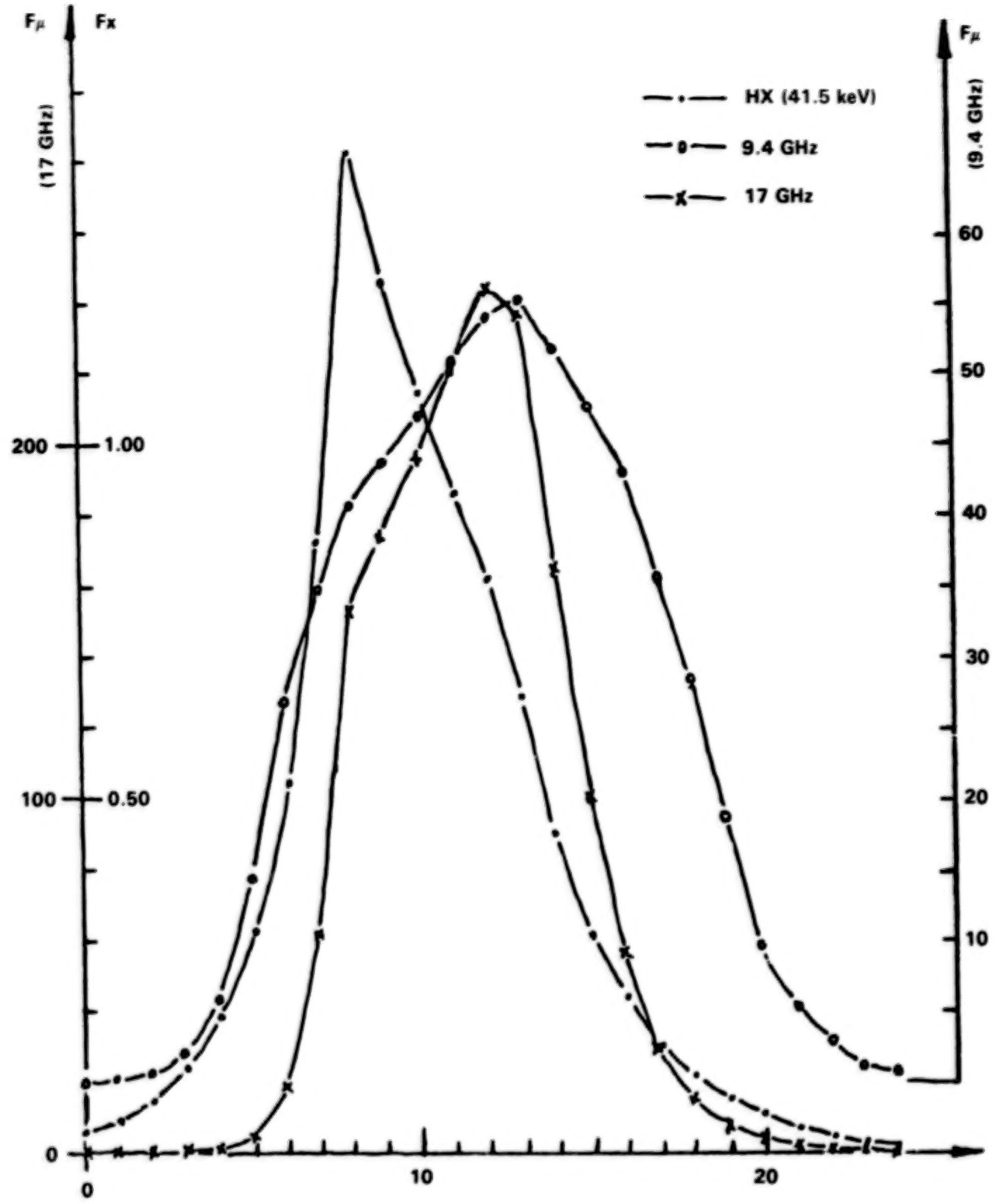

Figure 5a. The calculated time profiles of the HX flux at 41.5 keV and MW flux at 9.4 and 17 GHz, corresponding to case (a) in Figure 4, with a symmetric time profile of N(t).

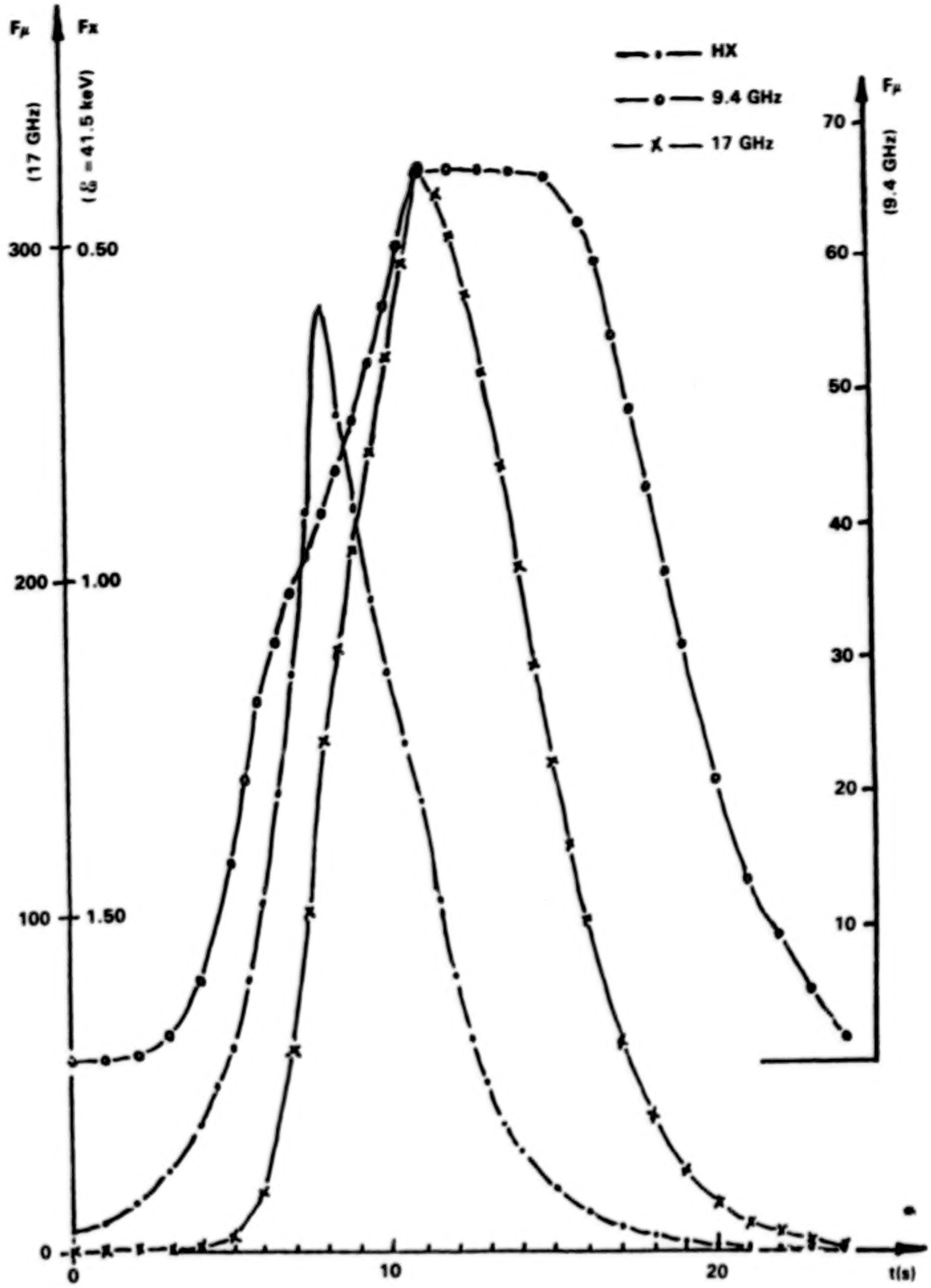

Figure 5b. The same as Figure 5a, but corresponding to case (b) in Figure 4, with an unsymmetric time profile for N(t).

V. Conclusions and Discussions

Starting with the systematic analysis of the spectra of the impulsive MW and HX bursts, we investigated the correlation of the spectral indices and found a possible way to distinguish between the thermal and nonthermal models. Comparisons of the theoretical results with the observations show that only the nonthermal models can explain the optically-thin MW spectrum and its relation to the HX spectrum. The results suggest that both the impulsive HX and MW bursts are produced by the same population of nonthermal electrons accelerated during the impulsive phase. The relative time delays of HX and MW can be explained consistently in a magnetic trap model if only the hardening of the electron spectrum is considered.

All the discussions above are simplified and the results are preliminary. We should have more data to plot the δ-γ correlation diagram and construct the model in more detail. In Figure 2 the δ-γ correlation is for different events. It would be obviously of great significance to analyse the δ-γ correlation during the lifetime of one event (or during its impulsive phase). But it is not easy to get the simultaneous HX and high-frequency MW spectral data.

References

Bai, T. et al. 1983, Ap.J., 267, 433
Benz, A.O. 1977, Ap.J., 211, 270
Brown, J.C. 1974 in Coronal Disturbances, Newkirk ed., IAU Symposium, No. 53, 395
Brown, J.C. 1976, Phil. Trans. R. Soc. Lond. A., 281, 473
Crannell, C.J. et al. 1978, Ap.J., 223, 620
Das, T.K. and Das Gupta, M.K. 1983, Bull. Astron. Inst., Czechoslovakia, 34, 229
Dulk, G.A. and Dennis, B.R. 1982, Ap.J., 260, 875
Dulk, B.A. et al. 1979, Ap.J., 234, 1137
Emsile, A.G. 1983, Solar Phys., 86, 133
Enome, S. 1982 in Hinotori Symposium on Solar Flares 1982, p. 263
Guidice, D.A. and Castelli, J.P. 1975, Solar Phys., 44, 155
Hoyng, P. et al. 1976, Solar Phys., 48, 197
Kane, S.R. et a. 1983, Ap.J., 271, 376
Kaufmann, P. et al. 1983, Solar Phys., 84, 311
Matzler, C. 1978, A.Ap., 70, 181
Takakura, T. et al. 1984, Solar Phys., 89, 379
Tandberg-Hansen, E. et al. 1984, Solar Phys., 90, 41
Wiehl, H. et al. 1980, A. Ap., 92, 260.

N87
21795
UNCLAS

N87-21795

HARD X-RAY IMAGING OBSERVATION OF FLUCTUATING BURSTS

K. Ohki

Tokyo Astronomical Observatory
Mitaka Tokyo, 181 Japan

M. Harada

Science University of Tokyo
Tokyo, Japan

Measurement has been done to obtain one-dimensional sizes of rapidly fluctuating bursts with fast spikes whose rise times are typically about one second, and in some extreme cases less than 0.1 seconds. The results of two bursts with fast spikes are presented here. One has a soft spectrum, and the other has a very hard spectrum. The measured one-dimensional size of both events indicates relatively a small size and simple structure. We can say, however, the source size is not so small as expected from its rapid time variations. Therefore, a thermal explanation of these bursts seems to be excluded.

1. Introduction

Among various electromagnetic radiations, the hard X-ray shows most complex temporal variations during the impulsive phase of flares as well as radio waves. This fact may simply indicate that both type of radiations come from most violently activated regions in the flare or the vicinity of them where energy is created from the nearby magnetic field. Then, a question may be naturally raised what causes the short time fluctuations. Do they indicate many different loops flaring up successively, or the repeated activations within the same loop?

It takes about 8 seconds to obtain two-dimensional flare images with the hard X-ray imaging telescope aboard the Hinotori (hereafter called SXT). However, if we restrict ourselves within one dimensional scan images,

PRECEDING PAGE BLANK NOT FILMED

the temporal resolution to make a single scan image is only about 100 milliseconds depending on the position angle of the scan. So,hard X-ray source location, size, and their time variation up to 100 millisec can be observed by using this one dimensional scan data.

2. Data Selection

To obtain the one-dimensional size of hard X-ray events with fast spikes, we searched for relatively intense events which contain at least several spikes with a total duration of well less than one second.

Another criterion of event selection is that the events should have fast spikes even in the lowest energy channel of the hard X-ray spectrometer, usually at 17 - 40 keV, because the SXT always observed at this energy range. Many hard X-ray bursts observed with the Hinotori show rather slow and broad spikes in the lowest energy channel in spite of fast and sharp spikes in the higher energies. Even in the case where fast spikes exist in the lowest channel, they are usually embedded in the gradual components, and the flux due to fast spikes seems relatively small as compared with those due to the gradual ones. Therefore we intentionally searched for those events in which the fast spike components constitute the major part of the total flux in the lowest energy channel.

Two typical events with such characteristics as above are found in the events of March, 1981. Mar 21 and Mar 24 event seem to be very similar in their appearance of the time history of the lowest channel. But the spectral characteristics of the two events are very different each other. Mar 21 event has a very hard spectrum, while Mar 24 has a rather soft one. In other words, these two events would show two extreme examples among similar events with fast spikes. Therefore, we will exclusively analyze these two events in this paper.

3. Method of Data Analysis

As indicated in Makishima(1982), the telescope SXT has the intrinsic roundness of the triangular beam pattern which is less than seven arcsec. Pre-launch calibration data also show five arcsec for the roundness of the beam pattern. Therefore, it would not be so implausible to start from a rigorous triangular pattern to analyze the one-dimensional data , if our goal of this analysis is restricted to 10 arcsec for the minimum detectable size of the hard X-ray sources.

Then, first we assume a triangular shape with FWHM of 28 arcsec as the SXT 2 (the name of the two SXT collimators) beam pattern. Second, we assume a gaussian profile as the structure of a single source. Then, the convolution between the triangular beam pattern and the gaussian profile of the source will give a calculated pattern after the transmission through an ideal collimator to be compared with the observed one-dimensional scan data.

Figure 1 shows the relationship between the FWHM of the assumed gaussian profile and the FWHM after convolution calculation described above. We can easily obtain the one-dimensional size by measuring the FWHM of the observed one-dimensional scan curve and by comparing it to the calculated FWHM in Figure 1, as far as the assumption of the gaussian profile is not so absurd.

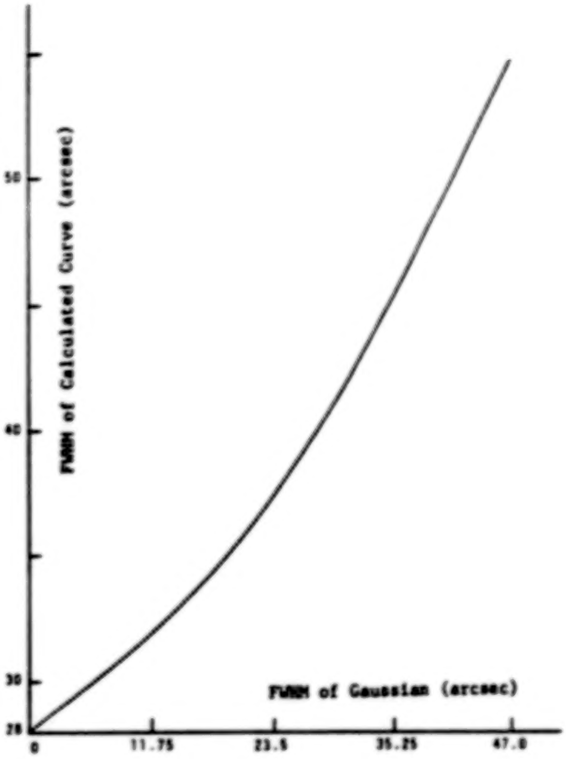

Fig.1. The relationship between the FWHM of the assumed gaussian profile and the FWHM of the calculated scan curve.

4.1. March 24, 1981 Event

In Figure 2(a), time histories of four energy bands are shown. Although this event has a moderate count rate at the lowest energy channel, the count rate at the third channel is very small and the highest channel shows almost no increase above the back-ground level, indicating a fairly soft spectrum of this event.

Figure 3 shows a detail time history with 0.125 sec temporal resolution and three examples of FWHM fitting of one-dimensional scan data. For comparison, the first scan data are accompanied by a standard scan profile taken from October 12, 1981 event which has an excellent single point source with the smallest size we have ever observed, with two-dimensional images for this event being obtained because this event has a smooth and gradual time variation. Generally, the March 24 event consists of a relatively small single source throughout the event. Exceptionally, a halo component is seen in the early phase of the event as can be seen in Figure 3(a1), though the brightness of this halo is less than 10 % of the main source. The measured FWHM sizes of the main source at various times are summarized in Table 1.

4.2. March 21,1981 Event

This event has the main source with larger size than March 24 event as shown in Figure 4. Especially, in the first half of the event, it contains intense halo components or some secondary weaker sources. Any way, it has a complex spatial structure. It should be noted here that a clear secondary source can be seen in a early phase of this first half period as shown in

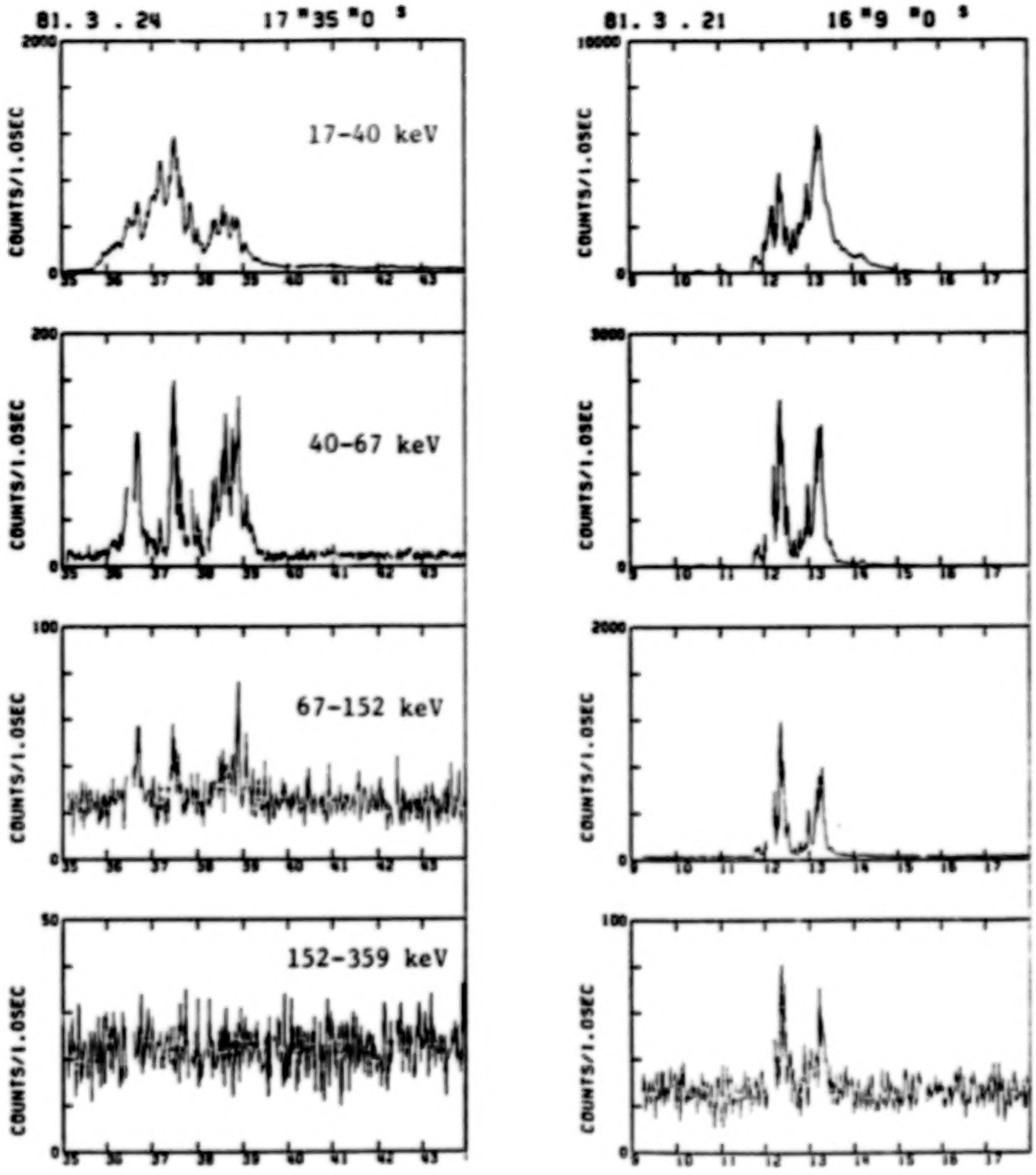

Fig.2. Time histories of March 24 and March 21, 1981 events. One division of the horizontal time axis corresponds to one minute. Four energy bands are illustrated.

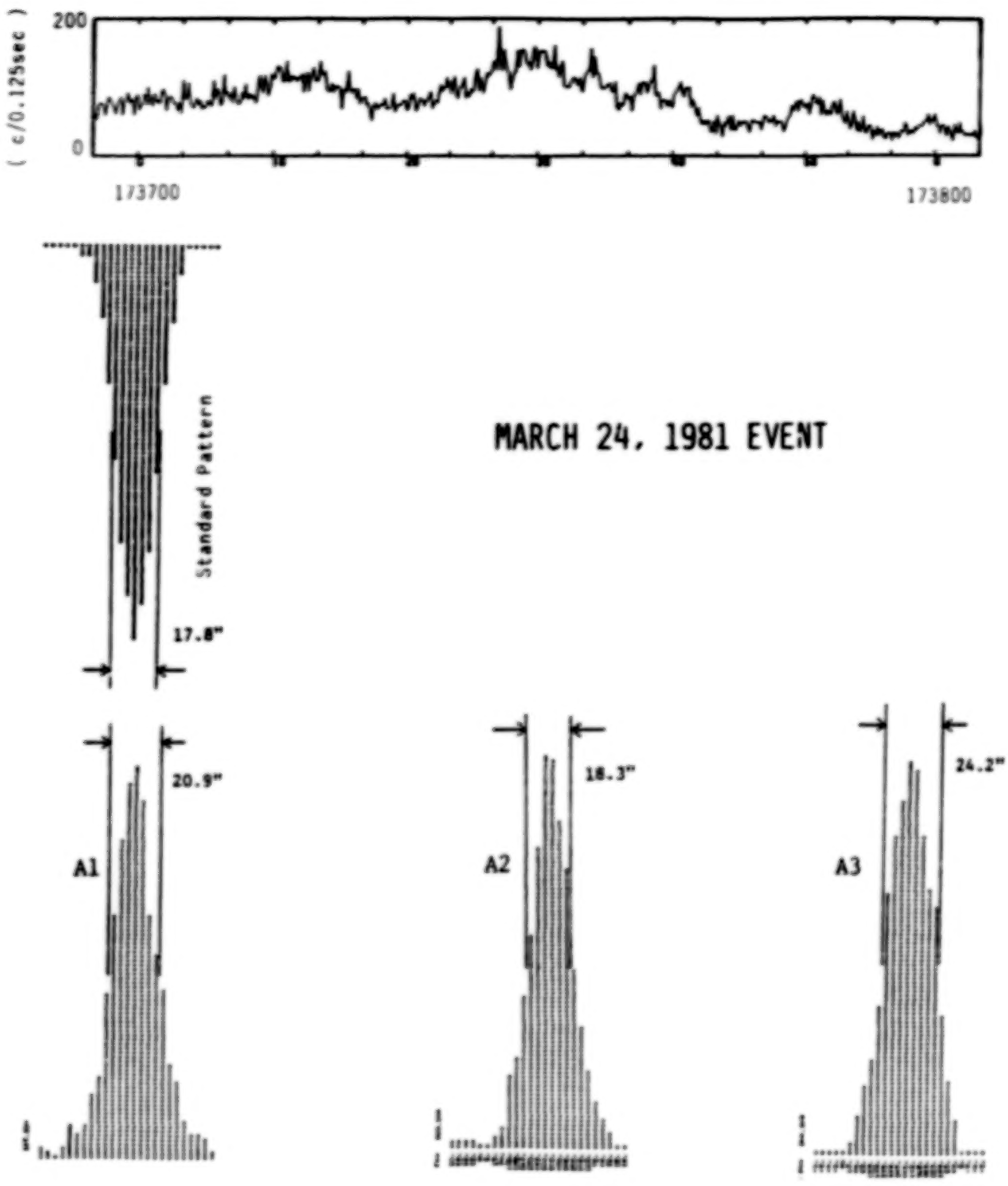

Fig.3. High resolution time history and three examples of the observed one-dimensional scan curves of March 24,1981 event. Resultant gaussian FWHM derived from the measurement of the observed FWHM after fitting to the curve in Figure 1 is illustrated in each scan data. The observation times and other data for each scan is summarized in Table 1.

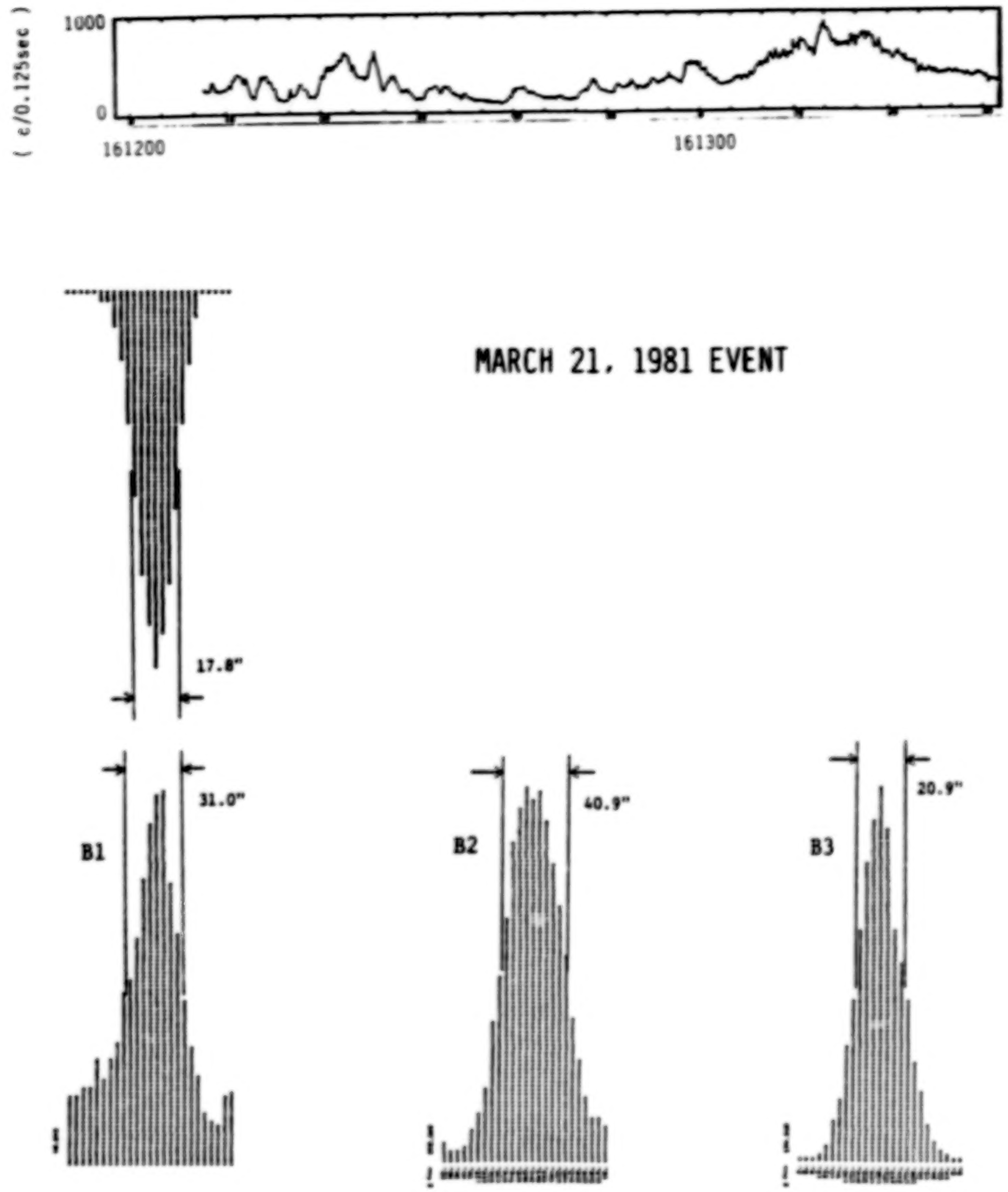

Fig.4. This is similar to Figure 3 but for the March 21, 1981 event. Above the scan data B1, a standard scan data from October 12, 1981 event is illustrated in upside-down position just for comparison. Note that all the observed FWHM of this event are larger than that of this standard scan data.

(continued)

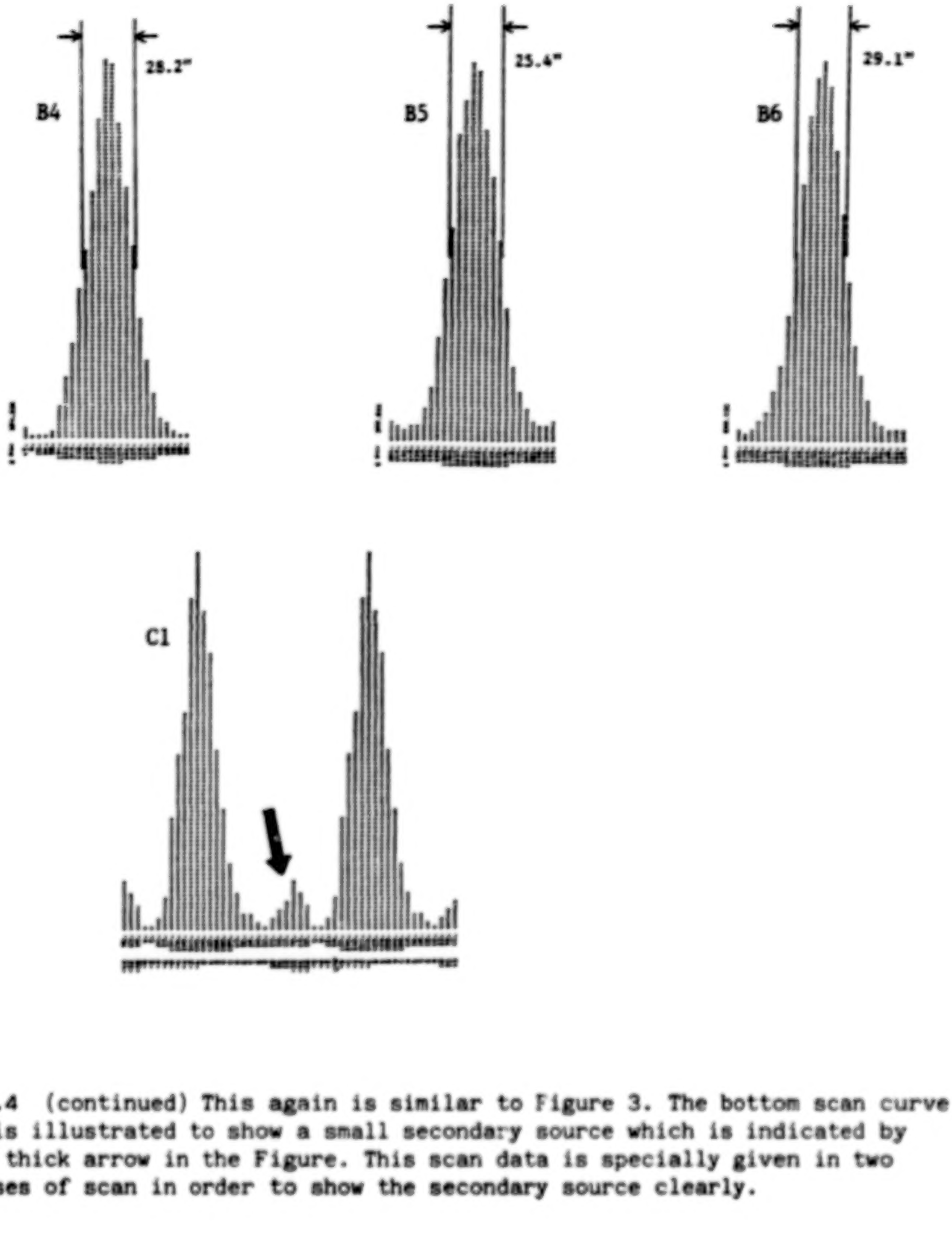

Fig.4 (continued) This again is similar to Figure 3. The bottom scan curve C1 is illustrated to show a small secondary source which is indicated by the thick arrow in the Figure. This scan data is specially given in two phases of scan in order to show the secondary source clearly.

Figure 4(C1). The spatial separation between this secondary source and the main source is as large as about one arcmin. Even in the second half, this event has a fairly large sized main source. The variation of the source sizes and the observed times are again summarized in Table 1.

Table 1. Summary of Observation

Date of Event	Scan No.	Obs.Time	Obs.FWHM (arcsec)	FWHM(arcsec) (gaussian)
MAR 24,1981	**A1**	**17:37:13**	**35.9**	**20.9**
	A2	**17:37:25**	**34.7**	**18.3**
	A3	**17:37:39**	**37.8**	**24.2**
MAR 21,1981	**B1**	**16:12:24**	**42.1**	**31.0**
	B2	**16:12:26**	**49.5**	**40.9**
	B3	**16:13:04**	**35.9**	**20.9**
	B4	**16:13:12**	**40.2**	**28.2**
	B5	**16:13:13**	**38.4**	**25.4**
	B6	**16:13:15**	**40.9**	**29.1**
	C1	16:12:19	—	—

5. Discussion

Many hard X-ray images of impulsive bursts has been already published. Among them, some images of spiky events were included, which showed relatively small and simple structures. For examples, two impulsive events on September 7, 1981 showed a small single source (Takakura et al. 1983). August 10, 1981 event also had a small source (Ohki et al. 1983).

However, we have had not hard X-ray images of rapidly fluctuating events composed of very fast spikes with total durations less than one second, since we can not reconstruct two-dimensional images for such events. About 8 seconds steady data are basically needed to obtain a two-dimensional image. Therefore, in this paper, we sought to have only one-dimensional informations of some fast spike events.

The observational results show relatively small single sources, in the case of March 24 event. One-dimensional sizes of March 21 event, however, show rather moderately sized, somewhat complex sources. The sizes are always larger than 20 arcsec, that is, more than 15000 km on the solar surface. If this size indicates the length of the flaring loop, 20 keV electrons take approximately 0.2 second to run through the entire loop. Since the energy generating region within the loop is localized in various flare models, a sharp spike with a rising time less than 0.1 second can not have a source size larger than 7500 km, that is, 10 arcsec.

If we take a thermally heated model for the fast spike burst, since the speed of heat conduction front is far less than the speed of 20 keV electrons, more difficulties would arise to be reconciled with the observed rapid time variations which should be originated from the 20 arcsec loop.

References

Makishima,K.1982. in Proc. Hinotori Sympo.on Solar Flares (Published by ISAS), p120.
Ohki,K., Takakura,T., Tsuneta,S., and Nitta,N.1983, Solar Phys., 86, p301.
Takakura,T., Ohki,K., Tsuneta,S., and Nitta,N.1983, Solar Phys., 86, p323.

N87
21796
UNCLAS

PRECEDING PAGE BLANK NOT FILMED

HARD X-RAY DELAYS

N87-21796

Richard A. Schwartz

Jet Propulsion Laboratory
National Aeronautics and Space Administration

High time resolution (8, 32, and 128 msec) hard X-ray rates with good counting statistics (up to >25,000 counts/sec) over 5 energy intervals (22-33, 33-60, 60-120, 120-235, and >235 keV) were obtained using a large area (300 cm^2) balloon-borne scintillation detector during the 27 June 1980 solar flare. The impulsive phase of the flare in comprised of a series of major bursts of several to several tens of seconds long. Superimposed on these longer bursts are numerous smaller ~ .5-1 second spikes.

The time profiles for different energies were cross-correlated for the major bursts. Below 120 keV, the bursts reached simultaneous peaks. Six of the bursts show ~ .5-2 second delays in the peaks above 120 keV. These six peaks cover over two minutes at the maximum of the impulsive phase.

The rapid burst decay rates and the simultaneous peaks below 120 keV both indicate a rapid electron energy loss process. Thus, the flux profiles reflect the electron acceleration/injection process. The delays could result from a second-step acceleration wherein the initial fast electron burst acts as a trigger or as a seed population.

The fast rate data (22-33, 33-60, and 60-120 keV) was obtained by a burst memory in 8 and 32 msec resolution over the entire main impulsive phase. We will cross-correlate these rates to look for short time delays and to find rapid fluctuations (<100 msec). However, a cursory examination shows that almost all fluctuations, down to the 5% level, are resolved with 256 msec bins.

PRECEDING PAGE BLANK NOT FILMED

N87
21797
UNCLAS

N87-21797

FAST FLUCTUATIONS OF SOFT X-RAYS FROM ACTIVE REGIONS

G. F. Simnett

Department of Space Research
University of Birmingham
Birmingham, England

B. R. Dennis

Code 682
Goddard Space Flight Center
Greenbelt, MD 20771

A selection of short lived $(\lesssim 10^2\mathrm{s})$ small soft X-ray bursts is studied using data from HXIS, and the results are compared with data from HXRBS with a view to understanding conditions at the onset of flares. Short-lived events provide an opportunity to study the radiation from the primary energy transfer process without confusion from the slowly-varying thermal X-ray emission which characterizes the decay of a large flare. The fast decay of the soft X-rays, only a few tens of seconds, suggests that they occur in the dense chromosphere, rather than in the corona, but this is of course a selection effect. The results indicate that the short events may be signatures of several different phenomena, depending on their characteristics. Some events occur in association with reverse-drift type III bursts and simultaneous flaring elsewhere on the Sun, thus suggesting dumping of particles accelerated at a remote site. Some events have hard X-ray bursts and normal type III bursts associated with them, while others have neither. The latter events place strong constraints on the non-thermal electron population present.

Introduction

There have recently been a number of analyses of solar flare phenomena which are characterized by a short, hard X-ray spike lasting $\lesssim 10^2$s. (Crannell et al. 1978, Wiehl and Desai, 1983, Batchelor et al. 1984). Part of the motivation for such studies is to understand (a) where in the solar atmosphere the X-rays are produced, (b) the X-ray production mechanism -thermal or non-thermal bremsstrahlung, and (c) the origin of the charged particles which carry the energy to power the flare. It has long been assumed that these particles are electrons. However, Simnett (1985) has argued that an energetically-dominant non-thermal ion population might be better able to explain a wider variety of flare phenomena than an energetically-dominant electron population.

With the advent of comprehensive data from recent spacecraft we believe progress can be made in understanding the above topics. Simple events should be easier to interpret than large, complex events, despite the relativity weak signals from some of the former. The large events are almost certainly a combination of two effects, the impulsive deposition of energy to give the short hard X-ray burst followed by ablation of heated chromospheric plasma into the corona. X-ray emission from this material in a typical large flare confuses

PRECEDING PAGE BLANK NOT FILMED

any attempt to isolate the radiation from the primary energy transfer process. In this paper we study a selection of short-lived soft X-ray events seen in 1980 by the Hard X-ray Imaging Spectrometer (HXIS) (van Beek et al (1980)) on the Solar Maximum Mission (SMM). We discuss them in the context of the >27 keV X-ray burst seen by the Hard X-ray Burst Spectrometer (HXRBS) (Orwig et al. 1980), also on SMM, and take into account simultaneous ground-based H_α and radio observations.

The X-ray emission is either thermal or non-thermal bremsstrahlung, or a combination of both. Non-thermal bremsstrahlung would naturally come from non-thermal electrons and rapid fluctuations of hard X-rays (>28 keV) are readily explained by modulation of the electron source. The spectrum radiated by such electrons will extend to the soft X-ray region (~3.5 keV). However, the majority of the soft X-rays have generally been assumed to reflect a thermal origin in plasma heated by the primary energy carriers, be they electrons or ions. If the radiation is thermal, then the very rapid decays (<<1s above 28 keV) are more difficult to understand, although the soft X-ray variations such as those reported here may be reasonable if the radiating region is in the chromosphere. The main problem with a rapidly declining thermal source is the cooling mechanism and for this reason it is unlikely that the X-ray source can be in the corona, where cooling times are longer than the time scales discussed here. Analysis of the events presented in this paper should have a direct bearing on these points.

The Observations

We have earlier presented observations of rapid soft X-ray flares (Simnett and Dennis, 1985). Figure 1 shows an example of the most rapid soft X-ray spike HXIS observed, on 1980, July 10 at 01:50 UT, which lasted <30s. The lower panel of Figure 1 shows an expansion of 40s of data from HXRBS where the accumulation periods for the two HXIS data points above background are shown in black. It is probable that the soft X-ray onset was no earlier than 01:50:18UT and that the intensity returned to background by 01:50:37 UT. From comparison of other fast events, the soft X-ray maximum may be reached just before the hard X-ray maximum. Under these assumptions the soft X-ray amplitude would be 50%-100% higher than plotted and the total width would be ~19s. The event was compact, imaged below the 8" x 8" resolution of HXIS, but on the limb. It was accompanied by a type III radio burst.

Figure 2 shows an example of an event with no hard X-ray, microwave, decimetric or metric emission. The clean fast decay event occurred at 07:07:46 UT on 1980, July 7 and the intensity-time history of 3.5-8.0 keV X-rays from four 8" x 8" HXIS pixels is shown in the upper right panel. The 3.5-5.5keV X-ray image of this event is shown in the lower panel. The left panels in Figure 2 show a similar, but more complex event, which occurred a few minutes earlier from a point approximately 14"E and 2"N of the former event. The active region being studied was then at N28 W48, but there was no reported H_α emission. (Unless otherwise acknowledged, ground based observations are from "Solar Geophysical Data", U.S. Dept. of Commerce, Boulder, CO.). At this position on the Sun, the observed separation of the two events corresponds to ~1.5 x 10^4km. Ten minutes later at 07:18 UT another small event occurred

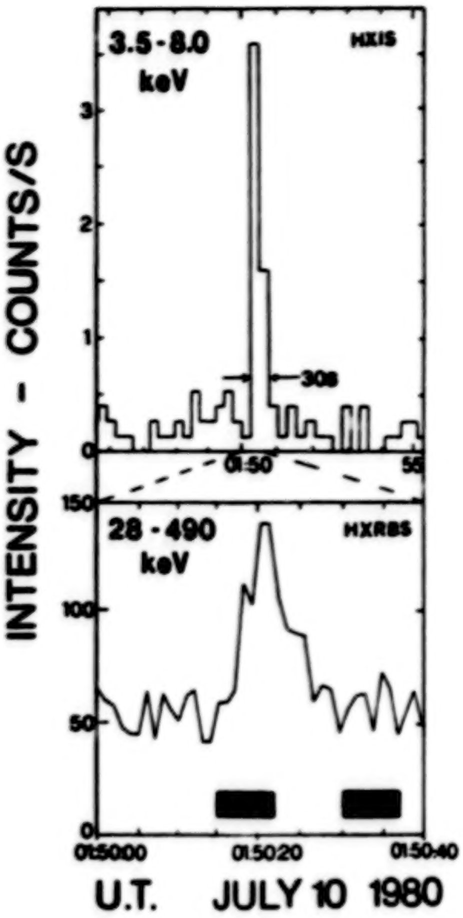

Fig. 1 The short soft X-ray spike on 1980 July 10. The hard X-ray intensity is shown expanded in the lower panel.

where the emission was in a band joining the bright points shown in Figure 2. One interpretation is that there is a magnetic loop linking these points and that the events in Figure 2 occur at opposite ends. There may even be small unresolved loops at these points which contain the bulk of the X-ray emitting plasma: the overlying loop would then be energized by the event at 07:18 UT. We stress then none of these events produced any detected hard X-ray or radio emission.

Some fast spikes occur when there is activity from a remote region. Figure 3 shows the intensity-time history of 16-30 keV (upper panel) and 3.5-5.5 keV (lower panel) X-rays from HXIS for the period 10:09 UT-10:20 UT on 1980, July 7. The feature of interest is the soft X-ray spike superimposed on the decay of the first event, which also had a hard X-ray burst reaching 280 c/s and extending to over 100 keV (shown hatched). The emission from HXRBS corresponding to the earlier, 10:14 UT event is not shown. If we assume the soft X-ray emission associated with the spike to be that above the heavy solid line drawn on the decay of the 3.5-5.5 keV X-rays, then the duration of the spike is 85s. Although there was microwave emission reported throughout the period covered by Figure 3, the maximum intensity at 9.1 GHz was at 10:17:48 UT, coincident with the spike. The spectrum of the burst is hard, as it is remarkable that such a weak event in soft X-rays would be detectable by HXIS above background in the 16-30 keV energy band. There was a 1N H_α flare reported from Hale region 16955, then at N29 W50, from 10:05 UT to10.23UT, with a maximum at 10:15 UT. This was the region studied by HXIS. However, there was another 1N H_α flare from 10:10 UT to 10:33 UT, with a maximum at 10:18 UT, from a region at N21 E44. There was also a reverse drift metric type III burst (A.O. Benz, private communication) at 10.17 UT which did not extend in frequency above 400 MHz. This would correspond to an electron density of $2 \times 10^9 cm^{-3}$ if the emission is at the plasma frequency. In the quiet Sun such densities are typically found at the top of the chromosphere or the base of the corona. (Vernazza et al, 1981) although during activity the altitude may be somewhat higher. The short spike was imaged a few arc-seconds to the southwest of the brightest point of the earlier, decaying flare. The data are consistent with an electron beam escaping from the easterly region and impacting the (presumably) density enhanced corona above region 16955. A similar event on 1980, June 24, was

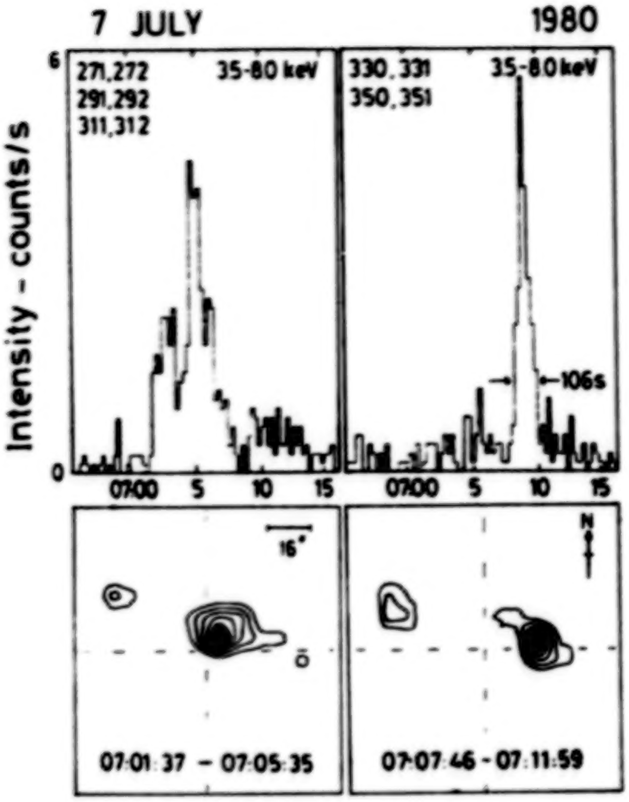

Fig. 2 The fast events with no hard X-ray emission from well-separated points.

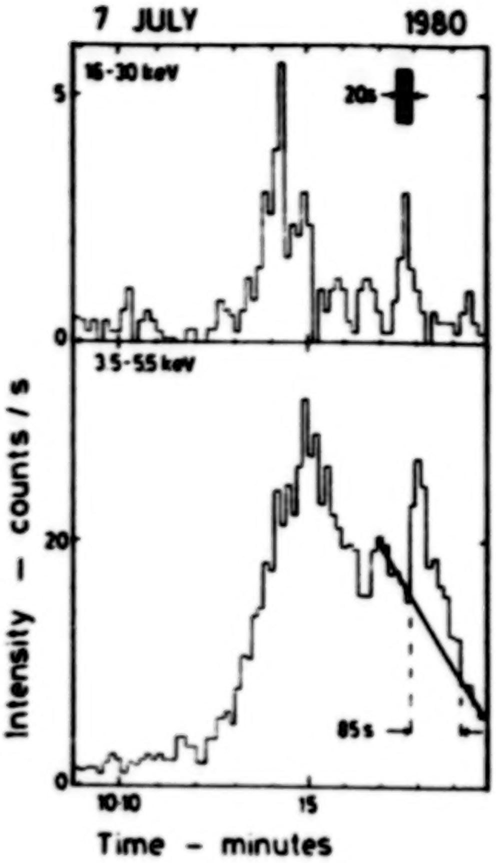

Fig. 3 The X-ray spike superimposed on the decay of an earlier event

reported by Simnett et al (1984) although in this instance both active regions were visible to HXIS.

We have assumed the spike is superimposed on an undisturbed, decaying background from the earlier flare. If this is correct, then the site of the spike and the site of the decaying flare must be physically separate, and not in good thermal contact. This either points to a vertical separation in the solar atmosphere, or to the existence of structures well below the 8" x 8" resolution of HXIS. If the spike is non-thermal bremsstrahlung from precipitating electrons which do not penetrate the 400 MHz plasma level (or the 200 MHz plasma level if the emission is at the second harmonic) then the former explanation would be consistent with the data.

Figure 4a, b, shows the 3.5-8.0 keV X-ray intensity-time history for two isolated events. The FW $^1/_{10}$M are 106s and 152s respectively, but they both have weak, long decays. Both are associated with hard X-ray bursts extending above 100 keV seen by HXRBS. That on 1980 September 26 started at 10:37:40 UT, reached a peak intensity of 349 c/s at 10:37:50 UT, and lasted 50s. That on 1980 July 10 reached a peak intensity of 535 c/s

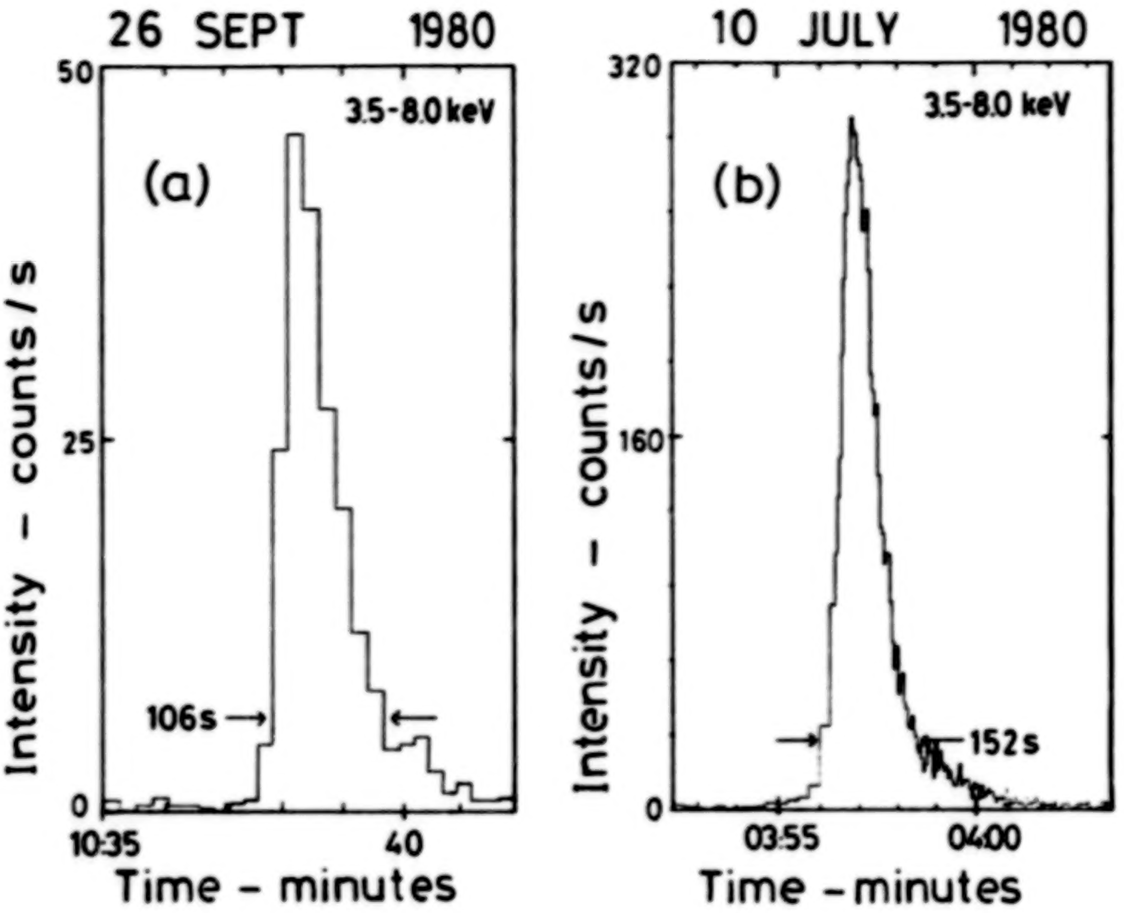

Fig. 4 (a) The fast event on 1980 September 26 (b) The fast event of 1980 July 10

at 03:56:55UT. slightly *after* the peak in soft X-rays.

The September 26 event was accompanied by a microwave burst which started at 10:37:30 UT and reached a maximum of 34×10^4 J_Y. at 19.6 GHz. at 10:37:48 UT. At this time HXIS was studying Hale region 17145. then at N17 W56. There was no optical flare reported from this region. but there was a -F H_α flare from region 17167. then at S19 E44. which reached maximum brightness at 10:37 UT. There was metric radio emission between 10:37:42 uT and 10:38:18 UT. including a reverse drift burst. The latter is indicative of downward moving electrons. If we apply the same reasoning to this event as we did to the event shown in Figure 3. then we might be witnessing X-ray emission from particles accelerated at one site and transferred to a remote site via the large scale coronal magnetic field. There was no evidence of any X-rays >16 keV from HXIS in this event. Considering the relative strengths of the events at 3.5-8.0 keV. and >28 keV for the event and that shown in Figure 3. this is surprising if all X-rays are coming from the area imaged by HXIS. It would be more reasonable if some of the hard X-ray burst seen by HXRBS was from a different region.

Figure 4b shows a much stronger event on 1980.July 10. There was a significant hard X-ray burst seen by HXIS, above 16 keV, capable of producing a weak image, yet the peak intensity seen by HXRBS was only 535 c/s. Therefore, a comparison with the September 26 event shows either that the X-ray spectra between the two events were very different or that the above conclusion that some, or most, of the hard X-rays from the September 26 event were from the east hemisphere flare is correct. There is an additional unusual feature about this event in that the soft X-ray intensity is already declining before the hard X-ray burst reaches maximum. The latter is very structured, with three prominant peaks, the last being the most intense. This event might be more consistent with other events, from spectral and temporal considerations, if the last and longest hard X-ray spike were from a region not imaged by HXIS. There was decimetric, metric and dekametric activity from 03:56-03:57 UT but no reported H_{α} flare.

The final event on 1980, July 11 at 05:31:30 UT is shown in Figure 5. The soft X-ray enhancement coincident with the hard X-ray burst fell virtually to background level before rising again for the small event at 05:33 UT. The 40s duration of the hard X-ray burst, which reached an intensity of 103 c/s and extended to beyond 100 keV, is indicated by the cross-hatched box in Figure 5. The 5.2 GHz microwave burst reached $8 \times 10^{4} J_{\gamma}$ at 05:31:30 UT, essentially coincident with the hard X-ray burst maximum at 05:31:35 UT. There was metric and decimetric type III activity from 05:31:30 UT-05:33 UT (A. O. Benz, private communication).

This small event was from N20 E55, associated with a -N H_{α} flare which started at 05:32 UT and had a maximum at 05:34 UT. The initial soft X-ray burst appears to be quite definitely associated with the hard X-ray burst, but yet the following stronger soft X-ray emission has no corresponding hard X-rays. The second burst is delayed long enough that any thermal effects of energy deposition at the time of the hard X-ray burst must have dissipated.

We note that there was a 1F H_{α} flare in progress at this time from S11 E83, with a maximum at 05:39: UT. In view of the associations discussed above in relation to other events it is plausible that this event is also associated with activity from a remote region. One might speculate that the first spike in Figure 5 is non-thermal bremsstrahlung from electrons, while the later emission is thermal X-rays from plasma heated by ions. If the distance travelled by the particles is 8×10^{-10}cm, consistent with the separation of the two flaring regions, cf e observed delay of ≈80s between the first spike and the subsequent soft X-ray emission may be accounted for by electrons of ≈30 keV and protons of ≈400 keV.

Conclusions

The events discussed above provide a unique insight into the correspondence between hard and soft X-ray emission in solar events which are not confused by large scale chromospheric ablation and its associated thermal X-ray signature. We have focused on the features of the events which we think provide good boundary conditions for a sound interpretation. The interpretations we have made appear reasonable, but they are not meant to exclude other explanations which match the boundary conditions. The soft X-ray spikes are compact events, typically, but not always, below the 8" x 8" resolution

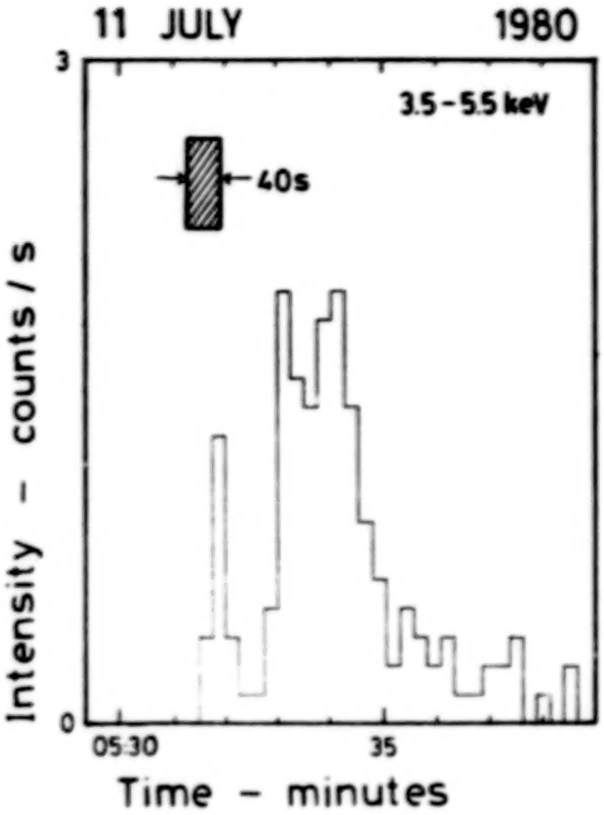

Fig. 5 A soft X-ray spike coincident with the hard X-ray burst (shown hatched) but separated from the main event.

HXIS. Some events, such as that on July 7 and on 1980, June 27 at 19.50 UT (Simnett and Dennis, 1985) had no reported radio activity at any wavelength. This would argue against non-thermal electrons as the dominant energy carrier in these events, especially as the hard X-ray intensity is also below the HXRBS threshold. The rapid decay of the soft X-ray events is unlikely to be a signature of hot plasma in the corona. Therefore we believe these events either take place at the top of the chromosphere, or are non-thermal electron bremsstrahlung. The very short spikes which occur in coincidence with hard X-rays, such as those shown in Figure 1 and 5, are most likely examples of the latter. Finally, we believe the events where (a) there is a reverse drift radio burst and (b) simultaneous flaring from widely separated regions argues strongly for a particle beam interpretaion, coupled with extensive magnetic coronal loops linking the flaring regions; where in the large loop the energy release and particle acceleration occur are open questions.

Acknowledgements

We are grateful to Dr. A. O. Benz for useful discussion and for making unpublished data available to us.

References

Crannell,C.J., Frost,K.J., Matzler,C., Ohki,K and Saba,J.L.:1978,Ap.J. 223, 620.

Batchelor,D.A., Benz,A.O. and Wiehl,H.J.:1984, Ap.J. 280,879.

Orwig,L.E., Frost,K.J. and Dennis,B.R.:1980, Solar Phys. 65,25.

Simnett,G.M., Harrison,R.A., Hoyng,P and Van Beek,H.F.:1984, in M.A.Shea, D.F.Smart and S.M.P. McKenna-Lawlor (eds) Proc STIP Symposium on Solar/Interplanetary Intervals Engineering International,inc. Huntsville, AL, USA, p273

Simnett,G.M. 1985, Proc. XIX Int.Cosmic Ray Conf. Vol.4, 70.

Simnett,G.M. and Dennis,B.R.:1985 Proc XIX Int.Cosmic Ray Conf. Vol 4,38.

Van Beek,H.F., Hoyng,P., LaFleur,H. and Simnett,G.M.:1980 Solar Phys. 65, 39.

Vernazza,J.E., Avrett, E.H. and Loeser,R.:1981, Ap.J.Supp. 45, 635.

Wiehl,H.J. and Desai,U.:1983, Ap.J. 270, 256.

RADIO AND MICROWAVE GROUP
SUMMARY OF DISCUSSIONS

Rapporteur: Arnold O. Benz

Institute for Astronomy, ETH
Zurich, Switzerland

Observers of solar flares in radio and microwaves have been confronted with rapid fluctuations for a long time. In fact, most radio bursts show variations on the time scale of one second or less. At long wavelengths (decimetric and longer) the radiation most often seems to consist of a sequence of peaks rather than a modulated emission. There are two main reasons for the great abundance of rapid fluctuations in radio and microwaves: The large collecting areas and high sensitivity of the receivers lead to a signal to noise ratio which usually far exceeds measurements at other wavelengths. Fluctuations, which also may exist, simply pass undetected in the noise at other wavelengths. The second reason is physical. At wavelengths longer than about 10 cm the emission process changes from incoherent synchrotron radiation to some coherent process. The cause of emission is one of many possible instabilities of a non-thermal electron velocity distribution. The limitation or saturation level of such instabilities is highly variable.

The group consisted of 2 distinct sets of people: observers at microwaves and observers at longer waves. The first question addressed was: **Are spikes seen in radio and microwaves the same?** G.D. Wells presented an example of National Geophysical Data Center archives data. A. Benz showed first quantitative spectras of spikes at 0.3 - 1.0 GHz having bandwidths of 1.5 % of the center frequency. K. Tapping discussed VLBI observations of a similar spike at 1.6 GHz with a possible source dimension of about 40 km. M. Stähli has discovered a narrowband spike at 5.1 GHz of a few tenths of millisecond duration, the highest frequency ever. A theoretical paper on millisecond spikes was presented by C.S. Li.

S. Enome and L. Orwig have studied the ratio of spike emission at 1 GHz to the hard X-ray flux. They find the narrowband spikes to emit much more than the broadband spikes. A very likely interpretation may be that the latter radiation is incoherent, i.e. synchrotron emission. Broadband spikes are generally seen at high microwave frequencies. They last typically 1 second and generally correlate well with hard X-rays. They have been discussed by E. Correia et al. in terms of inverse Compton losses. K. Kai and H. Nakayima find positions of such broadband spikes at microwaves to vary from peak to peak. P. Kaufmann and A.M. Zodi discussed ms-second structures at high frequency microwaves which are not broadband. They seem to be a modulation of a background or a fine structure of it. This is very different from the millisecond spikes at wavelengths longer than 10 cm, which are individual bursts with no (or differently polarized) background.

The group concluded that:

1) narrowband spikes are generally observed around 1 GHz, but up to 5.2 GHz, and are to be considered physically different from broadband spikes at higher frequency.
2) observations of bandwidths at all frequencies are of great importance.

The second topic concerned **pulsations**. They are observed as quasi-periodic fluctuations in the whole radio and microwave region. T. Kosugi has found microwave pulsations correlating with hard X-ray fluctuations. Pulsations at very high microwave frequencies were presented by P.

Kaufmann. The discussion, however, revealed that the position of some of such microwave pulsations were not identical. Oscillating flux tube models, however, would predict a constant source position. A. Benz presented metric radio oscillations (0.2 GHz) which were periodic and came from the same source. It was concluded in a general discussion that only position measurements can distinguish between real and apparent quasi-periodic pulsations.

N87

21798

UNCLAS

N87-21798

EXTREMELY RAPID RADIO SPIKES IN FLARES
(Review)

A. O. Benz

Institute of Astronomy, ETH
Zurich, Switzerland

ABSTRACT

Radio spikes of a few to tens of milliseconds of the solar radio emission have recently seen a surge of interest of theoreticians who are fascinated by their high brightness temperature of up to 10^{15} K, their association with hard X-ray bursts, and a possibly very intimate relation to electron acceleration. Their bandwidth and global distribution in frequency have quantitatively been measured only recently. This review is intended to emphasize the considerable extend of old and new observational knowledge which is hardly touched upon by theory. The wide range of spike observations is summarized and brought into the perspective of recent models. It is concluded that spikes yield a considerable potential for the diagnostics of energetic particles, their origin, and history in astrophysical plasmas.

1. Introduction

Millisecond radio spikes are a rapidly growing field of solar radio astronomy. Although their role and diagnostic capabilities for flare theory, nor even their emission mechanism are clear, considerable progress in our understanding has been achieved over the last few years. Spikes today are generally agreed to be a non-thermal, coherent emission closely connected with particle acceleration and energy release in flares.

Radio bursts with durations of less than 100 ms have first been noted by Dröge and Riemann (1961) and Elgarøy (1961). They have been studied by de Groot (1962), Elgarøy (1962), and later by Eckhoff (1966) and de Groot (1966). The first major articles on the subject did not appear until Dröge (1967) and Malville, Allen and Jansen (1967) summarized their observations. This work was extended by de Groot (1970) and Tarnstrom and Philip (1972a,b). The pioneers used various names for the new phenomenon: knots, pips, rain, flash bursts, etc. We will use the word "spike" introduced by de Groot, which today is well established in the community, and restrict it to narrowband peaks of less than 100 ms total duration. Note that in hard X-ray and high frequency microwave data the same expression sometimes is used for entirely different phenomena such as peaks with ten times or longer durations or tiny fluctuations of a background emission.

In the first decade of spike observations the observing frequencies were in the range from 200 to 350 MHz. This was extended by more than an order of magnitude in both directions in the following years. Barrow and Saunders (1972) have found spikes at 18 - 26 MHz associated with type III radio bursts. Their observation, however, has never been confirmed by spectral measurements. At microwaves, spikes were observed up to 1420 MHz by Dröge (1967 and 1977), at 2650 and 2840 MHz by Slottje (1978) and Zhao and Yin (1982). They have recently been discovered up to 5200 MHz by Stähli and Magun (1986). These authors did not find spikes (as defined above) at higher frequencies. It is clear today that spikes are most abundant in the decimetric range, i.e. from 300 to about 3000 MHz.

How many types of spikes are there? The report of Slottje (1978) of fully polarized spikes in a microwave event at the time was considered evidence for a species of spikes entirely different from the intermediately polarized kind at lower frequency. However, subsequent observations by Slottje (1980) and Stähli and Magun (1986) of a larger set of spikes at microwaves showed that the event was exceptional and the general polarization behaviour is similar to the one deduced by Benz, Zlobec, and Jaeggi (1982) at 300 MHz. Secondly, spike emissions may have different origins if they occur in different contexts as manifested by other radiations. Spikes have been found to be associated with metric type I storms (Elgarøy, 1962; Eckhoff, 1966), type III bursts (Elgarøy and Rødberg, 1963; Tarnstrom and Philip, 1972b), and type IV events (Dröge, 1961); Elgarøy, 1961; de Groot, 1962, and later authors). Malville et al. (1967) measuring only total flux at two frequencies could not find any difference between spikes and type I bursts except in duration. Elgarøy and Eckhoff (1966) noted a smooth transition from type I bursts to spikes and back during a noise storm. However, spectrographic observations by de Groot (1970) demonstrated that spikes associated with type III and type IV bursts preferentially occurred at higher frequencies than type I bursts. Finally, Benz et al. (1982) found significant differences to type I bursts in polarization, bandwidth, and spatial distribution on the solar disk. In conclusion, it seems that presently only two species of spikes can safely be distinguished: spikes in noise storms at metric frequencies, which seem to be identical to type I bursts except for their shorter duration, and "real" spikes, which extend to much higher frequencies and are associated with flares. This review concentrates on the second kind. Whether it is a homogeneous set of phenomena or needs to be divided along frequencies (such as decimetric vs. microwaves) or associated metric activity (type III vs. type IV) needs to be investigated. Nevertheless, this review follows the rule that phenomena have to be considered as manifestations of one type until shown to be different.

This article is the first summary of 25 years of spike research. The main emphasis is on a complete discussion of observations and their theoretical implications. The theory of spike emission is also briefly reviewed. The goal is to draw the attention of the larger community interested in solar flares to the rapidly growing set of spike observations, and most of all to bridge the gap which sometimes seems to separate theoreticians and observers.

2. The Spike Phenomenon

2.1. Time Profile

The duration of spikes, orders of magnitude shorter than any other type of radio emission, led to their discovery as soon as appropriate instruments were in operation. Early observations are shown in Figure 1. Many authors have reported contradictory values for the duration of single spikes. Limited instrumental resolution may explain some of the discrepancies. Other authors emphasized extremely short values which were, however, exceptional cases. In addition there seems to be a trend to shorter duration at higher frequencies noted already by Dröge (1967) and Tarnstrom and Philip (1972b).

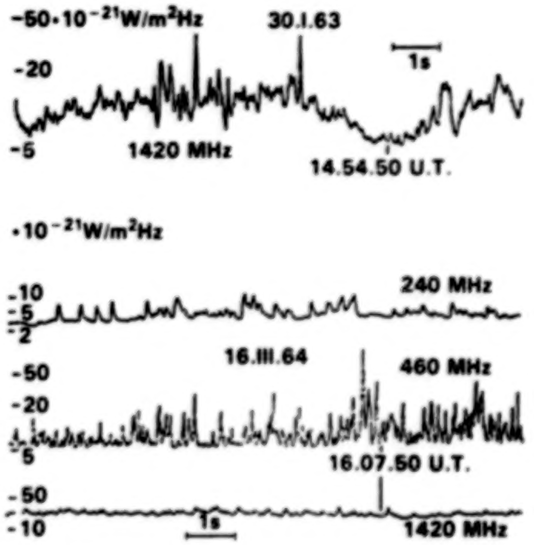

Fig. 1: Full Disk radio observations (total flux vs. time) of a solar flare at different frequencies. *Top*: Spikes superimposed on major type IV event in microwaves. *Bottom*: Spikes at 460 MHz associated with metric type III bursts at 240 MHz (from Dröge, 1967).

Considering only measurements with sufficient resolution, typical durations of single spikes around 250 MHz are 50 - 100 ms (Dröge, 1967, Benz et al., 1982). Barrow et al. (1984) measuring with 0.3 ms resolution noted structure down to 5 ms. The typical duration decreases to 10 - 50 ms at 460 MHz and to 3 - 7 ms at 1420 MHz (Dröge, 1967). It seems to be below 10 ms around 3000 MHz (Zhao and Yin, 1982; Stähli and Magun, 1986).

Tarnstrom and Philip noted that the duration of spikes is comparable to the electron-ion collision time interactions,

$$\tau = \frac{0.18\, T^{3/2}}{n_i \, ln\, \Lambda}\ , \tag{1}$$

(Zheleznyakov, 1970) assuming equal electron and ion temperature T. With $ln\ \Lambda \approx 11.2$ and for fundamental plasma emission

ORIGINAL PAGE IS
OF POOR QUALITY

$$\tau \approx 4.0\left(\frac{1}{\nu_{GHz}}\right)^2 \left(\frac{T}{2\cdot 10^6}\right)^{3/2} ms \tag{2}$$

where ν_{GHz} is the observing frequency in GHz. Several authors have derived upper limits on the source size, requiring it to be smaller than the duration divided by the speed of light. In the light of the above correlation of duration and collision frequency, it does not seem plausible that the source size decreases with frequency. More likely is the duration determined by some collision time, and the upper limit of the size derived from duration at high frequency is closest to the actual dimension.

2.2. Spectrum

A better estimate of the source size can be derived from the bandwidth of single spikes. Early spectras (e.g. de Groot, 1970) have already revealed that spikes are very narrow-banded. Reported observations of the bandwidth vary between 0.5 and 15 MHz. They have been measured with various methods and need to be considered with caution. Film recordings yield total bandwidth above threshold. The measured values thus depend on peak flux minus threshold. The firstquantitative spectra of spikes have been published only very recently (Benz, 1985). The half-power width at practically instantaneous time is typically 10 MHz, or 1.5 %, at a center frequency of 600 MHz. Figure 2 is an instructive comparison between spike and type III bursts in frequency and time. This extremely narrow width is a powerful restriction on possible emission processes.

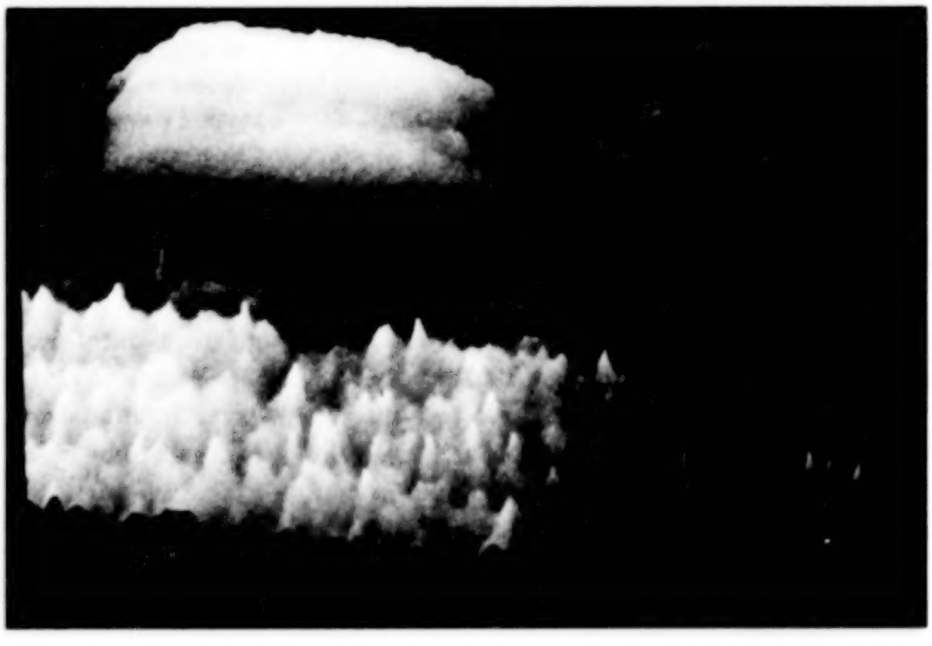

Fig. 2: Three-dimensional representation of spikes (front) and type III bursts (back): time increases to the right (total of 4 seconds is shown). Frequency decreases with depth (370-250 MHz), and flux is shown logarithmically in vertical direction. The data was recorded by the digital spectrometer (IKARUS) in Zurich on 1980, September 24, 0731 UT.

ORIGINAL PAGE IS
OF POOR QUALITY

Spikes have escaped detection by routine film-recording spectrographs for a long time. For this reason the total bandwidth of spike activity and the total number per event remained unclear. Single frequency observations by Dröge (1967) suggested total bandwidths of a few hundred MHz for spike activity in typical events. This has been confirmed with the digital spectrometer in Zurich. Using this instrument Benz (1985) has estimated the total number of spikes per event between 8200 and more than 13200 in 4 rich spike events. The multitude of spikes is evident in Figure 2 showing the contrast between type III and spike bursts. Spikes associated with type IV bursts may after some time of random occurrence arrange themselves to patterns in the frequency-time plane, which may resemble broadband pulsations or parallel drifting bands (Kuijpers et al., 1981). A global shift of spike activity from 3 GHz to $\leq$ 1 GHz has been noted by Fu et al. (1983) in the 1981, May 16 event. This may reflect a general shift of the spike sources to lower density and possibly higher altitude.

2.3. Polarization

De Groot (1962), Chernov (1976, 1978) and Slottje (1978) reported "strong" circular polarization of spikes. More recent measurements (Slottje, 1980; Benz et al., 1982; Stähli and Magun, 1986; Nonino et al., 1986) agree that the polarization is generally higher than e.g. for type III bursts, but it can vary from 0 to 100 %. It is interesting to note that these observers measured

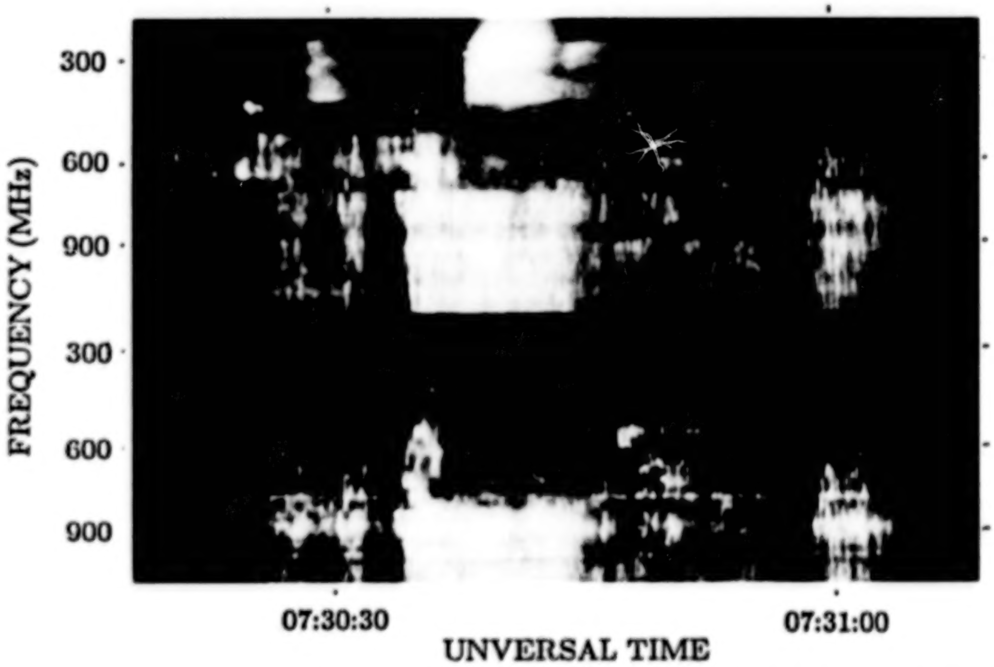

Fig. 3: Calibrated spectrogram of impulsive phase of a flare on 1980 September 24 observed by the digital spectrometer in Bleien (Zurich). **Top**: total flux. **Bottom**: polarization spectrum of the same time interval showing separation of type III and spike bursts. Left circular polarization is represented bright, right circular polarization dark, and zero polarization is gray (from Benz and Kane, 1986).

different frequencies (from 0.2 to 3.2 GHz) and associated with different metric activity (type III and type IV). An example of a polarization measurement is shown in Fig. 3. For this rare case the sense of polarization of the type III is opposite to the spikes. The polarization averaged over many spike events is between 25 and 30 %. Surprisingly, the value does not vary between 0.238 GHz (Zurich and Trieste observations) and 3.2, resp. 5.2 GHz (unpublished Bern observations).

2.4. Position

The center-to-limb variation of the rate of occurrence of spikes has been investigated by statistics on associated Hα flare positions. No longitudinal effect has been noted by Benz et al. (1982) at 0.3 GHz and Stähli and Magun (1986) at 3.2 GHz. It may thus be concluded that propagation effects do not play a major role in the spike process.

Only one direct measurement of the position of a spike event has been reported (Heyvaerts et al., 1978). The sources were found separated from the associated type III bursts by about 1 arcmin. Therefore it seems that not only the emission mechanisms of the two radiations are different, but also the source environment.

3. Phenomena Associated with Spikes

The timing of spike emission in relation of the flare process is an important indicator for the interpretation of spikes.

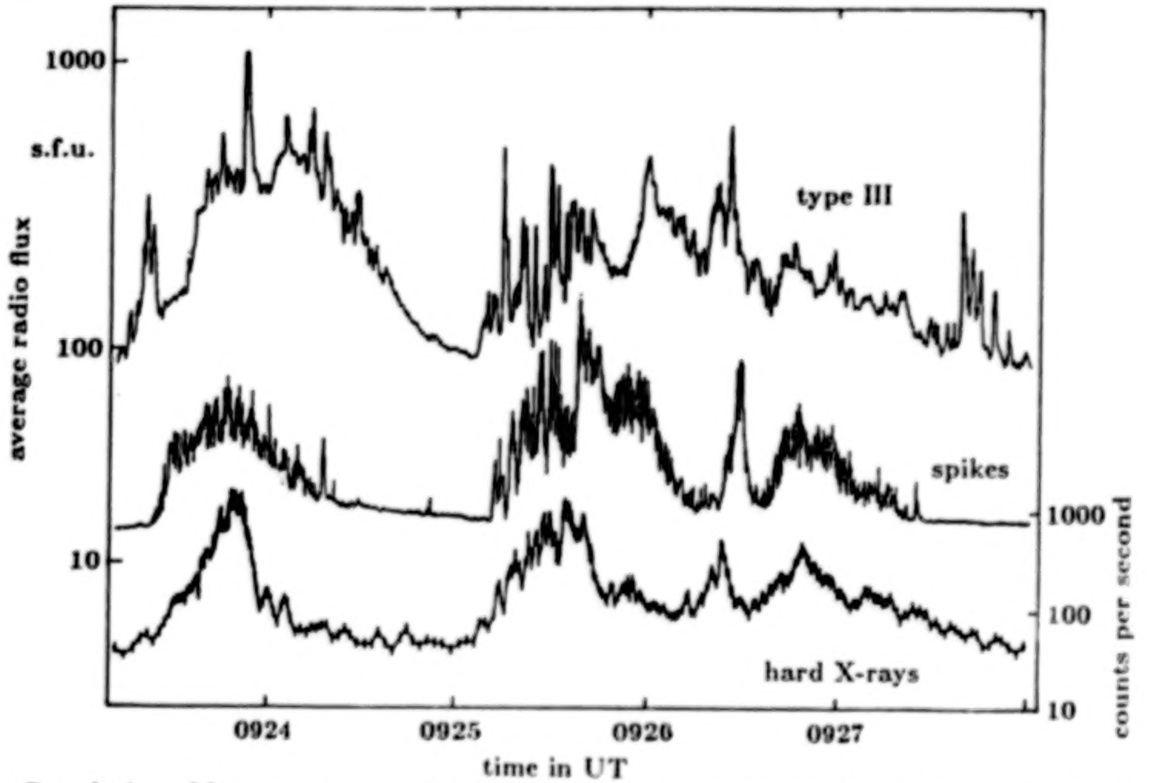

Fig. 4: Correlation of frequency-averaged spike flux in the frequency band 580-640 MHz (middle) with type III emission in the 250-310 MHz band (top) and HXR (bottom). The radio data has been recorded with the Zurich digital spectrometer (IKARUS), the HXR observations were made by HXRBS/SMM (from Benz, 1985).

3.1. Other Radio Emissions

Spikes most frequently appear at times of type III bursts, the radio signature of electron beams in the corona. Even with a modern film recording spectrograph spikes are observed near the starting frequency of type III bursts in 10 % of all cases (Benz et al., 1982). They are generally at higher frequency (and thus higher source density) than the associated type III bursts. Examples of type III-spike associations are given in Figs. 2 - 4. Figure 4 shows a relatively close correlation of the time variations. Details of type III and averaged spike emission sometimes, but not always, correlate. Some examples of detailed correlation of single type III bursts with clusters of spikes have been given by Benz et al. (1982). It seems very likely that spikes are caused by energetic electrons or their acceleration process.

Karlicky (1984) has analyzed spikes in big outbursts (usually type II and IV). He finds the spikes not always related to type III bursts. Some appeared shortly before the start of a type II or another manifestation of mass ejection. Spikes generally occurred before pulsations, which have been proposed to be caused by energetic particles trapped in magnetic loops. These observations suggest that spike emission neither requires streaming, nor trapped particles.

Stähli and Magun (1986) find from single frequency measurements at 3.2 GHz that 10 % of all events show temporal fine structure possibly caused by spikes. In agreement with Slottje (1978), Zhao and Yin (1982) and others, they find the spike activity to generally occur in the rise and maximum phase of the impulsive microwave (synchrotron) emission. An example of the phasing of spikes in relation to the impulsive microwave emission is given in Fig. 5.

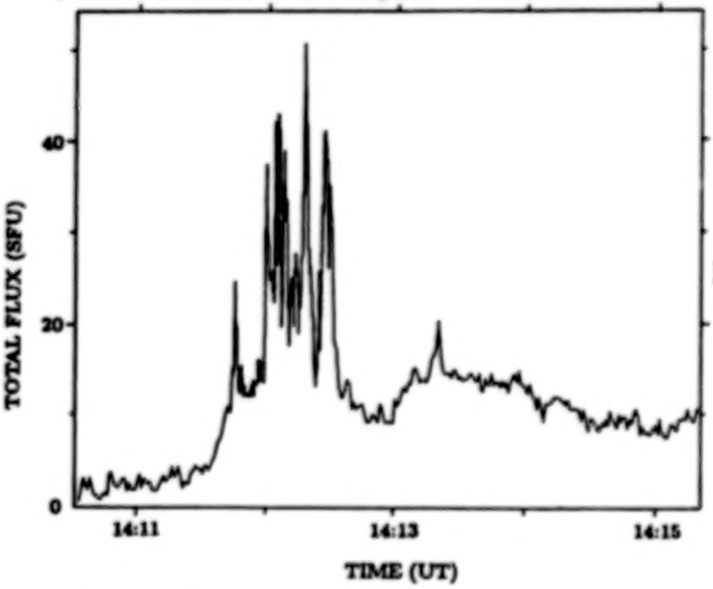

Fig. 5: Observation of spikes at 5.2 GHz by the Institute of Applied Physics in Bern on 1982, February 10. The spikes are superposed on the smoother, impulsive synchrotron emission (courtesy of M. Stähli).

3.2. X-Ray Emission

Hard X-ray (HXR) emission originates from bremsstrahlung and provides reliable information on the energy of fast electrons. Benz and Kane (1986) find enhanced X-ray emission above 26 keV in 71 % of well developed type III/spike events. All major spike events are accompanied by enhanced HXR. Benz and Kane (1986) have noted that HXR emission associated with spikes tends to be more impulsive and shorter in duration than the average HXR burst. The correlation of HXR and spikes can be very close as e.g. in Fig. 4. However, it is generally not as good and reliable as between HXR and microwave emissions. The occurrence of spikes seems to require additional conditions on the source or on the exciter. The occasionally close association of spikes with impulsive HXR emission suggests that spikes are intimately related to the energization of fast electrons. This is supported by the observed concentration of spikes in the rise and maximum phase of HXR bursts (Benz and Kane, 1986), which is contrary to the timing of all other decimetric emissions except type III. The understanding of spikes may thus yield information on the primary energy release in flares.

Soft X-ray observations of the 1980 August 31 flares by Strong et al. (1984) yield preflare densities with plasma frequencies in the range of the frequencies of the spikes observed later during the flare (Benz, 1985). It is generally believed that spike emission occurs at a frequency which is within a factor of two of the local plasma frequency. The observations then indicate that spikes occur near the flare site before the density increase by evaporation of chromospheric material. If shown to be generally true, the range of spikes in frequency would limit the density in the primary energy release region to about $10^9 - 10^{11} cm^{-3}$.

If the spike sources were located in an isothermal atmosphere, the derived density range would correspond to an extent of 5.5 scale heights or 550000 km at $2 \cdot 10^6$ K. The close correlation with hard X-rays (known to originate mostly from $\lesssim$ 2500 km, Kane, 1981) and the absence of drift in spike clusters clearly exclude such a possibility. The spread of spike activity in the spectrum thus seems to be caused by a density (or magnetic field) inhomogeneity other than gravitational. Compared with the much smaller inhomogeneity observed in type III or U bursts, the inhomogeneity of spike sources seems to be due to a gradient in perpendicular direction to the magnetic field which, in addition, is steeper at higher frequency (lower altitude). Benz and Kane (1986) have concluded that spikes emission (and thus acceleration) take place in a highly inhomogeneous region with density variations of about one order of magnitude.

4. Theory

Recent observations at decimeter and microwave frequencies have shown that millisecond spikes are a phenomenon associated with the impulsive phase of primary energy release in flares. They often correlate with HXR and type III radio emission, both manifestations of 10 - 100 keV electrons. Occasional absence of correlation has been interpreted in terms of unfavorable source conditions (Benz and Kane, 1986): Type III emission requires electrons streaming on quasi-open field lines, HXR have a high threshold for detection, and the conditions for spikes are unknown. It is generally agreed today that spikes are signatures of energetic electrons.

4.1. Source Size and Brightness Temperature

Estimates of the source size of spikes yield small values and thus lead to enormous brightness temperatures of spike radiation. They are a challenge to theory and have in the past attracted the attention of theoreticians. Upper limits based on duration may not be very meaningful, since the duration seems to depend on frequency and decreases approximately with the mean collision time (§ 2.1.). Estimates using the bandwidth seem to be more reliable. Let us assume that the emission frequency depends on a characteristic frequency (such as the local plasma frequency or gyrofrequency). The source dimension l of a spike is then determined by the scale length λ of the characteristic frequency and the bandwidth $\Delta\omega$ of the spike:

$$l = \lambda \frac{\Delta\omega}{\omega} \tag{3}$$

If the natural width of the emission frequency cannot be neglected, equ. (3) only gives an upper limit on the size. Quantitative measurements of all variables in equ. (3) yield $l \lesssim 200$ km (Benz, 1985). This is an order of magnitude smaller than the "speed of light dimension" derived from the duration of spikes at 600 MHz, but comparable to that upper limit at 3 GHz. It is interesting to note that the source size derived from equ. (3) agrees with the possible observation of a spike by VLBI technique yielding a diameter of approximately 50 km (Tapping et al., 1983).

With a diameter of 200 km and for a circular source the brightness temperature of spikes is up to $10^{15} K$. Only coherent emission processes can reach such an intensity.

4.2. Emission Process

Early ideas on the emission mechanism included plasma emission and electron cyclotron emission and were based on analogies to other impulsive radio emissions (Malville et al., 1967; Tarnstrom and Philip, 1972b). A plasma wave model was first presented by Zheleznyakov and Zaitsev (1975). They proposed emission at the harmonic of Langmuir waves generated by unstabilized electron beams. As soon as the "gentle- beam" instability stabilizes, the beam emits ordinary type III radiation. Chernov (1978) developed the model further and realized that such beams would have to be small in size (500 km) and nearly monoenergetic. Although plasma emission is still used today in modelling spike emission (Kuijpers et al., 1981, Karlicky, 1984) its predicted similarity to type III emission contradicts the observations. Spikes have a much smaller intrinsic bandwidth, higher polarization and, most of all, a 4 orders of magnitude higher brightness temperature. Spikes probably have a different emission mechanism.

Langmuir waves may still be the cause of spikes. Their transformation into radio emission, however, would have to be an extraordinary process (as examples we mention strong turbulence or direct conversion on density gradients). A further possibility has been studied by Vlahos et al. (1983) who considered the coherent wave-wave coupling of two antiparallel upper-hybrid waves. The random initial phase and finite coherence length produce a spiky radio emission. This emission process however still needs to be shown to agree with the wealth of observations summarized in sections 2 and 3.

Cyclotron emission is today's most favored process for spike radiation. Cyclotron waves grow exponentially in loss-cone velocity distributions of electrons. Such a distribution may be the result of trapping (or just one reflection) of energetic particles in magnetic mirrors. Of particular interest is the cyclotron maser instability, in which electrons with velocity v are in resonance with transverse electromagnetic waves (ω, k) if

$$\omega - s\,\Omega_e - k_\parallel\, v_\parallel = 0 \tag{4}$$

where the index $_\parallel$ is the component parallel to the magnetic field, s the harmonic number of the wave, and Ω_e the relativistic electron gyrofrequency. Equation (4) describes the equality of wave and particle gyrofrequency in the Doppler-shifted frame of the electron. The term "maser" was given to this instability, since it generally occurs for electron distributions depleted of particles with low perpendicular velocity constituing a reversed population. The instability directly converts particle energy into radiation and is able to produce very high brightness temperatures. For this reason it was proposed as the emission process of spikes by Holman et al. (1980).

Melrose and Dulk (1982a) have worked out the details of the growth and energetics of the maser emission. The effects of the ambient plasma have been included by Sharma et al. (1982). Growth and escape of the various modes and harmonics have recently been discussed for coronal conditions by Sharma and Vlahos (1984) and for auroral kilometric radiation by Melrose et al. (1984). It seems that the maser mechanism operates only in strong magnetic fields ($\omega_p/\Omega_e \lesssim 0.9$) and mainly emits on the fundamental ($s = 1$). Then it may not only be a strong radio source but can even considerably heat the ambient medium and thus may redistribute the flare energy (Melrose and Dulk, 1984) or accelerate particles (Sprangle and Vlahos, 1983).

While a considerable effort has been made to theoretically understand the maser instability and interprete the high brightness temperature, very little has been done to explain other features of spikes. In a model discussed by Vlahos and Sharma (1984) the bandwidth of spike emission is given by the inhomogeneity of the magnetic field (equ. 3). The short duration of spikes has been interpreted by Li (1986) in terms of injection of small beams at skew angles and fast relaxation of the anisotropic electron distribution.

It is concluded that the emission mechanism is still unclear. Although cyclotron masering looks attractive, other possibilities are still open and should be investigated.

4.3. Spikes and the Flare Process

Since spikes appear during the primary energy release in flares, it is most interesting to view spikes in the general context of flares. The close agreement of the source density of spikes with the preflare density of flare loops as derived from soft X-rays suggests that spikes are emitted from a source close to the primary acceleration region. Unless some novel coherent radiation mechanism is at work the exciter of spikes must be fragmented into 10000 or more single elements. This is usually assumed for maser models. Then, the simplest assumption is that the flare energy, i.e. at least its part taken up by fast electrons, is released in ten thousands of elements (microflares). This scenario has been considered by Benz (1985). These flare elements may be the result of a global MHD instability of the flare region.

Each flare element should not be much larger than the spike source (less than 200 km in diameter). The acceleration process in such a region may be caused by a constant electric field or double layer (run-away, considered by Kuijpers et al., 1981), stochastic acceleration (Benz, 1984), or small shocks (Vlahos and Sprangle, 1985). In any case, the extent of spike emission over more than an octave in frequency and the compactness of flare kernels suggests that the large range of different magnetic fields or densities is due to strong inhomogeneities.

The suggested fragmentation of flare energy release needs confirmation. It may be difficult to observe in hard X-rays, since most of the electrons may loose their energy far from the acceleration site at higher density. Also type III bursts may be the combined result of many elementary accelerations. They are well-known to often consist of superposed fine structures.

5. Conclusions

Spikes are an intriguing emission in the impulsive phase of flares. They are the most fragmented flare radiation consisting of ten thousands of individual elements. The most important question is whether this fragmentation is original or the result of a secondary process. If original, it will have a major impact on flare theory reducing flare time scales by several orders of magnitude.

The fact that spikes are not seen in every flare should not be overemphasized. Observations have mainly been done on frequencies below 1 GHz and only on a few single frequencies above. Many spike events have remained unobserved. Complete coverage from 0.3 to 5 GHz is urgently needed. In addition, propagation conditions in the source region may often prohibit the escape of spike radiation. This is particularly critical for cyclotron maser emission being strongly absorbed at skew angles to the magnetic field.

Future spike observations should be compared with other flare radiations. Spatial resolution and location in relation to the HXR flare are of great importance. Theoretical studies should proceed from merely considering the emission process to construction of models of spikes in the frame of current flare theory.

Acknowledgements

This work was partially supported by a grant from the Swiss National Science Foundation (No. 2.460-0.82).

References

Barrow,C.H. and Saunders,H.: 1972, Astrophys.Lett. **12**, 211.
Barrow,C.H., Flagg,R.S., and Perrenoud,M.R.: 1984, Solar Phys. **90**, 111.
Benz,A.O., Zlobec,P. and Jaeggi,M.: 1982, Astron.Astrophys. **109**, 305.
Benz,A.O.: 1984, Trends in Physics, Proc. 6th General Conference of EPS, **1**, 156.
Benz,A.O.: 1985, Solar Phys. **96**, 357.
Benz,A.O. and Kane,S.R.: 1986, Solar Phys., in press
Bernold,T.: 1980, Astron.Astrophys.Suppl.Ser. **42**, 43.
Chernov,G.P.: 1974, Sov.Astron. **17**, 788.
Chernov,G.P.: 1977, Sov.Astron. **21**, 612.
Dröge,F. and Riemann,P.: 1961, Inf.Bull.Solar Radio Obs.Europe **8**, 6.

Dröge,F.: 1967, Z.Astrophys. **66**, 176.

Dröge,F.: 1977, Astron.Astrophys. **57**, 285.

Eckhoff,H.K.:1966, Inst.Theor.Astrophys.Rep. **18**.

Elgarøy,Ø.:1961, Astrophys.Norv. **7**, 235.

Elgarøy,Ø.:1962, Inf.Bull.Solar Radio Obs.Europe **9**, **4**.

Elgarøy,Ø. and Rødberg,H.: 1963, Astrophys.Norv. **8**, 273.

Elgarøy,Ø. and Eckhoff,H.K.: 1966, Astrophys.Norv. **10**, 127.

Fu,Q.J., Li, C.S. and Yin,S.Z.: 1983, Kunming Workshop on Solar Physics, in press.

de Groot,T.: 1962, Inf.Bull.Solar Radio Obs.Europe **9**, 3.

de Groot,T.: 1966, Rech.Astr.Obs. Utrecht **XVIII-I.**

de Groot,T.: 1970, Solar Phys. **14**, 176.

Heyvaerts,J., Kerdraon,A., Mangeney,A., Pick,M., and Slottje,C.: 1978, Astron.Astrophys. **66**, 81.

Holman,G.D., Eichler,D., and Kundu,M.: 1980, IAU Symp. 86 (M. Kundu and T. Gergeley, eds.), p. 465.

Kane, S.R.: 1981, Astrophys.J. **247**, 1113.

Karlicky,M.: 1984, Solar Phys. **92**, 329.

Kuijpers,J., Van der Post,P. and Slottje,C.: 1981, Astron.Astrophys. **102**, 331.

Li,H.W.: 1986, Solar Phys., in press.

Malville,J.M., Aller,H.D., Jansen,C.J.: 1967, Astrophys.J. **147**, 711.

Melrose,D.B. and Dulk,G.A.: 1982, Astrophys.J. **259**, 844.

Melrose,D.B. and Dulk,G.A.: 1984, Astrophys.J. **282**, 308.

Melrose,D.B., Hewitt,R.G., and Dulk,G.A.: 1984, J.Geophys.Res. **89**, 2466.

Nonino,M., Abrami,A., Comari,M., Messerotti,M. and Zlobec,P.: 1986, Solar Phys., in press.

Sharma, R.R., Vlahos,L. and Papadopoulos,K.: 1982, Astron.Astrophys. **112**, 377.

Sharma,R.R., and Vlahos,L.: 1984, Astrophys.J. **280**, 405.

Slottje,C.: 1978, Nature **275**, 520.

Slottje,C.: 1980, Radio Physics of the Sun (M.R. Kundu and T.E. Gergeley, eds.), p. 195.

Sprangle,P., and Vlahos,L.: 1983, Astrophys.J.Lett. **273**, L95.

Stähli,M. and Magun,A.: 1986, Solar Phys., in press

Strong,K.T., Benz,A.O., Dennis,B.R., Leibacher,J.W., Mewe,R., Poland,A.I., Schrijver,J., Simnett,G.M., Smith,J.B. and Sylvester,J.: 1984, Solar Phys. **91**, 325.

Tapping,K.F., Kuijpers,J., Kaastra,J.S., van Nieuwkoop,J., Graham,D. and Slottje,C.: 1983, Astron.Astrophys. **122**, 177.

Tarnstrom, G.L. and Philip,K.W.: 1972a, Astron.Astrophys. **16**, 21.

Tarnstrom,G.L. and Philip,K.W.: 1972b, Astron.Astrophys. **17**, 267.

Vlahos,L., Sharma,R.R., Papadopoulos,K: 1983, Astrophys.J. **275**, 374.

Vlahos,L. and Sharma,R.R.: 1984, Astrophys.J. **290**, 347.

Vlahos,L. and Sprangle,P.: 1985, submitted to Astrophys.J.

Zhao,R.Y. and Yin,S.Z.: 1982, Scientia Sinica **25**, 422.

Zheleznyakov,V.V.: 1970, Radio Emission of the Sun and Planets, Pergamon Press, Oxford.

Zheleznyakov,V.V. and Zaitsev,V.V.: 1975, Astron.Astrophys. **39**, 107.

N87
21799
UNCLAS

N87-21799

RELATION BETWEEN SOLAR NARROW-BAND DECIMETER WAVE BURSTS AND ASSOCIATED X-RAY BURSTS

Shinzo Enome

Toyokawa Observatory
Nagoya University
Toyokawa 442, Japan

Larry E. Orwig

Code 682
NASA/GSFC
Greenbelt, MD 20771

Abstract

Results are reported of an initial comparison of solar narrow-band decimeter wave spike bursts with corresponding X-ray events for 25 solar flares. Contrary to the rather straightforward temporal and spatial relations which exist between typical impulsive microwave and X-ray bursts, narrow-band decimeter wave spike bursts show complex temporal structure relative to the associated X-ray features. The time delay between the hard X-ray and microwave emission peaks varies from -2 to 8 seconds. The asscoiated X-ray events are very weak in intensity, are spectrally very soft, and do not show any peculiar spectral features. Although the total number of bursts is small, it is found that decimeter spike bursts are 10^2 - 10^3 times stronger than normal impulsive microwave bursts for the same observed amount of hard X-ray emission. This feature, supplemented by the fact that 100% circular polarization is observed, strongly supports a maser origin for the decimeter spike bursts.

Published in Nature, 321, 421, (1986).

N87
21800
UNCLAS

N87-21800

POSITION MEASUREMENTS OF RAPIDLY FLUCTUATING MICROWAVE BURSTS

K. Kai and H. Nakajima

Tokyo Astronomical Observatory
University of Tokyo
Mitaka, Tokyo 181, Japan

ABSTRACT. We have investigated whether microwave source positions change while the total fluxes of hard X-rays and microwaves show remarkable rapid fluctuations of the order of seconds. The position measurements were made in one dimension (east-west direction) with the 17 GHz interferometer at Nobeyama. Position changes greater than a few arc seconds can be detected. The result shows that significant position changes are found for five of seven bursts but that no position changes greater than 3" are found for the remaining two bursts.

It is crucial for the understanding of the energy release mechanism in solar flares to know whether the flaring occurs repeatedly in a single loop or successively in adjacent different loops during X-ray and microwave bursts of multiple spikes with time scales of seconds. VLA observations show in some cases repeated flarings at the same position (Lang et al. 1981, Kundu, Bobrowsky, and Velusamy 1982) and in some cases rather erratic changes in flaring positions within complex active regions (Kundu, Schmahl, and Velusamy 1982, Wilson and Lang 1984). The spatial resolution of these observations are a few arc seconds, but the time resolution is 10 seconds. High time resolution observations with the WSRT reveal complex changes in flaring positions in the east-west direction; the source of spiky components often shows position shifts of the order of the source size (Kattenberg and Allaart 1983).

In this report we present time variations of circular polarization, position and size of the source of rapidly fluctuating microwave bursts simultaneously recorded with the HXRBS on SMM and the 17 GHz interferometer at Nobeyama. We are interested in particular to know if the position changes from one peak to the next of multiple spike bursts with time scales of seconds. The interferometer operated on a regular babis, ~5h a day, so that we had greater oppotunity of simultaneous recording of flares with the HXRBS

PRECEDING PAGE BLANK NOT FILMED

or the HXM on Hinotori.

The interferometer is one-dimensional in the east-west direction, and its maximum spacings are 3856λ and 7712λ before and after July 1981, which correspond to 50" and 25" respectively (Nakajima et al. 1980, 1984). Although these resolution are still poor, we can determine the source position or estimate the source size with an accuracy of a few arc seconds using all the observed Fourier components (Kosugi 1982): if the source shifts by more than a few arc seconds, we could detect them. The maximum recording rate of Fourier components is once per 0.8s for both RH and LH circular polarizations.

We present below the results of analysis of 7 microwave bursts with rapidly fluctuations of a few seconds. We have selected those bursts whose flux density is greater than 100 sfu at 17 GHz, recorded simultaneously with both the 17 GHz interferometer and the hard X-ray spectrometer on SMM (HXRBS). The selection was by no means complete in the present report. Examples are shown in Figures 1 to 3.

The first burst on 7 June 1980

This is a moderately strong burst occurring from an active region that gave rise to the 'famous' June 7 flare. In Figure 1(a) is shown the comparison between 17 GHz flux and 54-125 keV X-ray flux obtained with the HXRBS. The 17 GHz flux was recorded with the polarimeter with time constant of 0.3 s. The result of analysis of the interferometer data is illustrated in Figure 1(b): flux density, degree of circular polarization, east-west position, and source size. The observed source structure is simple and unipolar. However the east-west position of the centroid of the source shifts westward by ~ 5" at peaks relative to those at valleys. In addition the polarization degree becomes lower at peaks. On the other hand there are no changes in the estimated source size between peaks and valleys. The position and size were estimated by a model-fitting method developed by Kosugi (1982).

The second burst which occurred ~ 2 h later (0312 UT) shows no changes in position greater than 3" (p-p) between peaks and valleys but shows similar changes in the polarization degree, as previously described by Kane et al (1983).

The burst on 16 July 1982

The burst shows rapid fluctuations of a few seconds (Figure 2(a)). The source is single and of simple structue, and its center position remains at a fixed position at 0.8' west of the sun's center throughout the burst, as shown in Figure 2(b). The peak positions of RH and LH circular polarizations coincide to within errors of absolute position determination. There are no significant changes greater than 3" in the east-west direction, except the decay phase (> 03 22 30) when the source shows a progressive shift to west by ~ 2". The source size is estimated to be less than 8". However the degree of circular polarization significantly changes between 20 % and 40 % : it is

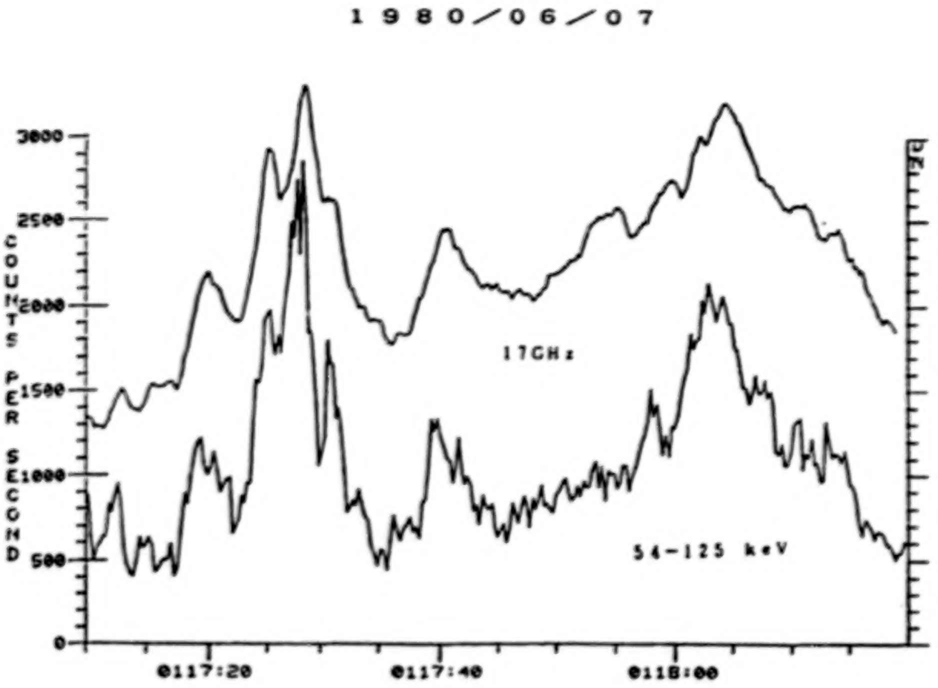

Fig.1(a) Time plots of 17 GHz flux and hard X-ray(54-125 keV) flux for the first burst on 7 June 1980.

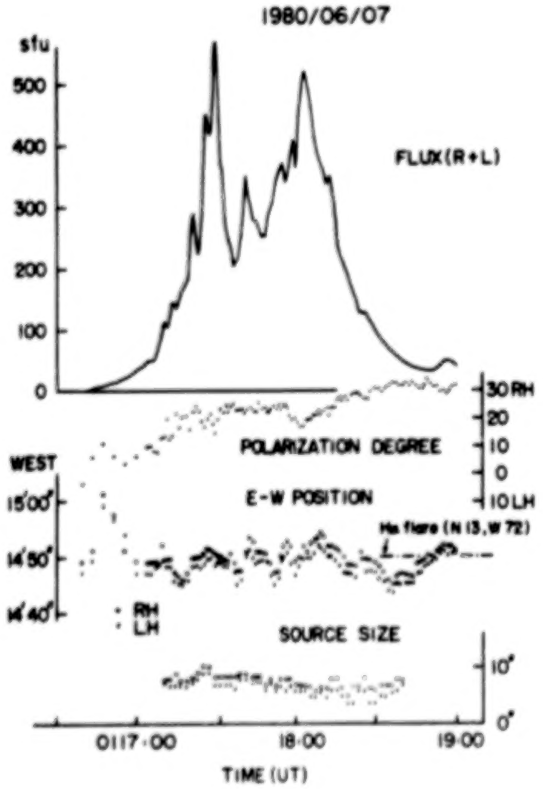

Fig.1(b) Time plots of flux, degree of circular polarization, east-west position, and source size, measured with the 17 GHz interferometer. The east-west position of the associated Hα flare center is indicated by dash-dot line.

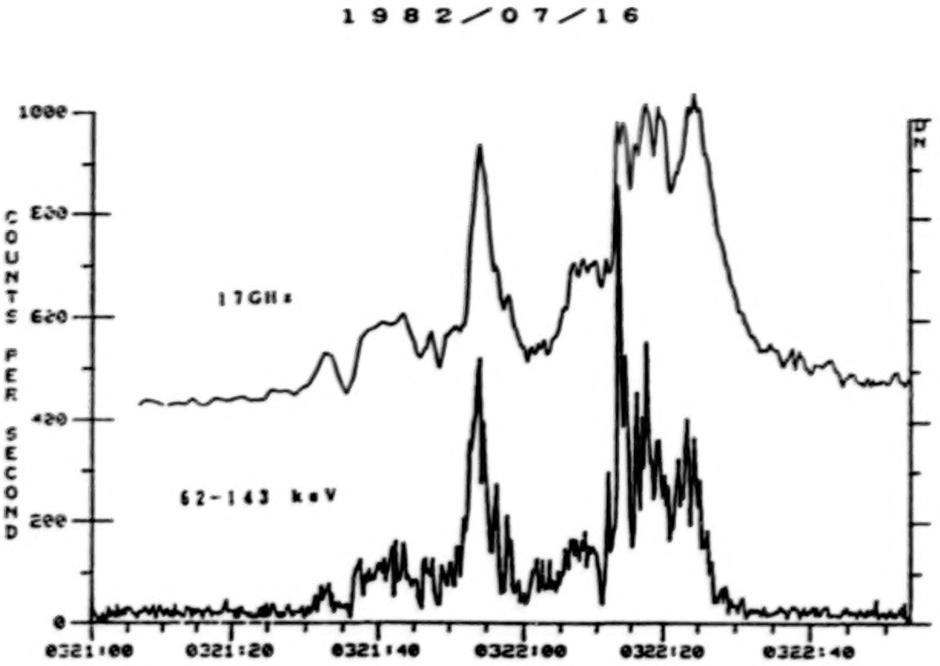

Fig.2(a) Time plots of 17 GHz flux and hard X-ray(62-143 keV) flux for the burst on 16 July 1982.

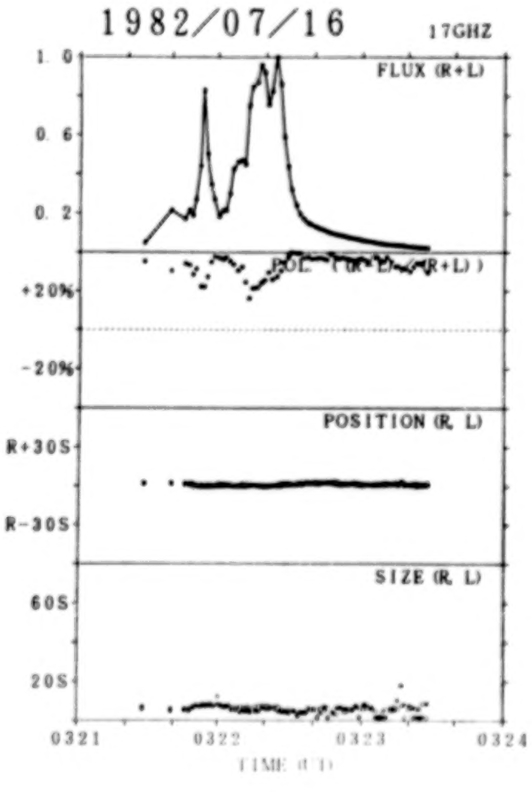

Fig.2(b) Time plots of flux, degree of circular polarization, east-west position, and source size. The position reference is 0.8' west.

smaller at peakes and larger at deep valleys.

The burst on 5 June 1982

The burst also shows rapid fluctuations of a few seconds. The source is single but slightly asymmetric with an extension on the east side, and the polarization structure is bipolar. As shown in Figure 3 the estimated source size is $\sim 30''$, much larger than the estimated sizes for the remaining bursts. Thereore it is likely that two sources of opposite polarizations are unresolved to be observed as an apparently single source. The east-west position changes from one pulse to the next and also between peaks and valleys.

We have made similar analyses for the remaining bursts. The result is summarized in Table 1. There are no significant ($> 3''$) position changes in the microwave sources for two bursts (the second burst on 7 July 1980 and the burst on 16 July 1982), although these two bursts show large amplitude fluctuations in both microwaves and hard X-rays. Even in these cases the degree of circular polarization changes in a systematic way : lower at peaks and higher at valleys. For the burst on 31 July 1981 there is a position shift of $\sim 5''$ between an initial small spike and the following main spikes, though no systematic shifts are found between peaks and valleys within the main spikes. The remaining four bursts show significant ($8'' - 12''$) position changes during rapid fluctuations. Systematic position shifts between peaks and valleys are seen for the first burst on 7 June 1980 and less clearly for the burst on 26 June 1982. Position shifts from pulse to pulse are found for the bursts on 26 June 1982 and 26 July 1981.

As far as the circular polarization is concerned, there is a systematic change: the polarization degree is lower at peaks and higher at valleys (c.f. Kundu et al., 1981). This tendency can be explained by the variation of optical depth τ of the source: $\tau > 1$ at peaks and $\tau < 1$ at valleys. Or alternatively there might be two unresolved components: one is less polarized and spiky, and the other more polarized and smoothly arying (c.f. Kattenberg and Allaart, 1983).

From the present observational evidence alone we cannot draw a general conclusion that microwave emission corresponding to different spikes always originates in different loops, because there are some bursts for which emission comes consistently at the same position. The latter case may be attributed to a limitted spatial resolution of the 17 GHz interferometer, because the two bursts showing no position changes have small source sizes ($< 3''$).

Finally we mention about spatial structures of impulsive flares observed in UV (Cheng et al., 1981, 1984). From the analysis of four impulsive flares observed with the UVSP on SMM, they presented diversity and complexity of temporal and spatial structures of the flares: in some flares there are several bright kernels which show different time behaviour and in some flares bright regions extend over many pixels all of which show a similar time behaviour.

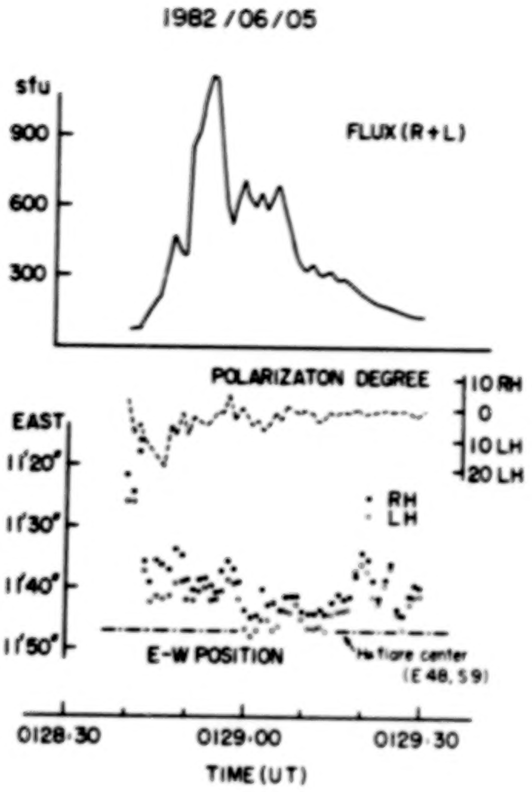

Fig.3 Time plots of flux, degree of circular polarization, and east-west position.

Table 1. Summary of Result

Date	Time	Position Change(p-p)		Size	Change of Pol.Degree
1980 June 7	0117-0119	yes	5"	8"	yes
1980 June 7	0312-0313	no	<3"	<5"	yes
1981 July 26	0411-0412	yes	10"	10"	yes
1981 July 31	0053-0054	yes	5"	9"	no
1982 June 5	0128:40-0129:30	yes	12"	30"	yes? (bipolar)
1982 June 26	0044-0048	yes	8"	20"	yes?
1982 July 16	0321:30-0322:40	no	<3"	<8"	yes

References

Cheng, Chung-Chieh, Tandberg-Hanssen, E., Bruner, E.C., Orwig, L., Frost, K.J., Kenny, P.J., Woodgate, B.E., and Shine, R.A. : 1981, *Astrophys. J.* **248**, 139.

Cheng, Chung-Chieh, Tandberg-Hanssen, E., and Orwig, L. : 1984, *Astrophys. J.* **278**, 853.

Kane, S.R., Kai, K., Kosugi, T., Enome, S., Landecker, P.B., and McKenzie, D.L. : 1983, *Astrophys. J.* **271**, 376.

Kattenberg, A. and Allaart, M. 1983, *Astrophys. J.* **265**, 535.

Kosugi, T. 1982, *Publ. Astron. Soc. Japan* **34**, 281.

Kundu, M.R., Bobrowsky, M., and Velusamy, T. 1981, *Astrophys. J.*, **251**, 342.

Kundu, M.R., Schamhl, E.J., and Velusamy, T. 1982, *Astrophys. J.*, **253**, 963.

Lang, K.R. and Wilson, R.F., and Felli, M. 1981, *Astrophys. J.*, **247**, 338.

Nakajima et al. 1980, *Publ. Astron. Soc. Japan* **32**, 639.

Nakajima et al. 1984, *Publ. Astron. Soc. Japan* **36**, 383.

Wilson, R.F. and Lang, K.R. 1984, *Astrophys. J.*, **279**, 427.

N87
21801
UNCLAS

N87-21801

THE ROLE OF NARROWBAND DM-SPIKES IN SOLAR FLARES

Marian Karlicky

Astronomical Institute of the Czechoslovak
Academy of Sciences
251 65 Ondřejov Observatory, Czechoslovakia

ABSTRACT

The main observational characteristics of narrowband dm-spikes are summarized. Since the spikes are observed in typical sequences of radio bursts, a global model of these bursts is presented. The intensity of the magnetic field in the spike source region, which is of principal importance, is discussed.

1. INTRODUCTION

Observations indicate that dm-spikes can be divided into two groups: narrowband dm-spikes (bandwidth $\Delta f \approx 3$-15 MHz, duration $t_s \lesssim 0.1$ s) and broadband spikes (blips)(15 MHz $< \Delta f < 100$ MHz, $t_s \lesssim 1$ s). Whereas the broadband spikes belong to the impulsive phase of the flare and are similar to type III radio bursts (Benz et al.1983,Wiehl et al.1985,Fárník et al. 1985), the narrowband dm-spikes were observed during the early stage of flare mass ejection (Karlický 1984). Due to their very high brightness temperature (Kuijpers et al.1981) the narrowband dm-spikes belong to the most interesting and important radio bursts. The purpose of this paper is to study these narrowband dm-spikes from the point of view of the flare process as a whole.

2. THE OBSERVATIONAL CHARACTERISTICS OF NARROWBAND DM-SPIKES

a) The duration of a separate spike is $\lesssim 0.1$ s.
b) The bandwidth $\Delta f \approx 3 - 15$ MHz.
c) The radio flux of a spike is typically 200 sfu (Kaastra 1985).
d) The dimension of the spike source of 500-6000 km and the brightness temperature of the spike of $1.4 \times 10^{12} - 6 \times 10^{15}$ K are estimated (Kuijpers et al.1981,Kaastra 1985).
e) In the radio spectrum, the spikes are observed in groups which sometimes consist of several hundreds of spikes.
f) Relationships between the dm-spikes and zebra pattern (Kaastra 1985) and the dm-spikes and brained zebra pattern (Kuijpers et al. 1981) were found.

PRECEDING PAGE BLANK NOT FILMED

g) Oscillations of a spike band were observed (Kaastra 1985).
h) Sequences of radio bursts were observed in several cases (dm-spikes, dm-pulsations and type II radio bursts) (Karlický 1984). The pattern of such a sequence from the January 31,1982 flare is depicted in Figure 1. The impulsive phase of the flare usually precedes this sequence by several minutes. The dm-spikes are observed at higher frequencies than the pulsations and type II radio bursts.
i) In the August 19,1981 flare, we observed an interesting radio spectrum (Figure 2a) which expresses the relationship between the narrowband dm-spikes, pulsations and fiber (intermediate drift) bursts (Karlický 1985). In this particular case, it is important that the sequence of radio bursts mentioned is followed (at lower frequencies) by a type II radio burst. This sequence, with the exception of the U-type and fiber bursts, is thus similar to the pattern in Figure 1.
j) The dm-spikes are considered to be the fine structure of type IV radio bursts (Slottje 1981). In some cases, a group of spikes were observed to change gradually into continuum radiation (type IV radio burst) in the spectrum - see Figure 2 in the paper by Karlický (1984).
k) The polarization of spikes may take any value and it is almost constant within a single group, both in time and at different frequencies. Their polarization is usually the same as that of near radio activity (e.g. pulsations) (Nonino et al. 1985).
l) The narrowband dm-spikes are usually related to two-ribbon flares (Karlický 1984).

3. MODEL OF BURST SEQUENCES WITH NARROWBAND DM-SPIKES

The observed burst sequences are best for verifying models of separate bursts, because these models must constitute the global model. Moreover, in this particular case the global model must agree with the model of the two-ribbon flare. Furthermore, the relation between narrowband dm-spikes and type II radio bursts indicates that the observed burst sequenes are connected with the process of flare mass ejection (Karlický 1984).

The first attempt to explain the burst sequence was made by Karlický (1985). The radio spectrum and the corresponding model is shown in Figure 2. In this model, the narrowband dm-spikes are interpreted as a radio manifestation of the spatially localized reconnections in the flare loop. The individual reconnection accelerates the dense electron beam, which cannot be stabilized by non-linear processes, and, consequently, the beam relaxes quasilinearly in a very short time. During this process, Langmuir`s waves are generated

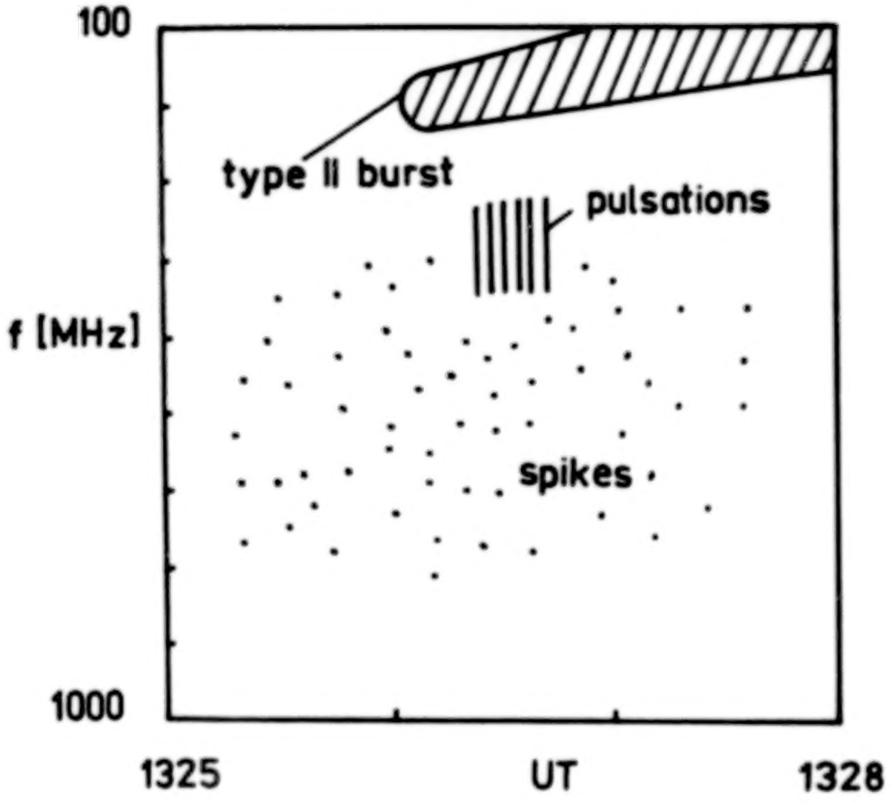
100
type II burst
pulsations
f [MHz]
spikes
1000
1325
UT
1328

Fig.1. Pattern of typical radio burst sequence (narrowband dm-spikes, pulsations and type II radio burst) observed during the January 31, 1982 flare.

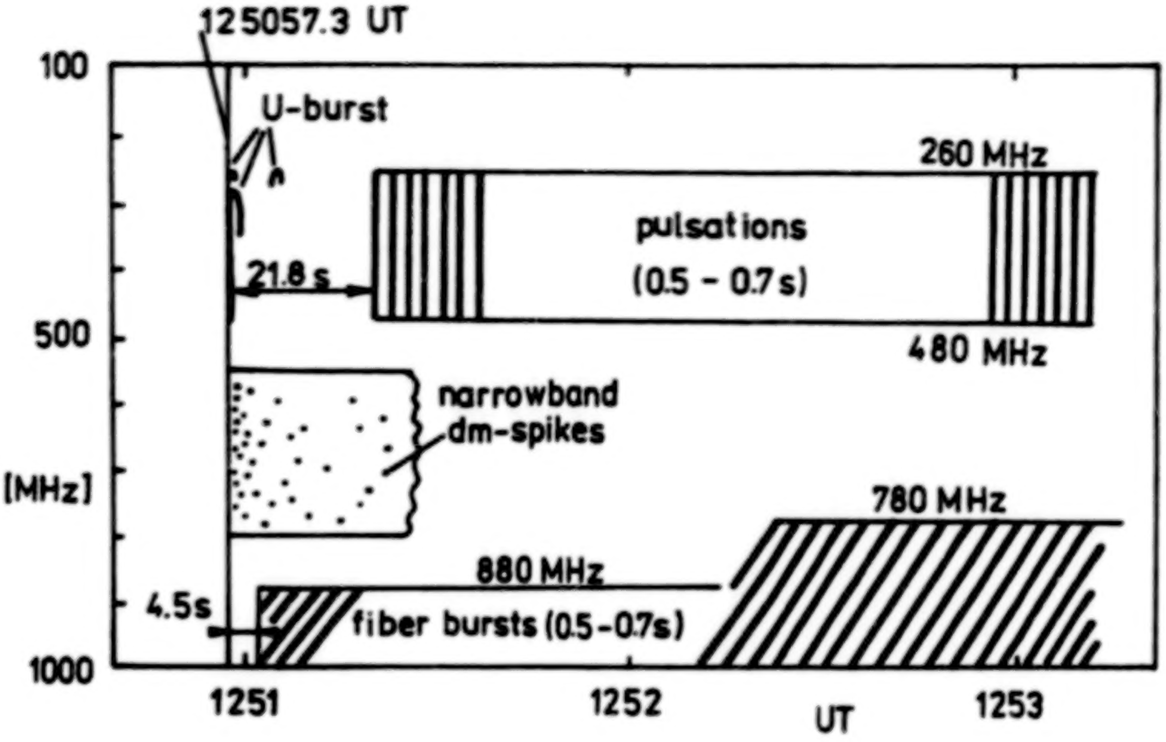

Fig.2a. A part of the radio spectrum of the August 19, 1981 flare.

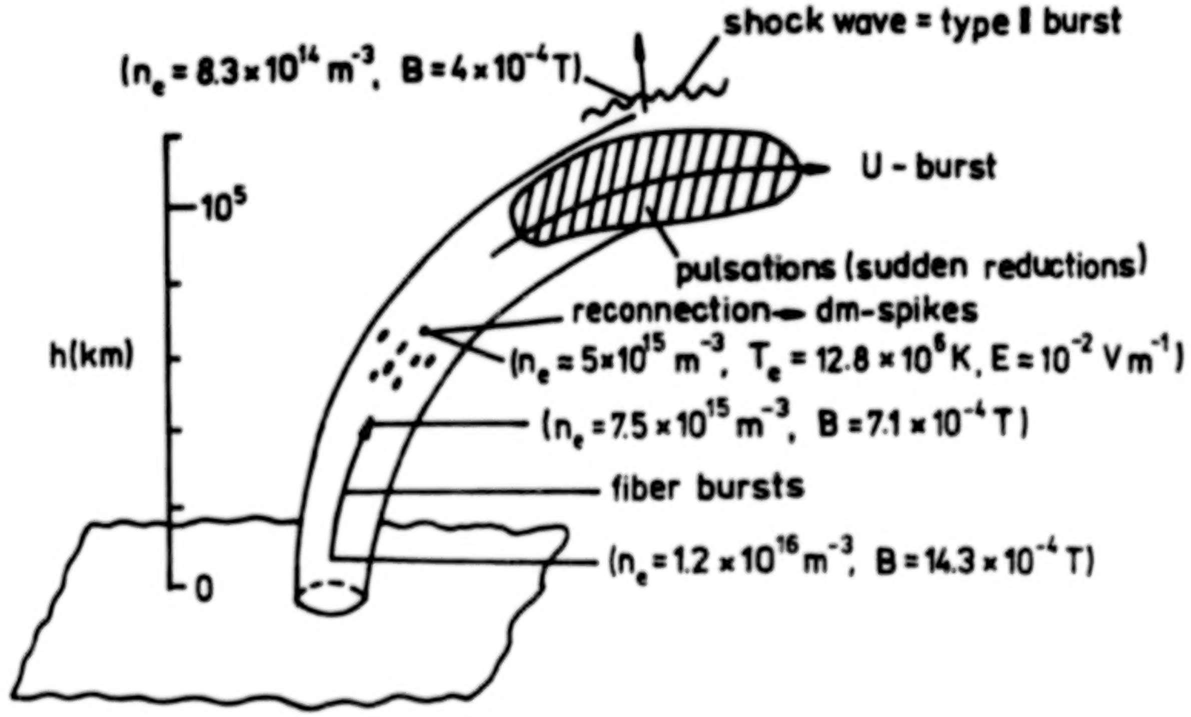

shock wave = type II burst
($n_e = 8.3 \times 10^{14}$ m^{-3}, $B = 4 \times 10^{-4}$ T)
U - burst
10^5
h(km)
0
pulsations (sudden reductions)
reconnection → dm-spikes
($n_e = 5 \times 10^{15}$ m^{-3}, $T_e = 12.8 \times 10^6$ K, $E = 10^{-2}$ V m^{-1})
($n_e = 7.5 \times 10^{15}$ m^{-3}, $B = 7.1 \times 10^{-4}$ T)
fiber bursts
($n_e = 1.2 \times 10^{16}$ m^{-3}, $B = 14.3 \times 10^{-4}$ T)

Fig.2b. The model corresponding to the radio spectrum in Figure 2a.

which, after transformation, lead to dm-spikes. The duration of a dm-spike is thought to be related to the thermal damping time of the generated Langmuir s waves. After quasilinear relaxation and space evolution, the superthermal electrons form the new electron beams which propagate along the flare loop and generate U-type bursts via two-stream instability. After some time, the superthermal electrons become trapped in the flare loop, and fiber bursts (the model by Kuijpers,1975) and pulsations (the model by Benz and Kuijpers 1976) are generated via the loss-cone instability. The same "periods" of the fiber bursts and pulsations (sudden reductions) are explained by the superthermal electrons which, after interacting with whistlers (fiber bursts) in the bottom part of the flare loop, interrupt the loss-cone instability (sudden reductions) also in the upper part of the flare loop. In the course of the whole process, the flare loop is heated and it, therefore, expands and generates a shock wave (type II radio burst). The parameters of the flare loop in the radio burst sources were estimated on the basis of this concept and of the models of the individual bursts mentioned (Figure 2b): The height of the flare loop from the U-type burst theory, the magnetic fields from the fiber and type II burst theory, the mean electric field in the reconnection process from the size of the spike source region and the energy of the superthermal electrons.

This model was developed for the August 19,1981 flare, but its significance is more general. It can also explain the typical burst sequence shown in Figure 1. The role of the spikes, pulsations and type II bursts remains the same, and the U-type and fiber bursts are not observed due to some effects (generation mechanism, propagation effects, weak intensity).

4. DISCUSSION

In all dm-spike models, their principal condition is expressed in terms of the ratio of the electron plasma ω_{pe} and electron cyclotron ω_{ce} frequencies. For example, the models by Kuijpers et al.(1981)(the runaway model) and by Melrose and Dulk (1982)(the electron-cyclotron maser) require relatively high magnetic fields, i.e. the condition $\omega_{pe} \lesssim \omega_{ce}$ must be satisfied. On the other hand, Kaastra (1985) established the condition $\omega_{pe} \gg \omega_{ce}$ in the spike source region on the basis of the relation between the dm-spikes and the zebra pattern. A similar result can also be obtained in our case with a relatively low magnetic field (Figure 2b). (However, a strong local concentration of the magnetic field can change this result).

In general, it is difficult to estimate the magnetic field in the spike source region. In our case, we have used Kuijper`s theory of fiber bursts (Kuijpers 1975). However, one thing requires an explanation: The H-alpha ribbons of the August 19,1981 flare were squeezed among a group of sunspots with a relatively high magnetic field. But Kuijper`s fiber burst theory cannot yield magnetic fields much higher than we estimated. (A higher magnetic field means a higher group velocity of the whistlers and a larger distance over which the whistlers must propagate during the time of the fiber burst. However, this distance must be smaller than the characteristic dimension of the flare). These contradictory facts can be explained in two ways:

a) By the structure of the flare`s magnetic field.

The magnetic field in the flare is strongly inhomogeneous, in other words, besides regions with strong magnetic fields there are also regions with weak magnetic fields.

b) By modifying fiber burst theory.

For example, if the whistlers are replaced by another type of low-frequency wave or if the ratio of whistler frequency and electron gyrofrequency is smaller than 0.25 (which is usually used), the estimated magnetic field may come out higher.

The situation is evidently very complicated. It should be emphasized, therefore, that the results reported above were obtained using determined models which still require verification.

REFERENCES

Benz,A.O.,and Kuijpers,J.1976,Solar Phys.46,275.

Benz,A.O.,Bernold,T.E.X.,and Dennis,B.R.1983,Ap.J.271,355.

Fárník,F.,Karlický,M.,and Tlamicha,A.1985,Relationship between Solar Radio Continua and X-ray Emission,CESRA Workshop,Duino 1985,Italy.

Kaastra,J.1985,Solar Flares - An Electrodynamic Model, Thesis,University of Utrecht.

Karlický,M.1984,Solar Phys.92,329.

Karlický,M.1985,Bull.Astron.Inst.Czechosl.,in print.

Kuijpers,J.1975,Solar Phys.44,173.

Kuijpers,J.,van der Post,P.,and Slottje,C.1981,Astr.Ap.103, 331.

Melrose,D.B.,and Dulk,G.A.1982,Ap.J.259,844.

Nonino,M.,Abrami,A.,Comari,M.,Messerotti,M.,and Zlobec,P. 1985,The Characteristics of Type IV Associated Spikes at Metric Wavelenght,CESRA Workshop,Duino 1985,Italy.

Slottje,C.1981,Atlas of Fine Structures of Dynamical Spectra of Solar Type IV-dm and Some Type II Radio Bursts, Dwingeloo Observatory.

Wiehl,H.J.,Benz,A.O.,and Aschwanden,M.J.1985,Solar Phys. 95,167.

N87
21802
UNCLAS

N87-21802

THE POSSIBLE IMPORTANCE OF SYNCHROTRON/INVERSE COMPTON LOSSES TO EXPLAIN FAST MM-WAVE AND HARD X-RAY EMISSION OF A SOLAR EVENT

E. Correia, P. Kaufmann, J. E. R. Costa, and A. M. Zodi Vaz

INPE: Instituto de Pesquisas Espaciais
C.P. 515, 12.200-São José dos Campos, S.P., Brazil

B. R. Dennis

Laboratory for Astronomy and Solar Physics
NASA: Goddard Space Flight Center
Greenbelt, MD 20771

ABSTRACT

The solar burst of 21 May 1984 presented a number of unique features. The time profile consisted in seven major structures (seconds), with a turnover frequency $\gtrsim$ 90 GHz, well correlated in time to hard X-ray emission. Each structure consisted in multiple fast pulses (10^{-2} seconds), which were analysed in detail. It has been confirmed a proportionality between the repetition rate of the pulses and the burst fluxes at 90 GHz and $\gtrsim$ 100 keV hard X-rays, and found an inverse proportionality between repetition rates and hard X-rays power law indices. A synchrotron/inverse Compton model has been applied to explain the emission of the fast burst structures, which appear to be possible for the first three or four structures.

A number of unique characteristics were found in a solar event observed in 21 May 1984, 1326UT at 30 and 90 GHz by Itapetinga Radio Observatory using high time resolution (1 ms) and high sensitivity (0.03 S.F.U.), and at hard X-rays by the HXRBS experiment on board of the SMM satellite, with 128ms time resolution. This event was also observed by patrol radio telescopes at 7 GHz (Itapetinga) and at 1.4, 2.7, 5, 8.8 and 15.4 GHz (AFGL; Cliver, 1984). The time profiles at hard X-rays, in two energy ranges, and at 90, 30 and 7 GHz radio frequencies are shown in Figure 1.

The event presented seven major time structures (1-2 sec duration) at 90 GHz, very well correlated to hard X-rays. They are labeled A-G in Figure 1. The 30 GHz emission enhanced only after the fourth structure, and was also well correlated to the 90 GHz and hard X-rays emissions. The radio emission intensity increased towards the shortest mm-waves, indicating a turnover frequency at about or above 90 GHz for all seven major time structures, as shown by the spectra in Figure 2.

Table I - Parameters of the burst major time structures, labeled A-G(Figure 1). The spectral indices $\bar{\alpha}$ and $\bar{q}$ are mean values at the maximum of each structure. Radio fluxes are in s.f.u., 1 s.f.u. = 10^{-22} w/m^2 Hz, and X-ray fluxes are in units of 3 x 10^{-25} erg/cm^2 s Hz. R is the repetition rate of fast pulses for each structure, R = N/Δt, with N the number of pulses, and Δt the duration of the major structures (or packet of pulses).

Structure	Flux 90 GHz	Flux 30 GHz	Flux X-ray		spectral indices				packet dur. (sec)	Nº pulses N	R (s^{-1})	e-fold. rise time (ms)	ΔF/F 90 GHz
			>30 keV	>100 keV	burst		slow comp.						
					$\bar{\alpha}$	$\bar{q}$	$\bar{\alpha}$	$\bar{q}$					
A	8	3	0.2	0.01	1.2	2.2	0.8	4.0	2.0	3	1.5	60	50
B	34	5	0.6	0.03	1.8	2.5	0.8	4.0	3.8	11	2.9	70	20
C	83	7	0.7	0.05	2.5	1.9	1.0	3.0	2.8	14	5.0	40	50
D	40	9	0.4	0.02	1.6	2.7	4.0	3.4	1.6	5	3.0	60	20
E	58	24	1.1	0.04	0.9	2.4	0.3	3.4	1.7	6	3.5	50	30
F	27	12	0.6	0.02	0.7	2.8	0.3	3.4	1.6	4	2.5	60	50
G	23	16	0.5	0.03	0.3	2.7	0.0	3.5	1.0	3	3.0	60	40

Interesting properties are found by correlating pulse repetition rates and the fluxes at 90 GHz and X-rays, for the various packets of pulses. The scatter diagrams (Figure 6) are for the seven structures which, together, included 46 fast pulses. The correlation coefficient was excellent at $\gtrsim$ 100 keV X-rays and 90 GHz (better than 90%) but not so good at $\gtrsim$ 30 KeV X-rays (60%). These results favour the well accepted assumption that the mm-wave emission are better associated to the higher energy X-rays and confirm the idea that the pulses emission are quasi-quantized in energy (Kaufmann et al., 1980; Correia, 1983; and Loran et al., 1985). The characteristic energy radiated by each pulse at the emitting source can be estimated as 5 x 10^{20} ergs at 90 GHz and 10^{20} ergs at $\gtrsim$ 100 KeV X-rays.

Another and new result was found by correlating the pulse repetition rates and hard X-ray power-law spectral index, shown in Figure 7. The correlation coefficient is very good (91%). This result suggest that the harder is the spectrum, the larger is the repetition rate.

The fast pulse emission and the high radio turnover frequency are difficult to be interpreted using models currently available which consider the acceleration of non-relativistic or mildly relativistic electrons (Kaufmann et al., 1985; and McClements and Brown, 1986).

One possible explanation assumes the acceleration of ultrarelativistic electrons which produce a synchrotron emission component spectrum peaking somewhere at $\nu \gtrsim 10^{11}$ Hz. The concurrent hard X-ray emission is attributed to inverse Compton quenching on the synchrotron photons produced in a compact, bright and short-lived source (Kaufmann et al., 1986). We analysed here this possible interpretation for all the seven major structures of the 21 May 1984 event.

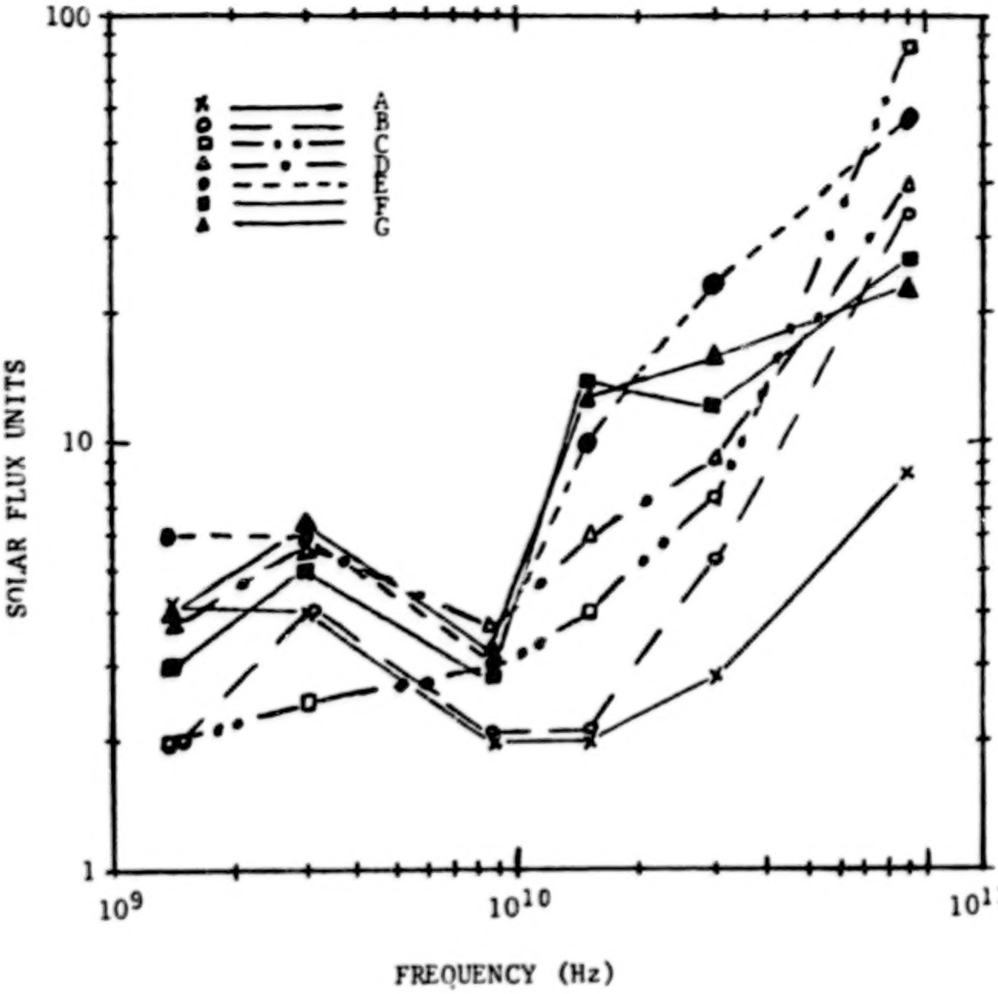

Figure 2 - Radio spectra for the maximum of each major time structure of the 21 May 1984 event, as indicated in Figure 1.

Table I summarizes the main characteristics of each major time structure of the burst. The spectral indices of the burst structures are distinguished from the indices of a slow underlying burst emission component (~20 seconds). At radio, the spectral indices α are defined as $F \propto \nu^{\alpha}$, where F is the flux density and ν the frequency. The spectral indices between 30-90 GHz enhanced for each superimposed structure with $\alpha \sim 0.3 - 2.5$, while the underlying slow component spectral index was varying slowly in the 0-1.3 range. The X-ray power-law spectral indices δ are defined as $F \propto E^{-q}$, where F is the flux, E the photon energy, and $q = \delta - 1$. The corresponding hard X-ray structures exhibited spectral indices reduction to ≈ 3, while the slow component remained at the $\delta \sim 4-5$. The spectra become harder in peak of each structure (Figure 5, Table I).

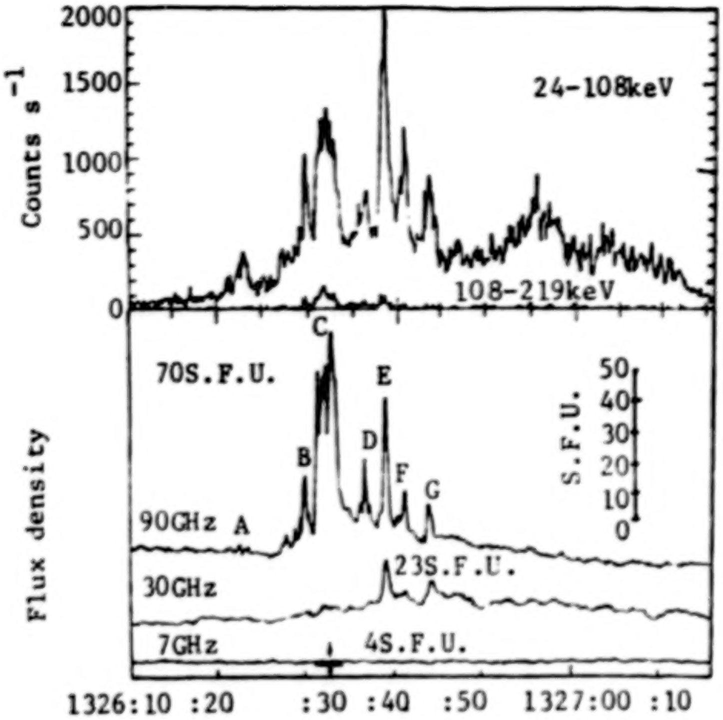

Figure 1 - The solar burst of 21 May 1984, 1326UT, observed at 7, 30 and 90 GHz (Itapetinga Radio Observatory) and hard X-rays (HXRBS-SMM). The seven major time structures are labeled A-G.

Each structure was expanded in 4 second sections, in order to analyse their time profiles in more detail. Using running mean technique,we filtered the 4 seconds sections to evidence pulses at 30 and 90 GHz (Figure 3). The plots show that each radio structure, consisted in packets of fast pulses with durations of tens of milliseconds and relative amplitude of ~50% at 90GHz and of less than 5% at 30GHz. After the fourth structure, when the 30 GHz emission was enhanced, we verified that the pulses between 30 and 90 GHz were generally in phase, to better than 10 ms (Figure 4).

Time expanded 4s sections were also analysed in comparison to hard X-rays, and in terms of spectral indices. Two examples are shown in Figure 5. At X-rays, the pulses are not visible because their durations (~60 ms) are shorter than the time resolution available (~128 ms). However, when compared with time integrated 90 GHz data, in the same 128 ms, the overall time structures appear to be well correlated. Therefore it is likely that the fast pulses are also present at hard X-rays and would be detected if enough sensitivity, and time resolution were available. In this case, it is plausible to assume that both, the radio and hard X-ray pulses, are produced by the same population of energetic electrons.

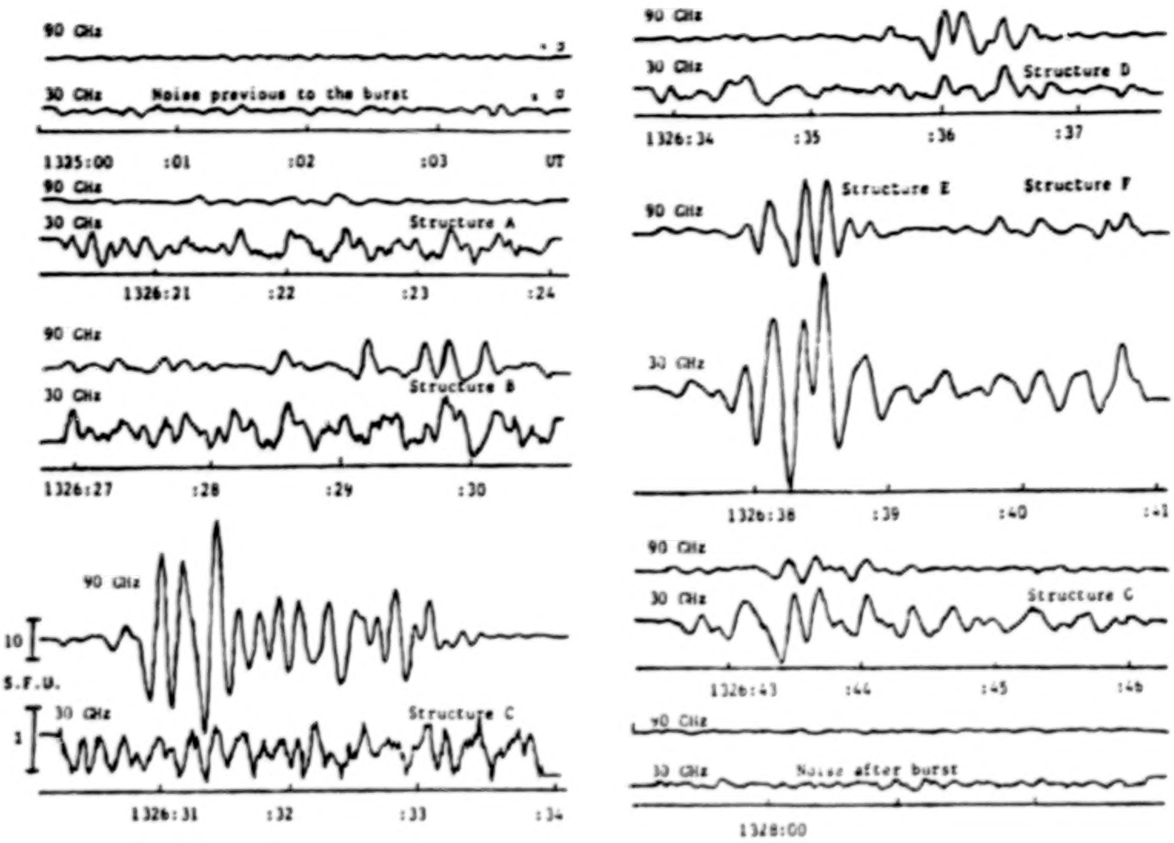

Figure 3 - All the structures at 90 and 30 GHz plotted on a 4s expanded time scale with a running mean subtracted from the measured fluxes at the two frequencies. The flux scales are indicated for structure C, and are kept the same for all the other 4s sections.

Using the formulation of the synchrotron/inverse Compton model given by Kaufmann et al., (1986), we obtained the pulse source characteristics in each one of major time structures. The results, considering a magnetic field of 500 gauss are given in Table II.

The application of the synchrotron/inverse Compton model seems to work self-consistently in the first four major time structures(A, B, C, D), which have turnover frequencies well above 10^{11} Hz. The estimated source parameters required to explain the high turnover frequency and the short pulse durations (~ 60 ms) are: source of $\sim 10^7$cm and $\sim 10^{11}$ cm^{-3} density of energetic electrons with Lorentz factor $\gamma \gtrsim 40$. The model predicts a turnover frequency around 10^{13} Hz.

For the last three structures (E, F, and G) exhibiting a turnover frequency at about 10^{11} Hz, the application of the model would require unrealistically high numbers of energetic electrons. The last three structures might be explained by existing models that do not require the acceleration of ultrarelativistic electrons (for example: Dulk and Marsh, 1982).

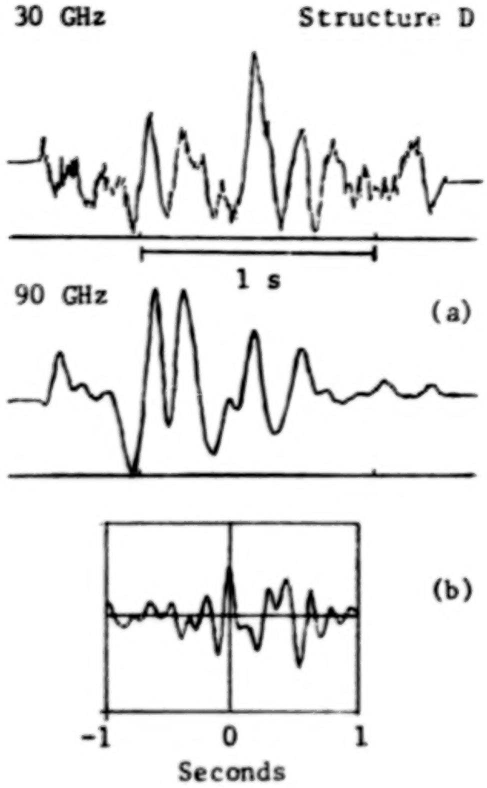

Figure 4 - Phase relationships are analysed for Structure D, with the pulses time profile in (a), and their cross-correlation in (b). Pulses are in phase to an accuracy better than 10ms.

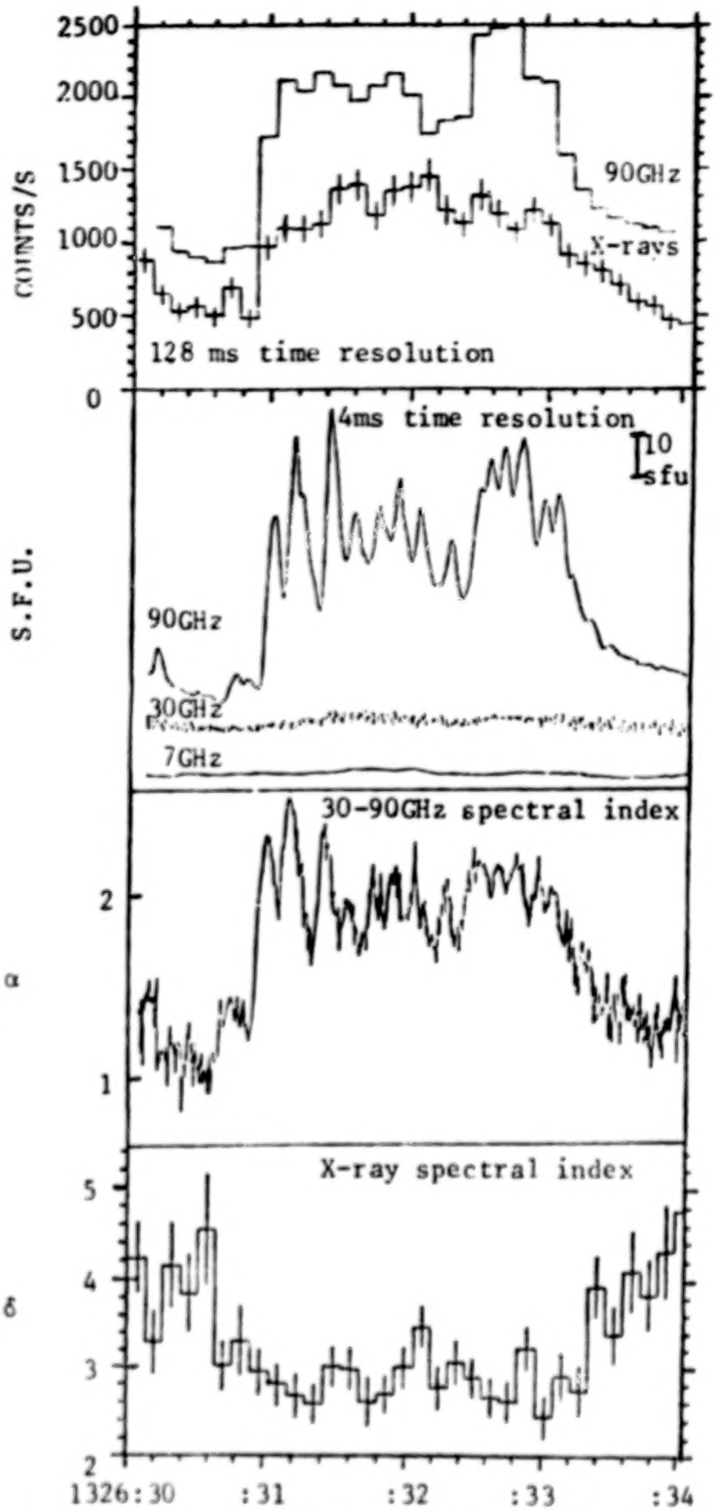

Figure 5(a) - A comparison of flux and spectral indices at 90 and 30 GHz, and hard X-rays (> 30 keV) for Structure C. The time resolution at hard X-rays was 128 ms, and at radio was 4 ms. In the upper plot the 90 GHz data was time integrated in 128 ms, in order to compare to the X-rays time profile.

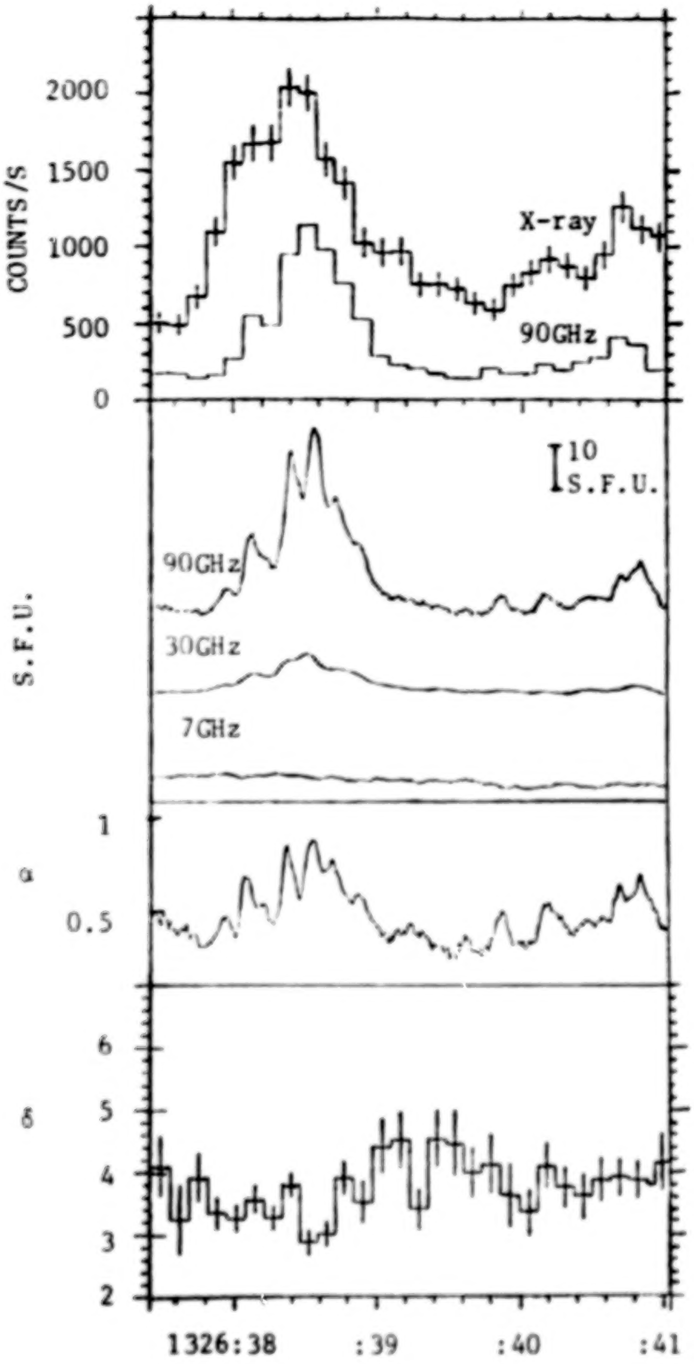

Figure 5(b) - Comparative plots, similar to Figure 5(a), for Structure E.

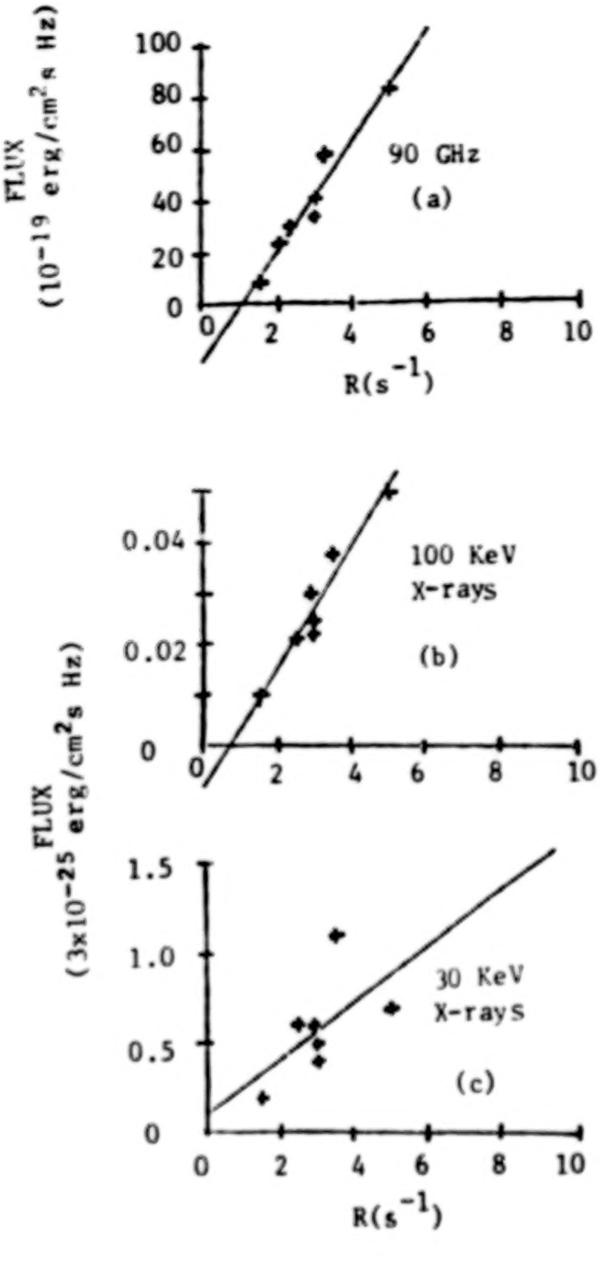

Figure 6 - Scatter diagrams: (a) Pulse repetition rates and fluxes at 90 GHz, (b) repetition rates at 90 GHz and fluxes at hard X-rays (> 100 keV), and (c) repetition rates at 90 GHz and fluxes at hard X-rays (> 30 keV), for all the seven structures.

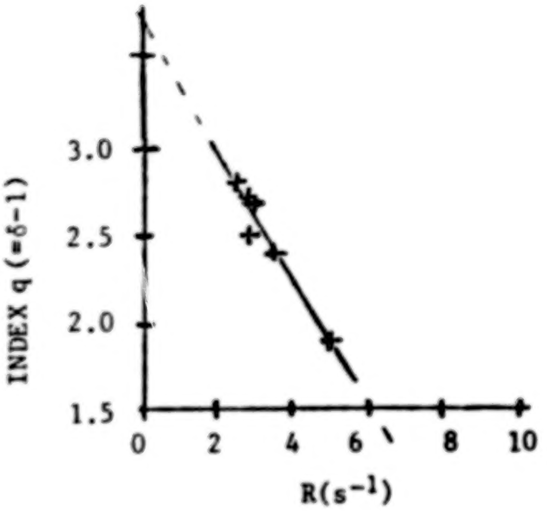

Figure 7 - Scatter diagram between pulse repetition rates and X-ray spectral index, for the last six burst structures.

Table II - Pulse source characteristics defined by Kaufmann et al., (1986) synchrotron/inverse-Compton model application of each major time structure as labeled in Figure 1. Parameters are defined at times $t = t_o$ (at the begining of the pulse) and $t = t_p$ (at the maximum of the pulse radio emission). γ is the Lorentz factor, ξ is the fraction of energy lost by the electrons, $\xi = \gamma(t = t_p)/\gamma(t = t_o)$; ν_{sm} is the maximum frequency of the spectrum produced by the accelerated ultrarelativistic electrons; K is the proportionality factor of the power law distribution $N(\gamma) = K\gamma^{-n}$; N and N_t are the density and total number of electrons accelerated per pulse; $r_{c/B}$ is the ratio of the inverse-Compton to bremsstrahlung losses "intrinsic" to the emitting pulse source.

STRUCTURE	ν_{sm} ($t=t_o$) Hz	ν_{sm} ($t=t_p$) Hz	ξ	KV electrons	N_t electrons	N cm^{-3}	γ ($t=t_p$)	$r_{c/B}$		scale size cm
								t_o	t_p	
A	7×10^{13}	3×10^{12}	0.21	2×10^{39}	2×10^{31}	2×10^{10}	47	10^{7}	10	10^{7}
B	8×10^{13}	4×10^{12}	0.26	10^{41}	2×10^{32}	2×10^{11}	40	10^{7}	56	10^{7}
C	7×10^{13}	2×10^{12}	0.17	4×10^{38}	8×10^{31}	8×10^{10}	39	10^{7}	2	10^{7}
D	9×10^{13}	4×10^{12}	0.21	9×10^{41}	2×10^{32}	2×10^{11}	45	3×10^{7}	24	10^{7}

Acknowledgements

This research was partially supported by the Brazilian research agency FINEP. INPE operates CRAAM and Itapetinga Radio Observatory. One of the authors (PK) is Guest Investigator on NASA-SMM Project.

REFERENCES

Cliver,E.W.: 1984, *private communication.*

Correia,E.: 1983, MS thesis, INPE, Brazil.

Dulk,G.A.; and Marsh,K.A.: 1982, *Astrophys.J.*, ***259***, 350.

Kaufmann,P.; Strauss,F.M.; Opher,R.; Laporte,C.: 1980, *Astron. Astrophys.*, ***87***, 58.

Kaufmann,P.; Correia,E.; Costa,J.E.R.; Zodi Vaz,A.M.; and Dennis,B.R.; 1985, *Nature*, ***313***, 380.

Kaufmann,P.; Correia,E.; Costa,J.E.R.; and Zodi Vaz,A.M.: 1986, *Astron. Astrophys.*, in press.

Loran,J.M.; Brown,J.C.; Correia,E.; and Kaufmann,P.: 1985, *Solar Phys.*, ***97***,363.

McClements,K.G.; and Brown,J.C.: 1986, *Astron. Astrophys.*, submitted.

N87
21803
UNCLAS

N87-21803

RAPID SPECTRAL AND FLUX TIME VARIATIONS IN A SOLAR BURST OBSERVED AT VARIOUS DM-MM WAVELENGTHS AND AT HARD X-RAYS

A. M. Zodi Vaz
P. Kaufmann
E. Correia
J. E. R. Costa

INPE: Instituto de Pesquisas Espaciais
C.P. 515, 12.200-S. José dos Campos, SP, Brazil

E. W. Cliver

Air Force Geophysical Laboratory
Space Physics Division
Hanscom Air Force Base
Bedford, MA 01731

T. Takakura

Department of Astronomy
Faculty of Science
University of Tokyo
Bunkyo-ku, Tokyo 113, Japan

K. F. Tapping

Herzberg Institute of Astrophysics
National Research Council
Ottawa, Ontario KIA OR6, Canada

ABSTRACT

A solar burst was observed with high sensitivity and time resolution at cm-mm wavelengths by two different radio observatories (Itapetinga and Algonquin); with high spectral time resolution at dm-cm wavelengths by patrol instruments (Sagamore Hill); and at hard X-rays (HXM-Hinotori). At the onset of the major burst time structure there was a rapid rise in the spectral turnover frequency (from 5 to 15 GHz), in about 10s, coincident to a reduction of the spectral index in the optically thin part of the spectrum. The burst maxima were not time coincident at the optically thin radio frequencies and at the different hard X-ray energy ranges. The profiles at higher radio frequencies exhibited better time coincidence to the higher energy X-rays. The hardest X-ray spectrum (-3) coincided to peak radio emission at the higher frequency (44 GHz). The event appear to be build up by a first major injection of softer particles followed by other injections of harder particles. Ultrafast time structures were identified as superimposed to the burst emission at the cm-mm high sensitivity data and at X-rays, with predominant repetition rates ranging 2.0-3.5 Hz.

1. INTRODUCTION

The 4 November 1981, 1828 UT solar burst was observed simultaneously at eleven dm-mm wavelengths (0.4-44 GHz), by Sagamore Hill (AFGL, USA), Algonquin (HIA, Canada) and Itapetinga (INPE, Brazil) observatories, and at seven energy ranges at hard X-rays by HXM experiment on Hinotori satellite(28-375keV). Radio spectral data were obtained by Sagamore Hill (0.4-15 GHz), with very

PRECEDING PAGE BLANK NOT FILMED

good time resolution (1 spectrum/second). The Algonquin (10.6 GHz) and Itapetinga (22 and 44 GHz) data were obtained with high sensitivity, and high time resolution (limited here to 30 milliseconds). The hard X-ray data were analysed with a time resolution of 30 milliseconds in the lower energy channel (28-38 keV). Hard X-ray spectral indices were obtained every 5-10 seconds throughout the major burst duration.

2. TIME SPECTRAL VARIATIONS

In Figure 1 we show the flux time profiles, the time variations of the radio turnover frequency and of the spectral indices. The radio spectral index α in the optically thin part of the spectrum was obtained from the fluxes at 22 and 44 GHz, and defined as $F \propto f^{\alpha}$, where F is the flux and f the frequency. The X-ray data for the seven energy channels (28-375 keV) were fitted to a power law spectrum (defined as $I \propto E^{\delta}$, where I is the flux, E the photon energy, and δ is the power law spectral index) and to a thermal spectrum (defined as $I \propto (kT)^{-0.2} \times E^{-1.3} \times \exp(-E/kT)$, where T is the temperature and k is the Boltzmann constant). The main burst phase (1828-1829 UT) exhibited three predominant structures at the softer X-ray (28-38 keV) time profile, with peaks at 1828:19, 1828:27 and 1828:38 UT, respectively.The corresponding maxima at radio occurred approximately at 10.6 GHz, 22 GHz and 44 GHz, respectively. The 10.6 GHz time profile is considerably smoother, compared to the time profiles at higher frequencies. This trend was also observed at 7 GHz, by a patrol instrument operated at Itapetinga Radio Observatory (Takakura et al., 1983).

Before 1828 UT, there was a precursor which was more pronounced at lower frequencies, presenting a spectral turnover frequency at about 5 GHz. Between 1828:10 and 1828:20 UT (corresponding to the first X-ray structure), there was a very rapid increase of the turnover frequency up to ~15 GHz, simultaneously to a decrease of the 22-44 GHz spectral index from about -3.7 to -4.9. The rapid change in the radio turnover frequency is shown in more detail in Figure 2.

The remaining part of the main burst (1828:20 to 1828:50 UT) was characterized by an increase of the radio and X-rays spectral indices (hardening) and a slight decline of the radio turnover frequency.

After 1828:50 UT, there was a softening of the X-rays index, but the 22-44 GHz spectral index continued to increase,reaching values between -3.0 and -3.5.

The increase and decrease of the X-ray spectral index δ can also be described in terms of increase and decrease of the temperature, if we assume the thermal fit (shown by open circles in Fig. 1). The χ^2 test applied to the two fits indicated that the thermal spectrum was better fitted than the power law spectrum during the main phase of the burst (1828:13-1828:43 UT). However, it is known that multiple injections of power law populations can produce apparent better thermal fits.

The errors bars marked in the plot of the radio spectral index refer to the uncertainty in the estimates of the 22 and 44 GHz flux densities at the beginning of the burst. After 1828:10 UT, this error becomes negligible. There is still an uncertainty of 0.4 in the absolute value of α,

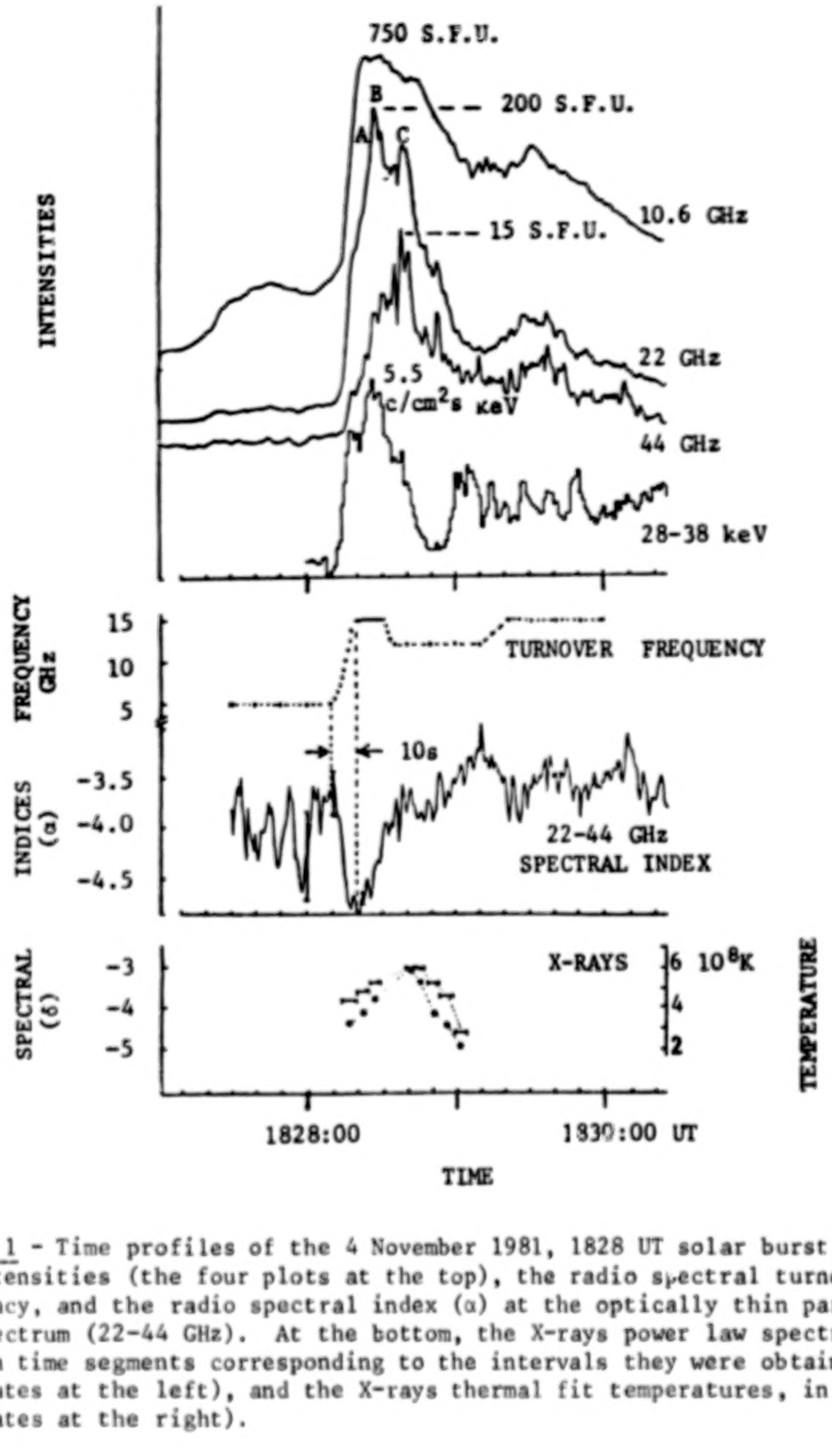

Figure 1 - Time profiles of the 4 November 1981, 1828 UT solar burst, including the intensities (the four plots at the top), the radio spectral turnover frequency, and the radio spectral index (α) at the optically thin part of the spectrum (22-44 GHz). At the bottom, the X-rays power law spectral index (δ), in time segments corresponding to the intervals they were obtained (ordinates at the left), and the X-rays thermal fit temperatures, in circles (ordinates at the right).

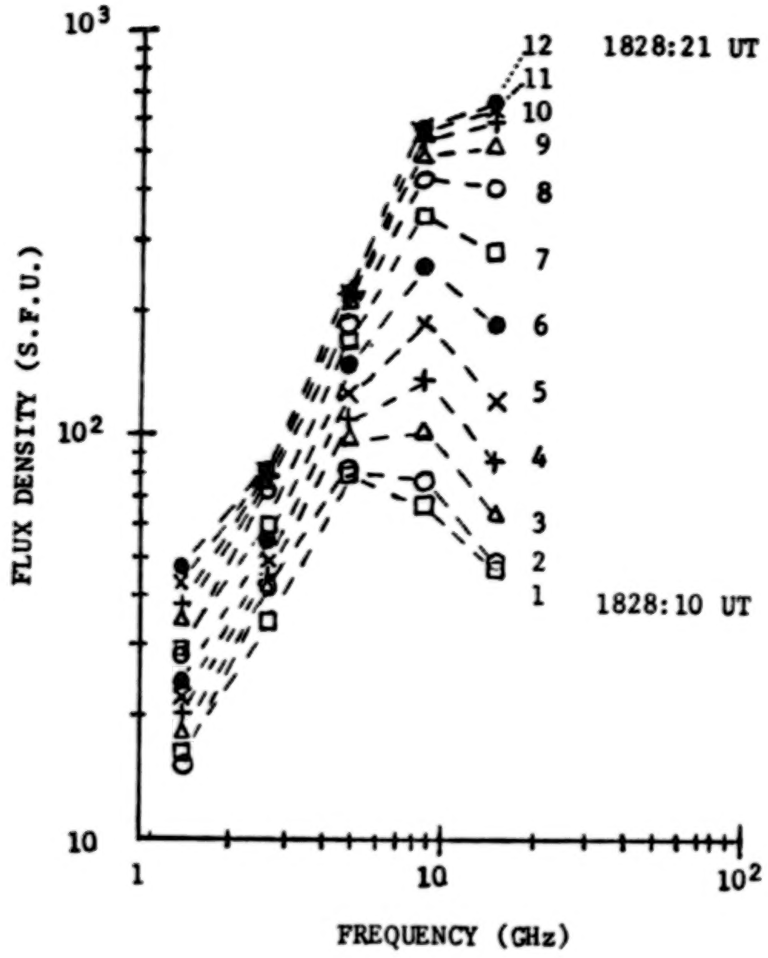

Figure 2 - The rapid variation of the turnover frequency between 1828:10 and 1828:21 UT, is shown by successive spectra, obtained every second, labeled 1-12, at five dm-cm frequencies by Sagamore Hill Radio Observatory (AFGL). The last three spectra (10, 11 and 12) are essentially identical. The shift in the turnover frequency (5-15 GHz) occurred in less than 10s.

due to the uncertainty of about 20% in the calibration of the 22 and 44 GHz flux scales. However, this effect is meaningless when we consider the time variation of α.

Figure 3 shows the X-rays time profiles at the six higher energy channels. There is a gap in the data between 1828:28 UT and 1828:37 UT, but it can be seen that the first structure at 1828:19 UT was more pronounced at the lower energies, while the third structure (1828:38 UT) was more pronounced at higher energies. As shown in Figure 1, the 44 GHz maximum occurred at the time of the third X-ray structure.

C-3

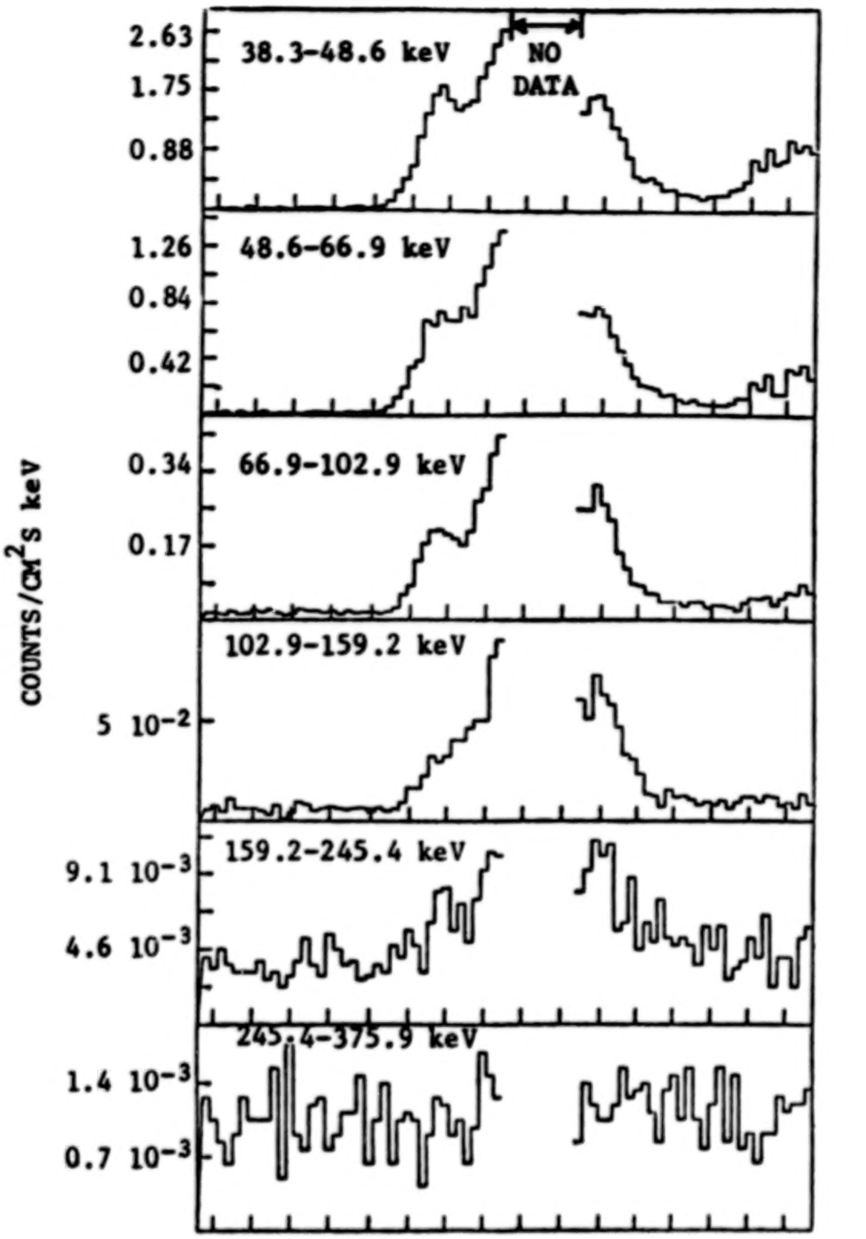

Figure 3 - X-rays time profiles at the harder energy ranges obtained by HXM experiment on board of the Hinotori satellite. The softer energy channel (28-38 keV) is shown in Figure 1. Note that the 22 GHz time profile (Figure 1) fits better to the 102.9-159.2 keV channel, while the 44 GHz time profile (Figure 1) fits better to the 159.2 - 245.4 keV channel.

3. SUB-SECOND TIME STRUCTURES

Time expanded sections of this burst reveal that sub-second pulsations were present in the radio and X-rays time profiles. This phenomenon was studied by Takakura _et al_. (1983), in the same burst. Their analysis, however, was restricted to two time intervals (of 2s), and the Algonquin 10.6 GHz high sensitivity data were not available. Figure 4 reproduces an expanded section of the original 22 GHz and 44 GHz time profiles obtained by two independent radiometers at the focus of the Itapetinga 45ft antenna. We have analysed in more detail three 4.3s intervals across the main burst structure, labeled A,B and C in Figure 1. The technique used was the subtraction of the data from running means, as described in the caption of Figure 5.

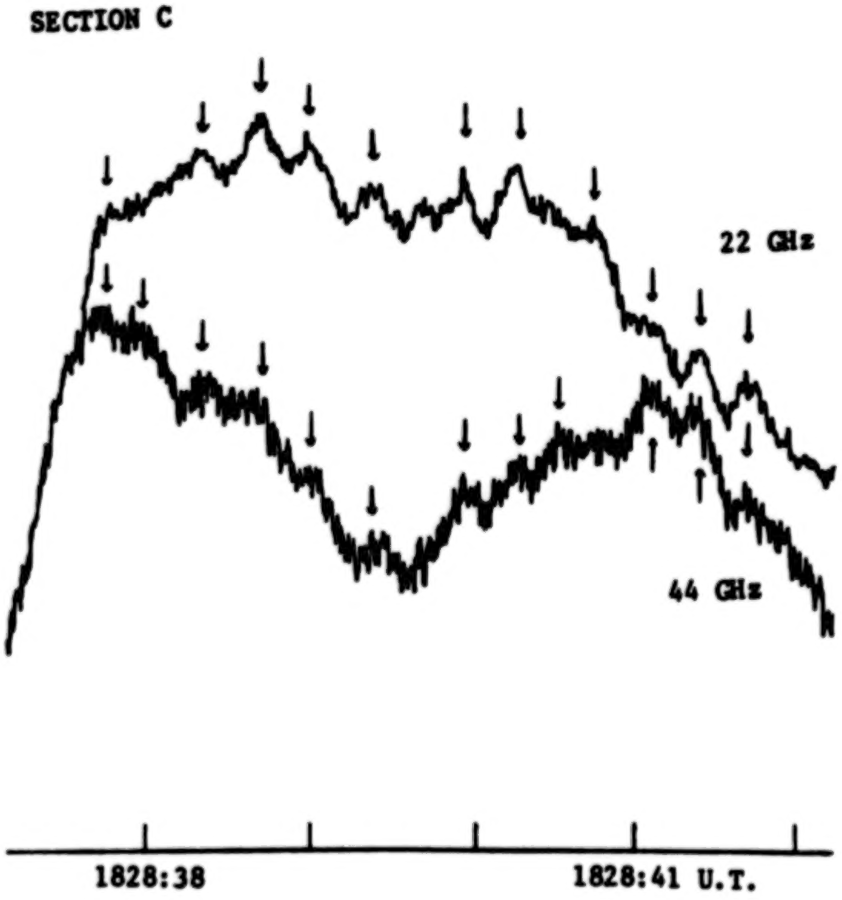

Figure 4 - Example of 22 and 44 GHz raw data without any filtering or processing, obtained for Section C (Figure 1). Superimposed fast structures are identified at the two frequencies by arrows. The mean time interval between consecutive well defined pulses is of about 0.3s, corresponding to a repetition rate of about 3.3 Hz. This burst section is analysed again in Figure 8, together with 10.6 GHz and hard X-rays data.

Figure 5 shows a sample of the uncertainties in fluctuations outside the burst period of time. They include the system noise and other fluctuations, which were due to excess noise at the data acquisition system (at 22 and 44 GHz), or to fluctuations of unknown origin (at 10.6 GHz). The figures 6-8 show the burst sections A,B and C, which compared to Figure 5 indicate clearly the presence of sub-second pulsations at the three radio frequencies and at 28-38 keV X-rays. The figure captions describe further details of the analysis. The repetition rates of the superimposed fast pulses ranged from 2-3.5 Hz. The subsecond pulses at 10.6 GHz were particularly pronounced at the main structures A and B, reducing substantially at structure C, as well as in the remaining part of the event. The relative amplitudes of the subsecond pulses at the corresponding maxima were of 0.7% (10.6 GHz), 3% (22 GHz), 7% (44 GHz), and 23% (at 28-38 keV X-rays). This result confirm the tendency of having better defined sub-second structures for higher mm-wave frequencies (Kaufmann et al., 1984; 1985).

We still observe that the time correlation between pulses at different radio frequencies and at X-rays is often poor or unexistent. The nature of this effect is not known, and deserves further analysis. One possibility might be that the fine time structures were not entirely resolved. Convolution effects may have produced the observed "ripple" structures, differently at the three radio frequencies and at X-rays (Brown et al.,1983; Loran et al., 1985).

The Fourier analysis techniques were highly criticized in the present Workshop, when applied to pulsed phenomena which are not strictly periodic. In spite of these restrictions, we obtained Fourier spectra for several sections throughout the burst duration. One example is shown in Figure 9, corresponding to the 4.3s burst section B (Figure 7). The results indicate the presence of several frequencies, with different relative amplitudes for different radio frequencies and hard X-rays, and confirm some repetition rates common to the four time profiles of section B (Figure 7).

4. CONCLUDING REMARKS

The impulsive burst may be interpreted as consisting of several major overlapping acceleration phases. In a first phase, the accelerated population of electrons are predominantly softer in energy. The sudden increase in turnover frequency may be attributed to the increase in density of accelerated electrons. The excess of particles with softer energies causes the decrease in the radio spectral index in the optically thin part of the spectrum. The following phases corresponded to a hardening of the radio and X-ray spectra, exhibiting peak emission, first at 22 GHz, followed by the peak at 44 GHz, nearly 20 seconds after the first phase. The phases appear to be build up of multiple rapid injections, which may also be superimposed or mixed up, producing complex power spectra or repetition rate frequencies.

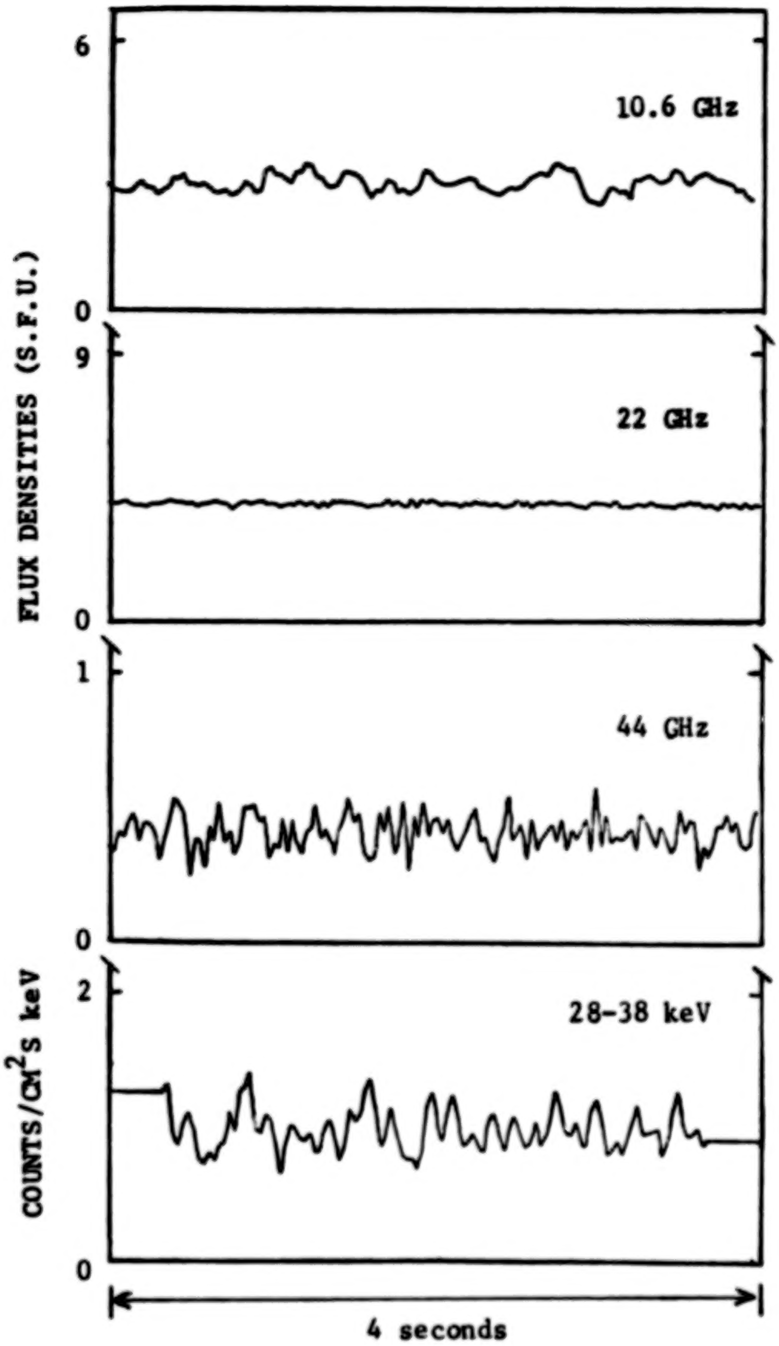

Figure 5 - 4 seconds of data obtained when tracking the active region previously to the event, in order to show the level of uncertainties in fluctuations at 10.6 GHz (Algonquin), 22 and 44 GHz (Itapetinga) and 28-38 keV (HXM-Hinotori). The plots were obtained by subtracting the data from 700 ms running mean baseline. The radio data was time integrated in 30 ms, in order to become comparable to the X-ray time resolution. The X-ray data was further smoothed out by a 90 ms running mean (this technique keeps the 30 ms time resolution).

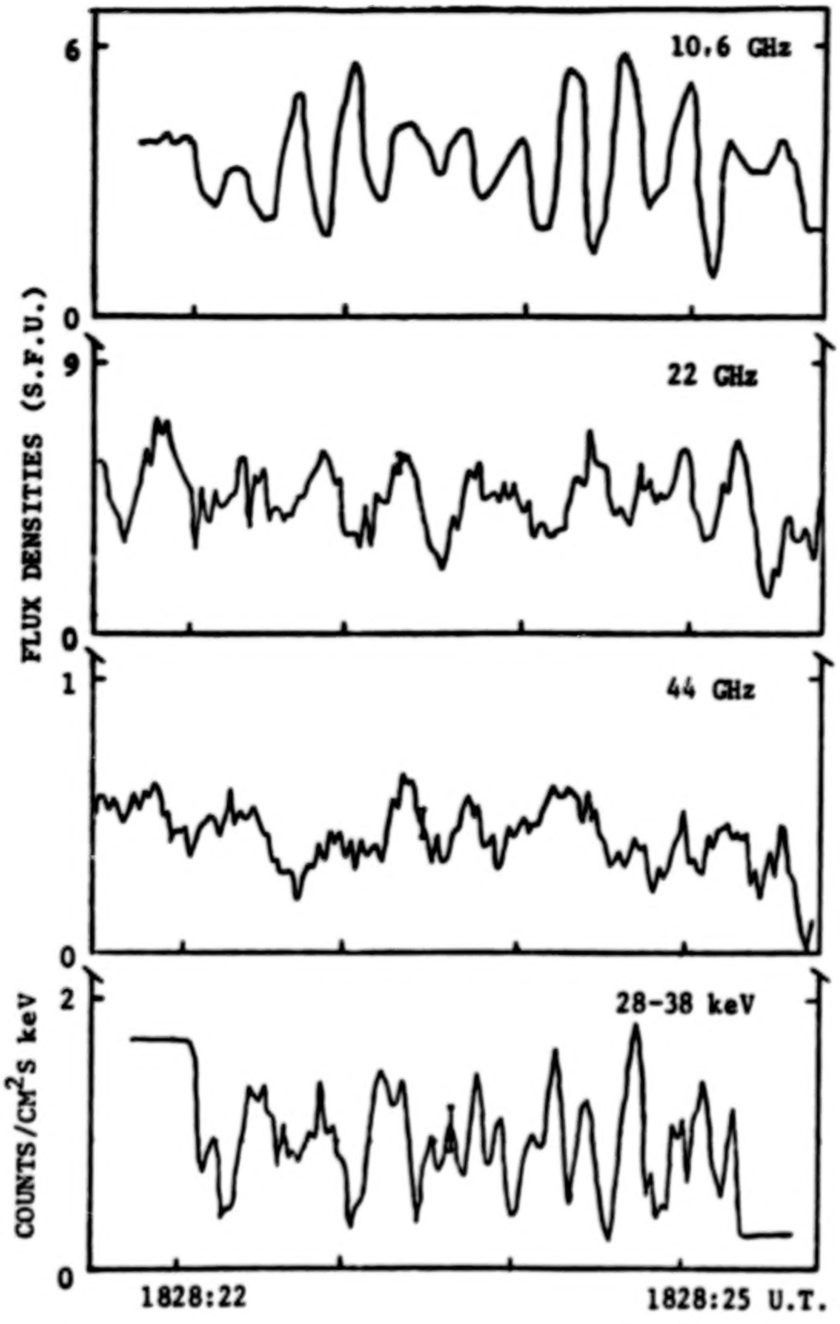

Figure 6 - 4.3 seconds interval of burst section A (Figure 1), obtained in the same scales and data reduction techniques used in the plots of Figure 5. The superimposed fast structures are clearly enhanced at the three radio frequencies and at hard X-rays. The error bars at 22 and 44 GHz take into account the increase in system temperature with the burst emission. Although there is a good correspondence between 22 and 44 GHz pulses, some of the pulses at 10.6 GHz and and at X-ray are not well correlated. The time intervals between two significant and consecutive pulses are nearly similar in the four plots, varying between 0.28s and 0.36s, corresponding to repetition rates ranging between 2.8 Hz and 3.5 Hz.

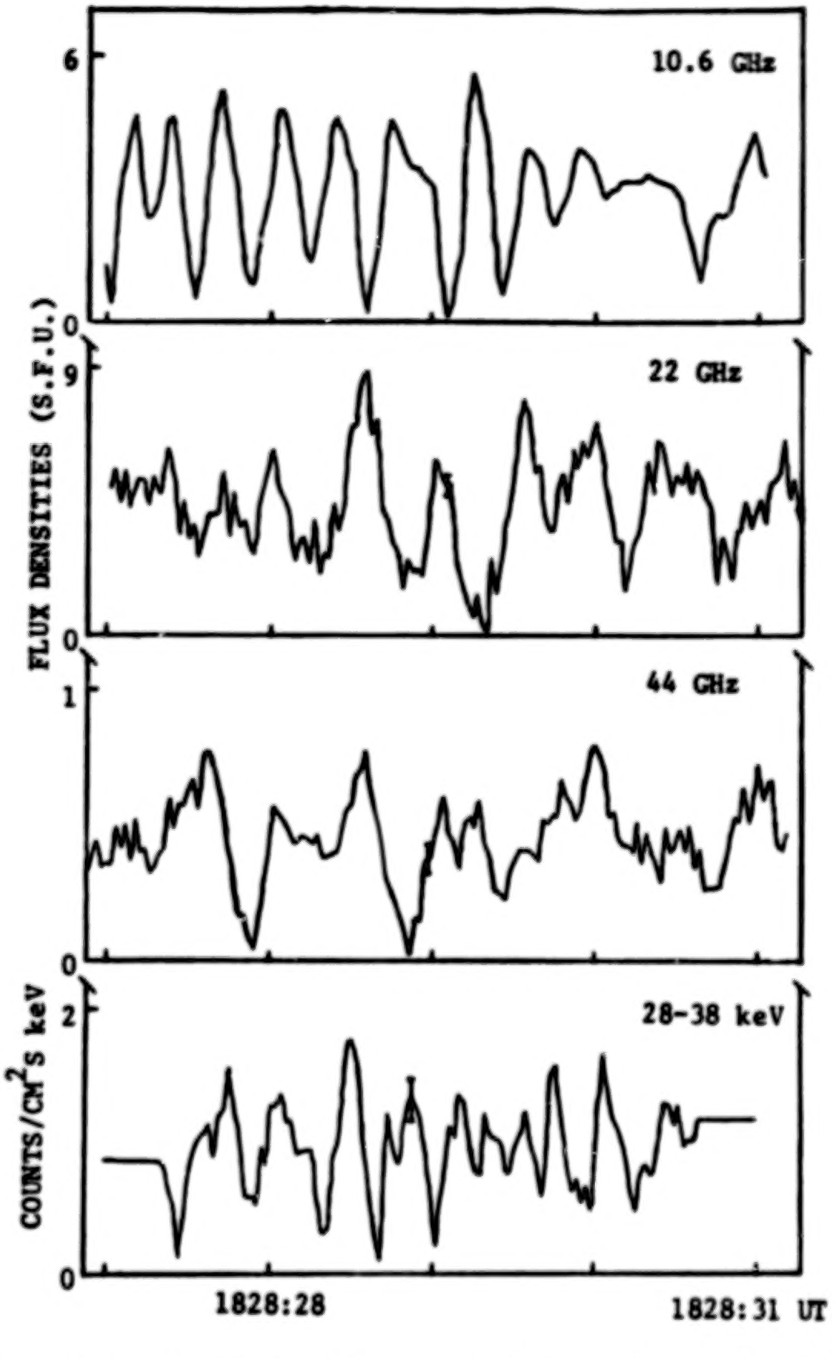

Figute 7 - 4.3 seconds interval of burst section B (Figure 1), obtained in the same conditions of the Figures 5 and 6. Fourier spectra of this section were also determined and are shown in Fig. 9. Like in section A (Figure 6), the time intervals between consecutive pulses denote the presense of more than one frequency, of about 2, 2.5 and 3.5 Hz. The Fourier spectra of Figure 9 also show these components, with different relative importance at the different radio frequencies and at hard X-rays.

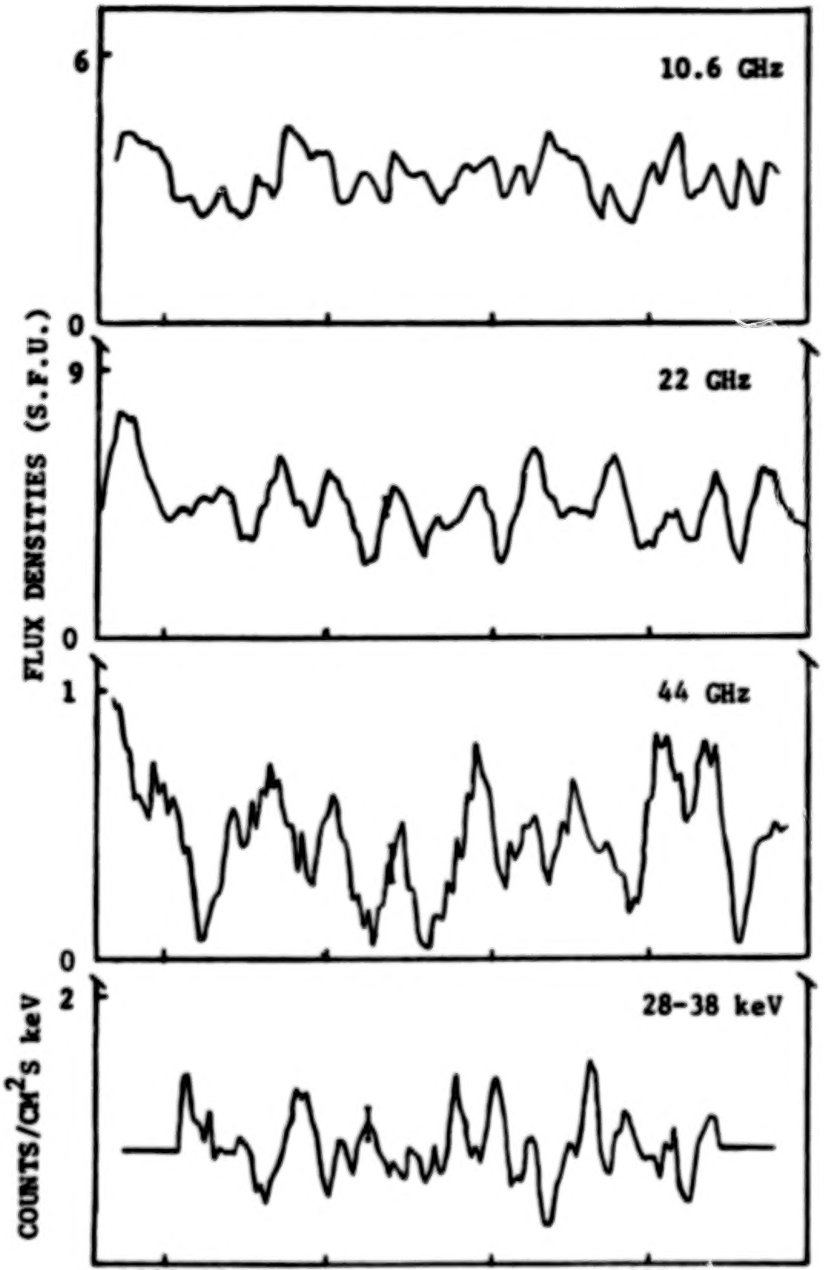

Figure 8 - 4.3 seconds interval of burst section C (Figure 1), obtained in the same conditions of the previous sections (Figure 5-7). In this section the fast pulses are better seen at 22 and 44 GHz. The original data at these frequencies were shown in Figure 4 and display the same structures.

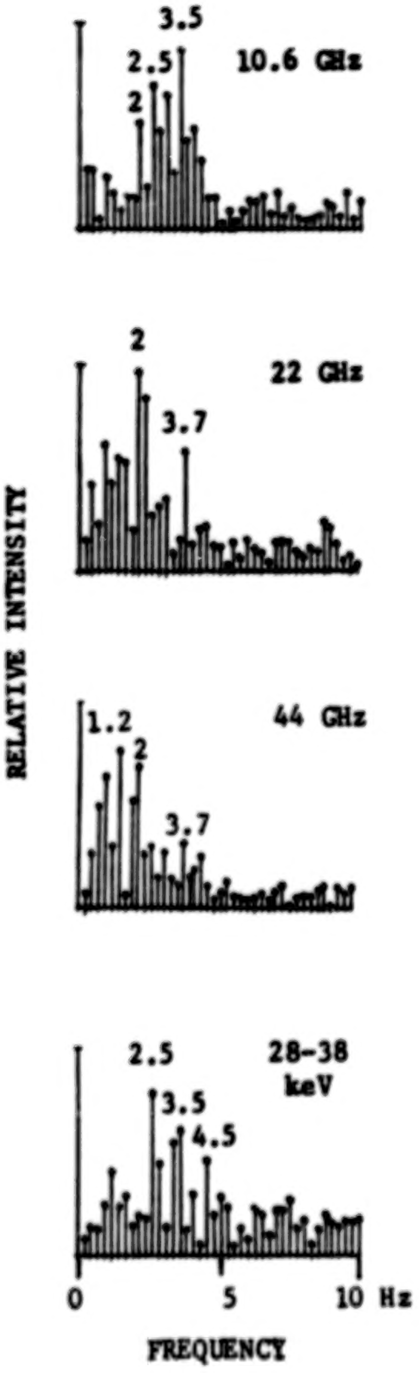

Figure 9 - Fourier spectra obtained for burst section B, about 4s in duration, which was shown expanded in Figure 7. The predominant time structures exhibit repetition rates of about 2.0-2.5 Hz and 3.5 Hz at the three radio frequencies and at hard X-rays, with different relative intensities.

Acknowledgements

This research was partially supported by the Brazilian research agency FINEP. INPE operates CRAAM and Itapetinga Radio Observatory. One of the authors (PK) is Guest Investigator on NASA-SMM Project.

REFERENCES

Brown,J.C., MacKinnon,A.L., Zodi,A.M., and Kaufmann,P.: 1983,*Astron.Astrophys.*, 123, 10.

Kaufmann,P., Correia,E., Costa,J.E.R., Dennis,B.R., Hurford,G.J., and Brown, J.C.: 1984, *Solar Phys.*, 91, 359.

Kaufmann,P., Correia,E., Costa,J.E.R., Zodi Vaz,A.M., and Dennis,B.R.: 1985, *Nature*, 313, 380.

Loran,J.M., Brown,J.C., Correia,E., and Kaufmann,P.: 1985, *Solar Phys.*, 97,363.

Takakura,T., Kaufmann,P., Costa,J.E.R., Degaonkar,S.S., Ohki,K., and Nitta,N.: 1983, *Nature*, 302,317.

N87
21804
UNCLAS

N87-21804

QUASI-PERIODIC PULSATIONS IN SOLAR HARD X-RAY AND MICROWAVE FLARES

Takeo Kosugi

NAS/NRC Research Associate
on leave from the Tokyo Astronomical Observatory

Laboratory for Astronomy and Solar Physics
NASA Goddard Space Flight Center
Greenbelt, MD 20771

Alan L. Kiplinger

Laboratory for Astronomy and Solar Physics
NASA Goddard Space Flight Center
Greenbelt, MD 20771
and
Systems Applied Sciences Corp.-Technologies
Lanham, MD 20706

For more than a decade, various studies have pointed out that hard X-ray and microwave time profiles of some solar flares show quasi-periodic fluctuations or pulsations (Parks and Winckler 1969, 1971; Frost 1969; Cribbens and Matthews 1969; Janssens and White 1969, 1970; Janssens et al. 1973; Maxwell and Fitzwilliam 1973; Anderson and Mahoney 1974; Cliver et al. 1976; Wiehl and Matzler 1980). Nevertheless, it was not until recently that a flare displaying large amplitude quasi-periodic pulsations in X-rays and microwaves was observed with good spectral coverage and with a sufficient time resolution. The event occurred on 1980 June 7 at ~ 0312 UT, and exhibits seven intense pulses with a quasi-periodicity of ~ 8s in microwaves ($f \gtrsim 3$ GHz), hard X-rays ($E \gtrsim 20$ keV) and gamma-ray lines. Details of this event are given by Kane et al. (1983), Kiplinger et al. (1983), Forrest and Chupp (1983), and Nakajima et al. (1983), and in several additional papers cited by them. This flare strongly suggests that, in the impulsive phase of a flare, electrons and ions are accelerated simultaneously in a train of quasi-periodic pulses which may arise as a consequence of some MHD/plasma

PRECEDING PAGE BLANK NOT FILMED

process such as a current loop coalescence (Tajima et al. 1982; Nakajima et al. 1984; Sakai et al. 1986). Therefore, a study of similar events for confirming common characteristics of this type of flare is expected to provide deeper insight into basic flare processes.

On 1983 May 12 at ~ 0253 UT, another good example of this type of flares was observed both in hard X-rays and in microwaves (Kiplinger et al. 1984). Time profiles of microwave intensity (R+L) at five frequencies are shown in Figure 1 together with curves representing the degree of polarization (R-L)/(R+L). Similar to the 1980 June 7 event, this event consists of seven dominant pulses with a remarkable regularity; the mean interval between pulses is ~ 16s with the ratio of the maximum interval to the minimum interval being ~ 2.1. It is to be noted that such a regularity should seldom occur as the result of randomly scattered pulses. The probability of such a regularity in the occurrences of seven pulses is ~ 3×10^{-4} if the pulses are distributed according to a Poisson distribution.

Temporal and spectral characteristics of this flare are compared with the event of 1980 June 7 in Table I. As can be seen from the table, the two flares resemble each other not only in their time profiles but also in other characteristics as follows:

a. The microwave source, observed with the Nobeyama 17 GHz interferometer for both cases, is almost stationary in the pulsating phase (see Figure 2). (The 1983 May 12 source shows an eastward motion in the decay phase after the pulsation. This motion may be a projection of an upward motion with a velocity of ~ 100 km s^{-1}.)

b. Several observed quantities vary in synchronism with the intensity variation, i.e.,
   (i) The hard X-ray spectrum hardens at the times peaks and softens at the times of valleys,
   (ii) The peak frequency of microwave spectrum, f_p, increases at the times of peaks and decreases at the times of valleys, and,
   (iii) The degree of circular polarization of microwaves at $f = f_p$ decreases at the times of peaks and increases at the times of valleys, while that at frequencies $f > f_p$ (data is not available for the 1980 June 7 event due to its high f_p) increases slightly at the times of peaks.

All these variations are superposed on a more gradual variation. It should be noted that the variation of hard X-ray spectrum between peaks and valleys is less pronounced in the 1980 May 12 event and that the 6th and 7th peaks of this event reveal a progressive hardening of X-ray spectra.

These common characteristics summarized above appear to be consistent

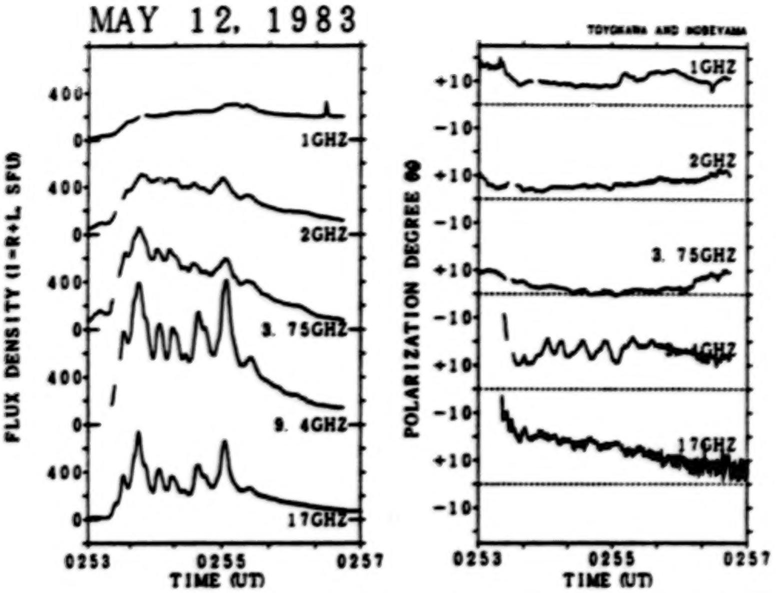

Figure 1: The flare of 1983 May 12 in microwaves. Time profiles in intensity (I=R+L, left) and the degree of polarization (p=(R-L)/(R+L), right) are shown at five frequencies. Observations were made at Toyokawa (1, 2, 3.75 and 9.4 GHz; by courtesy of S. Enome) and at Nobeyama (17 GHz).

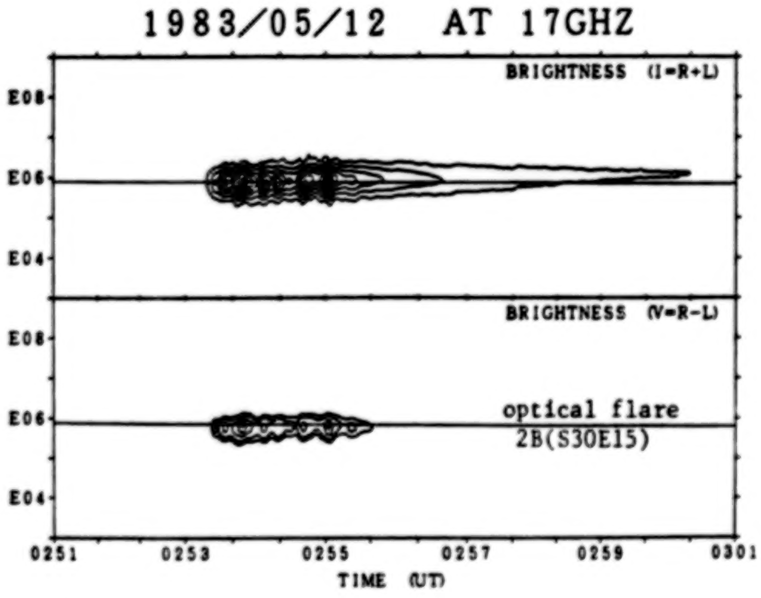

Figure 2: One-dimensional (E-W) contour map with time of the 1983 May 12 flare at 17 GHz. Contour lines are drawn at 90, 80 ..., 10, and 3% levels for the I=R+L map (upper), and at 20, 15, 10, 5, and 3% levels for the V=R-L map (lower), of the maximum brightness of I=R+L. The Hα flare position, S30E15, is denoted by a straight line.

Table I. Comparison between the 1980 June 7 and the 1983 May 12 flares.

<table>
<tr><th></th><th>1980 June 7</th><th>1980 May 12</th></tr>
<tr><td>A. Quasi-periodicity</td><td>$\tau \sim 8$s
$N = 7$
MW,HXR, γ-lines</td><td>$\tau \sim 16$s
$N = 7$
MW, HXR</td></tr>
<tr><td>B. Microwaves</td><td></td><td></td></tr>
<tr><td>B1. Source size
position
(17 GHz, East-West)</td><td>$\lesssim 5''$
stationary ($< 3''$)</td><td>$\sim 20''$
almost stationary ($\lesssim 5''$)
upward motion ($\sim$ 100km/s) after pulsation</td></tr>
<tr><td>B2. Spectra
(f_p: peak frequency)</td><td colspan="2">(f_p: increases at peaks, decreases at valleys)</td></tr>
<tr><td></td><td>$f_p \gtrsim 17$ GHz
gradually decreasing</td><td>$f_p \sim 9.4$ GHz
gradually increasing</td></tr>
<tr><td>B3. Degree of polarization at $f \sim f_p$</td><td colspan="2">(decreases at peaks, increases at valleys)
(i.e. anti-correlation with intensity)</td></tr>
<tr><td>at $f > f_p$</td><td>---</td><td>positive correlation with intensity</td></tr>
<tr><td>B4. Peak timings</td><td></td><td></td></tr>
<tr><td>with HXR's</td><td>0.3s delay</td><td>1-2s delay</td></tr>
<tr><td>high f vs low f</td><td>low-f delay</td><td>complex</td></tr>
<tr><td>C. Hard X-rays</td><td></td><td></td></tr>
<tr><td>C1. Spectra ($E^{-\gamma}$)</td><td colspan="2">(hardens at peaks, softens at valleys)</td></tr>
<tr><td></td><td>$\Delta\gamma \sim 1$</td><td>$\Delta\gamma \sim 0.4$</td></tr>
<tr><td></td><td>γ :2.5 → 3.5
(gradually softening)</td><td>γ :4.0 → 3.3
(gradually hardening)</td></tr>
<tr><td>C2. Peak timings</td><td>< 0.2s delay at high E</td><td>$\sim$1s delay at high E</td></tr>
<tr><td>D. Remarks</td><td>subpeak structure
homologous events</td><td></td></tr>
</table>

with a model in which acceleration of electrons (and also ions in the case of the 1980 June 7 event) takes place repeatedly in a single loop or a system of loops. The interval between this repeated acceleration is governed by some characteristic time scale such as the Alfven transit time, i.e., the length (or the radius) of the loop(s) divided by the Alfven velocity. At the times of peaks, electrons are accelerated in the loop(s) and stream down into a thick-target hard X-ray source where they give rise to hard X-rays by bremsstrahlung and lose their energy by collisions. Also a certain fraction of the electrons accelerated in the individual pulses are reflected and trapped in the loop(s) by magnetic mirrors. These electrons have a relatively long life-time and give rise to a gradual background component.

In this model, the differences in the hard X-ray spectra between the peaks and the valleys may be explained by the existence of more than one hard X-ray source. For simplicity, let us assume that hard X-rays are emitted only from the thick-target source at the times of peaks, whereas they are emitted only by trapped electrons at the times of valleys. Also we will assume that the spectral evolution of trapped electrons is negligible so that the thin-target approximation for the hard X-ray radiation is applicable. In this case, we get the maximum peak-to-valley difference in spectral index $\Delta\gamma = 1.5$. Note that the observed values, $\Delta\gamma \approx 1.0$ for the 1980 June 7 event and $\Delta\gamma \approx 0.4$ for the 1983 May 12 event, are smaller than this maximum value. This suggests that the above scenario is nearly correct but needs some modifications. It is likely that both the thick-target source and the trapped-electron source emit hard X-rays continuously with their relative contributions varying over the peaks and valleys. The smaller $\Delta\gamma$ observed in the 1983 May 12 event when compared to that observed in the 1980 June 7 event is in accordance with a higher trapping efficiency of electrons; this explanation seems consistent with several characteristics of the former event such as a progressive hardening of the X-ray spectrum and a delay of microwaves and higher-energy hard X-rays with respect to lower energy hard X-rays.

The higher peak frequency of the microwave spectrum, f_p, at the times of peaks than at the times of valleys is not only due to a larger number of energetic electrons but also due to a stronger magnetic field. The positive correlation between the degree of polarization and intensity at frequencies $f > f_p$ requires that the magnetic field is stronger at the times of peaks than at the times of valleys. This result is consistent with our scenario, because down-streaming electrons should encounter a stronger magnetic field than the trapped electrons. Finally, the anti-correlation between the variation in the degree of polarization and that in intensity, found at around the peak frequencies, $f \approx f_p$, is naturally explained by variations in optical depth. This variation in optical depth is observed as a positive correlation of f_p with intensity.

In order to further explore these observational results and theoretical scenarios, a study of nine additional quasi-periodic events has been incorporated with the results from the two flares described above. These 11 flares were selected from a sample of 135 digitally recorded events which were observed with the Nobeyama 17 GHz polarimeter from January 1979 through June 1983. All events were required to have a peak flux exceeding 150 sfu and were selected by criteria similar to those used by Cliver et al. (1976). Out of the 11 events selected, polarimeter data from Toyokawa Radio Observatory at 1, 2, 3.75 and 9.4 GHz are available for nine events (digital data kindly provided by S. Enome); Nobeyama 17 GHz interferometer data are available for seven events; and HXRBS data are available for four events.

A brief summary of the analyses of these events is:

(1) The mean periods identified in the 11 quasi-periodic events are scattered in the range of 8 to 36 s with the number of pulses varying between 4 and 15.

(2) The microwave source is stationary in three out of seven events (3/7), or shows a small shift of < 10" in the pulsating phase (4/7). In the latter cases, the motion appears continuous rather than random. Two events suggest an upward motion ($\sim$ 100 km s^{-1}) in the decay phase after the pulsation.

(3) The summaries b(i) to (iii) for the events on 1980 June 7 and 1983 May 12 apply to most cases:
  - (i) Hard X-ray spectral hardening at peaks (4/4), with $\Delta\gamma = 0.4 - 1.0$.
  - (ii) Increases of f_p at the times of peaks (6/9). In one out of the remaining three events, f_p is remains nearly constant. For the other two cases, the change in peak frequency cannot be estimated because $f_p >> 17$ GHz or because of small amplitude of pulses at $f < 10$ GHz.
  - (iii) The anti-correlation of the degree of polarization with intensity at frequencies $f \approx f_p$ (7/10). Two of the remaining three events are unpolarized. The other is the only exception whose degree of polarization decreases gradually with time and shows no correlation with the rapidly varying intensity.
  - (iv) Using data at 17 GHz, correlation of the degree of polarization with the intensity at $f > f_p$ has been examined for six events which exhibits $f_p < 17$GHz. We find that two events with $f_p < 9$ GHz show a weak positive correlation, one event with $f_p \approx 10$ GHz shows no correlation, two events with $f_p \approx 12$ GHz show a weak negative correlation, and the remaining one event is unpolarized. This result is consistent with the statement in point b(iii) in the previous summary.

(4) Flares from the same active region which produced a quasi-periodic

> event have been searched for homologous, quasi-periodic events. Such a homologous flare has been found in 6 of the 11 events, and the mean periods are similar between homologous pairs of flares in 5 out of the 6 cases. This is supporting evidence for a physical reality of the quasi-periodicities.

A more detailed examination is still in progress and will be summarized in a more extensive paper in the near future.

References

Anderson, K.A., and Mahoney, W.A. 1974, Solar Phys., 35, 419.
Cliver, E.W., Hurst, M.D., Wefer, F.L., and Bleiweiss, M.P. 1976, Solar Phys., 48, 307.
Cribbens, A.H., and Matthews, P.A. 1969, Nature, 222, 158.
Forrest, D.J., and Chupp, E.L. 1983, Nature, 305, 291.
Frost, K.J. 1969, Astrophys. J.(Letters), 158, L159.
Janssens, T.J., and White, III, K.P. 1969, Astrophys. J.(Letters), 158, L127.
Janssens, T.J., and White, III, K.P. 1970, Solar Phys., 11, 299.
Janssens, T.J., White, III, K.P., and Broussard, R.M. 1973, Solar Phys., 31, 207.
Kane, S.R., Kai, K., Kosugi, T., Enome, S., Landecker, P.B., and McKenzie, D.L. 1983, Astrophys. J., 271, 376.
Kiplinger, A.L., Dennis, B.R., Frost, K.J., and Orwig, L.E. 1983, Astrophys. J., 273, 783.
Kiplinger, A.L., Dennis, B.R., Frost, K.J., Orwig, L.E., and Kosugi, T. 1984, Bull. Amer. Astron. Soc., 16, 475.
Maxwell, A., and Fitzwilliam, J. 1973, Astrophys. Letters, 13, 237.
Nakajima, H., Kosugi, T., Kai, K., and Enome, S. 1983, Nature, 305, 292.
Nakajima, H., Tajima, T., Brunel, F., and Sakai, J. 1984, in Proc. Course and Workshop on Plasma Astrophysics (Varenna, Italy), p. 193.
Parks, G.K., and Winckler, J.R. 1969, Astrophys. J.(Letters), 155, L117.
Parks, G.K., and Winckler, J.R. 1971, Solar Phys., 16, 186.
Sakai, J., Tajima, T., Nakajima, H., Kosugi, T., Brunel F., and Zaidman, E. 1986, (in this issue).
Tajima, T., Brunel, F., and Sakai, J. 1982, Astrophys. J.(Letters), 258, L45
Wiehl, H.J., and Matzler, C. 1980, Astron. Astrophys., 82, 93.

N87
21805
UNCLAS

N87-21805

MICROWAVE MILLISECOND SPIKE EMISSION AND ITS ASSOCIATED PHENOMENA DURING THE IMPULSIVE PHASE OF LARGE FLARES

LI Chunsheng, JIANG Shuying, and LI Hongwei

Department of Astronomy
Nanjing University
Nanjing, China

FU Qijun

Beijing Observatory
Academia Sinina
Beijing, China

ABSTRACT

A tentative model is proposed to account for some features of the microwave millisecond spike emission and its links with the physical processes of associated phenomena during the impulsive phase of large flares by comparing the optical, radio and X-ray observations on May 16, 1981 to those on October 12, 1981.

I. INTRODUCTION

The emission of short duration (1-100 ms), high brightness temperature ($\gtrsim 10^{15}$ K) spikes at microwave frequencies during the impulsive phase of some solar flares is now well established [1,2]. The occurrences of these spikes may give us a clue to the physical process of microwave millisecond spike emission(MMSE) linked with its associated phenomena.

On the basis of the observations described in [1], Melrose and Dulk (1982) discussed the relation between the physical processes generating MMSE and hard X-ray

PRECEDING PAGE BLANK NOT FILMED

bursts. They suggested that MMSE was caused by the loss-cone driven electron-cyclotron maser in a flaring loop [3]. In this paper, we go further to find the physical processes of the MMSE and its links with associated phenomena druing the impulsive phase of some solar flares, but the MMSE is considered to be excited by the electron-cyclorton instability associated with a hollow beam of electrons [4].

We have analysed two major flare-burst events of May 16 and October 12, 1981. The following observational data during the impulsive phase of these two flares were used for comparison.

(1) Radio observations made at 2.84 GHz with the time resolutions of 1 second and 1 ms at the Beijing Observatory,

(2) H_α and photospheric magnetic field observations made at the Yunnan Observatory,

(3)Hard X-ray burst observations made on Hinotori (by courtesy of Dr.K.Tanaka)

(4) Radio spectra for type III and type IV_{DCIM} bursts published in Solar-Geophysical Data.

All the data staed above are summarized in Table 1.

II. A GENERAL DESCRIPTION OF THE TWO FLARE-BURST EVENTS

As shown by Table 1, there existed some similar features between these two events, such as the coincidence with H_α flares of importance 3B, two-ribbon flares, magnetic configurations of type δ and photospheric magnetic intensities $\gtrsim$2500G. However, we can see in the following their significant characteristics different from each other.

1. There appeared strong MMSE's ($T_b \gtrsim 10^{15}$ K) during the first event (1981 May 19) but appear during the second (1981 October 12).

2. A lot of intense decimetric bursts of type III_B , type III_G and type IV_{DCIM} occurred during the first event, but no decimetric burst and only weak metric bursts occurred during the second.

3. Although only the decay phase of hard X-ray bursts was recorded on Hinotori for the first event, the peak values (counts per second) of hard X-ray bursts for the first event still far exceeded those of the second in the same energy range.

4. However, the peak flux density of radio burst at 10.6 cm in the second

event is about six times larger than that in the first.

III. THE MODEL AND KEY PROCESSES

It has been pointed out in [2,6] that after the main phase of the microwave burst there still appeared MMSE's. This means that the fast electrons generating the microwave bursts and those exciting MMSE's do not come from the same source. Furthermore, the simultaneous observations of hard X-ray bursts by SMM and high resolution microwave observations by VLA indicate that the sources of these two bursts are not coincident with each other in space.

On the basis of these observations and a comparison between the two flare-burst events stated above, we propose a tentative model to account for the links of the physical processes of MMSE's with their associated phenomena as follows (Fig.1.).

1. During the impulsive phase of large solar flares, there probably appear two acceleration regions, One (region A) of them formed in the current sheet by a tearing mode instability is located over the top of the flaring loop, the other (region B) is established just at the top of the flaring loop by turbulence acceleration. Regions A and B are also the energy release regions.

2. A stream of fast electrons escaping outward from region A along open field lines is able to excite type III bursts with a negative frequency drift under certain conditions, while the other stream injected downward with a certain incident angle into the flaring loop is capable of establishing an anisotropic pitch angle distribution of "hollow beam" and stimulate an electron-cyclotron maser to radiate MMSE's or generate type IV_{DCIM} bursts with positive frequency drift. As soon as the fast electrons radiate away energy in the direction perpendicular to the magnetic field, they immediately precipitate into the transition region or the chromosphere, collide with the surrounding plasma and emit hard X-ray bursts (thick target model).

3. The background radiation, i.e. microwave radio bursts superimposed by MMSE's, is generally accepted as a gyrosynchrotron radiation emitted by nonthermal electrons, gyrating about field lines, with an isotopic pitch angle distribution and power law energy spectrum. The microwave burst source is located in region B at the top of the flaring loop.

Table 1. Observed Characteristics for the Events of May 16, 1981 and October 12, 1981

Date	Characteristic parameters	H_α Flare	Magnetic configuration	Radio Burst =10.6 cm	MMSE =10.6 cm	Hard X-ray Burst	Dynamic Spectrum	
							10cm----1 m	1m — 10m
May 16, 1981	Start Time(UT) Maximum(UT) End (UT) Peak Flux Density Importance Type Flare location	0806 0846 0916 3B Two Ribbons $N_{14}E_{14}$	Type δ	0806 0839 1002 1916 (sfu) 47GB	0806 0839 0920 5x10 (sfu)	$9^h00^m13^s$ 9 17 355 counts/sec (ε≿40KeV) 2016 counts/sec (40.7≻ε≻17 KeV)	0750.7 08105 0812 0812.5 0816.2 1000 1105 Insensity 2 3 3 3 III_B, III_G, IV_{DCIM}, IV_F	0810.5 0810.5 0816.2 1105 Intensity 3 3 III_G, IV_F
Oct. 12, 1981	Start Time(UT) Max. Time(UT) End (UT) Peak Flux Density Importance Type Flare Location	0626 0633 0830 3B Two Ribbons $S_{17}E_{08}$	Type δ	0614 0650.4 0720 10800 (sfu)	None	$6^h12^m53^s$ $6^h21^m17^s$ 6^h25^m 118 counts/sec (ε≿40 KeV) 158 counts/sec (40≻ε≿17KeV)	None	0616 0616.4 — — 1544 0617.8 Intensity 2 1 III_S III_G

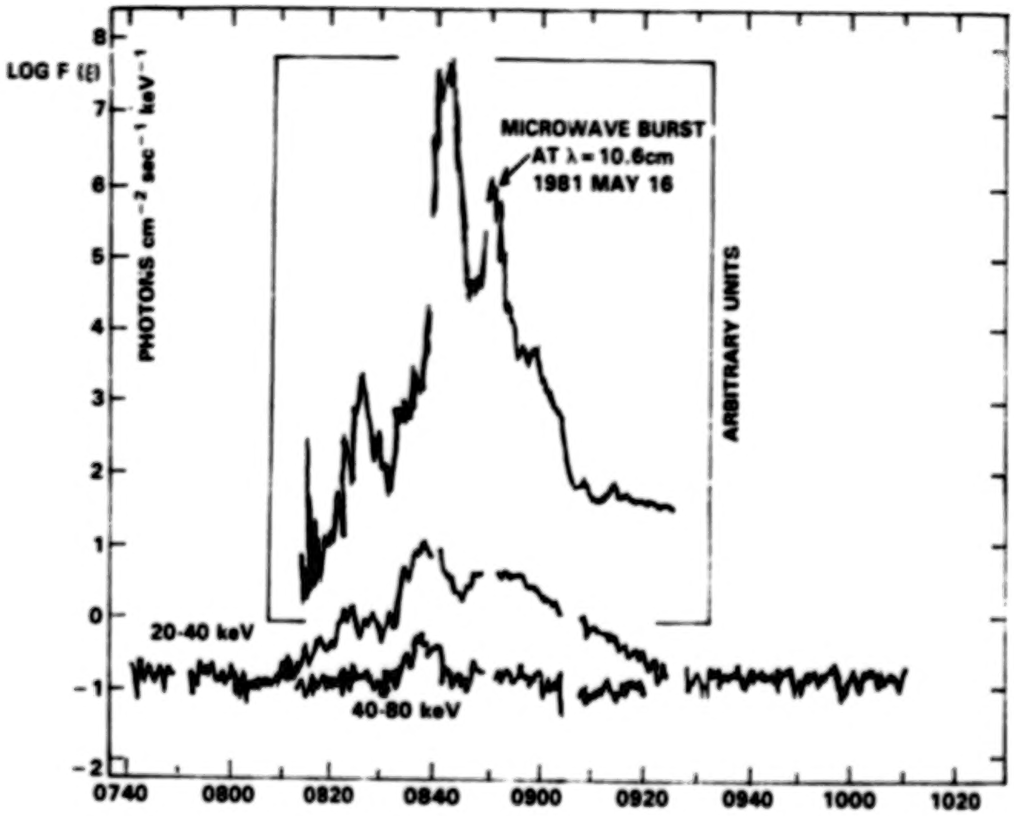

Fig. 1. The large microwave burst at λ = 10.6 cm and hard X-ray bursts recorded by Prognoz 8 satellite during the large flare-burst event of 1981 May 16 [5].

IV. EXPLANATION AND DISCUSSION

1. According to a quasilinear theory, the general formula for the growth rate at s-th harmonic for wave in the magneto-ionic mode is [3, Appendix B]

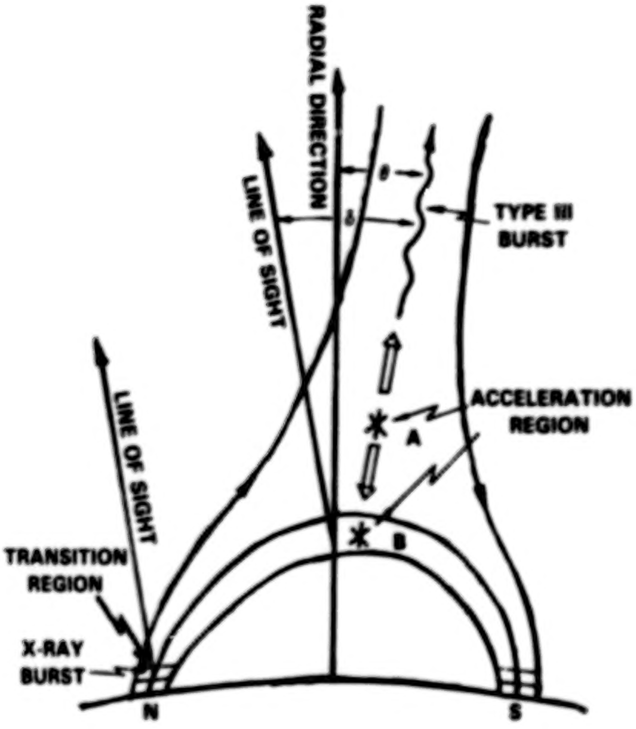
RADIAL DIRECTION
LINE OF SIGHT
θ
δ
TYPE III BURST
ACCELERATION REGION
A
B
LINE OF SIGHT
TRANSITION REGION
X-RAY BURST
N
S

Fig. 2 A model of MMSE and associated phenomena

$$\Gamma_s^{(\sigma)}(k) = \int d p \, A_s^{(\sigma)}(p,k)\,\delta(\omega - s\omega_B/\gamma - k_{\parallel} v_{\parallel})\left(\frac{s\omega_B}{\gamma v_{\perp}}\frac{\partial}{\partial p_{\perp}} + k_{\parallel}\frac{\partial}{\partial p_{\parallel}}\right) f(p_{\perp}, p_{\parallel}) \quad (1)$$

where $p = (p_{\perp}^2 + p_{\parallel}^2)^{1/2} = rmv$ is the electron's momentum, $\omega_B = \frac{eB}{mc}$ is the electron-cyclotron frequency, and $\perp$ and $\parallel$ denote components of wave number and velovity to the direction of the magnetic field B, $p_{\parallel} = p\cos\varphi$, $p_{\perp} = p\sin\varphi$, and φ is the pitch angle, r is the Lorentz factor.

It can be shown [8] that the sign of the integrand is determined by the sign of

$$\bar{D}f = \left(\frac{m s\omega_B}{p_{\perp}}\frac{\partial}{\partial p_{\perp}} + k_{\parallel}\frac{\partial}{\partial p_{\parallel}}\right) f(p_{\perp}, p_{\parallel}) \quad (2)$$

Positive contributions to $\bar{D}f$ favour the growth and negative contributions favour the damping of the waves.

Suppose that the distrioution function of nonthermal electrons with an isotropic pitch angle and power law energy spectrum for gyro-synchrotron radiation can be written as in [9, 10]

$$f(p)=\frac{G}{4\pi}\left(\frac{p}{mc}\right)^{-1}\left[1+\left(\frac{p}{mc}\right)^2\right]^{-1/2}\left[\sqrt{1+\left(\frac{p}{mc}\right)^2}-1\right]^{-g} \qquad (3)$$

here G is a constant and g is the spectral index, $g > 0$. one obtains $\frac{df}{dp} < 0$, so that $\Gamma_s^{(\sigma)} < 0$. Therefore, the distribution function of fast electrons in expression (3) is capable of producing gyrosynchrotron radiation of microwave bursts [9, 10] but it can not amplify the s-th harmonic waves and generate MMSE's.

Just on the contrary, the "hollow beam' distribution of fast electrons favours the growth of waves and leads to the generation of MMSE's [4].

2. The distribution of the pitch angles of the electrons injected from Region A to Region B on top of the magnetic arch is determined by the distance D between A and B. If D is sufficiently large, then the distribution is isotropic; otherwise, it will be anisotropic. This is because, the large the D, the greater will be the diffusion of the electrons; the smaller the D, the more restricted will be the angle of injection of the electron beams.

Table 1 shows that, for the event of May 16, the Type III bursts began in the decimetric wave range (aroung 60 cm, corresponding to a plasma frequency of 500 MHz, and a height of 23 x10^4 km above the photosphere, see below). For the Oct. 12 event, they began in the meter wave bands (e.g., 2 m, corresponding plasma frequency 150 MHz and height 2.3 x 10^5 km above photosphere). Since both events have the same type photospheric magnetic field with strengths $\gtrsim$2500 G, for both then, we may regard the microwave (10.6 cm) burst source in Region B at the top of the magnetic arch during the impulsive phase of the flare to have about the same size (or $10''$). It then follows that the angle of the cone subtended by the electron beams issuing from Region A (the height corresponding to the starting frequency of the Type III burst) must greater than 24°20' for the earlier event in order to achieve isotropic distribution, and need only 1°58' for the later event. Clearly it is easy to a beam ejected at A to be diffused through the collision with the background particls into a cone as small as 1°58' when reaching B. Thus, for the later event, of October 12, the electron beams injected from A into B had an isotropic distribution of pitch angle and so could not generate any spike emission or intense x-ray bursts. But such isotropic beams would add to the isotropic electrons in Region B and greatly increase the gyro-synchrotron radiation, hence the more intense at 10.6 cm.

For the earlier event of May 16, the Type III burst was strong, its starting frequency was high, the generating electrons had high energies, the downward injected beam was energetic and difficult to disperse, making the incident cone far below the value of 20°20' required for isotropization. The beam, then, was a "hollow-beam" and so generated intense spike emission and also led to strong bursts in hard X-ray. According to the radio dynamic spectrum measured at Dwingloo 5, during the impulsive phase, this event (May 16), at about 0814.5 UT, a Type III burst with a negative frequency drift appeared in 300-380 MHz, and at same time, one with a positive drift appeared in 509-666 MHz. This observed fact shows certainly that Region A in the neutral current sheet can simultaneously eject both one upward (towards the outer corona) and an inward (toward the coronal base) electron beams. It was estimated that the electron density in this acceleration region was about 3×10^4 km above the photospere.

3. Type III_G bursts are the type III bursts ($\lesssim 10$) appearing in groups. In the event of 1981 May 16, the MMSE's recorded at wavelength 10.6 cm often happended in a group-like type III_G burst. Since the radiating electrons of type III_G bursts and MMSE's escape from the same acceleration process. Probably, the duration of each group of MMSE's corresponds to that of each subburst in type III burst. The switch-off structure of MMSE's in [2] corresponds to the interval between two subbursts and the switch-on structure manifests the start of a group of MMSE's due to the injected electrons with a "hollow beam" distribution.

As can be seen in Table 1, an intense type-III burst appears from 0810 to 0816.2UT. It might be in correspondence with the significant switch-off and switch-on structures of MMSE's at about 0815UT during the rising phase in microwave burst (at 10.6 cm) of May 16, 1981.

About 0814.5UT in the band 300-480 MHz, type III bursts with negative frequency drifts of about 100MHz/sec were observed with Dwingloo radio-spectrograph, while at the higher frequencies 509-666 MHz positive drifting bursts about + 50 MHz/sec occurred [5]. This is a strong evidence indicating the simultaneous acceleration of electrons upwards and downwards. The electron density in the acceleration region was estimated to be $3\times10^9\ \mathrm{cm}^{-3}$ and the corresponding height about 2.3 x 10^4 Km.

5. Because the radiating electrons of hard X-ray bursts and type III bursts come from the same acceleration region A, the key problem is whether these electrons possess enough energy to radiate MMSE's and hard X-ray bursts. We should answer this question by evaluating the energy of these nonthermal electrons which may produce type III bursts.

Type III bursts present a rapid drift from high to low frequencies at a rate described in [11].

$$\frac{df}{dt} = (-0.01) f^{1.84} \quad (f \text{ in MHz}) \tag{4}$$

Generally speaking, Type III emission is ascribed to the scattering of Cerenkov plasma waves produced by fast electron streams. It is believed that most type III bursts are observed at the second harmonic of the local plasma frequency

$$f = 2f_p = 2 \times 8.98 \times 10^{-3} \sqrt{N(R)} \tag{5}$$

where R(t) represents the position of type III burst source at instant t. N(R) is the local electron density in cm^{-3}.

From equation (7), the drift rate in frequency can be expressed as

$$\frac{df}{dt} = \left(\frac{f}{2N}\right) \frac{dN}{dR} \cdot \frac{dR}{dt} \tag{6}$$

where $\frac{dN}{dR}$ is the gradient of coronal electron density and $\frac{dR}{dt} = v$ is the velocity vector of the fast electron stream. If θ is the angle between $\frac{dN}{dR}$ and v, and δ the angle between the line of sight and the direction of the electron stream, then for a relativistic electron stream and because of Doppler effect and $\beta^2 \ll 1$, we can obtain approximately $fv = \frac{c\beta f}{1-\beta\cos\delta}$. From Equation (6), the ratio $\frac{v}{c} = \beta$ can be given by

$$\beta(\theta,\varphi) = \frac{a}{\cos\theta + a\cos\delta} \tag{7}$$

and

$$a=\frac{2N}{cf}\cdot\frac{df}{dt}\cdot\frac{1}{\frac{dN}{dR}} \qquad (8)$$

For simplicity, we assume that the electron density of the corona is in spherically symmetric distribution and the fast electron streams move outward along the radial direction.

When $\theta = \delta = 0$, we have

$$\beta=\frac{a}{1+a}. \qquad (9)$$

The energy of the fast electrons producing type III bursts is given by

$$\mathcal{E}=\left(\frac{1}{\sqrt{1-\beta^2}}-1\right)\times 511\ \mathrm{Kev} \qquad (10)$$

Moreover, we use the model of N(R) for solar maximum activity fiven by Table 2 of reference [12]. Finally, the kinetic energy of fast electrons producing type III bursts for different frequencies is shown in Table 2.

If θ and δ are not equal to zero, the value of $\beta(\theta,\varphi)$ evaluated from equation(7) must be larger than that from equation (9) with the same frequency. Hence the energy of fast electrons increases. Therefore, as long as the fast electrons injected downward from acceleratiom region A possess the same energy as those exciting type III bursts, they are still able to produce hard X-ray bursts as those recorded on "Hinotori" or on Prognoz 8 satellite even after losing some energy about tens of kev due to MMSE's.

Table 2. Energy of fast electrons producing type III bursts at different frequencies

f(MHz)	600	300	200
$\mathcal{E}$ (KeV)	11.24	69	34

V. CONCLUDING WORDS

Based on our model and the mechanism of electron-cyclotron instability associated with a hollow beam of electrons, we have explained why there occurred strong MMSE's during the event of 1981 May 16 and why there appeared no MMSE but more intene microwave bursts at 10.6 cm during the event of 1981 October 12. Furthermore, we have shown that there exist some intimate links of MMSE's with their associated phenomena in the physical processes of generation and evolution during the impulsive phase of large flares. Obviously, the discovery of these links with one another is important for clarifying the mechanism of large flares.

ACKNOWLEDGEMENTS

The authors are indebted to Dr. K. Tanaka for sending us the data of hard X-ray bursts recorded on "Hinotori" satellite and to the Yunnan Observatory for the data of photospheric magnetic fields.

REFERENCES

[1] Slottje, C., Fast Fine Structure in Solar Microwave Flares, Nature, Vol. 157(1978), p. 20.

[2] ZHAO Renyan and JIN Shengzhen, Analysis of Ultrafast Fine Structures of Microwave Bursts, Scientia Sinica (Series A), Vol 25(1982), p. 422.

[3] Melrose D.B. and Duld C.A., Electron-Cyclotron Masers as the SOurce of Certain Solar and Stellar Tadio Bursts, Ap. J., Vol. 259(1982), p. 844

[4] LI Hongwei LI Chunsheng and FU Qijun, Electron-Cyclotron Masers and Solar Microwave Millisecond Spike Emission, This Workshop.

[5] Farnik F. et al., X-ray, H and Radio Observation of the Two-ribbon Flare of May 16, 1981, Dwingeloo Reprint.

[6] FU Qijun, LI Chunsheng and JIN Shengzhen, Spike Groups Event in Solar Microwave Bursts, submitted to Acta Astronomica Sinica

[7] Marsh K.A. et al., Properties of Solar Flare Electrons, Deduced from Hard X-ray and Spatially Resolved Microwave Observation, Ap. J. Vol. 251(1881), p. 797.

[8] Hewitt, R.G.et al., A Cyclotron Theory for the Beaming Pattern of Jupiter's Decimetric Radio Emission, Proc. ASA, Vol. 4(1981), p. 221.

[9] Takakura T. and Scalise, E.J., Gyro-synchrotron Emission in A Magnetic Dipole Field for the Application to the Center-To-Limb Variation of Microwave Impulsive Bursts, Solar Phys. Vol. 11(1970), p. 434.

[10] LI Chunsheng et al., The Mechanism of the U-shaped Spectrum of Type IV Solar Radio Bursts, Chinese Astronomy, Vol. 4(1980), No. 2, p. 155.

[11] Alvarez, H. and Haddock, F.T., Solar Wind Density Model from Km-Wave Type III Bursts, Solar Phys., Vol. 29(1973), p. 197.

[12] Zheleznyakov, V.V., Radio Emission from the Sun and Planets, Per Press, Oxford, 1970.

N87
21806
UNCLAS

N87-21806

THE MICROWAVE SPECTRUM OF SOLAR MILLISECOND SPIKES

M. Stähli and A. Magun

Institute of Applied Physics
University of Bern
Sidlerstrasse 5
CH-3012 Bern, Switzerland

Abstract. The microwave radiation from solar flares sometimes shows short and intensive spikes which are superimposed on the burst continuum. New observations at 3.47 GHz with high temporal and spectral resolution have revealed lifetimes of less than 10 ms and bandwidths between 0.5 and 200 MHz. Simultaneous measurements at two further frequencies showed no coincident spikes at the second and third harmonic. The spikes can be explained by the theory of electron cyclotron masering if the observed bandwidths are determined by magnetic field inhomogeneities or if the rise times are independent of the source diameters. The latter would imply source sizes between 50 and 100 km.

1. Introduction

Millisecond microwave spikes are intensive and very short fine structures which are occasionally superimposed on the microwave continuum of solar flares (Figure 1). They have mainly been observed at the lower end of the microwave spectrum up to ~6 GHz (Dröge, 1977; Slottje, 1978 and 1980; Zhao, 1983; Stähli and Magun, 1985). The duration of most of the spikes was reported to be shorter than 20 ms and the deduced brightness temperatures of the spikes were in the range between 10^{13} and 10^{15} K. In order to resolve and study the spectral and temporal fine structures of millisecond spikes a digital spectrometer with a time resolution of 5 ms was constructed (Stähli, 1983). Its center frequency was set at 3.47 GHz and its total bandwidth of 200 MHz was continuously covered by 30 channels with bandwidths varying between 0.5 MHz and 30 MHz. The frequency range was extended by two fixed frequency polarimeters at 3.1 and 5.205 GHz. For the simultaneous observation at the second and third harmonic of the gyrofrequency the latter was chosen at 3/2 of the spectrometer center frequency.

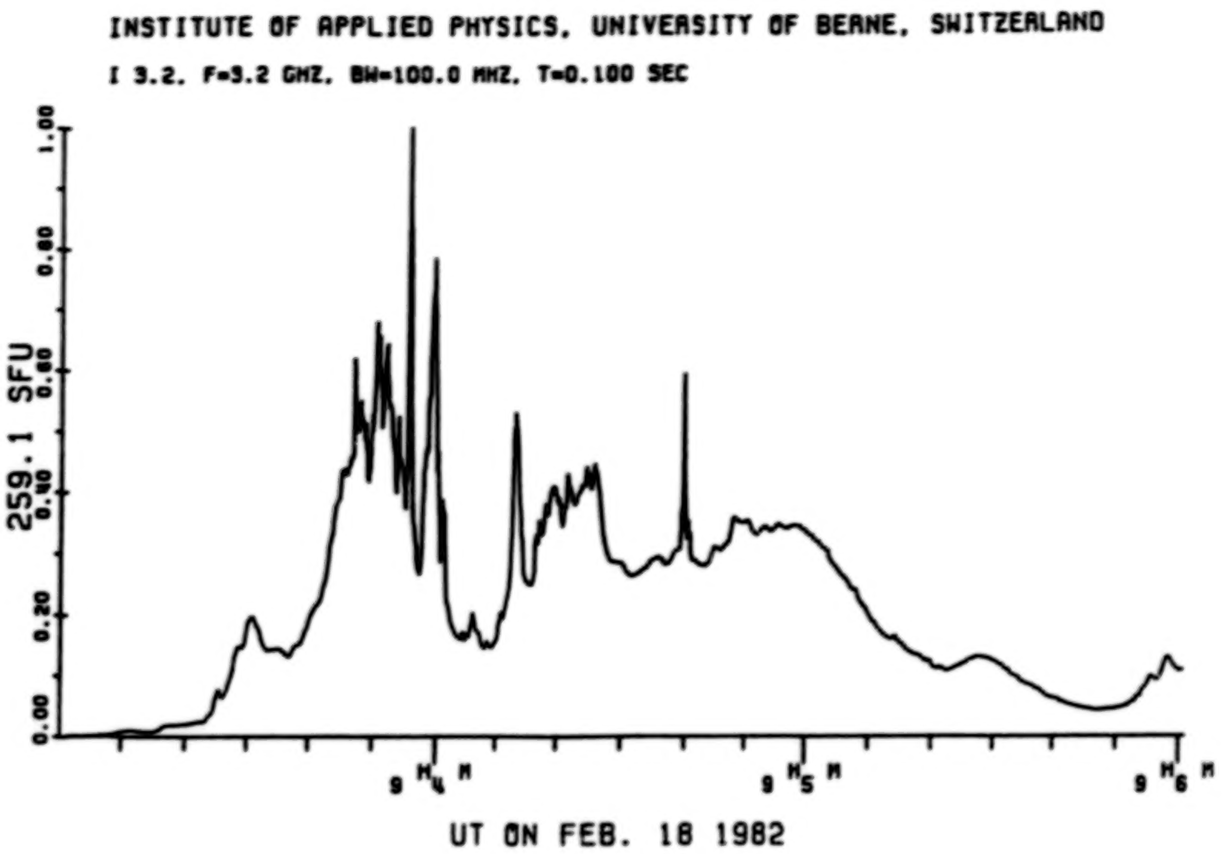

Fig. 1. Typical time profile of a solar radio burst at 3.2 GHz with superimposed millisecond spikes. The integration time is 100 ms.

In this paper new spectral observations of microwave spikes which were obtained with our fast spectrometer are presented and the proposed gyrosynchrotron maser emission tested. The concept of harmonic radiation by electron-cyclotron masers (Holman et al., 1980; Melrose and Dulk, 1982; Sharma et al., 1982) provides a plausible explanation for the observed characteristics of the spikes.

2. The spectrum of millisecond spikes

2.1. Observations

Between August 1982 and May 1983, 107 events have been observed, of which 14 exhibited microwave spikes. The fine structures appeared either as single spikes or in groups (Figure 2). The duration, rise and fall times of most of the spikes were between 5 and 10 ms. These values correspond to the instrumental resolution of 5 ms and we therefore believe that the temporal structures of these spikes could not be resolved.

ORIGINAL PAGE IS
OF POOR QUALITY

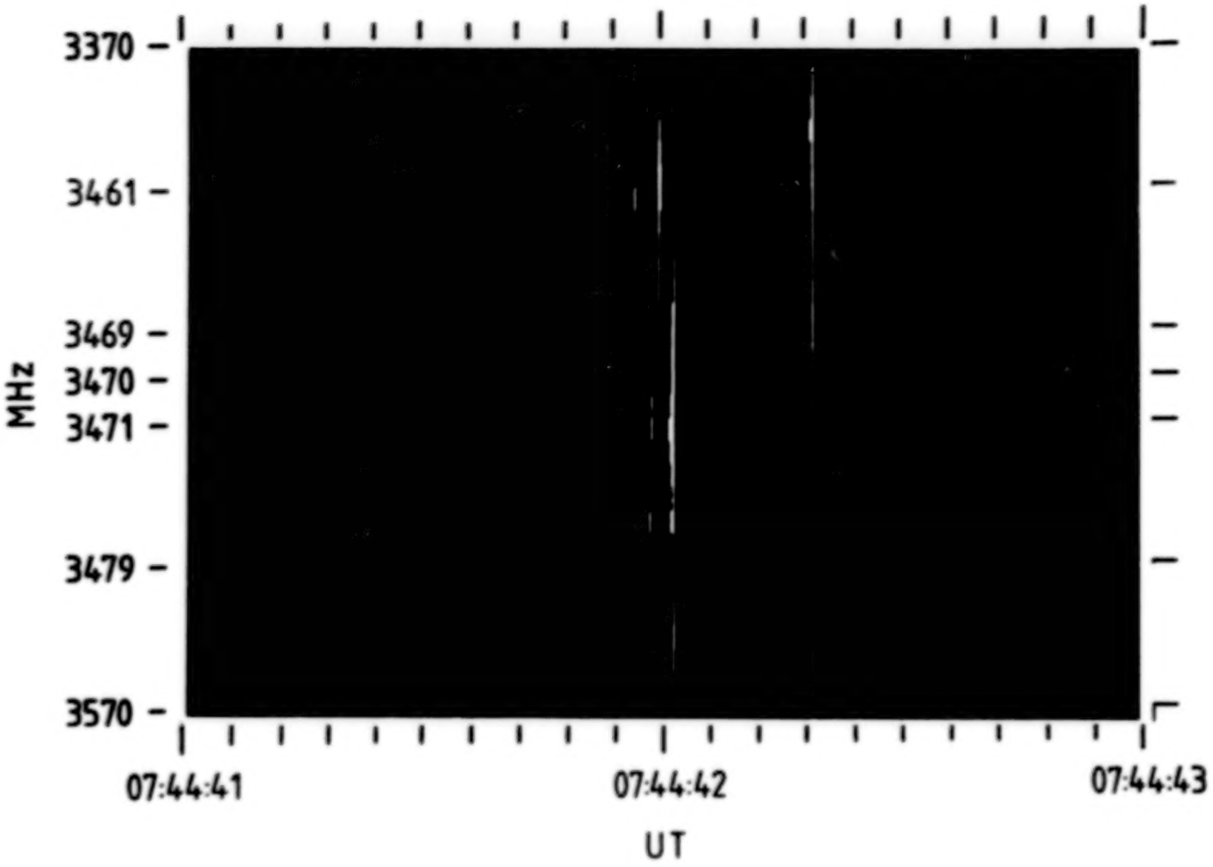

Fig. 2. Dynamic spectrum of millisecond spikes with subtracted continuum. The event of December 25, 1982 was observed with an integration time of 5 ms and a spectral resolution between 0.5 and 30 MHz.

The brightness temperatures of single spikes were derived from the rise time and the intensity under the assumption that the growing wave within the source propagates with the speed of light. Temperatures usually exceeded 10^{10} K but were always below 10^{11} K. The bandwidth of the spikes varied from less than 0.5 MHz to more than 200 MHz. However, the bandwidth must be smaller than approximately 300 MHz because no simultaneous spikes have been observed with the spectrometer centered at 3.47 GHz and the nearest single frequency polarimeter at 3.1 GHz. Additionally, no spikes were found to occur simultaneously at the second and third harmonic of the local gyrofrequency.

2.2. Discussion

The spectral data has been used to test the cyclotron maser theory (Melrose and Dulk, 1982). It predicts spike emission mainly slightly above the second or third harmonic of the local gyrofrequency with brightness temperatures up to 10^{13} K and very short rise times. The work of Melrose and

Dulk (1982) was used to derive relationships between observed spike parameters as flux density, brightness temperature and bandwidth, which are suitable for testing the proposed emission mechanism. Because of the many free parameters describing the loss cone and the ambient plasma only approximate formulae were used.

The relationship between brightness temperature T_b and relative bandwidth $\Delta\omega/\omega$ of the growing wave in the source was derived from (16) of Melrose and Dulk (1982):

$$T_b \approx m\, v_e^2 \left(\frac{2\pi c}{\omega}\right)^2 \frac{1}{L r_e}$$

where v_e : mean velocity of the radiating electrons
m : electron mass
c : velocity of light
ω : frequency
r_e : classical electron radius
L : trap length

With $\frac{\Delta\omega}{\omega} \approx v_e^2/c^2$, $\frac{\omega}{2\pi} \approx 3$ GHz and $L \approx 10^{10}$ cm this reduces to

$$T_b\ [\mathrm{K}] \approx 10^{15} \quad \frac{\Delta\omega}{\omega} \tag{1}$$

which is a linear relationship between the brightness temperature and the relative bandwidth of the spikes under the assumption of a homogeneous source. The above expression is only valid if the saturation is due to the fundamental radiation which usually grows fastest. A recent and more detailed analysis of the growth rates (Winglee, 1985) has shown that for $\omega_p/\Omega_e > 0.5$ the second harmonic dominates. This would lead to even higher brightness temperatures than given above.

The scatterplot (Figure 3a) shows the derived brightness temperatures and the relative bandwidths of the observed spikes, which were resolved in time and frequency. Relationship (1) is represented by a dashed line. It is obvious that the two parameters are uncorrelated in contrast to the prediction. The deduced temperatures are too low or the relative bandwidths are too large for which several explanations are possible: 1) Larger observed bandwidths than predicted could be due to magnetic field inhomogeneities within the source whose influence is not included in the theory. 2) The low brightness temperatures could be the result of overestimated source sizes. In this case source diameters and observed rise times must be uncorrelated which is for instance true if the latter is determined by the dynamics of the electron distribution.

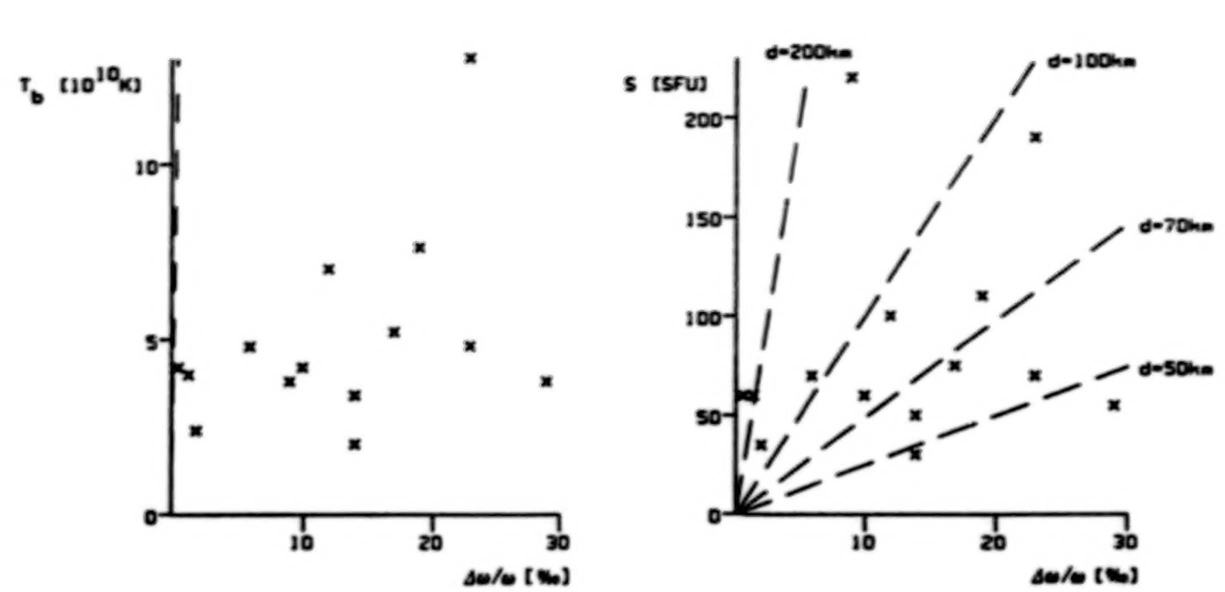

Fig. 3. Scatterplots of derived brightness temperature (a) and observed flux density (b) versus the relative bandwidth of observed spikes. The dashed lines represent the theoretical approximations. d is the source diameter.

In order to avoid the assumption of correlated source sizes and rise times the observed flux density of the same sample of spikes was plotted against the relative bandwidth (Figure 3b). The theoretical relationship for different source diameters was derived from (1) by using the Rayleigh-Jeans approximation:

$$S\ [\mathrm{SFU}] \approx d^2_{[\mathrm{km}]} \cdot \frac{\Delta\omega}{\omega} \tag{2}$$

S : flux density in SFU   d : source diameter in km
$\frac{\Delta\omega}{\omega}$: relative bandwidth

If we assume that the bandwidth is not determined by inhomogeneities and the rise time does not depend on the source geometry, diameters between 50 and 100 km could explain most of the spikes.

These first observations of the spectral fine structures of millisecond spikes establish several new features. However, they also indicate that for a detailed analysis, better observations with higher temporal and spectral resolution including circular polarization are essential. For further investigation of the important electron spectrum it is also necessary to correlate microwave data with spike observations in other spectral ranges (hard X-ray, decimetric radio waves).

Acknowledgements

The authors are indebted to Prof. E. Schanda for the opportunity to undertake this work. They would also like to thank Prof. G.A. Dulk for valuable discussions. The work was supported by the Swiss National Science Foundation under grant No. 2.604.0.82.

References

Dröge, F. 1977, Astron. Astrophys., 57, 285.
Holman, G.D., Eichler, D. and Kundu, M.R. 1980, in M.R. Kundu and T.E. Gergely (eds.), 'Radio Physics of the Sun', IAU Symp., 86, 457.
Melrose, D.B. and Dulk, G.A. 1982, Astrophys. J., 259, 844.
Sharma, R.R., Vlahos, L. and Papadopoulos, K. 1982, Astron. Astrophys., 112, 377.
Slottje, C. 1978, Nature, 275, 520.
Slottje, C. 1980, in M.R. Kundu and T.E. Gergely (eds.), 'Radio Physics of the Sun', IAU Symp., 86, 195.
Stähli, M. 1983, 'Das Mikrowellen-Spektrum von solaren Millisekunden-Spikes', Diploma Thesis, Institute of Applied Physics, Bern.
Stähli, M. and Magun, A. 1985, submitted to Solar Phys.
Winglee, R.M. 1985, submitted to J. Geophys. Res.
Zhao, R. 1983, Adv. Space Res., 2, 177.

N87
21807
UNCLAS

N87-21807

SOLAR VLBI

K. F. Tapping

Herzberg Institute of Astrophysics
Ottawa, Ontario, Canada, K1A OR6

J. Kuijpers

Sterrekundig Instituut
Zonnenburg 2
3512NL Utrecht, The Netherlands

1. Introduction

The use of data recording systems having milli-second time resolution for solar radio observations has revealed the presence, at both decimeter and centimeter wavelengths, of spikes and intensity fluctuations having durations of tens of ms. If the associated mechanical disturbances propagate at the Alfvén speed then such time-scales imply spatial dimensions of the order of 100 km. Indications of bright radio sources having such compact dimensions are of considerable interest in the study of solar plasma processes, so there would be great value in being able to determine the properties of the sources directly, rather than by inference.

The required angular resolution is beyond the reach of single antenna radio telescopes or of connected-element interferometers. The only observing technique currently available which will yield the required angular resolution is that of Very Long Baseline Interferometry (VLBI). Since this technique was developed primarily for the observation of extra-galactic and other sources having intensities varying slowly with time, it does not lend itself well to the study of transient, solar phenomena. Subject to certain restrictions however, it can be used for solar studies. A general discussion of (non-solar) VLBI is given in Meeks (1976).

There are two areas of particular applicability, namely the study of the initial plasma instabilities in solar flares, and of the sources of the milli-second spikes observed at decimeter wavelengths. The work so far has been mainly with respect to the former application.

2. Current Work

In April, 1981, radio telescopes at Dwingeloo (The Netherlands) and Onsala (Sweden) were used as a long-baseline interferometer at a wavelength of 18 cm. The baseline of 619 km gave a spatial resolution on the sun of about 45 km. The experiment and results are described by Tapping et al. (1983). Strong suggestions were obtained of the occurrence of multiple sources of short duration ($\lesssim 0.2$s) during a small solar burst. If the maximum size of the sources was 45 km, the inferred brightness temperature was at least 10^{12}K at 18cm wavelength. In 1984 a further experiment was made by the same workers, this time using one of the antennas of the Westerbork Synthesis Radio Telescope (The Netherlands) in conjunction with a radio telescope at Onsala. Several bursts were observed, some strong and at least two showing transient, spike structures, so therefore good candidates for compact sources. The results are still being analyzed.

3. The Technique

A detailed discussion of the major problems of Solar VLBI and its associated problems is given by Tapping (1985); only a few notes will be given here. There are four major difficulties to be encountered in Solar VLBI which are not encountered in non-solar VLBI:

(a) The position of the source cannot be predicted to within arc-minutes. The experiment must be designed to accommodate the expected values of the positional errors.

(b) The source is moving. Besides the annual motion of the sun against the celestial sphere, and the solar rotation, the source may have an intrinsic velocity. This is a consequence of the flare event itself and cannot be predicted.

(c) On the basis of the 1981 results and the inferred sizes of spike events, the lifetime of the sources is likely to be less than the cycle time of the processor.

(d) The source has to be observed against the bright background made up by the solar disc emission and the contributions from resolved sources in the parent flare.

In order to process the data, an estimate of the position and motion of the source is required. The receiver bandwidth used must be sufficiently small that the error in the estimate of the source position lies within the acceptance range of the processor. Since the processor operates on the assumption that the source is fixed to the celestial sphere, a compensating "incremental fringe rate" must be used to correct for the motion of the source against the sky. The annual solar motion and the solar rotation are easily calculable, but the intrinsic source velocity is usually unknown. The processors now in use can accommodate the contribution to the fringe rate for the velocities observed for Type II events. Consequently this component can be ignored with reasonable safety.

Since the sources can have a duration shorter than a processor cycle time, the correlated amplitudes may be considerably degraded even within the correlator cycle. No integration of multiple cycles can be carried out. Also, the rate of change of fringe phase cannot be determined. Thus, only the correlator delay can be used to estimate the position of the source. With only one antenna baseline, only one source coordinate can be measured accurately.

The sources studied in non-solar VLBI are usually observed against a cold sky; the system sensitivity is determined by the receiver and signal processing hardware. In the solar case the source appears against the bright solar disc, and against a background of emission components from resolved sources in the flare. Accordingly, the system sensitivity is quite poor (in the 1981 experiment, a source brightness of the order of 10^{12}K yielded a signal to noise ratio of about unity). The bandwidth must therefore be as large as possible in order to maximize the system sensitivity. In the experiments carried out so far, only single interferometer baselines were used. In the 1981 experiment, the Westerbork Synthesis Radio Telescope was used at 6cm wavelength, simultaneously with the VLBI observations. It was intended that positional information may be obtained which would facilitate the analysis of data. One of the major difficulties in the analysis of the 1984 experiment has been the absence of collaborative data from which estimates of source position within the active region can be obtained.

4. Further Observations

There is a real need for further observations. However, unlike the experiments done so far, multiple baselines should be used. These will provide confirmation of the occurrence of sources. If the baselines are at an angle to each other, estimates of the position and spatial size in more than one dimension of the sources will be available. The sources detected in the 1981 experiment had durations small compared with the processor cycle time, there can be no reliable estimates of the difference between the estimated and actual fringe rate. This residual fringe rate component can be used to estimate one of the components of the source position. However, even if the residual fringe rate can be determined, in the case of single baseline measurements it is not possible to separate the contribution due to the source position and that due to source motion. The use of multiple baselines would make it possible to determine the source positions from measurements of delay alone. Any estimates of the residual fringe rate can then be used to estimate the source velocity and direction.

The more accurate the estimate of the source position that can be used for the data correlation and processing, the more it is possible to design the experiment for maximum sensitivity. The use of a high resolution, real-time synthesis instrument such as the Very Large Array in parallel with the Solar VLBI observations would provide high quality observations of the burst position. It would also give information concerning the relationship of the compact sources to the larger components of the burst emission. Solar VLBI has considerable potential in the study of solar plasma processes, so despite its limitations and the difficulty in its application, further experiments will be highly worthwhile.

References

Meeks, M.L.; "Methods in Experimental Physics", Vol. 12, Part C (Astrophysics), Chapter 5, Academic Press, New York.

Tapping, K.F., Kuijpers, J., Kaastra, J.S., van Nieuwkoop, J., Graham, D., Slottje, C.; Astronomy and Astrophysics, Vol. 122, 177, 1983.

Tapping, K.F.; Proceedings of the Trieste Workshop (1985), Italy, Solar Physics (In Press).

N87
21808
UNCLAS

N87-21808

TEMPORAL FREQUENCY OF RADIO EMISSIONS FOR THE APRIL 25, 1984 FLARE

G. D. Wells, B. A. Hausman, and H. W. Kroehl

National Geophysical Data Center (E/GC2)
325 Broadway
Boulder, Colorado 80303

ABSTRACT

The National Geophysical Data Center archives data of the solar-terrestrial environment. The USAF Radio Solar Telescope Network (RSTN) data allow performance of time series analyses to determine temporal oscillations as low as three seconds. For our study, we selected the X13/3B flare which erupted in region 4474 (S12E43) on 24-25 April 1984. The soft X-rays, 1-8 A, remained above X-levels for 50 minutes and the radio emissions measured at Learmonth Solar Observatory reached a maximum of 3.15 x 10^5 SFUs at 410 MHz at 0000 UT. A power spectral analysis of the fixed frequency RSTN data from Learmonth shows possible quasi-periodic fluctuations in the range two to ten seconds. Repetition rates or quasi-periodicities, in the case of the power spectral analysis, generally showed the same trends as the average solar radio flux at 245 and 8800 MHz. The quasi-periodicities at 1415 MHz showed no such trends.

1. Introduction

Solar radio emissions in the microwave range have been monitored for many years, but only within the last 20 years have investigators realized the rapid fluctuations superimposed on these bursts were not "noise" or interference. Since then, several physical mechanisms have been proposed to explain these rapid fluctuations. They may be caused by a modulation of the source radiation by waves or oscillating magnetic fields, or by quasi-periodic accelerations of electrons or successive occurrences of elementary bursts either in a single or several source regions (Zodi et al. 1984). The last two proposed explanations will be resolved with improved spatial resolution of the recording instruments. The first explanation involves several mechanisms of solar physics which may be distinguished by their fundamental periods as they give clues to the scale of the emitting source.

Zodi et al. (1984) separated these quasi-periodic pulsations into categories. The first, and most common, class occurs in chains of a few pulses (not more than a few tens of pulses) separated by nearly constant time intervals such as the burst analyzed by Parks and Winckler (1969). A second class consists of long-lasting uniform oscillations which persist throughout the event, such as the 28 March 1976 burst examined by Kaufmann et al. (1977). The third class consists of the extremely fast (tens of milliseconds) structures superimposed on mm-microwave bursts, with repetition rates (quasi-periodicity) that are directly proportional to the average flux level (Zodi et al. 1984).

These quasi-periodic fluctuations have been detected over a broad range of periodicities. Kaufmann et al. (1984) detected some of the finest structure yet with a periodicity at 30-60 ms and a "slow" structure at 1 s, whereas, Cribbens and Matthews (1969) reported a periodicity of 385 ±15 s. Quasi-periodic fluctuations in the range 2-10 s have been reported by many authors (Janssens et al. 1973; Kaufmann et al. 1972; Cliver et al. 1976; Gaizauskas and Tapping, 1980; Urpo et al. 1981; Kaufmann et al. 1977; and Zodi et al. 1984).

This RSTN data set was chosen for several reasons. Although the RSTN is of fairly low resolution, 1 s, compared to Itapetinga recordings, it has provided a nearly continuous, 24-hour record of solar radio emissions since 1981. Also, the RSTN data is readily available from the NGDC in Boulder, Colorado, USA. Additionally, most studies of quasi-periodic bursts have used microwave bursts with peak fluxes on the order of hundreds of SFUs (1 SFU = 10^{-22} watts/m^2/sec) or less and durations of minutes; whereas, the burst presented here had a peak flux on the order of a few hundred thousand SFUs at 245, 410 and 610 MHz and a duration of hours. This burst also had very distinct impulsive and gradual phases. The length of the burst gives a sufficiently large number of data points to analyze for "true" periodicities in considerable detail using power spectral analysis techniques at various stages of the burst. Finally, although the data is not of sufficient resolution for "quasi-quantization" studies, the temporal resolution is sufficient for studies of "elementary" bursts with durations of 5-20 s (Sturrock et al. 1984) and "quasi-periodicity" in the range of seconds to hours.

2. Equipment

The RSTN network monitors the Sun with an analog sweep frequency recorder and at eight discrete frequencies, i.e., 245, 410, 610, 1415, 2695, 4995, 8800 and 15400 MHz. It consists of three observatories: Sagamore Hill, Massachusetts (actually a prototype RSTN site); Palehua, Hawaii; and Learmonth, Australia. Except for a "window" over Europe, these sites provide nearly 24-hour coverage of solar radio emissions. The RSTN discrete frequency radio telescopes monitor the power output of the solar disk and not just for a specific region. The system consists of an automatic tracking antenna system, a radiometer, an automated "event" detection system and an analog recording system. The radiometers employed in the RSTN system are Dicke radiometers and are designed to automatically compensate for rapid gain changes within the equipment. The Dicke operates at a 500 Hz rate and is located between the antenna signal and the matched load, a 50 ohm precision noise source. The RSTN system uses shielded coaxial cable for frequencies below 8800 MHz and precision wave guides for 8800 and 15400 MHz to transfer the energy from the feed to the receiver system. The 30 MHz intermediate frequency (IF) section within each receiver limits the signals to an approximate 8 MHz bandwidth.

The lower frequencies (245-1415 MHz) have double IF amplifiers to provide approximately 55 dB gain for the medium and low gain channels and 99 dB gain for the very high and high gain channels. The output from the 30 MHz IF amplifier is detected and filtered to extract the audio modulation introduced by the action of the RF switch by the lock-in amplifier. Details are listed by frequency in Table 1 (Air Weather Service Pamphlet 105-61).

Table 1
A summary of technical data for the discrete frequency radiometers and their associated antennas.

Frequency (MHz)	HPBW (deg)	Antenna Diameter (m)	Effective Bandwidth (MHz)	Efficiency (%)	Maximum Flux (SFUs)
15400	1.49	0.9144	14	45	50,000
8800	.976	2.4384	14	22	50,000
4995	1.72	2.4384	14	31.5	50,000
2695	3.187	2.4384	7	45	50,000
1415	6.115	2.4384	7	50	100,000
610	4.068	8.5344	2	50	500,000
410	6.0	8.5344	2	53.2	500,000
245	10.09	8.5344	2	55	500,000

3. Data and Data Reduction

Although we had data for all eight frequencies from about 30 minutes before the event to four hours after the burst maximum, we selected only three of the frequencies (245, 1415 and 8800 MHz) and limited our analysis interval to no more than 15 minutes (900 points). We also limited the analysis to four intervals: the preburst or interval A, the impulsive rise or interval B, the post-maximum or interval C, and the gradual or interval D. Figure 1 shows the general trends of the entire burst for the three frequenies produced from 20-second averaged data from 2330 UT on 24 April to 0400 UT on 25 April. The analysis intervals are 15 minutes each except for interval B where the duration depends on the implusive rise to maximum time.

Data quality should be good. The relative values used are reportedly accurate to within 1 SFU (Near 1985). As mentioned in the previous section, the equipment automatically attempts to remove system noise. In addition,

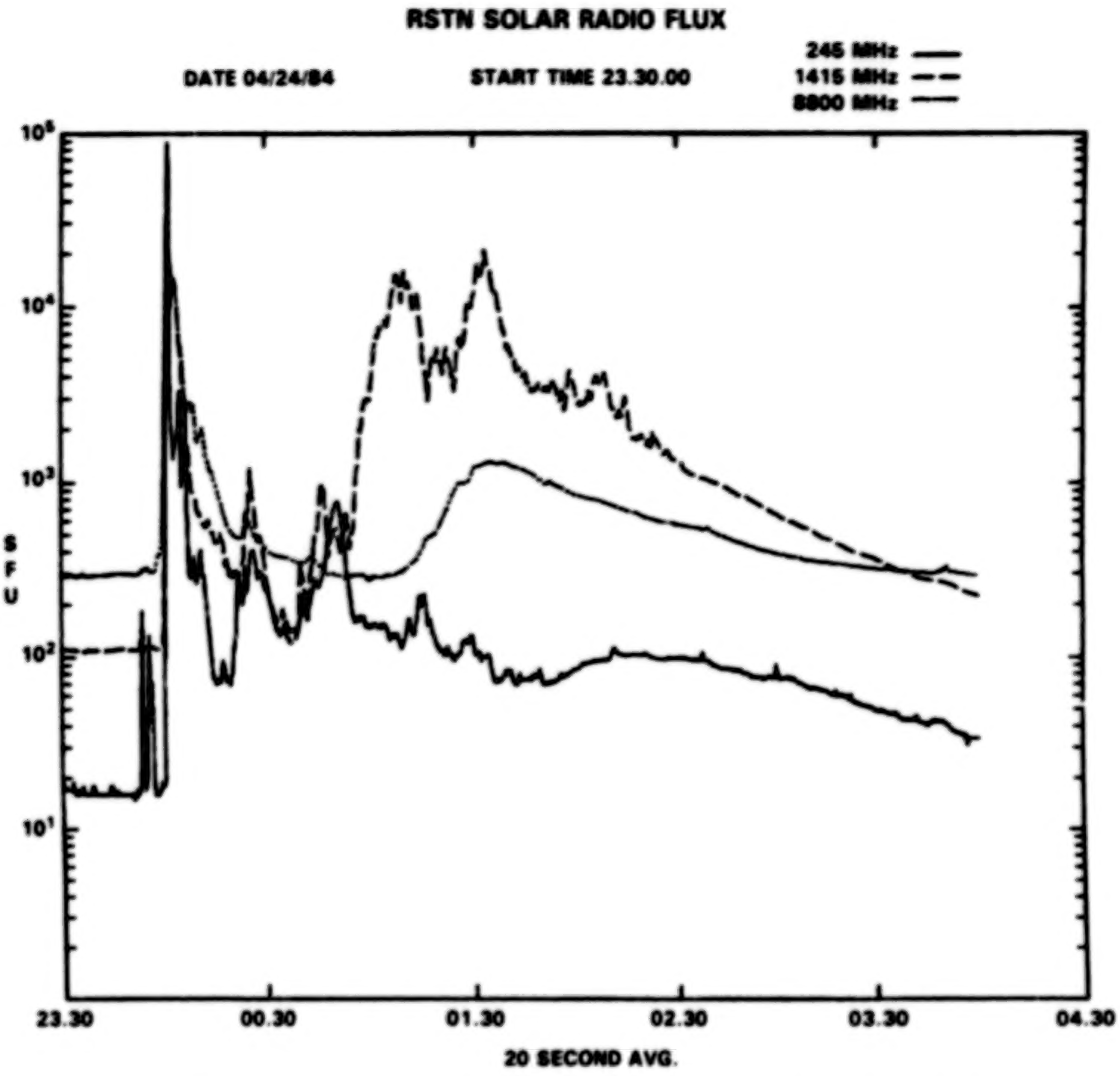

Figure 1. Plots of the 24-25 April 1984 radio burst using 20-second averages at 245, 1415 and 8800 MHz. Data from Learmonth, Australia.

since Learmonth is remotely located in northwest Australia (Exmouth), local interference should be minimal. Finally, since the RSTN system measures the flux of the whole disk, pulsations due to the antenna beam oscillating across a fixed source, as region 4474, are not a factor. Unfortunately, this also introduces uncertainty as to the source of the pulsations. However, except for the preflare interval (A), the average flux is on the order of a few thousand SFUs and any emission from nonflaring regions should be negligible. Higher-time resolution plots of intervals A-D are shown in Figures 2-5.

The data were filtered to remove all periodicites greater than 10 s. This was done for two reasons. The first, and most obvious, reason is that we were only looking for periods on the order of two (the Nyquist frequency) to ten seconds. The second reason involves the desire to know whether the peak is at or below the 95% confidence level, which is shown on the normalized Fourier power plot. Unfortunately, once a peak drives the trace above the 95% confidence level, the confidence level of subsequent peaks is uncertain. Therefore, we wanted the first peak to exceed the 95% confidence level to have a periodicity of 10 seconds or less. In an attempt to resolve peaks of less than five seconds when there was a significant peak between 5 and 10 s, we also filtered out all periodicities greater than 5 s for intervals C and D.

4. Data Analysis

The Fourier power spectrum, the normalized Fourier power spectrum, and the maximum entropy spectrum analysis (MESA) were estimated for each frequency for each interval using the filtered data. The Fourier power spectrum and normalized power spectrum are used to determine, statistically, whether a given peak is significantly above background noise. The maximum entropy is an attempt to measure the degree to which the randomness of the data has been lost or gained by using power spectral analysis. Nine hundred points (15 minutes) were used as input to the filter routine. However, since the filter reduces the number of points, only 850 points were input into the power spectral analysis program, except for interval B. As part of the power spectral program, the significance was estimated both by the Fisher statistic and the 95% confidence interval in the normalized Fourier power plot.

To check for any dominant preflare periodicities due to system, environmental, or local sources, interval A was included as one of the power spectral analysis intervals.

Following the Fourier analysis, we went back into the data plots to locate the "quasi-periodicities" found in Tables 2-3. This was done by measuring the peak to peak temporal spacing. We then marked those peaks which closely (± .5 s) agreed with the Fourier "quasi-periodicities".

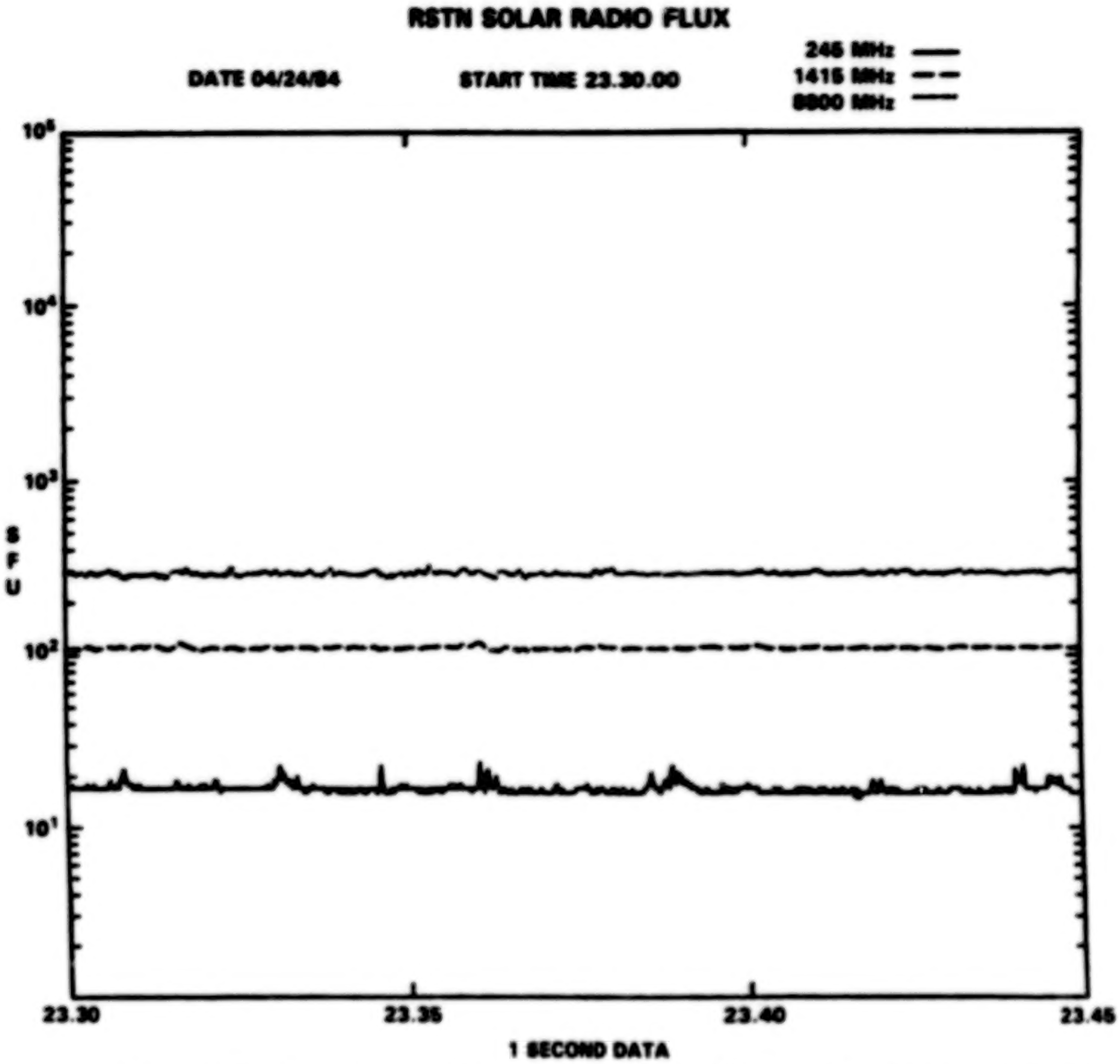

Figure 2. Preflare interval (interval A) for 245, 1415 and 8800 MHz. Data are at 1-second resolution from 2330 UT to 2345 UT on 24 April.

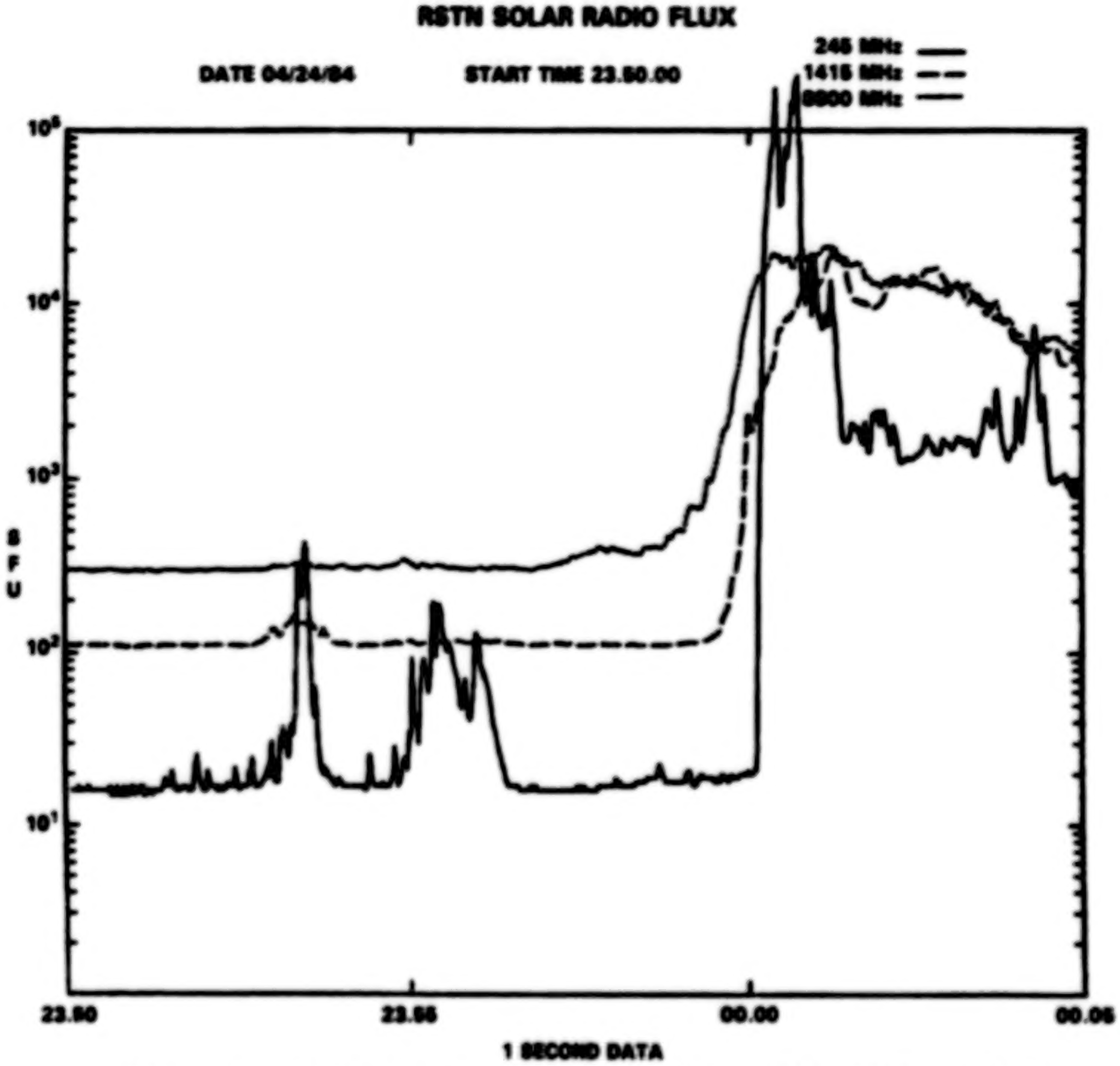

Figure 3. Impulsive Rise (interval B) for 245, 1415 and 8800 MHz. Data are at 1-second resolution from 2350 UT on 24 April to 0005 UT on 25 April.

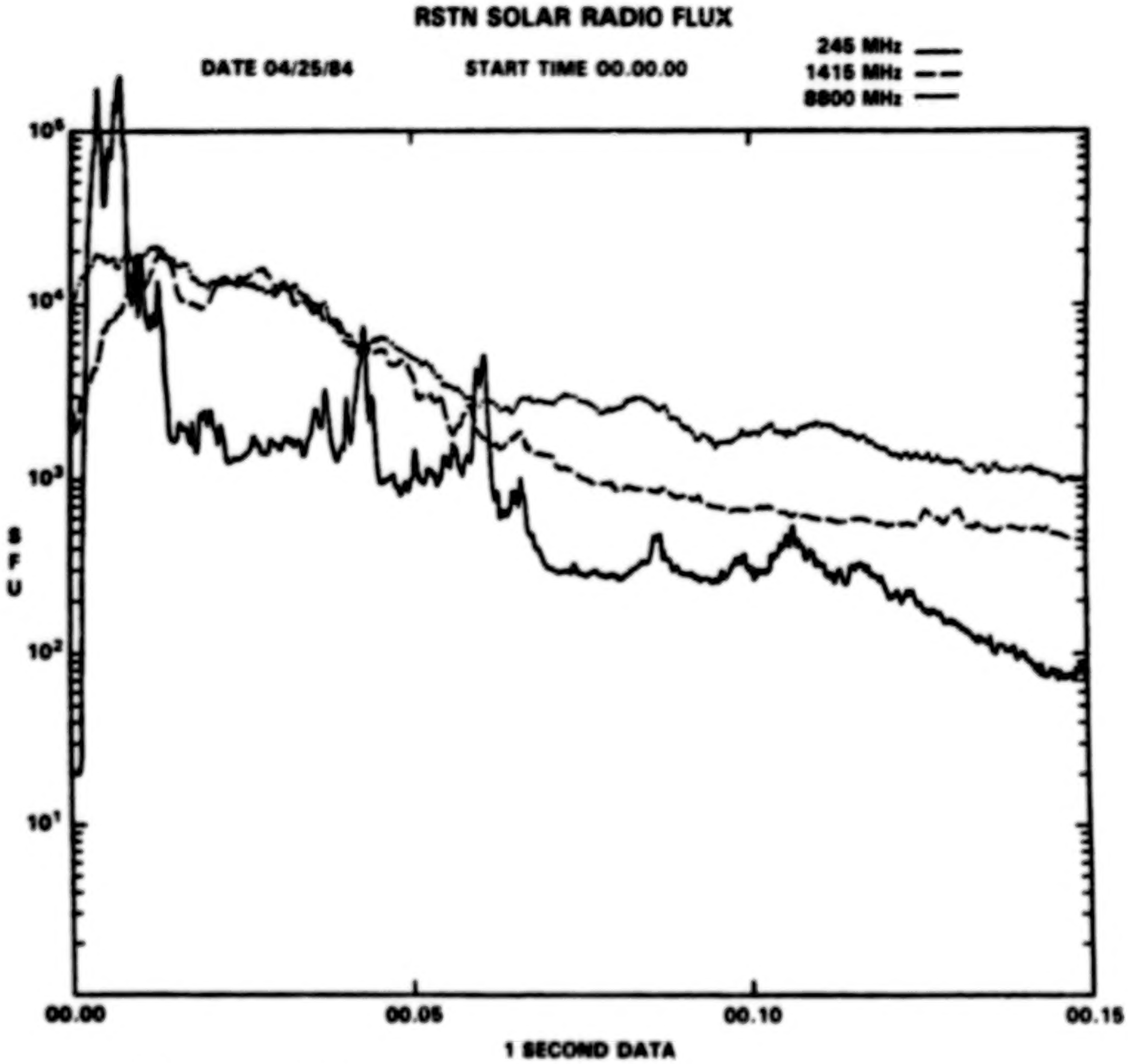

Figure 4. Post-maximum (interval C) for 245, 1415 and 8800 MHz. Data are at 1-second resolution from 0000 UT to 0015 UT on 25 April.

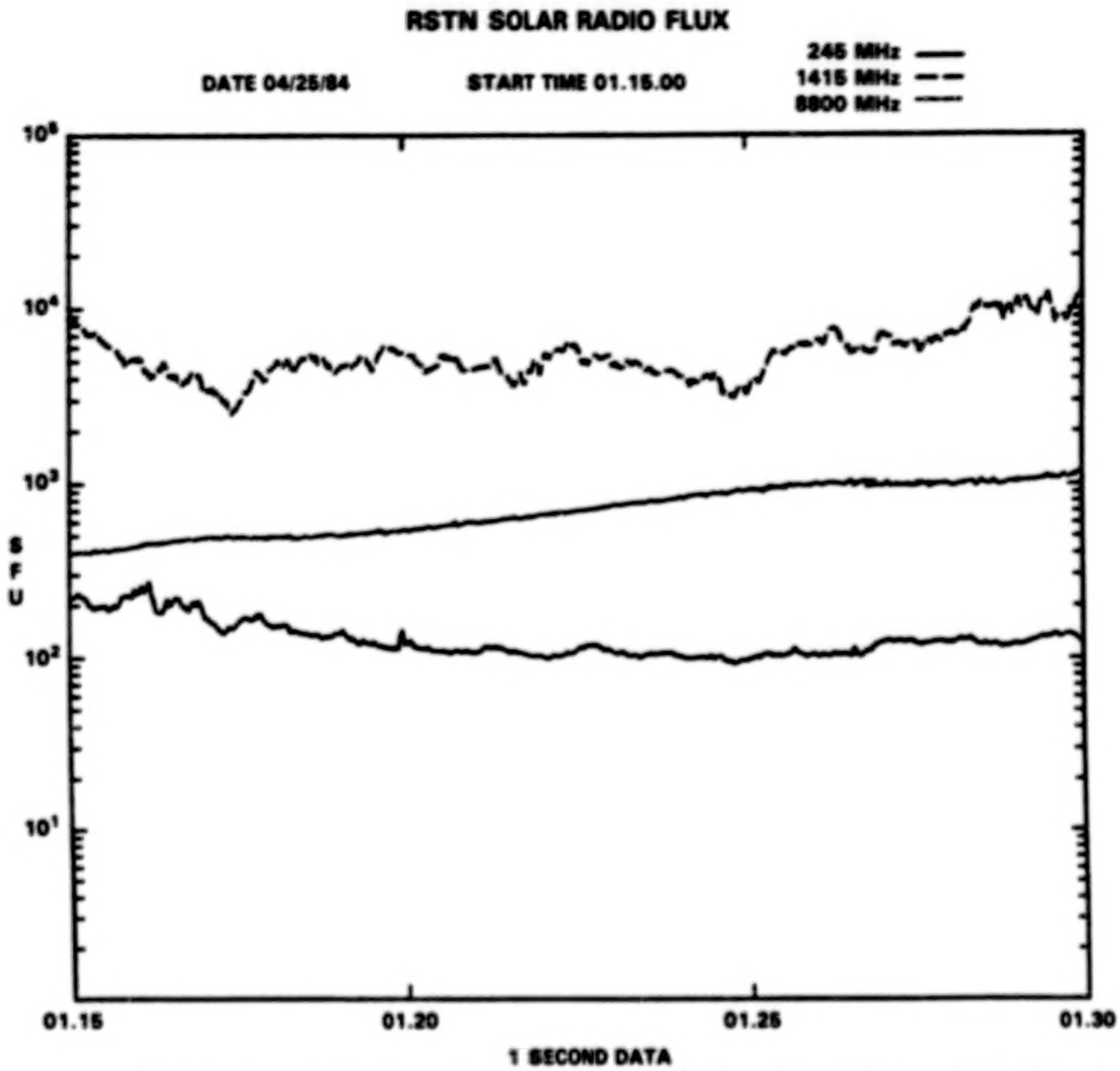

Figure 5. Gradual phase (interval D) for 245, 1415 and 8800 MHz. Data are at 1-second resolution from 0115 UT to 0130 UT on 25 April.

5. Results

For interval A, no periods with a 95% or greater confidence level, hereafter referred to as significant, occurred at 410 or 610 MHz. The maximum peak at 1415 MHz did not prove significant, but a secondary peak at 3.7 s did prove significant. Maximum, significant periodicities ranged from 3.7 to 8.2 s. A summary of the preflare interval (interval A) is found in Table 2.

Table 2
Summary of significant periods for interval A and whether they are significant based on the Fisher statistic and normalized power spectrum.

Frequency	Interval	Quasi-Period (sec)	Fisher	Normalized
245	2330-2345	7.02	Yes	Yes
410	2330-2345	None		
610	2330-2345	None		
1415	2330-2345	3.7	Unk	Yes
2696	2330-2345	8.17	Yes	Yes
4995	2330-2345	4.78	Yes	Yes
8800	2330-2345	8.02	Yes	Yes
15400	2330-2345	6.2	Yes	Yes

For the impulsive phase (interval B), we did not have a sufficient number of data points at 245 (30 points) and 1415 MHz (100 points) to give significant results. Therefore, the results at these two frequencies will not be presented. We did have a sufficiently large number of points at 8800 MHz (220 points) and found a double peak in the Fourier power curve around 6.8 s, which did prove significant (Figure 6). Interval B results are summarized in Table 3.

The post-maximum interval (interval C) was analyzed in two runs. In the first run, the data was filtered to remove periodicities greater than 10 s; in the second, periods greater than 5 s were filtered out. In the first run, significant peaks occurred at 8.4 s and 9.8 s for 1415 and 8800 MHz, respectively. The peak at 5.03 s was not significant using the Fisher statistic, but did prove significant using the normalized Fourier power plot (Figure 7) and the maximum entropy plot. In the second run, significant peaks occurred at 2.1 s, 4.4 s, and 3.3 s at 245, 1415, and 8800 MHz, respectively. See Table 3.

Interval D was analyzed using the same techniques as interval C. For the first run significant peaks occurred at 7.7 and 8.1 s for 245 and 1415 MHz, respectively. The significant peaks during the second run were 3.9 s based on the Fisher statistic, Fourier power spectrum, and the maximum

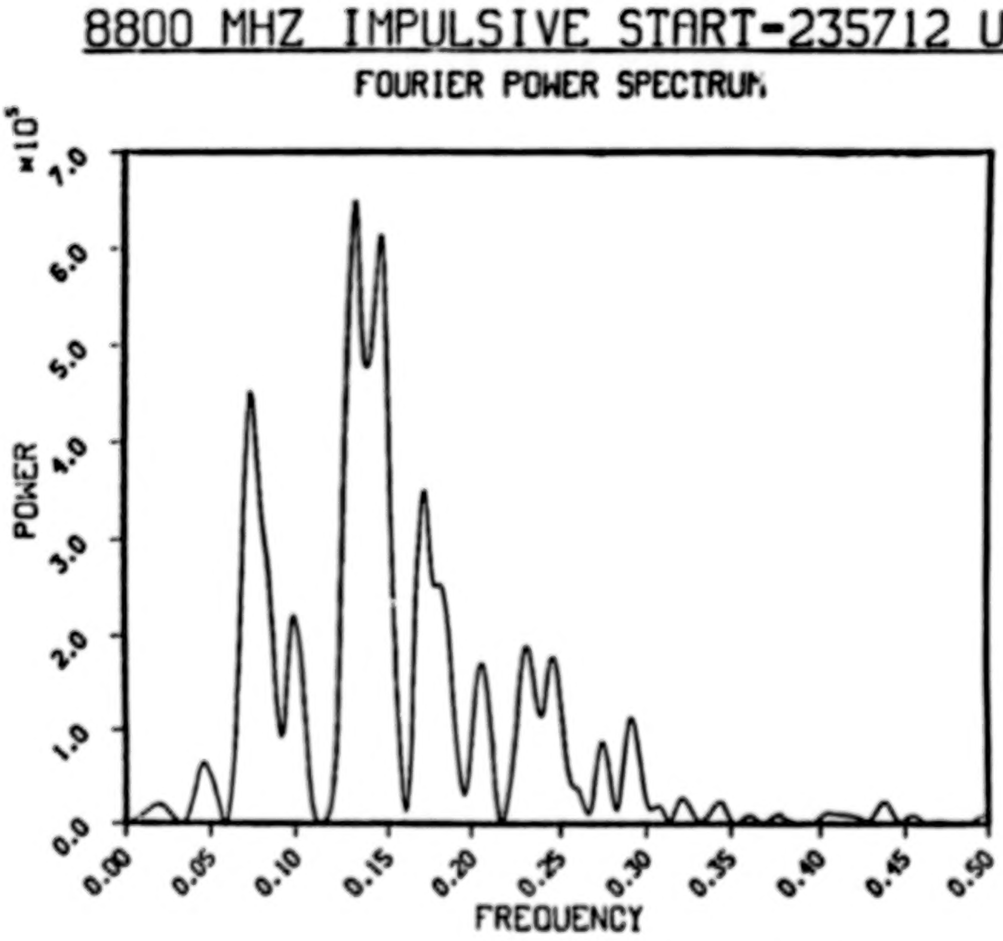

Figure 6. Fourier power spectral plot for 8800 MHZ during the Impulsive phase or interval B. Data have been filtered to remove periodicities greater than 10 s. Data are at 1-second resolution from 2357.2 UT on 24 April to 0000.87 UT on 25 April.

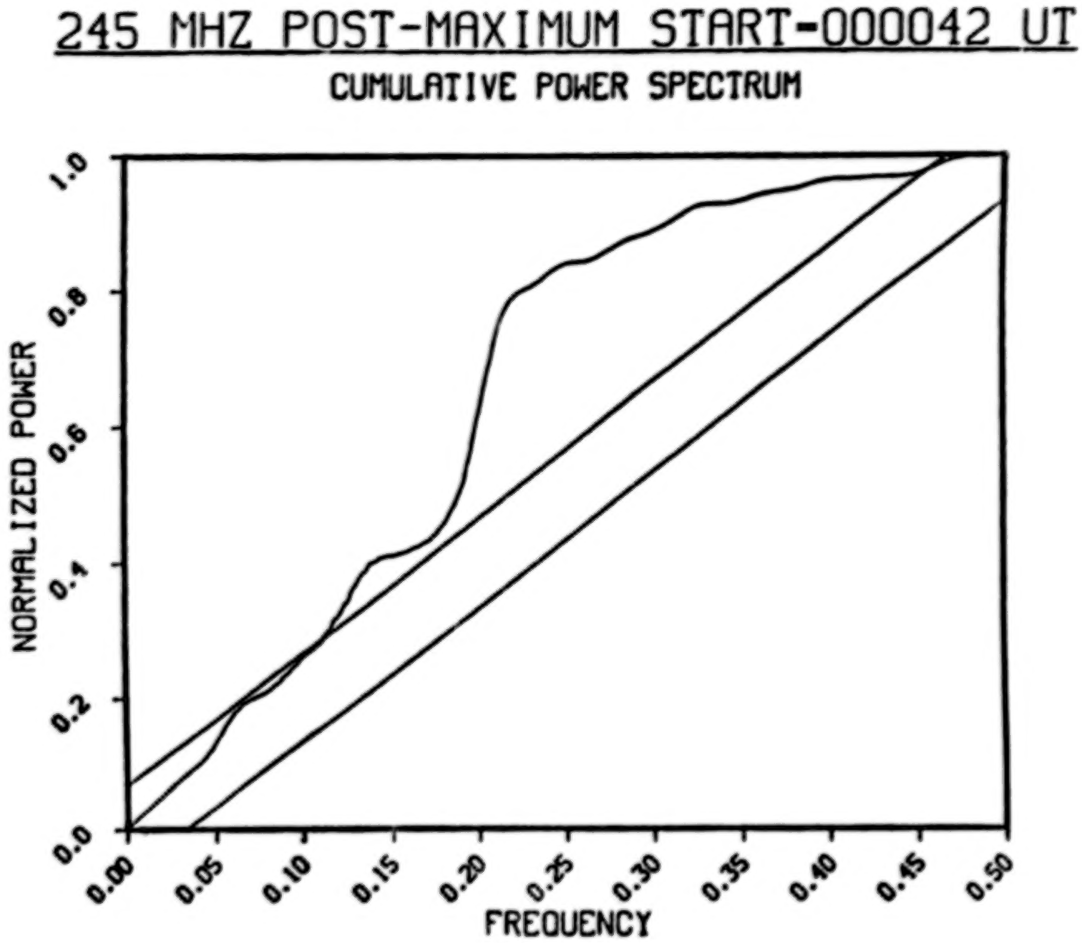

Figure 7. Cumulative Fourier power spectrum plot for 245 MHz during the Post-maximum or interval C. Data has been filtered to remove periodicities greater than 10 s. Data are at 1-second resolution from 0000.7 UT to 0014.87 UT on 25 April. The portion of the curve above the upper diagonal line is significant at the 95% confidence level.

entropy plots (Figure 8); but it was 3.1 s based on the normalized Fourier power plot. The peak at 1415 MHz occurred at 4.0 s. No significant peaks were noted at 8800 MHz.

Table 3
Summary of significant periodicities for intervals B, C and D and whether they are significant based on the Fisher statistic and the normalized power spectrum.

Frequency	Interval	Time (hhmmss)	Quasi-Period (sec)	Fisher	Normalized
8800	B	235712-000111	6.8	No	Yes
245	C10	000042-001541	5.03	No	Yes
245	C5	000042-001541	2.1	Unk	Yes
1415	C10	000216-001715	8.42	Yes	Yes
1415	C5	000216-001715	4.45	Unk	Yes
8800	C10	000111-001610	9.77	Yes	Yes
8800	C5	000111-001610	3.32	Yes	Yes
245	D10	011500-013000	7.66	Yes	Yes
245	D5	011500-013000	3.95	Yes	Yes
1415	D10	011500-013000	8.09	Yes	Yes
1415	D5	011500-013000	4.67	No	Yes
8800	D10	011500-013000	None		
8800	D5	011500-013000	None		

Although crude and not nearly as complete as the Fourier analysis. the peak to peak measurements did yield some interesting results. First of all. those peaks exhibiting the "quasi-periodic" oscillations indicated by the Fourier analysis generally occurred in pairs, and were very rarely organized into groups of more than three successive pulses. Notable exceptions to this generalization occurred at 1415 MHz beginning at 0013.36 UT (Figure 9), and at 8800 MHz beginning at about 0012 UT (Figure 10) on 25 April 1984. In the first case (1415 MHz), there were five peaks spaced at approximately 8.4 s intervals, and in the second case (8800 MHz) there were four peaks spaced at approximately 9.8 s intervals. Secondly, the longest "quasi-periodic" episode lasted on the order of one minute, which was considerably shorter than our 15 minute analysis intervals. Finally, we noted intervals where two "quasi-periodic" episodes were occurring simultaneously though out of phase with respect to each other (Figure 11).

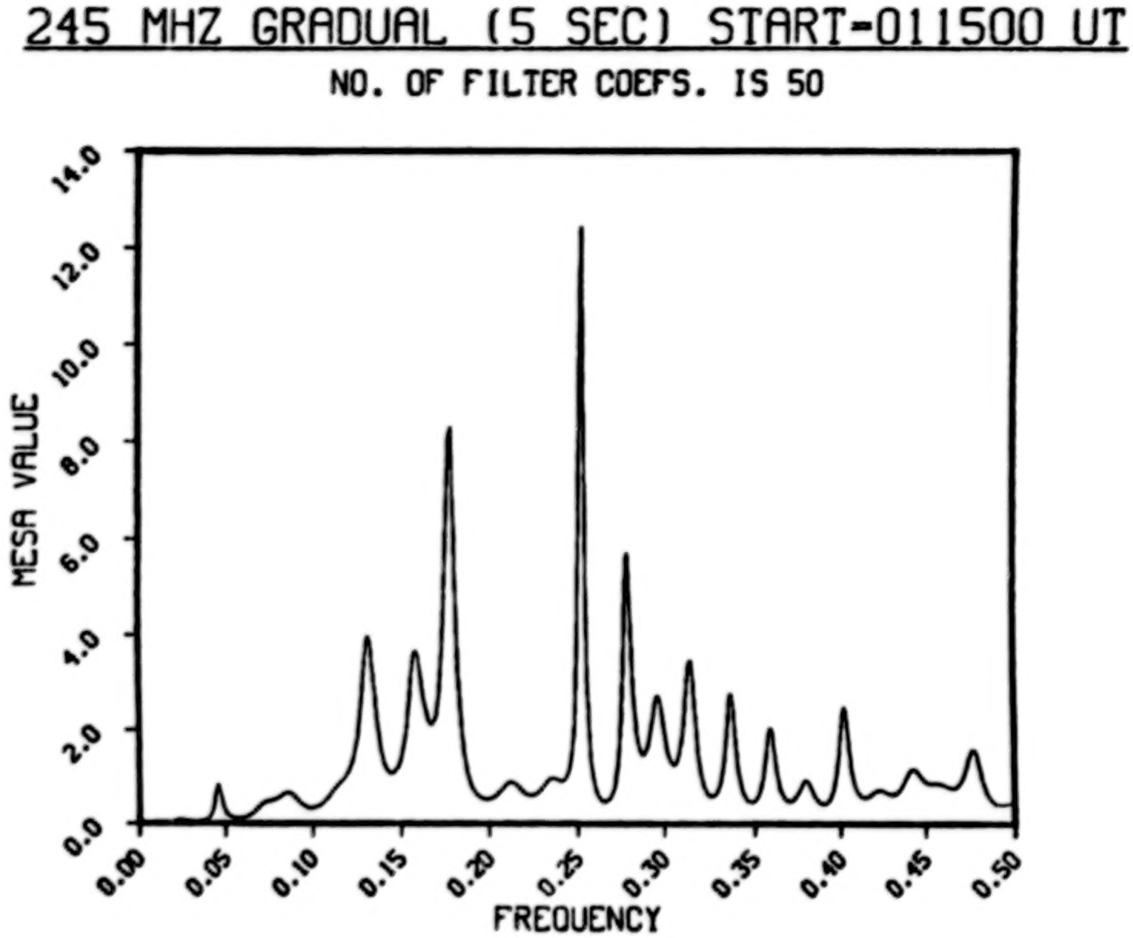

Figure 8 . Maximum entropy plot for 245 MHz during the Gradual phase or interval D. Data has been filtered to remove periodicities greater than 5 s. Data at 1-second resolution from 0115 UT to 0129.17 UT on 25 April.

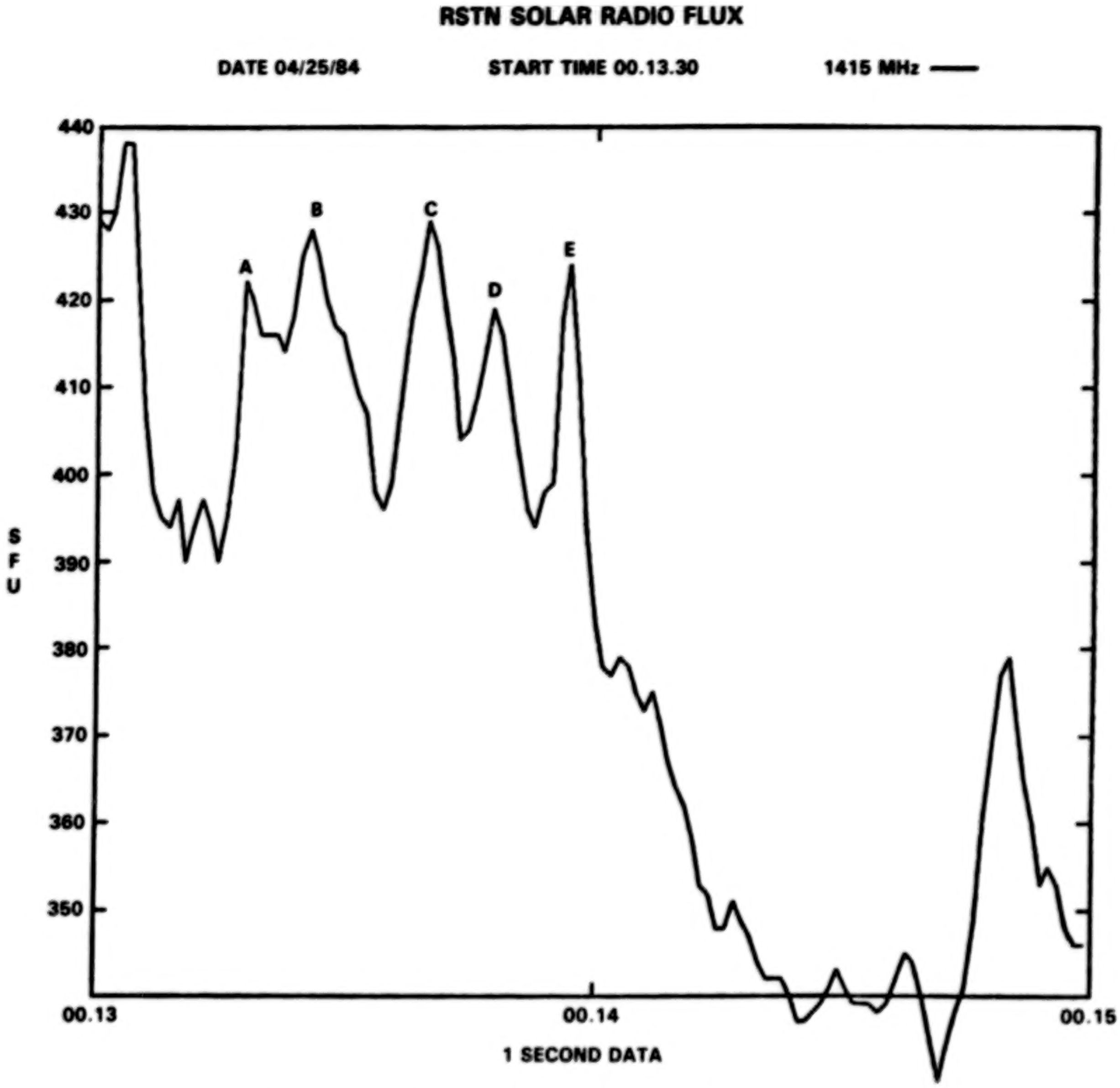

Figure 9. Quasi-periodic pulses at 1415 MHz. Data are at 1 s resolution from 0013.5 to 0015.5 UT on 25 April 1984.

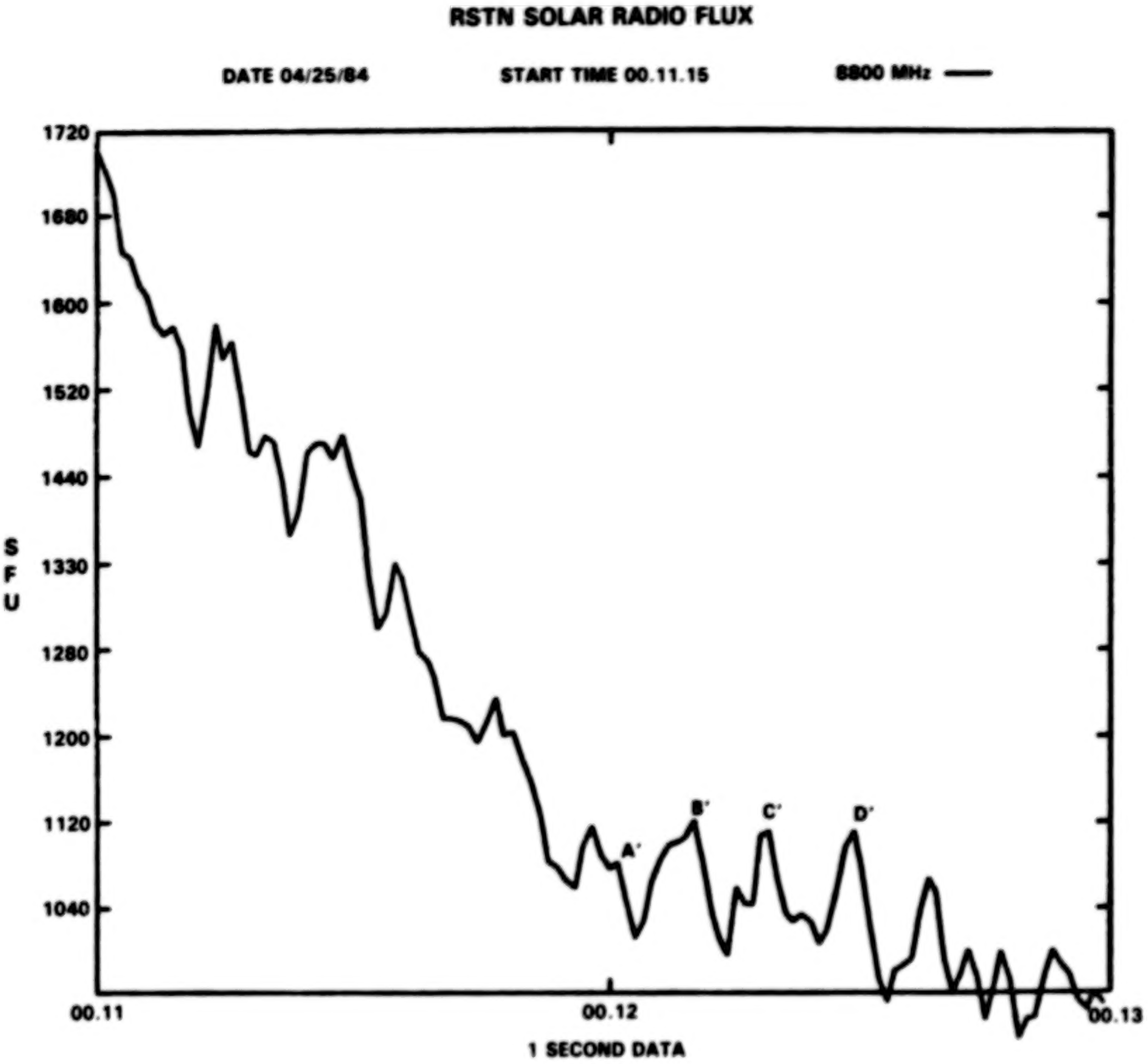

Figure 10. Quasi-periodic pulses at 8800MHz. Data are at 1 s resolution from 0011.25 to 0013.25 UT on 25 April 1984.

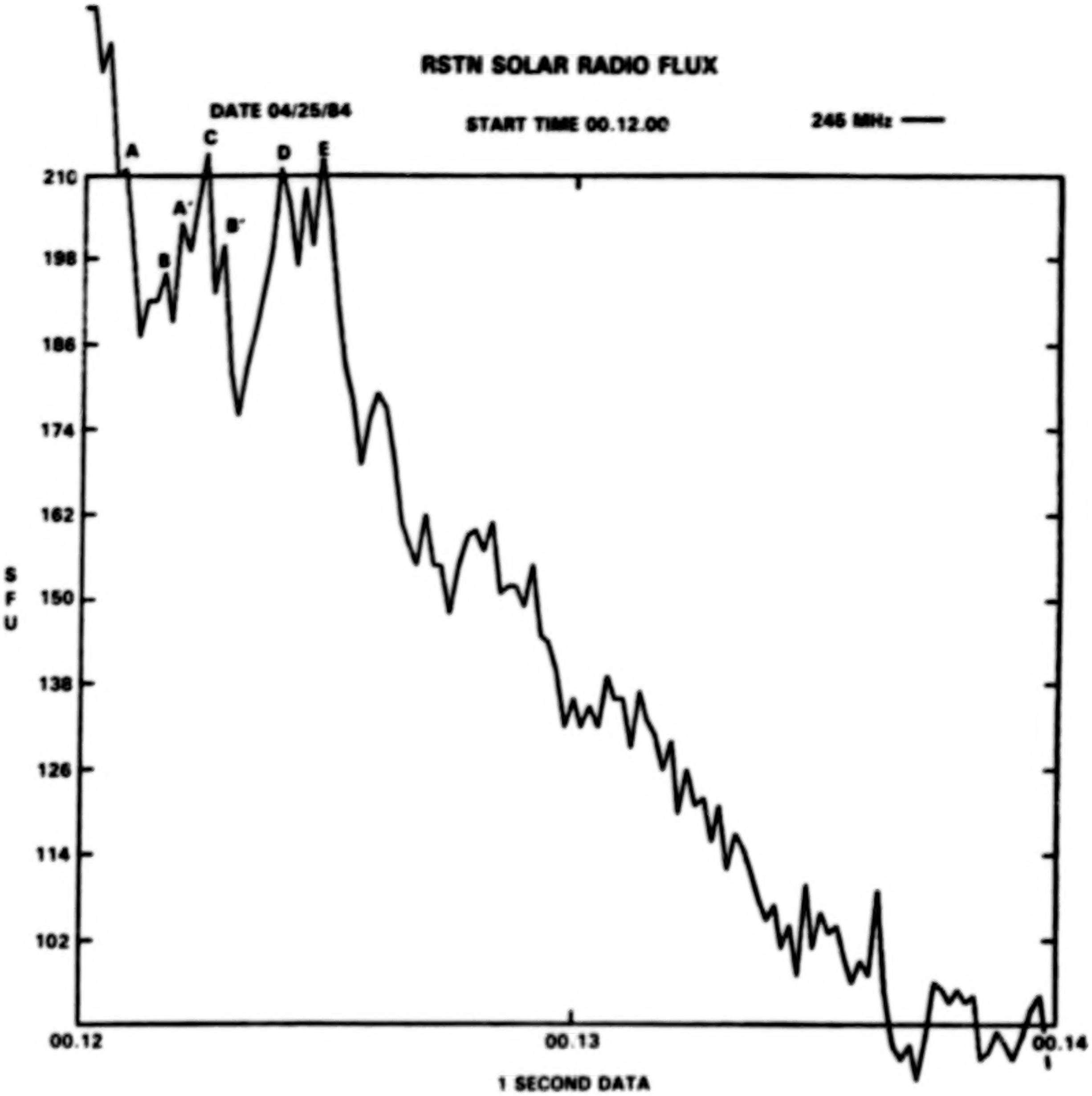

Figure 11. Overlapping (out-of-phase) quasi-periodic pulsations at 245 MHz. Data are at 1 s resolution from 0012 to 0014 UT on 25 April 1984.

6. Discussion

In this study, we sought to define the dominant periodicities in the range two to ten seconds in each of three radio frequencies monitored by the RSTN telescopes during each phase of the flare. The observed "quasi-periodicities" seem real since observed trends in periodicity at 245 MHz and 8800 MHz fit well with what would be expected based on Kaufmann et al.'s (1980) findings concerning the relationship between changing repetition rates and changing radio flux. For instance, Figures 2, 4 and 5 show an increase in repetition rates for the post-maximum phase and then a decrease by the gradual phase. These observations are consistent with the results of the power spectral analysis which show the same trend. Also, the apparent loss of significant periodicity at 8800 MHz by the gradual phase supports our premise that the periodicities during the preflare interval at this frequency were caused by the "background" solar emission. The absence of any significant periodicity during interval D is probably due to the relative insignificance of the "background" emission when compared to the average flux of 600 SFUs, which is well above quiet sun values. Indeed, the power spectral analysis at 8800 MHz shows the largest frequency during the impulsive phase, a smaller frequency during the post-maximum phase and the disappearance of any significant frequencies by the gradual phase. Figure 5 confirms this decrease in repetition rate by the gradual phase at 8800 MHz.

For interval A, the spread in periodicities and the absence of a dominant periodicity throughout all eight frequencies suggest that the data is free from strong periodicities in the range two to ten seconds attributable to broadband system noise or local interference. However, the Fourier power spectrum plot for 610 MHz (Figure 12) clearly shows the data is "noisy". A possible source for some of this "noise" could be rounding of values, especially at lower frequencies where the variance is of the same order as the data accuracy. For example, the periodicity at 245 MHz during interval A appears questionable. It is uncertain whether the observed periodicity results from rounding of values due to the very small amplitudes of the the fluctuations, 1 to 5 SFUs, or from the cumulative effect of many, very short-lived bursts with peak fluxes around 10 SFUs (evident in Figure 2). Another explanation could be the changing or unstable periodicities noted when we searched the plots for the Fourier "quasi-periodicities". In this case, there might be significant periodicities, but these periodicities would not remain constant throughout the analysis interval (Rust 1985). At higher frequencies (greater than 2695 MHz), the observed periodicities seem to result from a "background noise" from the Sun, but they may also be due to a succession of small, impulsive bursts or some atmospheric phenomena. However, the possibility that they may be due solely to some random process cannot be eliminated.

Based on the appearance of our Fourier power analysis plots, it becomes evident that there are no "true" periodicities; but we did find evidence of "quasi-periodicities". We use the term "quasi-periodic" because the observed periodicities tend to occur over a range of values evidenced by double or even multiple peak maximum, the peaks were not necessarily of equal amplitudes, and their temporal spacing could only be determined to

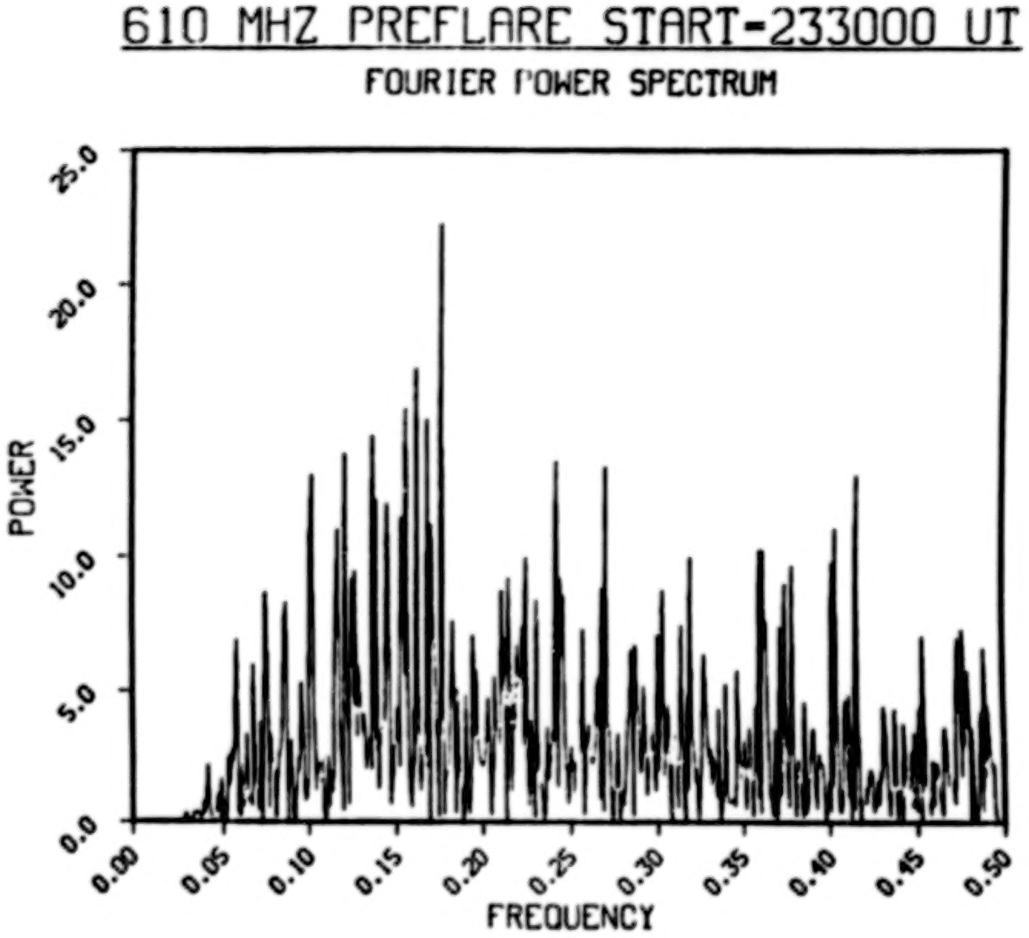

Figure 12 · Fourier power spectrum plot for 610 MHz during the Preflare interval or interval D. Data has been filtered to remove periodicities greater than 10 s. Data are at 1-second resolution from 2330 UT to 2344.17 UT on 24 April.

closely fit the Fourier values since the analysis program does not identify those peaks contributing to the "quasi-periodicity". The "quasi-periodic" episodes shown in Figures 9 and 10 (interval C) seem to closely fit the "quasi-periodic" events of the Parks and Winckler (1969) type. However, the vast majority of the peaks fitting the Fourier results occurred only in pairs indicating a random process rather than some physical mechanism. We, therefore, felt that the Fourier analysis techniques did not show conclusively that "quasi-periodicity" was present in all intervals in which they showed peaks in the power spectrum curves at the 95% confidence level. Based on the results of our subsequent searches for "quasi-periodicities", we felt Fourier analysis techniques do not adequately analyze for the presence of periodicities.

The suggested presence of two, out-of-phase, "quasi-periodic" events occurring simultaneously as shown in Figure 11 may indicate two emission sources. Indeed, observations from Tokyo Astronomical Observatory, Japan, did show two flaring areas within the region after 0100 UT (they were not observing before this time) (Kai, 1985). The presence of two emission sources would certainly contribute to making any results ambiguous. Additionally, the peaks analyzed were composed of an overlapping fine structure poorly resolvable using 1 s data (Kaufmann, 1985).

Our results may have been more conclusive had we analyzed more events, or if we had had some correlative data. As it turned out, Palehua Solar Observatory observed the event manually but was unable to record the radio data due to electrical power problems. This eliminated our hopes for simultaneous observations from two observatories using the same equipment and monitoring the same frequencies. These simultaneous observations are particularly critical for microwave frequencies below 10 GHz since radio emissions in this range do not correlate well with hard x-ray emissions.

Finally, our observations of quasi-periodicities of 4, 6, 9 and 10 seconds agree fairly well with quasi-periodicities reported by Cliver et al. (1976) using 2.8 GHz and with Kaufmann et al. (1977), who used 7 GHz data. Our use of a highpass filter is similar to work done by Urpo et al. (1981).

7. Conclusions

From our analysis, we conclude the following: (1) The RSTN data does contain a significant amount of "noise" which should be filtered out if one is interested in the very fine structure in the data. (2) The "noisiness" of the Fourier plots is partially due to shifting periodicities (Rust 1985). (3) Periodicities in the range two to ten seconds should be resolvable from the RSTN data, but higher resolution data would have been more desirable since the longest interval of "quasi-periodicity" noted was on the order of one minute. (4) These "quasi-periodicities" are similar to those reported by others at other microwave frequencies. (5) Simultaneous observations are critical for studies in this range of frequencies because Fourier techniques do not appear to adequately rule out periodicities due to random processes. (6) Analysis intervals should be on the order of one to two minutes for periodicities in the range two to ten seconds.

8. Acknowledgments

We are grateful to E. W. Cliver for converting the RSTN data to ASCII format and for his helpful discussions. Additionally, we appreciate C.D. Wells' help in writing the graphics programs and B.W. Rust's help with the Fourier analysis interpretation.

References

Air Weather Service Pamphlet 105-61, 1 April 1982, Scott AFB. IL., USA.
Cliver, E. W., Hurst, M. D., Wefer, F. L., and Bleiweiss, M. P. 1976, Solar Phys. 48, 307.
Cribbens. A. H. and Matthews, P. A. 1969, Nature 222, 158.
Gaizauskas, V. and Tapping, K. F. 1980, Ap. J. 241, 804.
Janssens, T. J., White III, K. P., and Broussard, R. M. 1973, Solar Phys. 31, 207.
Kai. Keizo 1985, private communication.
Kaufmann, P. 1972, Solar Phys. 23, 178.
Kaufmann, P., Piazza, L. R., and Raffaelli, J. C. 1977, Solar Phys. 54, 179.
Kaufmann. P., Strauss, F. M., Opher, R., and Laporte, C. 1980, Astr. Ap. 87, 58.
Kaufmann, P., Correia, E., Costa, J. E. R., Dennis, B. R., Hurford, G. J., and Brown. J. C. 1984, Solar Phys. 91, 359.
Kaufmann, P. 1985, private communication.
Near, J. 1985, private communication.
Parks. G. K. and Winckler, J. R. 1969, Ap. J. 155, L117.
Rust, B. W. 1985, private communication.
Sturrock, P. A., Kaufmann, P., Moore, R. L., and Smith, D. F. 1984, Solar Phys. 94, 341.
Urpo, S., Tiuri, M., Tlamicha, A., Pracka, M., and Karlicky, M. 1981, Astr. Ap. 93, 121.
Zodi, A. M., Kaufmann, P., and Zirin, H. 1984, Solar Phys. 92, 283.

N87
21809
UNCLAS

N87-21809

SOLAR MICROWAVE MILLISECOND SPIKE AT 2.84 GHZ

Qi-jun Fu*

Astronomy Program
University of Maryland
College Park, MD 20742

Sheng-zhen Jin, Ren-yang Zhao, Le-ping Zheng, Yu-ying Liu, Xiao-cong Li, Shu-lan Wang, Zhi-jun Chen, and Chu-min Hu

Beijing Observatory
Academia Sinia
Beijing, China

ABSTRACT

Using the high time resolution of 1 ms, the data of solar microwave millisecond spike (MMS) event more than two hundred times at the frequency of 2.84 GHz have been recorded at Beijing (Peking) Observatory since May 1981. The present paper has made a preliminary analysis. It can be seen from these data that the MMS-events have a variety of the fast activities such as the dispersed and isolated spikes, the clusters of the crowded spikes, the weak spikes superimposed on the noise background, and the phenomena of absorption. The marked differences from that observed with lower time resolution are presented. Using these data, a valuable statistical analysis has been made. There are close correlation between MMS-events and hard X-ray bursts, and fast drifting radio bursts. The MMS-events are highly dependent with the type of active regions and the magnetic field configuration. It seems to be crucial to find out the accurate positions on the active region where the MMS-events happen and to make co-operative observations at different band during the special period when specific active regions appear on solar disk.

I. INTRODUCTION

At Beijing Observatory, a fast sampling recorder with time constant of 1 ms for solar observation at 2.84 GHz was devised in 1981 (Jin, Zhao and Fu). From April 1981 to June 1983, these systems worked in 480 days, about 250 events have been recorded. These results have given us a clue to the researching on the physical process of microwave millisecond spike (MMS) emission linked with its associated phenomena.

---

*Permanent address: Beijing Observatory, Academia Sinica, Beijing, China

PRECEDING PAGE BLANK NOT FILMED

II. ANALYSIS OF FEATURES OF THE MMS-EVENTS

There are many and varied structures of the spikes in the MMS-events. They may be classified as follows:

1) Dispersed or isolated spike clusters:

Among all MMS-events recorded spike bursts grouped in isolated clusters occur most frequently. The duration of the clusters is often 10-100 ms and the time interval between clusters is about 100-1000 ms. Each single spike generally last about 3-10 ms, sometimes longer, with peak flux density higher than 2000 sfu., sometimes higher than 1000 sfu.

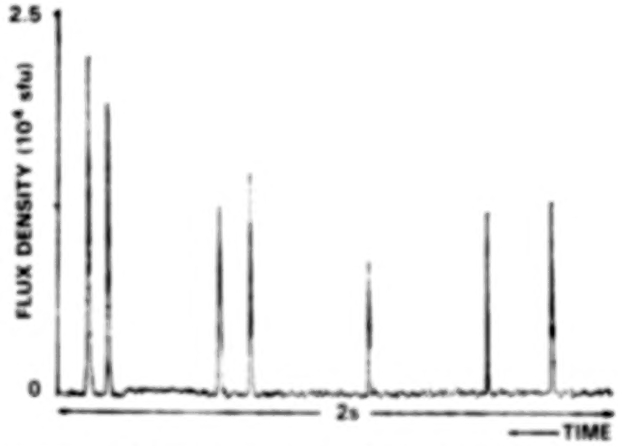

Fig. 1 Isolated spike cluster occurring at 0544 UT, on Feb. 3, 1982

Generally, the isolated spike clusters correspond with subflares and/or impulsive radio bursts (type 3s, 5s and 8s). Fig. 1 shows the record of MMS-event occurring at 0544 UT on Feb. 3, 1982. The duration of the largest spike is 19 ms, with the amplitude of 2.2 x 10^4 sfu. Most MMS-events contained isolated spike clusters, while about 1/3 of the events were completely composed of isolated spike clusters.

2) Crowded spike clusters

Such clusters are composed of a number of crowded spike pulses. Duration of each cluster amounts to tens to hundreds of ms, even more than 10 s. Individual spike in the cluster has short duration (not more than a few ms) and high flux density (about ten thousands sfu.). About half of

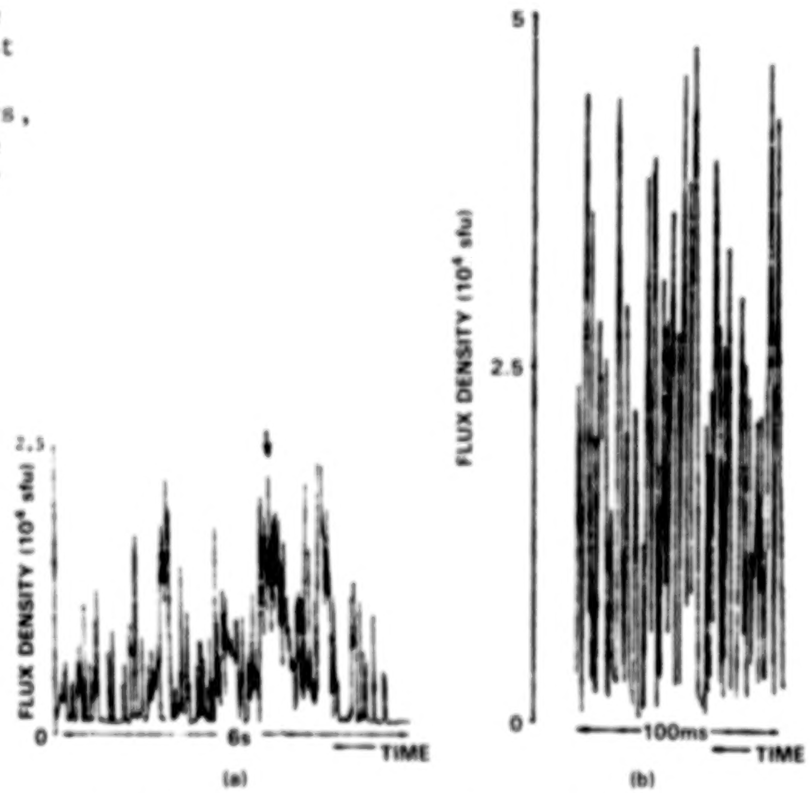

(a) (b)

Fig. 2 a) A part of the crowded spike cluster occurring at 0839 UT on May 16, 1981.
b) The details indicated by an arrow in Fig 2a.

the MMS-event recorded contained crowded spike clusters. About 10 events of such clusters occurred without other types of clusters during the period mentioned above. Fig. 2 indicates a part of the crow spike clusters contained in the May 16, 1981 event. It is the biggest event among the whole record we obtained. There were 37 spikes in the 100 ms time interval. The average duration of individual spike is 2-3 ms. Some of them has a duration of less than 1 ms, the time resolution of the radio telescope. The amplitude of the largest spikes in the time interval is 4.8×10^4 sfu., with the duration of less than 4 ms. The most crowded cluster recorded had 430 spike each minute.

3) Long lasting weak spike clusters

They display as some small spike on the noise background. The spikes sometimes are isolated, sometimes crowded in groups. Their flux density is generally of the order of 1000 sfu. The clusters have a duration of several minutes to tens minutes, even a couple of hours. They look like a "noise storm" at microwave band. Generally, the long-lasting weak spike clusters correspond to weak radio burst or flares. About a half of all MMS-events recorded belong to this type, which generally happens when some specific active region appears. Fig. 3 shows the long-lasting weak spike cluster recorded on July 15, 1981.

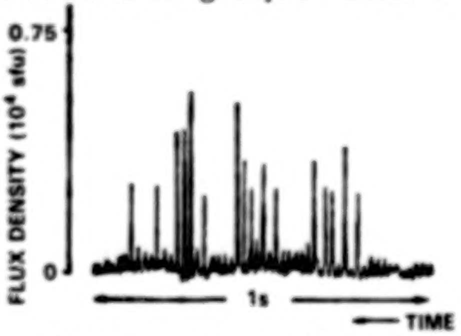

Fig. 3 Weak spike cluster in the noise background occurring at 0910 UT. on July 15, 1981.

4) Absorption phenomena

Besides the upward spike pulses, we have recorded a number of downward negative ones, namely absorption phenomena. Their flux density is obviously lower than that of slow burst level. Of all the MMS events analyzed about 10 events contained such absorption phenomena. Fig. 4, Fig. 5 shows a part of the MMS recorded at 0901 UT. on July 30, 1981 and at 0403 UT on July 21, 1981, respectively . It can be seen that there are at least two kinds of aborption phenomena in the MMS-events.

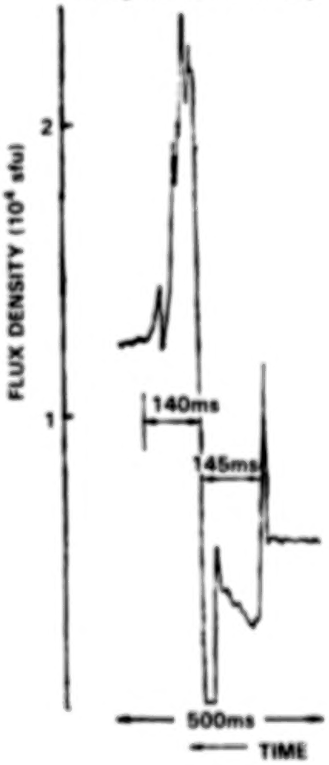

Fig.4 Absorption phenomenon occurring at 0901 UT. on July 30, 1981

Figs. 6, 7, 8, and 9 show four typical MMS-events recorded on May 16, 1981 (Zhao, R., and Jin, S. 1982), July 31, 1981 (Fu, Q. and et al. 1982) Feb. 3, 1982 and Mar. 30, 1982.

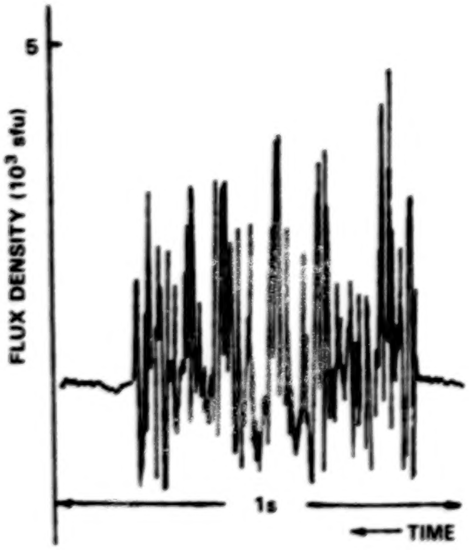

Fig. 5 Absorption phenomenon occurring at 0403 UT. on July 21, 1981.

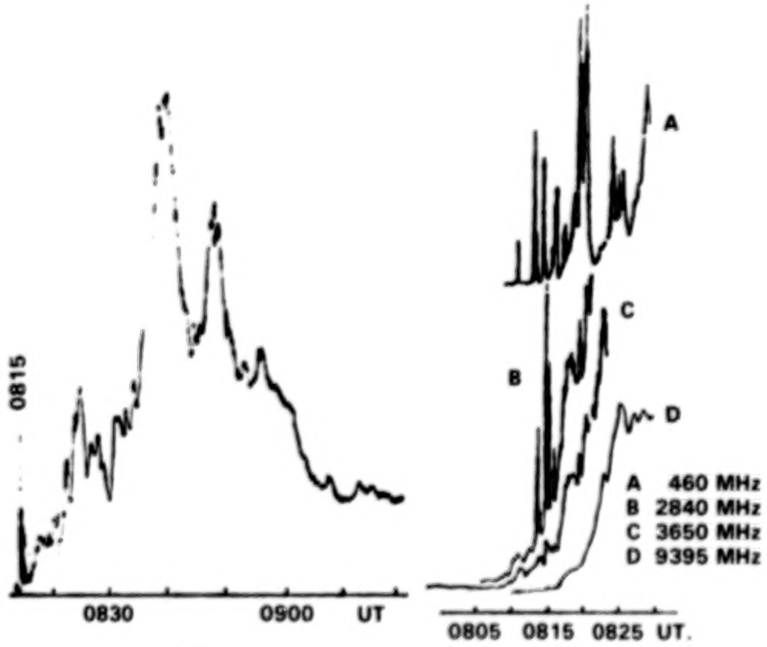

(a) (b)

Fig. 6 Microwave outburst associated MMS-event (Figures 2, 10) occurred on May 16, 1981
a) slow record at 2.84 GHz
b) impulsive structures during initial rising phase at 460, 2840, 3650, and 9395 MHz

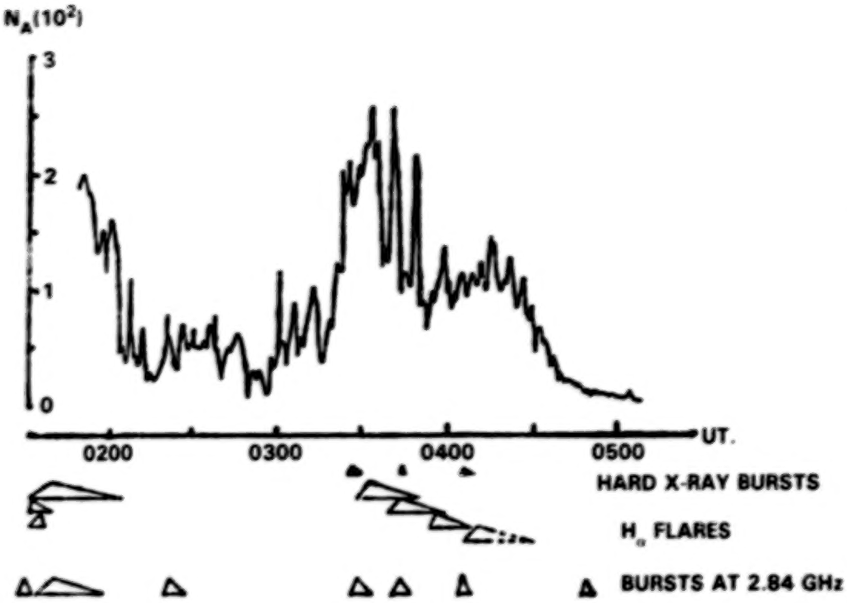

Fig. 7 Spike's number per minute (N_A) and X-ray bursts, flares, and radio bursts at 2.84 GHz associated on the event of July 31, 1981.

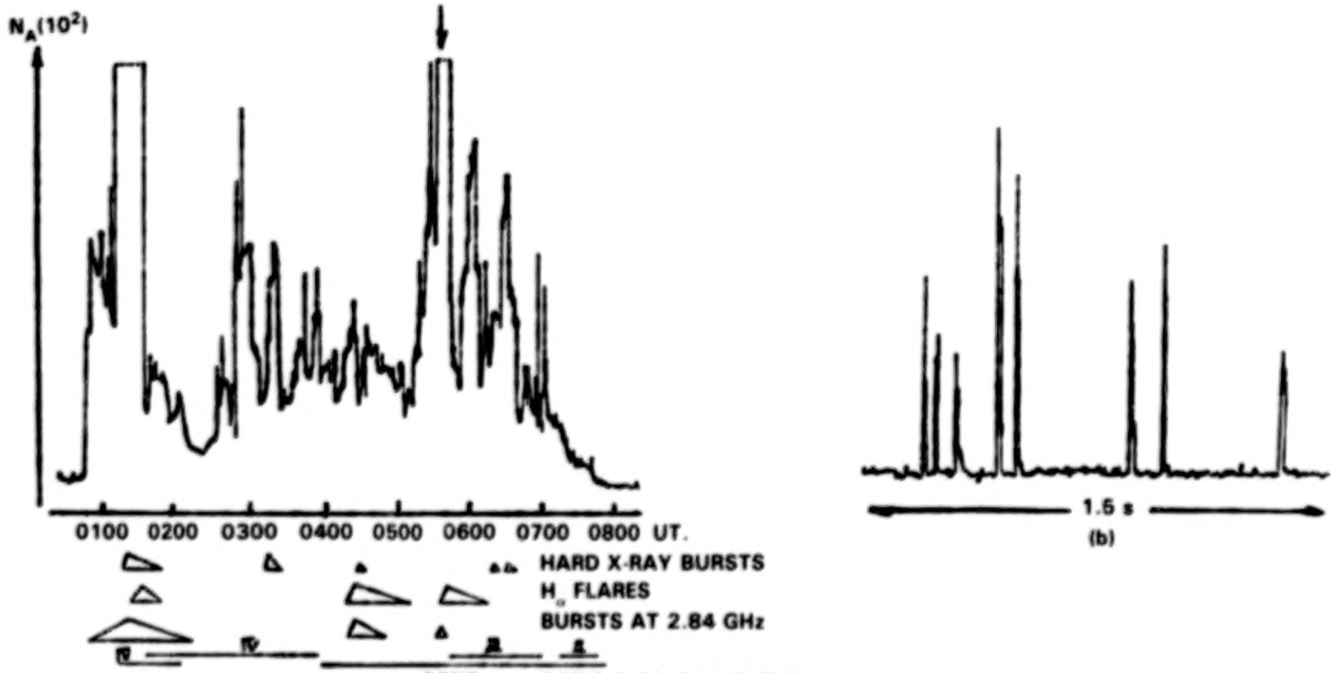

(a)

(b)

Fig. 8 The event of Feb 2, 1982.
a) spike's number per minute (N_A) and other solar activities associated.
b) the details of flux density at the time indicated by an arrow in Fig. 8a.

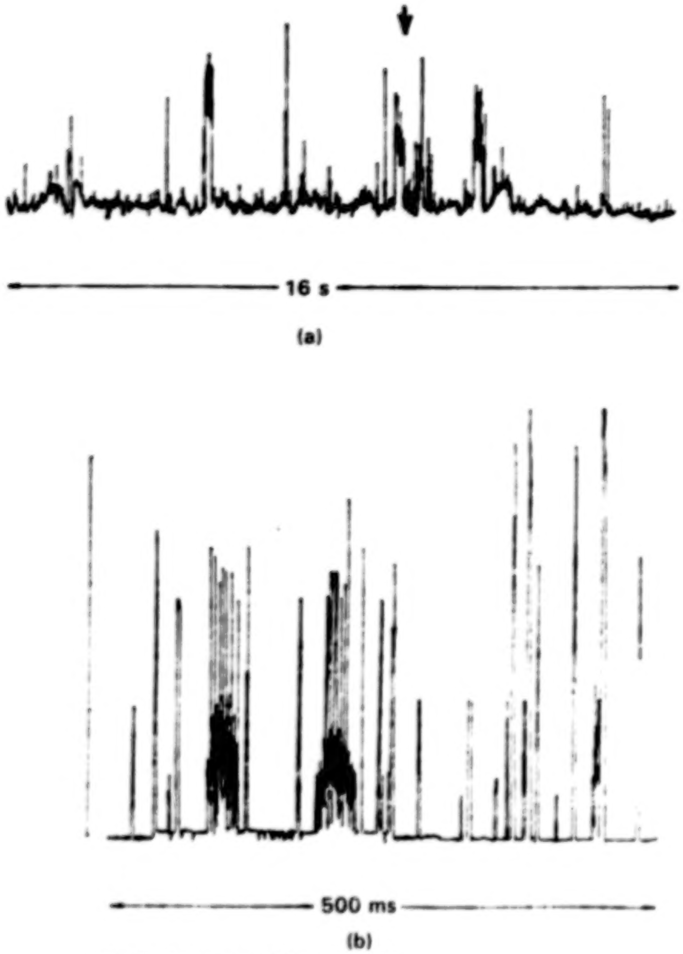

Fig. 9 The event of Mar. 30, 1982
a) a part of record of 16 seconds
b) the details indicated by an arrow in a).

III. CHARACTERS OF OUR OBSERVATIONS

Owing to the time resolution obtained by us is higher than those obtained by Slottje, C. (1980) and Drago, F. (1977), the morphology of events observed by us is markedly different from that by them and reflect MMS emission more accurately. It has been found that:

1) The amplitude of the largest spike is more than 5×10^4 sfu. (possibly larger than 10^5 sfu.).

2) The duratioan of most spikes in great events is less than 4 ms. Some are less than 1 ms (Fig. 1).

3) The ratio of the amplitude of individual spike to the slow burst background in the event of May 16, 1981 is 100 to 500.

4) Some spikes which cannot be resolved with lower time resolution have been resolved. Fig. 10a show a recorded group of spikes. Fig. 10b shows the same groups of spikes with a time constant of 10 ms. It can be clearly seen that the group of spikes has become a noise pattern with random fluctuations. The amplitude has decreased to less than one half of the original pattern, while the continuous background has increased greatly.

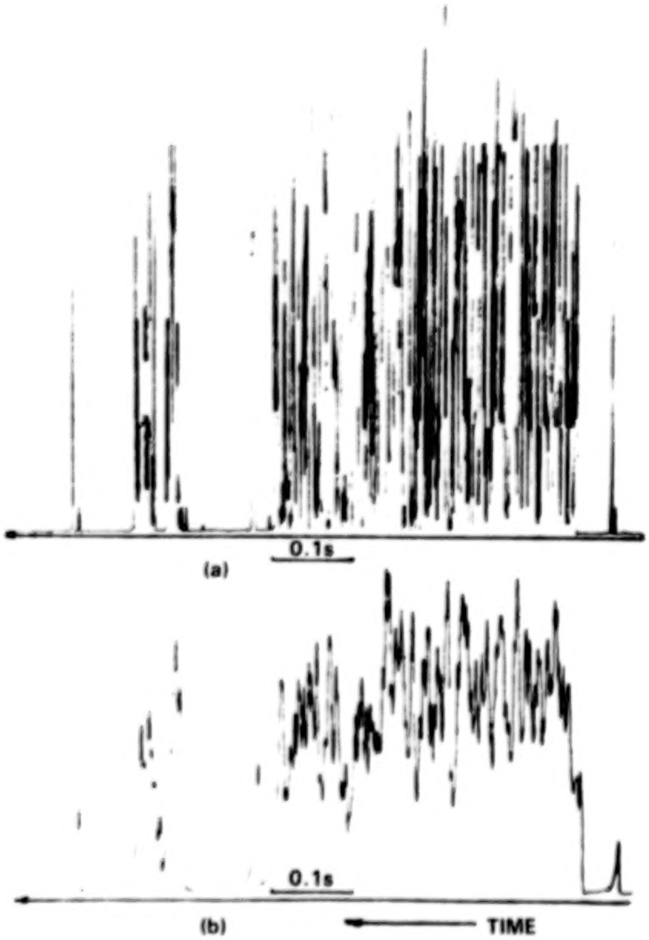

Fig. 10 A part of spikes occurring at 0815 UT. on May 16, 1981
a) with time constant of 1 ms
b) with time constant of 10 ms

5)Because of the many records with high temporal resolution, its seems likely that the basic unit of MMS structure is a spike having a duration from less than 1 ms to tens or hundreds of ms. Spikes appear individually to form a sparse cluster as a "noise storm" (Fig. 3), or in groups with a group duration of tens or hundreds of ms and even tens of seconds. There are a number of groups in an event. With a lack of temporal resolution, these groups become noise pattern with random fluctuation. Some "switch-on and switch off structures" (Slottje, C. 1980) recorded with a lower time resolution are possibly an assembly of a large number of unresolved spikes. The first spike marks the begining of the assembly, and the last spike the end. Its rising time or falling time amounts to only 1 ~ 2 ms (Fig. 10).

6) Owing to continuous patrolling and maintaining a record of N_A, spike's number each minute, a valuable statistical analysis was made with using the events recorded.

IV. CORRELATION BETWEEN MMS-EVENTS AND OTHER SOLAR ACTIVITIES:

1) The correlation between MMS event at 10 cm and solar activity period:

Table 1 and Fig. 11 show the number of MMS-events recorded at different periods of solar activity. It indicates that the appearance of MMS-events decreases as solar activity decends.

Table 1

	May-Dec. 1981	Jan.-Mar. 1982	Mar.-Sept. 1982	Jan.-June 1983
No. of MMS events/100^h	11.2	10.8	4.6	2.3

2) From Oct. 1981 to July 1982, the MMS-events were recorded in 142 days, in these days, 299 hard x-ray bursts recorded ("NASA Technical Memorandum 84998", and "Listing of x-ray flares on HINOTORI"). 94 of them are found to be co-occurrence with the MMS events. This amounts to a percentage of 31.4%, which is much higher than those for the radio bursts and optical flares with only 17.5% and 8.6% respectively are associated MMS-events. If taken the "satellite nights" into consideration, the significance of x-ray burst and MMS-event association may even be enhanced.

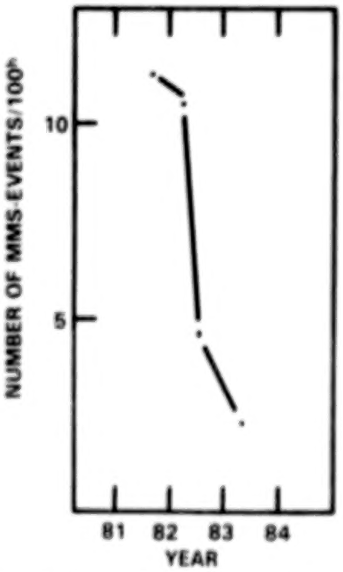

Fig. 11 The correlation between MMS-event at 10 cm and solar activity period

3) Table 2 gives the statistics of the percentage of MMS events that were associated with the radio bursts, optical flares, hard x-ray burst and radio spectral events. It should be pointed out that the most of radio burst assocaited with MMS events contain impulsive structure (Fig. 6). Some of the impulsive structure has been proved that they are integrated with a great number of spikes (Fu, Q., Li, C., and Jin, S. 1985), and the most of radio spectral events associated with MMS-events are type III.

Table 2

	radio bursts	optical flare	hard x-ray bursts	radio spectral events
MMS-events	82%	59%	34.6%	61.5%
Peaks* in MMS-events	64%	59.6%	49.2%	

*The amount of peaks in the plot of spike's number per minute via time.

4) Relation between MMS-events and solar active regions:

For those MMS-events associated with solar flares, we can relate former with the active regions where the flares located. 149 such cases have been found for statistical study. Results are listed in Table 3.

We notice that 87.3% of such MMS events occurred in the regions with magnetic field more than 2000 Gauss, while in δ and $\beta\gamma$ magnetic configurations, which are rather rare as a whole, concentrated 54.6% of the MMS-events generation. When referring to sunspot group, we find that 84.8% of the events are associated with type D, E and F. These lead to the conclusion that strong and complex magnetic field is an important indicator for the happening of MMS-events.

Table 3

Relation Between MMS-Events and Solar Active Regions

Type of Magnetic Structure	Percentage of MMS-events associated	Magnetic field strength (Gauss)	Percentage of MMS-events associated	Type of Sunspot group	Percentage of MMS-events associated
α	4.2	> 2000	87.3	E	34.8
β	41.2	> 2500	62.0	F	24.6
$\beta\gamma$	17.5			D	25.4
δ	37.1			other	15.2

5) The closeness of association between the MMS-events and hard x-ray bursts differs significantly at different periods. The period Oct. 8-24, 1981 is a noticeable example. During this period 24 MMS-events (with 28 peaks) and 62 hard x-ray events were registered when the time intervals of our radiometer's working. 93% of the peaks of events has x-ray association and for all the x-ray events, 41% are co-occurrence with MMS-events. These correlations are much higher than the average values over all periods (49.2% and 31.4% respectively as stated before). Almost

whole of them were located on active regions 17906 and 17923. This means that for some particular solar active regions, the probability of co-occurrence of MMS-events and x-ray events can be very high.

6) The longitude distribution of the flares associated with MMS-events: Fig. 12 and Fig. 13 show the distribution of these flares in longitude of solar disk and in Carrington longitude, respectively. As one may expect, there is obvious directivity of the emission of these events. The "half-power" beamwidth of emission is estimated to be 45^0 to 50^0. The distribution is somewhat asymmetric, in favor of the west part of the disk. There are some active longitude (as 300^0) on solar disk for the flares associated with MMS-events as the normal flares, from the Fig. 13. It means that, similarly to normal flares, MMS-flares correlate to certain active places wiht long living on the solar disk.

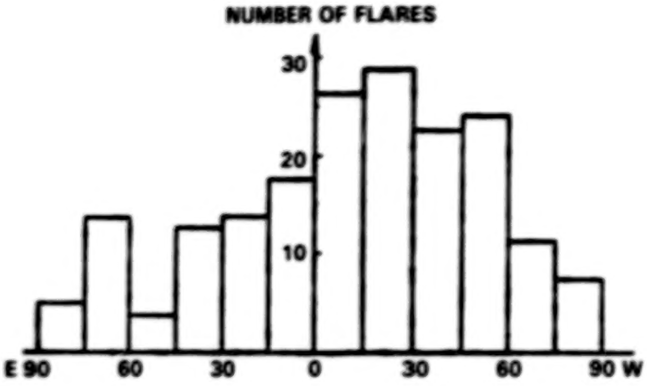

Fig. 12 The distribution of the flares associated with MMS-events in longitude of solar disk

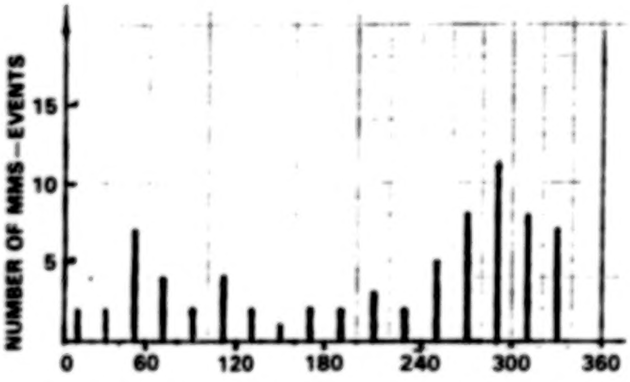

Fig. 13 The distribution of the flares associated with MMS-events in Carrington longitude

V. DISCUSSION:

Owing to the systematic observation with equipment of high time resolution (1 ms), some interesting new features of fast fine structure of solar microwave bursts have been revealed. For example, the MMS emission has shorter duration and higher flux density than were previously known, and the basic units of such fast activities are single spike crowded together forming separate clusters. Observation shows that many spikes are not yet resolved. Therefore, it is of importance to have the time resolution further improved.

With the observational data accumulated so far, the following results are worth noticing: the MMS events are closely correlated with hard x-ray bursts and with fast drifting dm bursts. Some MMS-events found no correspondence with the bursts at the same frequency on slow speed record but corresponded to the bursts occurring in other wavelengths. It is likely that the contribution of the spike clusters were smoothed out on the slow speed record, it seems that they originate from different physical processes. Thus, such fast activity may be a fundamental process different from the flares and normal radio bursts. The MMS events are highly dependent with the type of active regions and the magnetic configuration of the active regions. Possibly, it is crucial to find out the accurate positions on the active region where the MMS-events happen and the position relative to the places where other solar activities associated occur, for judging what is better mechanism for MMS emission.

Since the discovery of solar microwave spike emission with high time resolution observations at cm wavelengths, much theoretical work on the interpretation of its high brightness temperature and polarized characteristics has been proposed. The mechanisms for generating MMS emission have been reviewed in more detail by the authors (Holma, G.D., 1982; Melrose, D.B., and Dulk, G.A., 1982). There is another type of cyclotron maser instability with a "hollow beam" distribution of electrons (Li, H., Li, C., and Fu, Q., 1985) seems to be more important than that associated with a loss-cone distribution. Possibly, different kinds of MMS emission have different mechanisms. It is important to make co-operative observations at different radio wavelengths, optical wavelengths, x-ray and others during the special period when specific, as mentioned in section IV, active region appear on solar disk for clarifying the essence of the fast fine structure emission.

REFERENCES

Dröge, F. 1977, Astro. Astrophys., 57, 285.

Fu, Q., et al. 1982, Astronomical Circular No. 13, March 25.

Fu, Q., Li, C., and Jin, S. "Microwave Millisecond Spike Groups Superimposed on Solar Microwave Bursts", 1983, Kunming International Workshop of Solar Physics, China (submitted to Acta Astrophysica Sinica).

Holman, G.D., 1982, Advanced Space Research, vol. 2, 181.

Jin, S., Zhao, R., and Fu, Q., "Solar Microwave Bursts Recorded at 2.84 GHz with Millisecond Time Resolution", (submitted to Solar Physics).

Li, H.W., Li, C.S., and Fu, Q.J., 1985, Acta Astrophysica Sinica, (in Chinese) Vol. 5, No. 4, 300.

Melrose, D.B. and Dulk, G.A., 1982, Ap.J., 259, 844.

Slottje, C., 1980, Radio Physics of the Sun, M.R. Kundu and T.E. Gergely (eds.) p. 195.

Zhao, R., and Jin, S., 1982, Scientia Sinica, 25, 422.

N87
21810
UNCLAS

N87-21810

THE SENSITIVITY OF Hα PROFILES TO RAPID ELECTRON BEAM FLUCTUATIONS*

Richard C. Canfield and Kenneth G. Gayley

Center for Astrophysics and Space Sciences and Department of Physics
University of California
San Diego, California

ABSTRACT

In order to understand the temporal relationship between Hα and hard X-ray emission predicted by the nonthermal electron thick target model of impulsive-phase energy transport we have computed time-dependent theoretical Hα profiles for the dynamic model atmospheres of Fisher, Canfield and McClymont (1985b), which simulate the effects of an impulsively initiated power-law beam of electrons.

On the basis of our physical analysis we expect a very rapid Hα response to an instantaneous increase in the flux of a nonthermal deka-keV electron beam, as compared to the timescale associated with the propagation of these electrons over characteristic flare coronal loop spatial scales. The amplitude and timescale of this response vary over the Hα profile, and show effects which arise from three different physical mechanisms. First, there is an impulsive initial rise, on the chromospheric heating timescale, which has greatest amplitude at line center. Second, there is a slower component, on hydrogen thermal ionization timescales, which is most apparent in the blue wing, Third, there is a delayed response, associated with the formation of the chromospheric condensation, which is most apparent in the red wing. This latter component dominates over ionization effects on the red side of Hα and, to a lesser extent, at line center.

We conclude that observational efforts to test the thick target nonthermal electron model through detection of impulsive Hα brightenings associated with impulsive hard X-ray or microwave bursts should initially focus attention on Hα line center. Additional simultaneous blue-wing measurements will have substantial diagnostic potential. However, red wing measurements are potentially deceptive, since the prompt enhancements on the chromospheric heating timescale are much smaller than the ~1 s delayed enhancements due to chromospheric condensations, which are not uniquely associated with either nonthermal electron beams or conduction fronts.

INTRODUCTION

Study of the morphology and timing of Hα emission, relative to hard X-ray and microwave emission, during the impulsive phase provides a useful test through which one can discriminate between alternate models for impulsive phase energy transport. For example, are deka-keV electrons the dominant mechanism of energy transport from the hot flare corona (Lin and Hudson, 1976), or are lower

---

* Supported by the National Aeronautics and Space Administration, under grant NSG-7406, and by the National Science Foundation, under grant ATM84-15793.

PRECEDING PAGE BLANK NOT FILMED

energy electrons in a nonclassical conduction front (Brown, Melrose, and Spicer 1979) more important? In the former case, one expects synchronism between Hα and microwaves or hard X-rays on timescales much less than 1 s, whereas in the latter delays of several seconds are to be expected between the hard X-ray or microwave event and its primary Hα counterpart.

Temporal resolution of order 1 s is required to discriminate between conduction-front and energetic-particle energy tranport models. It is also necessary to have spatial resolution, since not all parts of the flare necessarily reflect the same transport process. In the past the lack of adequate temporal resolution led to much confusion about time delays between hard X-rays (or microwaves) and Hα (cf. Vorpahl 1972 and Zirin 1978). However, the development of two-dimensional digital detector systems enabled the first observations with sufficient temporal resolution, which have been obtained recently by Kaempfer and Schoechlin (1982) and Kaempfer and Magun (1983). In a study of one flare with 1.4 s and 100 ms temporal resolution in Hα and microwaves respectively, Kaempfer and Magun found evidence for both fast electron transport, at one site of a flare, and hydrodynamic or nonclassical conductive transport, at other sites of the same flare. At the former site they observed Hα and microwave synchronism within two seconds; the lack of delays at different microwave frequencies also supported an energetic electron interpretation. At the latter sites, delays of about 10 s were observed. The authors showed that these delays are consistent with the propagation of disturbances at about 2000 km/s, i.e. roughly the same velocities expected for collisionless conduction fronts.

In this paper we address a specific technical question: for such simultaneous observations with microwaves or hard X-rays, what is the most appropriate point within the Hα line profile? The observations by Kaempfer and Schoechlin (1982) and Kaempfer and Magun (1983) were made with a narrow-band filter centered on the Hα line. Other observations are currently in progress elsewhere, some of which use a filter centered on the line, while others use the red wing. Which of these positions within the Hα line profile is the best test of energy tranport mechanisms? Which of these positions, or combinations of positions, offers the most valuable diagnostic potential? To answer these questions, our approach is not to try to simulate all the complexity found in real flares; we know from hard X-ray data that, for example, that there is no compelling evidence for preferred values of beam durations or intensities. Instead we discuss in this paper a highly idealized computer simulation which leads to an understanding that can be used to both guide and interpret simultaneous observations in Hα and microwaves or hard X-rays.

COMPUTATIONS

In this paper we compute theoretical time-dependent Hα line profiles for selected times in the sequence of model atmospheres of Fisher, Canfield and McClymont (1985b), henceforth FCM. These models simulate the dynamic response of a loop atmosphere to Coulomb heating by a power-law beam of nonthermal electrons injected at the coronal loop apex. FCM assumed that an electron beam was turned on instantaneously, at a specified value of F_{20} (the equivalent flux of nonthermal electrons above a 20 keV energy cutoff) and then turned off after 5 s. To study the response of Hα on short timescales, we focus our attention on the first few seconds.

The method used for the computation of the time dependent Hα profiles in this paper is an extension of the previous static calculations of Canfield, Gunkler and Ricchiazzi (1984), henceforth CGR. For the model atmospheres at certain instants, available from FCM, we solve the probabilistic radiative transfer equation (Canfield, McClymont, and Puetter 1984) for a 4-level-plus-continuum hydrogen atom. Complete redistribution within a pure Doppler absorption coefficient profile is adopted for the Lyman lines (following Milkey and Mihalas 1973). The absorption coefficient profile for all subordinate transitions has a Doppler core and wings due to both the linear Stark effect (we assume a Holtsmark profile) and resonance broadening (hydrogen-hydrogen collisions; see Mihalas 1978). Our use of probabilistic radiative transfer in the computations of Hα line profiles is consistent with its use by FCM in the energy equation, and its physical limitations are discussed in detail in FCM and CGR. The major limitations on accuracy of radiative transfer aspects of our calculation probably accrue both from the use of probabilistic methods and from the assumption of Doppler core redistribution for the Lyman lines. We estimate that the Hα profiles computed here are limited in their quantitative accuracy to about a factor of two, as a result of these two factors.

The sole difference between the methods used here and those used by CGR lies in the treatment of velocity fields and radiative transfer in the equations describing the level populations of the model hydrogen atom. In the present calcuation the fractional population ϕ_i of the quantum state i of hydrogen is determined by the rate equation

$$\dot{\phi}_i = \partial\phi_i/\partial t = \sum_{j\neq i} \left[R_{ji}\phi_j - R_{ij}\phi_i\right] \tag{1}$$

and the radiative and collisional transition rate coefficients R_{ij} between states i and h, subject to the constraints that

$$\dot{\phi}_2 = \dot{\phi}_3 = \dot{\phi}_4 = 0 \tag{2a}$$

$$\dot{\phi}_1 = -\dot{\phi}_C \tag{2b}$$

and

$$\dot{\phi}_C = \dot{\phi}_C^{(2)}, \tag{2c}$$

where $\dot{\phi}_C^{(2)}$ is the value computed for a 2-level-plus-continuum hydrogen atom by FCM. These constraints given allow us to use the FCM results, rather than having to replace them by a simulation that includes, from the beginning, a full 4-level-plus-continuum hydrogen atom. The use of the more complete model of the hydrogen atom would have only minor effects on the ionization state and energy loss rate as a function of time, yet would impose stringent computational demands. There is no reason to doubt the validity, on the factor of two level that characterizes the calculations throughout, of the approximations made in imposing these constraints, because the rates among the bound levels are so much faster than the rates from bound levels to the continuum; for completeness, we will return to a quantitative discussion of the self-consistency of this assumption below. Our solution to the combined set of radiative transfer and atomic population equations (2) for any FCM model atmosphere at any chosen time gives a self-consistent set of radiation fields and source functions for all transitions within the 4-level-plus-continuum hydrogen atom, including Hα. From

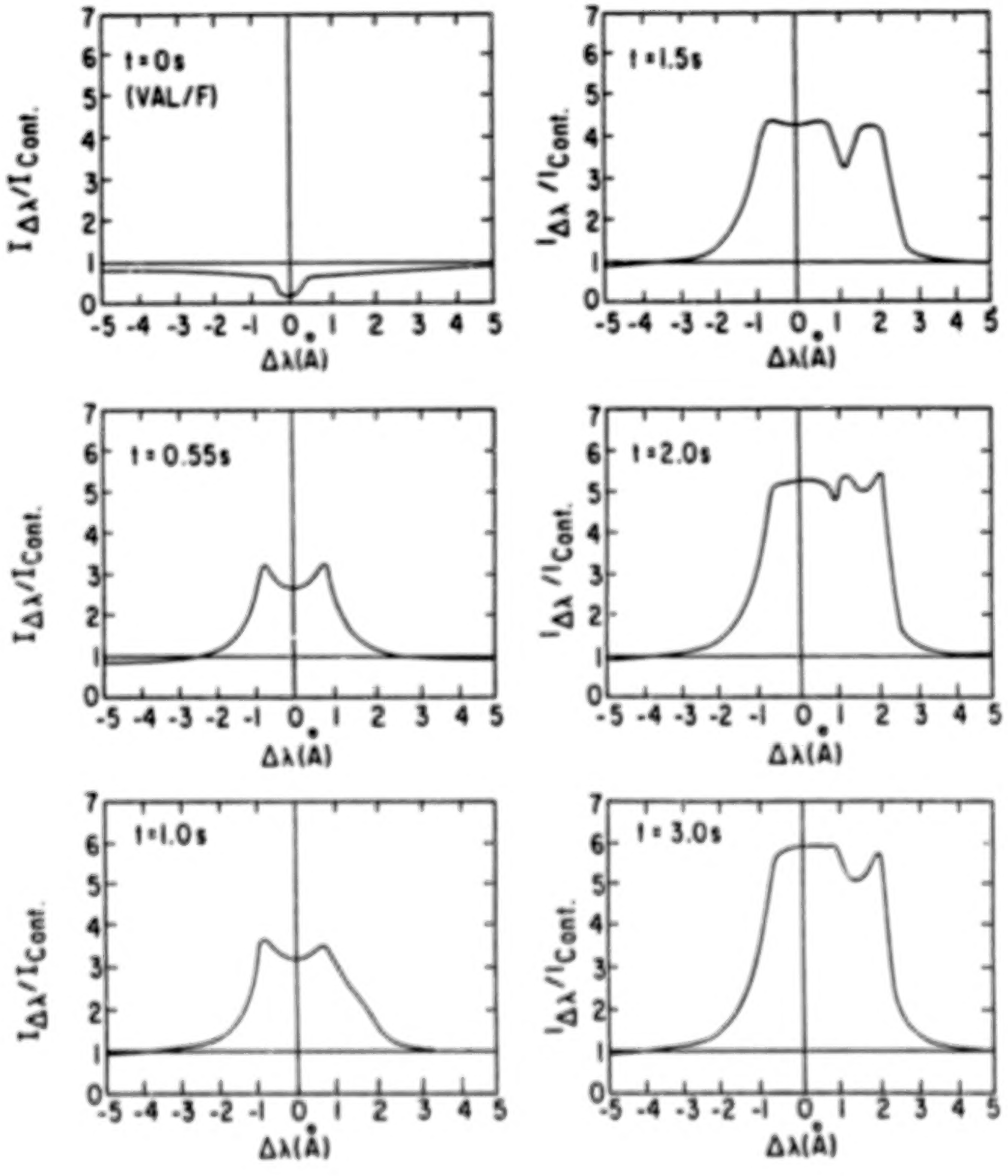

Fig. 1. - Theoretical Hα line profiles for the electron beam heated model atmospheres of Fisher, Canfield and McClymont (1985b), at the indicated times relative to the instantaneous start of flare heating.

this solution, and the columnar dependence of density, hydrogen ionized fraction, and velocity from the FCM models, we know all quantities required to compute the Hα line profiles.

Figure 1 shows Hα profiles at 6 selected times of interest from the FCM $F_{20} = 10^{11}$ ergs cm^{-2} s^{-1} simulation; the electron beam heating in the FCM simulation was turned on instantaneously at $t = 0$ and remained constant for the entire period shown in the figure. It is clear that at $t = 0.55$ s the Hα-emitting chromosphere is enhanced considerably; its behavior on timescales shorter than 0.55 s is discussed below. The profile at 0.55 s is still symmetric; the Hα-emitting chromosphere is not yet moving. By $t = 1.0$ s an enhanced red wing is formed, which is the first indication of chromospheric mass motions. By $t = 1.5$ s one sees that there are two components of the Hα line profile, one shifted and one not. The further evolution of these two components can be seen in the subsequent panels at $t = 2.0$ and 3.0 s. The unshifted component is broad and is initially centrally reversed; it fills in as time passes. This tendency for the reversal to fill in is primarily a consequence of the shifting of the region of formation to a more dense region of the chromosphere, as the region of formation of unshifted Hα emission rapidly shifts to greater column depths. It is secondarily due to seeing even further into the chromosphere at line center due to Doppler shifting of overlying reversing material in the condensation. The shifted component is unreversed initially, while it is optically thin, but a central reversal appears as the moving material becomes optically thick. The moving material is the chromospheric condensation, shown by FCM to be a thin slab of chromospheric material rapidly cooled by the enhanced radiative loss rate associated with compression of this region driven by explosive chromospheric evaporation of adjacent overlying material. The redshift of the emission from the condensation decreases perceptibly between 1.5 and 3 s, as a consequence of its rapid slowing.

We note that the computed Hα profiles are much brighter than typical observed line profiles. The profiles show that this emission comes from both the moving condensation and the essentially static underlying chromosphere, both of which exhibit high pressure. CGR showed that high pressure static atmospheres produce very bright Hα profiles when the conductive flux is not large enough to evaporate much of the flare chromosphere. It is premature, however, to compare these theoretical profiles to observations. As shown by Canfield and Ricchiazzi (1980), the probabilistic radiative transfer methods upon which both the FCM model atmospheres and our Hα profiles are based are only accurate to the factor of two level for static atmospheres such as the VAL/F (Vernazza, Avrett, and Loeser 1981). For dynamic atmospheres in which velocity gradients exceed well-understood limits additional systematic errors arise due to the use of the probabilistic methods. It is known that these limits are exceeded in the FCM atmospheres, in the vicinity of the condensation front. Hence it is important to recognize that while the Hα profiles of Figure 1 are qualitatively well founded, and are based on a method that correctly describes the dominant physical processes associated with photon escape in static atmospheres, one should not attribute significance to the intensity, relative to the background continuum, on the factor of two level.

In Figure 2 we contrast the time dependence of the relative intensity of various parts of the Hα line profile. Bearing in mind that the intensity scale used in the upper panel of Figure 2 is much different from that used in the center and lower panels, it is clear that there is considerable difference, in

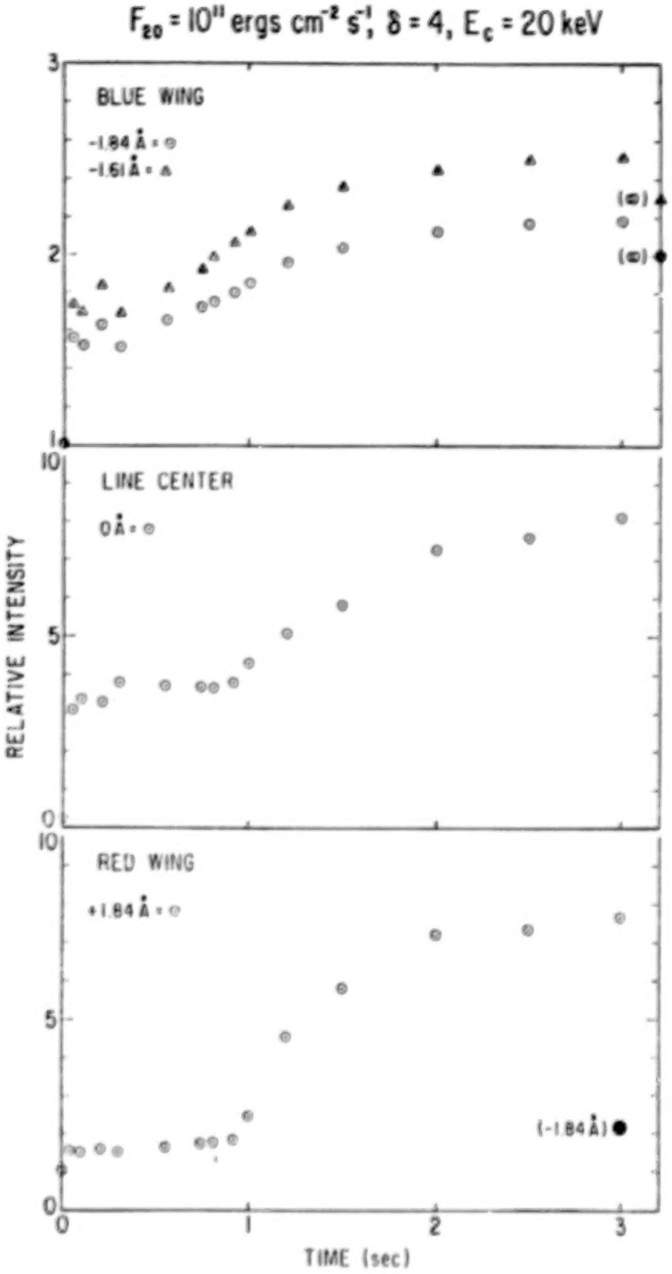

Fig. 2. - The relative intensity of the Hα line profile at the indicated spectral positions, for electron-beam-heated dynamic model atmospheres of Fisher, Canfield and McClymont (1985b), as a function of time relative to the moment of instantaneous initiation of flare heating. The filled symbols marked (∞) in the upper panel are from the hydrostatic calculation of Canfield, Gunkler and Ricchiazzi (1984). The filled symbol in the lower panel is our blue wing result at $t = 3$ s.

both amplitude and functional form, of the time dependence between the blue wing, the line center, and the red wing. Each point in Figure 2 corresponds to one of a limited number of times at which a dynamic model atmosphere from the FCM simulation is available. Between the first and second points (at $t = 0$ and 0.05 s respectively) the intensity jumps on a timescale not resolved in the figure, but temporally and spatially resolved in the computations themselves. The relative increase of this initial jump is much greater at line center than in either wing. In the blue wing, at both -1.61 and -1.84 Å, there is also a slower increase, on a timescale ~0.3 – 0.4 s; our analysis suggests that this is an ionization effect. Finally, at both line center and in the red wing, one sees a delayed increase (starting at about 1 s), which is due to the formation of the chromospheric condensation. We now turn to a discussion of the physical origins of these effects.

ANALYSIS

The three timescales on which the Hα line profile varies in our numerical simulation can understood in terms of the timescales for electron beam heating, thermal ionization, and chromospheric condensation.

ELECTRON BEAM HEATING

In the first approximation, the flare chromosphere reaches a quasi-equilibrium on the longer of two timescales, those for heating

$$t_h = E_{th}/Q_b \tag{3}$$

and radiative cooling

$$t_r = E_{th}/R. \tag{4}$$

The duration of this quasi-equilibrium is limited to values much less than the hydrodynamic timescale

$$t_p = H/c_s. \tag{5}$$

Here E_{th} is the specific (per hydrogen nucleus) mean thermal energy $\frac{3}{2}kT(1+x)$, T is the electron and ion temperature, k is Boltzmann's constant, x is the hydrogen ionized fraction, Q_b is the specific electron beam heating rate, R is the specific radiative cooling rate, H is the local density scale height for hydrogen nuclei, and c_s is the sound speed. The value of t_p is of order 5 – 10 s in the flare chromosphere. For the impulsive phenomena that interest us here we need consider only t_h and t_r.

In this study we are interested primarily in the region of the atmosphere from which the flare Hα emission originates. Table 1 identifies physical parameters of interest in this region: N is the column depth of maximum contribution to the Hα emission at the specified spectral location within the line profile and x and T are the hydrogen ionized fraction and temperature at this depth. We focus our attention on the depths of maximum contribution at two times: 1) $t = 0$ s, before any shift of the emitting region into the deeper chromosphere has started, and 2) at $t \sim 1.5$ s, after the emitting region has shifted into the deeper chromosphere and the condensation has been formed. Table 2 shows that if $F_{20} = 10^{11}$ ergs cm^{-2} s^{-1}, the heating timescale t_h is very short at the depths that are of interest when the beam is first turned on—less than 10 ms. Because the radiation timescale t_r is so long, and the t_h is so much less than the pressure equilibration timescale t_p, it is clear that either the temperature or the hydrogen ionized fraction is going to increase very rapidly. Since both the rate and amount of energy that can go into ionization is limited, while the rate and amount that can go into thermal form is much more weakly constrained, the temperature of the beam-heated chromosphere will increase on timescales less than 10 ms, if the beam energy flux $F_{20} = 10^{11}$ ergs cm^{-2} s^{-1}. At $t = 1.5$ s the heating timescale is longer, especially in the wings of Hα, but is still about an order of magnitude less than the electron transit timescale $t_e = L/v_e$, where L is the characteristic length of a flare loop and v_e is the characteristic velocity of a nonthermal electron, if $L = 10^4$ km and $E_e = 100$ keV. A range of values is given for the red wing at $t = 1.5$ s because this emission is distributed rather evenly over the condensation and the upper uncondensed material.

TABLE 1. - PHYSICAL PARAMETERS IN THE Hα CHROMOSPHERE AT DEPTHS OF MAXIMUM CONTRIBUTION TO Hα EMISSION

$t = 0$ s	$N(cm^{-2})$	T(K)	x
Blue Wing (-1.8 Å)	1.5×10^{20}	6700	0.05
Line Center	6.2×10^{18}	7600	0.50
Red Wing (+1.8 Å)	1.5×10^{20}	6700	0.05

$t = 1.5$ s	$N(cm^{-2})$	T(K)	x
Blue Wing (-1.8 Å)	3.6×10^{20}	11,800	0.95
Line Center	6.0×10^{19}	59,000	1.00
Red Wing (+1.8 Å)†	3.6×10^{20}	11,800	0.95
	2.7×10^{19}	22,400	1.00

† Red wing emission originates in both the condensation and the uncompressed upper chromosphere.

TABLE 2. - TIMESCALES (SECONDS) IN THE Hα CHROMOSPHERE $F_{20} = 10^{11}$ ergs cm^{-2} s^{-1}

	$t = 0$ s		$t = 1.5$ s	
Wavelength (Δλ)	heating	radiation	heating	radiation
Blue Wing (-1.8 Å)	7×10^{-3}	$1\times10^{+2}$	2×10^{-1}	2×10^{-1}
Line Center	2×10^{-3}	$6\times10^{+0}$	2×10^{-2}	2×10^{-2}
Red Wing (+1.8 Å)	7×10^{-3}	$1\times10^{+2}$	$1\times10^{-1-2}$	$1\times10^{-1-2}$

Several comments are in order. It is apparent that the sudden jump in the Hα intensity at all three $\Delta\lambda$ values in Figure 2 in the interval $0 < t < .05$ s is a consequence of the short heating timescale in the region of initial formation of Hα. Hence, except for other complications (see below), it appears that all three spectral positions within Hα would be useful for high-intensity electron beam timing experiments, since all heating timescales are much less than beam transit timescales. Even though the heating timescale is 1 - 2 orders of magnitude longer after the beam is established, it still remains about one order less than t_e. Third, the table confirms the quasi-equilibrium interpretation of the slowly-rising plateau seen at line center and the red wing during the first second of Figure 2; to the precision given in Table 2, $t_h = t_r$. One should therefore expect Hα to track beam temporal variations, at high electron beam flux levels, down to timescales well under 1 s. Finally, it is hardly surprising that substantial Hα emission is generated in the flare chromosphere, given the large temperatures at the depths of maximum contribution given in Table 1. The hydrogen ionized fraction is much higher in the Hα flare chromosphere than in the preflare, but no so high that the chromosphere is optically thin at line center.

THERMAL IONIZATION

The gradual increase in the blue wing emission evident in Figure 2 on a timescale of about 0.3 - 0.4 seconds suggests a slow drift toward an equilibrium that must be only quasi-steady on a grander timescale as macroscopic effects such as pressure equilibration set in. What physical effect controls the timescale of this approach to equilibrium, or more accurately, what is the slowest of the many physical effects present? The temperature and density of the emitting region are important to the total emission, but the temperature equilibrates rapidly, as described above. Also, the density changes only on the much longer hydrodynamic timescale. Is then the relevant timescale that for the atomic level populations to equilibrate? The bound-bound rate coefficients in equation (1) are so large that the level populations equilibrate with each other extremely rapidly, but the continuum rates are much slower and so the continuum equilibration takes much longer. Thus the ionization timescale is a likely candidate for the slow-paced driving timescale in this equilibration process.

The ionization timescale manifests itself in a gradual increase in the optically thin component of the wing emission. This is due to the effects of Stark broadening of the Hα absorption coefficient profile caused by interactions of hydrogen atoms with free electrons. As ionization progresses and the free electron density increases, the broadened profiles produce an enhancement of the wing emission from the ionizing region. (This emission is optically thin, so is superimposed on top of the fairly constant optically thick wing emission from the photosphere, but it contributes strongly to the total wing emission.) Thus we expect a close correlation between the local ionization timescale and the timescale for increase of the local contribution to the total wing emission. This assumption can be tested by focusing on the region where emission in the wings (e.g. at $\Delta\lambda = -1.8$ and -1.6 Å) is most important, and calculating the ionization timescales directly from the local rate equations (1).

There are two ways in which the local populations effect the local contribution to the Hα wing emission. First, the absorption coefficient profile may become wider due to larger free electron density and associated increased Stark broadening, as mentioned above. Second, the population of the second level of hydrogen may increase, increasing the Hα opacity (recall that the emission being considered is optically thin). This second effect is highly dependent on the rate coefficient primarily responsible for populating level 2, which is the 1 → 2 radiative rate, and as such is proportional to the local Lα radiation field, whose origins are highly nonlocal. If these nonlocal effects dominated the local wing rise, it would be impossible to analyze the timescale in terms of local equilibration timescales such as the ionization timescale. Fortunately, our results indicate that the dominant effect is the absorption coefficient profile, not the second level opacity. Hence the ionization timescales are the most relevant to the wing rise, and these can be found at least approximately by considering only the local conditions, i.e., the local rate coefficients.

Finding a simple approximation to these ionization timescales based on the local conditions is complicated by the fact that the rate equations (1) are nonlinear, owing to the dependence of the collisional and radiative recombination rate coefficients on the electron density and thus on the continuum population itself. But the local behavior of these equations can be approximated by linearizing about a given point taken from the simulations. The problem then reduces to the solution of a linear system of first order differential equations, whose eigenvalues are thus the equilibration rates of the various normal modes of decay to equilibrium. The smallest of these eigenvalues will correspond to the most slowly decaying mode, and will therefore give the overall net equilibration rate. Of course, this can only approximate the true equilibration rate because the equilibrium approached by the linearized system will deviate from the true equilibrium. This probably introduces an uncertainty of a factor of two or so in the rate predicted by this simple analysis.

Linearization of the rate coefficients with respect to their dependence on the continuum population is accomplished by writing the vector ϕ of atomic level populations ($\phi_1, \ldots \phi_4, \phi_C$ in our case) as $\phi = \phi_0 + \delta\phi$, where ϕ_0 is the locally determined equilibrium population vector. The linearized form of equation (1) is then

$$\delta\dot{\phi} = R\,\phi_0 + R\,\delta\phi + (\delta\phi_C\,\partial R/\partial\phi_C)\,\phi_0, \tag{6}$$

where R is the rate matrix evaluated at the point of maximum wing emission, and the first term on the right side of the equation vanishes, by definition of equilibrium. We can rewrite (6) as

$$\delta\dot{\phi} = [DR]\,\delta\phi \tag{7}$$

where

$$[DR]_{ij} = [R]_{ij} + \delta_{jC}\,\phi_0 \cdot \partial r_i/\partial\phi_C \tag{8}$$

where δ is the Kroneker delta of rank two and r_i is row i of R.

DR is the desired linearization of the rate matrix in equation (1). It is a 5 by 5 matrix equation, whose size makes its eigenvalues hard to obtain in a simple way. This is further complicated by the fact that there is a very broad spread in the magnitudes of the matrix elements, so that slight errors in the eigenvectors can produce contamination by drastically larger eigenvalues, which makes determination of the actual eigenvalue impossible from knowledge of the approximate normal mode. But since the overall behavior of the system was obtained from the two-level plus continuum model of FCM and it is assumed that inclusion of levels 3 and 4 cannot drastically effect the overall behavior, we looked at the reduced 3 by 3 linearized system and were able to obtain the eigenvalues by simply factoring the characteristic polynomial. This was further aided by the fact that since the rate matrix (and the linearized version) must conserve particle number and therefore must produce time derivatives that add up to zero, it is singular, it has determinent zero, and its range forms a two-dimensional subspace. This singularity results in one of the eigenvalues being zero (corresponding to the non-decaying equilibrium mode itself). Thus finding the remaining eigenvalues amounts to factoring the quadratic polynomial to which the characteristic polynomial reduces.

The results of this simple analysis show that, although the eigenvalues vary over the atmosphere, in the region of greatest wing emission at $\Delta\lambda = -1.6$ and -1.8 Å we find one dominant eigenvalue of order 10^8 s^{-1}, which is essentially equal to the large 2 → 1 spontaneous decay rate, and a second eigenvalue of size roughly 5 - 10 s^{-1}, which arises from the sum of all the linearized continuum rates except the large 2 → c rate. The corresponding eigenmodes are the direct exchange of electrons between levels 1 and 2, and the exchange of electrons between the continuum and levels 1 and 2 in proportion to the equilibrium ratio between these two levels. It is this second eigenvalue that is related to the ionization timescale, and is believed to account for the equilibration time seen in the blue wing of Figure 2. Since the eigenvalue gives the equilibration rate, its inverse gives the corresponding timescale, which in this case is 0.1 - 0.2 seconds.

This rate appears to be a little too fast to explain the 0.3 - 0.4 s Hα timescale. This could be due to the fact that the linearized rates are high by some factor of order unity owing to the fact that the eventual equilibrium point is not actually within the local range of the validity of the linear approximation until equilibration is nearly attained. Thus during the times of primary interest ($0.5 < t < 1.5$ s), we are experiencing a drift of the equilibrium point of the local linearization in addition to the linear time evolution toward this point, which extends the equilibration timescale somewhat. This could be enhanced by the nonlocal effects of the radiation field. Since the discrepancy is of order unity, we believe that the ionization process described here does successfully account for, and is the dominant physical effect in, the observed 0.3 - 0.4 s equilibration timescale in the blue wing. Other effects such as changes in the opacity of the optically thin emitting region and variations in the optically thick wing emission from the photosphere due to changes in the total opacity of the chromosphere play a lesser role, and certainly depend on the ionization timescale also.

CHROMOSPHERIC CONDENSATION

Another important timescale that can be inferred from Figure 2 is the timescale for the onset of strong Hα emission from the chromospheric condensation. This is visible as a rapid increase in both line center and red wing emission starting at t ~ 1 s. Shortly thereafter, condensation emission dominates both the red wing and, to a lesser extent, line center. Awareness of this ~1 s delay time is important because this condensation emission could be confused observationally with the initial brightening that occurs when the electron beam is "turned on", particularly in the red wing where the red-shifted condensation emission becomes much stronger than the normal wing emission (which comes from deeper in the chromosphere and produces the initial red wing brightening).

A rough way to see how this ~1 s formation delay time comes about is to imagine a simple two-step model of the effects of the explosive evaporation of the upper chromosphere when the beam is "turned on". In the first step, explosive evaporation causes the pressure to increase very rapidly at the top of the chromosphere. Fisher (1986) has shown that this first step can be understood quantitatively with a simple "gasbag" model of the explosively evaporating region (see Fisher, Canfield and McClymont 1985a). We refer the interested reader to Fisher (1986), and will not discuss this first step further here; we will make the simplifying assumption that this pressure increase is instantaneous (both the FCM simulations and the gasbag model show that it actually takes a few tenths of a second to reach its maximum value). In the second step, the high pressure region moves down into the chromosphere as a compression wave and forms the condensation. This can be modelled most simply as a piston with constant pressure excess Δp behind it moving down into a chromosphere of density ρ, compressing the material ahead of it to the piston pressure. Since we are interested in only ~1 s timescales here, the piston is taken to move at a constant velocity v -- the velocity of the compression wave. Then setting the pressure discontinuity equal to the rate of change of momentum in the compressed material (i.e.,the condensation), we obtain the accretion rate of condensation mass m:

$$\Delta p = \frac{dm}{dt}\, v = \rho\, v^2,$$

so that

$$v = \left[\frac{\Delta p}{\rho}\right]^{\frac{1}{2}}.$$

Taking from the simulation a characteristic $\rho \approx 4\text{x}10^{-12}$ g cm^{-3} and $\Delta p \approx 200$ dynes cm^{-2} gives $v \approx 70$ km s^{-1}, comparable to the initial condensation velocity in the $F_{20} = 10^{11}$ ergs cm^{-2} s^{-1} simulation. Then the column accretion rate of hydrogen with a density of roughly 2-3x10^{12} cm^{-3} is about 1-2x10^{19} cm^{-2} s^{-1}. Now from the simulation it is found that the condensation begins to become visible in Hα when it has accumulated a column depth of about 5x10^{18} cm^{-2} and becomes optically thick at about 2x10^{19} cm^{-2}. This simple model thus provides a consistent picture of why it takes about 1 s to begin seeing condensation effects. It should be noted that this delay time will depend on the F_{20} value, and may vary by perhaps a factor of two over a plausible range of explosive F_{20} values.

CONCLUSIONS

We find an Hα response to a instantaneously initiated intense beam of nonthermal electrons that is rapid compared to the timescale associated with the propagation of these electrons over characteristic flare loop dimensions. The amplitude and timescale of this response vary over the Hα profile, and show effects which arise from three different physical mechanisms. First, there is an impulsive initial rise on the chromospheric heating timescale; this rise has greatest amplitude at line center. Second, there is a slower component, on hydrogen ionization timescales, which is most apparent in the blue wing. Third, there is a delayed response associated with the formation of the chromospheric condensation, which is most apparent in the red wing. This latter component dominates over ionization effects on the red side of Hα.

We conclude that observational efforts to detect impulsive Hα brightenings associated with impulsive hard X-ray or microwave bursts should initially focus their attention on line center. Additional simultaneous blue-wing measurements will have diagnostic potential because of their sensitivity to the thermal ionization timescale and the fact that even for very intense electron heating ($F_{20} = 10^{11}$ ergs $\mathrm{cm}^{-2}\ \mathrm{s}^{-1}$) the timescale is in a readily observable range (>0.1 s). However, red wing measurements are potentially deceptive, since the prompt enhancements on the chromospheric heating timescale are much smaller than the ~1 s delayed enhancements due to chromospheric condensations, which are not uniquely associated with either nonthermal electron beams or conduction fronts.

REFERENCES

Brown, J. C., Melrose, D. B., and Spicer, D.S.: 1979, *Astrophys. J.*, 228, 592.
Canfield, R. C., Gunkler, T. A., and Ricchiazzi, P.J.: 1984, *Astrophys. J.*, 282, 296.
Canfield, R. C., McClymont, A. N., and Puetter, R. C..: 1983, in *Methods in Radiative Transfer*, ed. W. Kalkofen (Cambridge: Cambridge University Press), p. 101.
Canfield, R. C. and Ricchiazzi, P. J.: 1981, *Astrophys. J.*, 239, 1036.
Fisher, G. H. 1986, in preparation.
Fisher, G. H., Canfield, R. C. and McClymont, A. N.: 1985a, *Astrophys. J.*, 289, 425.
Fisher, G. H., Canfield, R. C. and McClymont, A. N.: 1985b, *Astrophys. J.*, 289, 434.
Kaempfer, N., and Magun, A.: 1983, *Astrophys. J.*, 274, 910.
Kaempfer, N., and Schoechlin, W.: 1982, *Solar Phys.*, 78, 215.
Lin, R. P., and Hudson, H. S.: 1976, *Solar Phys.*, 50, 153.
Mihalas, D.: 1978, *Stellar Atmospheres* (2nd ed.), W. H. Freeman and Co., San Francisco.
Milkey, R. W., and Mihalas, D.: 1973, *Astrophys. J.*, 185, 709.
Vernazza, J. E., Avrett, E. H., and Loeser, R. 1981: *Astrophys. J. Suppl.*, 45, 619.
Vorpahl, J.: 1972, *Solar Phys.*, 26, 397.
Zirin, H.: 1978, *Solar Phys.*, 58, 95.

N87
21811
UNCLAS

N87-21811

A SEARCH FOR FAST VARIATIONS IN THE Fe XXI EMISSION DURING SOLAR FLARES

Chung-Chieh Cheng

E.O. Hulburt Center for Space Research
Naval Research Laboratory
Washington, DC 20375-5000

ABSTRACT. The main results are: 1) No periodic oscillation in Fe XXI emission detected. 2) The shortest timescale of rapid variation persistently present in the Fe XXI emission is about 20 sec. 3) Statistically significant isolated bursts of duration 3 to 5 sec are present in some of the flares.

1. INTRODUCTION

Observations have shown that the intensity of soft X-ray bursts from solar flares varies smoothly with a gradual rise and decay time profile. The timescales of soft X-ray burst variations range from minutes to hours. On the other hand, the impulsive hard X-ray bursts typically show fast variations and spiky time structures, with timescales as short as one tenth of a second (Hoyng et al., 1976; Kiplinger et al., 1983). Since the soft X-ray burst is generally regarded as the result of energy transfer from the hard X-ray electrons, either by direct heating or by the process of chromospheric evaporation, it is of interest to ask whether the fast variations observed in the impulsive hard X-ray burst are in any way reflected in soft X-ray bursts. Studies of the Fe XXV and Ca XIX emissions in solar flares obtained from the P78-1 (Doschek, Kreplin, and Feldman 1979, Doschek et al. 1980; Feldman et al. 1980) have shown that these emissions have a very smooth intensity profile, when observed with a time resolution of about 30 sec. During the SMM in 1980, many flares were observed in the UV line of Fe XXI at 1354 Å, which originates in plasmas with a temperature of about 10 million K. Examinations of high-time resolution Fe XXI observations generally show gradual rise and fall profiles, representative of typical soft X-ray bursts. However, these gradually varied time profiles do show intensity fluctuations. In this paper we make a quantitative study of the Fe XXI intensity variations, and assess whether the observed rapid fluctuations represent intrinsic variations in the emission or are just due to photon counting statistics.

2. DATA ANALYSIS

The Fe XXI observations were obtained with the Ultraviolet Spectrometer and Polarimeter (UVSP) on the SMM satellite. In order to study fast variations, we have chosen flares that were observed with a field of view of 30" x 30" and a slit size of 10" x 10". These 3 x 3 raster element images

PRECEDING PAGE BLANK NOT FILMED

were taken every 1.215 seconds for a period of ten minutes. This time resolution was the highest observed by the UVSP in the Fe XXI mode. Out of 26 flares in the fast Fe XXI mode, 10 were observed from the beginning of the flare, and showed appreciable Fe XXI emission in the small field of view. These were chosen for analysis. Figure 1 (upper panel) shows an example of the time evolution of the Fe XXI emission in the 1 November 1980 flare at 1924 UT; the intensity is for the brightest pixel in the field of view (FOV).

Figure 1 shows there are large fluctuations superimposed on the generally gradual rise and fall profile. In all figures, the count rate is count per 0.063 sec. As is well known in photon detection and cosmic ray observations, such fluctuations are most often due to photon counting statistics rather than due to real signals. How does one determine whether the observed variation is statistically significant in the inherently noisy data? If such fluctuation

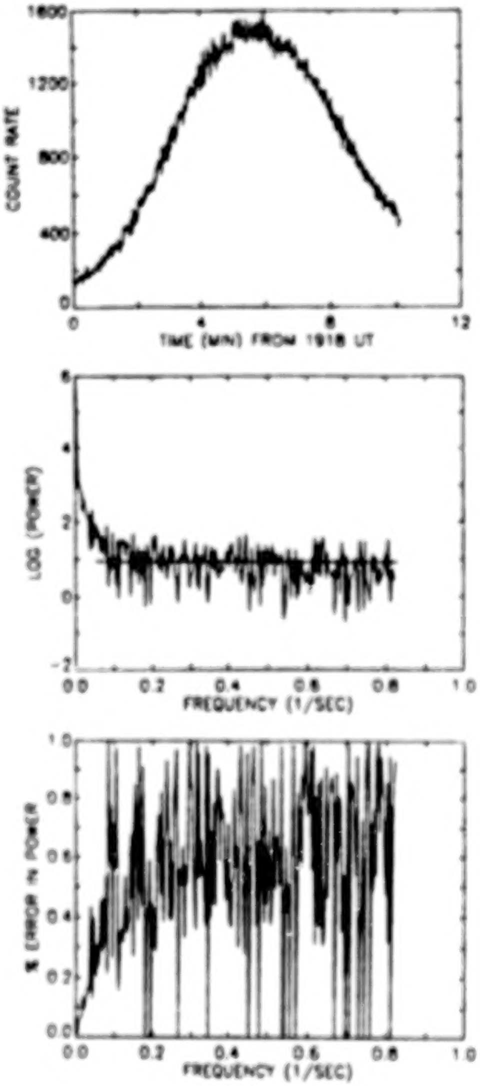

Figure 1

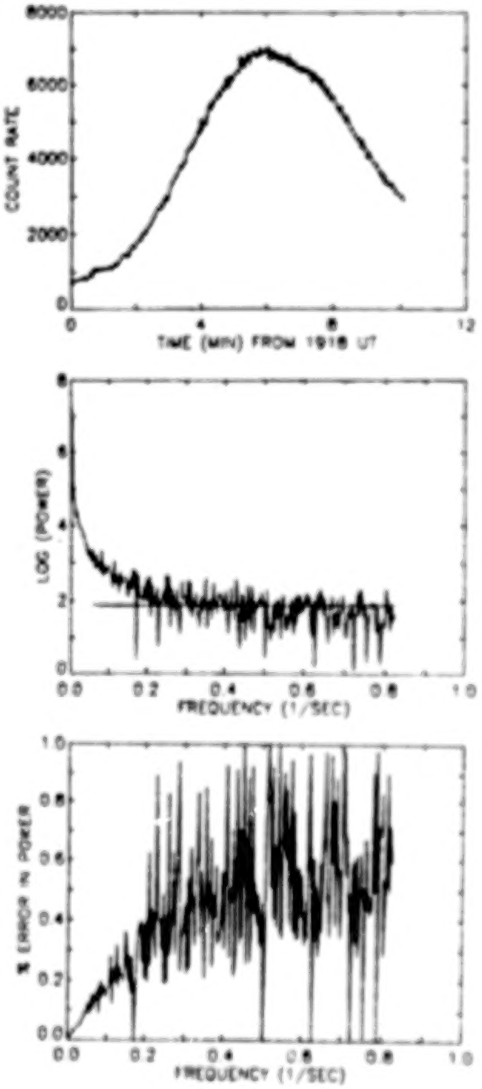

Figure 2

is real, what is its timescale? One technique to answer such questions is the use of Fourier power spectral analysis. This technique was used by Hoyng _et al._ (1976) and Brown, Loran, and MacKinnon (1985) to determine the shortest timescale present in solar impulsive hard X-ray bursts.

We have calculated the power spectra for the 10 flares selected for analysis, using a standard fast Fourier transform code. Since the analyses are the same for the flares we studied, we shall present calculations for three flares to illustrate the results.

In Figure 1 we have already shown the light curve for the brightest Fe XXI pixel in the FOV for the 1 November 1980 flare. The flare occurred in AR 2776 (NOVA designation), and is classified as a 1B in Hα and M1 in soft X-ray. In Hα the flare began at 1915 UT, reached maximum at 1922 UT, and ended at 1931 UT. The Fe XXI emission started to increase at 1918 UT and reached peak intensity at 1924 UT. Figure 1 also shows the power spectrum. As expected, the power spectra is dominated by the zero frequency component. The power decreases sharply towards higher frequencies and levels off at about the frequency f = 0.2 sec^{-1}. The high frequency powers are dominated by random noises. Since the noise in the photon counting experiment generally obeys Poisson statistics, it is possible to calculate the expected level for the high frequency powers that are due to noise presented in the data. Hoyng (1976) has derived such an expression as well as calculated the relative error in a power spectrum for Poisson distribution. The horizontal line in the power spectrum graph is the calculated high frequency power expected from noise, and the relative error in the power spectrum as a function of frequency is shown in the lower panel of Figure 1. As can be seen, the power does not rise above the noise level until the frequency has decreased to below f = 0.1 sec^{-1}. At f = 0.1 sec, the relative error in the power is about 30%, and the error approaches unity at high frequencies, again demonstrating the dominance of noise at high frequencies. Considering the errors involved in the power spectrum, it is only for f < 0.05 sec^{-1} do we see any appreciable power in the data. If we take f = 0.05 sec^{-1}, where the error is relatively small, as the cut off frequency beyond which the power is due to noise, then the corresponding timescale is about 20 sec. We emphasize that this is the fluctuation timescale that is persistently present in the data that is not masked by noise. There are no isolated peaks in the power spectrum, indicating the absence of any periodic variations in the Fe XXI emission.

We also obtained the power spectrum for the total intensity of Fe XXI summed over the FOV. This is done to increase the count rate to improve its statistics. Figure 2 shows the total intensity variation, the power spectrum, and the relative error in the power spectrum. We see that the power spectrum rises above the noise level at the frequency about f = 0.05 sec^{-1} with relatively smaller error than that shown in Figure 1. This is because of the increased count rate and comparatively lower noise level. It is clear that for the 1 November flare, the shortest timescale persistently present in the data is about 20 sec. This timescale of variability is similar to those found for Fe XXV emission in some flares observed by the XRP instrument on _SMM_ (Zarro, Strong, and Saba, 1985).

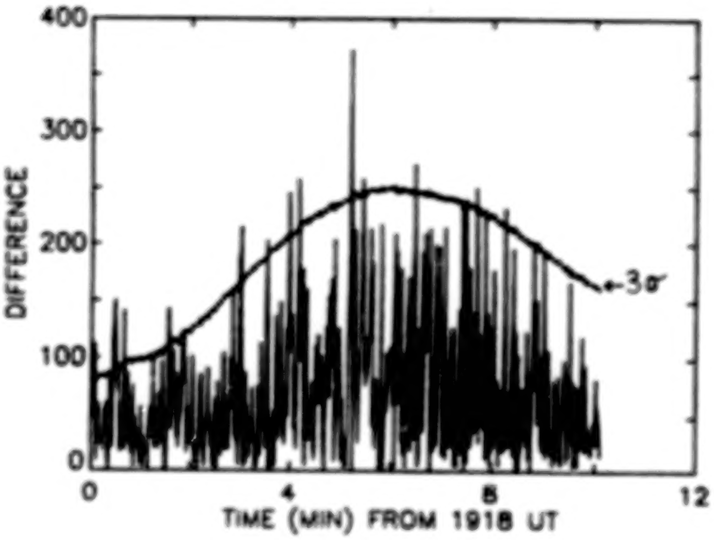

Figure 3

The detection of persistent variations in the Fe XXI emission by the Fourier analysis does not preclude the existence of isolated bursts that have timescales much shorter than those indicted by the Fourier Power spectrum. Close examination of the data shows there are isolated large changes; see Figures 1 and 2. To examine the reality of such isolated fast variations, we plotted the difference (absolute value) between the observed intensity and a calculated mean intensity (Figure 3). The calculated mean is obtained by a seventh power polynominal fitting of the observed data. Also plotted in the figure is the 3σ level calculated from Poisson statistics for the observed data. Out of 500 intervals (a total time period of 10 minutes), there are about 22 intervals in which the observed intensities are above the 3σ level. This represents a probability of 4.4% of occurrence of a signal that is above the mean. From the Poisson distribution, we know that the probabilty of occurrence of a 3σ signal is 0.3% (Bevington, 1969). Therefore, the occurrence of a 3σ signal above the mean in the observed data is 15 times greater than that indicated by the Poisson statistics. In other words, we would only expect less than 2 intervals in which the signal rises above the mean, if the 3σ signals are purely random fluctuations. We can conclude that the observed fast variations, with large amplitudes, are statistically significant, and, to a reasonable degree of certainty, real. One particular isolated change with large variation can be seen in Figure 1 just before maximum intensity. The intensity jumps about 15% in about 4 sec. Other isolated bursts show similar timescales of fast variation. We emphasize that the existence of isolated fast bursts in our data should only be understood in the statistical sense.

In Figure 4 we present the Fe XXI light curve for the whole raster as well as its power spectrum for the 6 November 1980 flare. This flare occurred in AR 2779 which in Hα started at 1228, reached maximum at 1236, and ended at 1258 UT. The Hα class is unknown but the X-ray class is M3. The Fe XXI observations started at 1232 UT and continued until 1233 UT. The FOV of the UVSP covered only part of the flare. The figure shows that the shortest timescale of fluctuations in the Fe XXI emission is about 20 sec, corresponding to a cutoff frequency of about 0.05 sec.

Another example of the Fourier analysis of the Fe XXI emission is the 11 November 1980 flare. This flare also occurred in AR 2779. It was a SN flare in Hα, which started at 0625 UT, peaked at 0632 UT, and ended 0645 UT. In

X-ray, the flare was a M1. The Fe XXI observation started at 0628 UT and lasted for 10 minutes. This flare is interesting in that the FOV of the fast Fe XXI mode covered an area located at the top of the flaring loop (Cheng and Pallavicini, 1985). In Figure 5, we show the total Fe XXI intensity and its power spectrum. The power rises above the noise level at about f = 0.1 sec^{-1}, which gives a time scale of 10 sec. The relative error at f = 0.1 sec^{-1} is about 10% (Figure 5). When the light curve of the brightest pixel is Fourier analyzed, as shown in Figure 6, the cutoff frequency that can be identified in the power spectrum is about f = 0.05 sec^{-1}, corresponding to a period of about 20 sec. For this flare there are 3 intervals out of 500 that are 3σ above the mean. This is what is expected from the Poisson statistics, and therefore, we would not claim that the isolated large variations in the data are real.

3. SUMMARY AND DISCUSSIONS

We have made a search for fast variations in the Fe XXI emission for ten flares using the Fourier analysis. Examples of three flares were described in the previous section. Here we summarize the main results:

1) We do not detect any periodic oscillation in the Fe XXI emission in any of the flares studied.

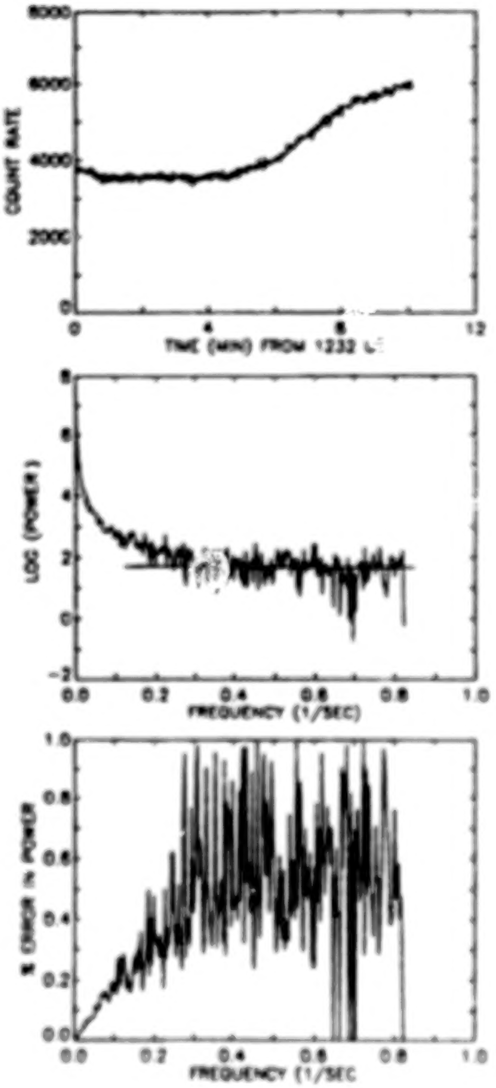

Figure 4

2) The shortest timescale of rapid variation, persistently present, in the Fe XXI emission is about 20 sec or longer.

3) Statistically significant isolated bursts of 3 to 5 sec duration are found in some of the flares. These isolated bursts, superimposed on the general gradual time profile of the Fe XXI emission, have an intensity variation from the mean by as much as 15%.

The main purpose of the paper is to find the shortest timescale, persistently present, in the Fe XXI emitting plasma. A timescale of about 20 sec in the Fe XXI emission is considerably greater than the subsecond variation found for the impulsive hard X-ray bursts (Kiplinger et al. 1983). If the heating of the Fe XXI emitting plasma or the soft X-ray emitting plasma is due to the energy deposition of the energetic electrons responsible for the impulsive hard X-ray burst, as is commonly assumed, then there might be some is due to the energy deposition of the energetic electrons responsible for the impulsive hard X-ray burst, as is commonly assumed, then there might be some

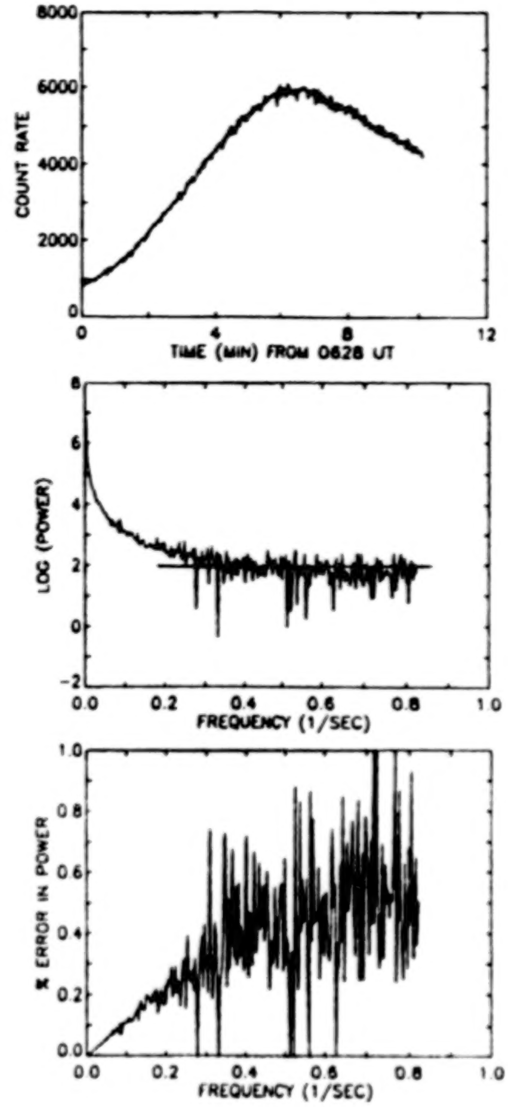

Figure 5

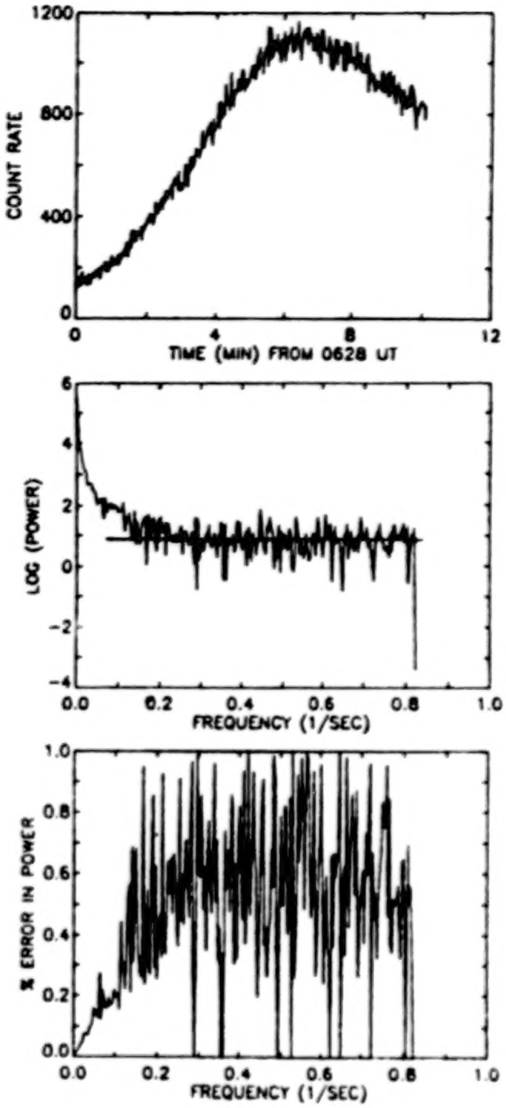

Figure 6

causal relationship between the time variations of the two components. We note that the chromospheric evaporation, which in the electron deposition model is the mechanism by which the soft X-ray bursts are powered, begins within seconds after the electron beam has heated the chromosphere (see, for example, Fisher et al. 1985; MacNeice et. al. 1984). If a variable electron beam is responsible for the fast variations in hard X-ray bursts, then we would also expect the thermal response of the chromosphere in the form of evaporation to vary accordingly, thereby manifested in the variations of the soft X-ray emissions. We then might expect to find intensity variation on the order of seconds in the Fe XXI emission. As we have seen, the shortest time

C-4

scale of variation we found in our data is about 20 sec. Since the energy transfer process and the thermal response of the chromosphere are complicated and are not precisely known, it is difficult, at the present time, to conclude whether the timescales we found for the Fe XXI emitting plasma are due to variations in the electron energy depositions. A better understanding of the timing relationship between the various emission components in the electron energy deposition model has to wait for more realistic numerical calculations (see Canfield et al. 1986).

This work is supported in part by NASA under Contract DPR W-15367.

REFERENCES

Bevington, P.R. 1969, Data Reduction and Error Analysis for the Physical Sciences (New York : McGraw Hill).
Brown, J.C., Loran, J.M., and MacKinnon, A.L. 1985, Astron. Astrophys. 147, L10.
Canfield, et al. 1986, in Proceedings of the SMM Workshops on Solar Flares.
Cheng, C.-C., and Pallavicini, R. 1985, preprint.
Doschek, G.A., Kreplin, R.W., and Feldman, U. 1979, Ap. J. (Letters), 233, L157.
Dosheck, G.A. et al. 1980, Ap. J., 239, 725.
Feldman, U., et al. 1980, Ap. J., 241, 1175.
Fisher, G.H., Canfield, R.C., and McClymont, A.N. 1985, Ap. J., 289, 414.
Hoyng, P. 1976, Astron. Astrophys. 147, L10.
Hoyng, P., Brown, J.C., and Van Beek, H.F. 1976, Sol. Phys., 48, 197.
Kiplinger, A. et al. 1983, Ap. J. (Letters), 265, L99.
MacNeice, P., McWhirter, R.W.P., Spicer, D.S., and Burgess, A. 1984, Sol. Phys., 90, 357.
Zarro, D., Strong, K., and Saba, J. 1985, preprint.

N87
21812
UNCLAS

N87-21812

FAST TEMPORAL CORRELATION BETWEEN HARD X-RAY AND ULTRAVIOLET CONTINUUM BRIGHTENINGS

Marcos E. Machado*

Space Science Laboratory, ES52
NASA Marshall Space Flight Center
Alabama 35812, U.S.A.

Pablo J. Mauas

Instituto de Astronomia y Fisica del Espacio
Buenos Aires, Argentina

ABSTRACT

Recent Solar Maximum Mission (SMM) observations have shown fast and simultaneous increases in hard X-rays (HXR, E>25 keV) and ultraviolet continuum (UVC, λλ ≈ 1600 and 1388 A) radiation. We give a simple and natural explanation for this phenomenon to happen, which does not involve extreme conditions for energy transport processes, and confirms earlier results on the effect of XUV photoionization in the solar atmosphere.

1. INTRODUCTION

Recent SMM observations, see Orwig and Woodgate elsewhere in these proceedings, have shown that besides the close temporal correlation between UV line emission originating in the transition zone (TZ) and HXR emission at E > 30 keV (Woodgate et al., 1983), a similar relationship exists between HXR's and ultraviolet continuum (UVC). As shown by Orwig and Woodgate, the correlation holds in some cases to better than 0.1 s, with details that can be found in their paper, thus extending the relationship between HXR and UV emission to radiation originating in deep atmospheric levels around the temperature minimum region (TMR).

As shown by Vernazza et al. (1976, 1981) for the quiet Sun and Machado et al. (1980) and Machado and Hénoux (1982) for the case of flare atmospheres, the continuum radiation within λλ 1350 -1680 A originates close to the TMR and is primarily due to SiI. It is also known (Vernazza et al., 1981) that the source function of the silicon continua, with edges at 1682 and 1525 A, is significantly decoupled from the local Planck function, due to the strong effect of the photoionization term in the ionization balance equation

$$n(\mathrm{SiII})/n(\mathrm{SiI}) = \frac{4\pi \int (\sigma_\lambda J_\lambda/h\nu)\, d\lambda + C}{R}\,, \qquad (1)$$

---

*NAS/NRC Research Associate, on leave from CNIE, Argentina.

PRECEDING PAGE BLANK NOT FILMED

where C and R are the collisional ionization and recombination rates respectively, and σ_λ is the photoionization cross section which we take from Vernazza et al. (1976). Since the radiation field that SiI "sees" is characterized, even in the quiet Sun, by a radiation temperature larger than the local electron temperature, T_e, it results that the source function of the continuum, S_λ, is

$$S_\lambda(\mathrm{SiI}) > B_\lambda(Te) \ , \tag{2}$$

where B_λ is the Planck function, at and around the optical depth unity ($\tau = 1$) level in both continua. This, in turn, leads to emergent intensities characterized by radiation temperatures larger than the local T_e at those depths.

Therefore, any increase in the UVC radiation, which basically reflects an increase in $S_\lambda(\mathrm{SiI})$ at $\tau \approx 1$ for each of the continua, may either be due to an increase in the J_λ term of equation (1), which would further increase the S_λ decoupling with respect to $B_\lambda(T_e)$, or by a strong increase in the collisonal term C, associated with an increase in the local temperature at the TMR. If by some means, presumably a large increase in the electron density n_e, the C term becomes dominant under flare conditions, then $S_\lambda \approx B(T_e)$ and the brightness temperature changes, which have been reported to be $\Delta T_b > 560$ K (see below) for uniform filling over the observed area (Woodgate, private communication), would represent local changes in the TMR temperature during the flare. Such an increase would then imply a change in the internal energy of the plasma,

$$\Delta E = 1.5 \ n_H \ k \ \Delta T > 460 \ \mathrm{erg \ cm^{-3}} \ , \tag{3}$$

where we have taken $n_H = 4 \times 10^{15}$ cm^{-3} at the depth of SiI continuum formation. Considering that radiative loss rates, primarily due to H^-, can be estimated to be of the order of 10 erg cm^{-3} s^{-1} under such conditions (Machado et al., 1986; Mauas and Machado, 1986), the large ΔE value from (3) implies extremely large energy deposition rates at the TMR, unlikely to be attained by any canonical energy transport mechanism like accelerated particles or XUV heating, not to mention heat conduction which is totally ineffective at those depths (Emslie et al., 1981).

Furthermore, it can be easily demonstrated (Mauas and Machado, 1986) that nonthermal electron beam ionization of hydrogen (Ricchiazzi and Canfield, 1983), which can lead to a local increase in n_e without any accompanying large change in T_e, is rather ineffective at these depths, due to the strong attenuation of the beam above the TMR.

We are thus left with either the possibility that strong and rapid local heating, as specified in (3), occurs at the TMR during the HXR/UVC bursts, or that the observed increase is due to a change in the J_λ term of equation (1). Bearing in mind the unlikeness of the first, for conventinal energy transfer conditions, we explore in the next section the effect of the second.

2. THE EFFECT OF ULTRAVIOLET IRRADIATION

As shown by Machado and Hénoux (1982), the photoionization term on the right hand side of equation (1) can be decomposed into a J_λ^o term, reflecting the undisturbed quiet Sun conditions, and an additional J_λ^T term which corresponds to flare irradiation from lines formed in the chromosphere/corona TZ. The net effect of J_λ^T, which is principally related to the increase in the CIV line emission at 1549 A, is to alter the SiII/SiI ionization balance, through photoionization from the ^1D level (1682 A continuum) which is very effectively coupled through collisions, and thus in detailed balance, with the most populated ^1S level (1525 A continuum, see Vernazza et al., 1981; Machado and Hénoux, 1982). Therefore, the effect of the largely increased flare J_λ^T term is to overionize SiI through the TMR, as compared with the results of equation (1) for undisturbed model atmospheres like those of Vernazza et al. (1981).

The effect of the increase in n(SiII)/n(SiI) is twofold, it increases the depth at which τ (continuum) = 1 in the atmosphere, while at the same time it enhances the already present decoupling between S_λ and $B_\lambda(T)$, increasing the inequality of equation (2) and leading to brightness temperatures much larger than the local T_e.

Using spatially averaged values of UV irradiation, I(UV), as measured by Skylab, Machado and Hénoux (1982, see references therein) found that for $I(UV) = 4 \times 10^5$ erg cm^{-2} s^{-1} sr^{-1} the variation of S_λ leads to a $\Delta T_b \approx 280$ K, without any associated increase in the local temperature as compared with the Vernazza et al. (1976) values. We have now performed a similar calculation using Vernazza et al. (1981) model C atmospheric parameters, with ad-hoc constant irradiation values $1 \times 10^6 < I(UV) < 5 \times 10^6$ erg cm^{-2} s^{-1} sr^{-1}, which are more appropriate for flare kernels during the impulsive phase as compared with the averaged flare decay values of Machado and Hénoux. The details of these straightforward statistical equilibrium calculations, in which we have kept all model C parameters and ionization equilibrium of elements other than SiI unchanged, will be reported elsewhere in conjunction with a self consistent, time varying modeling of specific burst observations (see below). It suffices to say here that these increased irradiation values lead to correspondingly larger equilibrium T_b increases, of the order

$$360 \text{ K} < \Delta T_b < 690 \text{ K}, \qquad (4)$$

in both the 1525 and 1682 A continua. These values are to be compared to the $\Delta T_b \approx 560$ K as observed at $\approx$ 1600 A in the 20 May, 1984 event, and $\Delta T_b \approx 870$ K at 1388 A in the 24 April, 1985 flare (Woodgate, private communication; see Orwig and Woodgate in these proceedings).

Furthermore, the characteristic rate of increase of n(SiII) at the optical depth unity level in the ^1D continuum ($h \approx 400$ km in the irradiated model C), is given by

$$dn(SiII)/dt \approx 7.8 \times 10^{10}\, dF(UV)/dh = 1.32 \times 10^{10} \text{ cm}^{-3} \text{ s}^{-1}, \qquad (5)$$

for $I = 10^6$ erg cm^{-2} s^{-1} sr^{-1}, for $F = 2\pi I$ and assuming that the ionizing flux is concentrated in the CIV line. This gives, for characteristic silicon densities at these depths (see Vernazza et al., 1981), a characteristic e-folding time of SiII increases of the order of $\approx$ 1.7 seconds, and commensurably shorter values for larger ionizing fluxes.

3. DISCUSSION

In the preceding section we have reported that increases in the UVC brightness temperature can be effected, as far as steady state statistical equilibrium calculations show, by the strong photoionization effect of transition zone UV irradiation under flarelike conditions. Irradiation fluxes of the order of $\approx 10^7$ erg cm^{-2} s^{-1} seem to be enough to explain the observed increases in the UVC brightness and, furthermore, they should occur extremely rapidly.

On the other hand, we would like to clearly note here that our results are of very preliminary nature, since they are based on ad-hoc conditions of constant UV irradiation, as compared with the spiky nature of the bursts. In a subsequent study we shall model the HXR-TZ emission-UVC correlation for a set of events, taking into account the observed temporal dependence and absolute value of the TZ irradiation. In spite of these shortcomings in our present study, there are a few aspects worth pointing out in the results which would still stand up after a more detailed study:

a) The strong temporal correlation between TZ and UVC bursts was a definite prediction of the irradiation model (Machado and Hénoux, 1982; Machado et al., 1986), which has been at least qualitatively confirmed by the SMM observations.

b) A temporal correlation between HXR and UVC bursts can only be possible, in our model, through an equally strong correlation between HXR's and transition zone UV emission. Since this correlation is known to exist (Tandberg-Hanssen et al., 1983; Woodgate et al., 1983) and to support the nonthermal thick target model, the HXR/UVC correlation also supports the thick target model for as much as the previous one does, even though there is no direct cause-effect relationship between particle heating or ionization and UVC increases.

c) We further note that the observed increases can simply be due to a relatively minor energy transport towards the deep atmosphere, as compared with any model that invokes localized heating at and around the TMR. For example, instead of the $\approx 10^7$ erg cm^{-2} s^{-1} needed in our computations, Aboudarham and Hénoux (1986) have found that in order to heat the TMR by electron beams, the power in the accelerated particles should exceed 10^{11} erg cm^{-2} s^{-1} for electrons with energies above 20 keV.

ACKNOWLEDGEMENTS

We thank A.G. Emslie, E. Tandberg-Hanssen and B.E. Woodgate for useful discussions and for providing data in advance of publication.

REFERENCES

Aboudarham, J. and Henoux, J.-C., 1986, Astron. Ap., in press.

Emslie, A.G., Brown, J.C. and Machado, M.E., 1981, Ap. J. 246, 337.

Machado, M.E., Emslie, A.G. and Brown, J.C., 1978, Solar Phys. 58, 30.

Machado, M.E. and Henoux, J.-C., 1982, Astron. Ap. 108, 61.

Machado, M.E., Emslie, A.G. and Mauas, P.J., 1986, Astron. Ap., in press.

Mauas, P.J. and Machado, M.E., 1986, Proceedings of the NSO Workshop on the Physics of the Low Temperature Flare, in press.

Tandberg-Hanssen, E., Reichmann, E. and Woodgate, B.E., 1983, Solar Phys. 86, 159.

Vernazza, J.E., Avrett, E.H. and Loeser, R., 1976, Ap. J. Suppl. 30, 1.

____________________, 1981, Ap. J. Suppl. 45, 635.

Woodgate, B.E., Shine, R.A., Poland, A.I. and Orwig, L.E., 1983, Ap. J. 265, 530.

N87
21813
UNCLAS

N87-21813

COMPARISON OF SOLAR HARD X-RAY AND UV LINE AND CONTINUUM BURSTS WITH HIGH TIME RESOLUTION

L. E. Orwig and B. E. Woodgate

Laboratory for Astronomy and Solar Physics
NASA/Goddard Space Flight Center
Greenbelt, MD 20771

ABSTRACT

The close temporal correlation between the ultraviolet line emission from OV (λ 1371Å) and hard X-rays above 30 keV has been previously established from a comparison of data sets from the Ultraviolet Spectrometer and Polarimeter (UVSP) and Hard X-Ray Burst Spectrometer (HXRBS) instruments on SMM. Corresponding features were found to be concident to within 1 s. Following the SMM repair, similar measurements were made for a flare occurring on May 20, 1984 at 0259 UT, this time with UVSP observing in the continuum near 1600Å with much higher time resolution (75ms). The simultaneity of several features in this flare have been established to better than 0.1 s, thus reinforcing the close relationship between hard X-ray and UV emission.

Following the repair of the UVSP wavelength drive, similar measurements were repeated for a flare occurring at 0148 UT on April 24, 1985. This event was observed simultaneously in the OV line, the UV continuum and in hard X-rays by the same SMM instruments. Temporal comparisons of the three data sets show that, for a few selected features, simultaneity of the hard X-ray and UV emissions does exist. However, cross-correlation analyses of the entire data sets indicate that there is a trend for the fastest OV emission features to be delayed with respect to the hard X-rays by ~ 260 ms. On the other hand the fast OV and UV continuum features are simultaneous to within the instrumental uncertainty.

The combined results have established the close relationship of the impulsive phase hard X-ray and UV continuum and OV line emissions. They lend support to the argument that both the hard X-ray and UV radiations originate low in the solar atmosphere. Such results place severe constraints on models which attempt to explain impulsive phase hard X-ray and UV emission and may be important in proving the existence, or lack thereof, of electron beams in the impulsive phase of flares. These results indicate that alternative processes for impulsive phase UV continuum production should be considered. Models currently under investigation include an electron beam "hole boring" mechanism (Woodgate and Orwig) and a photoionization radiation transport mechanism (Machado and Mauas).

Published in Proceedings of the NSO/SMM Summer Meeting on Relationships Between Low Temperature Plasmas and High Enegy Emissions, 1986.

PRECEDING PAGE BLANK NOT FILMED

N87
21814
UNCLAS

N87-21814

OV AND HARD X-RAYS, OBSERVATIONS AND MODEL CALCULATIONS

A. I. Poland

Laboratory for Astronomy and Solar Physics
NASA/Goddard Space Flight Center
Greenbelt, MD

J. T. Mariska

E. O. Hulburt Center for Space Research
Naval Research Laboratory
Washington, DC

Abstract

This paper is an amalgamation of two published works that discuss the observation and theoretical calculations of OV (T~250,000K) and Hard X-rays (30-100kev) emitted during flares. The papers are by Poland et al (1984) and Mariska and Poland (1985). The observations of Hard X-rays and OV show that the excitation processes for each type of emission are closely coupled. Except for small differences the two types of emission rise and fall together during a flare. Model calculations are able to reproduce this behavior to a large extent, only when conductive processes do not dominate the energy transport processes.

PRECEDING PAGE BLANK NOT FILMED

Discussion of Figures

Figure 1 shows the light curves for one flare in OV and HXR. The upper curve shows emission in OV for the entire flare area as a function of time (actual values are 10^{23} times larger than shown), while the lower curve shows HXR emission above 25kev (actual values are 3.84×10^{20} times larger than shown). The noise errors for a single measurement are shown as vertical bars. It can be seen from this figure that OV and HXR peaks occur simultaneously and that OV and HXR rise and fall together.

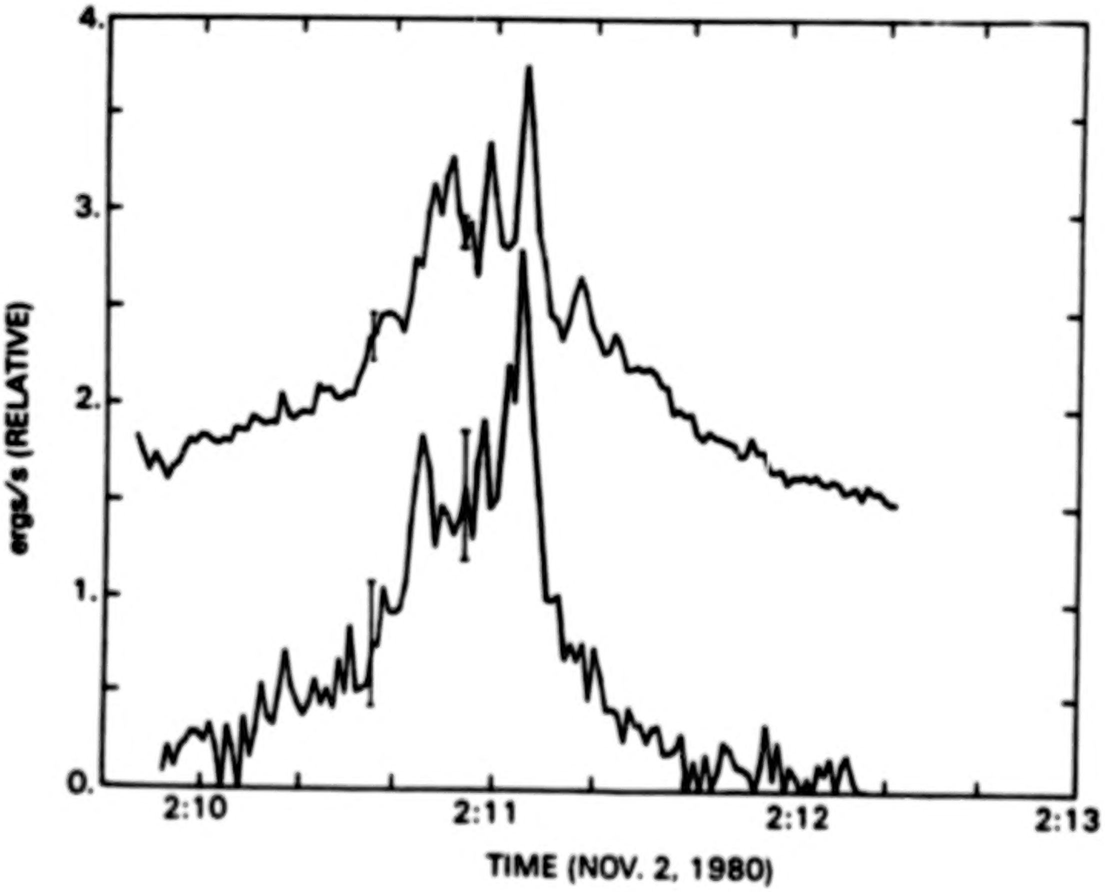

Figure 1

Figure 2 shows the energy emitted in HXR as a function of energy emitted in OV on a log - log scale. Squares are before flare maximum, diamonds are within 5 s of maximum, and plus signs are after flare maximum. Only every third point has been plotted for clarity of the figure. It can be seen that for this flare they both rise and fall together and peak at the same time. There has been some discussion in the past about the importance of the slope of this curve and the large change in HXR for a small change in OV. First, it can be seen from Figure 1 that most of the range of HXR in Figure 2 is from the lowest brightnesses and may be due mostly to noise. Second, the lowest brightnesses of OV are highly influenced by the size of the area chosen for measurement and the background brightness. Only the brightest few points have a significantly measurable slope which is not clearly unique, so the physical significance of this is unclear. The significant result is that HXR and OV rise and fall together with only a small hysteresis.

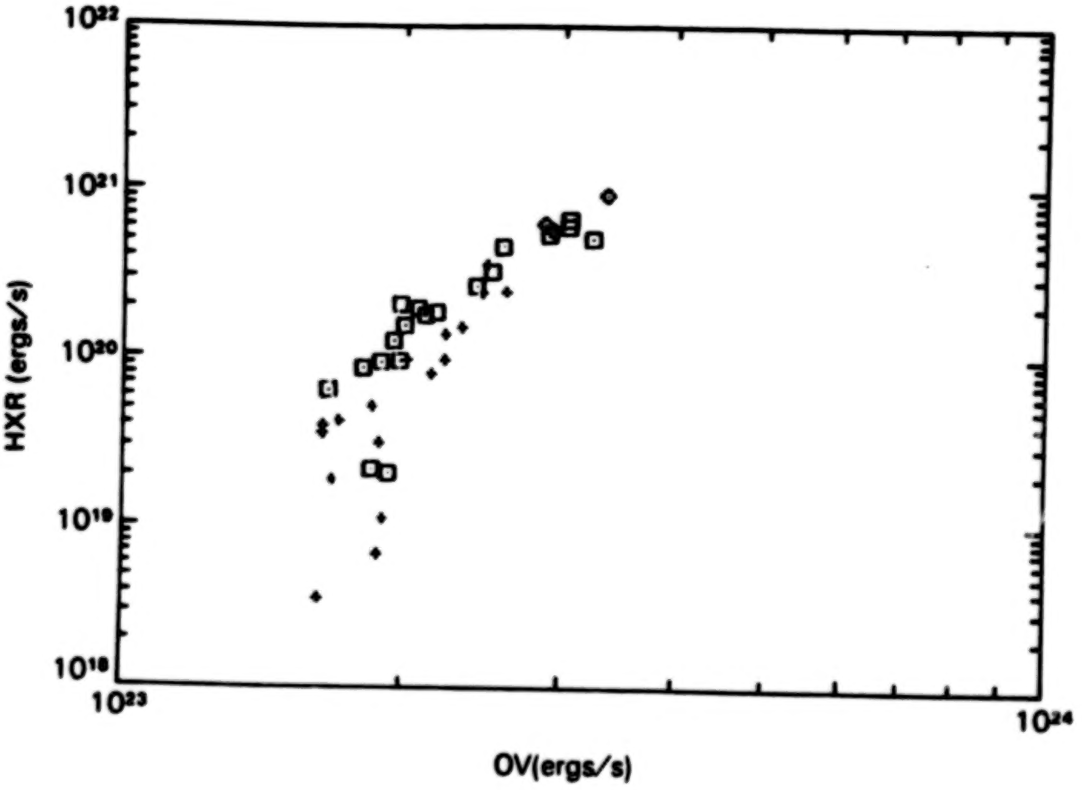

Figure 2

Figure 3 shows a plot similar to Figure 2 for several flares. Note that while most flares rise and fall together some show a lag in the fall of OV. This lag behavior is what is expected when conduction begins to become an important factor in the energy transport. The numbers refer to the flare number (see Poland et al 1984). Curves labeled with a solid line are disk flares; -.- are limb flares; and - - - are on the disk but near the limb. Arrows on the split curves show the direction in time. Number 7 is the same flare shown in Figures 1 and 2.

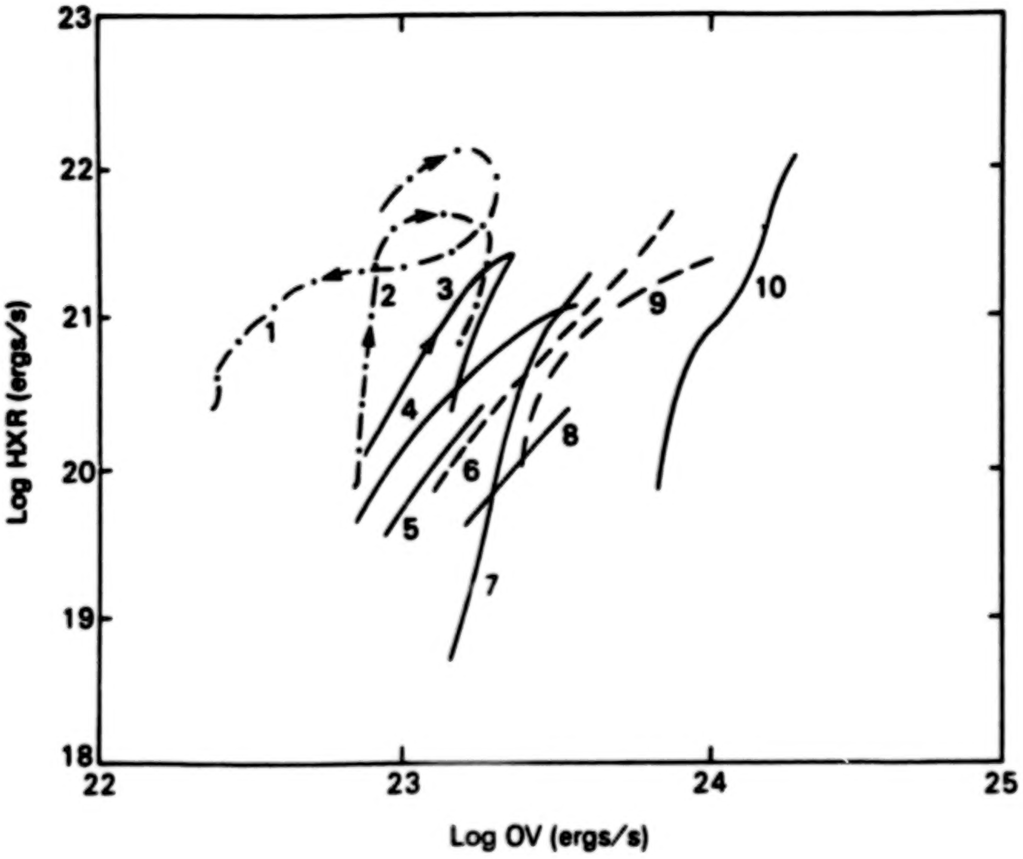

Figure 3

Figures 4 and 5 show the effect of heating location on the model calculations. We plot temperature vs. column mass with the temperature of OV formation bracketed by the two horizontal lines. Time evolution is shown by the numbers 0., .5, 1. etc.. It can be seen that when heat is deposited below the transition region (a) there is obviously an enhancement of OV until later times when the temperature gradient steeps due to conduction. Even at these later times OV is enhanced because Ne^2 dominates the smaller Δm. In the case where heat is deposited above the transition region (b) it is not obvious that OV is enhanced. The steepening temperature gradient reduces Δm but because the transition region is driven deeper into the atmosphere Ne^2 increases. Detailed calculations show that it increases in this case also but the results are highly model dependent. Once the heat source is turned off in these cases OV does not immediately decrease because conduction continues to supply heat from the now enhanced corona or flare loop.

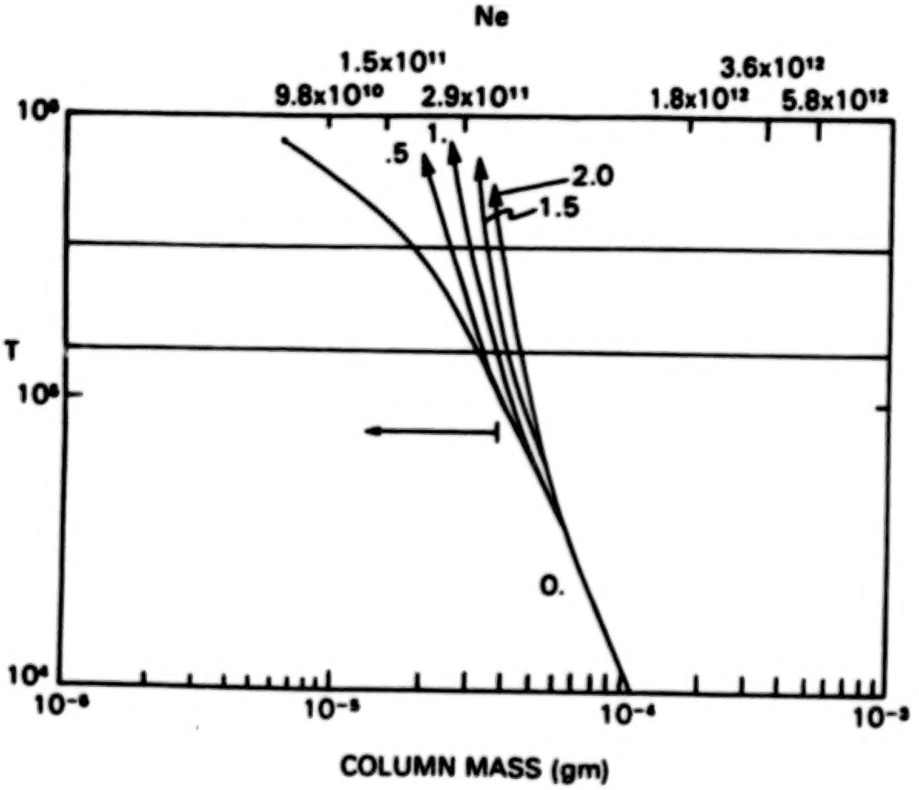

Figure 4

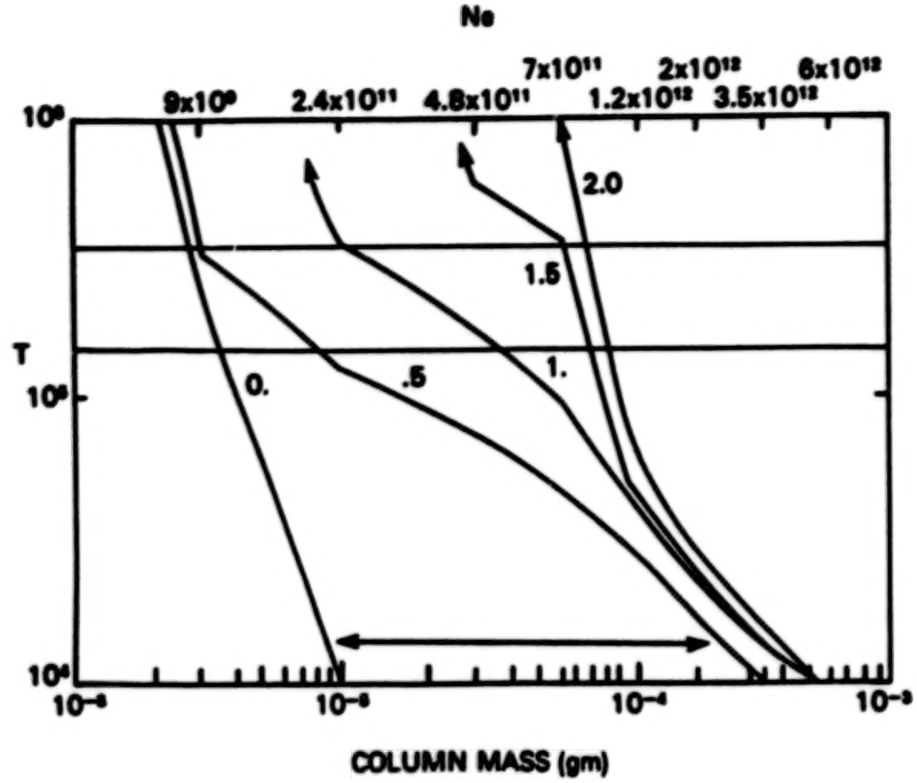

Figure 5

Figure 6 shows the more detailed calculations discussed in Mariska and Poland (1985). The figure shows temperature and emission measure distributions at various times during the flare for one model. The order of the times listed on the left panels corresponds to the ordering in temperature of the peaks in the 1600km region and the ordering of the emission measure curves between log T of 4.8 and 5.0. For clarity the plots are separated into pre and post maximum sections. The initial model parameters are indicated in the upper left panel.

Figure 7 shows the relation between the power emitted in HXR and the power emitted in OV 1371 A for the four different combinations of initial pressure and beam flux discussed in Mariska and Poland (1985).

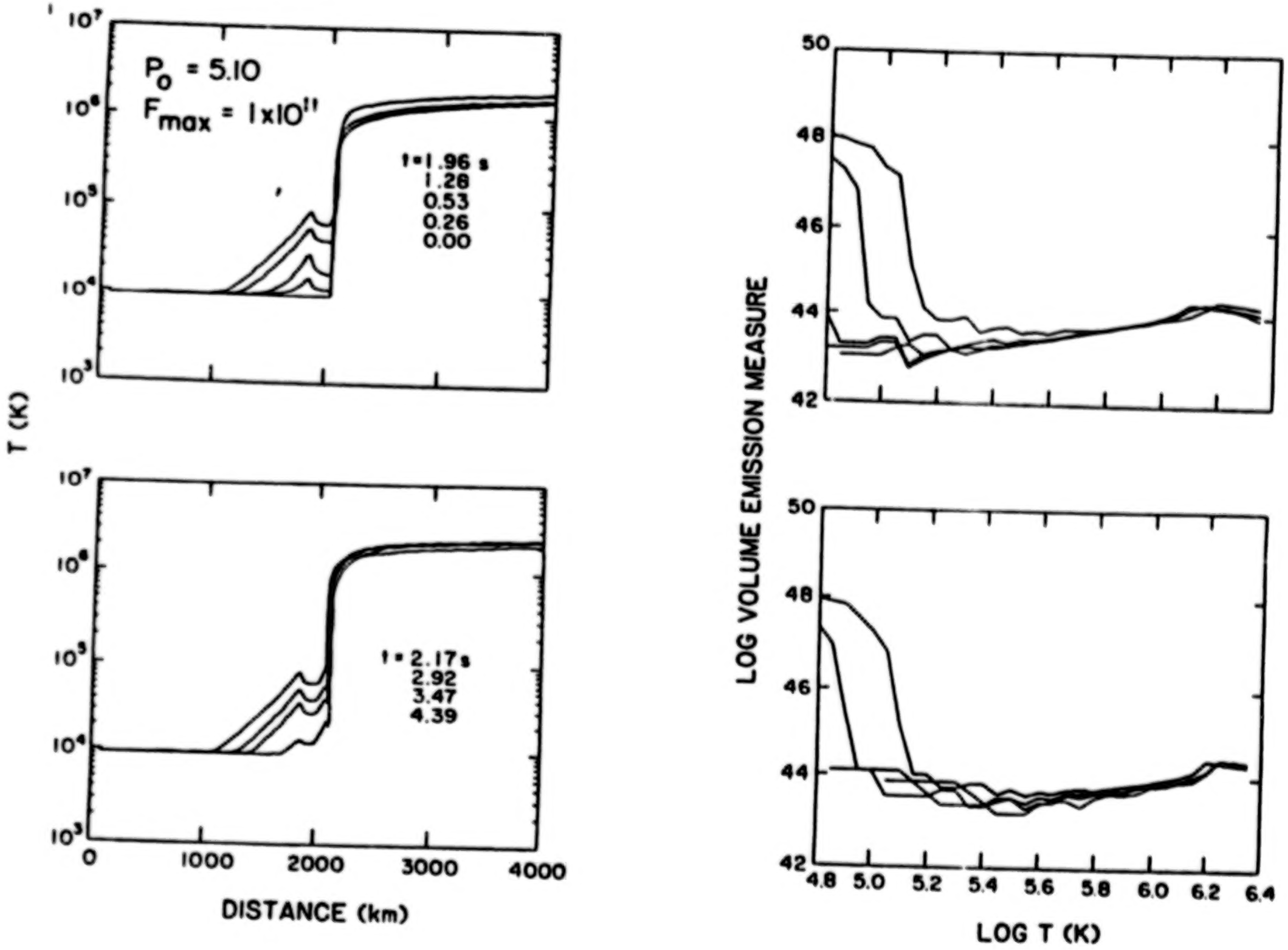
P_o = 5.10
F_{max} = 1x10^{11}
t=1.96 s
1.28
0.53
0.26
0.00
t=2.17s
2.92
3.47
4.39
T (K)
10^3
10^4
10^5
10^6
10^7
0
1000
2000
3000
4000
DISTANCE (km)
LOG VOLUME EMISSION MEASURE
42
44
46
48
50
4.8
5.0
5.2
5.4
5.6
5.8
6.0
6.2
6.4
LOG T (K)

Figure 6

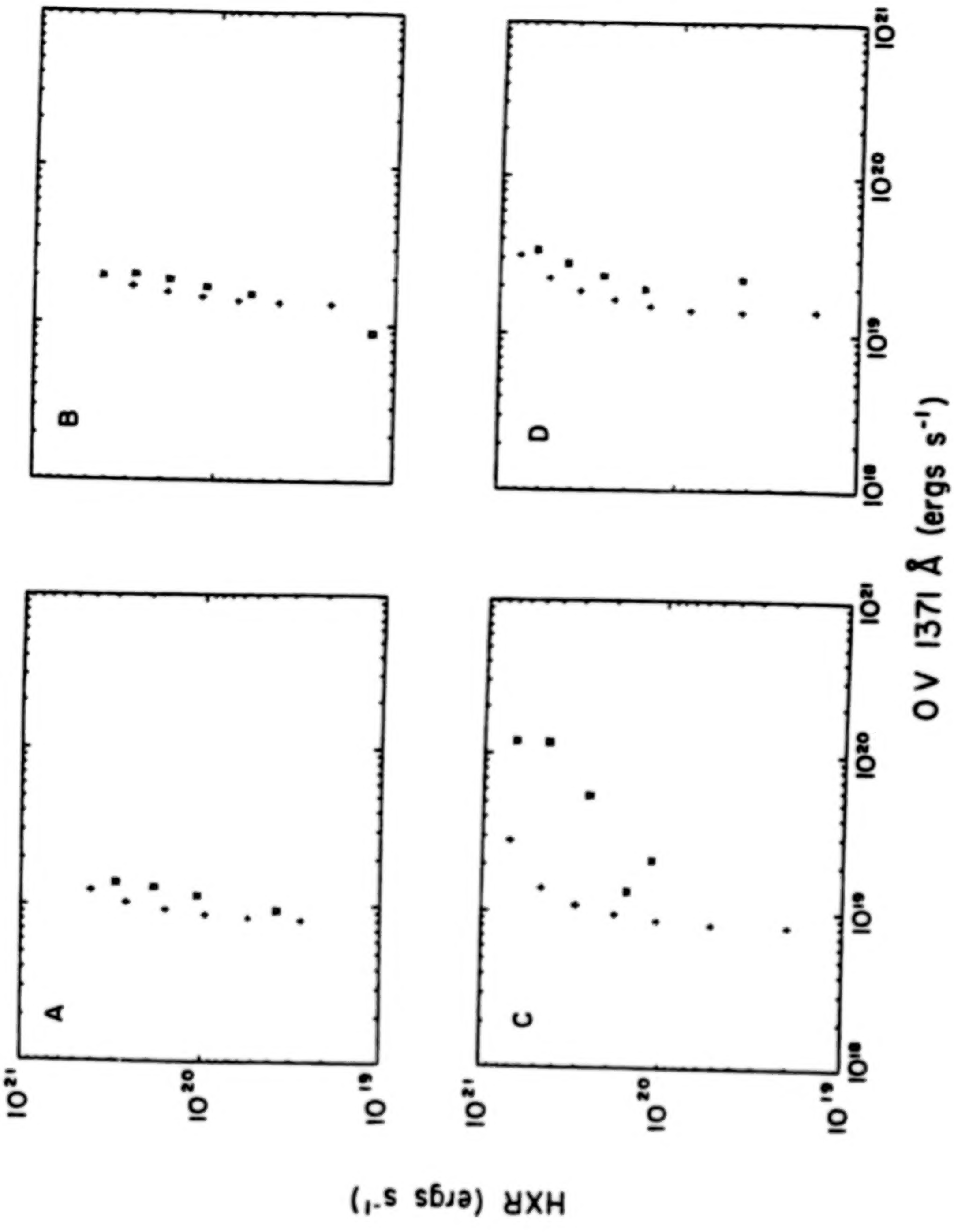

Figure 7

Premaximum points are indicated with pluses and postmaximum points are indicated with stars. The time separation between each point is roughly 0.25s. This figure shows that to avoid the hysteresis observed in case c, it is essential that conduction not become the dominant source of enhanced heating. This required a relatively high density, and a short heat input. If the heat input is long and of low energy, temperature enhancements in the chromosphere will be of too low a value to provide the observed enhancements.

Conclusions

We can think of few possibilities that would allow the OV and HXR to follow each other as is observed. These are: 1) The impulsive phase loops are separate from the the gradual phase loops and do not reach temperatures greater than approximately $2\mathrm{x}10^6$K. There are many loops each "firing" for a second or two and relaxing for several seconds before "firing" again. 2) Conduction is almost totally inhibited so that the transition region is heated only directly by the electron beam.

Acknowledgments

The work of J.T. Mariska was supported by a NASA/SMM guest investigator grant and by the Office of Naval Research.

References

Poland, A.I., Orwig, L.E., Mariska, J.T., Nakatsuka, R., and Auer, L.H.: Ap J 280, 457, 1984.
Mariska, J.T., and Poland, A.I.: Solar Physics 96,317, 1985

N87
21815
UNCLAS

N87-21815

RAPID SOFT X-RAY FLUCTUATIONS IN SOLAR FLARES OBSERVED WITH THE X-RAY POLYCHROMATOR

D. M. Zarro and J. L. R. Saba

Applied Research Corporation
Landover, MD

K. T. Strong

Lockheed Palo Alto Research Laboratories
Palo Alto, CA

ABSTRACT

We have studied three flares observed by the Soft X-Ray Polychromator on the Solar Maximum Mission. Flare light curves from the Flat Crystal Spectrometer and Bent Crystal Spectrometer were examined for rapid signal variations. Each flare was characterized by an initial fast (<1 min) burst, observed by the Hard X-Ray Burst Spectrometer (HXRBS), followed by softer gradual X-ray emission lasting several minutes. From an autocorrelation function analysis, we have found evidence for quasi-periodic fluctuations with rise and decay times of 10 s in the Ca XIX and Fe XXV light curves. These variations were of small amplitude (<20%), often coincided with hard X-ray emissions, and were prominent during the onset of the gradual phase after the initial hard X-ray burst. We speculate that these fluctuations were caused by repeated energy injections in a coronal loop that had already been heated and filled with dense plasma associated with the initial hard X-ray burst.

1. INTRODUCTION

Soft X-ray emission from solar flares is usually characterized by timescales ranging from several minutes to many hours. However, this impression is based on observations by instruments of limited spatial, spectral, and temporal resolution and coverage. In this paper we use Solar Maximum Mission (SMM) observations to demonstrate the existence of soft X-ray fluctuations with faster timescales of seconds to minutes.

The X-Ray Polychromator (XRP) on board the SMM is composed of two soft X-ray instruments: the Bent Crystal Spectrometer (BCS) and the Flat Crystal Spectrometer (FCS) (Acton *et al.* 1980). These instruments are ideal for high time resolution studies since they have good temporal resolution (0.5-10 s for the BCS and 0.256 s for the FCS), high spectral resolution ($\lambda/\delta\lambda > 1000$), and well-collimated fields of view (6 arcmin FWHM for the BCS and 14 arcsec FWHM for the FCS). Among the various techniques for analysing time series data, the autocorrelation function (ACF) provides a direct method of extracting the mean timescale of rapid variations that are superimposed on a slowly varying background (Jenkins and Watts 1968). The following is a brief description of the technique and its application.

Given a sequence of N observations $Y(i)$, the ACF is calculated by the formula:

$$\mathrm{ACF}(u) = \sum_{i=1}^{N-u} [Y(i) - \langle Y \rangle][Y(i+u) - \langle Y \rangle],$$

PRECEDING PAGE BLANK NOT FILMED

where u is the lag time in units of the accumulation time and $< Y >$ is the data mean. For statistically significant variations in the data, the characteristic timescale is related to the $1/e$ width of the ACF (Jenkins and Watts, 1968). This relationship is demonstrated in the following simulation. We model a fluctuating data stream by a first order autoregressive series defined by the algorithm:

$$Y(i) = aY(i-1) + bZ + c,$$

where Z denotes a random noise variable and $\tau = -\ln(a)^{-1}$ is the characteristic fluctuation timescale. The constants b and c are chosen such that the mean and variance of the autoregressive series match those of the observations. For example, figure 1a shows an example of fluctuations with $\tau = 17.5$ s, generated with a poisson noise random number generator. Figure 1b illustrates the corresponding ACF with a superposed exponential fit based on the first ten points. The timescale implied by this function is approximately $\tau = 20$ s. The error in this value may be estimated via a simple iterative procedure whereby a new autoregressive series is generated based on the current τ. An autocorrelation function is then calculated and a new τ derived. This procedure is repeated to yield a set of timescales from which a corresponding mean and standard deviation can be assigned. Thus, in the above example, five iterations with different random number seeds gave $\tau = 19.5 \pm 4$ s. Note that the autocorrelation width is an approximate measure of the mean temporal width of spike-like enhancements occuring within the data train. Hence, for example, an autocorrelation width of less than 20 s would imply that the rise and decay times of significant fluctuations are typically faster than 10 s (i.e., $\tau_{rise} \approx \tau_{ACF}/2$). In the following section we apply this autocorrelation technique to X-ray light curves for three strong solar flares observed with SMM.

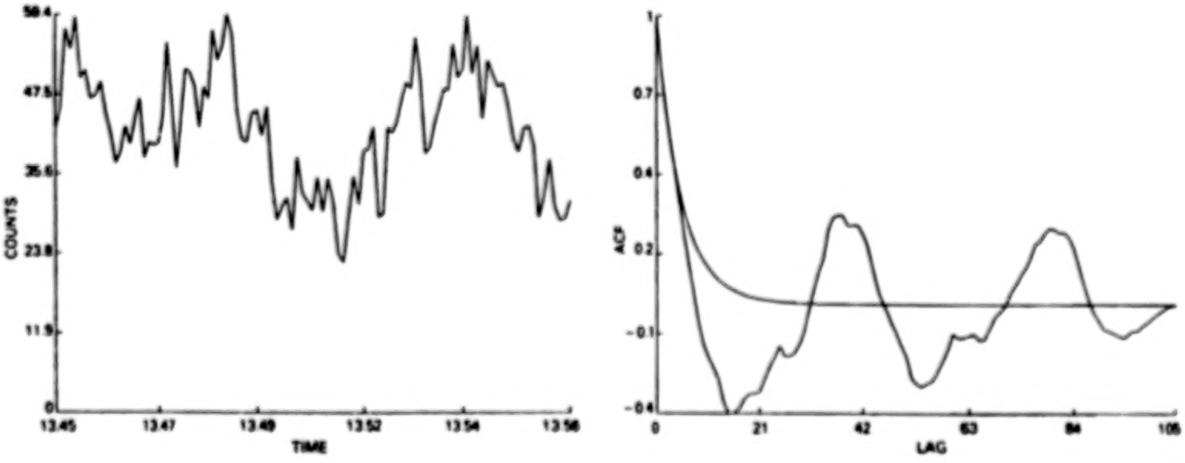

Figure 1a (left panel). Light curve representing an autoregressive series with a 17.5 s timescale fluctuation above a mean background of 42 counts. The series is generated using the algorithm described in the text. Time axis is in units of hours.

Figure 1b (right panel). Autocorrelation function of the above light curve (normalised to unity at zero lag). The smooth curve represents a fitted exponential with 20 s $1/e$ width. Time-lag axis is in units of 3.8 s accumulation bins.

2. OBSERVATIONS AND ANALYSIS

Flare 1 - GOES class M3 at UT 13:25 on 21 May 1984

This event was studied by Kaufmann *et al.* (1984), who demonstrated that hard X-ray structures and intensity fluctuations at 90 Ghz were well-correlated during the burst phase. Figure 2a indicates that hard X-ray fluctuations persisted with much weaker intensity for several minutes beyond the initial hard X-ray burst and were evidently correlated with soft X-ray features in the BCS Fe XXV (1.85 Å) and Ca XIX (3.18 Å) channels; with typical delays of less than 10 s.

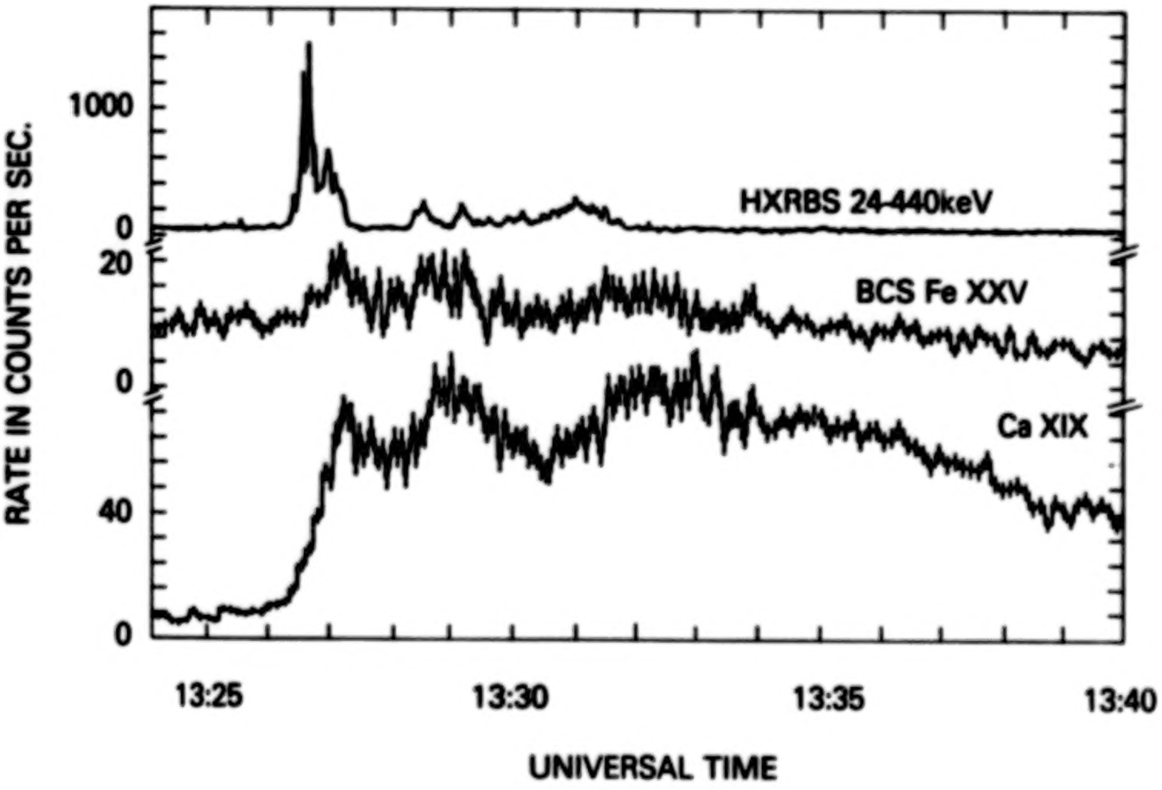

Figure 2a. HXRBS (1 s resolution) and BCS (3.8 s resolution) light curves are compared for flare 1. After the initial hard X-ray burst, there appear to be quasi-periodic fluctuations in the three light curves. Error bars denote σ variations

Figures 3a-c illustrate the HXRBS and BCS light curves in the period following the initial hard X-ray burst. The poisson error bars indicate that rapid 2-3 σ level fluctuations are present within the longer-term variation. Figures 4a-c show the corresponding autocorrelation functions for the above light curves. The fluctuation timescales implied by the $1/e$ widths are 14.1, 17.7, and 14.6 s for the HXRBS, Fe XXV, and Ca XIX light curves, respectively, with associated errors of ± 4 s. Hence, to within our measurement errors, the soft and hard X-ray emissions following the initial burst in flare 1 fluctuate with similar timescales of 15 - 20 s. Equivalently, the X-ray rise and decay times are typically faster than 10 s.

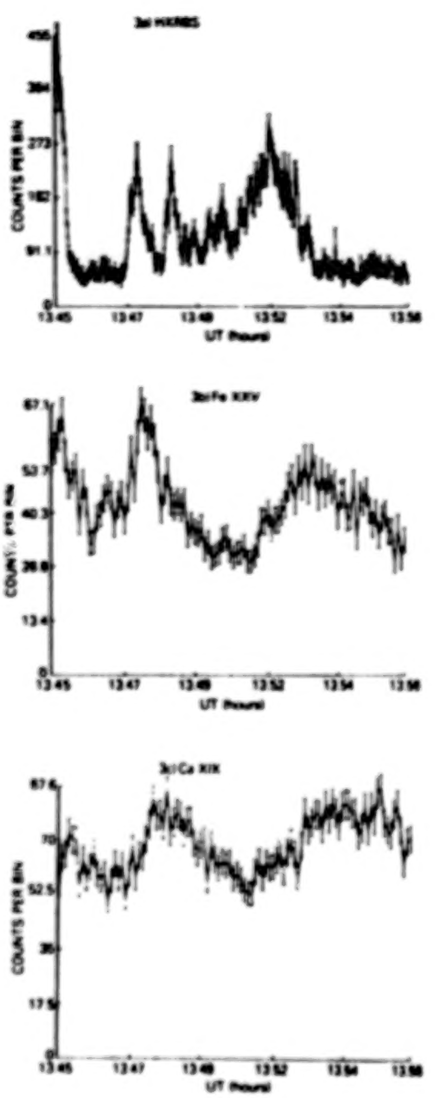

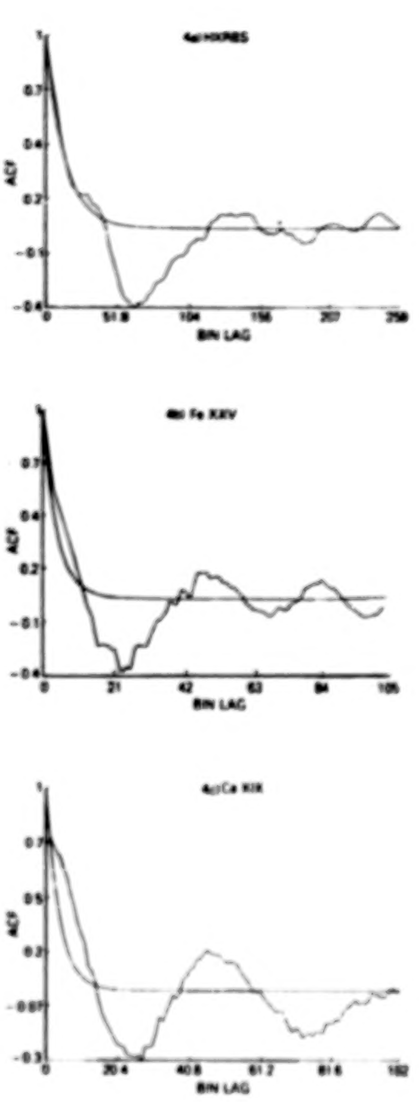

Figure 3a-c (left panel). Post impulsive phase light curves for flare 1 commencing at UT 13:27 are shown with σ poisson error bars. Intensity is in units of counts per bin resolution.

Figure 4a-c (right panel). Corresponding autocorrelation functions for the above curves with fitted exponentials.

Flare 2 - GOES class C3/M2 at UT 12:48 on 8 August 1980

Figure 2b illustrates the double event nature of this strong flare, with the second component (M2) exhibiting rapid fluctuations in the BCS Ca XIX light curve. As in flare 1, these soft X-ray features corresponded to specific hard X-ray spikes. From an autocorrelation function analysis of the second event, we inferred a characteristic spike width of 15 ± 5 s in both soft and hard X-rays. Note that this timescale is similar to the mean value obtained in flare 1.

The dynamics of flare 2 was studied by Strong *et al.* (1984), who found that the evolution of the second event was influenced significantly by the thermodynamic initial conditions created

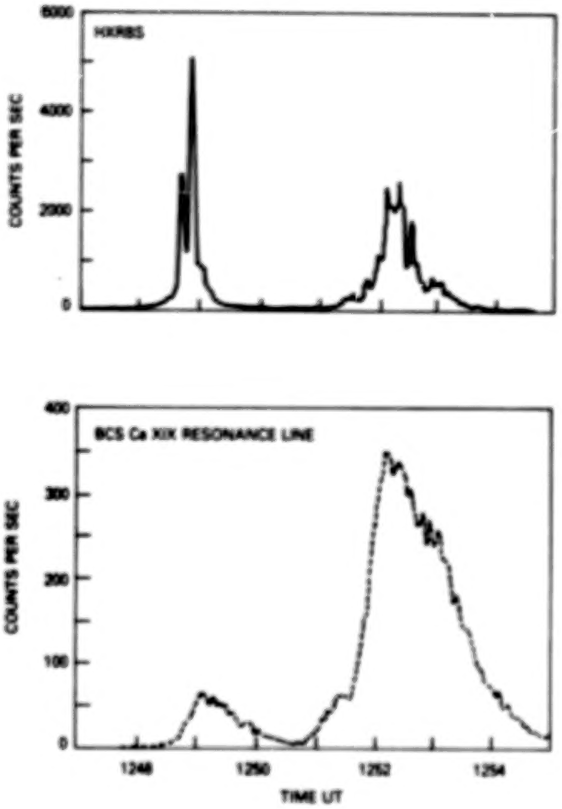

Figure 2b. HXRBS (top panel) and BCS Ca XIX (lower panel) light curves for the double-event flare 2. Note the prominence of fluctuations in hard and soft X-rays at approximately UT 12:53.

by the first event. In particular, prior to the first event, coronal plasma was relatively cool ($T_e \approx 3 \times 10^6$ K) and tenuous ($N_e \approx 4 \times 10^9 \mathrm{cm}^{-3}$). However, at the onset of the second event, the temperature and density had both increased ($T_e \approx 5 \times 10^6$K, $N_e \approx 3 \times 10^{11} \mathrm{cm}^{-3}$) due to previously heated chromospheric material being evaporated into the corona. Accordingly, Strong *et al.* (1984) suggested that a large fraction of the energy emitted subsequent to the first event would be absorbed high in the hot dense corona, with only a small proportion reaching the denser transition region and chromosphere. In view of this circumstance, we speculate that the rapid soft X-ray fluctuations that characterize the second event are a consequence of local heating by energy deposition in the upper flaring corona. This model will be examined further in section 3.

Flare 3- GOES class M3 at UT 01:25 on 20 May 1984

This flare exhibited fast fluctuations in the high-temperature FCS channels during the rise and decay phase of the soft component. The FCS Fe XXV channel light curve is shown in figure 2c. We used a 1 min running mean of the data to approximate the soft X-ray background and then subtracted it to produce the residuals shown in the upper curve. Comparison with the HXRBS light curve reveals a close correspondence between features, with FCS fluctuations being most prominent in the post-impulsive phase. From an autocorrelation analysis of the Fe XXV residuals, we derived a fluctuation timescale of 12 ± 5 s, which is comparable with timescales determined for the previous two flares.

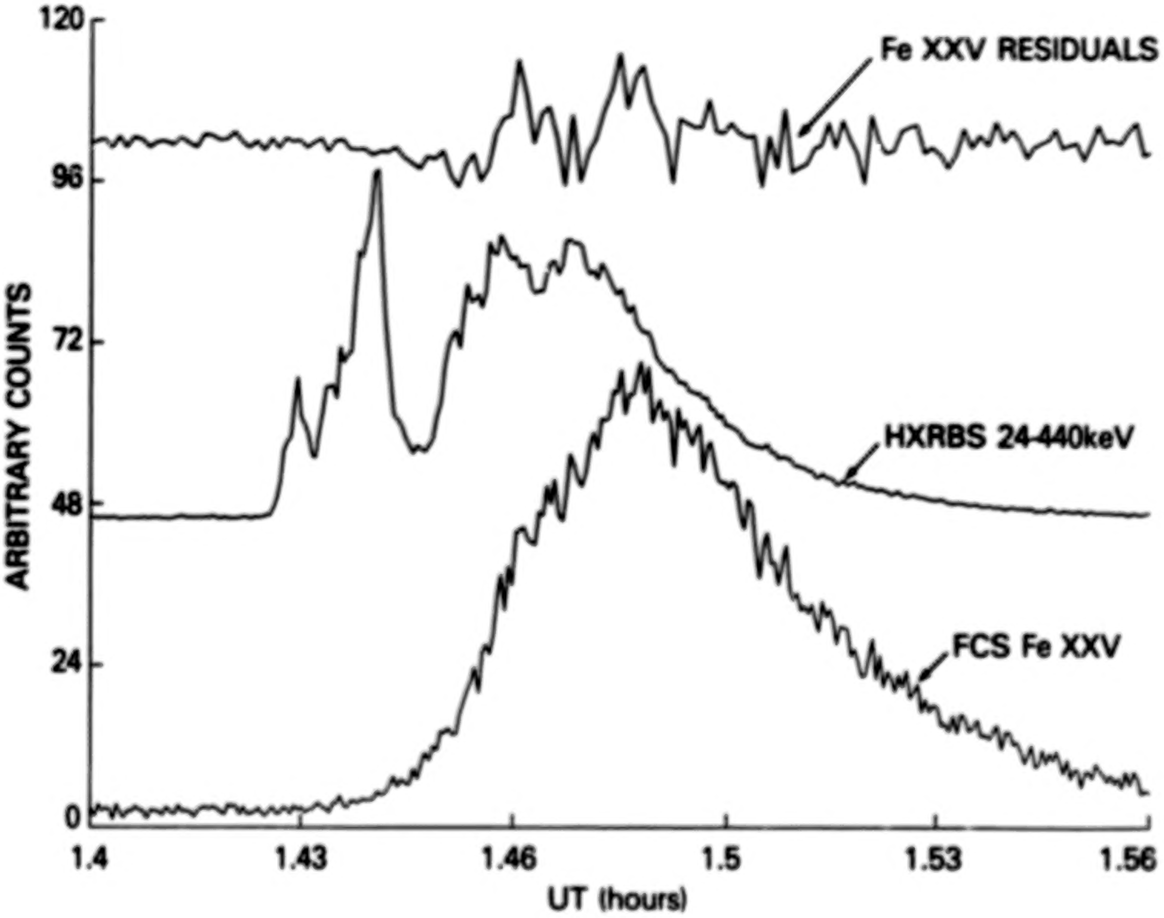

Figure 2c. FCS Fe XXV light curve (lower) for flare 3 is plotted at 2 s resolution. The middle curve shows the hard X-ray counterpart at equivalent resolution. The upper curve displays the Fe XXV residuals (magnified x 10) obtained after subtraction of a 1 min running mean of the FCS light curve. There is good qualitative correspondence between variations in the residuals and hard X-ray features. Note that the soft X-ray fluctuations became prominent after the initial hard X-ray burst.

To a first approximation, we can assess the statistical significance of these fluctuations by computing the deviation of the FCS residuals from the mean soft X-ray background. For example, figure 5 illustrates the Fe XXV residuals during the the first 1 min of the gradual rise phase plotted with constant σ lines (σ calculated from the square root of the smoothed soft

X-ray background). There are two features (A and B) that rise 2 to 3 σ above the background.

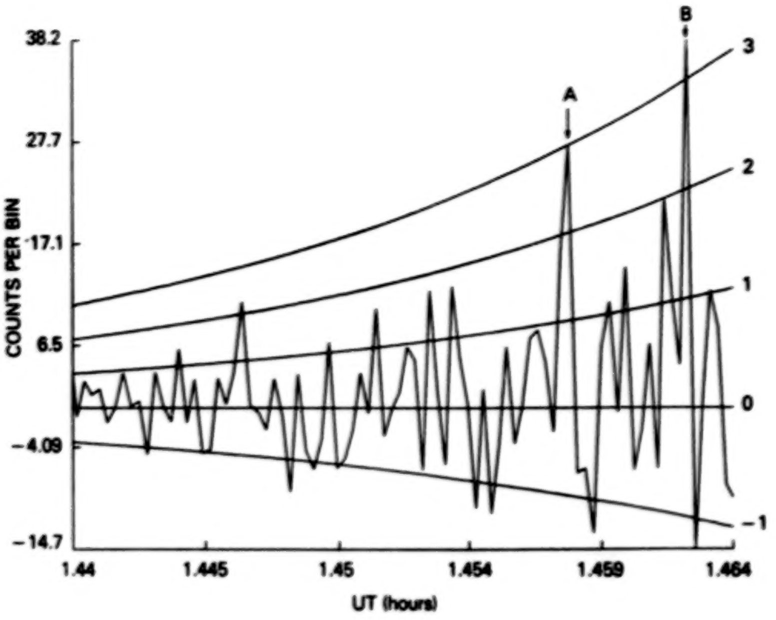

Figure 5. FCS Fe XXV residuals during the first 1 min of flare 3, plotted at 0.256 s resolution. The curves of constant σ are computed by assuming poisson counting statistics. Two features (A and B) lie approximately 3σ above the background.

Further analysis of this flare revealed that the prominence of fast intensity fluctuations decreased in the cooler-temperature sensitive FCS channels. For example, in figure 6 we compare the Fe XXV ($T_e \approx 2 \times 10^7$ K) channel light curve with the less temperature sensitive S XV (5×10^6 K) and Mg XI (3×10^6 K) channel light curves obtained simultaneously. The lack of stong fluctuations in the cooler-ion channels is further indication that these fluctuations are temperature-related phenomena. In particular, Peres *et al.* (1985) have indicated that the Fe XXV light curve represents the shape of the heating function, with the Fe XXV emissivity function being very steep at typical flare temperatures of 15 - 20 x 10^6 K. Accordingly, sudden temperature changes produced by heating would be strongly reflected as rapid changes in Fe XXV intensity. By contrast, the emissivity functions for the lower temperature sensitive ions such as Mg XI are broader and, thus, less responsive to sudden temperature changes.

3. DISCUSSION

The gradual soft X-ray phase of a flare is the response of the corona to the initial energy release – presumably characterized by the hard X-ray burst – and the thermalization of the non-thermal energy components of the flare (Strong *et al.* 1984). During the flare impulsive stage, energy is deposited deep down in the transition region and chromosphere. Whether this energy

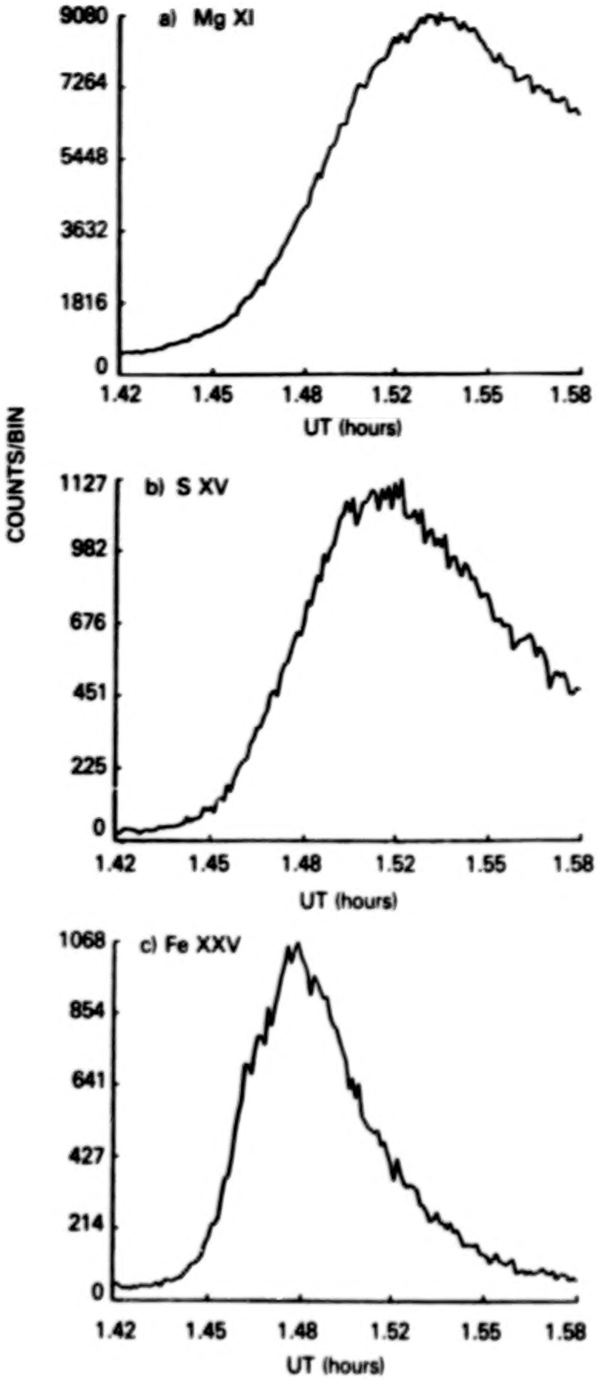

Figure 6a-c. FCS light curves of Mg XI, S XV, and Fe XXV, respectively, for flare 3 flare plotted at 4 s resolution. Note the decreasing prominence of fast spikes in the cooler-temperature sensitive channels.

is transported by a particle beam or by a thermal conduction front, chromospheric evaporation should result. This phenomenon is commonly observed as a high-velocity ($V \approx 400 \mathrm{kms}^{-1}$) stream of hot ($T_e > 10^6$ K) coronal plasma (Antonucci *et al.* 1982). The timescale to fill typical coronal loops of about 10^9 cm length is of the order of 30 s, which is comparable with the observed delay time between the hard and soft X-ray maxima.

The observations reported in this paper provide evidence for fast soft X-ray flare fluctuations with timescales that are shorter than expected for simple hydrodynamic processes. For example, an upward velocity in excess of 1000 km s^{-1} would be required to evaporate hot, dense chromospheric material sufficiently fast to produce a 10 s soft X-ray enhancement. Such a large blueshift was not observed in, for example, the BCS Ca XIX resonance line wing. Consequently, the observed intensity brightenings in soft X-rays are more probably due to local temperature enhancements that occur in the upper layers of the flaring coronal loop. This is consistent with our observation that the rapid soft X-ray fluctuations often corresponded with hard X-ray emissions.

The amplitudes of the soft X-ray fluctuations were typically less than 20% in the three flares studied. Based on the theoretical emissivity functions for Ca XIX and Fe XXV, such intensity changes would require a temperature increase of about 5 x 10^6 K. A possible driver for this increase could be magnetic reconnection occuring after the initial hard X-ray burst. Following each local heating episode, the hot plasma is likely to cool conductively within a timescale given by the expression:

$$\tau_c \approx 2 \times 10^{-10}\ N_e\ L^2\ T_e^{-5/2},$$

where L denotes the conductive lengthscale (Svestka 1976). Setting $T_e \approx 2 \times 10^7$ K for the enhanced temperature of the soft X-ray emitting plasma (Strong *et al.* 1984), assuming $N_e \approx 10^{11} \mathrm{cm}^{-3}$ as characteristic of the peak coronal electron density (Veck *et al.* 1984), and adopting the 10 s soft X-ray decay time as representative of τ_c, we derive $L \approx 10^8$ cm. Note that this value is an order of magnitude less than typical loop lengths, indicating that the locally injected heat energy is conducted quite rapidly into the surrounding cooler medium. This is in contrast with the energy associated with the initial hard X-ray burst, which is dissipated over much longer length scales ($L \approx 10^9$ cm).

4. CONCLUSIONS

We have presented evidence for fast soft X-ray fluctuations during the onset of the gradual component in three solar flares. These variations occurred in conjunction with similar features in hard X-rays, although they were not necessarily correlated in intensity. The timescales of these fluctuations were shorter than the typical hydrodynamic timescales expected for solar flares.

It is generally accepted that the initial hard X-ray burst in a solar flare is responsible for heating dense chromospheric material which subsequently evaporates into the corona. It is likely that in the ensuing soft X-ray gradual phase, secondary heating may occur (e.g., by magnetic reconnection). Since the coronal density is already enhanced by evaporation ($N_e > 10^{11} \mathrm{cm}^{-3}$), this energy is absorbed *in situ* rather than being transported to lower transition region layers. We have speculated that such secondary heating may be responsible for the observed soft X-ray intensity spikes. A more detailed study of this mechanism would demand theoretical calculations that are beyond the scope of this exploratory investigation. However, past numerical simulations of rapid heating of coronal loop plasma predict that, among the many non-equilibrium effects to arise, burst-like enhancements in soft X-ray flux are indeed likely to be a very common phenomenon (Shapiro and Moore 1977).

Acknowledgements

This work was performed at the Goddard Space Flight Center and supported by NASA contract NAS5-28713 and the Lockheed Independent Research Programme. We thank Allyn F. Tennant for helpful discussions on autocorrelation techniques.

REFERENCES

Acton, L. W., *et al.* 1980, *Solar Phys.*, **65**, 53.

Antonucci, E., *et al.* 1982, *Solar Phys.*, **78**, 107.

Jenkins, G.M., and Watts, D.C. 1968, in *Spectral Analysis and its Applications*, ed. (San Francisco: Holden-Day).

Kaufmann, P., Correia, E., Costa, J.E.R, Zodi Vaz, A.M., and Dennis, B.R. 1985, *Nature*, **313**, 380.

Peres, G., Serio, S., and Pallavicini, R. 1985, submitted to *Astrophys. J.*

Shapiro, P.R., and Moore, R.T. 1977, *Ap. J.*, **217**, 621.

Strong, K.T., *et al.* 1984, *Solar Phy.*, **91**, 325.

Svestka, Z. 1976, in *Solar Flares*, ed. (Reidel: Dordrecht).

Veck, N.J., Strong, K.T., Jordan, C., Simnett, G.M., Cargill, P.J., and Priest, E.R. 1984, *M.N.R.A.S.*, **210**, 443.

N87
21816
UNCLAS

N87-21816

SOFT X-RAY OSCILLATIONS DURING THE FLARE OF 7 AUGUST 1972

Roger J. Thomas and Werner M. Neupert

Laboratory for Astronomy and Solar Physics
Goddard Space Flight Center
Greenbelt, MD 20771

William T. Thompson

Applied Research Corporation
8201 Corporate Drive
Landover, MD 20785

Unique observations from OSO-7 of the intense flare on 7 August 1972 are presented, showing 1.6 second oscillations in it's soft X-ray emission which are long enduring, extremely regular, and initially of large amplitude. For approximately 20 minutes just after flare maximum, the X-ray intensity of an area 20 arc second square near the flare's core was monitored with 160 millisecond time resolution in two channels, 2-8Å and 8-16Å. Each channel recorded over 700 cycles of the X-ray oscillations, which remained remarkably stable in phase and period throughout the entire observations, but with gradually diminishing amplitude. The observed period does not corrrespond to any known operational periodicity in either the instrument or the spacecraft and cannot be attributed to aliasing with any other oscillatory component. Although radio pulsations of similar period were reported earlier in the flare, they had apparently died out by the time that the X-ray measurements began. Channel ratios indicate that both the temperature and electron density of the emitting plasma are enhanced at the peak of each cycle. There is indirect evidence that the X-ray pulsations are occurring only in a relatively small portion of an elongated feature, presumed to be a loop or arcade of loops. Such an effect could be caused by periodic kink mode instabilities within the arch, but seems to be incompatible with the idea of shock-induced oscillations of the whole loop, as had been proposed to explain the radio pulsations. Furthermore, the duration and stability of the oscillations set stringent conditions either on the mode in which they are driven or else on the physical characteristics of the oscillating flare structure.

N87
21817
UNCLAS

N87-21817

RAPID CHANGES IN Hα-FLARES CORRELATED WITH MICROWAVES

J-P. Wülser and N. Kämpfer

Institute of Applied Physics
University of Bern
Sidlerstrasse 5
CH-3012 Bern, Switzerland

Abstract. We have studied the time evolution of several flares in Hα with a time resolution of 1.4 seconds. The time profiles of the linecenter intensity show fast fluctuations and spikes. During the impulsive phase, prominent spikes occur in different kernels and they are correlated with microwave and Hard X-ray spikes. Spectrally resolved observations show major changes of the ratio between Hα line width and Hα linecenter intensity at time scales in the order of 1 minute. No significant fluctuations occured at shorter time scales.

1. Introduction

By studying the chromosphere with a sufficiently high temporal resolution and comparing the results with microwave and hard X-ray data one can draw conclusions about the flare heating mechanism in the chromosphere. Different energy transport mechanisms show different time delays between the initial energy release in the corona and the chromospheric response. Conductive flux results in a significant time delay in the order of some ten seconds. Non-thermal electrons, on the other hand, imply time delays of much less than a second, and fast fluctuations (order of seconds) in the primary energy release should also be seen in the chromospheric response.

We have studied the time evolution of several flares in Hα. Microwave observations from Bern (in the range of 3.1 to 35 GHz) and hard X-ray data from the HXRBS on SMM have been used for correlation purposes. Hα linecenter observations, which can be done with high temporal resolution are important for the measurement of fast fluctuations and small delays between the time profiles in different spectral regions. Spectrally resolved observations are limited in the temporal resolution because of the higher amount of data to be observed and stored. However, lineprofiles contain more physical information on the low-temperature flare plasma than does the intensity in the linecenter alone. Because Hα is optically thick, the lineprofiles reflect the dependence with height of the physical parameters in the chromosphere. Furthermore, they seem to be sensitive to the flare heating mechanisms (non-thermal electrons, conductive flux). Recently, theoretical lineprofile calculations have been carried out (Dinh, 1980; Canfield, Gunkler and Ricchiazzi, 1984) which may be used for quantitative comparisons with observed lineprofiles.

PRECEDING PAGE BLANK NOT FILMED

2. Hα Observations

Hα linecenter observations have been done with a digital CCD camera taking images at a rate of 1 frame per 1.4 seconds (Kämpfer and Schöchlin, 1982). Before analysis the raw data has been calibrated for CCD inhomogeneities.

The lineprofile observations have been carried out with an imaging spectrograph equipped with a CCD array sensor (Wülser, 1984). The instrument scans an active region every 5.4 seconds, acquiring images in 15 spectral channels simultaneously.

The analysis of the time evolution of the lineprofile as a whole is rather difficult. It is more adequate to use single spectral signatures instead, e.g. linewidth, line shift, or total power in Hα. In this paper we concentrate on the analysis of the linewidth because it is supposed to be sensitive to the flare heating mechanism. Canfield, Gunkler and Ricchiazzi (1984) have theoretically found that broad Stark emission wings of obviously non-Gaussian form are produced by non-thermal electrons.

In order to get a parameter which is most sensitive to changes in the line wings, we measured the effective linewidth at those points where the flare profile exceeds the intensity of the adjacent continuum by 10 percent (Fritzova, 1964). As a consequence of this definition, linewidth and intensity at linecenter are not independent. Therefore, we looked for relative changes of linewidth and linecenter intensity. Figure 4b shows the time evolution of the linewidth of a flare on November 20, 1982, and Figure 4a its intensity at linecenter. The different evolution of the two parameters can be seen on a correlation diagram where linewidth is plotted as a function of linecenter intensity and time as free parameter (Figure 5).

3. Discussion

a) linecenter observations. Figure 1 shows the light curves for two individual kernels of the flare on December 17, 1980. The two kernels develop quite differently. Kernel A starts earlier and peaks later than kernel B, which shows a rather fast rise. Both kernels have spikes in their light curve but most fluctuations are prominent in only one of the kernels. As an example, consider the spike at 12h07m48s. It is a major feature in kernel A but not in B. The same spike is clearly seen in the light curve of the whole flare, in the microwave regions and in X-rays at 29keV (Figure 2). The close temporal coincidence between Hα and microwaves indicates a rapid energy transfer by electrons from the microwave source down to the chromosphere. Besides the rapid fluctuations this event also shows a close correspondence of the impulsive phase in the two spectral regions.

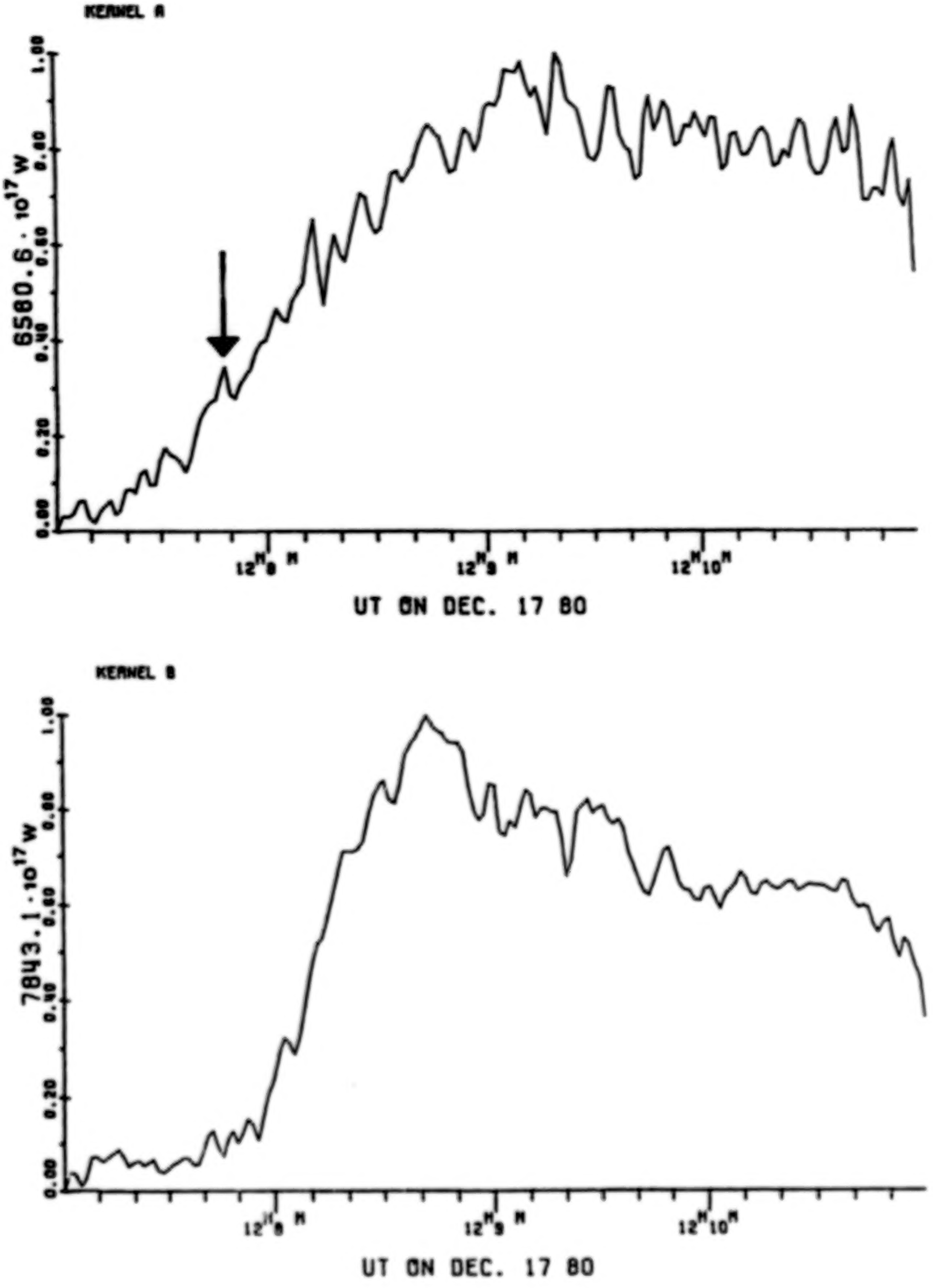

Fig. 1. Lightcurves for two individual kernels in Hα. The spike at 12h07m48s is very prominent in kernel A but not so much in kernel B.

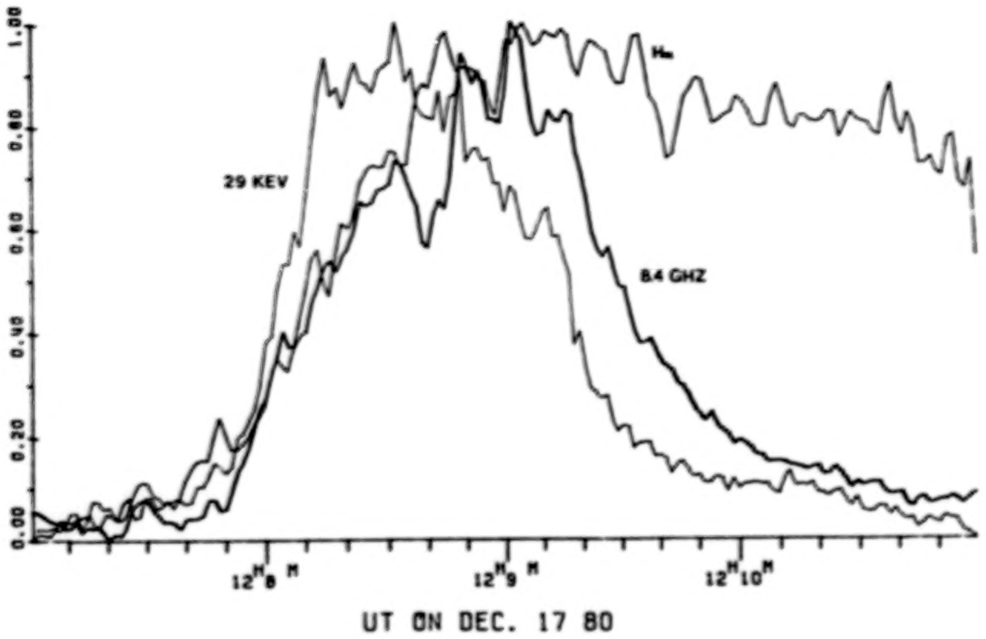

Fig. 2. The comparison of the Hα lightcurve with the corresponding event in the microwave region at 8.4 GHz and in hard X-rays at 29 keV clearly shows the close correspondence of some prominent spikes.

The flare of June 17, 1982, is an example of an another type of event where the development of the total Hα intensity is delayed compared with the microwave emission (Figure 3a). However, if the evolution of a specific kernel is considered, no time delay can be observed and there is a close correspondence between the individual spikes in Hα and microwaves during the impulsive phase (Figure 3b).

b) spectrally resolved observations. Figure 4 shows the time evolution of intensity and linewidth of the flare of November 20, 1982. The two time profiles show a spiky structure, but the ratio of both parameters does not change much on short timescales in the order of 10 seconds. On longer timescales, (some ten seconds to minutes) the ratio is changing significantly. By comparing intensity and linewidth (Figures 4a, 4b and 5), we can distinguish 3 phases: During the first phase until 10h13m15s, both parameters show a fast rise. The second phase lasts until about 10h15m and is characterised by a further increase of intensity, whereas the linewidth fluctuates around a constant value. In the third phase both parameters decrease. A comparison with microwaves (Figure 6) shows, that the first phase coincides with the impulsive burst. The fast increase of the Hα linewidth indicate a heating of the chromospheric flare by fast electrons. However, broad Hα emission wings as a clear indicator for massive electron heating do not exist. At the beginning of phase 2, a qualitative change occurs. The microwave flux begins to decrease substantially and the Hα linewidth remains at about a constant value. These facts suggest that the further increase of the Hα intensity is not primarily due to electron heating.

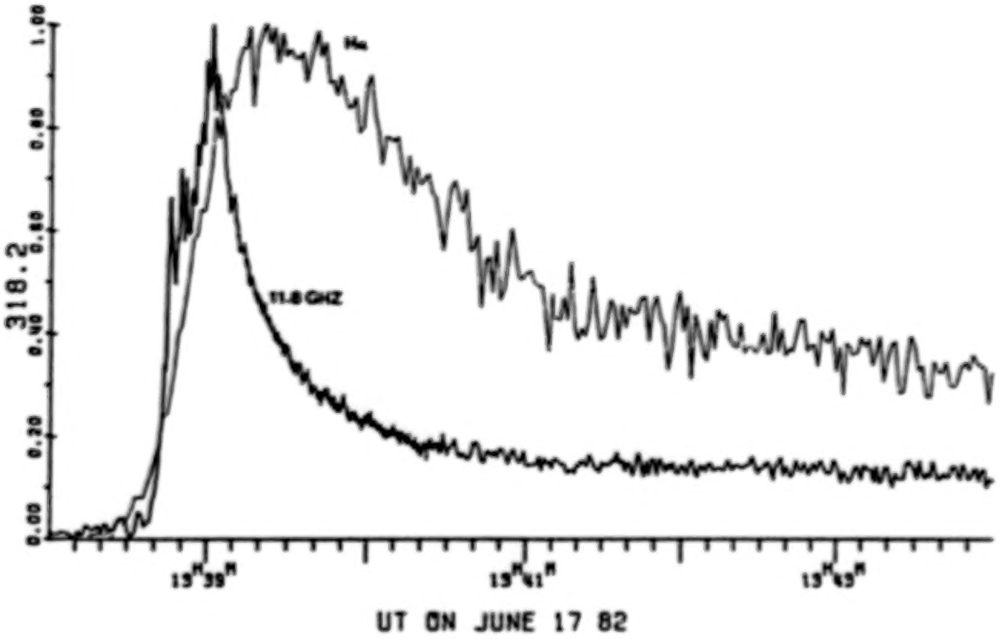

Fig. 3a. In this flare a time delay between the overall development of the Hα-intensity and the microwave region is present.

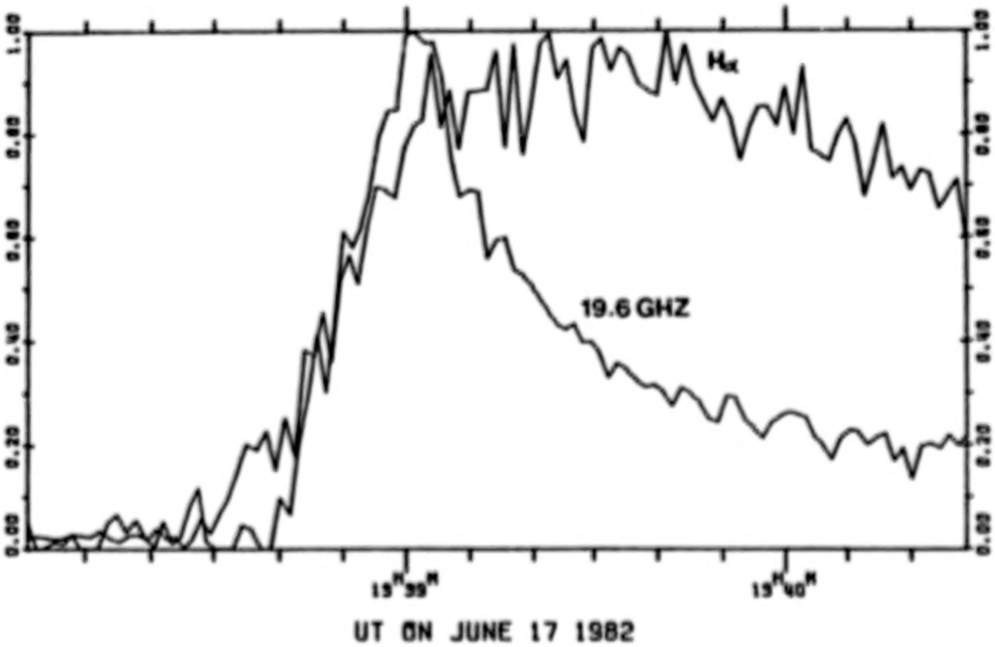

Fig. 3b. Temporal evolution of a specific kernel and the microwave event at 19.6 GHz which shows no time delay between the two spectral regions. Integration time in both cases is 1.4 sec.

a) INTENSITY

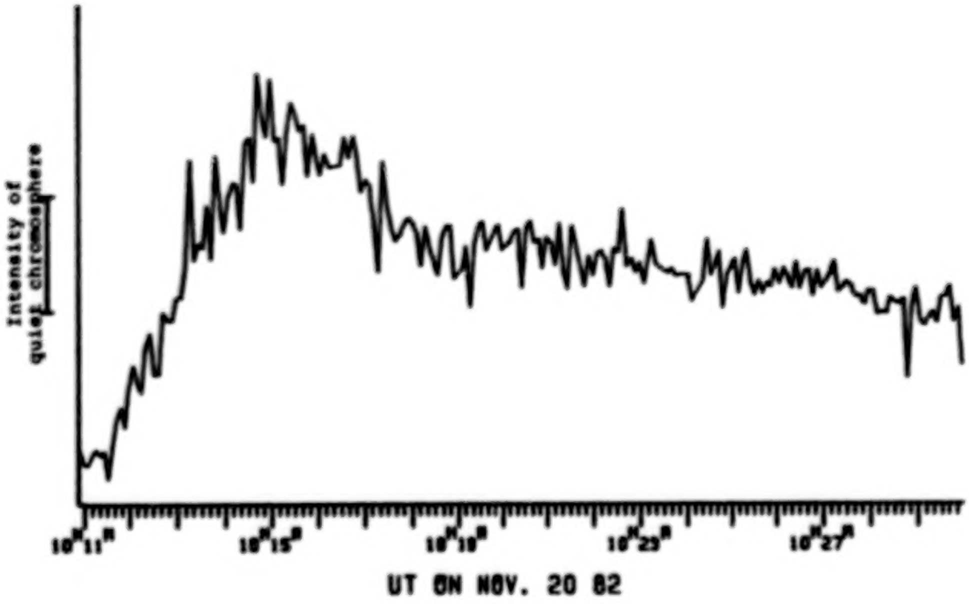

b) LINEWIDTH

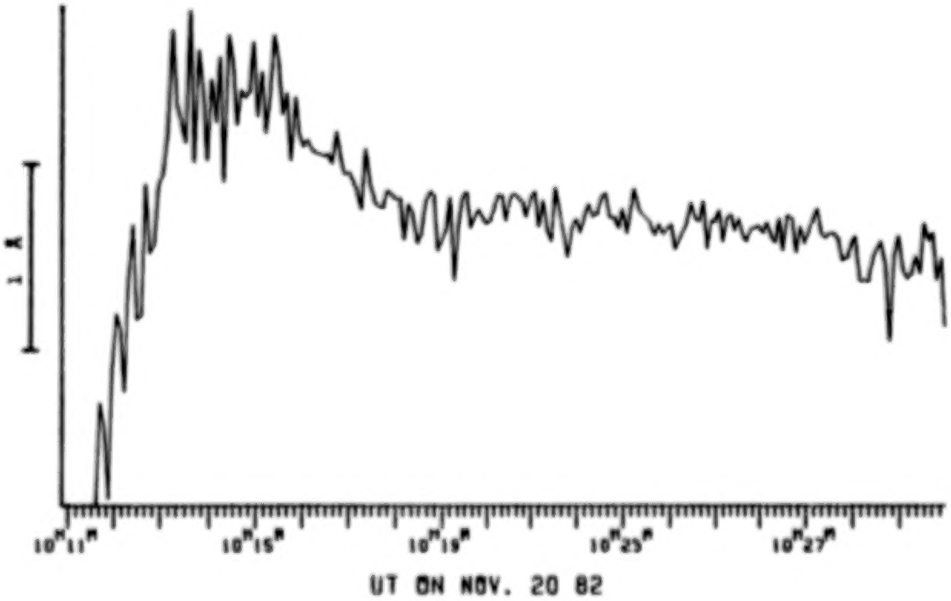

Fig. 4. Flare of Nov. 20, 1982: Time evolution of linecenter intensity (a) and linewidth (b) at the center of the strongest flare kernel.

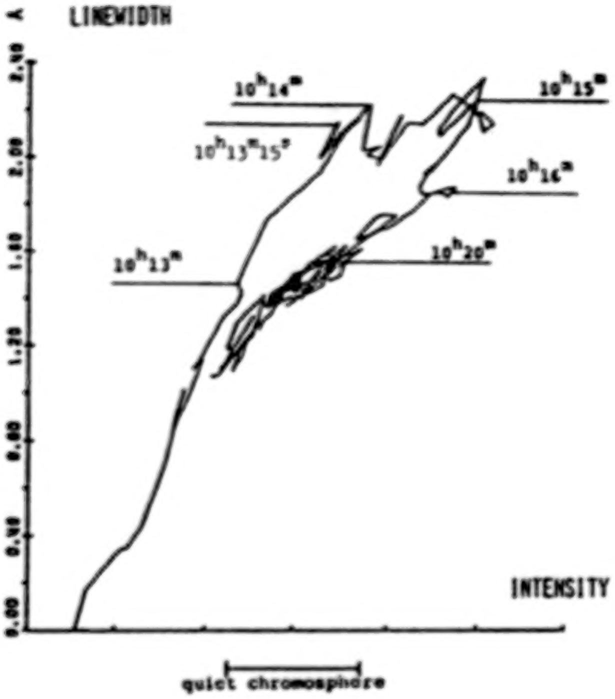

Fig. 5. Flare of November 20, 1982: Correlation diagram. Linewidth as a function of intensity at linecenter. Free parameter is time. Changes in the ratio of linewidth and intensity mainly occur between 10h14m and 10h15m.

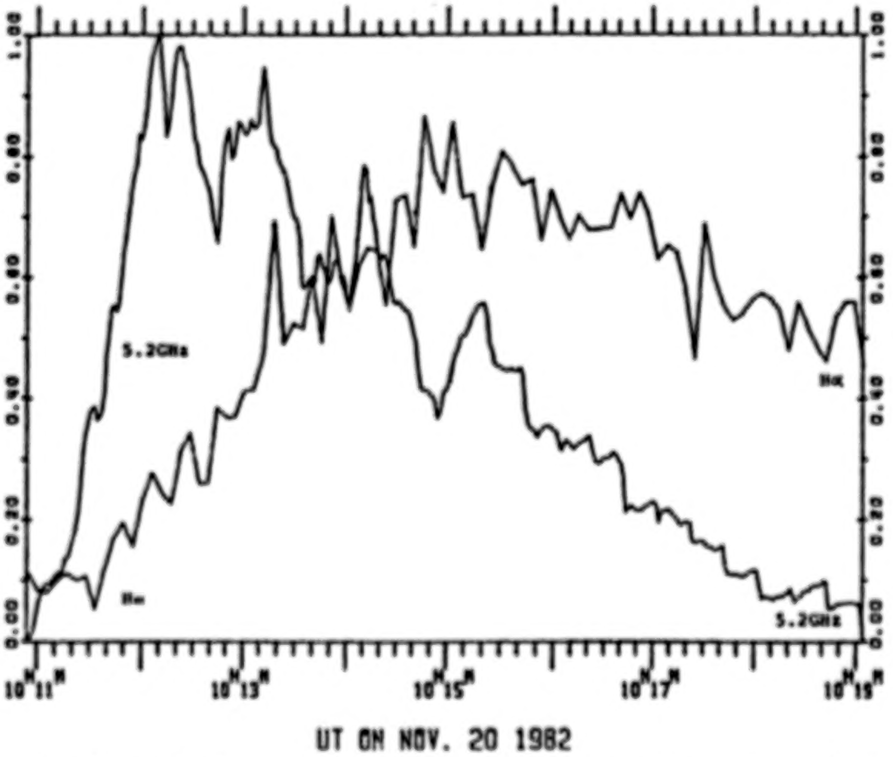

Fig. 6. Time evolution of microwaves at 5.2 GHz and Hα-intensity of the flare of November 20, 1982.

ORIGINAL PAGE IS
OF POOR QUALITY

An other flare (November 21, 1982) did not show these 3 phases in Hα: There was no difference between the temporal evolution of linewidth and linecenter intensity. On the correlation diagram (Figure 7) the flare rises and falls along the same line of path. The absolute amplitudes of linewidth and Hα intensity were larger in this flare. It consisted of a single loop, in contrast to the previously discussed event of November 20, which showed a more complex structure (4 Hα kernels). Presently it is not clear to the authors wether the 3 phase evolution in Hα only occurs above some minimum value of released energy and loop size.

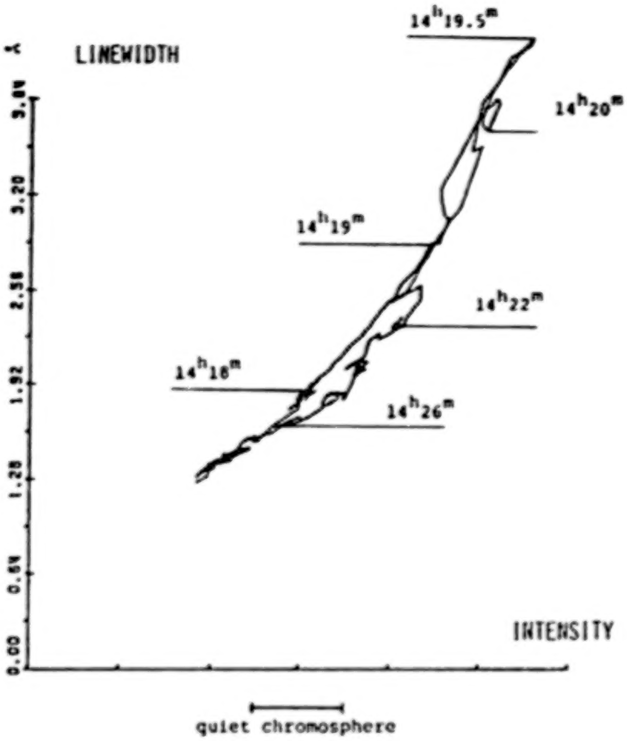

Fig. 7. Flare of November 21, 1982: Correlation diagram. This flare rises and falls along the same line of path.

4. Summary

The time evolution of the total Hα intensity during the impulsive phase shows fast fluctuations and spikes which are correlated with microwaves and hard X-rays. These spikes indicate chromospheric heating by fast electrons. Different peaks can originate from different kernels.

Spectrally resolved Hα observations showed no significant changes of the shape of the line profile during the spikes. However, the time resolution of the imaging spectrograph may have been too low to resolve the changes properly. On longer timescales, one of two investigated flares shows an enhanced linewidth during the impulsive phase, which is another indicator for electron heating of the chromosphere. We conclude, that Hα observations with high temporal resolution are a valuable tool for the analysis of the chromospheric flare. Together with microwave and hard X-ray measurements, they especially can give us additional information about the flare heating mechanism.

Acknowledgements

The authors are indebted to Prof. E. Schanda for the opportunity to undertake this work. They would also like to thank Dr. A. Magun for his helpful advices and comments. The work was supported by the Swiss National Science Foundation under grant No. 2.604.0.82.

References

Canfield, R.C., Gunkler, T.A. and Ricchiazzi, P.J. 1984, Astrophys. J., 282, 296.
Dinh, Q.-V. 1980, Publ. Astron. Soc. Japan, 32, 515.
Fritzova, L. 1964, Bull. Astron. Inst. Czech., 15, 34.
Kämpfer, N. and Schöchlin, W. 1982, Solar Phys., 31, 143.
Kämpfer, N. and Magun, A. 1983, Astrophys. J., 274, 910.
Wülser, J-P. 1984, 'Beobachtung und Analyse von Hα-Linienprofilen solarer Flares', Diploma Thesis, Institute of Applied Physics, Bern.

N87
21818
UNCLAS

N87-21818

PLASMA TURBULENCE AND IMPULSIVE UV LINE EMISSION IN SOLAR FLARES

John C. Brown

Department of Astronomy
University of Glasgow
G12 8QW, Scotland

ABSTRACT

Observations show that hard X-ray burst and UV lines rise and fall simultaneously on time scales of seconds. Hydrodynamic simulations of beam-heated atmospheres, based on collisional transport, however, produce only a gradual fall in UV emission, when the beam flux falls, due to the long time scale of conductive relaxation. It is suggested that this discrepancy might be explained by onset of plasma turbulence driven by the strong heat flux or by the beam return current going unstable. Such turbulence greatly reduces electrical (σ) and thermal (κ) conductivities. Fall in σ reduces the hard X-ray flux by enhanced ohmic dissipation of the return current, while fall in κ may cause the UV line to fall by reducing the transition region thickness.

1 Introduction

Simultaneous SMM data in hard X-ray and UV lines exhibit synchronism of both rise and fall of impulsive spikes down to time scales of order of seconds. The driving mechanism for both is believed to be a thick target electron beam. However, numerical simulation of the atmospheric response to such a beam (Mariska and Poland, 1985) does not reproduce synchronous fall in the two emissions. In such simulations, UV line emission rises because of the direct heating effect of the beam and because of the increased conductive flux in the transition region driven by beam heating of the corona (cf Section 2). Though the direct heating turns off with the beam, the fall in the enhancement due to conduction is gradual because the corona acts as a heat reservoir.

This paper gives a very preliminary discussion of how onset of beam generated plasma turbulence might modify the simulation results through anomalous transport effects.

PRECEDING PAGE BLANK NOT FILMED

2 Line Formation in the Flare Transition Region

An injected electron beam dominates flare atmosphere heating in the corona and in the low chromosphere, where the temperature gradient is rather small, while in the upper chromosphere and transition region, after a brief initial transient, the steep temperature gradient results in energy transport being dominated by thermal conduction (driven by the coronal beam heating) - e.g. Shmeleva and Syrovatskii (1973) and subsequent authors. In a quasi-steady transition region there is negligible direct beam heating, because of the small column mass, and essentially constant conductive flux down to the temperature ($\sim 10^5$K) where radiative losses become stable and maximal, and where densities become high enough for conductive deposition to be radiated away. Furthermore, because of the small column mass, the transition region can be adequately described as having spatially uniform pressure.

For a conductive energy flux F emanating from the corona, the thermal structure of the transition region is then described by

$$\kappa(T) \frac{dT}{dz} = F \qquad (1)$$

where $\kappa(T)$ is the thermal conductivity at temperature T, at geometric depth z. Since the bulk of the energy of a beam is deposited in the corona, F is essentially the energy flux of the beam.

An optically thin collisionally excited transition region line of wavelength λ, with emissivity $n^2 f_\lambda(T)$ (erg cm^{-3}s^{-1}) at plasma density n, temperature T, will have a total luminosity per unit area

$$I_\lambda = \int_Z n^2(z)\, f_\lambda\, (T(z))\, dz \qquad (2)$$

where n is determined by the constant pressure condition $nT = n_o T_o$ where n_o is the atmospheric density at the upper chromospheric level where the bolometric radiative loss curve maximises at temperature T_o ($\sim 10^5$K). n_o will, of course, depend on the magnitude of F, the higher value associated with a flare pushing the base of the transition region deeper in the atmosphere to the depth where n_o is high enough to radiate off the input. For lines formed in the upper transition region ($T \geq 10^5$K), (2) then becomes

$$I_\lambda = n_o{}^2 T_o{}^2 \int_Z \frac{f_\lambda(T)}{T^2}\, dz \qquad (3).$$

As a first approximation, a typical line may be approximated as being formed over a fixed interval ΔT centred on the peak temperature T of line formation and (3) can be approximated, using (1), as

$$I_\lambda = n_o{}^2 T_o{}^2 \int_T \frac{f_\lambda(T)}{T^2} \frac{dT}{F/\kappa(T)} = \left\{ \frac{T_o{}^2}{T^2}\, f_\lambda(T) \Delta T \right\} \frac{n_o{}^2 \kappa(T)}{F} \qquad (4)$$

where $\kappa(T)$ is a mean value of κ over ΔT approximated by its value at line peak T.

It follows that if $\kappa(T)$ remains of the same form, I_λ is determined by

n_o^2/F. Increase in F alone during a flare would result in a decrease in I_λ due to the transition region becoming thinner. However, as already noted, increase in F also results in increase in n_o and steady state numerical simulations (Emslie, 1985) show that the rise in n_o more than offsets the decrease in $\Delta Z = \kappa(T)\Delta T/F$ and the nett result is a rise in UV flux I_λ accompanying an increase in thick target hard X-ray flux due to the increased F. Time dependent simulations (Mariska and Poland, 1985) confirm this and show that the rise is closely synchronous but that when F falls, the thermal conduction relaxation time is too long for I_λ to track F. All of these calculations, however, assume that $\kappa(T)$ retains the same form throughout and in particular neglect the consequences of onset of anomalous transport processes.

3 Effect of Onset of Plasma Turbulence on Transition Region Lines

3.1 Qualitative Description

Suppose that instead of assuming the beam flux F to peak at the observed peak of a radiation spike, while transport is still classical, we suppose that during its rise F exceeds a threshold for anomalous transport effects to set in. This may be due to one or more of three processes: two-stream instability of the beam itself, resulting in Langmuir wave generation (e.g. Emslie and Smith 1983; McClements et al 1985 - this Workshop); drift current instability of the beam driven return current resulting in generation of electrostatic (ion-cyclotron, ion-acoustic) waves (e.g. Hoyng et al 1977; Cromwell et al 1985, Holman 1985 - this Workshop); heat flux instability resulting in electrostatic wave generation by the currents associated with steep thermal gradients (Mannheimer 1977, Brown et al 1979, Smith and Lilliequist 1979). Here we will concentrate our attention on the last two processes as it is these which will directly affect thermal and electrical conductivities.

When such plasma waves appear, the effective electron collision frequency will increase, resulting in a fall in both electrical (σ) and thermal (κ) conductivities. Decrease in σ will increase the electric field required to drive the return current, reducing beam electron lifetimes, and consequently the X-ray bremsstrahlung from the beam. Decrease in κ, on the other hand, will result in a decrease in the transition region thickness (1) and consequently in I_λ provided n_o does not rise enough to offset this factor. The extent to which n_o will eventually rise for a given change in κ will have to be determined by a steady state numerical calculation (cf Machado and Emslie 1979). For the moment we will assume that n_o is determined mainly by the input flux F rather than by details of $\kappa(T)$ and that the κ factor in I_λ overwhelms the n_o^2 factor. Likewise, the time scale on which the transition region thins will have to be found by time dependent numerical simulation. We note, however, that a change in structure purely due to a change in coronal heating when F changes will take roughly the time of propagation of a thermal front along the coronal loop length. On the other hand, re-adjustment of the transition zone structure due to an in situ change of κ (typically in a few plasma periods) will occur in the much shorter time needed for a thermal front to cross the transition region.

3.2 Conditions for Onset of Anomalous Transport in the Flare Transition Region

If beam electrons are injected into the transition region at a total rate $\mathcal{F}(s^{-1})$ over an area A then the condition for return current instability can be written

$$n\left(\frac{kT_e}{m_e}\right)^{1/2} f(T_e/T_i) < \mathcal{F}/A \qquad (5)$$

where f declines from about unity as T_e/T_i increases from unity (e.g. Hoyng et al 1977, Brown and Hayward 1981).

On the other hand, the heat flux $F = E\mathcal{F}/A$ is likely to drive wave generation if it significantly exceeds the saturated value $\simeq \frac{1}{6}n\left(\frac{kT_e}{m_e}\right)^{1/2}kT$ or roughly

$$n\left(\frac{kT_e}{m_e}\right)^{1/2} \frac{kT_e}{E} \leq \mathcal{F}/A \qquad (6)$$

where E is the mean energy of beam electrons.

From (5) and (6) we see that which effect sets in first depends on the value of f compared to kT_e/E. With $E \gtrsim 10\,\mathrm{KeV}$ and $kT_e \lesssim 6.5\,\mathrm{KeV}$ for the transition region, it seems almost certain that heat flux instability will set in first except for very high T_e/T_i values and near the top of the transition zone. (Noting the condition nT_e = constant we see that the left side of (5) varies as $T_e^{-1/2} f(T_e/T_i)$ which increases with depth in the atmosphere whereas the left side of (6) varies as $T_e^{1/2}$ and so decreases with depth - i.e. the heat flux is most unstable at low T_e.) In absolute numerical terms, the separate criteria are as follows.

Heat Flux Instability

If the transition region pressure is $P(\mathrm{dyne\ cm^{-2}}) = 10^2 P_2 \simeq nkT_e$ and with $T = 10^6 T_6(\mathrm{K})$, $\mathcal{F} = 10^{36}\mathcal{F}_{36}(s^{-1})$, $A = 10^{18}A_{18}(\mathrm{cm^2})$ and $E = 10E_1(\mathrm{KeV})$ then (6) becomes

$$\frac{\mathcal{F}_{36}E_1}{A_{18}} \gtrsim 2.3P_2T_6^{1/2} \qquad (7).$$

Thus for typical flare transition region pressures $P_2 \simeq 0.3-3$ (e.g. Machado et al 1979) and temperatures $T_6 \simeq 1$ and with the electron beam parameters $\mathcal{F}_{36} \simeq E_1 \simeq 1$ typical of large hard X-ray bursts, heat flux instability in the transition zone is likely if the injection area $A \lesssim 4 \times 10^{17}\mathrm{cm^2}$ which is very possible.

Return Current Instability

With the same notation and $f = 0.1f_{-1}$, (5) becomes

$$\frac{\mathcal{F}_{36}}{A_{18}} \geq 27 P_2 f_{-1} \quad (8).$$

This condition will be satisfied only if f is particularly small, due to large T_e/T_i, or if the injection area A is << $10^{18}\mathrm{cm}^2$, for typical flare transition region pressures. It is more readily satisfied in the corona, where P is smaller (and $\mathcal{F}$ larger), and so may contribute strongly there to beam deceleration, and hence to the fall in bremsstrahlung from the beam.

3.3 Quantitative Effect of Plasma Turbulence in the Transition Region

Both the electrical (σ) and thermal (κ) conductivities are determined by the effective collision frequency ν_{eff} of the electrons, viz

$$\kappa \simeq 6 \times 10^{11} n_{10} T_6 / \nu_{eff} \quad \mathrm{erg\,cm^{-1}\,s^{-1}\,K^{-1}} \quad (9)$$

and

$$\sigma \simeq 2 \times 10^{18} n_{10} / \nu_{eff} \quad \mathrm{s^{-1}} \quad (10)$$

where $n_{10} = \frac{n}{10^{10}}$.

In the classical regime $\nu_{eff} = \nu_{coll}$ given by

$$\nu_{coll} = 7 \times 10^2 \; n_{10} / T_6^{3/2} \quad (11)$$

whereas in the presence of (e.g. ion-acoustic) waves of energy density W, ν_{eff} becomes of order

$$\nu_{eff} = \nu_{pe} \left(\frac{W}{nKT}\right) = 10^9 n_{10}^{1/2} \left(\frac{W}{nKT}\right) \quad (12)$$

where ν_{pe} is the plasma frequency. Thus the classical and anomalous transport coefficients become

$$\kappa_{class} = 10^9 T_6^{5/2} \quad (13a)$$

$$\kappa_{AN} = 6 \times 10^2 n_{10}^{1/2} T_6 \Big/ \left(\frac{W}{nKT}\right) \quad (13b)$$

and

$$\sigma_{class} = 3 \times 10^{15} T_6^{3/2} \quad (14a)$$

$$\sigma_{AN} = 2 \times 10^9 n_{10}^{1/2} \Big/ \left(\frac{W}{nKT}\right) \quad (14b).$$

If then, during a UV/HXR burst, waves are generated by either return current or heat flux instability, at wave onset the thermal conductivity and hence the transition region scale thickness will fall by a factor (Equation

(1))

$$\frac{\Delta Z_{AN}}{\Delta Z_{class}} = \frac{\kappa_{AN}}{\kappa_{class}} \simeq 6 \times 10^{-7} n_{10}^{1/2} T_6^{-3/2} / \left(\frac{W}{nKT}\right) \qquad (15).$$

The actual value of W/nKT depends on how the waves are driven. Simulations of return current instability (Cromwell et al 1985 - these proceedings) lead to values of W/nKT as high as 10^{-3} at saturation and around 10^{-5} in marginal stability. In the more relevant case of heat flux instability, Brown et al (1979) found that in the case of extreme temperature gradients, unstable generation of ion sound waves led to $W/nKT \simeq (m_e/m_p)^{1/2} \simeq 1/43$ for which (15) gives

$$\frac{\Delta K_{AN}}{\Delta K_{class}} \simeq 2 \times 10^{-4} P_2^{1/2} / T_6^{2}$$

Consequently, neglecting any compensating factor due to increase of P_o, Equations (4) and (16) show that a small increase in F past a critical threshold can result in a reduction in UV line strength by several orders of magnitude. Furthermore, we expect this decrease to be very fast - roughly the time it takes for F to rise above the instability threshold across the temperature domain of formation of the line concerned.

Whether wave generation is driven by heat flux or return current instability , its effect on σ will act on the electron beam in two ways. Firstly, it will increase the electric field driving the return current and so decelerate the beam in the region of its propagation. Secondly, and more speculatively, it may feed back on the region of acceleration of the beam and interfere with beam production (Brown and Melrose 1977). To see the consequences of the first effect on the HXRB, we can compare the thick target bremsstrahlung yield in the case of collisional losses only (the usual thick target case - Brown 1971) with that when strong return current losses dominate. In each case the bremsstrahlung photon yield at energy ϵ from an electron of initial energy E_o is roughly $\nu = nQ_B v\tau$ where Q_B is the bremsstrahlung cross section (appropriately averaged over electron energies between ϵ and E_o), v is the electron velocity and τ is stopping lifetime. In the classical (collisional case) $\tau = E_o^2 / 2\pi e^4 \Lambda n v$ and so

$$\nu_{class}^{Brems} \simeq \frac{Q_B E_o^{\,2}}{2\pi e^4 \Lambda} \qquad \text{(photons per electron)} \qquad (17).$$

In the case of return current losses dominating (e.g. Brown and Hayward 1981) $\tau = m_e v_o/(ej/\sigma) = \sigma A E_o / e^2 \mathcal{F} v_o$ so that the photon yield is

$$\nu_{AN}^{Brems} \simeq nQ_B \sigma_{AN} A E_o / e^2 \mathcal{F} \qquad (18).$$

Taking the ratio of (18) to (17) substituting, for σ_{AN} from (14b) and inserting numerical values then gives

$$\left(\frac{\nu_{AN}}{\nu_{class}}\right)_{Brems} \simeq 3 \times 10^{-8} \frac{n_{10}^{3/2} A_{18}}{\mathcal{F}_{36} E_1} \Big/ \left(\frac{W}{nKT}\right) \qquad (19)$$

which even with W/nKT as small as 10^{-4} implies a fall in thick target bremsstrahlung yield of over 3 orders of magnitude, effectively switching off the hard X-ray production entirely.

4 Conclusions

In summary, when the electron beam flux in a beam heated flare becomes large enough for onset of wave generation either directly by the beam return current, or via production of heat flux beyond saturation, we expect an immediate reduction in both hard X-ray burst intensity (due to anomalous return current dissipation) and simultaneously in the emission of UV lines from the transition region (due to reduction in its thickness by anomalous thermal conductivity). The exact magnitude and time scales of this effect require further investigation by numerical simulation, hopefully as a sequel to this Workshop. In particular, the effect of reducing κ on the transition region pressure (i.e. n_o) and its effect on the above conclusions is the topic of Workshop related collaborations.

References

Brown J.C. 1971, Solar Phys. 18, 489
Brown J.C. and Melrose D.B. 1977, Solar Phys. 52, 117
Brown J.C. , Melrose D.B. and Spicer D.S. 1979, Ap.J. 228, 592
Cromwell D., McQuillan P. and Brown J.C. 1986, these proceedings
Emslie A.G. 1985, Solar Phys. 98, 281
Emslie A.G. and Smith D.F. 1983, Ap.J. 279, 882
Hoyng P., Knight J.W. and Spicer D.S. 1977, Solar Phys. 58, 139
Machado M.E., Avrett G., Vernazza J. and Noyes R. 1979, Ap.J. 242, 336
Machado M.E. and Emslie A.G. 1979, 232, 903
Mannheimer W.M. 1977, Phys. Fluids 20, 265
Mariska J.T. and Poland A. 1985, Ap.J., in press
Shmeleva O.P. and Syrovatskii S.I. 1973, Solar Phys. 33, 341
Smith D.F. and Lilliequist C.Q. 1979, Ap.J. 232, 582.

N87
21819
UNCLAS

N87-21819

ELECTRON-CYCLOTRON MASER AND SOLAR MICROWAVE MILLISECOND SPIKE EMISSION

Li Hong-wei
Li Chun-sheng

Department of Astronomy
Nanjing University

Fu Qi-jun

Beijing Observatory
Academia Sinica

I. Introduction

An intense solar microwave millisecond spike emission (SMMSE) event has been observed on May 16, 1981 by Zhao and Jin at Beijing Observatory ($\omega = 2\pi \times 2.84$ GHz)[1]. The peak flux density of the spikes is high to 5×10^5 s.f.u., and the corresponding brightness temperature (BT) reaches $\sim 10^{15}$ K.

In order to explain the observed properties of SMMSE, we propose in this paper that a beam of electrons with energy of tens kev injected from the acceleration region downwards into an emerging magnetic arch forms so-called hollow beam distribution and causes electron-cyclotron maser (ECM) instability. The growth rate of second harmonic X-mode is calculated and its change with time is deduced. It is shown that the saturation time of ECM is $t_s \approx 0.42$ ms and only at last short stage ($\Delta t < 0.2\, t_s$) the growth rate decreases to zero rather rapidly. So a SMMSE with very high BT ($T_b > 10^{15}$ K) will be produced if the ratio of number density of nonthermal electrons to that of background electrons, n_s/n_e, is larger than 4×10^{-5}.

II. Model and Excitation of X-mode

If the induced electric field is larger than the Dreicer field, it will be able to accelerate electrons along the field to energy of tens kev in one millisecond. The injected electrons with a large pitch angle gyrate around the magnetic field B and form so- called hollow beam distribution (Fig. 1) as following equation[2]:

$$F(v_\perp, v_{\parallel}) = (\pi^{3/2}\, d_\perp^2\, d_{\parallel}\, v_{0\perp}^2\, v_{0\parallel})^{-1}$$

$$\exp\left\{-\left(\frac{v_\perp - v_{0\perp}}{d_\perp\, v_{0\perp}}\right)^2 - \left(\frac{v_{\parallel} - V_0}{d_{\parallel}\, v_{0\parallel}}\right)^2\right\}$$

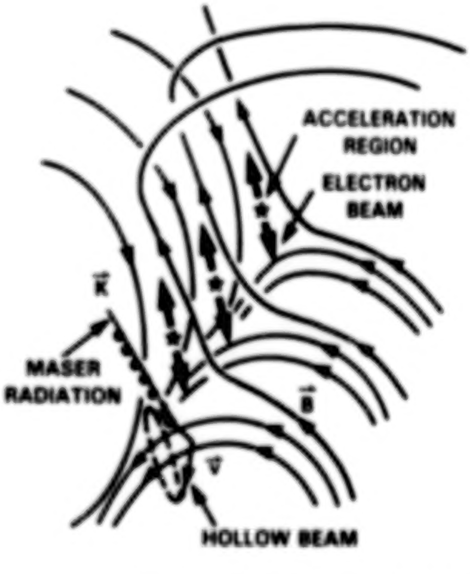

Figure 1. Model of hollow beam driven ECM for SMMSE.

PRECEDING PAGE BLANK NOT FILMED

It drives ECM and we have the growth rate at the m-th harmonic[2]

$$\omega_i^{(m)} = \frac{\pi^2 c^3}{2^{2m-1}[(m-1)!]^2}\cdot\frac{n_s}{n_e}\cdot\frac{\omega_p^2}{\omega^2}\left\{\left[2-n^2-\frac{2\omega_p^2}{\omega(\omega+\Omega_e)}\right]\left(1-\frac{\omega_p^2}{\omega^2}-n^2\sin^2\alpha\right)\right.$$
$$\left.-\,n^2\cos^2\alpha\left(1-\frac{\omega_p^2}{\omega^2}\right)\right\}\frac{\Omega_e}{G\,n\sin\alpha}\cdot\int_{v_-}^{v_+}dv_{11}\cdot b_m^{2m-1}$$
$$\times\left(\frac{m\Omega_e}{\omega}\cdot\frac{\partial}{\partial\cdot v_m}+\frac{v_m}{c}n\cos\alpha\frac{\partial}{\partial v_{11}}\right)F(v_m,\ v_{11}) \qquad (2)$$

where

$$G = 2n^4\left[\frac{\omega^2\omega_p^2\sin^2\alpha}{(\omega^2-\Omega_e^2)^2}+\frac{\omega_p^2}{\omega^2}\cos^2\alpha\right]+4n^2\left[\frac{\omega_p^2(\omega_p^2-\Omega_e^2)}{(\omega^2-\Omega_e^2)^2}-1\right.$$
$$\left.-\frac{\omega_p^2\Omega_e^2\sin^2\alpha}{2(\omega^2-\Omega_e^2)^2}\right]+2\left[\left(2-\frac{\omega_p^2}{\omega^2}\right)\left(1-\frac{\omega_p^2}{\omega^2-\Omega_e^2}\right)^2-\frac{\omega_p^4\Omega_e^2}{\omega^2(\omega^2-\Omega_e^2)^2}\right.$$
$$\left.+2\left(1-\frac{\omega_p^2}{\omega^2}\right)^2\cdot\frac{\omega^2\Omega_e^2}{(\omega^2-\Omega_e^2)^2}\right]$$

$$\frac{v_m}{c} = \left\{1-\left(\frac{\omega}{m\Omega_e}\right)^2+2\left(\frac{\omega}{m\Omega_e}\right)^2\frac{v_{11}}{c}n\cos\alpha-\left[1+\left(\frac{\omega}{m\Omega_e}\right)^2n^2\cos^2\alpha\right)\frac{v_{11}^2}{c^2}\right\}^{1/2}$$

$$\frac{v_\pm}{c} = \frac{\left(\frac{\omega}{m\Omega_e}\right)^2 n\cos\alpha\pm\sqrt{1-\left(\frac{\omega}{m\Omega_e}\right)^2(1-n^2\cos^2\alpha)}}{1+\left(\frac{\omega}{m\Omega_e}n\cos\alpha\right)^2}$$

c is light velocity, n is refraction index satisfying the Appleton-Hartree dispersion relation, α is the angle between wave vector K and B, ω is wave frequency,

$$\Omega_e = \frac{eB}{m_ec},\ \omega_p^2 = \frac{4\pi n_e e^2}{m_e},\ K_\perp = K\sin\alpha,\ K_{11} = K\cos\alpha,\ b_m = \frac{K_\perp v_m}{\Omega_e}.$$

Assuming that the energy of nonthermal electrons [illegible] 60 keV, pitch angle $\phi = 60°$, i.e., $v_{0\perp}/c = 0.386$, $v_{011}/c = 0.223$, and $d_\perp = 0.2$, $d_{11} = 0.4$, ω_p/Ω_e [illegible] 0.4, it is found that the second harmonic ($m = 2$) X-mode will grow fastest if $\omega = 2.02\ \Omega_e$, $\alpha = 65°$, and the growth rate is

$$\omega_i^{(2)} = 0.096\frac{n_s}{n_e}\Omega_e$$

III. Saturation of ECM

The excitation of ECM leads to diffusion of energetic electrons in velocity space, which in turn weakens the instability. According to quasilinear theory we have[3]

$$\frac{\partial}{\partial t} F(v_\perp, v_\parallel) = D(t, v_\perp, v_\parallel) \frac{1}{v_\perp} \frac{\partial}{\partial v_\perp} v_\perp \frac{\partial}{\partial v_\perp} F(v_\perp, v_\parallel) \tag{3}$$

$$D(t, v_\perp, v_\parallel) = \frac{4\pi^2 e^2}{m_e^2} \int d\vec{K}\, \mathcal{E}_{\vec{K}}(t)\, \delta\left(\omega - \frac{m\Omega_e}{\gamma} - K_\parallel v_\parallel\right) \tag{4}$$

$$\frac{\partial}{\partial t} \mathcal{E}_{\vec{K}}(t) = 2\omega_i (\vec{K}, t) \mathcal{E}_{\vec{K}}(t) \tag{5}$$

where $\gamma = (1 - (v_\perp^2 + v_\parallel^2)/c^2)^{-1/2}$, $D(t, v_\perp, v_\parallel)$ is the diffusion coefficient and $\mathcal{E}_{\vec{K}}$ the wave spectral density. Let

$$\tau = \int_0^t dt'\, D(t', v_\perp, v_\parallel) \tag{6}$$

we can rewrite Eq. (3) as

$$\frac{\partial F}{\partial \tau} = \frac{1}{v_\perp} \frac{\partial}{\partial v_\perp} v_\perp \frac{\partial F}{\partial v_\perp}$$

then obtain the distribution for t > 0 (i.e. t > 0).

$$F(\tau, v_\perp, v_\parallel) = \frac{1}{2\tau} \int_0^\infty dy\, F(0, y, v_\parallel)\, e^{-\frac{v_\perp^2 + y^2}{4\tau}} I_0\left(\frac{v_\perp y}{2\tau}\right) y$$

where $F(0, v_\perp, v_\parallel)$ is the initial distribution of Eq. (1), $I_0(x)$ is modified Bessel function of zero order with argument x.

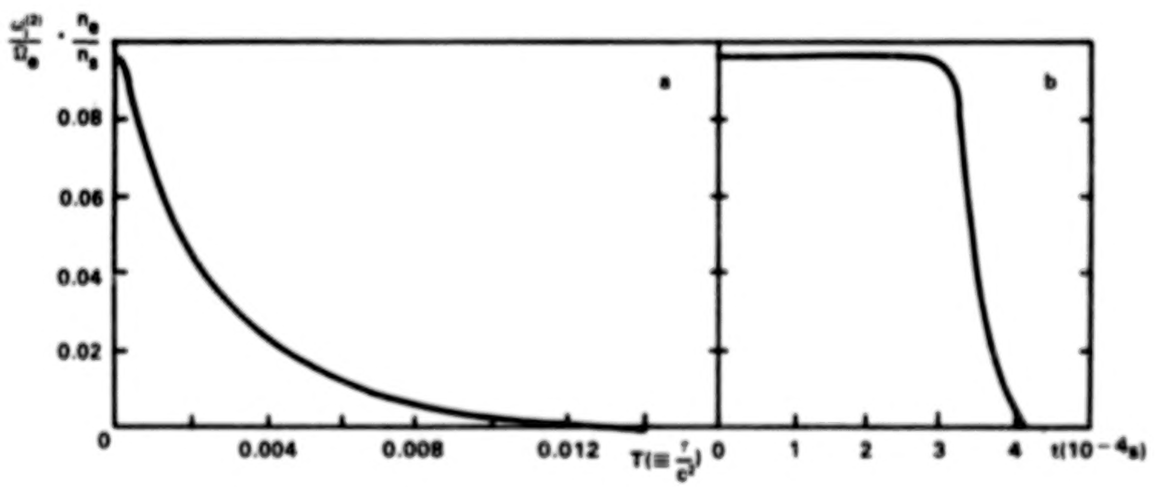

Figure 2. Plots of $\omega_i^{(2)}/\Omega_e \cdot n_e/n_s$: (a) vs τ, (b) vs time t, all for X-mode with parameters: E = 60 keV, $\phi = 60°$, $\alpha = 65°$, $\omega_p = 0.4\Omega_e$, $d_\perp = 0.2$, $d_\parallel = 0.4$ and $\omega = 2.02\Omega_e$.

Substituting Eq. (7) into Eq. (2) and using the following relations

$$\left(\frac{\partial F}{\partial v_{\parallel}}\right)_t = \left(\frac{\partial F}{\partial v_{\parallel}}\right)_\tau + \left(\frac{\partial F}{\partial \tau}\right)_{v_{\parallel}} \left(\frac{\partial \tau}{\partial v_{\parallel}}\right)_t$$

$$\approx \left(\frac{\partial F}{\partial v_{\parallel}}\right)_\tau - \frac{\tau}{v_{\parallel}} \left(\frac{\partial F}{\partial \tau}\right)_{v_{\parallel}}$$

$$\left(\frac{\partial F}{\partial v_{\perp}}\right)_t \approx \left(\frac{\partial F}{\partial v_{\perp}}\right)_\tau$$

and Eqs. (4)–(6), we obtain the change of $\omega_i^{(2)}$ with τ (Fig. 2a) and then with time t (Fig. 2b), which gives the saturation time of ECM t_S ($\tau = \tau_S$) corresponding to $\omega_i^{(2)} = 0$. We have $t_S \approx 0.42$ ms and find out that $\omega_i^{(2)}$ almost doesn't change until $t \approx 0.8\ t_S$ and only at last short stage ($\Delta t \lesssim 0.2\ t_S$) it decreases to zero rapidly. In addition we have obtained the following relations

$$t_s \approx \frac{1}{2\ \omega_{io}}\ \ell n\left(2\ \frac{W(t_s)}{W_o}\right) \tag{8}$$

$$W(t_s) \approx \frac{m_e^2}{4\pi^2 e^2}\ \tau_s\, \omega_{io}\, K_{\parallel}^{*}\ v_{0\parallel} \tag{9}$$

where $W(t_S)$ and W_O are the saturation and initial energy density of the wave, respectively, ω_{iO} is the initial growth rate and $K_{\parallel}^{*} = \eta\omega/c\ \cos\alpha$.

The above calculation is rather complicated. For simplicity we give an evaluation for saturation value τ_S.

Taking only the part of distribution (1) containing $v_\perp$ and introducing $\chi \equiv v_\perp/c$, $v \equiv v_{0\perp}/c$, $A = d_\perp v$, we have

$$F_o(\chi) = (\pi c^2 A^2)^{-1} \exp\left\{-\left(\frac{\chi - v}{A}\right)^2\right\}$$

$$\frac{\partial F_o}{\partial \chi} = -\frac{2(\chi - v)}{\pi c^2 A^4} \exp\left\{-\left(\frac{\chi - v}{A}\right)^2\right\}$$

If $\chi = \chi_O \equiv (1 - d_\perp/\sqrt{2})\ v$, then $\partial F_O/\partial\chi > 0$ (so $\omega_i > 0$) and has its maximum. Introducing $T = \tau/c^2$, $\chi = \chi_O$, $z = y/c$, we have for $\tau > 0$ ($t > 0$)

$$F(T,\chi) = \frac{1}{2\pi c^2 A^2 T} \int_0^\infty dz\ I_o\left(\frac{\chi z}{2T}\right) z \exp\left\{-\frac{\chi^2 + z^2}{4T} - \left(\frac{z - v}{A}\right)^2\right\}$$

$$\frac{\partial F}{\partial \chi} = \frac{1}{4\pi c^2 A^2 T^2} \int_0^\infty dz \left[z\, I_1\left(\frac{\chi z}{2T}\right) - \chi\, I_o\left(\frac{\chi z}{2T}\right)\right] z \exp\left\{-\frac{\chi^2 + z^2}{4T} - \left(\frac{z - v}{A}\right)^2\right\} \tag{10}$$

we can divide the integration in Eq. (10) into two parts:

$$Q_1 = \int_0^{z_0} dz\, z\left[\frac{z^2\chi}{16T^2}(2T-\chi^2) + \frac{z^4\chi^3}{3\cdot 2^{10}T^4}(4T-3\chi^2) + \frac{z^6\chi^5}{9\cdot 2^{14}T^6}(T-\chi^2) - \chi\right]$$

$$\exp\left\{-\frac{\chi^2+z^2}{4T} - \left(\frac{z-v}{A}\right)^2\right\}$$

$$Q_2 \approx \sqrt{\frac{T}{\pi\chi}}\int_{z_0}^{\infty} dz\sqrt{z}\,(z-\chi)\exp\left\{-\frac{\chi^2+z^2}{4T} - \left(\frac{z-v}{A}\right)^2\right\}$$

where $z_0 \approx 10T/\chi$ and in Q_1 $(0 \leq z \leq z_0)$ the Bessel functions I_0, I_1 have been expressed approximately for small argument but in Q_2 $(z_0 \leq z < \infty)$ for large argument. It is easy to see that in general we have $Q_1 < 0$ and $Q_2 > 0$.

If $z_0 << \chi$, i.e. $T << 0.1\,\chi^2$, Q_2 is dominant and $\partial F/\partial\chi > 0$. This is the case at the start of the growing wave.

If $z_0 >> \chi$, i.e. $T >> 0.1\,\chi^2$, Q_1 becomes dominant, so $\partial F/\partial\chi < 0$. This is the case after saturation.

If $z_0 \sim \chi$, i.e., $T \sim 0.1\,\chi^2$, we have $Q_2 > |Q_1|$ and $\partial F/\partial\chi > 0$, but $|Q_1|$ gets larger. This corresponds to the case that the growth rate decreases obviously.

Hence we can take $T_s = 0.1\,v^2$ or $\tau_s = 0.1\,v_{0\perp}^2$ as the saturation value when Q_1 can be comparable with Q_2. For the chosen parameter, $v_{0\perp}/c = 0.386$, we have $T_s \approx 0.015$ which is in agreement with numerical calculation ($T_s \approx 0.013$).

IV. Gyroresonance Absorption and BT of Radiation

The gyroresonance absorption (GA) is a serious problem for maser radiation. The optical depth of the mth layer ($m \geq 2$) for χ-mode is[4]

$$\tau_m = \left(\frac{\omega_p}{\omega}\right)^2 \frac{m^{2m}\sqrt{2}}{2^{m-1}m!} \cdot \frac{\omega L_B}{c}\left(\frac{T_e}{m_e c^2}\right)^{m-1}$$

with $L_B = B\left|\frac{dB}{dL}\right|^{-1}$. For $\omega = 2\pi \times 2.84$ GHz and $m = 3$ we have

$$\tau_3 \approx T^2\left(\frac{\omega_p}{\omega}\right)^2\left(\frac{T_e}{10^6}\right)^2 \frac{L_B}{10^8}$$

Because $L_B > 1000$ km in general, an intense maser radiation ($T_b > 10^{14}$K) can hardly be received unless $T_e < 2\times 10^6$K and $\omega_p/\omega \lesssim 0.1$

It seems possible, however, that some magnetic arches with smaller dimension and higher magnitude may emerge from an active region where the magnetic configuration is more complicated, then it may be true that $L_B < 1000$ km (e.g. $L_B = 500$ km) at larger angle to $\vec{B}$ and the third GA will be weaker, so the radiation may escape from the corona.

The BT (T_b) and flux density (S) received are

$$T_b = \left(\frac{2\pi c}{\omega}\right)^3 \left(\frac{\Delta\omega}{\omega}\right)^{-1} \frac{W}{\Delta\Omega_r} e^{-\tau_s} \tag{12}$$

$$S = 2\, T_b \left(\frac{\omega}{2\pi c}\right)^2 \frac{A}{R^2} \tag{13}$$

where W is the energy density of the wave, $R = 1.5 \times 10^{13}$ cm is the distance between the Sun and the Earth, A is the surface area of the radiation source, which is about 10^{15} cm^2 for SMMSE, $\Delta\omega$ is the bandwidth of the radiation ($\Delta\omega/\omega \approx 0.01$ according to Droge[5] and our calculation), $\Delta\Omega_r$ is the radiation solid angle. It is easy to see from Fig. 3 that the propagation angle α will be from 60° to 70° if the pitch angle $\phi = 60°$, hence $\Delta\Omega_r = 1$.

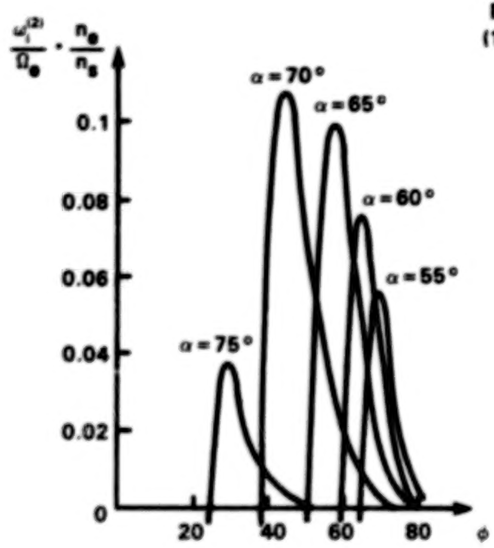

Figure 3. A plot of $\omega_i^{(2)}/\Omega_e \cdot n_e/n_s$ vs ϕ for different α: 55°, 60°, 65°, 70° and 75°. Other parameters are the same as in Fig. 2.

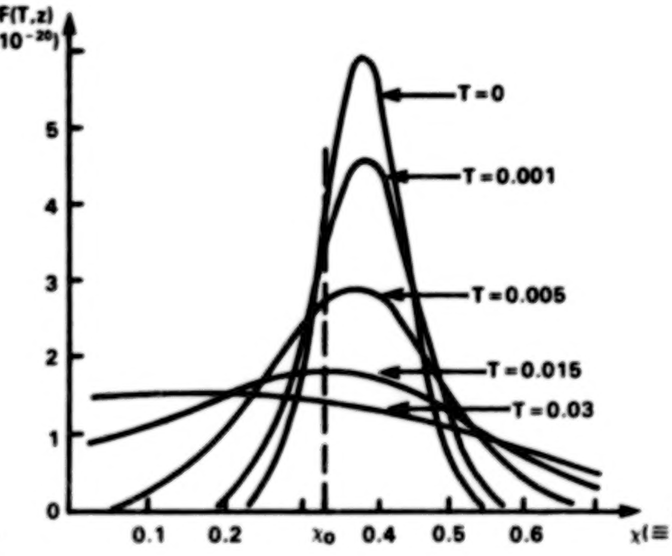

Figure 4. A plot of $v_\perp$ part of distribution of nonthermal electrons for different T with $\chi \equiv v_\perp/c$, $T \equiv \tau/c^2$, $v \equiv v_{o_\perp}/c = 0.386$, and $\chi_o = 0.86v$.

Assuming $n = 0.97$, $\alpha = 65°$ (for the fastest growing second harmonic of X-model) and $n_s/n_e = 4 \times 10^{-5}$, $\tau_s/c^2 = 0.013$, $W(t_s)/W_o = 2 \times 10^{10}$, $e^{-\tau_s} = 0.1$, we have obtained from Eqs. (8)–(13)

$$t_s \approx 0.36 \text{ ms}, \; W(t_s) \approx 5.9 \times 10^{-5} \text{ ergs cm}^{-3}$$
$$T_b \approx 5 \times 10^{15} \text{ K}, \; S \approx 5.5 \times 10^{5} \text{ s.f.u.}$$

These results are in agreement with observations.

V. Summary and Concluding Remarks

It has been shown that ECM is an effective mechanism to produce electromagnetic radiation. Its BT may be higher than 10^{15} K and it can escape from the solar corona without any transformation. The simple procedure, high efficiency, short time scale, strong directivity of radiation, and high degree of circular polarization are its advantages over the plasma radiation mechanism to explain SMMSE. It is calculated in this paper that SMMSE with very high BT ($T_b \approx 5 \times 10^{15}$ K) would be produced by hollow beam driven ECM if $E = 60$ keV, $\phi = 60°$, $\alpha = 65°$, $n_s/n_e = 4 \times 10^{-5}$, $\omega_p/\Omega_e = 0.4$, $L_B = 500$ km, and $T_e = 2 \times 10^6$K.

It is shown that the range of pitch angle ϕ for exciting ECM is very wide (> 30°, see Fig. 3) and the energy of nonthermal electrons may be from ~10 keV to 100 keV or higher. Besides the hollow beam distribution, other velocity anisotropy as a loss-cone distribution can also excite ECM under appropriate conditions. Hence it seems that ECM is often produced above solar active regions. The main reasons why there appear rarely intense SMMSE events may be due to the powerful directivity of radiation and strong third GA.

It is easy to see from Eq. (7) and Fig. 4 that with the evolution of the energetic electron's distribution, the transverse velocity component of them is decreased but the parallel one isn't. As a result, the pitch angle is getting smaller, so the electrons, after losing most of their transverse energy, get through the magnetic mirror points and rush into the transition region to produce hard X-ray bursts, so with which the SMMSE correlate very well[6].

Acknowledgements

Professor C.S. Wu is thanked for his helpful discussion after the paper was finished.

References

[1] Zhoa, R.Y. & Jin, S.Z., Ultra-fast fine structures of a microwave outburst, Scientia Sinica (series A), Vol. XXV, No. 4 (1982), pp. 422-429.

[2] Frend, H.P., et al., An electron cyclotron maser instability in high-density plasma, Phys. Fluids, (1985) in press.

[3] Wu, C.S., et al., Saturation and energy-conversion efficiency of auroral kilometric radiation, Ap. J., 248 (1981), pp. 384-391.

[4] Zheleznyakov, V.V., Radio Emission of the Sun and Planets, Oxford: Pergamon Press, p. 454, 1970.

[5] Dröge, F., Millisecond fine-structure of solar burst radiation in the range 0.2–1.4 GHz, Astron. Astrophys., 57 (1977), pp. 285-290.

[6] Li Chun-sheng, Fu Qi-jun, Yan Yu-hua, Jiang Shu-ying & Li Hong-wei, Microwave millisecond spike emission and its associated phenomena during the impulsive phase of flares, These proceedings (1986).

N87
21820
UNCLAS

N87-21820

THE EFFECT OF BEAM-DRIVEN RETURN CURRENT INSTABILITY ON SOLAR HARD X-RAY BURSTS

D. Cromwell, P. McQuillan, and J. C. Brown

Departments of Astronomy and Natural Philosophy
University of Glasgow
Glasgow, G12 8QW, U.K.

ABSTRACT

The problem of electrostatic wave generation by a return current driven by a small area electron beam during solar hard X-ray bursts is discussed. The marginal stability method (cf. Duijveman et al. 1981) is used to solve numerically the electron and ion heating equations for a prescribed beam current evolution. When ion-acoustic waves are considered, we find that the method appears satisfactory and, following an initial phase of Coulomb resistivity in which T_e/T_i rises, predicts a rapid heating of substantial plasma volumes by anomalous ohmic dissipation. This hot plasma emits so much thermal bremsstrahlung that, contrary to previous expectations, the unstable beam-plasma system actually emits more hard X-rays than does the beam in the purely collisional thick target regime relevant to larger injection areas. Inclusion of ion-cyclotron waves results in ion-acoustic wave onset at lower T_e/T_i and a marginal stability treatment yields unphysical results. Specifically, negative resistivity occurs when the ion-acoustic instability is excited at an electron-to-ion temperature ratio of $T_e/T_i \lesssim 4{\cdot}5$, showing the marginal stability analysis of ion acoustic waves to be invalid in this regime. Discarding marginal stability and adopting a simple wave-energy equation, the time-dependent effect of ion-acoustic turbulence generated by the return current is investigated.

1 Introduction

It is commonly believed that electron beams, propagating downwards in the solar atmosphere, play a major role in the production, by collisional bremsstrahlung, of hard X-ray bursts during the impulsive phase of solar flares (see review by Brown and Smith 1980) and that they may also be

PRECEDING PAGE BLANK NOT FILMED

instrumental in flare atmospheric heating. In addition, it is recognised (e.g. Hoyng, Brown and van Beek 1976) that the large electron flux, demanded by the observed X-ray photon flux in such an interpretation, requires that a beam-neutralising return current be set up, such that:

$$\frac{n_b}{n_p} = \frac{v_d}{v_b} \qquad (1)$$

where $\frac{n_b}{n_p}$ is the ratio of beam density to ambient plasma density, v_b is the (sub-relativistic) beam velocity (a beam with single injection energy E_o, representing the mean energy of a real beam, is considered here) and v_d is the drift velocity of the ambient plasma electrons (which constitute the return current). If we consider, for simplicity, a model in which v_d increases during the impulsive phase, due to the rising beam flux $n_b v_b$, threshold velocities for the generation of various microinstabilities may be reached and so unstable wave growth may take place in the atmosphere. The resultant anomalous resistivity will affect hard X-ray production in two ways:

(a) The electric field required to drive the return current will increase and so reduce the lifetime of beam electrons. The nonthermal bremsstrahlung efficiency, which is already small, is therefore further reduced.

(b) Enhanced plasma heating will take place and thereby affect the observed thermal radiation signature.

The aim of this paper, then, is to describe preliminary results of calculations attempting to determine the effect of such return current instability on hard X-ray bursts during solar flares.

2 Marginal Stability Analysis

We consider a quasi-steady state consisting of a monoenergetic driving electron beam, with specified current density $j_b(t)$, current neutralising ($j_p = - j_b$) hot drifting electrons at temperature T_e, and hot stationary ions at temperature T_i. While recognising the possibility of beam-return current interaction, we concentrate here on the return current electron-background ion instability. The quasi-linear relaxation of the electron beam is considered elsewhere in these proceedings by McClements et al.

A typical large solar flare value is chosen for the peak total electron injection rate, $\mathcal{F}_o(s^{-1})$, but the beam area, A, is taken to be well below the upper limit set by hard X-ray images in order to ensure that unstable return current drift velocity thresholds are exceeded before this peak, viz.

$$\mathcal{F}_o = 10^{36}s^{-1}; \quad A = 10^{16}cm^2 \qquad (2)$$

(Brown and Melrose 1977, Hoyng, Knight and Spicer 1978). If we assume that this rate (2) is obtained after a linear increase over 10s, a typical time-scale for the impulsive phase, then our specified $j_b(t)$ is:

$$j_b(t) = 5.10^9 t \quad \text{statamp cm}^{-2} \qquad (3).$$

The electron beam is decelerated by the electric field that drives the return current and ignoring electron time-of-flight effects, it has a "stopping length", s (Brown and Hayward 1981) due to ohmic losses, given by

$$s = \frac{E_o}{e\eta j_b} \qquad (4)$$

where E_o is the injected electron energy, here taken to be 100 keV and η is the resistivity of the plasma. Finally, we also assume a homogeneous and initially isothermal plasma with density $n_p = 10^{11}\text{cm}^{-3}$ and temperature $T_o = 5.10^6\,\text{K}$.

The heating equations for the plasma electrons and ions, neglecting collisional heating by the beam, and also convection, thermal conduction and radiation losses, are

$$\frac{3}{2} n_p \kappa \frac{dT_e}{dt} = \frac{3}{2} n_p \kappa \frac{(T_i - T_e)}{\tau} + \sum_i \chi_i \eta_i j_p^2\,(t) \qquad (5)$$

$$\frac{3}{2} n_p \kappa \frac{dT_i}{dt} = \frac{3}{2} n_p \kappa \frac{(T_e - T_i)}{\tau} + \sum_i (1 - \chi_i)\eta_i j_p^2\,(t) \qquad (6)$$

where κ is Boltzmann's constant, τ is the ion-electron energy exchange time, $\chi_i = \chi_i(T_e/T_i)$ and $(1 - \chi_i)$ are the fractions of the ohmic power dissipation $\eta_i j_p^2(t)$ absorbed by the electrons and ions respectively as a result of collision process i, and η_i is the resistivity due to this process; e.g. in the case of classical Coulomb collisions, $\chi = 1$ and η is the usual Spitzer (1962) resistivity, proportional to $T_e^{-3/2}$.

With the onset of turbulence, anomalous resistivity sets in due to wave-particle collisions and so the ohmic heating term $\sum_i \eta_i j_p^2$ rises, leading to increased plasma heating. Note that this model, with a prescribed j(t), is fundamentally different from the Duijveman et al. (1981) problem where the electric field $\mathcal{E}(t)$ is specified. Specifically, their ohmic heating term, $\sum_i \frac{\mathcal{E}^2}{\eta_i}$, is reduced by any turbulent increase in η, a fact they appear to have overlooked. In other words, having a prescribed $\mathcal{E}$-field leads to reduced, rather than increased, plasma heating when anomalous resistivity sets in.

To solve equations (5) and (6) for $T_e(t)$, $T_i(t)$ and $\eta(t)$ we use the hypothesis of marginal stability (Manheimer and Boris 1977). States of marginal stability (i.e. states with zero growth-rate) in the present case can be represented by critical drift velocity (v_{crit}) curves in the $\left(\frac{v_d}{v_e}, \frac{T_e}{T_i}\right)$ plane, where $v_e = \left(\frac{\kappa T_e}{m_e}\right)^{1/2}$ is the electron thermal speed. We apply the marginal stability hypothesis by setting $v_d = v_{crit}$ at onset of turbulence, thereby constraining the system to evolve thereafter along the marginal stability curve. This gives us a relationship between T_e and T_i which, using the forms of χ for ion-cyclotron (IC) and ion-acoustic (IA) waves derived by

Duijveman et al. (1981), then allows us to solve numerically the heating equations (5) and (6).

We first consider the simplest case of an unmagnetised plasma, i.e. zero B-field. Figure 1 shows the evolution of the plasma in the $\left(\frac{v_d}{v_e}, \frac{T_e}{T_i}\right)$ plane. In the initial phase of classical resistivity, collisions cause an increase in T_e/T_i, from its initial value of 1.0, while the drift velocity rises, until the IA marginal stability curve is reached. The system then evolves along the curve. Figure 2 shows the variation of the normalised resistivity with time, ion-acoustic turbulence switching on after about 6s. Finally, the increases in T_e and T_i are seen in Figure 3. These profiles relate only to a plasma layer of thickness s_{min}, $\simeq 5.10^9$cm (emission measure $n^2As_{min} \simeq 5.10^{47}cm^{-3}$), the smallest depth of beam penetration into the atmosphere, because it is this region which is heated continuously during the simulation. The final temperatures obtained ($T_e \simeq 300\ T_o$, $T_i \simeq 35\ T_o$) will tend to be reduced by losses (neglected here) but we should note that wave generation will reduce thermal conductivity by the same factor as the electrical conductivity.

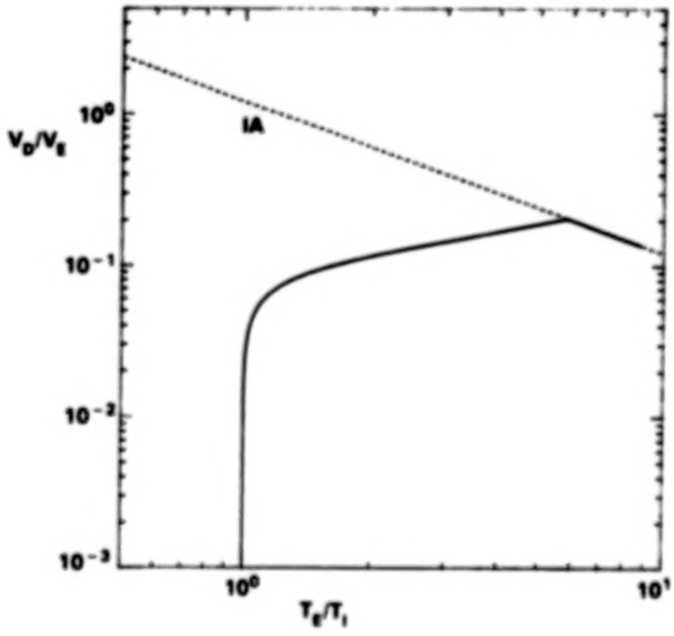

Figure 1. Evolution of the plasma in the $\left(\frac{v_d}{v_e} - \frac{T_e}{T_i}\right)$ plane, assuming marginal stability. IA denotes the ion-acoustic marginal stability curve.

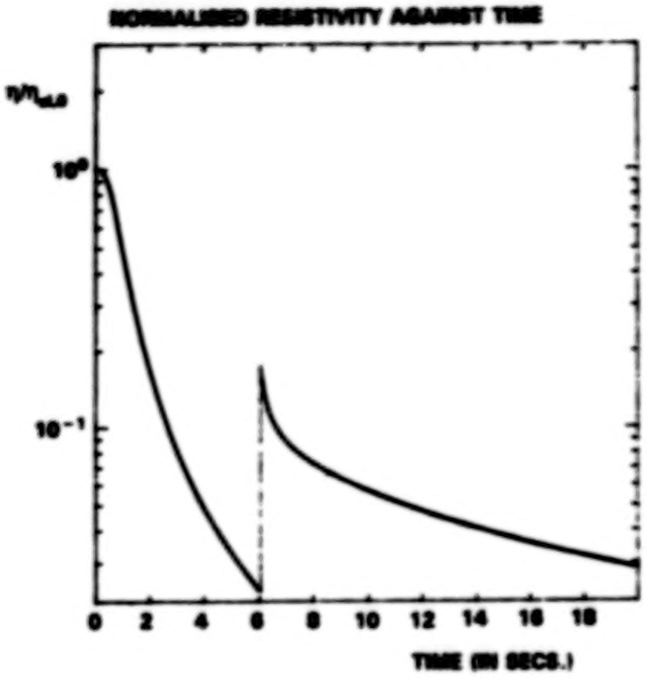

Figure 2. Variation of resistivity, normalised to the initial classical (i.e. Spitzer) resistivity. IA turbulence is generated at about 6s.

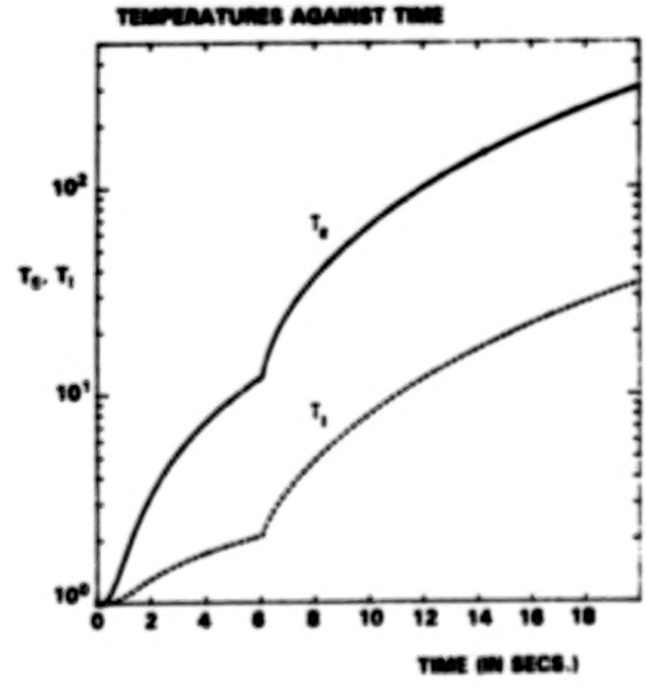

Figure 3. Rise in electron and ion temperatures, normalised to the initial temperature $T_0 = 5.10^6$ K, showing the increases at onset of IA turbulence.

We now attempt to repeat the analysis for a magnetised plasma. For $T_e/T_i \lesssim 8$, the critical drift velocity for the generation of ion-cyclotron waves has the lowest threshold. These preferentially heat ions and so tend to reduce T_e/T_i. However they quickly saturate and do not contribute greatly to the total resistivity. The system then evolves away from the IC marginal stability curve, with T_e/T_i once again increasing due to the dominant effect of Coulomb collisions, until the IA marginal stability curve is reached. In this case, onset of IA turbulence occurs at lower T_e/T_i and we often find unphysical behaviour in the form of negative resistivity. Investigating further, by assuming a simple analytic form for the IA marginal stability curve and by using the form of $\chi_{IA} = \chi_{IA}(T_e/T_i)$ derived by Duijveman et al. (1981), we find that η is negative if $T_e/T_i \lesssim 4.5$. In other words, the application of marginal stability leads to negative values of anomalous resistivity, if the onset of ion-acoustic turbulence occurs at $T_e/T_i \lesssim 4.5$. We discuss this failure of marginal stability further in Section 5.

3 Wave Growth Analysis

In the previous discussion we did not incorporate any equations describing the growth of the ion-acoustic waves, which occurs on very short timescales in comparison to $v_d/\dot{v}_d$, the rise time of the return current. Here we adopt the following equation for the evolution of W, the wave energy,

$$\frac{dW}{dt} = \gamma W \tag{7}$$

where γ, the linear growth rate, is taken to be $10^{-2}\omega_{pi}$ (ω_{pi} is the ion plasma frequency). This growth rate corresponds to a drift velocity just in excess of the marginally stable drift velocity (Stringer 1964). Provided that $\frac{W}{n_p \kappa T_e} \ll 1$, (i.e. weak turbulence), we can relate the effective collision frequency, ν_{eff}, and the wave level using:

$$\nu_{eff} \simeq \omega_{pe} \frac{W}{n_p \kappa T_e} \tag{8}$$

(see, e.g. Hasegawa (1974)) where ω_{pe} is the electron plasma frequency. The effective (i.e. total, including classical) resistivity is then obtained using:

$$\eta_{eff} = \frac{4\pi \nu_{eff}}{\omega_{pe}^2} \tag{9}$$

(see, e.g. Papadopoulos 1977).

We can, therefore, solve equations (5) and (6) numerically in conjunction with equations (7), (8) and (9). The wave level grows from the thermal level, obtained by substituting the classical collision frequency in the left hand side of equation (8). There are several possible saturation mechanisms limiting the growth of ion-acoustic waves (Hasegawa 1974) and the relevant process for solar flare conditions is by no means certain. Hasegawa gives three possible processes, the saturation level being lowest for the nonlinear two-wave interaction investigated by Tsytovich (1971). The effective collision frequency at saturation for this process is

$$\nu_{eff} \gtrsim 10^{-2}\, \omega_{pi}\, \frac{v_d}{c_s} \qquad (10)$$

where $c_s = \left(\frac{\kappa T_e}{m_i}\right)^{1/2}$ is the ion sound speed.

Our approach then, is to let classical heating proceed as v_d rises until the critical drift velocity for onset of ion-acoustic turbulence is reached. The wave energy then grows from the thermal level in the classical regime until saturation occurs. During the ion-acoustic heating phase, v_d/v_e decreases due to the rapid increase in T_e, until the system drops below the IA marginal stability curve (see Figure 4). The waves are then allowed to decay, with the same e-folding time $(1/\gamma)$ as the wavegrowth, until the wave level has dropped to the thermal level, where, once again, classical heating only takes place.

Initial investigations show a rise in anomalous resistivity to $\sim 10^5$ times the initial classical value (see Figure 5), while T_e and T_i rise to $\sim 50\,T_o$ and $\sim 8\,T_o$ respectively (see Figure 6). These values are obtained in a very short time: the rise, saturation and decay of the IA waves takes place in $\sim 10^{-5}$s . Again we note that the final temperature values are attained in the beam layer of thickness s_{min}, here found to be only $\gtrsim 3.5.10^3$ cm (emission measure $\gtrsim 3.5.10^{41}$cm^{-3}), because of the very high resistivity attained during IA turbulence. In our simulations, it is found that saturation occurs at $\frac{W}{n_p \kappa T_e} \gtrsim 10^{-3}$ thus satisfying the requirement for weak turbulence.

The above analysis has, of necessity, been a very simple approach to the problem. For example, a wave energy equation with a proper averaging over the wavenumber, k, of the wave spectrum W(k) would be more realistic. In addition, the controversial issue of the relevant saturation mechanism for solar flare parameters needs to be looked at in more detail.

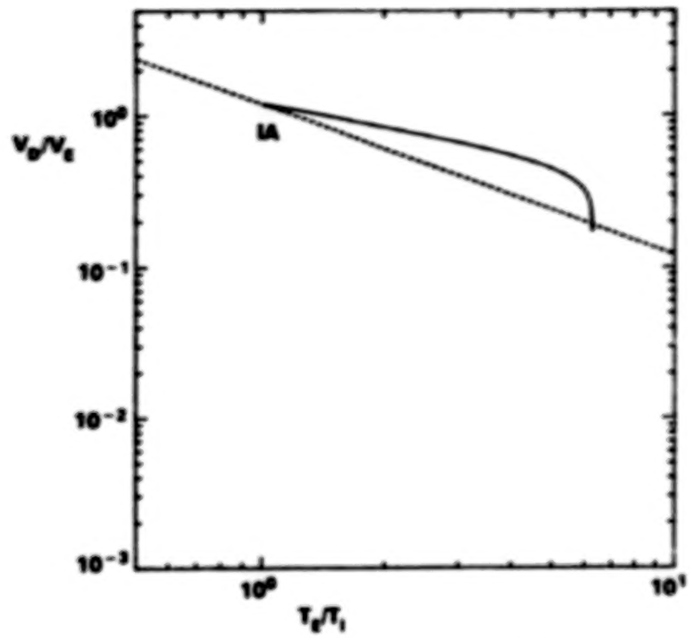

Figure 4. Evolution of the plasma in the $\left(\frac{v_d}{v_e} - \frac{T_e}{T_i}\right)$ plane using the wave growth analysis. The initial value of v_d is chosen such that the IA curve is reached after just a few numerical timesteps.

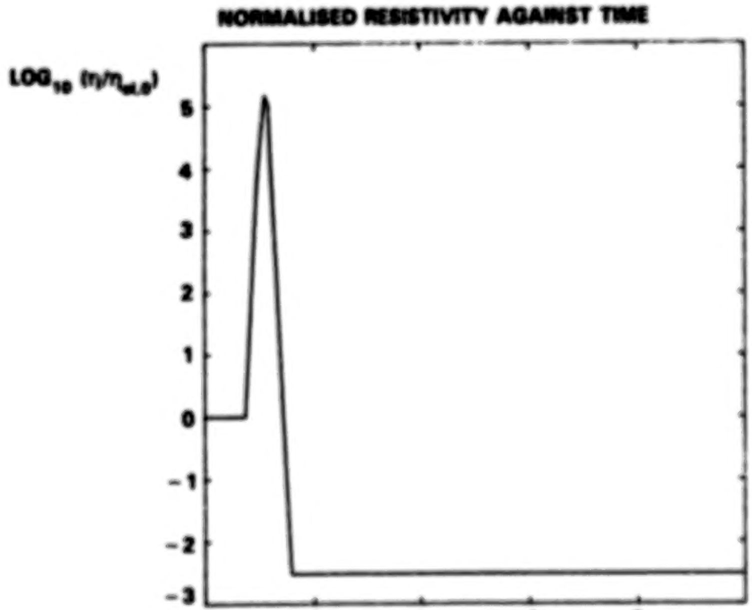

Figure 5. The variation of normalised resistivity with time, showing the growth, saturation and decay of IA resistivity in $\sim 10^{-5}$ s.

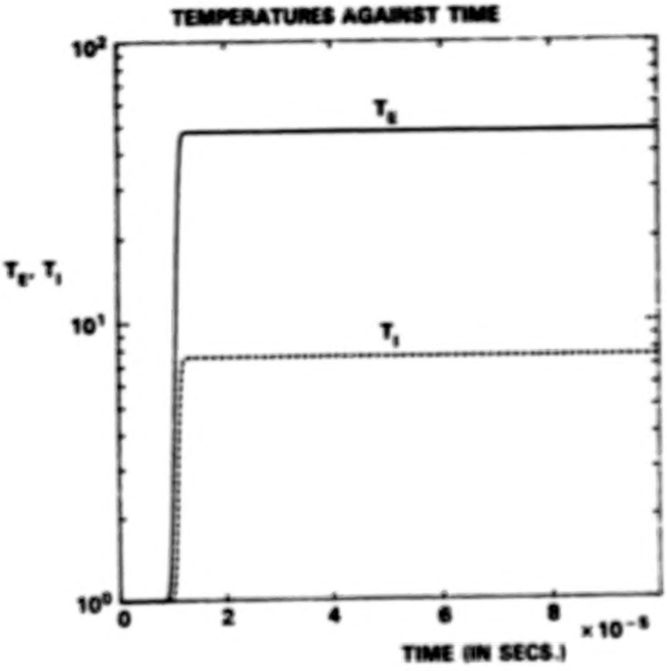

Figure 6. The electron and ion temperature profiles over the evolution time of 10^{-4} s.

4 The Effect of Return Current Instability on the Radiation Signature

In this section we briefly compare the thermal and non-thermal bremsstrahlung emitted at the instant when the beam has shrunk to its minimum length s_{min}. From equation (4) it can be seen that when η rises at onset of turbulence, the beam length is reduced by the same factor (over the short time-scale involved, the current density $j_b(t)$ is virtually constant). In other words, the electron beam lifetime is reduced and, correspondingly, the non-thermal bremsstrahlung. The enhanced ohmic dissipation of the return current, however, causes rapid local heating of the plasma and hence increases its thermal bremsstrahlung.

Below, we calculate the ratio of thermal to non-thermal radiation in the case of beam return current losses only, which as we will show, in some circumstances, dominate collisional losses from the beam when η is anomalous. For comparison, we also evaluate the ratio of the thermal bremsstrahlung in the anomalous case to the beam bremsstrahlung evaluated from the usual thick target formula which incorporates collisional losses only. The thermal emissivity from the volume $V = A.s_{min}$ is

$$\left(\frac{dJ}{d\varepsilon}\right)_T = Vn_p \int_\varepsilon^\infty v(E)\, \frac{dn}{dE}\, \frac{dQ}{d\varepsilon}\, (\varepsilon, E)\, dE \qquad (11)$$

where $\frac{dn}{dE}$, the number density of electrons per unit energy range, is given by the Maxwellian distribution function and $\frac{dQ}{d\varepsilon}(\varepsilon, E)$ is the bremsstrahlung cross-section differential in photon energy. Here, as a simple first approximation, we assume Kramer's cross-section:

$$\frac{dQ}{d\varepsilon}(\varepsilon, E) = \frac{Q_o m_e c^2}{\varepsilon E} \tag{12}$$

where $Q_o = \frac{8}{3}\alpha r_e^2$ in the usual notation. The thick-target non-thermal emissivity (Brown 1971) is

$$\left(\frac{dJ}{d\varepsilon}\right)_{NT} = \int_{\varepsilon}^{\infty} \mathcal{F}(E)\nu(\varepsilon, E)\, dE \tag{13}$$

where $\mathcal{F}(E) = \mathcal{F}_o\delta(E - E_o)$ (s^{-1} per unit electron energy) is the electron flux and $\nu(\varepsilon, E)$ is the number of photons of energy ε emitted by an electron with initial energy E, given by:

$$\nu(\varepsilon, E) = n_p \int_{E_*=E}^{E_*=\varepsilon} \frac{dQ}{d\varepsilon}(\varepsilon, E_*) \frac{v(E_*)}{\left(\frac{dE_*}{dt}\right)}\, dE_* \tag{14}$$

In the case of beam losses due to ohmic dissipation of the return current only, the energy loss equation is

$$\frac{dE_*}{dt} = -e\mathcal{E}v(E_*) \tag{15}$$

where $\mathcal{E}$, the electric field, is given by

$$\mathcal{E} = e\eta\frac{\mathcal{F}_o}{A} \tag{16}.$$

The ratio of thermal to non-thermal emissivities (in the case of return current losses only) is then:

$$\frac{\left(\frac{dJ}{d\varepsilon}\right)_T}{\left(\frac{dJ}{d\varepsilon}\right)_{RC}} = \left(\frac{8}{\pi m_e \kappa T_e}\right)^{1/2} \frac{e^2 \eta\, n_p s_{min}}{\ell n\left(\frac{E_o}{\varepsilon}\right)} \exp\left(-\frac{\varepsilon}{\kappa T_e}\right) \tag{17}.$$

Equation (13) also applies to the case of beam Coulomb collisional losses only. The energy loss equation in this case is

$$\frac{dE_*}{dt} = -\frac{K\, n_p v(E_*)}{E_*} \tag{18}$$

where $K = 2\pi e^4 \Lambda$ in the usual notation. The ratio of thermal bremsstrahlung in the anomalous case to the non-thermal emissivity in the case of Coulomb collisional losses only is then:

$$\frac{\left(\frac{dJ}{d\varepsilon}\right)_T}{\left(\frac{dJ}{d\varepsilon}\right)_{CC}} = \left(\frac{8}{\pi m_e \kappa T_e}\right)^{1/2} \frac{n_p^2 VK}{\mathcal{F}_0 (E_0 - \varepsilon)} \qquad (19)$$

Applying equations (17) and (19) to the results of Section 2 (Marginal Stability) and Section 3 (Wave Growth Analysis) we find the following:

(a) Marginal stability analysis (Figures 1 - 3) gives, at $\varepsilon = 20\,\mathrm{keV}$:

$$\frac{\left(\frac{dJ}{d\varepsilon}\right)_T}{\left(\frac{dJ}{d\varepsilon}\right)_{RC}} \simeq 15 \; ; \quad \frac{\left(\frac{dJ}{d\varepsilon}\right)_T}{\left(\frac{dJ}{d\varepsilon}\right)_{CC}} \simeq 2.6 \qquad (20).$$

Here the thermal emissivity is over one order of magnitude greater than the non-thermal (return current) emissivity, and substantially exceeds that from a collisional thick target beam. Thus, when one considers a beam injection rate $\mathcal{F}_0$ and reduces the beam area, A, until the return current goes IA unstable, the beam length and bremsstrahlung are greatly reduced as usually assumed (e.g. Hoyng, Knight and Spicer 1978) but enhanced thermal bremsstrahlung from the rapidly heated plasma exceeds the thick target bremsstrahlung which is produced by the same beam over a large area A.

(b) Using the wave growth analysis (Figures 4 - 6), when unphysical behaviour is found in a marginal stability treatment, gives at $\varepsilon = 20\,\mathrm{keV}$:

$$\frac{\left(\frac{dJ}{d\varepsilon}\right)_T}{\left(\frac{dJ}{d\varepsilon}\right)_{RC}} \simeq 4 \; ; \quad \frac{\left(\frac{dJ}{d\varepsilon}\right)_T}{\left(\frac{dJ}{d\varepsilon}\right)_{CC}} \simeq 8.10^{-7} \qquad (21)$$

i.e. the thermal and return current non-thermal emissivities are comparable but the thermal emissivity is negligible in comparison with the collisional non-thermal emissivity. This is due to the small size of the emitting volume defined by s_{min}. In comparing these results with those of (a), we should note that the evolution time in each analysis is very different - 20s in the marginal stability case compared to 10^{-4} s in the wave growth case. However, we anticipate that over longer evolution times the wave growth analysis will result in a greater volume of material heated to $\sim 10^8$ K and a greater thermal emissivity (and emission measure).

5 The Failure of Marginal Stability

We return now to the problem of why the application of marginal stability leads in some cases to negative values of resistivity. There appears to be confusion in the literature as to whether or not there is a lower limit of T_e/T_i below which the ion-acoustic instability cannot be excited and therefore below which the marginal stability curve used by us, by Duijveman et al. (1981) and by Holman (1985) for v_{crit} (IA) is irrelevant. For example, Kaplan, Pikel'ner and Tsytovich (1974) state quite explicitly (p.53) that "... it is necessary that $T_e \gtrsim 5T_i$" (for the growth of ion-acoustic waves). If this is correct, then it would be inappropriate to use our v_{crit} and χ - IA curves below $T_e/T_i \gtrsim 5$, and so it would not be surprising that unphysical results arise in this region. Similar statements are to be found in Melrose (1985) and in Stix (1962) (p.214) where a precise lower limit of $T_e/T_i \simeq 3.5$ is set. However all of these statements appear to be based on the assumption that $v_d << v_e$. In contrast, Fried and Gould (1961) and Kadomtsev (1965) state that the ion-acoustic instability can arise in an isothermal (i.e. $T_e/T_i \sim 1.0$) plasma if the drift velocity is high enough: $v_d \gtrsim v_e$.

By examining the roots of the linearised dispersion relation describing longitudinal plasma oscillations for drifting Maxwellians, we have ourselves confirmed the latter case: the so-called "ion-acoustic" mode will become unstable in an isothermal electron-ion plasma, described by drifting Maxwellians, if the relative drift velocity > $1.34 v_e$. We hope to justify this in a subsequent paper. We are, of course, still left with the problem of explaining the failure of marginal stability for $T_e/T_i \lesssim 4.5$. It is possible that the form of the χ-function (Tange and Ichimaru, 1974) for ion-acoustic waves is the source of this difficulty and we intend to investigate this.

6 Discussions and Conclusions

We have presented a simple analysis of the problem of electrostatic wave generation by a beam-driven return current. The marginal stability approach fails below an electron-to-ion temperature ratio $T_e/T_i \gtrsim 4.5$. We believe that this is not due to any lower limit of T_e/T_i necessary for the generation of unstable ion-acoustic waves: the ion-acoustic instability will arise in an isothermal electron-ion plasma provided $v_d \gtrsim v_e$.

Both the marginal stability and wave growth analyses presented here allow us to calculate the uniform plasma heating only in the volume bounded by s_{min}, the minimum stopping length of the beam. A 2-D treatment of the combined spatial and temporal dependence is required to extend the problem to plasma heating outside this region. Future work should also incorporate a less idealised injected electron spectrum (e.g. power law). However, we believe that the essential result presented here of enhanced ohmic return current dissipation leading to rapid plasma heating to hard X-ray temperatures in milliseconds (i.e. typical spike burst durations) or less, will remain unaltered.

Acknowledgements

We would like to thank R. Bingham, E.W. Laing, A.L. MacKinnon and P.A. Sweet for helpful discussions relating to this paper. Two of us (D.C. and P.McQ.) gratefully acknowledge financial support from SERC.

References

Brown, J.C.: 1971, Solar Phys., 18, 489.
Brown, J.C. and Melrose, D.B.: 1977, Solar Phys., 52, 117.
Brown, J.C. and Smith, D.F.: 1980, Rep. Prog. Phys., 43, 125.
Brown, J.C. and Hayward, J.: 1981, Solar Phys., 73, 121.
Brown, J.C., Hayward, J. and Spicer, D.: 1981, Ap.J., 245, L91.
Duijveman, A., Hoyng, P. and Ionson, J.A.: 1981, Ap.J., 245, 721.
Fried, B.D. and Gould, R.W.: 1961, Phys. Fluids, 4, 139.
Hasegawa, A.: 1974, Rev. Geophys. Space Phys., 12, 273.
Holman, G.D.: 1985, Ap.J., 293, 584.
Hoyng, P., Brown, J.C. and van Beek, H.F.: 1976, Solar Phys., 48, 197.
Hoyng, P., Knight, J.W. and Spicer, D.S.: 1978, Solar Phys., 58, 139.
Kadomtsev, B.B.: 1965, "Plasma Turbulence", Academic Press (London).
Kaplan, S.A., Pikel'ner, S.B. and Tsytovich, V.N.: 1974, "Plasma Physics of the Solar Atmosphere", Physics Reports, Volume 15C, Number 1.
Manheimer, W. and Boris, J.P.: 1977, Comments Plasma Phys. Controlled Fusion, 3, 15.
Melrose, D.B.: 1985, in "Solar Radiophysics" (eds. D.J. McLean and N.R. Labrum), Cambridge University Press; Chapter 8.
Papadopoulos, K.: 1977, Rev. Geophys. Space Phys., 15, 113.
Spitzer, L.: 1962, "Physics of Fully Ionized Gases", Interscience (New York).
Stix, T.H.: 1962, "The Theory of Plasma Waves", McGraw-Hill (New York).
Stringer, T.E.: 1964, J. Nucl. Energy C6, 267.

N87
21821
UNCLAS

N87-21821

ELECTRON-CYCLOTRON MASER EMISSION DURING FLARES: EMISSION IN VARIOUS MODES AND TEMPORAL VARIATIONS

R. M. Winglee

Institute of Geophysics and Planetary Physics
University of California
Los Angeles, California 90024

G. A. Dulk

Department of Astrophysical, Planetary and Atmospheric Sciences
University of Colorado
Colorado 80309

ABSTRACT. Absorption of radiation at the electron-cyclotron frequency, Ω_e, generated by the electron-cyclotron maser instability has been proposed as a possible mechanism for transporting energy and heating of the corona during flares. Radiation from the same instability but at harmonics of Ω_e is believed to be the source of solar microwave spike bursts. The actual mode and frequency of the dominant emission from the maser instability is shown to be dependent on (i) the plasma temperature, (ii) the form of the energetic electron distribution and (iii) on the ratio of the plasma frequency ω_p to Ω_e. As a result, the emission along a flux tube can vary, with emission at harmonics being favored in regions where $\omega_p/\Omega_e \gtrsim 1$. Changes in the plasma density and temperature in the source region associated with the flare can also cause the characteristics of the emission to change in time.

1. INTRODUCTION

Solar microwave spike bursts and very bright and highly polarized spike bursts from flare stars and close binaries have been attributed to the electron-cyclotron maser instability (Holman et al., 1980; Melrose and Dulk, 1982a; Sharma et al., 1982; Gary et al., 1982; Dulk et al., 1983). Partial absorption of the radiation as it propagates through the corona is also thought to produce heating of coronae during solar and stellar flares (Melrose and Dulk, 1982b, 1984; Winglee, 1985a,b).

The maser instability arises as follows. Electrons are accelerated at some point along a flux tube tied to the star. As they propagate toward the footpoint of the flux tube (i.e., towards increasing magnetic field) their perpendicular velocity increases at the expense of their parallel velocity due to the conservation of the adiabatic invariant. With the precipitation of low pitch angle electrons, two types of distributions can develop: a loss-cone distribution if the electrons are injected continuously into the flux tube, or a distribution which is peaked at high pitch angles if the electrons are injected impulsively (White et al., 1983). Both types of distributions have a positive $\partial f/\partial v_\perp$ which can drive the maser instability. Maser emission at the fundamental is likely to be reabsorbed in the corona and produce heating; higher harmonic radiation can escape to produce the observed radio burst.

PRECEDING PAGE BLANK NOT FILMED

The mode and frequency of the dominant emission from the maser instability are dependent on the plasma temperature, the form of the energetic electron distribution and on the ratio of the plasma frequency ω_p to the electron-cyclotron frequency Ω_e (Winglee, 1985a,b). In this paper we review the characteristics of the maser emission and discuss the implications for maser emission during flares.

2. KINEMATIC CONDITIONS

The mode and frequency of the dominant maser emission is dependent on ω_p/Ω_e due to restrictions on the frequency of a given mode imposed by the cut-offs and/or resonances of the mode (Winglee, 1985a,b). These cutoffs and/or resonances are increasing functions of ω_p so that for a fixed s and a sufficiently high ω_p, these cutoffs can exceed $s\Omega_e$ and growth at harmonic s becomes suppressed.

Specifically, the dominant maser emission assuming that the energetic particles have velocities of the order of 0.1c is

(i) fundamental x mode when $\omega_p/\Omega_e \lesssim 0.3$;

(ii) fundamental z or o mode or second harmonic x mode when $0.3 \lesssim \omega_p/\Omega_e \lesssim 1$;

(iii) fundamental z mode or second harmonic x mode when $1 \lesssim \omega_p/\Omega_e \lesssim \sqrt{2}$;

(iv) second harmonic o mode or third harmonic x mode when $\sqrt{2} \lesssim \omega_p/\Omega_e \lesssim \sqrt{3}$;

(v) second harmonic z mode when $\sqrt{3} \lesssim \omega_p/\Omega_e \lesssim \sqrt{6}$.

3. VARIATIONS WITH PLASMA TEMPERATURE

The above ranges in which growth in a given mode can dominate are only approximate and they can be significantly modified when the plasma becomes sufficiently hot. This is most pronounced for the x mode when $\omega_p^2/\Omega_e^2 \ll 1$. Under these conditions, a non-zero plasma temperature can significantly reduce the x-mode cutoff and allow x-mode growth to dominate at larger ω_p/Ω_e, up to about 0.6 (Winglee, 1985a).

This dependence of the maser emission on the plasma temperature is illustrated in Fig. 1 which shows the maximum growth rates in ω - $\underset{\sim}{k}$ space for the o, x and z modes at the fundamental. The electrons are assumed to have a Dory, Guest and Harris (DGH) distribution of the form

$$f = \left((2\pi)^{3/2} v_T^3 j!\right)^{-1} \left(v_\perp/\sqrt{2}\, v_T\right)^{2j} \exp\left(-v^2/2v_T^2\right)$$

which is peaked at $v_z = 0$, $v_\perp = \sqrt{2j}\, v_T$. In Fig. 1, $j = 1$ with (a) $v_T/c = 0.2$ and (b) $v_T/c = 0.3$. It is seen that in each case, the maximum growth rate for the x mode initially increases with ω_p/Ω_e. However, in Fig. 1a once ω_p/Ω_e increases past 0.45 the x-mode growth rate decreases rapidly and z-mode growth rate dominates. In Fig. 1b, x-mode growth does not become suppressed until $\omega_p/\Omega_e = 0.65$.

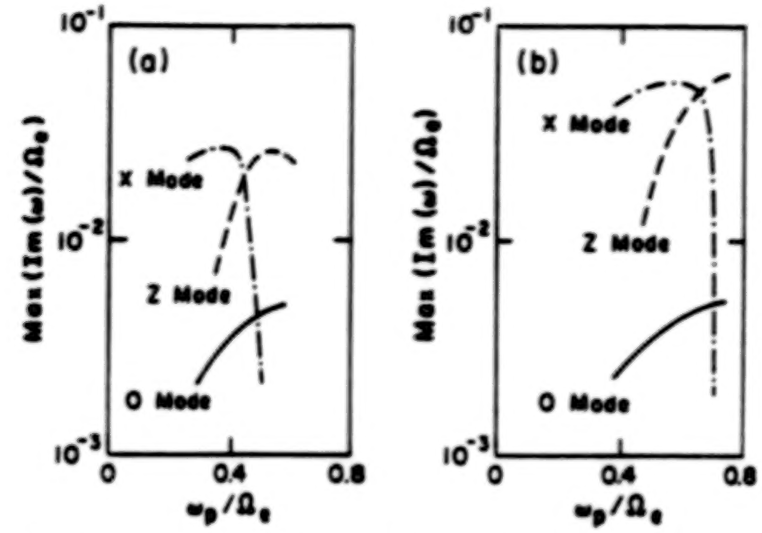

Fig. 1. Maximum growth rates for the o, x and z modes at the fundamental at a function of ω_p/Ω_e for a $j= 1$ DGH distribution with (a) $v_T/c = 0.2$ and (b) $v_T/c = 0.3$.

4. VARIATIONS WITH THE ELECTRON DISTRIBUTION

When ω_p/Ω_e is sufficiently high that fundamental x-mode growth is suppressed, then growth is not necessarily restricted to one mode and frequency for a given ω_p/Ω_e. Rather the dominant mode depends on the form of the electron distribution, specifically on:

(a) the relative density of the energetic electrons to any background component;

(b) the pitch angle of the energetic electrons driving the maser instability.

In particular when ω_p/Ω_e is $\lesssim 1$ and sufficiently large that fundamental x-mode growth is suppressed, fundamental z-mode growth tends to dominate if the density of the energetic electrons is much larger than that of the background component. This is illustrated in Fig. 2 which shows the maximum growth rates for $0.4 \lesssim \omega_p/\Omega_e \lesssim 2.4$ and where the energetic electrons have a $j = 1$ DGH distribution with $v_T/c = 0.075$. In Fig. 2a there is no cold background component while in Fig. 2b the plasma frequency of the energetic component ω_{pE} is held fixed at $0.2\ \Omega_e$ and the plasma frequency of the cold component ω_{pc} is varied. (For the illustrated range of ω_p/Ω_e, fundamental x-mode growth is suppressed.) In Fig. 2a fundamental z-mode growth dominates for $\omega_p/\Omega_e \lesssim 0.7$ while in Fig. 2b, for the same range of ω_p/Ω_e, both fundamental x-mode and z-mode growth are suppressed and fundamental o-mode dominates.

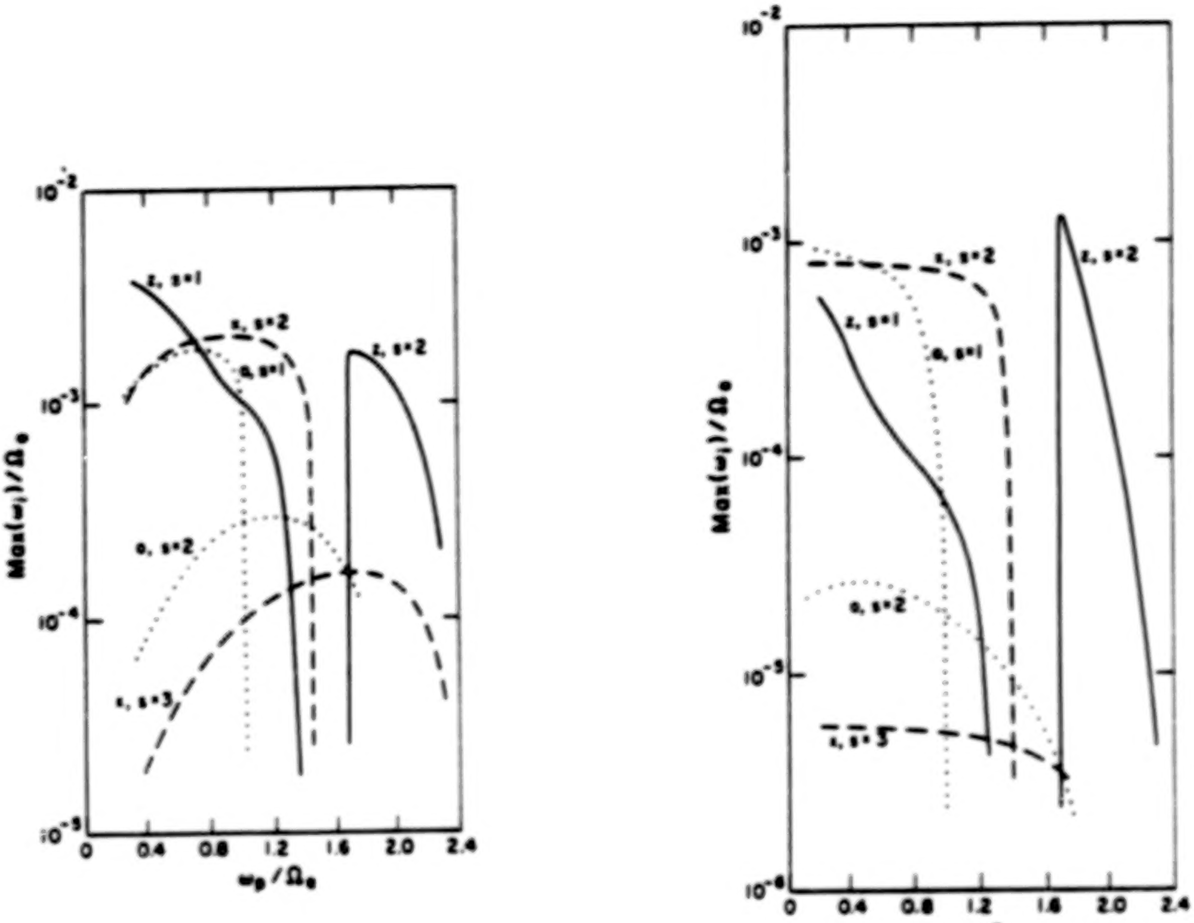

Fig. 2. Maximum growth rates for the o, x and z modes for the case where the energetic electrons have a j = 1 DGH distribution with $v_T/c = 0.075$. In (a) there is no background component (i.e., $\omega_{pc} = 0$, $\omega_p = \omega_{pE}$), and, in (b) ω_{pE} is held fixed at 0.2 Ω_e.

The pitch angles of the energetic electrons driving the maser instability also play an important role in determining the fastest growing mode. Specifically, when the distribution is such that $\partial f/\partial v_\perp > 0$ lies in regions of velocity where $v_\perp^2/v_z^2 \lesssim 1$ (i.e., where the electrons driving the instability have small pitch angles) o-mode growth is favored over x-mode growth; when $\partial f/\partial v_\perp > 0$ lies in regions where $v_\perp^2/v_z^2 >> 1$, x-mode growth is favored (Winglee, 1985b). This is illustrated in Fig. 3 which shows the maximum growth rates for the same parameters as in Fig. 2b except that j = 2 rather than j = 1. The effect of the larger j is to move the peak of the distribution to higher pitch angles. In Fig. 3 there is no value of ω_p/Ω_e for which the o-mode growth rate is largest, contrary to Fig. 2b. On the other hand, when the energetic electrons have a loss-cone distribution with a small loss-cone angle, growth of the o-mode tends to be faster than that of the x mode at $s > 2$ (i.e., except at the fundamental for $\omega_p/\Omega_e \lesssim 0.3$ (Melrose et al., 1984)).

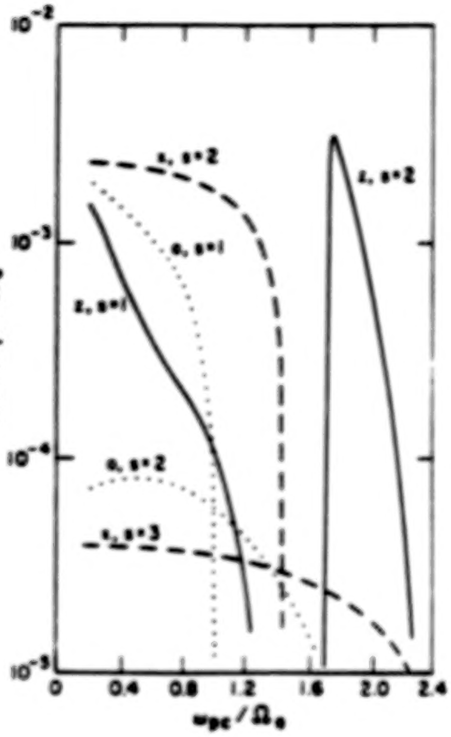

Fig. 3. As in Fig. 2b except that j = 2 rather than j = 1.

5. SUMMARY AND DISCUSSION

In this paper, the characteristics of the dominant emission from the electron-cyclotron maser instability have been examined. As ω_p/Ω_e is increased, the mode of the dominant emission changes and the frequency moves to higher harmonics of Ω_e. Fundamental x-mode growth tends to be restricted to plasmas where $\omega_p/\Omega_e \lesssim 0.3$; growth at higher ω_p/Ω_e can occur if the plasma becomes sufficiently hot. When fundamental x-mode growth is suppressed and $\omega_p/\Omega_e \lesssim 1$, the dominant emission can be fundamental o- or z-mode or second harmonic x mode, depending on the form of the energetic electron distribution. Growth of the x-mode over the o-mode is favored if $\partial f/\partial v_\perp > 0$ lies in regions where $v_\perp^2 \gg v_z^2$ (e.g., if the energetic electrons are impulsively injected into the flux tube) while o-mode growth is favored if $\partial f/\partial v > 0$ lies in regions where $v_\perp^2 \lesssim v_z^2$ (e.g., if the electrons are continuously injected into the flux tube).

During a flare, the above dependences of the emission on ω_p/Ω_e, the plasma temperature and the form of the distribution may cause the characteristics of the maser emission to change. For example, suppose that the initial conditions within the flaring flux tube favor fundamental z-mode growth. This radiation is trapped in the vicinity of the source region and is likely to be reabsorbed locally and heat the ambient electrons. If most of the electrons in the flaring flux tube become hot, the increase in temperature can cause the dominant radiation from the maser instability to switch from the z-mode to the x-mode. This x-mode radiation can escape from the source region, but, it is likely to be reabsorbed higher in the corona (the plasma overlying the source region is believed to be optically thin only for radiation at $\omega \geq 2\,\Omega_e$). This reabsorption can produce heating of the plasma away from the source region. Should the plasma in the flaring flux tube then cool (e.g., by radiation or conduction losses) the maser emission may switch back to the z-mode, and the process of switching between x- and z-modes may repeat.

Furthermore the maser emission at the beginning of a flare may be different from that at the end. The flow of cold electrons evaporated from the bottom of the flux tube and/or electrons associated with the return current for the precipitating electrons can cause ω_p/Ω_e to increase within the flaring flux tube. In this case the emisson can move to a different mode or to a higher harmonic of Ω_e. Also the distribution of the energetic electrons is most likely to have a loss-cone anisotropy at the end of the flare since this type of anisotropy tends to occur when the acceleration of the electrons lasts for any extended period. Hence, at least in the final stages of the flare, o-mode growth may be favoured, provided that $\omega_p/\Omega_e \gtrsim 0.3$ and the density of the energetic electrons is not too large.

Acknowledgements. This work was supported by NASA's Solar Terrestrial Theory Program under grants NAGW-78 to the University of California and NAGW-91 to the University of Colorado.

References

Dulk, G.A., Bastian, T.S., and Chanmugam, G. 1983, Astrophys. J., **273**, 249.

Gary, D.E., Linskey, J.L., and Dulk, G.A. 1982 Astrophys. J., **263**, L79.

Holman, G.D., Eichler, D., and Kundu, M.R. 1980, in "Radio Physics of the Sun", ed. M.R. Kundu and T.E. Gergely (D. Reidel), p. 457.

Melrose, D.B., and Dulk, G.A. 1982a, Astrophys. J., **259**, 844.

Melrose, D.B., and Dulk, G.A. 1982b, Astrophys. J., **259**, L41.

Melrose, D.B., and Dulk, G.A. 1984, Astrophys. J., **282**, 308.

Melrose, D.B., Hewitt, R.G., and Dulk, G.A. 1984, J. Geophys. Res., **89**, 897.

Sharma, R.R., Vlahos, L., and Papadopoulos, K. 1982, Astron. Astrophys., **112**, 377,

White, S.M., Melrose, D.B., and Dulk, G.A. 1983, Proc. Astron. Soc. Aust., **5**, 188,

Winglee, R.M. 1985a, Astrophys. J., **291**, 160.

Winglee, R.M. 1985b, J. Geophys. Res., **90**, 9663.

N87
21822
UNCLAS

N87-21822

IMPULSIVELY GENERATED FAST CORONAL PULSATIONS

P. M. Edwin* and B. Roberts

Department of Applied Mathematics
University of St. Andrews
North Haugh St. Andrews
Fife, Scotland KY16 9SS

*Also at The Open University in Scotland

Abstract

Rapid oscillations in the corona will be discussed from a theoretical standpoint, developing some previous work on ducted, fast magnetoacoustic waves in an inhomogeneous medium. In the theory, impulsively (e.g. flare) generated mhd waves are ducted by regions of low Alfvén speed (high density) such as coronal loops. Wave propagation in such ducts is strongly dispersive and closely akin to the behaviour of Love waves in seismology, Pekeris waves in oceanography and guided waves in fibre optics. Such flare-generated magnetoacoustic waves possess distinctive temporal signatures consisting of periodic, quasi-periodic and decay phases. The quasi-periodic phase possesses the strongest amplitudes and the shortest time scales. Time scales are typically of the order of a second for inhomogeneities (coronal loop width) of 1000 km and Alfvén speeds of 1000 kms^{-1}, and pulse duration times are of tens of seconds.

Quasi-periodic signatures have been observed in radio wavelengths for over a decade and more recently by SMM. It is hoped that the theoretical ideas outlined above may be successfully related to these observations and thus aid the interpretation of oscillatory signatures recorded by SMM. Such signatures may also provide a diagnostic of coronal conditions.

New aspects of the ducted mhd waves, for example their behaviour in smoothly varying as opposed to tube-like inhomogeneities, are currently under investigation. The theory is not restricted to loops but applies equally to open field regions.

1. Introduction

Since the end of the 1960's many observations of coronal oscillations have been reported, the bulk of the evidence being provided by radio wave and hard X-ray data (Abrami, 1970, 1972; Rosenberg, 1970; McLean et al, 1971; Gotwols, 1972; Kai and Takayanagi, 1973; McLean and Sheridan, 1973; Kaufmann et al, 1977; Pick and Trottet, 1978; Tapping, 1978; Dennis et al, 1981; Trottet et al, 1981; Kane et al, 1983, Kiplinger et al, 1983 a,b; Takakura et al, 1983), though coronagraph observations have also been reported (Koutchmy et al, 1983; Pasachoff and Landman, 1984). Besides the long period (one minute and greater) radio pulsations reported by, for example, Trottet et al (1979) there are numerous observations of short period oscillations with periodicities of around one second. An interesting feature of these short period observations is the form of the observed signature, the temporal variation. Short bursts of oscillatory behaviour are seen to occur, the wave packet or wave train behaviour being described variously as periodic, quasi-periodic or as a sequence of spikes. Kiplinger (1984, private communication) has pointed out that of the various criteria that any successful model of these oscillations must meet, one is certainly that the process is not an enduring one. Theory must be able to explain the termination of the pulses. Kiplinger also stresses two other observed features of the hard X-ray (and also microwave and γ-ray) pulse train phemonena: the source appears to be more or less stationary and compact, and the oscillations are very irregular. A model should ascribe a time scale of the variations rather than a well-defined period i.e. one phase of the motion is quasi-periodic.

How are these rapid oscillations generated? It is suspected that the source is impulsive, perhaps a solar flare, as in the examples given by McLean and Sheridan (1973) and Kiplinger et al (1983 a,b). However, Tapping (1978) and Gaizauskas and Tapping (1980) have reported bursts of oscillations with which there appears to be no associated flare activity.

2. Model of a Coronal Structure

The open and closed 'loops' of the magnetically dominated corona vary in size and are often twisted, hot and dense. Structures may have cool cores and it is thought that brightness variations over them may imply density variations. Not all these observed properties can be incorporated into a model which is simple enough to exhibit the wave-like phenomena associated with the corona. Here the effects of gravity (not so important for a region of scale $\gtrsim 3 \times 10^5$ km above the photosphere), curvature (more important for closed loops) and twist (important in knowing if an equilibrium exists) will be neglected. Since transverse dimensions are usually much smaller than longitudinal ones, the structure will be modelled by a straight cylinder and will be regarded as a density inhomogeneity. This may take the form of a uniform magnetic cylinder or alternatively the density may vary across the inhomogeneity but in either case we consider this to be an intrusion into an otherwise uniform magnetic environment.

It has been shown previously (Roberts, Edwin and Benz, 1984) that a uniform, high density coronal cylinder of radius a, its axis lying along the z-direction, acts as a wave guide for the free modes of oscillation ($e^{i(kz+\omega t)}$, ω, k real) of the structure. A high density ($v_{Ae} > v_A$, where v_A, v_{Ae} are the Alfvén speeds in the cylinder and its environment respectively) coronal loop can oscillate freely (that is without radiating energy to infinity) in the fast magnetoacoustic mode. Motions in the environment of the coronal loop arise simply in response to those within the loop; the loop acts as a wave duct trapping the fast mhd oscillations, which penetrate only a small distance into the environment.

The dispersion relation for these ducted, free modes of oscillation is (Meerson et al, 1978; Wentzel 1979; Wilson 1980; Spruit 1982; Edwin and Roberts 1983; Roberts et al, 1984)

$$\rho_o(k^2v_A^2 - \omega^2)m_e\,\frac{K_n'(m_e a)}{K_n(m_e a)} = \rho_e(k^2v_{Ae}^2 - \omega^2)n_o\,\frac{J_n'(n_o a)}{J_n(n_o a)}, \qquad (1)$$

where

$$m_e^2 = \frac{(k^2v_{Ae}^2 - \omega^2)(\omega^2 - k^2c_e^2)}{(c_e^2 + v_{Ae}^2)(\omega^2 - k^2c_{Te}^2)}\,, \quad m_o^2 = \frac{(\omega^2 - k^2v_A^2)(\omega^2 - k^2c_o^2)}{(c_o^2 + v_A^2)(\omega^2 - k^2c_T^2)},$$

and ρ_o and ρ_e are the equilibrium densities inside and outside the cylinder, respectively. The sound and Alfvén speeds inside the cylinder are c_o and v_A, outside c_e and v_{Ae}. Also,

$$c_T^2 = \frac{c_o^2v_A^2}{(c_o^2 + v_A^2)}\,, \quad \text{and} \quad c_{Te}^2 = \frac{c_e^2v_{Ae}^2}{(c_e^2 + v_{Ae}^2)}.$$

K_n, J_n are Bessel functions (modified and first kind, respectively). $n = 0$ give the symmetric (sausage) modes (those in which the axis of the cylinder is undisturbed by the vibration) and $n = 1$ the kink or asymmetric modes.

Figure 1 illustrates the solutions of Equation (1) for a dense coronal loop: two sets of waves feature which, because the sound and Alfvén speeds differ by an order of magnitude, have widely separated frequencies. One class of oscillations has slow, acoustic time scales, for both kink and sausage modes, and the waves are only mildly dispersive. In a low β plasma the tube speed c_T is close to the sound speed c_o so the frequencies of both these slow modes are given (to a good approximation, provided ka is not too large) by

$$\omega \sim kc_T \simeq kc_o. \qquad (2)$$

Of the fast waves (with phase-speeds satisfying $v_A < \omega/k < v_{Ae}$) only the principal kink mode exists for all wave numbers k (i.e. does not have a cut-off). It has a typical frequency given by

$$\omega \sim kc_k, \qquad (3)$$

where

$$c_k^2 = \frac{\rho_e v_{Ae}^2 + \rho_o v_A^2}{\rho_o + \rho_e}.$$

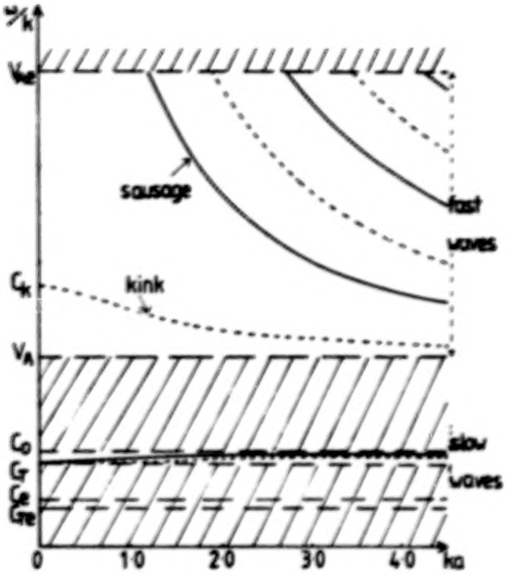

Figure 1 The phase speed ω/k (ω, k real) as a function of ka ($k > 0$) where a is the radius of a dense coronal structure, illustrated here for $v_{Ae} = 5c_o$, $c_e = 0.5c_o$ and $v_A = 2c_o$. The mildly dispersive, slow band of oscillations has infinitely many modes, on acoustic time scales, for both sausage (——) and kink (- - -) modes. Here only two are shown. Except for the principal kink mode, which exists for all wave numbers k, the fast waves have cut-offs. Hatching denotes regions where there are no free modes (After Edwin & Roberts, 1983).

In a coronal loop of length L, with its footpoints anchored in the dense chromosphere/photosphere both the slow and fast waves may occur as standing modes. Then Equation (2) and (3) would give rise to two time scales $\tau_s \sim 2L/c_o$ and $\tau_f \sim 2L/c_k$, corresponding to the slow and fast waves respectively. For typical coronal parameters, for example a sound speed of 200 km s^{-1}, an Alfven speed of $\sim$ 2000 km s^{-1} and a loop length of 2×10^4 - 10^5 km, τ_s and τ_f are estimated to be of order 200-1000s and 15-70s respectively.

3. Impulsively Generated Modes

A solar flare, considered as either a single or multiple impulsive source, will initiate propagating rather than standing waves. Alternatively, there may be other less energetic sources generating the waves, which may arise either in a closed coronal loop, if the motions have insufficient time to reflect from the far ends of the loop, or in open field regions.

To simplify the discussion and interpretation of these propagating waves it will be assumed that the plasma is cold. This is reasonable for the low β corona and involves no loss of essential physics as far as the fast modes are concerned. Mathematically it means that $c_o = c_e = 0$ in Figure 1 and that just the fast band of waves remains. For the fast sausage waves in particular the dispersion relation (1) with $c_e = c_o = 0$ reduces to

$$- n_o \frac{K_1(m_e a)}{K_0(m_e a)} = m_e \frac{J_1(n_o a)}{J_0(n_o a)} \qquad (4)$$

where

$$n_o^2 = \frac{\omega^2 - k^2 v_A^2}{v_A^2} \quad \text{and} \quad m_e^2 = \frac{(k^2 v_{Ae}^2 - \omega^2)}{v_{Ae}^2}.$$

For a cylindrical structure of large radius, (4) reduces to

$$\tan(n_o a - \pi/4) = - n_o/m_e, \qquad (5)$$

which, except for a phase shift of $\pi/4$, is identical to the dispersion relation given by Pekeris (1948) for the propagation of explosive sound in shallow water.

Thus Eqn (4) describes the highly dispersive, fast, symmetric (cold plasma) waves of Figure 1. If such waves are generated impulsively, then the resulting disturbance ϕ may be represented as a Fourier integral over all frequencies ω and wave numbers k. In general, a wave packet results. For example, if ω is related to k from (4) by $\omega = \pm W(k)$, then $W'(k)$ describes the group velocity of the waves and ϕ has the form (Pekeris, 1948; Whitham, 1974):

$$\phi \sim \begin{cases} A(z,t)e^{i\psi(z,t)}, & W''(k) \neq 0, \qquad (6a) \\ \dfrac{1}{(t|W'''(k)|)^{1/3}}\, e^{i\psi(z,t)}, & W''(k) = 0, \qquad (6b) \end{cases}$$

where

$$A(z,t) = \sqrt{\frac{2\pi}{t|W''(k)|}}\; e^{-(\pi i/4)\mathrm{sgn}W''(k)}, \text{ and } \psi(z,t) = zk - W(k)t.$$

Thus Eqn (6a) describes an oscillatory wave train with ψ giving the variation between local maxima and minima. However, since A, k and ω are not constant the wave train is not uniform. The distance and *time* between successive maxima, and the amplitude, are not constant i.e. there is a *quasi-periodic* behaviour. It is obvious from Eqns (6) that extrema, $W''(k) = 0$, of the group velocity are important since then expression (6b), the so called Airy phase, describes the disturbance rather than (6a).

The group velocity curve for the ω-k dispersion relation (Eqn (4)) for a *uniform* cylinder of density inhomogeneity is found to possess a minimum.

So too does the group velocity curve for a μ-power density intrusion into an otherwise uniform medium. If the density variation across the loop has the form

$$\rho_o(r) = \begin{cases} \rho_o(0)\left[1 - \left[\frac{r}{a}\right]^{\mu}\left[1 - \frac{\rho_e}{\rho_o}\right]\right], & 0 < r < a, \\ \rho_e, & r > a, \end{cases} \tag{7}$$

then the ω-k dispersion relation becomes (Edwin, 1984)

$$-\frac{v\,K_0(v)}{K_1(v)} - \frac{\left\{1 - \frac{K_0(v)\,K_2(v)}{K_1^2(v)}\right\} v^2}{\mu + 2} = \frac{u\,J_0(u)}{J_1(u)}, \tag{8}$$

where $u^2 = \frac{\mu}{\mu + 2} n_o^2 a^2$ and $v^2 = m_e^2 a^2$. Letting $\mu \to \infty$ in the relation (8) recovers the uniform density dispersion relation Eqn (4).

Typical group velocity plots for the lowest order sausage modes of the uniform ($\mu \to \infty$) and parabolic ($\mu = 2$) density variation cylinders are shown in Figure 2.

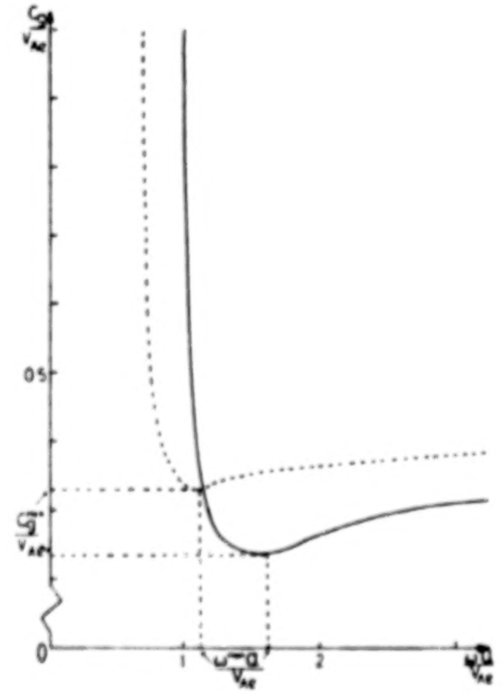

Figure 2 The dimensionless group velocity c_g/v_{Ae} as a function of dimensionless frequency $\omega a/v_{Ae}$ of the lowest order fast sausage mode of Figure 1, shown for uniform (- - -) and parabolic (——) density profiles across a coronal structure. Here $\rho_o(0)$, the density on the axis of the structure is 6 times that in the exterior of the loop, ρ_e. (After Edwin, 1984).

Since each curve has a minimum there is a point where $W'(k) = 0$. The disturbance resulting from an impulsively generated fast symmetric mode may thus be described as follows. At time $t = 0$ a pulse is generated at a point source $z = 0$, say, which is composed of all frequencies. The disturbance observed at a (large) distance $z = h$ from the source, on the basis of one of the group velocity curves in Figure 2, initially has a frequency given by

$$\omega_c = k_c v_{Ae}, \qquad (9)$$

where the wave number k_c at cut-off is found from (4) or (8) with $\omega/k \simeq v_{Ae}$. Specifically,

$$k_c = \frac{f . j_s^{(0)}}{(\rho_o(0)/\rho_e - 1)^{\frac{1}{2}} a}, \quad s = 1,2,3,... \qquad (10)$$

where $f = 1$ and $\rho_o(0) = \rho_o$ for the uniform cylinder, and $f = (1 + 2/\mu)^{\frac{1}{2}}$ for the μ-power density variation; $j_s^{(0)}$ ($\simeq$ 2.40, 5.52, ...) are the zeros of the Bessel function J_o. This disturbance has taken a travel time of $t = h/v_{Ae}$ from the source and initiates the *periodic phase*. As time progresses the frequency and amplitude of this nearly sinusoidal wave (Eqn (6a)) grow slowly until a time h/v_A when high frequency information arrives from the source. So a new train of high frequency waves, due to the right-hand branch of the group velocity curve, is superimposed on those arriving from the left-hand branch. The result is a strong increase in amplitude and the oscillation becomes quasi-periodic (see (6a) where the amplitude varies inversely as the square root of the slope of the group velocity curve). During this *quasi-periodic phase* the frequencies of the waves in the right-hand and left-hand branches of the curve continue to decrease/increase respectively (see Figure 2) until at a time $t = h/c_g^{min}$, where c_g^{min} is the minimum group velocity, they coincide. The disturbance then consists of the single frequency ω^{min} (Figure 2) and, though the disturbance continues to oscillate with this constant frequency, the amplitude declines rapidly according to (6b) ($W(k) = \omega^{min}$) in the *Airy* or *decay phase*. The behaviour at a location $z = h$ from the impulsive source is well known (Pekeris, 1948; Ewing et al, 1957; Brekhovskikh, 1960; Tolstoy, 1973; Kennett, 1983) and the sequence of phases just described can be illustrated as in Figure 3.

In order to draw comparisons between observations and theory the particular frequencies and time scales associated with Figure 3 must be identified. The frequency representative of the periodic phase is given by (9) and (10), and setting $s = 1$ for the lowest order sausage mode. In terms of period this means that the *largest periodicity* of the disturbance is given by

$$\tau_c = \frac{2\pi a}{f j_1^{(0)} v_{Ae}} \left[\frac{\rho_o}{\rho_e} - 1\right]^{\frac{1}{2}}. \qquad (11)$$

For a very dense inhomogeneity ($\rho_o \gg \rho_e$), Eqn (11) reduces to

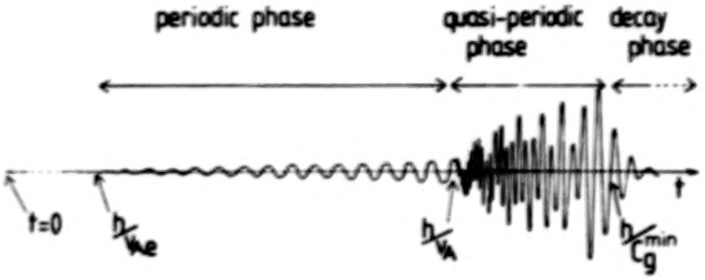

Figure 3 A sketch of the evolution of the lowest order fast sausage mode of Figure 1 in the low β extreme (c_o, c_e << v_A, v_{Ae}) showing the various phases in the disturbance as recorded at an observation level $z = h$ away from an impulsive source at $z = 0$.

$$\tau_c \simeq \frac{2.6a}{fv_A} . \qquad (12)$$

The other important frequency is that representative of the quasi-periodic phase, though this is a variable quantity because of the very quasi-periodicity. ω^{min}, which characterizes the frequency at the end of the quasi-periodic phase is larger than ω_c and so has an associated period τ^{min} which is *smaller* than τ_c. Thus rapid oscillations occur during the quasi-periodic phase.

4. Relation to observations

The mechanism by which fast magnetoacoustic waves ducted in a density enhancement of the corona may be manifest as radio wave observations was discussed in Roberts et al (1984). Here we merely summarise the properties of such mhd waves when they are impulsively generated, perhaps by a solar flare, and show that several of the desirable features of observed rapid oscillations can be explained by our model.

When the lowest order, fast, symmetric mode is generated impulsively it exhibits both periodic and quasi-periodic signatures as shown in Figure 3, the vast majority of the wave power appearing as a well-defined packet. The time signature thus resembles the pulsations recorded in the radio wave (and other) data (see e.g. Pick and Trottet, 1978; Tapping, 1978). The time scales associated with such a disturbance are indeed rapid and of the order of 1 second, as observations require. For example, taking a particle density of ~ $10^9 cm^{-3}$, a magnetic field intensity of 40G and a loop radius of ~ 10^3km, Eqn (5) shows that the periodicity at cut-off for a uniform loop is 0.94s. Again it must be remembered that this is the largest time scale of the motion, the periodicity within and at the end of the quasi-periodic phase being much smaller. Also coronal loops having a gradual density variation with radius rather than forming a step-like density inhomogeneity, would according to the μ-power model have even larger values of ω^{min} and a correspondingly reduced time scale of oscillation in the quasi-periodic phase.

Apart from periodicities, there are time scales associated with the durations of the periodic and quasi-periodic phases. Observational determination of the onset of the periodic phase is expected to be difficult because the lower amplitude oscillations may be lost in background noise, but the quasi-periodic phase is theoretically distinctive (Figure 3) and so comparisons with estimates of its duration, τ_{dur}, given by

$$\tau_{dur} = h \left[\frac{1}{c_g^{min}} - \frac{1}{v_A}\right], \qquad (13)$$

and observed signatures of similar form should be possible. It was suggested also in Roberts *et al*, (1984) that the width of the inhomogeneity and the associated Alfvén speeds may be obtained by plotting a/h (in units of τ^{min}/τ_{onset}, where $\tau_{onset} = h/v_A$) against τ_{dur} (in units of τ_{onset}), so that the theory may be used to determine physical conditions in the corona using radio pulsation data.

The picture presented by Figure 3 depends largely on the comparative sizes of v_A, v_{Ae} and c_g^{min}. If the density of the inhomogeneity is not very different from that of its surroundings, so that v_A is close to v_{Ae} and the structuring is weak, then the quasi-periodic phase is of fairly short duration because $c_g^{min} \sim v_A$ (see Figure 2). Consequently, with the periodic phase lost in noise, the observed pulse train will start abruptly. Also it will decay more gradually because the Airy phase is correspondingly extended. (The curvature of the group velocity curve at the minimum is not so pronounced for $v_A \sim v_{Ae}$ so $|W''(k)|$ in (6b) is smaller.) This theoretical possibility may correspond to the event observed by McLean and Sheridan (1973). Density variations across the loop would produce a lower c_g^{min} and longer duration times (see Figure 2 and Eqn (13)).

5. Concluding Remarks

A mechanism has been offered to try to explain some of the quasi-periodic, rapid, oscillatory behaviour observed in the solar corona. It has been shown that the explanation does not depend on the coronal loop having uniform density. Variations in density across the loops would modify the duration of the quasi-periodic phase and the time scale of the periodic phase, but observations and results from radio wave, hard X-ray and other data could still be accounted for.

Most of the foregoing analysis (the group velocity curves, etc) has been carried out for both sausage and kink modes. (For the asymmetric kink mode in a wide cylinder $ka \gg 1$, the phase-shifted Love's equation

$$\tan(n_o a - \pi/4) = m_e/n_o,$$

describing seismological waves ducted in the Earth's crust, is obtained instead of Eqn (5).) All modes would be generated by an impulsive source so a combination of the above features is to be expected. Moreover disturbances could be generated by a series of impulses at various times so that a quasi-periodic phase resulting from one disturbance may interact with the periodic phase of a subsequent impulse to give a much more complicated picture than that presented in Figure 3. Interactions between impulses and the various combinations of modes could therefore produce a far more distorted signature than that described here for a single mode and a single impulse.

Whilst it is recognised that the real situation in a coronal loop is unlikely to be that of a single, symmetric mode in a dissipationless, linear system arising from a single impulse, the theory nevertheless offers an idea which can be tested against further observations. The marriage of observation and theory offers the possibility of a fruitful diagnostic of *in situ* coronal conditions.

References

Abrami, A. 1970, Solar Phys., 11, 104.
Abrami, A. 1972, Nature, 238, 25.
Brekhovskikh, L.M. 1960, *Waves in Layered Media* (New York: Academic Press), Chap. 5.
Dennis, B.R, Frost, K.J. and Orwig, L.E. 1981, Ap. J. (Letters), 244, L167.
Edwin, P.M. 1984, Ph.D. thesis, University of St Andrews.
Edwin, P.M. and Roberts, B. 1983, Solar Phys., 88, 179.
Ewing, W.M., Jardetzky, W.S. and Press, F. 1957, *Elastic Waves in Layered Media* (New York: McGraw-Hill), Chap. 4.
Gaizauskas, V. and Tapping, K.F. 1980, Ap. J., 241, 804.
Gotwols, B.L. 1972, Solar Phys., 25, 232.
Kai, K. and Takayanagi, A. 1973, Solar Phys., 29, 461.
Kane, S.R., Kai, K., Kosugi, T., Enome, S., Landecker, P.B. and McKenzie, D.L. 1983, Ap. J., 271, 376.
Kaufmann, P., Rizzo Piazza, L. and Raffaelli, J.C. 1977, Solar Phys., 54, 179.
Kennett, B.L.N. 1983, *Seismic Wave Propagation in Stratified Media* (Cambridge: Cambridge University Press), Chap. 11.
Kiplinger, A.L., Dennis, B.R., Emslie, A.G., Frost, K.J. and Orwig, L.E. 1983a, Ap. J. (Letters), 265, L99.
Kiplinger, A.L., Dennis, B.R., Frost, K.J. and Orwig, L.E. 1983b, Ap. J., 273, 783.
Koutchmy, S., Zhugzhda, Y.D. and Locans, V. 1983, Astr. Ap., 120, 185.
McLean, D.J., Sheridan, K.V., Stewart, R.T. and Wild, J.P. 1971, Nature, 234, 140.
McLean, D.J. and Sheridan, K.V. 1973, Solar Phys., 32, 485.
Meerson, B.I., Sasorov, P.V. and Stepanov, A.V. 1978, Solar Phys., 58, 165.
Pasachoff, J.M. and Landman, D.A. 1984, Solar Phys., 90, 325.
Pekeris, C.L. 1948, *Geol. Soc. Amer. Mem.*, Vol 27, 117 pp.
Pick, M. and Trottet, G. 1978, Solar Phys., 60, 353.
Roberts, B., Edwin, P.M. and Benz, A.O. 1984, Ap. J., 279, 857.

Rosenberg, H. 1970, Astr. Ap., 9, 159.
Spruit, H.C. 1982, Solar Phys., 75, 3.
Takakura, T., Kaufmann, P., Costa, J.E.R., Degaonkar, S.S., Ohki, K. and Nitta, N. 1983, Nature, 302, 317.
Tapping, K.F. 1978, Solar Phys., 59, 145.
Tolstoy, I. 1973, *Wave Propagation* (New York: McGraw-Hill), Chap. 5.
Trottet, G., Kerdraon, A., Benz, A.O. and Treumann, R. 1981, Astr. Ap., 93, 129.
Trottet, G., Pick, M. and Heyvaerts, J. 1979, Astr. Ap., 79, 164.
Wentzel, D.G. 1979, Astr. Ap., 76, 20.
Whitham, G.B. 1974, *Linear and Nonlinear Waves* (New York: Wiley and Sons), Chap. 11.
Wilson, P.R. 1980, Astr. Ap., 87, 121.

N87
21823
UNCLAS

N87-21823

SHOCK ACCELERATION OF ELECTRONS AND IONS IN SOLAR FLARES

Donald C. Ellison

Astronomy Program
University of Maryland
College Park, MD

Reuven Ramaty

Laboratory for High Energy Astrophysics
NASA/Goddard Space Flight Center
Greenbelt, MD

Abstract

We compare the simultaneous first-order Fermi shock acceleration of electrons, protons, and alpha particles to observations of solar energetic particle events. For each event, a unique shock compression ratio in the range ~ 1.6 to 3 produces spectra in good agreement with observation. The range in compression ratios predicts that the more than 5 orders of magnitude spread in electron to proton intensity ratios observed at MeV energies is compressed to about 3 orders of magnitude at an assumed injection energy of 100 keV. The remaining spread can be accounted for with a modest range of injection conditions. The model predicts that the acceleration time to a given energy will be approximately equal for electrons and protons and, for reasonable solar parameters, can be on the order of 1 second to ~ 100 MeV.

Published in Ap.J. 298, 400 (1985)

[1] Also at NASA Goddard Space Flight Center

PRECEDING PAGE BLANK NOT FILMED

N87
21824
UNCLAS

N87-21824

THE GENERATION OF RAPID SOLAR FLARE HARD X-RAY AND MICROWAVE FLUCTUATIONS IN CURRENT SHEETS

Gordon D. Holman

Laboratory for Astronomy and Solar Physics, Code 682
NASA/Goddard Space Flight Center
Greenbelt, MD 20771

Abstract. The generation of rapid fluctuations, or spikes, in hard X-ray and microwave bursts via the disruption of electron heating and acceleration in current sheets is studied. It is found that 20 msec hard X-ray fluctuations can be thermally generated in a current sheet if the resistivity in the sheet is highly anomalous, the plasma density in the emitting region is relatively high ($\sim 10^{11}$ cm^{-3}), and the the volume of the emitting region is greater than that of the current sheet. A specific mechanism for producing the fluctuations, involving heating in the presence of ion acoustic turbulence and a constant driving electric field, and interruption of the heating by a strong two-stream instability, is discussed. Variations upon this mechanism are also discussed. This mechanism also modulates electron acceleration, as required for the microwave spike emission. If the hard X-ray emission at energies less than $\sim$100 keV is nonthermal bremsstrahlung, the coherent modulation of electron acceleration in a large number ($>10^4$) of current sheets is required.

1. Introduction

Fluctuations in the impulsive hard X-ray emission from solar

PRECEDING PAGE BLANK NOT FILMED

flares with rise and fall times as short as 20 msec have been reported (Kiplinger et al. 1983). Spikes in the microwave emission from solar and stellar flares with time scales as short as 1 msec are also observed (Slottje 1978, 1980; Kaufmann et al. 1980, 1985; Zhao and Jin 1982; Gary et al. 1982; Lang et al. 1983). The high brightness temperature and polarization of the microwave spikes clearly indicate that this emission is nonthermal, while the hard X-ray emission may be either thermal or nonthermal. Mechanisms that might be responsible for these rapid fluctuations are (1) an instability in the heating/acceleration region, (2) rapid compression and expansion of the emitting and/or heating/acceleration region, or (3) an instability in the "beam" of streaming, accelerated particles when the emission is nonthermal.

Flares are generally understood to be associated with the formation and instability of current sheets. This paper therefore addresses mechanisms of the first type for producing the observed fluctuations or spikes; specifically, unstable electron heating and acceleration in current sheets. In a previous study of electron heating and acceleration in current sheets (Holman 1985; hereafter, H85) it was found that impulsive phase solar flare hard X-ray and microwave emission can be generated in a single current sheet if the bulk of the X-ray emission is thermal, while a large number of oppositely directed sheets ($>10^4$) is required if the bulk of the hard X-ray emission is nonthermal (see also Spicer 1983, Hoyng 1977). Hence, the following section is concerned with the generation of thermal hard X-ray fluctuations in a single current sheet. The general physical conditions required for the fluctuations to be produced are determined, and a specific mechanism for generating the fluctuations is discussed. In Section 3 the generation of microwave and nonthermal hard X-ray spikes is discussed.

2. Thermal Hard X-ray Fluctuations

The results of Kiplinger et al. (1983) indicate that the X-ray flux can increase by a factor of two on a time scale of 20 msec. For one such fluctuation they deduce a peak temperature and emission measure of 2.4×10^8 K and 6×10^{44} cm^{-3}. Since the bremsstrahlung emissivity is proportional to $T^{1/2}\exp(-E_{min}/kT)$, where E_{min} is the minimum observed photon energy (29 keV), if the emission measure remains constant the temperature must increase by a factor of 1.4 in 20 msec, and the initial electron temperature, T_0, is 1.7×10^8 K. These values will be used in the following paragraphs.

The characteristic time required to heat the plasma within a current sheet, $\tau_J \equiv nkT/JE$, where J is the current density and E the electric field strength, can be written as (see H85, Eqns. 4 and 20)

$$\tau_J = (v_e/v_d)^2 \nu_e^{-1}, \tag{1}$$

where v_e is the electron thermal speed, v_d is the drift speed of the current-carrying electrons, and ν_e is the thermal collision frequency. The precise relationship between this time scale and the actual rise time, t_r, depends upon which quantities vary or remain constant while the heating is occurring. When the electric field E and the total current I are both held constant, and $\nu_e \propto T^{-3/2}$, this relationship is (H85, Eqn. 24)

$$t_r = (3/2)[(T/T_0)-1]\tau_J. \tag{2}$$

Writing, in general, $t_r = \alpha\tau_J$, $T/T_0 = 1.4$ gives $\alpha = 0.6$. Since $T/T_0 \sim 1$, other conditions give comparable values for α. Holding E and the volume of the current sheet constant gives a smaller value (0.3), while holding J and I constant gives a slightly

C-5

larger value (0.8) for α.

In addition to obtaining the 20 msec rise time, the emission measure, $EM = n^2V_J$, must also be correct. The current sheet volume can be written as $V_J = wL\delta r$, where w, L, and δr are the width, length, and thickness of the sheet. All three dimensions are constrained to be less than ct_r, where c is the speed of light, and δr is further constrained by the requirement that the induction magnetic field associated with the current sheet not be unacceptably large. Taking w and L to be $\leq ct_r$, using Eqn. 8 from H85 for δr, and combining this with $t_r = \alpha\tau_J$ and Eqn. 1 for τ_J gives the following expression for ν_e:

$$\nu_e \geq 1.89 \times 10^{11}\ \alpha(EM_{44})^2 T_8 (B_2)^{-2}(n_{11})^{-2}(t_{r(-2)})^{-5}\ \ s^{-1}, \quad (3)$$

where all parameters are in cgs units and the numerical subscripts indicate the exponent of the value assumed for each parameter ($n_{11} = n/10^{11}$). With B = 300 gauss and n = 10^{11} cm^{-3}, a collision frequency of 3×10^{10} s^{-1} is obtained. This is well above the classical collision frequency. A plasma density of 10^{12} cm^{-3} brings this down to a value that is comparable to the highest anomalous collision frequency expected from the ion acoustic instability, but the corresponding value of v_d is, from Eqn. 1, $3 \times 10^{-4} v_e$, much too small to drive such an instability. Electron acceleration in such a sheet would also be negligible. The reason for the low value of v_d (and the correspondingly large value of ν_e) is the need for the thickness of the sheet, δr, to be large enough for the required emission measure to be obtained. Therefore, in the following an emission volume that exceeds the current sheet volume is considered.

The collision frequency required for the Joule heating of a volume $V > V_J$ in time t_r is found from Eqn. 22 of H85 to be

$$\nu_e = 4.36 \times 10^6\, \alpha (EM)_{44} (T_{o(8)})^{1/2} (B_2)^{-1} (n_{11})^{-1} (t_{r(-2)})^{-3} \cdot$$

$$\cdot (v_e/v_d) \;\; s^{-1}. \tag{4}$$

With B = 300 gauss, $n = 10^{11}$ cm^{-3}, and $(v_e/v_d) = 16$, the collision frequency $\nu_e = 1.4 \times 10^7$ s^{-1} is obtained. This is well above the classical collision frequency, but an order of magnitude smaller than the maximum effective collision frequency expected from the ion acoustic instability. The ion acoustic instability will be driven by this current when $T_e/T_i \sim 10$, and this current and resistivity will result in significant electron acceleration. The length and width of the X-ray emitting region have been taken to be 6,000 km (ct_r), and the thickness of the emitting region is found from the emission measure to be 1.7 km. Hence, the rise time of the X-ray fluctuations can be attained with Joule heating if the resistivity in the current sheet is highly anomalous and the volume of the X-ray emitting region exceeds that of the current sheet. It is interesting, however, that, because of the strong dependence of ν_e upon t_r, rise times shorter than 10 msec rapidly become more difficult to obtain.

Since $V > V_J$, for the 20 msec rise time to actually be achieved the heat generated in the current sheet must be transported to the larger emission volume in 20 msec or less. Both classical and anomalous (Bohm) cross-field conduction are too slow to do this. This could easily be achieved with classical conduction along field lines, however. Hence, a bent or tangled field structure would allow the source volume to be achieved. Alternatively, if the heat is transported convectively or behind a shock or conduction front, a propagation speed of at least 40 km/sec is required.

Producing the X-ray fluctuations requires a mechanism for interrupting the enhanced heating of the flare plasma. If the current is driven so that E remains constant, and the plasma resistivity decreases with increasing temperature, as for classical resistivity, the fluctuations can be produced as follows. The Joule heating rate is E^2/η, where η is the resistivity in the current sheet, and, hence, is regulated by η. The current density $J = nev_d$ in the sheet is $J = E/\eta$ and, therefore, is also regulated by η. Hence, if the resistivity decreases as the temperature in the sheet increases, both the heating rate and J increase as T increases. The number of electrons accelerated out of the thermal plasma increases as well. If a new instability sets in because of the increased current of either thermal or accelerated electrons, η will increase, causing both the heating rate and J to decrease. The fall time of the fluctuation will be determined by either (a) the growth time of the new instability, (b) the time required for heat to be transported out of the emitting volume, or (c) the size of the emitting region ($t_f \sim L/c$). The longest of these time scales will dominate. After the enhanced turbulence dissipates, heating will be occurring at the initial lower level and, as T increases again, the process can repeat itself.

It should be noted that the rise time of the fluctuation can also be determined by either (b) or (c) if the heating time is shorter than t_r. If the rise is dominated by heating and the fall by heat transport, then the X-ray spectrum is expected to harden during the rise and soften during the falling phase. If heat transport dominates both the rise and fall, the spike will be fairly symmetric ($t_r \sim t_f$) with the X-ray spectrum becoming softer throughout the spike. The spike (0.25 sec rise time) studied by Kiplinger et al. (1984) may be of this type.

A likely source of the anomalous resistivity during the rise phase of the fluctuation is ion acoustic turbulence, since it can provide the required collision frequency, and the current drift speed is likely to be near the threshold for the ion acoustic instability. Whether or not the effective resistivity has the required temperature dependence will most likely be determined by how the instability saturates. The instability required to interrupt the heating must also be strong, since the turbulence level required in the sheet to attain the 20 msec rise time is already high. The oscillating two-stream instability, associated with the accelerated electrons, is a likely instability that can generate the required level of turbulence. Determining when the oscillating two-stream instability will occur is difficult, since it depends upon the details of the electron distribution. Since the instability grows rapidly compared to the msec time scale of the X-ray bursts, the growth time of the instability is not likely to be the time scale that determines the fall time of the fluctuations.

A variation upon this scenario might be to have the initial level of turbulence determined by the oscillating two-stream instability, and the heating interrupted by the ion acoustic instability when J reaches the instability threshold. It is not apparent that the oscillating two-stream effective resistivity can have the required temperature dependence, however, since it is proportional to the number density of accelerated electrons. Other likely sources of anomalous resistivity in the current sheet are the electrostatic ion cyclotron instability and the lower hybrid drift instability. One of these may be able to supply the required initial level of turbulence if the plasma density is higher and B is larger or v_e/v_d is smaller than assumed above. In the extreme case of $v_e/v_d \sim 1$, the Buneman instability could be the interrupting instability.

An alternative mechanism for interrupting the plasma heating has been studied by Krishan and Kundu (1985; see also Spicer 1977, 1981). In direct analogy to the sawtooth oscillations seen in Tokamaks, the current is interrupted by the onset and nonlinear growth of the m=1 tearing mode. A difficulty with this analogy is that the tearing mode is driven by an internal kink instability, requiring that the system oscillate about the threshold for this instability, q = 1, where

$$q = rB_z/LB_\theta = cB_z/2\pi LJ_z = (cB_z/2\pi enLv_e)(v_e/v_d) \qquad (5)$$

is the system safety factor. A cylindrical current channel of radius r with uniform current density, J_z, is assumed here, as for the Tokamak. B_z is the magnetic field strength in the direction of the current, and B_θ is the azimuthal magnetic field associated with the current. For solar parameters, however, q is found to be orders of magnitude smaller than one and, therefore, the oscillations cannot occur (the system is very unstable, however). This mechanism may still be able to operate as required if, instead of being distributed throughout a cylindrical volume, the current is concentrated in a thin sheet at the surface of the cylinder. The right side of Eqn. 5 then becomes multiplied by the factor $\pi(r/\delta r)$, where δr is the thickness of the sheet, and, for the parameters used above, $r \sim 10^6 \delta r \sim 10^3$ km is obtained for q = 1. Hence, although the formal analogy with the Tokamak disruption is no longer valid because of the different current geometry, this mechanism may also be able to provide the required interruption of the current heating.

3. Nonthermal Microwave and Hard X-ray Spikes

In the above mechanism for generating thermal hard X-ray fluctuations the acceleration of electrons in the current sheet is modulated as well. The rate at which runaway electrons is produced is sensitive to the value of $v_e/v_d = E_D/E$, where E_D is the Dreicer electric field. With $\nu_e \propto T^{-3/2}$, $E_D/E \propto T^{-1}$ and the flux of accelerated electrons increases as the temperature in the current sheet increases. When the heating is interrupted by a sudden increase in resistivity, the rate of runaway production suddenly drops. For the parameters obtained above (§2), electrons can be accelerated to energies of up to 1 GeV. If the particles are pitch angle scattered within the current sheet, however (e. g., Holman, Kundu, and Papadopoulos 1982, Moghaddam-Taaheri et al. 1985), the maximum energy will be smaller, ∿a few MeV, since electrons with a perpendicular energy greater than a few MeV have gyroradii that exceed the thickness of the sheet.

Microwave emission generated by the accelerated electrons is not likely to directly mimic the X-ray fluctuations, since the rise and fall of the microwave spikes is likely to be determined by the growth and saturation of the emission mechanism. If the emission mechanism is gyrosynchrotron masering (Holman, Eichler, and Kundu 1980, Melrose and Dulk 1982, Sharma, Vlahos, and Papadopoulos 1982; for a review of possible emission mechanisms, see Holman 1983) a delay is also involved in the time required for the accelerated electrons to propagate to a mirroring point within the flaring loop. Only when conditions are right for both the X-ray fluctuations and the masering will both be seen simultaneously.

Generating the hard X-ray fluctuations at photon energies below ∿100 keV through nonthermal bremsstrahlung requires modulating simultaneously, to within the time scale of the fluctuations, electron acceleration within a large number of current sheets. For a typical electron flux requirement of 10^{35} electrons/sec for $\gtrsim$25 keV X-rays, at least 10^4 sheets are required. For a typical sheet thickness of 100 cm, the total thickness of the sheets is ∿10 km if the sheets are arranged adjacently, well below $ct_r = 6{,}000$ km (and on the order of $v_A t_r$, where v_A is the Alfven speed). Hence the sheets can in principal be driven with the required degree of coherency. The interruption of the Joule heating within the sheets must keep the temperature (or emission measure) of the thermal X-ray source low enough so that it does not dominate the nonthermal emission.

Acknowledgements

This work was supported in part by NASA Grant 188-38-53-01. The author thanks Dr. Daniel Spicer for a helpful comment.

References

Gary, D. E., Linsky, J. L., and Dulk, G. A.: 1982, Ap. J. (Letters), 263, L79.

Holman, G. D., Eichler, D., and Kundu, M. R.: 1980, in IAU Symp. 86, Radio Physics of the Sun, ed. M. R. Kundu and T. E. Gergeley (Dordrecht: Reidel), p. 457.

Holman, G. D., Kundu, M. R., and Papadopoulos, K.: 1982, Ap. J., 257, 354.

Holman, G. D.: 1983, Adv. Space Res., Vol. 2, No. 11, p. 181.

Holman, G. D.: 1985, Ap. J., 293, 584.

Hoyng, P.: 1977, Astron. Astrophys., 55, 23.

Kaufmann, P., Strauss, F. M., Opher, R., and Laporte, C.: 1980, Astron. Astrophys., 87, 58.

Kaufmann, P., Correia, E., Costa, J. E. R., Sawant, H. S., and Zodi Vaz, A. M.: 1985, Solar Phys., 95, 155.

Kiplinger, A. L., Dennis, B. R., Emslie, A. G., Frost, K. J., and Orwig, L. E.: 1983, Ap. J. (Letters), 265, L99.

Kiplinger, A. L., Dennis, B. R., Frost, K. J., and Orwig, L. E.: 1984, Ap. J. (Letters), 287, L105.

Krishan, V., and Kundu, M. R.: 1985, in IAU Symp. 107, Unstable Current Systems and Plasma Instabilities in Astrophysics, ed. M. R. Kundu and G. D. Holman (Dordrecht: Reidel), p. 299.

Lang, K. R., Bookbinder, J., Golub, L., and Davis, M. M.: 1983, Ap. J. (Letters), 272. L15.

Melrose, D. B., and Dulk, G. A.: 1982, Ap. J., 259, 844.

Moghaddam-Taaheri, E., Vlahos, L., Rowland, H. L., and Papadopoulos, K.: 1985, Phys. Fluids, submitted.

Sharma, R. R., Vlahos, L., and Papadopoulos, K.: 1982, Astron. Astrophys., 112, 377.

Slottje, C.: 1978, Nature, 275, 520.

Slottje, C.: 1980, in IAU Symp. 86, Radio Physics of the Sun, ed. M. R. Kundu and T. E. Gergeley (Dordrecht: Reidel), p. 195.

Spicer, D. S.: 1977, Solar Phys., 53, 305.

Spicer, D. S.: 1981, Solar Phys., 70, 149.

Spicer, D. S.: 1983, Adv. Space Res., Vol. 2, No. 11, p. 135.

Zhao, R., and Jin, S.: 1982, Scientia Sinica (Series A), 25, 422.

N87
21825
UNCLAS

N87-21825

THE QUASI-LINEAR RELAXATION OF THICK-TARGET ELECTRON BEAMS IN SOLAR FLARES

K. G. McClements and J. C. Brown

Department of Astronomy
The University
Glasgow G12 8QQ, Scotland, UK

A. G. Emslie

Department of Physics
The University of Alabama in Huntsville
Huntsville, AL 35899, USA

ABSTRACT

The effects of quasi-linear interactions on thick-target electron beams in the solar corona are investigated. Coulomb collisions produce regions of positive gradient in electron distributions which are initially monotonic decreasing functions of energy. In the resulting two-stream instability, energy and momentum are transferred from electrons to Langmuir waves and the region of positive slope in the electron distribution is replaced by a plateau. In the corona, the timescale for this quasi-linear relaxation is very short compared to the collision time. It is therefore possible to model the effects of quasi-linear relaxation by replacing any region of positive slope in the distribution by a plateau at each time step, in such a way as to conserve particle number. The X-ray bremsstrahlung and collisional heating rate produced by a relaxed beam are evaluated.

Although the analysis is strictly steady state, it is relevant to the theoretical interpretation of hard X-ray bursts with durations of the order of a few seconds (i.e. the majority of such bursts).

1. Introduction

It is widely accepted that hard X-ray bursts observed during solar flares are produced by the bremsstrahlung of non-thermal electrons, but relatively few authors have considered the possible consequences of collective plasma effects on the dynamics of thick-target electron beams. Considerable attention has been paid recently to the importance of reverse current Ohmic losses due to collisional resistivity (e.g. Emslie 1980), but the effects of plasma wave generation resulting from beam instability (as described by quasi-linear theory) have been neglected by most authors. Emslie and Smith (1984) pointed out that the effect of Coulomb collisions is to produce regions of positive gradient in electron distributions which are initially monotonic decreasing functions of energy: this gives rise to the well-known "bump on

PRECEDING PAGE BLANK NOT FILMED

tail" instability, and Langmuir wave generation is set up.

In this paper we examine the effect of quasi-linear relaxation on the bremsstrahlung emission and collisional heating rate associated with an electron beam in the corona. In Section 2, the quasi-linear equations and their asymptotic solutions are discussed. In Section 3, the collisional energy loss rate of an electron in a warm target is used to infer the evolution of the electron beam in a collisionally dominated thick target. Numerical computations of the distribution function, with and without quasi-linear relaxation, are presented. Computations of the corresponding hard X-ray spectra and heating rates are presented in Section 4. In Section 5 we compare our results with those of previous authors and consider their implications.

2. The Quasi-linear Equations

In the following we will assume that the source region is a homogeneous fully ionized hydrogen plasma. The beam electrons will be assumed to be non-relativistic and to be streaming in one direction only: for simplicity, pitch angle scattering will be neglected. In order to simplify the quasi-linear equations, only Langmuir waves propagating in the streaming direction will be considered.

Let f(v) and W(v) denote respectively the electron velocity distribution (differential in velocity space) and the energy density in Langmuir waves (differential in phase velocity space). Then the quasi-linear equations may be written as (Melrose 1980)

$$\frac{df}{dt} = \frac{\pi\,\omega_p}{mn}\,\frac{\partial}{\partial v}\left[v\,W(v)\,\frac{\partial f}{\partial v}\right] \qquad (1)$$

$$\frac{dW}{dt} = \frac{\pi\,\omega_p}{n}\,v^2\,W(v)\,\frac{\partial f}{\partial v} \qquad (2)$$

where m is the electronic mass, n is the ambient density and ω_p is the electron plasma frequency. In general, $^d/_{dt}$ denotes the total (i.e. advective) time derivative. We will now argue that, if there exists a region of positive slope in the electron distribution (i.e. positive $\frac{\partial f}{\partial v}$, corresponding to wave growth) then quasi-linear interactions will dominate over Coulomb interactions in the corona. The wave growth rate associated with equation (2) is

$$\gamma_w = \pi\,\frac{\omega_p}{n}\,v^2\,\frac{\partial f}{\partial v} \qquad (3)$$

Now consider the situation shown schematically in Figure 1 in which a beam distribution is superimposed on a background Maxwellian, a region of substantial positive slope lying between v_1 and v_2. Putting
$\frac{\partial f}{\partial v} \simeq \frac{f}{\Delta v}$ $(\Delta v = v_2 - v_1)$ and defining

$$n_1 \equiv \int_{v_1}^{v_2} f\,dv \simeq f\,\Delta v$$

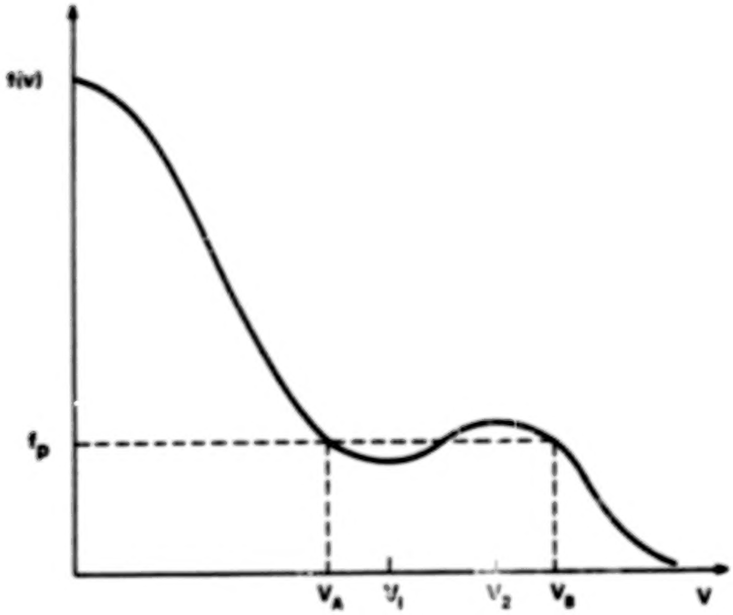

Figure 1. The form of the combined electron distribution giving rise to the "bump on tail" instability. A region of positive slope lies between velocities v_1 and v_2. The plateau of the relaxed distribution is defined by the three parameters v_A, v_B and f_p.

the growth rate may be written as

$$\gamma_w = \pi \omega_p \frac{n_1}{n} \left(\frac{v}{\Delta v}\right)^2 \tag{3a}$$

while the collisional damping rate is given by (Ginzburg 1961)

$$\gamma_c \simeq \frac{5.5n}{T^{3/2}} \ln\left(10^4 \frac{T^{2/3}}{n^{1/3}}\right) \simeq 70\ nT^{-3/2} \tag{4}$$

where T is the electron temperature, and the logarithmic factor has been set equal to a constant with $T \sim 10^7$K and $n \sim 10^{10}\,\mathrm{cm}^{-3}$ (i.e. typical coronal values). From equations (3a) and (4) we obtain, assuming $\Delta v \simeq v$ (a reasonable assumption in practice),

$$\Gamma \equiv \frac{\gamma_w}{\gamma_c} \simeq 2500\, n_1 \left(\frac{T}{n}\right)^{3/2}. \tag{5}$$

The value of n_1 depends principally on the total injected electron flux. For fluxes of the order of $10^{19}\mathrm{cm}^{-2}\mathrm{s}^{-1}$ (fluxes as large as this are required by the thick target interpretation of some hard X-ray bursts) it turns out that $n_1 \gtrsim 10^6\ \mathrm{cm}^{-3}$. Putting $T \sim 10^7$K and $n \sim 10^{10}\ \mathrm{cm}^{-3}$ as before indicates that $\Gamma \gtrsim 10^5$, so that the timescale for quasi-linear relaxation is extremely short compared to the collision time. This justifies the omission of collisional terms in equation (1) and enables us to model the effects of relaxation by applying the asymptotic solution of equations (1) and (2) (in the chromosphere, $\Gamma << 1$, so that the effects of quasi-linear relaxation may be neglected in that region).

The quasi-linear equations can only be solved numerically. Grognard (1975) obtained a solution of the one-dimensional quasi-linear equations including spontaneous emission terms, with the initial conditions of zero wavelevel and a Gaussian electron distribution. As expected, the asymptotic solution for f(v) is a plateau in velocity space. However, Grognard points out that the time for the plateau to be formed is considerably longer than the characteristic growth time associated with equation (3). In fact the asymptotic solution is only valid for times $\tau \gtrsim 100/\gamma_w$: this does not, however, alter our conclusion that quasi-linear interactions dominate over Coulomb interactions in the Corona.

Although a numerical treatment of equations (1) and (2) is essential for studying the details of the relaxation process, the asymptotic value of the wavelevel may be readily determined for any given initial distribution f(v,0). Melrose (1980) obtained such an asymptotic solution in the case of a delta function velocity distribution. An explicit calculation of the wavelevel to be expected is important because of the (possibly observable) plasma radiation it excites. In fact Emslie and Smith (1984), on the basis of their calculation, estimated that the wavelevel would give rise to a microwave flux far in excess of that observed in a typical event, unless the microwaves are strongly gyroresonance absorbed. A convincing explanation of this anomaly, consistent with the thick-target model, does not yet exist.

3. The Evolution Of The Electron Distribution with Depth

We will assume that instability (i.e. wave generation) will always occur whenever a region of positive slope appears in the electron distribution. The combined distribution function is given by

$$f(v) = f_b(v) + f_o(v) \tag{6}$$

where f_o is the distribution function for the background plasma and f_b is the distribution function of a vertically injected beam of electrons. Following Knight and Sturrock (1977) we will consider the beam distribution corresponding to the injected differential energy spectrum

$$F_o(E_o) = (\delta - 1) F_{oo} \frac{E_{oo}{}^{\delta-1}}{(E_{oo} + E_o)^{\delta}} \tag{7}$$

where F_{oo} is the total injected flux (cm^{-2}), and E_{oo} and δ are constants. Neglecting pitch angle scattering, the instantaneous steady state electron energy spectrum F(E) is given by the continuity equation

$$F(E)\,dE = F_o(E_o)\,dE_o \tag{8}$$

and the beam distribution function is given by

$$v\,f_b(v)\,dv = F(E)\,dE$$

i.e.

$$f_b(v) = mF(E). \tag{9}$$

To evaluate E_o from any given E we require the beam electron energy loss rate. It turns out that the relaxation process affects f(v) at energies of typically a few kT (depending on the model parameters, such as F_{oo}), and therefore it is not self-consistent here to use the cold target formula for the energy loss rate assumed by, for example, Brown (1971). The energy loss rate of an electron in a warm fully ionized target, taking into account only electron-electron collisions (cf Emslie 1978), is given by

$$\frac{dE}{dt} = -\frac{2\pi e^4 \ln\Lambda}{E} nv\,(\Phi(x) - 2x\Phi'(x)) \tag{10}$$

(Spitzer 1962) where $\ln\Lambda \simeq 25$ is the Coulomb logarithm, e is the electronic charge, $x = (E/kT)^{1/2}$ and Φ is the error function. Writing $\psi(x) = \Phi(x) - 2x\Phi'(x)$, $K = 2\pi e^4 \ln\Lambda$ and defining the usual column depth variable

$$N = \int_0^z n\,dz' = nz$$

equation (10) becomes

$$\frac{dE}{dN} = -\frac{K}{E}\psi(x). \tag{10a}$$

The numerical solution of equation (10a) yields E_o for prescribed E, N. dE_o/dE is then given by

$$\frac{dE_o}{dE} = \frac{E}{E_o}\,\frac{\psi(x_o)}{\psi(x)} \tag{11}$$

where $x_o = (E_o/kT)^{1/2}$.

Using equations (9), (10a), and (11) we can evaluate f(v) (neglecting the effects of quasi-linear relaxation) for any prescribed set of parameters (F_{oo}, E_{oo}, δ, T and n). Quasi-linear relaxation can be incorporated in the scheme in the following way: if a region of positive slope is found in the combined distribution, it is immediately replaced by a plateau which conserves particle number. The three parameters which define the plateau are, as indicated in Figure 1, v_A, v_B and f_p. These are (uniquely) defined by the condition that

$$\int_{v_A}^{v_B} (f(v) - f_p)\,dv = 0. \tag{12}$$

Although there are three unknown parameters, only one of these is independent: they may all be readily determined numerically. The smoothed-out distribution function minus the background Maxwellian can then be taken to be the new $F_o(E_o)$, and the distribution function F(E) corresponding to the subsequent N-step can be evaluated as before. $E_o - E$ is thus the energy lost by an electron in a single N-step. If E_o lies in the plateau region then

$$m\,F_o(E_o) = f_p - f_o(E_o). \qquad (13)$$

Otherwise, $F_o(E_o)$ is given by the function $F(E)$ as evaluated in the previous step.

In Figure 2 we present numerical computations of the combined distribution function $f(v)$, for typical thick-target parameters, at a depth of 10^{21} cm^{-2}. The plateau formed by relaxation extends from 13 keV to 130 keV.

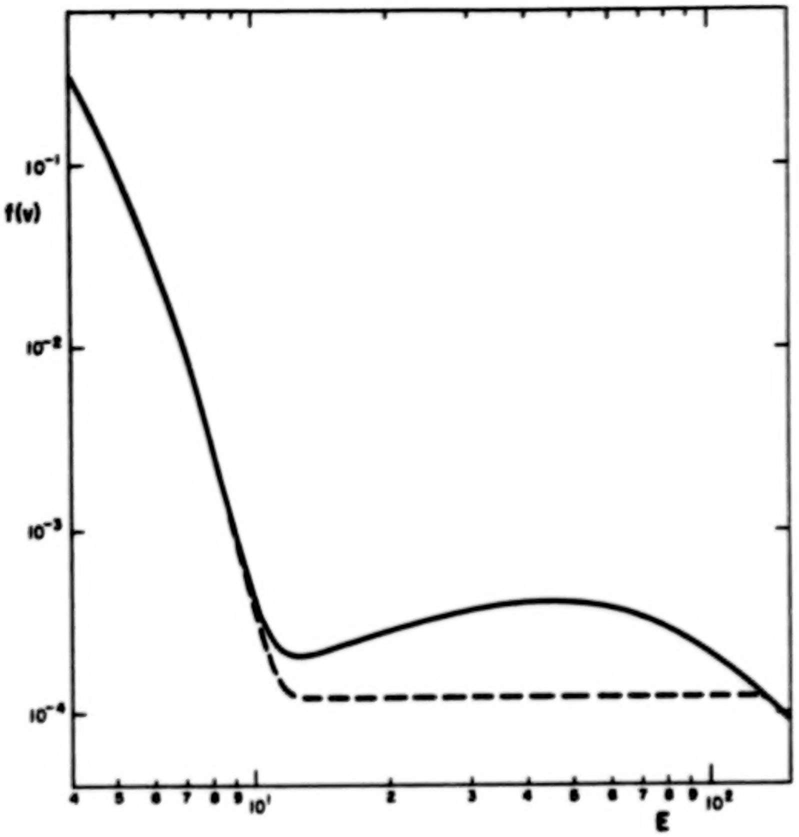

Figure 2. The combined distribution function for the model parameters $T = 10^7$K, $n = 10^{11}$ cm^{-3}, $F_{oo} = 10^{19}$ cm^{-2} s^{-1}, $E_{oo} = 20$ keV, $\delta = 4$. The column depth is 10^{21} cm^{-2}. The dotted line shows the plateau formed by relaxation. (f is measured in electrons cm^{-3} (cms^{-1})$^{-1}$ and E is measured in keV.)

4. The Bremsstrahlung Emission and Heating Rate

Figure 3 shows the local bremsstrahlung spectrum corresponding to the distribution function shown in Figure 2 (the non-relativistic Bethe-Heitler cross-section, averaged over solid angle, was used). The dotted line shows the spectrum obtained by including quasi-linear relaxation. It may be seen

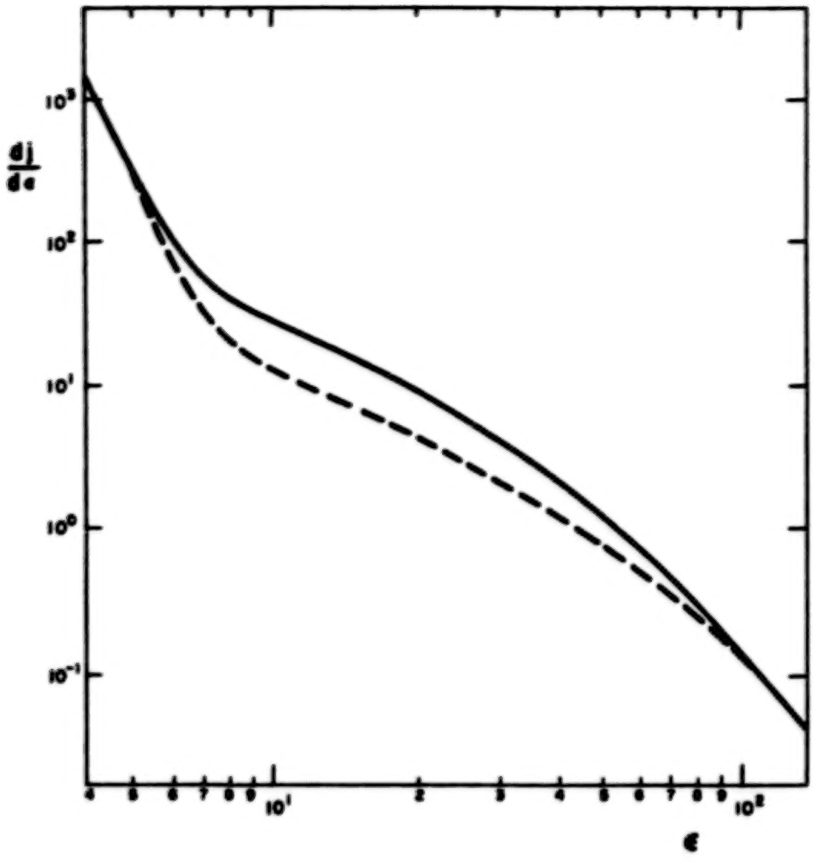

Figure 3. X-ray bremsstrahlung emissivity spectrum corresponding to the distribution function shown in Figure 2. ($dj/d\varepsilon$ is measured in photons cm^{-3} s^{-1} keV and ε is measured in keV.)

that relaxation has relatively little effect on the X-ray spectrum. Qualitatively, the emissivity is reduced in an energy range corresponding roughly to the plateau region in the electron distribution: the reduction is never more than about 50%. If the X-ray emissivity is integrated over the source volume, the overall effect of relaxation on the spectrum is much smaller: the reduction is $\lesssim$ 10%.

The above results are in qualitative agreement with those of Hoyng, Melrose and Adams (1979). They may be attributed to the "filtering" property of the Bethe-Heitler cross-section. What this means is that the source function $f(v)$ is very sensitive to small perturbations on the photon spectrum. Conversely, different electron distributions can give rise to bremsstrahlung spectra which are almost identical (cf Brown 1975, Craig 1979).

In Figure 4 the collisional heating rate is shown as a function of column depth with the same beam and source parameters as before. The dotted line again indicates the case in which quasi-linear interactions are included. There is a considerable reduction in the heating rate for $N \gtrsim 10^{20}$ cm^{-2}

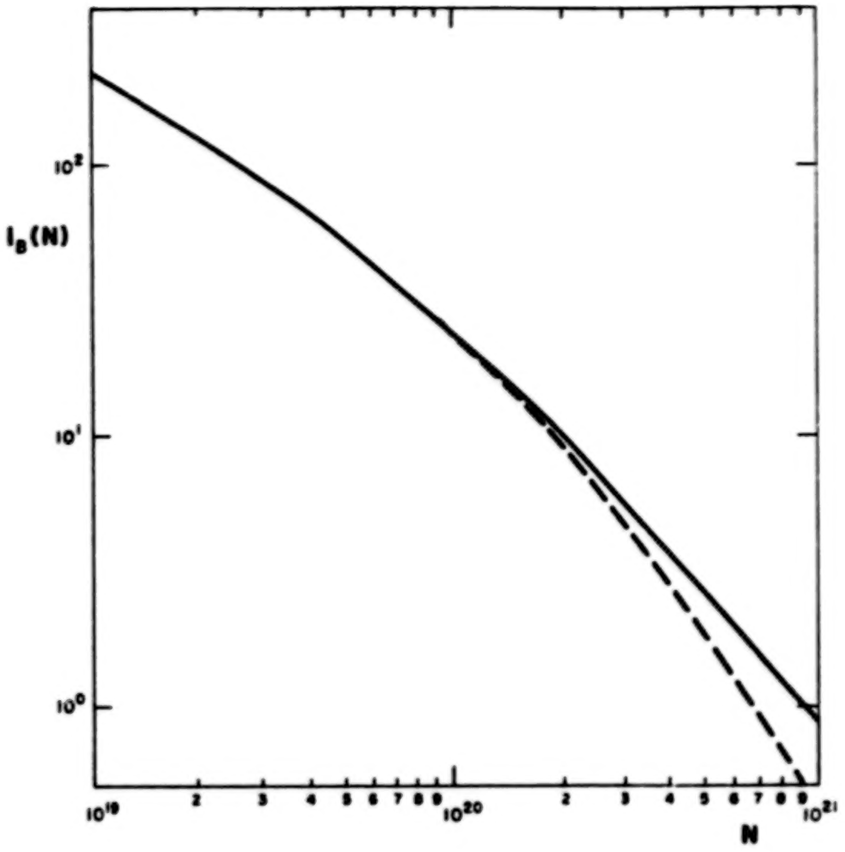

Figure 4. Collisional heating rate as a function of column depth with the same beam and plasma parameters as before. (I_B is measured in ergs cm^{-3} s^{-1} and N is measured in cm^{-2}.)

($\sim 50\%$ at $N = 10^{21}$ cm^{-2}): this is to be expected since energy is being lost from the beam in the form of Langmuir waves. These waves are then damped and thereby heat the plasma: the total energy deposition rate is therefore greater than that indicated by the dotted line in Figure 4. The bremsstrahlung efficiency is consequently reduced and greater fluxes of electrons are required to explain hard X-ray bursts on the basis of a thick-target interpretation.

5. Discussion

As indicated previously, our results are consistent with those of Hoyng, Melrose and Adams (1979). These authors used a rather different technique, involving a Legendre series expansion of the three-dimensional quasi-linear equations. The form of the initial particle distribution was similar to that considered in this paper. It was found that bremsstrahlung spectra were not greatly affected by quasi-linear relaxation. It is quite likely, however, that the total energy requirement of the thick-target model (with the inclusion of quasi-linear effects) may depend critically on the form of the injected electron spectrum. Our choice of a modified power law was governed by the aim of reproducing power law photon spectra, while at the same time having an acceptably small beam density to plasma density ratio. As mentioned previously, Melrose (1980) evaluated the asymptotic wave energy density in the case of a delta function injected particle distribution and showed that the particles eventually lose two thirds of their initial energy to waves. We would therefore expect the effects of quasi-linear relaxation on the energy requirement and the beam lifetime to be quite substantial in this case. For the beam and plasma parameters assumed in this paper, however, it appears that wave-particle interactions have an observationally negligible effect on the integrated bremsstrahlung emission.

There remains the problem of determining the wavelevel generated by a thick-target electron beam - this requires the numerical solution of the quasi-linear equations with collisional damping terms. The wavelevel so obtained may exceed the threshold for strong turbulence, with important consequences for the stability of both the beam and the reverse current (Vlahos and Rowland 1984, Rowland and Vlahos 1985).

Acknowledgement

This work was supported by NASA, SERC and Glasgow University.

References

Brown, J.C. 1971, Solar Phys., 18, 489

Brown, J.C. 1975, in S.R. Kane (ed.) "Solar gamma-, X- and EUV radiation", IAU Symp. No.68, 245

Craig, I.J.D. 1979, Astron. Astrophys., 79, 121

Emslie, A.G. 1978, Ap.J., 224, 241

Emslie, A.G. 1980, Ap.J., 235, 1055

Emslie, A.G. and Smith, D.F. 1984, Ap.J., 279, 882

Ginzburg, V.L. 1961, "Propagation of Electromagnetic Waves in Plasmas" (Gordon and Breach)

Grognard, R.J.-M. 1975, Aust. J. Phys., 28, 731

Hoyng, P., Melrose, D.B., and Adams, J.C. 1979, Ap.J., 230, 950

Knight, J.W. and Sturrock, P.A. 1977, Ap.J., 218, 121

Melrose, D.B. 1980, "Plasma Astrophysics", Vol.2 (Gordon and Breach)

Rowland, H.L. and Vlahos, L. 1985, Astron. Astrophys., 142, 219

Spitzer, L.W. 1962, "Physics of Fully Ionized Gases" (Interscience)

Vlahos, L. and Rowland, H.L. 1984, Astron. Astrophys., 139, 263

N87
21826
UNCLAS

N87-21826

THE PROPAGATION OF SOLAR FLARE PARTICLES IN A CORONAL LOOP

J. M. Ryan

Space Science Center
University of New Hampshire
Durham, New Hampshire 03824 USA

ABSTRACT

Energetic solar flare particles, both electrons and protons, must survive the turbulent environment of a flaring loop and propagate to the lower corona or chromosphere in order to produce hard x-ray and γ-ray bursts. This plasma turbulence, often observed in soft x-ray line widths to be in excess of 100 km/s, is presumably capable of efficiently scattering the fast flare particles. To some degree this prevents the free streaming of accelerated particles and, depending on the amplitude of the turbulence, restricts the particle transport to diffusive propagation along the length of the loop to the target chromosphere. In addition this turbulence is capable of performing additional acceleration on the fast particles by the second order Fermi mechanism. For compact flares with rise times < 2s, the acceleration effect is small and the propagation of the particles is governed by spatial diffusion and energy loss in the ambient medium.

A time-dependent diffusion equation with velocity-dependent diffusion and energy-loss coefficients has been solved for the case where energetic solar particles are injected into a coronal loop and then diffuse out the ends of the loop into the lower corona/chromosphere. The solution yields for the case of relativistic electrons, precipitation rates and populations which are necessary for calculating thick and thin target x-ray emission. It follows that the thick target emission is necessarily delayed with respect to the particle acceleration or injection by more than the mere travel time of the particle over the loop length. In addition the time-dependent electron population at the top of the loop is calculated. This is useful in estimating the resulting μ-wave emission. The results show relative timing differences in the different emission processes which are functions of particle species, energy and the point of injection of the particles into the loop. Equivalent quantities are calculated for non-relativistic protons.

1. Introduction

Short bursts of energetic solar radiation are frequently ascribed to energetic particles precipitating onto the lower corona or chromosphere after being accelerated higher in the corona. The duration or rise time of these bursts (x-rays or γ-rays) bears upon the acceleration time of the particles (electrons or protons/ions). However, the duration and rise time of the bursts of precipitating particles is also affected, sometimes greatly, by their propagation to these denser regions of the solar atmosphere.

PRECEDING PAGE BLANK NOT FILMED

Many of the papers presented in these volumes focus upon the nature of the brief or rapid fluctuations in x- or γ-ray emission from flares, and it is the aim of this paper to consider the effects of particle propagation on these observed rapid fluctuations. Without such a discussion incorrect conclusions about acceleration processes can be drawn from the time profiles of these bursts. One of the major findings of the SMM program is the discovery of a new time domain for bursts or spikes of hard x-rays and γ-rays. Bursts have been observed in x-rays on the order of tens of milliseconds (Kiplinger et al., 1983) while bursts of γ-rays have been as short as ~ 1 second (Kane et al., 1985). These times are on the order of the travel times of electrons or protons over 2×10^4 km.

The propagation of electrons in a solar flare also affects the nature of μ-wave emission. The μ-wave opacity of a coronal loop or a flaring region is a strong function of electron density and thus altitude. The controversy as to whether μ-wave and x-ray emissions are results of the same electron population is further complicated by the fact that one initial population of electrons can spatially fractionate due to propagation effects which then leads to different signatures in x-rays and μ-waves due to the spatial dependence of the emission process.

A variety of scenarios exists for how particles once accelerated and injected into a coronal loop make their way to a region where they can emit observable radiation. The model chosen for study here is a simple one where particle propagation is separate and distinct from the acceleration process. Such a distinction is not clear for stochastic acceleration processes such as shocks and second order Fermi acceleration. In those cases, the propagation of particles is intimately linked to their acceleration. The problem of time scales in the related processes of stochastic acceleration and spatial diffusion is discussed by Schlickeiser (1985). In the environment of a solar flare where the spatial scale, magnetic field strength and ion density are 2×10^4 km, 100G and 10^9 cm^{-3} respectively, the product of the spatial diffusion time constant and the stochastic acceleration time constant is 80 s^2. Thus, if we restrict the discussion to the spatial diffusion time scale of 2 s, it implies that the acceleration time scale is 40 s making acceleration a minor feature in the propagation of particles within the loop. Thus, for these brief events the subsequent transport of particles after rapid acceleration involves negligible additional acceleration.

2. Model

We can analyze theoretically the transport of particles within a coronal loop after a rapid episode of acceleration, where the time domain of interest is under 2 seconds for the buildup or peaking of particle precipitation or the transport of electrons to optically thin regions of the corona. This model describing the particle transport and the rates of interest (e.g., precipitation rates, etc.) is a one-dimensional diffusion equation with an energy dependent diffusion coefficient and energy loss term.

To pose the basic problem simply, we assume that a coronal loop contains a uniform distribution of thermal material and is connected at both ends to the chromosphere. A distribution of particles is impulsively injected at an arbitrary point within the loop whereby the particles diffuse within the loop according to an energy dependent diffusion coefficient which is independent of time and space. The particles diffuse along the length of the loop away from the point of injection or acceleration. The diffusion process itself is one of elastic pitch angle scattering of the particles off an MHD wave field. We have assumed here no specific origin of the wave field, which could be anything ranging from an ambient wave field produced by photospheric turbulence to a wave field generated by the particles themselves.

In the process of diffusing, these energetic particles emit x-rays, γ-rays and μ-waves as the electrons and proton/ions interact with the ambient material and magnetic field inside the loop. When the electrons and/or protons reach the footpoints of the loop, they emit a burst of x-/γ-rays. Similarly, when the electrons reach an optically thin point in the loop, they emit observable μ-waves. The material inside the loop which is responsible for the initial thin target x-/γ-rays also serves to slow down the energetic particles through collisions with ambient thermal electrons. It is therefore necessary to follow the population of energetic particles in space, time and energy as they diffuse away from an assumed impulsive injection or acceleration. The case of finite duration injections can be handled by integrating the solution of the impulsive injection case over the injection time interval. If, however, the scattering wave field is due to the energetic particles themselves then the diffusion coefficient must also be time dependent. This complication is not addressed here.

The basic equation is the following

$$\frac{\partial f}{\partial t} - \frac{\partial}{\partial x}\kappa(E)\frac{\partial f}{\partial x} + \frac{\partial}{\partial E}\dot{E}(E)f = Q \qquad (1)$$

where f = distribution function of particles,
x = distance along loop,
κ = diffusion coefficient,
E = energy of particle,
$\dot{E}$ = energy loss rate for collisional deceleration and
Q = injection profile.

We take $Q = \delta(x - x')\delta(t)S(E)$ where S is the input particle distribution and then (1) can be solved with the boundary conditions $f = 0$ at $x = 0, \ell$, where ℓ is the total loop length. Using a Laplace transformation in time and by expanding in eigenfunctions in x (1) yields

$$f(x,x';E,t) = \sum_m \frac{2}{\ell}\sin\frac{m\pi x'}{\ell}\sin\frac{m\pi x}{\ell}\exp(-\eta_m(E,E'))S(E'). \qquad (2)$$

Here E' is determined by the slow down relationship

$$t + \int_{E}^{E'} \frac{d\varepsilon}{\dot{E}(\varepsilon)} = 0 \tag{3}$$

and

$$\eta_m(E,\ E') = \int_{E}^{E'} \frac{-\frac{\partial \dot{E}}{\partial \varepsilon} - \kappa(\varepsilon)\,\frac{m^2\pi^2}{\ell^2}}{\dot{E}}\, d\varepsilon . \tag{4}$$

The quantity E' is thus the particle energy projected backward in time to $t = 0$. Integrating over x space, the total loop population is

$$f(E,t) = \frac{4}{\pi}\ S(E') \sum_{m\,=\,1,3,5,\ldots} \frac{1}{m}\ \sin\frac{m\pi x'}{\ell}\ \exp(-\eta_m(E,E')) \tag{5}$$

The total flux of particles diffusing out the ends of the loop is the quantity

$$\dot{f}(E,t) = \kappa(E)\ \left(\nabla f(x{=}0,E) - \nabla f(x{=}\ell,E)\right) \tag{6}$$

which is

$$= \frac{4\pi}{\ell^2}\, \kappa(E)\ S(E') \sum_{m=1,3,5,\ldots} m\ \sin\frac{m\pi x'}{\ell}\ \exp(-\eta_m(E,E')). \tag{7}$$

Other quantities of interest can be calculated similarly.

Two cases of interest can be investigated, that of (1) relativistic electrons where the energy loss is constant (as is the diffusion coefficient) and (2) ∿ 20 MeV protons which are sub-relativistic ($\kappa \sim E^{+\frac{1}{2}}$ and $\dot{E} \sim E^{-\frac{1}{2}}$). The energy dependence of κ is only due to velocity differences, i.e. the mean free path of the particle is taken to be constant. As will be seen, the results are similar so that the relativistic electron calculation can be taken to be representative of the basic physics.

X-rays and γ-rays can be emitted by electrons and protons, respectively, from both the regions of precipitation at the ends of the loop and from the interior of the loop where tenuous thermal material resides; μ-waves on the other hand might very well only be emitted from the highest parts of the loop which are presumably optically thin. Appropriate time profiles for such emissions can be derived by calculating the population or population flux of the parent particles for various injection positions and material densities within the loop.

Figure 1 is a plot of total particle precipitation rate with an input spectrum of $E^{-2.5}$ at $t = 0$. These profiles would be identified with total instantaneous thick targe x-/γ-ray emissions. Here particles are injected at the midpoint of the loop ($x/\ell = \frac{1}{2}$) and at $x/\ell = \frac{1}{4}$ and 1/10. The time axis is normalized to the characteristic diffusion time of the particles $\tau_d = (\kappa(E)/\pi^2\ell^2)^{-1}$ and the density effect is included as a parameter τ_d/τ_c where $\tau_c = E/\dot{E}$. The vertical axis, i.e. precipitation rate, is in units of τ_d^{-1} normalized to the total injection population. Values of τ_d/τ_c are 0, 1 and 5 which represent respectively, the case with no material inside the loop, the case with a quantity of material such that energy loss competes with diffusive losses and the case where energy losses dominate.

Curves with equal τ_d/τ_c show that the peak precipitation rate is solely a function of injection position but the actual time of peaking is weakly dependent on the ambient density. The density effect is mostly seen in the amplitude of the precipitation in the latter half of the pulse. The earlier peaking of the curves for smaller x'/ℓ show that particles diffuse preferentially out the closest end of the loop, the distance to which is strongly related to peak time. In terms of the dimensionless quantities τ_d/τ_c, there is little difference between the curves for relativistic electrons and subrelativistic protons.

Figure 2 is a similar plot where the precipitation rate for each loop end is shown separately. This sort of time profile would be expected from observations by an instrument which could spatially resolve two emission points. The density effects here are seen as a variation in the amplitude of the precipitation rate at the far end of the loop. The relative peaking times again are only a function of position. The loop end closest to the injection position shows the greatest precipitation and the closer the injection point is to the end, the earlier the peak in the precipitation rate. The peak time of the precipitation out the farthest loop end is not sensitive to the injection position as the particles must diffuse rather uniformly through the loop to produce any significant precipitation at the remote site. This time is roughly the same for all cases, i.e., τ_d.

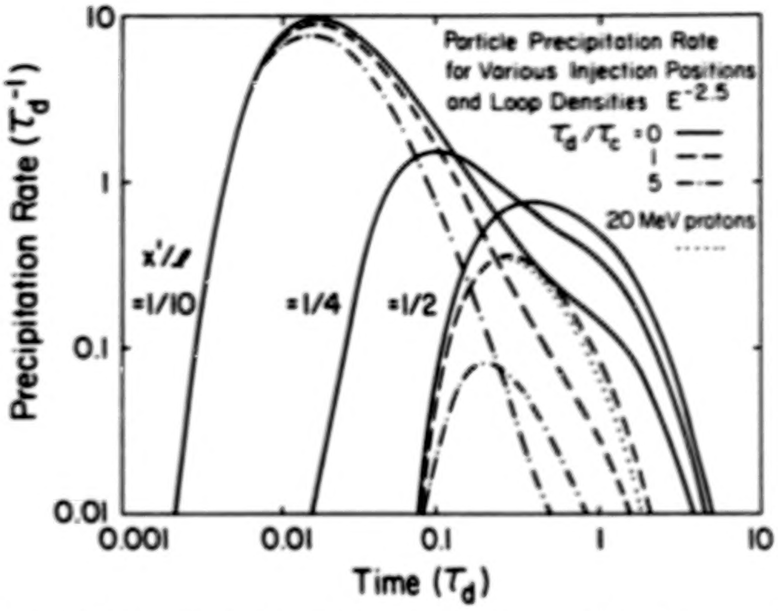

Figure 1. Total particle precipitation rate versus time for various injection positions and loop densities, where the time axis is in units of the characteristic diffusion time. The precipitation rate is in dimensionless units of inverse diffusion time, and the loop densities are parameterized by τ_c the collisional slow-down time and then normalized to the characteristic diffusion time. An injection position of $x'/\ell = 1/10$ means that energetic particles in this case with a spectrum of $E^{-2.5}$ are injected at one tenth the way from one end of the loop to the other. Also shown are the corresponding curves for 20 MeV protons which have a different energy dependence for collisional braking.

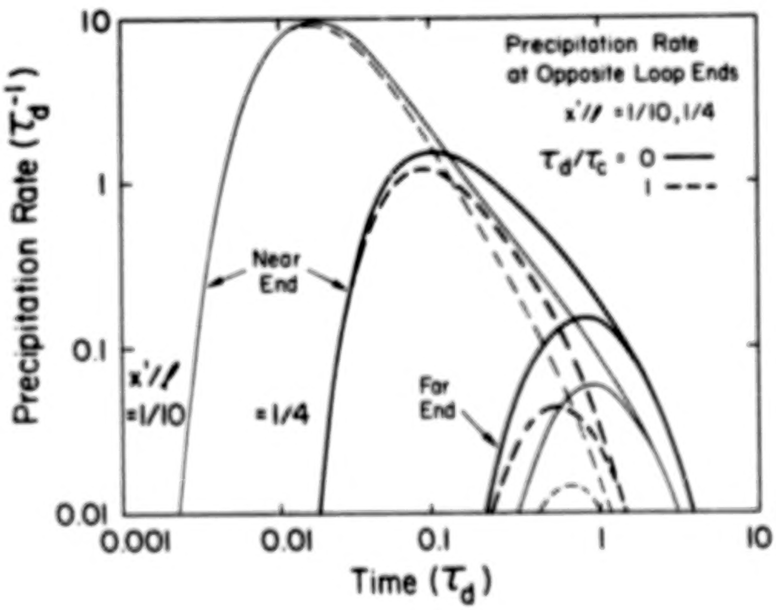

Figure 2. The particle precipitation rate for opposite ends of the loop for injection positions of 1/10 and 1/4. Curves are shown for the precipitation

rate at the loop end nearest the injection point and the loop end farthest from the injection. There is almost two orders of magnitude difference between the rates at opposite ends of the loop when particles are injected very close to one end. Collisional braking further suppresses the rate at the far end due to the greater time required to diffuse to the far end.

We expect that x- and γ-ray emission comes not only from the footpoints of the loop, but also from the interior of the loop due to the non-zero matter density. This thin target emission will be proportional to the number of particles still within the loop. In Figure 3 is the total loop population as a function of time plotted along with the precipitation rate illustrating the relative rates of thin versus thick target emission. These are plotted for the case where $x'/\ell = \frac{1}{4}$ and $\tau_d/\tau_c = 1$. Also shown is the ratio of these two quantities. It should be noted again that the emission physics is not included in these calculations but the total emission will scale by the quantities shown. The ratio of loop population to precipitation reaches a constant value as time approaches τ_d. At this time particles have uniformly distributed themselves throughout the loop and from that time forward the precipitation rate is simply proportional to the loop population. The positional dependency at t = 0 has been lost.

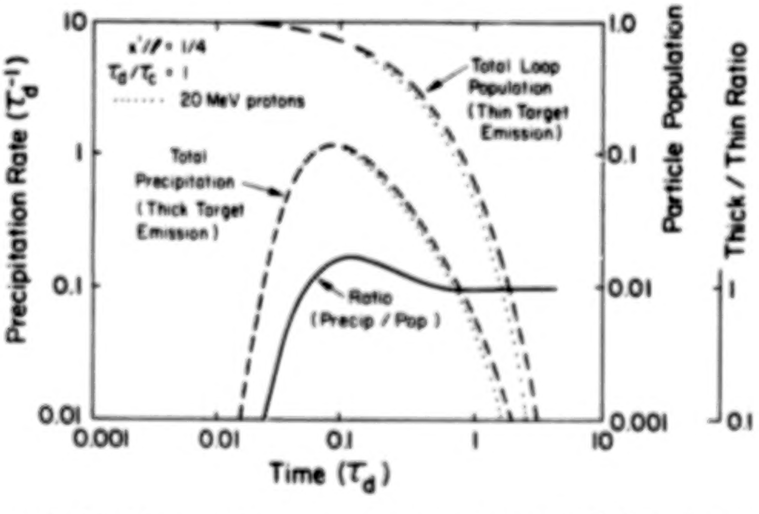

Figure 3. Total precipitation rate representative of thick target emission processes and the time behavior of the total particle population representative of thin target emission processes. The ratio of the two quantities is also shown where thin target emission dominates at the very earliest times due to the fact that no particles have diffused to the ends of the loop. Also shown are equivalent curves for the 20 MeV protons.

Figure 3 has other relevancy if the whole contents of the loop is optically thin to μ-waves. In this case the thin target emission and the μ-wave emission will follow the total loop population. The total loop population, of course, peaks at $t = 0$ as would the μ-wave emission in this case. The precipitation produced x-rays peak at a later time, a function of x'/ℓ.

If the case exists, however, that only part of the loop is optically thin to μ-waves, specifically the top quarter of the loop, then the emission will follow the particle population in that top quarter of the loop. This is shown in Figure 4 again with the accompanying precipitation profile for the case of $x'/\ell = 1/10$ and for a few values of τ_d/τ_c. In this configuration the x-ray flux (precipitation) will lead the μ-wave flux (population) since the injection point is closer to the loop end than to the top of the loop.

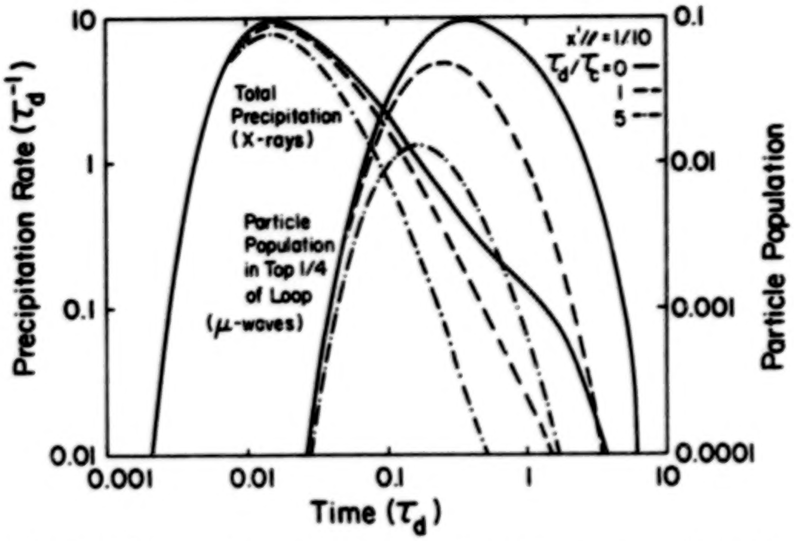

Figure 4. Total precipitation rate representing hard x-ray emission and the time behavior of the electron population representing μ-wave emissions at the very top 1/4 of the loop (presumed to be optically thin). The material density inside the loop has little impact on the relative timing of the two emissions.

Parameterizing all these curves in terms of τ_d and τ_c is a useful exercise even though we expect significantly different profiles from subrelativistic protons as opposed to relativistic electrons. But in terms of these quantities the profiles are very similar as seen in Figures 1 and 3. Thus the energy dependences of any of these profiles are imbedded in the scaling of the axes. A different profile, though, is to be expected if κ exhibits an abrupt change of form. This would occur for mildly relativistic electrons as they interact with whistlers at lower energies and MHD waves at higher energies.

3. Discussion

Since second order stochastic acceleration occurs due to the same scattering or diffusion process, it is possible that acceleration is not negligible compared to spatial diffusion effects. However, this is true only when the mean-free path is very short compared to loop length in which case the particles are accelerated efficiently but do not propagate beyond the acceleration region. If in fact, the turbulence in the flaring loop is not associated with the acceleration of the energetic particles, the particle transport is truly decoupled from the acceleration. In this scenario episodic acceleration could occur in one region of the loop and then the particles which escape this region into the remainder of the loop are the ones described by the above formalism. The turbulence necessary for the diffusion approximation to be valid could then come from three potential sources, photospheric turbulence propagating upward and cascading to larger κ values, flare generated waves or waves excited specifically by the fast particles. Particle excited waves would allow for scatter-free propagation of electrons prior to the development of a sufficient intensity wave field to isotropize the distribution. Thus it would be possible to achieve the very short time scale phenomena observed by Kiplinger et al. (1983), yet the majority of the particles would obey diffusive transport once the wave field develops. This is consistent with the observations of Kiplinger et al., (1983) as these short (< 50 ms) bursts of x-rays are infrequent occurrences with an energy content far less than the total x-ray flux. The majority of hard x-rays and γ-rays reside within a time envelope which has a longer time scale than that of the very shortest spikes. These could be photons from a majority of particles which obey diffusive propagation while the infrequent but rapid spikes derive from particles (electrons) which freely propagate to the loop footpoints before a sufficient scattering wave field develops.

The concept of diffusive transport of energetic particles within a flaring coronal loop is an attractive one in that we assume that the flare environment is turbulent and noisy, a likely situation. This contrasts with precipitation models based on simple strong pitch angle diffusion at a single point while the remainder of the loop is quiet, e.g. (Zweibel and Haber, 1983; Kawamura et al., 1981). It is unfortunately difficult to verify the existence of the MHD wave field necessary for pitch angle scattering over such a large spatial extent. Large scale turbulence (> 100 km/s) is commonly seen in broad soft x-ray lines but this normally takes place very early in the event. If the wave field is generated by the fast particles, only a small fraction of the particle energy density is required in a small range of wave number resonant with the particles. This may be entirely unobservable. However, this can be observed in situ at the Earth's bow shock (Lee, 1982) where fast ions generate the waves necessary for their own acceleration in the environment of that shock.

In summary, the physics of short time scale phenomena must take into account the effects of particle transport between the times of particle acceleration and production of observable radiation. Diffusive particle propagation effects are capable of producing a number of timing features seen in solar flares by varying geometrical parameters such as the length of the loop, the relative position of the particle injection and the position of the portion of the loop optically thin to μ-waves. If such a transport concept is used as a working model in hard x-ray, μ-wave and γ-ray emission, then the time profile of these emission processes become diagnostic tools in probing the interior of flaring coronal loops.

4. References

Kane, S. R., Chupp, E. L., Forrest, D. J., Share G. H., and Rieger, E. 1986, Vol. 2, these proceedings.
Kawamura, K., Omukoda, T., and Suzuki, I. 1981, Solar Phys., 11, 55.
Kiplinger, A. L., Dennis, B. R., Emslie, A. G., Frost, K. J., and Orwig, L. E. 1983, Ap. J. (Lett.) 265, L99.
Lee, M. A. 1982, J. Geophys. Res., 87, 5063.
Schlickeiser, R. 1985, Proc. 4th Intl. Summer School on Cosmic Ray Astrophys., ed. M.M. Shapiro, (Dordrecht: D. Reidel) in press.
Zweibel, E., and Haber, D 1983, Ap. J., 264, 642.

N87
21827
UNCLAS

SIGNATURES OF CURRENT LOOP COALESCENCE IN SOLAR FLARES

J. Sakai

Faculty of Engineering
Toyama University
Toyama 930 Japan

H. Nakajima

Tokyo Astronomical Observatory
University of Tokyo
Japan

E. Zaidman and T. Tajima

Department of Physics
University of Texas
Austin, Texas U.S.A.

T. Kosugi

NASA-NRC Research Associate on leave from
Tokyo Astronomical Observatory
University of Tokyo
Japan

F. Brunel

National Research Council
Ottawa, Canada

ABSTRACT

The nonlinear coalescence instability of current carrying solar loops can explain many of the characteristics of the solar flares such as their impulsive nature, heating and high energy particle acceleration, amplitude oscillations of electromagnetic emission as well as the characteristics of 2-D microwave images obtained during a solar flare. The physical characteristics of the explosive coalescence of currents are presented in detail through computer simulation and theory.

Canonical characteristics of the explosive coalescence are:
(1) a large amount of impulsive increase of kinetic energies of electrons and ions,
(2) simultaneous heating and acceleration of electrons and ions in high and low energy spectra,
(3) ensuing quasi-periodic amplitude oscillations in fields and particle quantities,
(4) the double peak (or triple peak) structure in these profiles,

A single pair of currents as well as multiple currents may participate in the coalescence process, yielding varieties of phenomena.

In particular, double sub-peak structures in the quasi-periodic osillations found in the time profiles of two solar flares on June 7, 1980 and November 26, 1982 are well explained in terms of the coalescence instability of two current loops. This interpretation is supported by the observations of two microwave sources and their interaction for the November 26, 1982 flare.

1. Introduction

The solar flare phenomenon is a manifestation of an explosive release process of energy stored in the lower corona, involving the plasma heating up to 5×10^7K, the acceleration of charged particles up to the order of the rest mass energy of electrons and ions, as well as the production of electromagnetic radiation from the radio band to γ-ray wavelengths. (for a previous summary of solar flares, see Svestka, 1976; Sturrock, ed., 1980; Priest, 1982).

After launching of the Solar Maximum Mission (SMM) and Hinotori satellites, it becomes clear from the observations of hard X-rays and γ-rays that the electrons with energies up to MeV as well as ions with energies up to GeV can be simultaneously accelerated within a second during the impulsive phase of a solar flare. In a particular flare (03:12UT of June 7, 1980) the γ-rays showed a quasi-periodic amplitude oscillation which closely correlated with the quasi-periodicity in both microwave bursts and hard X-ray bursts.

Direct observations in soft X-rays (Howard and Svestka, 1977) showed that in the active regions there exist multiple coronal loops which might carry plasma currents. The interconnecting coronal loop might be a quite important physical process for energy release in the solar corona.

Recently, the observations of the interacting coronal loops which lead to solar flares have increased in various kinds of observations from H_α (Kurokawa et al., 1985), radio (Nakajima et al., 1984, Kundu, 1985) as well as hard X-ray (Machado, 1985).

In order to explain the rapid quasi-periodic particle acceleration of both electrons and ions observed in the June 7, 1980 flare, (Tajima et al., 1982, 1985) showed that the most likely mechanism for the impulsive energy release in solar flares is the current loop coalescence instability (Finn and Kaw, 1977, Pritchett and Wu, 1979).

It has been shown that by simulation and theory (Tajima and Sakai, 1985) that during the coalescence of two current loops, the magnetic energy stored by the plasma current can be explosively transformed to the plasma heating as well as the production of high energy particles within a transit Alfven time across the current loop (which is about 1~10 seconds for appropriate radius of the loop) through the magnetic reconnection process. Furthermore, the energy release can be achieved with quasi-periodic fashion whose periodicity depends on plasma parameters such as plasma beta ratio (β), the ratio B_P/B_T between the magnetic field, B_P produced by the plasma current and B_T the potential magnetic field, as well as the colliding velocity of two current loops that is determined mostly from the initial total plasma loop current.

The plasma can be heated up to 60 times of the initial temperature and the electrons and ions can be accelerated simultaneously by the transverse electrostatic field which can be produced during the explosive coalescence process.

The present paper is to show results obtained from current loop coalescence plasma dynamics with applications to solar flares. The current loop coalescence itself is similar with Gold and Hoyle model (1960) and emerging flux model (Hayverts et al., 1977) in its morphological spirit of the model. However, the details are quite different from each other. In particular, Tajima and Sakai (1985) presented the physical basis of such a morphological model, i.e., the physics of magnetic reconnection process, as well as particle acceleration mechanism. We found basically two types of magnetic reconnection, namely, slow and explosive processes: the reconnected magnetic flux $\Delta\psi$ is proportional to t^m $(m>1)$ the slow reconnection process and $\Delta\psi$ is proportional to $(t_0-t)^{-m}$ $(m>0)$, in the explosive process. We also found in the ensuing stage the quasi-periodic reconnection with quasi-periodic acceleration during the coalescence of current loops.

2. Physical Characteristics of Current Loop Coalescence

In the problem of solar flares, the reconnection of field-lines is believed to take place due to finite resistivity. The paper based on a boundary layer analysis by Furth, Killeen, and Rosenbluth found an instability (the tearing instability) which grows at a growth rate $\Gamma = C\tau_r^{-3/5}\tau_A^{-2/5} \propto \eta^{3/5}$.

Sweet and Parker, on the other hand, obtained a steady-state solution which has a narrow x-point angle; the time scale τ_{sp} of reconnection is characterized by $\tau_{sp} = \sqrt{\eta}\,(n_i/n_e)^{1/2}(v_A/L)^{1/2}\chi_e^{-1} \propto \sqrt{\eta}$, where 2L is the length of the impinged plasma, and are the densities inside and outside of the singular layer. Petschek similarly obtained a steady-state solution which has a large x-point angle; the reconnection time scale τ_p is independent of resistivity, $\tau_p^{-1} \propto \eta^0$. The time scale of reconnection due to the mechanism of the Sweet-Parker process is characterized by $\epsilon^{-1/2}$ $(\epsilon = \tau_A/\tau_R)$, while that of Petschek is by ϵ^0. It may be said that the paper by Furth et al. is appropriate for situations of spontaneously growing tearing modes, while the papers by Sweet et al. are for problems of driven reconnection, although the distinction is yet to be clarified in more precise scientific terms.

Since the paper Furth et al. was published, a considerable amount of literatures have been written which further investigate the nonlinear processes of the tearing instability. A paper by Rutherford discussed nonlinear secular growth of a single tearing mode, while a paper by Drake and Lee found the collisionless equivalent to the Rutherford regime. The Rutherford time scale τ_R is characterized by $\tau_R^{-1} \simeq C\eta\Delta'(B_y\psi)^{1/2}$, where C is a constant less than unity, B_y is the shear field, and ψ the reconnecting flux. Carreras, Rosenbluth, Diamond et al. discussed nonlinear stages of many tearing modes with different helicities (i.e., on different rational surfaces), emphasizing mode couplings. With more than one helicity, the coupling is inherently three dimensional.

It has been recognized that the processes of magnetic reconnection are quite different depending upon whether reconnection is driven or spontaneous. For the spontaneous cases, as we briefly reviewed in the above paragraph, the current sheet becomes unstable against the tearing instability evolving from the unstable magnetic configuration. It is customary to argue that the Rutherford regime follows the linear stage and then the highly nonlinear mode coupling stages come into play. There are natural disturbances such as solar flares and geomagnetic storms, in which some of the observed time scales of the entire process of explosive phenomena are as small as the Alfven time. The scenario for reconnection based on spontaneous tearing has to confront the observed rapid reconnection processes, although the nonlinear stages of spontaneous reconnection can be quite rapid, as reviewed in the preceding paragraph. In this case, one has to maintain the unstable configuration in equilibrium long enough to reach the disruptive stage. On the other hand, driven reconnection is much faster and therefore quickly enters the nonlinear stage. This is one of the reasons why the driven reconnection has been studied by many authors.

In order to rapidly convert magnetic energy into kinetic one by a substantial amount, it seems necessary that the bulk of magnetic energy has to participate in the conversion process: the resistive heating at the x-point alone is to meager. This is because the available magnetic energy at the x-point is small by itself. On the other hand, the ideal MHD instabilities such as the kink instability and the coalescence instability are the processes that involve the bulk current redistribution in a matter of the Alfven time scale.

In the present paper we pick the coalescence instability as the primary instability to investigate its nonlinear consequences. we do so because (1) although it is an ideal MHD instability for drive in the linear sense, it would not nonlinearly evolve if there is no resistive (non-ideal MHD) effect; (2) therefore, it can involve a large amount of conversion of magnetic to kinetic energies in a short time; (3) it is essentially a two-dimensional instability, thus more amenable to thorough analysis of the fundamental processes of the instability. It is interesting to observe that with this two-dimensionality restriction we still find an explosive process as we shall see. The coalescence instability starts from the Faddeev equilibrium, which is characterized by the current localization parameter ϵ_c : The equilibrium toroidal current (in the z-direction) is given as $J_z = B_{0t} k (1-\epsilon_c^2)(\cosh ky + \epsilon_c \cos kx)^{-2}$. The parameter ϵ_c varies from 0 to 1 with small ϵ_c corresponding to a weak localization and ϵ_c close to unity corresponding to a peaked localization; in the limit of $\epsilon_c \rightarrow 1$ the current distribution becomes delta function-like. The rate of reconnection was that of Sweet-Parker for small ϵ_c, while the reconnection rate experiences two phases for larger ϵ_c (but smaller than 0.8). This emergence of

two phases is similar to the case of the driven reconnection. The intensity of coalescence and the rate of subsequent reconnection are controlled by just one parameter, the current localization (ϵ_c). In this problem there is no ambiguity as to the nature of the driver in contrast to the reconnection driven by external boundary conditions. For the case with $\epsilon_c = 0.7$, the second phase showed the reconnected flux increasing as t^{α} with $1<\alpha<2$. (Brunel-Tajima scaling) This indicates that the more the current localizes, the faster the reconnection becomes.
As seen in the next section, for the case with $\epsilon_c = 0.85$ we found more rapid reconnection called explosive reconnection, in which the reconnected flux $\Delta\Psi$ increases as $(t_0 - t)^{-4/3}$. (Tajima-Sakai scaling)

2.1 Summary of Simulation Results

We combine both a MHD model and a kinetic model of simulation. The results from these two different models are consistent in basic points, but are complementary in many detailed aspects. The kinetic simulation model we adopt here is the electromagnetic particle code with 2- dimensions.

The MHD simulation model we use is the MHD particle code with $2\frac{1}{2}$ dimensions. The MHD particle code is robust in applications to problems even with strong turbulence, flows, convections, and density depression. This is helpful because the present problem involves fast (explosive) reconnection, strong density depression and compression, and strong flows.

Results from the electromagnetic particle model are now discussed. Figure 1 displays the typical time history of various field and particle quantities observed in our simulation in which after the initial transient (up to $t=4\Omega_i^{-1}$ in the code unit to be explained in the following section) the phase of coalescence of two magnetic islands commences. It is seen in Figs. 1(a)-(c) that around t=27 the magnetic and electrostatic field energies shoot up explosively as well as the ion temperature in the direction of coalescence (the x-direction). The unit of computational time is omitted hereafter whenever it is unambiguous. It is also seen in Figs. 1(a)-(c) that (1) after the explosive increase of the field energies and temperature this overshooting results in synchronous amplitude oscillations of all these quantities with the period being approximately the compressional Alfven period; and (2) superimposed on these overall amplitude oscillations is a distinct double-peak structure in the electrostatic field energy and the ion temperature. Although we are interested in analyzing the entire episode of the run including the initial phase and the post-explosive phase, we focus particularly on the explosive phase of the coalescence. We replot Figs. 1(a)-(c) into Figs. 1(d)-(f) to find the way in which these quantities increase toward the catastrophic point. We find from Figs. 1(d)-(f) that (1) the magnetic energy explodes as $(t_0 - t)^{-8/3}$; (2) the electrostatic energy explodes as $(t_0 - t)^{-4}$; and (3) the ion temperature in the coalescing direction explodes as $(t_0 - t)^{-8/3}$ until saturation due to

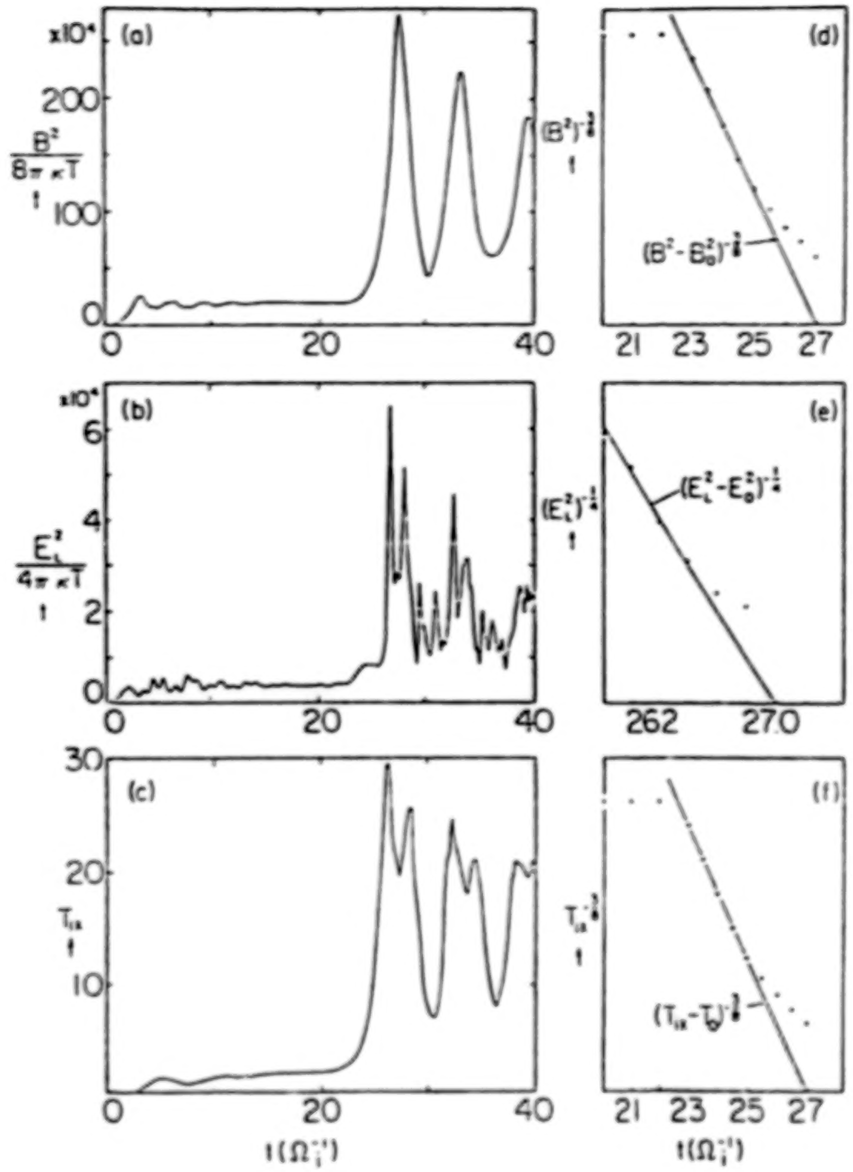

1. Explosive increase of field energies and temperature during the coalescence of two magnetic islands: EM particle simulation results. For the case $\Omega_{ei} = 0.2$. Other parameters are given in Sec. II. Toward the same explosion time $t = t_0 = 27(\Omega_i^{-1})$, the magnetic energy B^2 (a), electrostatic energy E_L^2 (b), and the ion temperature in the z-direction T_{iz} (c) diverge as $(t_0 - t)^{-8/3}$, $(t_0 - t)^{-4}$, and $(t_0 - t)^{-8/3}$, as shown in (d), (e), and (f), respectively. [We took $B_0^2 \sim 1.6 \times 10^5$, $E_{L0}^2 \sim 7.5 \times 10^3$, and $T_{iz0} \sim 0.85$ for the pre-explosive phase values; see Figs. 1(a)-(c)].

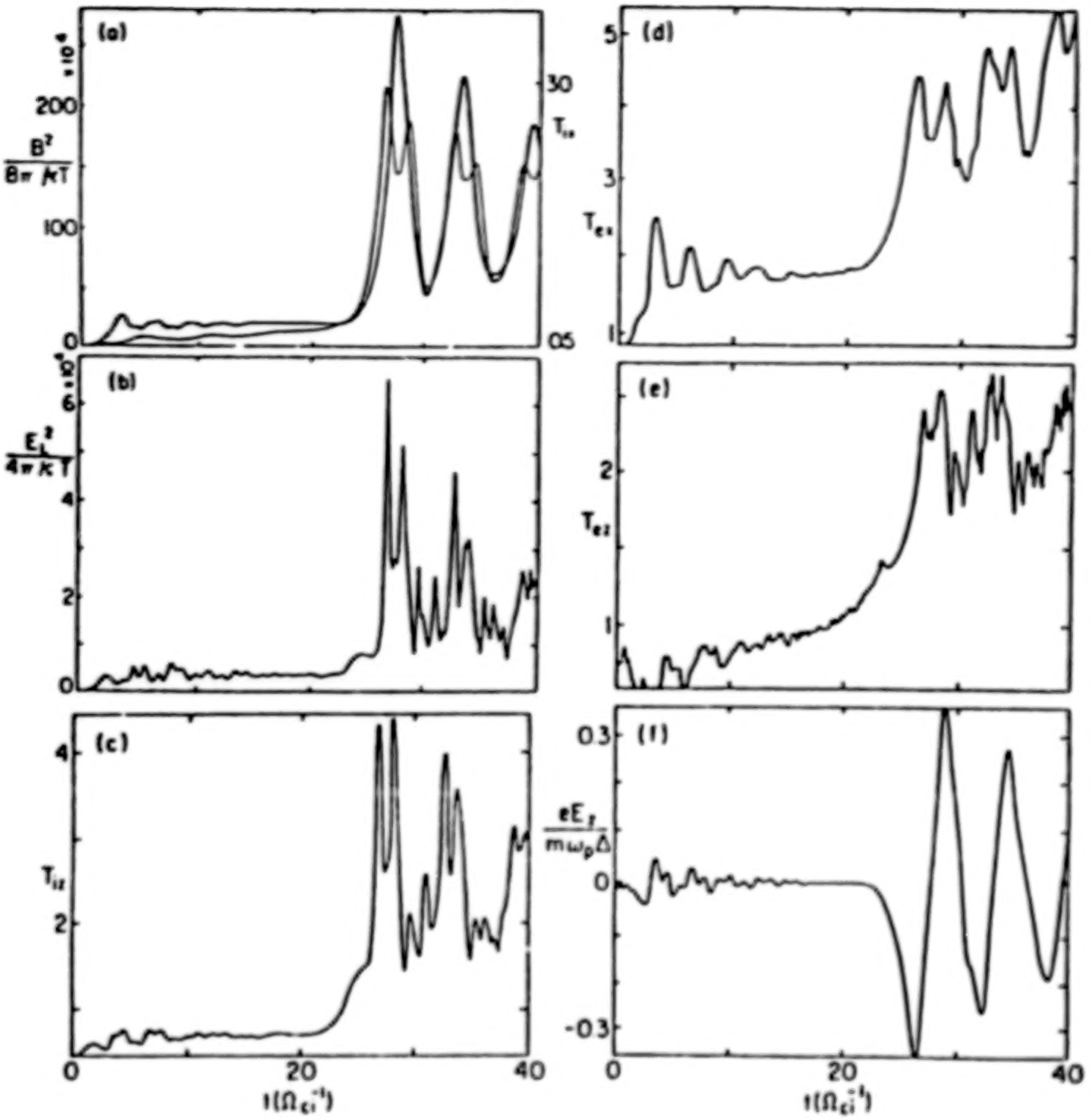

2. Temporal profiles of particle and field quantities for the coalescence process obtained from the EM particle simulation. $\Omega^{et} = 0.2$. (a) The thick line represents the magnetic energy, the thin one the ion temperature in the z-direction. (T_{iz} at $t = 0$ was 0.5). (b) Electrostatic field energy in time. (c) Ion temperature in the z-direction. (d) Electron temperature in the x-direction. (e) Electron temperature in the z-direction (f) Inductive electric field (E_z) in time.

overshooting sets in, where t_e is the explosion time measured here to be $t_e \sim 27(\Omega_i^{-1})$ in this run. Figure 2 presents the time history of various field quantities and temperatures in the course of the early formation and the coalescence with the toroidal field being such that $eB_z/m_e c=\Omega_{ez}=0.2\omega_{pe}$. In Fig. 2(a) both the magnetic field energy and the ion temperature in the direction of coalescence (x) show that after the early $(t \leq 3\,\Omega_i^{-1})$ rise which corresponds to the magnetic islands formation by tearing a long relatively dormant period (t=3-22) sets in, followed by a stage (t=22-27) rapid and huge increase in these quantities. It is also evident that after the rapid increase $(t \geq 27)$ salient amplitude oscillations ensue due to overshooting. It is to be remarked that all the other quantities shown in Fig. 2 (a)-(e) closely follow the pattern of Fig. 2(a) with their characteristic events simultaneously occurring. It is also noted that the amplitude oscillations of the temperatures (T_{ix} and T_{iz} as well as T_{ex} and T_{ez}) and the electrostatic field energy have a structure of marked double peaks. The valley of the double-peak structure coincides with the peak of the magnetic field energy amplitude. As mentioned in Sec. 1, it is important to notice that the rapidness of the increase of each quantity differs and that each quantity explosively increases characterized by a certain definite, but different, index of explosion (i.e., the exponent to the time measured backward from the point of explosion time) until the saturation stage sets in. The stop of rise (t 3) of each quantity in Fig. 2(a)-(e) corresponds to the completion of islands formation. The following quiescent period $(3<t<20)$ corresponds to the stage where the formed islands slowly attract each other. The rapid explosive rise $(t \geq 20)$ marks the commencement of the explosive coalescence. The following stage of amplitude oscillations correspond to the "breathing" (or pulsations) of coalesced islands (compressional Alfven oscillations). The induced electric field E_z explosively increases when there is rapid flux reconnection during the explosive coalescence and then oscillates as the magnetic flux in the coalesced island is compressed and decompressed.

Some of the above findings can be given by a qualitative explanation. Since we shall discuss the explosive phase in greater detail later, we try to pay attention to the amplitude oscillation phase in particular here. Once two current blobs coalesce, they are bound by common magnetic flux. The larger coalesced island continues to vibrate. Within the coalesced island the colliding two plasma blobs cause turbulent flows which dissipate their energy quickly into heat, thereby reducing the amplitude oscillations of temperatures and field. As a result as we shall see, the momentum distribution of plasma electrons and ions exhibit an intense bulk heating and acceleration of the tail. The heating in the poloidal direction (x) is due to adiabatic compression and decompression of the coalesced current blobs. The eventual bulk heating is a result of turbulent dissipation of counterstreaming instabilities. The heating in the toroidal direction is due to heating/acceleration by the inductive toroidal electric field which is several times the classical Dreicer field and the $v_p \times B$ acceleration. The double peak in the time development of the temperatures occur just before ($t=t_1 \sim 27$) and after ($t=t_3 \sim 29$) the maxima of magnetic field ($t=t_2 \sim 28$). In Fig. 3 schematic sequential pictures of plasma dynamical behavior during coalescence are shown. At $t=t_1$ the magnetic (JxB) acceleration of ions becomes maximum so that the magnetic flux the behind the colliding plasma blobs as well as the plasma blobs are themselves strongly compressed. This plasma compression causes the first temperature peak at $t=t_1$. After this maximum acceleration phase ions aquire substantial velocities along the direction of collision so that they detach from the magnetic flux against which ions have been compressed. This result in an expansion phase ($t=t_2$) of ions, and hence in an adiabatic cooling of the plasma as the magnetic fields obtain maximum values. The process reverses after the maximum of the magnetic fields at $t=t_3 \sim 29\Omega_i^{-1}$, which gives rise to the second peak of the temperature.

The high energy tail particle acceleration of ions and electrons may be qualitatively discussed here. The tail formation is probably due to a combination of localized electrostatic field acceleration across the poloidal magnetic field and magnetic acceleration of the poloidal to toroidal directions.

Electrons are magnetized and are carried away with the accelerating magnetic flux, while bulk ions are accelerated by the JxB force. On the other hand, the high energy ions are produced and dragged by the charge separation created near the compressed flux. The difference of motions between ions and electrons around $t=t_1$ causes a strong localized shock-like electrostatic field, E_x, which propagates with a phase velocity of the structure $v_p = v_x$. This $v_p \times B$ acceleration causes the formation of high energy particle in the toroidal direction. By this acceleration process, ions and electrons are accelerated to relativistic energies in opposite directions along the toroidal magnetic field.

Next we present the simulation results of the case of multiple coalescence process (Fig. 4). A number of islands are induced as the crowbar current is turned on. An interesting phenomenon here is that these islands begin to coalesce one by one to form slightly larger ones. In turn, these larger islands coalesce further into still larger islands. Finally, we are left with only two (big) islands that more resembles two sheets of plasma. Eventually these two islands also coalesce into but one. In this multiple coalescence process, the early stage presents many less regular or spiky time profiles of fields and particle quantities. As time goes on, larger and more organized time profiles of these quantities come to dominate. Eventually, large scale oscillations are observed in Fig. 5, which are set off after the final two islands coalesce into one. This is, therefore, a similar process to the previous two islands coalesce process. In this particular

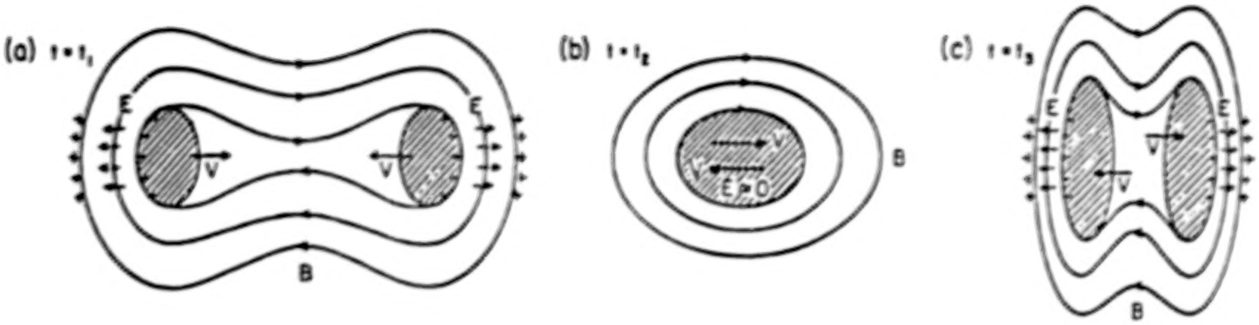

3. Schematic sequence of snapshots of the plasma and electric and magnetic fields during the coalescence process.

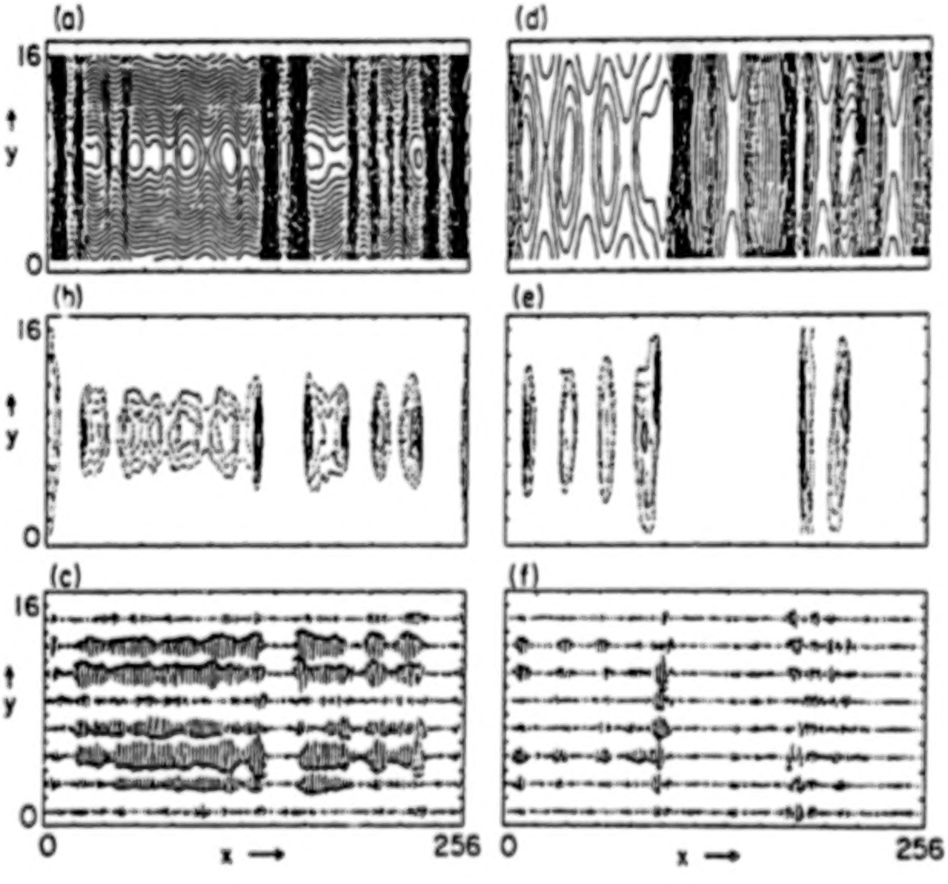

4. Multi-loop coalescence ; (a) (d) ;magnetic field line, (b) (e) ;density
(c) (f) ;electrostatic field.
(a) (b) (c) correspond to the same time,
and (d) (e) (f) follow.

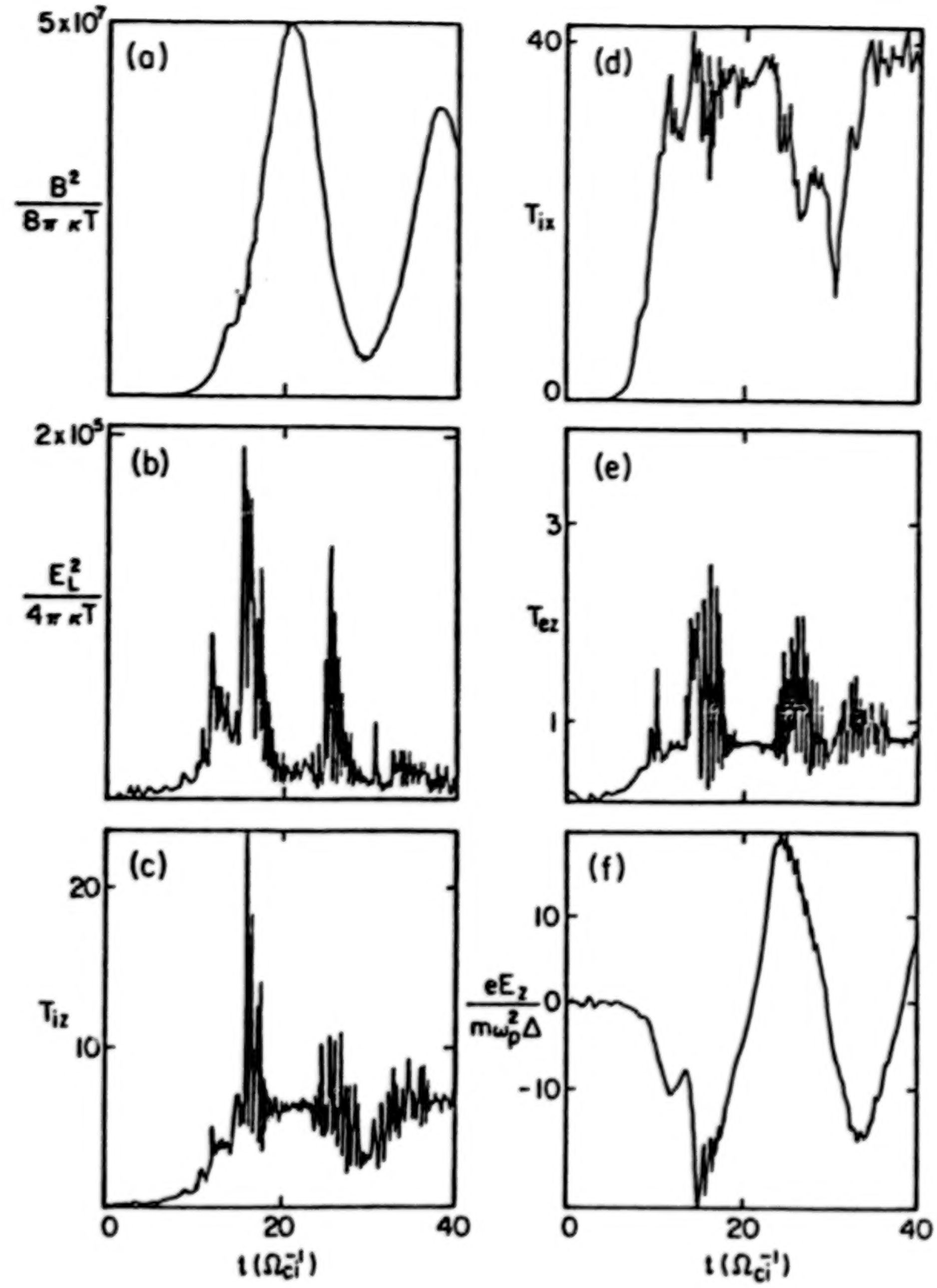

5. Time hisroty of physical quantities in the case of multi-loop coalescence.

choice of parameters heating and acceleration of particles are more intense than the previous case. Corresponding energy distributions (spectrum) show a longer and more populous tail, indicating a harder spectrum. However, the basic feature of two (for perpendicular) and three (for the z-directional distribution) distinct distribution regimes is still unchanged, implying the same heating/acceleration mechanism at work. When we inspect the electron z-direction distribution, the highest energy of the tail oscillates as the overall coalesced island vibrates. On the other hand, the maximum ion energy of the tail in the z-direction, although also oscillating, is less sensitive to the island vibration.

Results from the magnetohydrodynamic particle models are presented hence. Fig. 6 shows kinetic energy and the reconnected flux upon coalescence as a function of time for the case with ϵ_c=0.85. A theoretical curve $(t_0-t)^{-4/3}$ is superimposed on the simulation result. During the phase of the rapid increase of reconnected flux (t=50-90Δc_s^{-1}) the simulation result matches reasonably with the theoretical curve. Beyond t=90Δc_s^{-1} the increase begins to be mitigated due to a saturation effect (the flux depletion).

Figure 7 displays the case with ϵ_c=0.7. The reconnected flux increases rapidly with $\Delta\psi \propto t^m$ (m=1.9). It is, however, less rapid than the case with ϵ_c =0.85. The released energy is also less in present case. The case with ϵ_c =0.3 was treated, where $\Delta\psi \propto t^m$ with m=1. Thus, it is clear that as increases, the process of reconnection becomes faster, changing from the Sweet-Parker rate to the Brunel-Tajima rate to the explosive rate. It is also remarkable that the explosive increase of reconnected flux during the coalescence is observed in the MHD simulation as well as in the kinetic simulation discussed earlier.

The structure and its evolution of the plasma and magnetic fields during the coalescence are examined.

These signatures are consistent with our hypothesis (a) that the reconnection takes place by the mechanism of Sweet and Parker for coalescence with ϵ_c=0.3. The signatures found in ϵ_c=0.3, on the other hand, imply that the reconnection process is not that of Sweet and Parker. It shows instead that (1) the reconnection angle at the x-point has enlarged ; (2) a high density spot near the x-point is formed ; (3) the reconnected flux increases faster than the Sweet-parker process ($\Delta\psi \propto t^m$ with m ~ 2). These are consistent with our further hypotheses (b) that the reconnection is through the process of Brunel, Tajima and Dawson for coalescence with ϵ_c =0.7. Later (t=160), the system approaches saturation when most of the flux available has reconnected as seen in ϵ_c=0.7 (at t=140 for this frame) and the high density region shifted from the x-point to the coalesced island hedge. The flow is randomized.

To supplement our kinetic simulation in order to make comparison with the MHD particle simulation, we present a run starting from the Faddeev equilibrium. In this case the

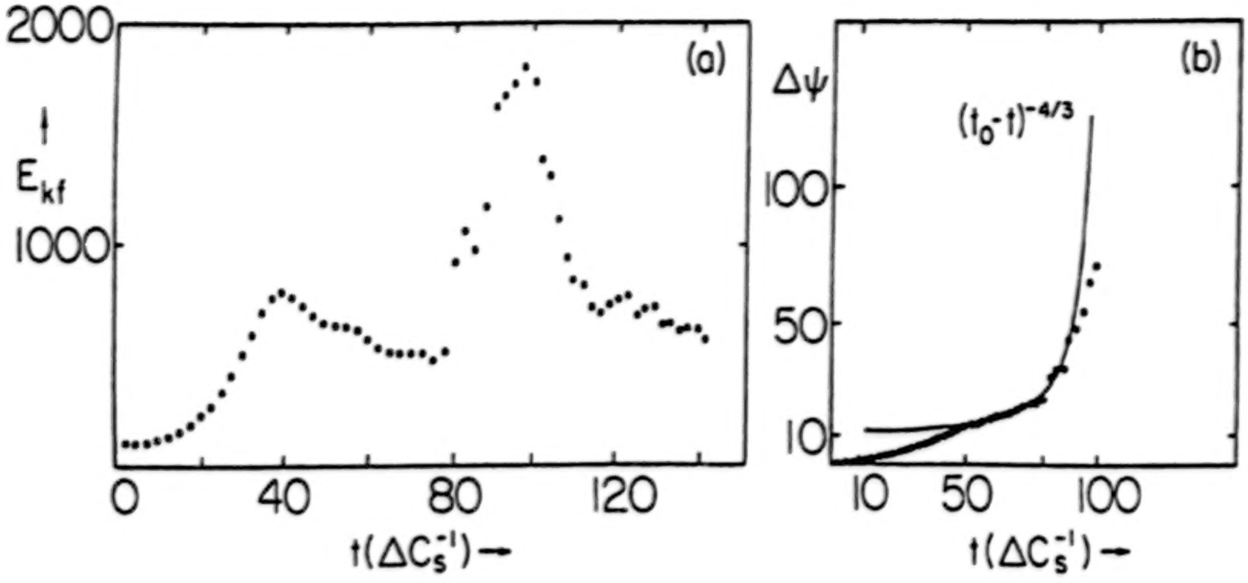

6. Temporal profiles of the fluid energy (a) and the reconnected flux (b) for $\epsilon_c = 0.85$ obtained from the MHD particle simulation. A solid line in (b) is a theoretical curve discussed in Sec. III.

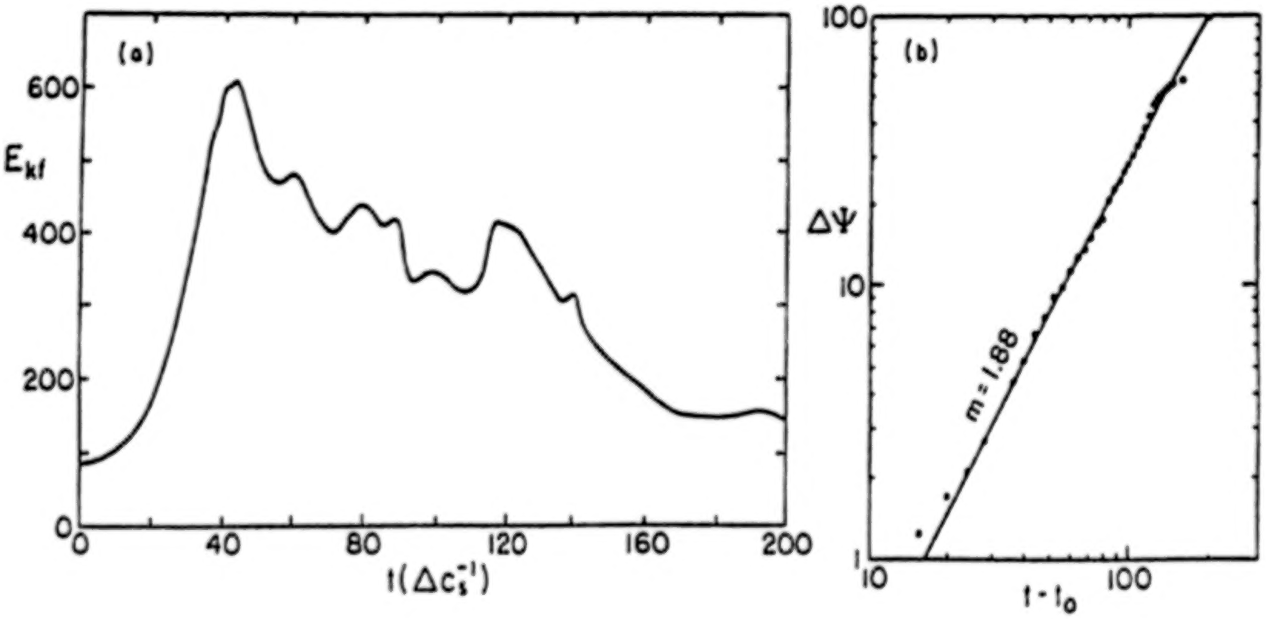

7. Temporal profiles of the fluid energy (a) and the reconnected flux (b) for $\epsilon_c = 0.7$ obtained from the MHD particle simulation. A solid line in (b) is a fit to the observation.

equilibrium is the same as the MHD particle run, although the parameters such as the collisionless skin depth are different because of the difference in model.

Figure 8 presents the pattern of the plasma and fields of the case ϵ_c =0.85, where we see faster and explosive reconnection (Fig.6). We are advancing our third hypothesis (c) that the coalescence with ϵ_c =0.85 is explosive whose reconnection process is to be characterized by the present paper. In frames of Figs.8 (a)-(d)(t=50) one sees the coalescence behavior before it becomes explosive. Although, in Figs.8(a) and (b), in particular, one can detect some deviation from the Sweet-Parker type for ϵ_c =0.3, it is qualitatively similar to the ϵ_c =0.3 case and the ϵ_c =0.7 case at this stage. In Figs. 8 (e) and (f) (t=75), we now see significant deviations in pattern from the cases with less . A much wider reconnection angle than the previous ones is observed in Fig. 8 (e). From these observations it can be argued that the widening of the reconnection angle has to be accmopanied by fast or explosive coalescence.

2.2. Theoretical Model of Explosive Coalescence

As shown in the previous section, the current sheet of nearly one-dimensional structure is formed in the explosive stage of the coalescence instability. As the coalescence proceeds further, the magnetic field structure approaches an x-type (Petsheck type) configuration. We assume that $\partial/\partial x \gg \partial/\partial y, \partial/\partial z$, in which x is the direction of coalescence, while y is the direction of poloidal magnetic field line and z is the direction of plasma current. We treat the external plasma dynamics of the explosive stage as a one-dimensional problem.

As we shall see in our separate paper(Tajima and Sakai,1985), in one-dimensional limiting case of two-dimensions, we get essentially the same results as we obtain in this section.

We start from the two-fluid model equations of plasma and the Maxwell equations, neglecting the displacement current. We assume the adiabatic law of states for both electrons and ions. The basic equations read as follows:

$$\frac{\partial n_j}{\partial t} + \nabla \cdot (n_j \mathbf{v}_j) = 0 \tag{1}$$

$$m_j n_j \frac{d\mathbf{v}_j}{dt} = n_j e_j \left(\mathbf{E} + \frac{\mathbf{v}_j}{c} \times \mathbf{B}\right) - \nabla p_j, \tag{2}$$

$$\nabla \times \mathbf{B} = \frac{4\pi}{c} \sum_j n_j e_j \mathbf{v}_j, \tag{3}$$

$$\nabla \cdot \mathbf{E} = 4\pi \sum_j n_j e_j, \tag{4}$$

$$\nabla \times \mathbf{E} = -\frac{1}{c} \frac{\partial \mathbf{B}}{\partial t}, \tag{5}$$

ORIGINAL PAGE IS
OF POOR QUALITY

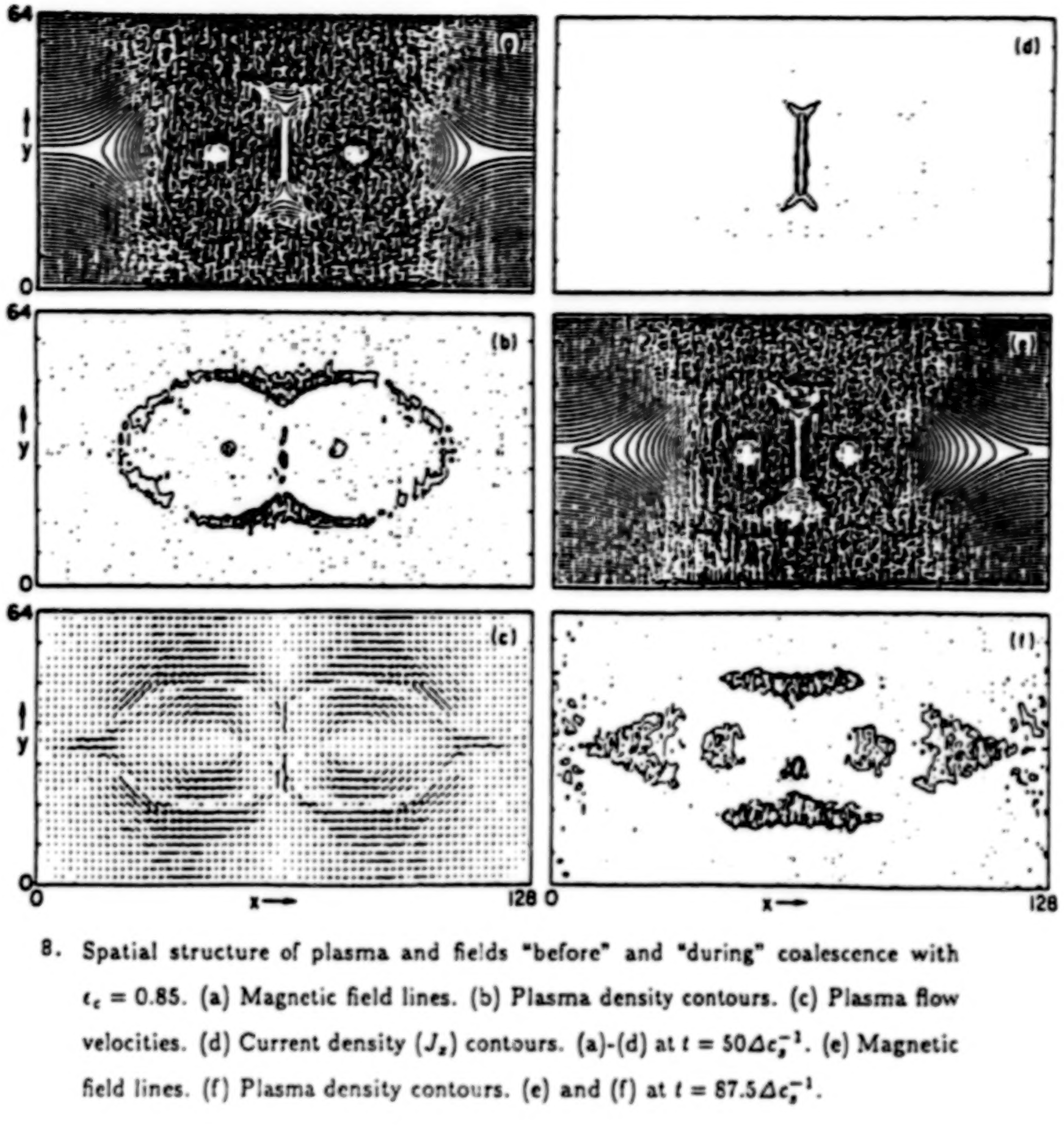

8. Spatial structure of plasma and fields "before" and "during" coalescence with $\epsilon_c = 0.85$. (a) Magnetic field lines. (b) Plasma density contours. (c) Plasma flow velocities. (d) Current density (J_z) contours. (a)-(d) at $t = 50\Delta c_s^{-1}$. (e) Magnetic field lines. (f) Plasma density contours. (e) and (f) at $t = 87.5\Delta c_s^{-1}$.

$$\frac{\partial p_j}{\partial t} + \mathbf{v}_j \cdot \nabla p_j + \gamma p_j \mathrm{div} v_j = 0, \tag{6}$$

where j denotes the species of particles and γ is the ratio of heat capacity which is related to the degree of freedom of the system f as $\gamma = 1 + 2/f$.

During coalescence, there is no specific scale length. The scale length characterizing the current sheet varies continuously in time without deformation of global structure of current sheet. If one looks at the evolution of the system locally in time (in the neighborhood of $t = t_s$), the system undergoes the rapid field and temperature swelling, compression of plasma and the size of the current sheet, change of the reconnection angle etc. in a certain specific fashion which was detailed in Sec. 2. If one looks at the same system locally in time a little later (in the neighborhood of $t = t_s + t_s'$), the system undergoes these changes with different magnitudes, but still in the same specific fashion. That is, the relations (laws) that govern the explosive coalescence themselves are invariant under the change of time scale. This was the manifestation of the presence of self-similarity in the system during explosive coalescence.

Such a physical situation may best be described by self-similar solutions in which scale factors vary continuously. We introduce scale factors a(t) and b(t) as follows,

$$v_{ez} = \frac{\dot{a}}{a} x, \tag{7}$$

$$v_{iz} = \frac{\dot{b}}{b} x, \tag{8}$$

where a dot represents the time derivative. An ansatz is imposed here that the velocities are linear in x. The linear dependence on x of the velocity implies that ions and electrons stream in the opposite direction around the center of current sheet, x = 0. The scale factors a and b will be determined from the above basic equations. From the continuity equations of electrons and ions, Eq. (1), we obtain

$$n_e = n_0 / a, \tag{9}$$

$$n_i = n_0 / b, \tag{10}$$

where n_0 is a constant. Equations (9) and (10) show that the densities of ions and electrons are nearly homogeneous in space and vary only in time during coalescence. The self-similar solutions obtained here are local solutions in space whose physical process dominates near the current sheet. We therefore neglect the higher order terms in space proportional to x^3 and higher hereafter. The current J_z in the sheet is nearly constant. This means that as n_j is nearly constant, v_{zj} is also approximately constant in space. Neglecting the term with x^3 in Eq. (3), we obtain

$$\frac{B_0(t)}{\lambda} = \frac{4\pi e n_0}{c}\left(\frac{v_{iz}^{(0)}}{b} - \frac{v_{ez}^{(0)}}{a}\right), \tag{11}$$

where we assumed the magnetic-field B_1 varies as $B_1=B_0(t)\frac{x}{\lambda}$, where λ is the magnetic field scale length. This ansatz is consistent with the assumption that the sheet current is constant in space.

From the y-component of Eq. (5) and the z-component of equation of motion for electrons Eq. (2) we obtain

$$\dot{B}_0 = 2c\frac{E_{z1}}{\lambda}, \tag{12}$$

$$E_{z1}\frac{x^2}{\lambda^2} + \frac{\dot{a}}{a}\frac{B_0(t)}{\lambda c}x^2 = 0, \tag{13}$$

$$\frac{\partial v_{ez}^{(0)}}{\partial t} = -\frac{e}{m_e}E_{z0}, \tag{14}$$

where

$$E_z = E_{z0}(t) + E_{z1}(t)\frac{x^2}{\lambda^2}.$$

Equations (12) and (13) yield

$$B_0(t) = \frac{B_{00}}{a^2}, \tag{15}$$

where B_{00} is a constant. From the z-component of equation of motion for ions, we get

$$\frac{\partial v_{iz}^{(0)}}{\partial t} = \frac{e}{m_i}E_{z0}. \tag{16}$$

From Eqs. (14) and (16) we have

$$v_{iz}^{(0)} = -\frac{m_e}{m_i}v_{ez}^{(0)}. \tag{17}$$

From Eqs. (15), (17) and (11), we get for $v_{ez}^{(0)}$ and E_z

$$v_{ez}^{(0)} = -\frac{cB_{00}b}{4\pi e n_0\lambda a^2(\frac{b}{a} + \frac{m_e}{m_i})}, \tag{18}$$

$$E_z = -\frac{B_{00}\dot{a}x^2}{ca^3\lambda} + \frac{m_e c B_{00}}{4\pi n_0 e^2\lambda}\frac{d}{dt}\left(\frac{b}{a^2(\frac{b}{a} + \frac{m_e}{m_i})}\right). \tag{19}$$

Assuming that the electrostatic field E_x varies like $E_x=E_0(t)x/\lambda$, we obtain from Poisson's equation (4)

$$E_0 = 4\pi e n_0\lambda\left(\frac{1}{b} - \frac{1}{a}\right). \tag{20}$$

Furthermore, the equations of state for electrons and ions give rise to

$$P_e = \frac{P_{0e}}{a^\gamma} - \frac{P_{0e}}{2a^{\gamma+2}}\frac{x^2}{\lambda^2}, \qquad (21)$$

$$P_i = \frac{P_{0i}}{b^\gamma} - \frac{P_{0i}}{2b^{\gamma+2}}\frac{x^2}{\lambda^2}. \qquad (22)$$

We now go back to the x-component of equations of motions for electrons and ions in order to obtain the basic equations for a(t) and b(t). If we neglect the small terms of the order of the mass ratio m_e/m_i, we obtain

$$\ddot{a} = -\omega_{pe}^2\left(\frac{a}{b} - 1\right) - \frac{B_{00}^2}{4\pi m_e n_0 \lambda^2 a^2} + \frac{P_{0e}}{m_e n_e \lambda^2 a^\gamma}, \qquad (23)$$

$$\ddot{b} = \omega_{pi}^2\left(1 - \frac{b}{a}\right) + \frac{P_{0i}}{m_i n_0 \lambda^2 b^\gamma}. \qquad (24)$$

Furthermore, assuming that the plasma is quasi-neutral n =n , i.e., a = b, by adding Eqs. (23) and (24)

$$\ddot{a} = -\frac{v_A^2}{\lambda^2 a^2} + \frac{c_s^2}{\lambda^2 a^\gamma}, \qquad (25)$$

where

$$v_A^2 = \frac{B_{00}^2}{4\pi n_0(m_i + m_e)} \quad \text{and} \quad c_s^2 = \frac{(P_{0e} + P_{0i})}{(m_e + m_i)n_0}.$$

In Eq. (25) the first term of the RHS corresponds to the J x B term. This is the term that drives magnetic collapse. The second term corresponds to the pressure gradient term. This term may eventually be able to balance the magnetic compression (collapse) when γ = 3. The condition γ = 3 means that the plasma compression takes place in a nearly one-dimensional fashion so that the degree of freedom of the system f becomes unity. When γ = 3, we obtain

$$\ddot{a} = -\frac{v_A^2}{\lambda^2 a^2} + \frac{c_s^2}{\lambda^2 a^3}. \qquad (26)$$

When γ = 2 (f = 2), on the other hand, we obtain

$$\ddot{a} = -\frac{(v_A^2 - c_s^2)}{\lambda^2 a^2}. \qquad (27)$$

Once the behavior of the scale factor a(t) is determined from the above equations, we obtain various kinds of physical quantities as follows, in the quasi-neutral plasmas, and neglecting the mass ratio ($m_e/m_i \to 0$),

$$B_y = \frac{B_{00}}{a^2}\frac{x}{\lambda} \qquad (28)$$

$$E_x = \left(-\frac{m_i}{e_\lambda}\frac{v_A^2}{a^3} + \frac{P_{0e}}{e_\lambda a^4 n_0}\right)\frac{x}{\lambda} \qquad (29)$$

$$E_x = -\frac{B_{00}\dot{a}x^2}{ca^3\lambda} - \frac{B_{00}m_e c\dot{a}}{4\pi n_0 e^2 \lambda a^2} \tag{30}$$

$$v_{ex} = -\frac{cB_{00}}{4\pi e n_0 \lambda a} \tag{31}$$

$$v_{ix} = v_{ex} = \frac{\dot{a}}{a}x \tag{32}$$

$$n_i = n_e = \frac{n_0}{a} \tag{33}$$

where the electrostatic field E_x in the quasi-neutral plasmas is determined from the equation of motions for ions, not from Poisson's equations.

From Eqs. (28) and (29) we find as important result that in the explosive phase (a 0) the electrostatic field $E_x \propto (a^{-3} + a^{-4})$ grows more rapidly than the magnetic field ($B_y \propto a^{-2}$) does. This effect comes into playing a pivotal role for high energy particle production.

Now we investigate the global time behavior of coalescence by making use of the first integral of Eq. (26). Equation (26) may be rewritten as

$$\ddot{a} = -\frac{\partial V(a)}{\partial a}, \tag{34}$$

where the effective (Sagdeev) potential V(a) is given by

$$V(a) = -\frac{v_A^2}{\lambda^2 a} + \frac{c_s^2}{2\lambda^2 a^2}, \tag{35}$$

where the first term may be reminiscent of the "gravitational potential" while the second of the "centrifugal potential." The schematic graph of the effective potential is drawn in Fig. 9. The value a which satisfies $V(a_1) = 0$ is given by

$$a_1 = \frac{1}{2}\frac{c_s^2}{v_A^2}. \tag{36}$$

The minimum of the potential, V_{min}, obtained from $\partial V/\partial a = 0$ is

$$V_{\min} = \frac{-v_A^4}{2\lambda^2 c_s^2}, \tag{37}$$

at $a = 2a_1 = c_s^2/v_A^2$. The potential becomes deeper when the ratio of the kinetic to magnetic energy densities $\beta = c_s^2/v_A^2$ approaches zero. This means that the driving force J B is dominant compared with the pressure term. The first integral of Eq. (34) is given by

$$\dot{a}^2 = \frac{2v_A^2}{\lambda^2 a} - \frac{c_s^2}{\lambda^2 a^2} + \mathcal{E}, \tag{38}$$

where $\mathcal{E}$ is the initial (Sagdeev) "energy" (dimension: $1/\text{time}^2$) in space of stretching factor a.

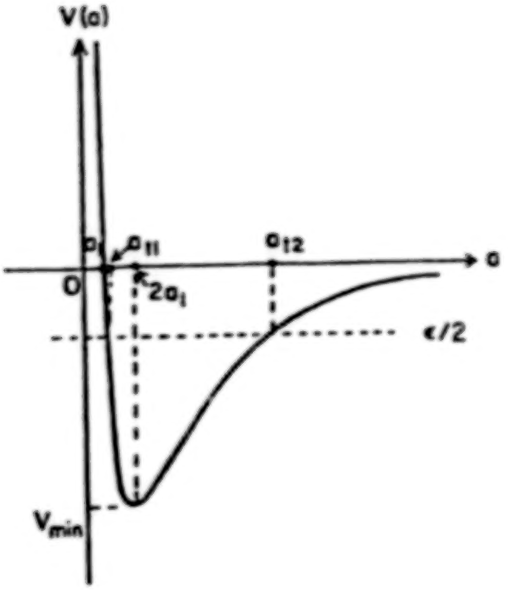

9. The Sagdeev potential for the scale factor of the explosive coalescence.

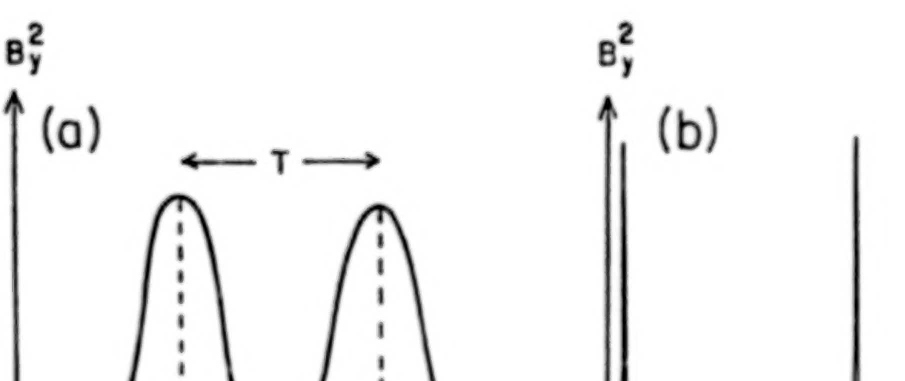

10. The temporary behavior of the magnetic field energy constructed from the Sagdeev Potential (a) and numerical result (b).

$$\mathcal{E} = \dot{a}_0^2 - \frac{2v_A^2}{\lambda^2 a_0} + \frac{c_s^2}{\lambda^2 a_0^2}. \tag{39}$$

As seen from Fig. 9 , the explosive magnetic compression corresponds that the scale factor a(t) rapidly changes in time by orders of magnitude and vanishes. We may call this an explosive magnetic collapse. Such an explosive collapse can be realized (1) when the effective potential has a sharp and deep potential well and this means that $\beta = c_s^2/v_A^2$ is very small; (2) when the initial total energy /2 is nearly zero. On the other hand, when $\mathcal{E}/2$ is close to $-V_{min}$, we have oscillations near the potential minimum and no explosive collapse.

If the total energy is given in Eq. (38), we can find the period T_{os} of nonlinear oscillations by integrating Eq. (38)

$$T_{os} = 2\int_{a_{t1}}^{a_{t2}} \frac{a\,da}{\left[\mathcal{E}\left(a + \frac{v_A^2}{\mathcal{E}\lambda^2}\right)^2 - \frac{v_A^2}{\mathcal{E}\lambda^2} - \frac{c_s^2}{\lambda^2}\right]^{1/2}}$$

$$= 2\pi \frac{v_A^2}{\mathcal{E}^{3/2}\lambda^2} = 2\pi\mathcal{E}^{-3/2} t_A^{-2}, \tag{40}$$

where a_{t1} , a_{t2} are roots of the equation which gives $\dot{a} = 0$:

$$a^2 + \frac{2v_A^2}{\mathcal{E}\lambda^2}a - \frac{c_s^2}{\mathcal{E}\lambda^2} = 0, \tag{41}$$

and $t_A = \lambda/v_A$. In the limit of $\mathcal{E} \to -V_{min}$, we find the minimum period T_{min} as

$$T_{min} = 2\pi\beta^{3/2} t_A. \tag{42}$$

Equation (40) indicates that the period T_{os} of nonlinear oscillations becomes longer when $\mathcal{E}$ tends to zero.

Let us examine the time history of various physical quantities based in the qualitative time behavior of a(t) derivable from the effective potential V(a). The magnetic field energy is proportional to B_y^2, which is given by

$$B_y^2 = \frac{B_{00}^2}{a^4}\left(\frac{x}{\lambda}\right)^2.$$

If the scale factor a becomes smaller, B_y^2 must increase. The maximum is given by

$$\frac{\partial B_y^2}{\partial t} = 0,$$

which yields $\dot{a} = 0$, namely $a = a_{t1}$. After the maximum, B_y^2 decreases again and reaches minimum at $a = a_{t2}$. The oscillatory behavior of the magnetic field energy is schematically drawn in Fig. 10 . The period of the oscillation is given by Eq. (40).

The electrostatic field E is given by Eq. (29). The time history of the electrostatic field energy, which is proportional to E_x^2, is analyzed by investigating

$$\frac{\partial E_x^2}{\partial t} = 0.$$

This condition is equivalent to

$$\mathcal{E}_0 = 0, \tag{43}$$

or

$$\frac{\partial \mathcal{E}_0}{\partial t} = 0, \tag{44}$$

where $\mathcal{E}_0(t) = -\frac{m_i v_A^2}{e\lambda a^3} + \frac{P_{0e}}{e\lambda n_0 a^4}$. The first condition $\mathcal{E}_0 = 0$ occurs at $a = a_3 = P_e / m_i n_e v_A^2 = c_s^2 / v_A^2$. The second condition $\partial\mathcal{E}_0/\partial t = 0$ gives two conditions, namely

(i) $\dot{a} = 0$, which occurs at $a = a_{t1}, a_{t2}$

(ii) $a = a_4 = \frac{4}{3}\frac{P_{0e}}{m_i n_0 v_A^2} \cong \frac{4}{3}\frac{c_s^2}{v_A^2}$.

The above considerations give us the schematic time history of the electrostatic field energy E_x^2 as drawn in Fig. 11. Figure 11 indicates a triple-peak structure in the electrostatic field energy. When the plasma β is small, a_3, a_{t1} are close. In this case, the triple-peak structure in the electrostatic field energy would become double-peak structure. The maximum value of the electrostatic field, E_{max}, achieved at $a = a_4$ is given by

$$E_{max} = \frac{1}{4}\left(\frac{3}{4}\right)^3 \frac{m_i}{e\lambda}\frac{v_A^8}{c_s^6}\frac{x}{\lambda} \cong 0.1\frac{m_i}{e\lambda}\frac{v_A^2}{\beta^3}\frac{x}{\lambda}. \tag{45}$$

The induced electric field E_z is given by Eq. (30), which shows that E becomes zero, when $\dot{a} = 0$. E_z changes its sign around $\dot{a} = 0$ because $\dot{a} = 0$ is the point where the magnetic field achieves maximum or minimum.

Next, the time behavior of ion temperature T_{ix} is examined. In the early stage of coalescence, the plasma should be adiabatically compressed. However, as the magnetic field energy increases near the peak and approaches the peak, the ion flow energy becomes dominant over the thermal energy. From the consideration that v_x^2 gives maximum or minimum, namely $\frac{\partial v_x^2}{\partial t} = 0$, we find two conditions for the extrema; (i) $v_x = 0$, which gives $\dot{a}$, (ii) $\frac{\partial v_x}{\partial t} = 0$, which gives

$$a\ddot{a} = \dot{a}^2. \tag{46}$$

When the explosive coalescence takes place ($\mathcal{E} = 0$), we estimate the condition (46) as

$$a = a_5 \simeq \frac{2}{3}\frac{c_s^2}{v_A^2}.$$

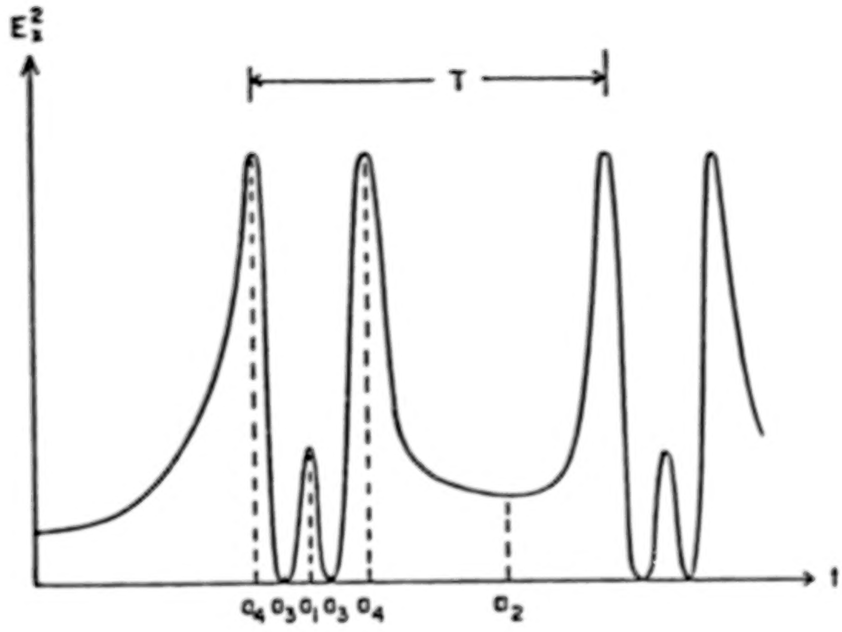

11. The temporal behavior of the electrostatic field energy constructed from the Sagdeev potential.

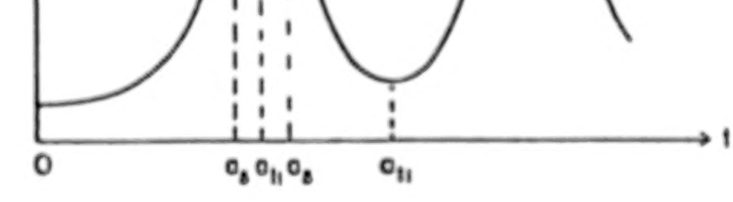

12. The temporal behavior of the ion-temperature in the x-direction (in the direction of coalescence) constructed from the Sagdeev potential.

After $a = a_\xi$, the kinetic energy must decrease, which means that the plasma is in the state of colliding phase. The above considerations give us the schematic time history of the ion temperature, which is shown in Fig. 12 . Figure 12 shows a double-peak structure in the ion temperature. In the limit of quasi-neutrality, we can estimate the dominant term governing the explosive phase where the adiabatic compression is predominant. The temperature T is given by $T = P / n$, while the dominant term in pressure changes in time as $P \sim a^{-5}$ when $\gamma = 3$, $P \sim a^{-4}$ when $\gamma = 2$, while $n \sim a^{-1}$. Therefore we find

$$T = P/n \simeq \frac{1}{a^4}(\gamma = 3) \tag{47}$$

$$\simeq 1/a^3(\gamma = 2). \tag{48}$$

We investigate in more detail the explosive phase of the coalescence in a case that we can neglect the effect of plasma pressure: it only acts as a saturation mechanism. However, if we take $\gamma = 2$, the pressure does not take the role of a saturation mechanism as seen in Eq. (27). In the explosive phase, therefore, we can neglect the second term in the right-hand side of Eq. (26);

$$\ddot{a} = -\frac{v_A^2}{\lambda^2 a^2}. \tag{49}$$

Furthermore, we need a second condition for explosive collapse, namely the initial total energy must be close to zero. For example, if the oscillation period of magnetic energy is of the order of the transit Alfven time $t_A = \lambda / v_A$, we can estimate the total energy $\mathcal{E}$ by making use of Eq. (40) as

$$T_{os} = 2\pi \mathcal{E}^{-3/2} t_a^{-2} \approx t_A, \tag{50}$$

which gives

$$\mathcal{E} \sim \frac{(2\pi)^{2/3}}{t_A^2}. \tag{51}$$

The solution of Eq. (49) with small $\mathcal{E}$ is given by

$$a(t) \cong \left(\frac{9}{2}\right)^{1/2} \left(\frac{v_A}{\lambda}\right)^{2/3} (t_0 - t)^{2/3} + 0(\mathcal{E}), \tag{52}$$

where we neglect the order of $\mathcal{E}$, t_0 is the explosion time. Once the solution a(t) is given by Eq. (52), we can find the various physical quantities as follows, which is valid in the explosive phase of the coalescence;

$$v_x = v_{ix} = v_{ex} = -\frac{2}{3}\frac{x}{(t_0 - t)}, \tag{53}$$

$$n = n_i = n_e = \left(\frac{2}{9}\right)^{1/3} \frac{\lambda^{2/3} n_0}{v_a^{2/3} (t_0 - t)^{2/3}}, \tag{54}$$

$$E_x = -\frac{2}{9}\frac{m_i}{e}\frac{x}{(t_0 - t)^2}, \tag{55}$$

$$B_y = \left(\frac{2}{9}\right)^{2/3}\frac{B_{00}\lambda^{1/3}x}{v_a^{4/3}(t_0 - t)^{4/3}}, \tag{56}$$

$$E_z = \frac{2}{3}\left(\frac{2}{9}\right)^{2/3}\frac{B_{00}\lambda^{1/3}x^2}{v_A^{4/3}c(t_0 - t)^{7/3}} + \frac{2}{3}\left(\frac{2}{9}\right)^{1/3}\frac{B_{00}c}{\omega_{pe}^2\lambda^{1/3}v_a^{2/3}(t_0 - t)^{5/3}}. \tag{57}$$

The explosion time t_0 is related to the initial condition. From Eq. (53) we find the initial velocity v_{x0} at t = 0 as

$$v_{x0} = \frac{\dot{a}_0}{a_0}x = -\frac{2x}{3t_0}, \tag{58}$$

where a_0 , $\dot{a}_0$ are the initial values of a, $\dot{a}$ at t = 0. From Eq. (58) we find

$$t_0 = -\frac{2}{3}\frac{a_0}{\dot{a}_0}(> 0), \tag{59}$$

where $\dot{a}_0$ must be negative when magnetic collapse occurs. On the other hand, a and a are related to the initial total energy as

$$\mathcal{E} = \dot{a}_0^2 - \frac{2v_A^2}{\lambda^2 a_0} \tag{60}$$

when the pressure term is neglected. If $\mathcal{E} \to 0$, we obtain from Eqs. (59) and (60)

$$t_0 \simeq \frac{\sqrt{2}}{3}a_0\sqrt{a_0}t_A. \tag{61}$$

Combining eqs. (55) and (56), we find an important result that in the explosive phase the electrostatic field $E_x \propto (t_0 - t)^{-2}$ more rapidly grows compared with the magnetic field $B_y \propto (t_0 - t)^{-4/3}$. This fact becomes very important when we consider the high energy particle production by E during the explosive phase of the coalescence.

Let us compare the theoretical results obtained here for the explosive phase with the computer simulation results. The global structure of the magnetic field energy, electostatic field energy, ion temperature in the x-direction observed in the simulation is well explained by the theoretical model obtained here. Especially, the double-peak structure in the ion temperature, and the triple-peak structure in the electrostatic field energy are also observed in the simulation (see Figs. 1 and 2). Table 1 summarizes the results of comparison between the theory and the collisionless simulation.

In Table 1 we show the index m of explosiveness (the exponent to the time $(t_0 - t)^{-m}$). Table I shows a good agreement between simulation and theory in the electrostatic energy. When the ttoroidal field becomes comparable the poloidal field (B_T / B_P = 1 case), there appears two-dimensional motion, plasma

Table I

Indices of Explosion [exponents to the $1/(t_o-t)$] During Coalescence

	$\Omega_{ce}=0$ $L_x \times L_y=128\times 32$ [NB $L_x \times L_y=256\times 32$ many islands]	$\Omega_{ce}=0.2\omega_{pe}$ $L_x \times L_y=128\times 32$	$\Omega_{ce}=1.0$ $L_x \times L_y=128\times 32$	$\Omega_{ce}=2.0$ $L_x \times L_y=128\times 32$ No formation of islands
Magnetic Energy (S)	8/3	8/3	2	
B^2 (T)	8/3	8/3	2*	N/A
Electrostatic Energy (S)	4	4		
E_L^2 (T)	4	4	4	N/A
Ion Temperature in x-direction (S)	8/3	8/3	3	
T_{ix} (T)	8/3	8/3	2	N/A
Explosive Time (S) t_o	$24.3\Omega_i^{-1}$	$27\Omega_i^{-1}$	$19\Omega_i^{-1}$	N/A
Compressional Alfvén Oscillation (S) Period τ_{os}	$6.3\Omega_i^{-1}$	$6.0\Omega_i^{-1}$	$8.8\Omega_i^{-1}$	N/A

* incompressibility is assumed. Derivation from observation might be due to plasma rotation in $\Omega_{ce}=1$ case.

S is for simulation results and T for theory.

rotational motion, which makes a more complex electrostatic field configuration. When $B_t/B_p = 1$, the magnetic time behavior of field energy also deviates from the one-dimensional analysis for the same reason. For the ion temperature we find its explosiveness from Eq. (47) as

$$T \sim \frac{1}{a^4} \sim \frac{1}{(t_0 - t)^{8/3}} \tag{62}$$

when $\gamma = 3$. The above scaling also is close to the results obtained in the simulation, except for the case of $B_t/B_p = 1$.

Figure 13 shows the spectral intensity $S(k, \omega)$ obtained from the simulation run that corresponds to Fig. 2. Since the spectral intensity is integrated over time, the most intense period of various modes is most heavily weighted. For most of modes this intense period corresponds to that after the coalescence. Thus, it becomes necessary to recalibrate the plasma density and magnetic field strength, etc. at that stage. These recalibrated eigenfrequencies are indicated near the edge of the frame of Fig. 13. We observe that the lower hybrid range frequency contains strongest spectral intensity, followed by the compressional Alfven modes that correspond to the coalescence and ensuing oscillations, and the plasma oscillations ($\omega \simeq \omega_{pe}$). The frequency happens to be outside of the frame so that we do not know if they are prominent or not.

Finally, comments in the effect of non-quasineutrality are due. In the explosive phase, we can neglect the effect of pressure terms in Eq. (23) and Eq. (24):

$$\ddot{a} = -\omega_{pe}^2\left(\frac{a}{b} - 1\right) - \frac{v_{Ae}^2}{\lambda^2 a^2}, \tag{63}$$

$$\ddot{b} = \omega_{pi}^2\left(1 - \frac{b}{a}\right). \tag{64}$$

From the analysis of numerical calculations of Eqs. (63) and (64), we can conclude that b is slowly varying in time during the variation of a. Therefore if we use the result of $b \simeq b_0 = \text{const.}$ in Eq. (63), we find the effective potential $V(a)$ as

$$\ddot{a} = -\frac{\partial V(a)}{\partial a},$$

$$V(a) = \omega_{pe}^2\left(\frac{a^2}{2b_0} - a\right) - \frac{v_{Ae}^2}{\lambda^2 a}, \tag{65}$$

The schematic graph of the potential is given in Fig. 14. Here we write the effective potential including the effect of plasma pressure. The curve that incorporates the pressure effect is shown as the broken line near $a = 0$. Figure 14 shows a second minimum at $a = a_{min}$ which is caused by the effect of charge separation. When the J x B force dominates, the charge separation effect is unimportant. Such is the case of explosive phase of coalescence (where charge neutrality is maintained to a good degree). However, after the coalescence in the late stage of

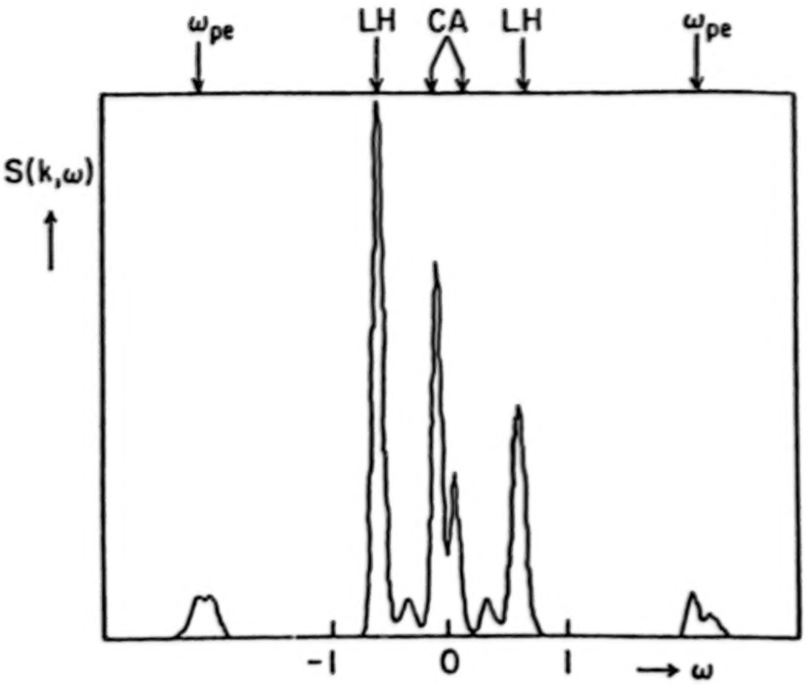

13. Radiation spectrum during explosive current loop coalescence.

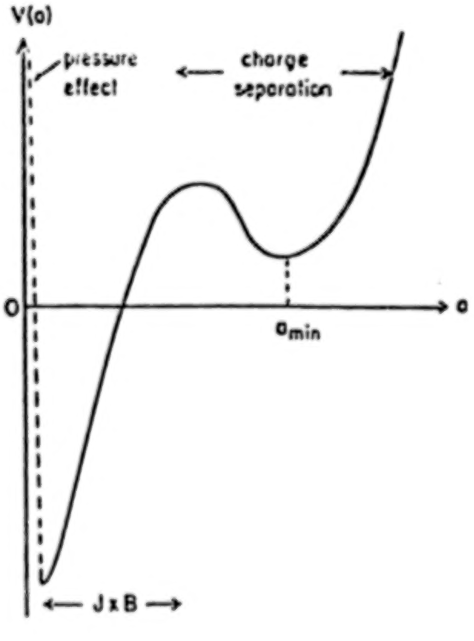

14. The Sagdeev potential for the scale factor including the plasma pressure.

amplitude oscillations, the J x B force becomes weaker. Then the charge separation may become important. In this stage electrons can be trapped and oscillate in the potential well near the second minimum in Fig.14 . The electrostatic field oscillations are similar to the dipole oscillations near the current sheet. Such dipole oscillations may be able to radiate the electromagnetic wave ($\omega \sim \omega_{pe}$ or ω_{pi}), if the plasma is not evanescent. The simulation results obtained show certain high frequency oscillations in the frequency range of $\omega \sim \omega_{pe}$, ω_{LH} . The detailed comparison will be reported elsewhere. Once other effects such as the two-dimensional curvature effect are included , it might be possible to have additional minima in the effective potential and thus for the system to be temporarily trapped in the potential well and exhibit pulsations.

We have found that in the explosive phase of magnetic collapse the electrostatic field can be explosively generated and more rapidly grow compared with the magnetic field.

The explosiveness of the electrostatic field $E_x \sim (t_0 - t)^{-2}$, and magnetic field $B_y \sim (t_0 - t)^{-4/3}$ well agree with the results obtained in the simulations (see Fig.1)

As shown later, the kinetic simulation finds that in the explosive phase ions and electrons are simultaneously accelerated in the z-direction, opposite each other. When a particle moves across the magnetic field driven by the electrostatic field E the particle can be accelerated in the direction (z-direction) perpendicular both to the electric field (x-direction) and the poloidal magnetic field (y-direction). This acceleration mechanism was considered by Sugihara and Mizuno (1979). On the other hand, Sagdeev and Shapiro discussed the same physics in another point of view, namely the large amplitude wave damping due to trapped electrons. These previous works are applicable to the cases in which the large amplitude electrostatic waves can propagate across the static magnetic field. In the explosive phase during magnetic collapse, a similar situation can be realized; now the magnetic field and electrostatic field can vary in time and space.

Figure 15 shows the distribution functions of electrons and ions in the coalescence simulation from the electromagnetic particle code. In Fig.15 we compare the distribution of electrons and ions before the explosive coalescence with the distribution after that.

It is clear that the distribution functions have very rapidly changed during the explosive coalescence and strong heating of ions in the coalescence direction has occurred during this time. It is also observed that there is a very small but energetic population of electrons has been created in the z-direction perhaps due to the inductive acceleration. A similar pattern is observed in the ion distribution in the z-direction with the appropriate parity difference because of the charge difference between electrons and ions. It should be noted that the explosive coalescence produces extremely energetic ions which form a

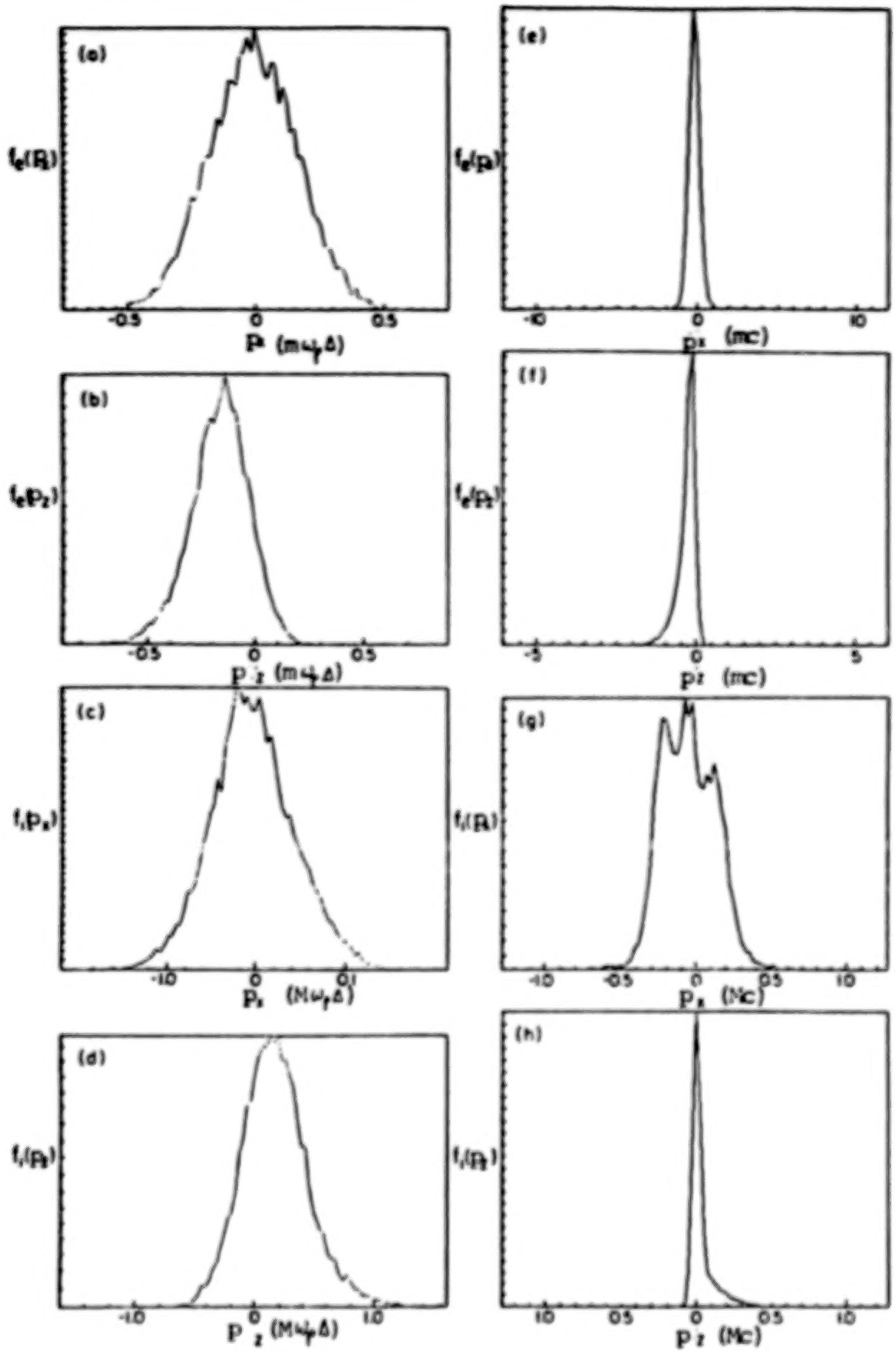

15. Distribution functions of electrons and protons before coalescence (a)-(d) and after coalescence (e)-(h).

relatively flat and long plateau.

3. Current Loop Coalescence in Solar Flares

Recent observations of x-ray continuum emission, γ-ray line, and continuum emission from solar flares with instruments on the Solar Maximum Mission (SMM) and Hinotori satellites show that energetic ions and relativistic electrons are accelerated almost simultaneously with non-relativistic electrons during the impulsive phase of solar flares. These observational results make it necessary to revise the widely accepted hypothesis of particle acceleration that energetic ions and relativistic electrons are produced in the second phase a few minutes after the impulsive phase (Wild et al., 1963; de Jager, 1969; Svestka, 1976). Although Bai and Ramaty (1979), Bai (1982), and Bai et al. (1983) revised the hypothesis as the secondstep acceleration taking note of a small delay of γ-ray line emission from hard x-ray emission, Kane et al. (1983), and Forrest and Chupp (1983) pointed out that such a small delay can be explained simply by either the injection, propagation, or energy loss processes of particles which are accelerated in a single step.

Recently Nakajima et al. (1983) and Kiplinger et al. (1983) reported observations of quasi-periodic pulses with double sub-peak structure seen in hard x-ray, γ-ray and microwave emissions in the two intense solar flares of June 7, 1980 and June 21, 1980. We are interested in the close similarity between the observed time profiles and those obtained with the computer simulation given in the previous section.

We present the results of our analysis of the June 7, 1980 and November 26, 1982 events, both of which are widely different from each other in duration, source size, source height, etc., they provide a stringent test for examining the validity of our model of particle acceleration in solar flares in terms of the coalescence instability. Our study shows that observational features of the two events are consistent with the results of our computer simulation.

3.1 Summary of Observations

(a) June 7, 1980 Event

The impulsive burst of the June 7, 1980 solar flare (Fig. 16) has been investigated by many authors (Forrest et al., 1981; Kane et al., 1983; Forrest and Chupp, 1983; Nakajima et al., 1983; Kiplinger et al., 1983). We summarize below some essential points from these observations.

(1) The burst is composed of seven successive pulses with a quasi-periodicity of about 8 seconds. Each of the pulses in hard x-rays, prompt γ-ray lines, and microwave is almost synchronous and similar in shape.

(2) The microwave pulses consist of double sub-peaks as seen

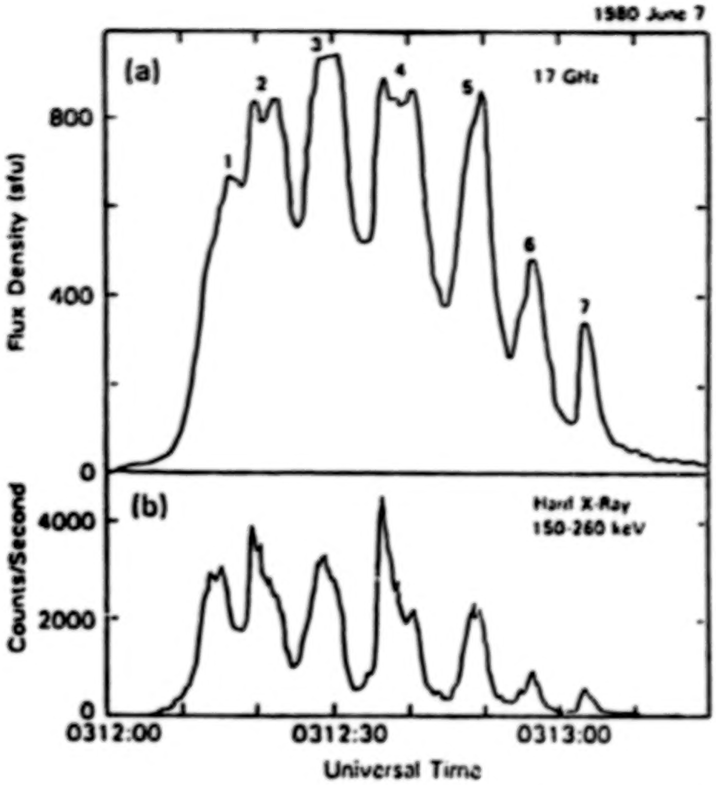

16. Time profiles of 17 GHz microwave and 150-260 kev X-ray emissions (from the Hard X-ray Burst Spectrometer on SMM) of June 7, 1980 Flare.

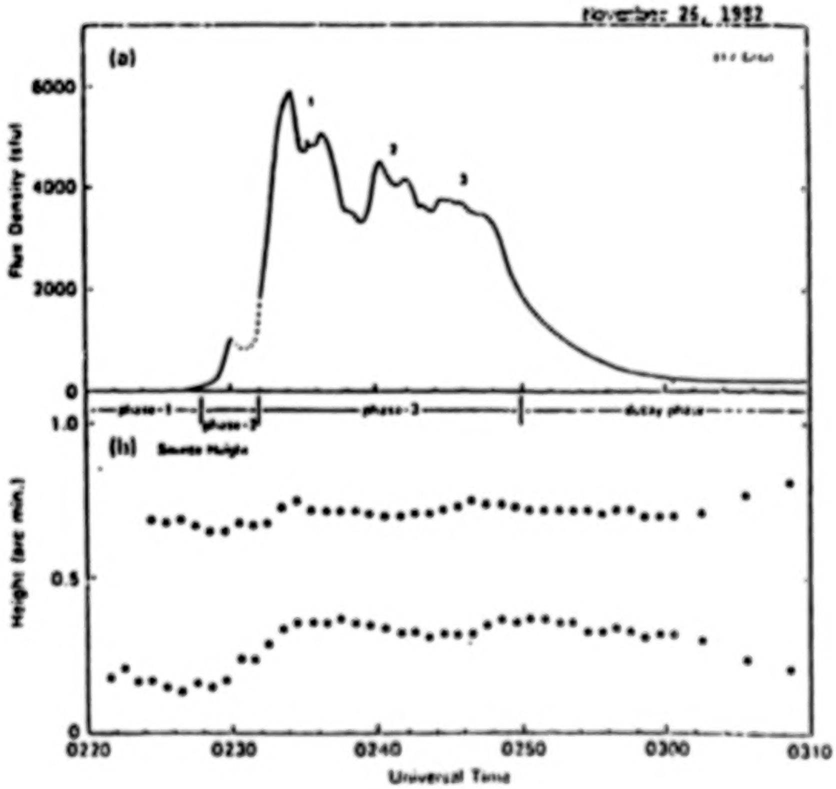

17. (a) time profiles of 17 GHz microwave and (b) time variation of the height of two microwave (17 GHz) sources during the 1982 November 26 Flare.

especially in the second and fourth pulses in Fig. 16(a).

(3) The starting times of hard x-rays, prompt γ-ray lines, and microwaves coincide within ±2.2 seconds.

(4) The time scales of acceleration for both electrons (up to energies above 1 MeV) and ions (above 10 MeV/nucleon) are less than 4 seconds. The accelerations must occur almost simultaneously.

(5) The height of the microwave source is estimated to within 10 arc sec above the photosphere (H_α flare; N12 , W64). The source has a small size of less than 5 arc sec in the east-west direction and shows no motion.

The H_α photographs from the Peking Observatory (H. Chow, private communication) add a new finding. The flaring region has two structures that appear to be in contact with each other, one stretching in the east-west direction and the other in the north-south.

(b) November 26, 1982 Event

We briefly outline the characteristics of the Nobember 26, 1982 flare (Fig.17). This event is of much longer duration than the event on June 7, 1980, about 20 minutes compared to about 1 minute. The microwave observations were made with the 17-GHz interferometer at Nobeyama, Japan, and the hard x-ray observation with the hard x-ray Burst Spectrometer (HSRBS) on SMM.

(1) The microwave burst is composed of three successive peaks with a quasi-periodicity of about 6 minutes as indicated by number 1-3 in Fig.17(a).

(2) Each of the microwave peaks further consists of two sub-peaks. The hard x-ray time profiles seem to coincide with the microwave sub-peaks. The SMM hard x-ray data are available only for the first peak.

(3) The microwave and hard x-ray emissions start almost simultaneously within 10 seconds.

(4) The microwave source is composed of two sources, one at a height of $\sim 10^4$ km and the other at $\sim 3\times10^4$ km. These values are derived on the assumption that the sources are located directly above the H_α flare (S10, W88).

Figure 17(b) shows the height of the two microwave sources as a function of time. In the pre-burst phase (phase 1: 0220-0228 UT), the upper source appears at a height of $\sim 2.9\times10^4$ km above the photosphere and the lower one at $\sim 0.7\times10^4$ km. In phase 2, the lower source rises at a velocity of ~ 30 km/ s . The main phase (phase 3) started when the lower source reaches a height of 1.5×10^4km. It is suggested that the two sources collide with each other at this time. In fact, a small up-and-down motion of the lower source is observed in the main phase. The oscillation period and peak-to-peak amplitude of the up-and-down motion are $\sim$min and $\sim 2\times10^3$ km (significantly larger than the fluctuation level due to the signal to noise ratio), respectively. After the main phase, the lower source begins to go down towards its previous position. On the other hand, the upper source rises gradually, though it remains at almost the same height until the decay phase.

The observational facts summarized above, especially the collision of the two microwave sources and the small up-and-down motion of the lower source in the November 26, 1982 event, suggest that the current loop coalescence takes place. The existence of two H_α bright components in the June 7, 1980 event also supported this interpretation.

3.2 Interpretation by Simulations

Two parallel current loops are unstable against the coalescence instability. They are attracted by and collide with each other and finally coalesce into one loop. Its nonlinear development can release a large amount of poloidal magnetic energy associated with the current loops into particle energies. We investigated this process, i.e., the global plasma dynamics, heating and acceleration of particles, and so on, through computer simulations as described in Chapter 2. Here, we made two different types of simulations in order to experiment with a wide variety of plasma parameters: one is a MHD particle simulation, and the other a collisionless full-electromagnetic particle simulation, both of which are two-dimensional in space across the plane perpendicular to the current loops and three dimensional in velocity space.

(a) Explosive Coalescence --- June 7, 1980 Flare

The case that two parallel loops have sufficient electric currents so that they attract each other fast enough (in about one Alfven transit time) was simulated using the collisionless full-electromagnetic particle code.

The resultant time history of the electron temperature is shown in Fig. 2. We can clearly see a quasi-periodic oscillation, the period of which is about one Alfven transit time ($8\,\omega_{ci}^{-1}$). The cause of this oscillation is as follows: after explosive reconnection of poloidal magnetic fields takes place at the X-point between approaching current loops, the two plasma blobs pass through each other and overshoot, resulting in repetition of this process.

Fig. 2 also shows that the electron temperature oscillation is characterized by prominent double sub-peak structure. The double sub-peaks occur just before and after each peak in the magnetic field intensity. Just before a peak, the magnetic acceleration of the plasma by JxB becomes strongest so that the magnetic flux behind the colliding plasma blobs as well as the plasma blobs themselves are strongly compressed. This plasma compression causes the first sub-peak of the electron temperature. Then, the plasma particles acquire velocities close to the Alfven velocity along the colliding direction, so that they detach from the magnetic flux against which they have been compressed, resulting in an expansion and hence in an adiabatic cooling of the plasma as the magnetic fields obtain peak values. After the peak in the magnetic fields, the process reverses giving rise to the second sub-peak of the electron temperature.

A similar time history is obtained for the kinetic energy of high-energy tail electrons and protons as well as for proton temperature. The acceleration of the high energy-tail particles is due to the $V_p \times B$ acceleration mechanism, which can lead simultaneous electron and proton acceleration within about second. Since these processes accompany the local plasma compression/decompression just before and after coalescence, it is not surprising that the time profile of the microwave emissions caused by high-energy tail electrons resembles that of Fig. 2(d).

The result of this simulation can also explain the observed period of the quasi-periodic oscillation of the June 7, 1980 event. The period(4 sec) which is estimated with source size (~5 arc sec), magnetic field(~200 Gauss: Kiplinger et al., 1983) and emission measure($\sim 10^{49}$ cm^{-3} from the GOES soft x-ray data).

We discuss the energy spectrum of electrons and protons, after the explosive coalescence of two current loops. The energy spectrum consists of three components; (a) background thermal component due to the adiabatic heating, (b) intermediate component due to inductive electric field, (c) high energy component due to the $V_p \times B$ acceleration. Fig. 18 shows the energy spectrum without the background thermal component which was reproduced from the previous figures given in Chapter 2.

The intermediate non-thermal component has $\gamma \simeq 2$ as the power-law index near the peak, while near the valley the spectrum becomes more soft. The global structure of the electron energy spectrum is consistent with observations. (Kane et al., 1984; Kiplinger et al., 1984)

The spectrum for ions is shown in Fig. 18b in which two cases are given. The one is just after the coalescence($T=28\,\Omega_i^{-1}$) and the other is at $T = 40\,\Omega_i^{-1}$. As seen in the figure, the spectrum becomes harder which means that the number of high energy proton increases. The range (b) and (c) for protons corresponds to the production of observed γ-rays.

Finally, we make brief comments about the energy spectrum in the multiple coalescence. The global behavior consisting of three energy components is still the same as the two loop coalescence (see Fig. 19). The maximum energy obtaind by $V_p \times B$ acceleration depends on total released energy. Therefore the bigger flare can produce stronger -rays and neutrons.

(b) Slow Coalescence --- November 26 1982 Flare

When two parallel loops have insufficient electric currents or are not well separated and hence the attracting force of them is weaker than that of the previous case, reconnection of poloidal magnetic fields during loop coalescence becomes slower. (However, this reconnection rate is still faster than what would be predicted by a classical tearing theory (Furth et al., 1963)). This case was also simulated using the MHD particle code. Figure

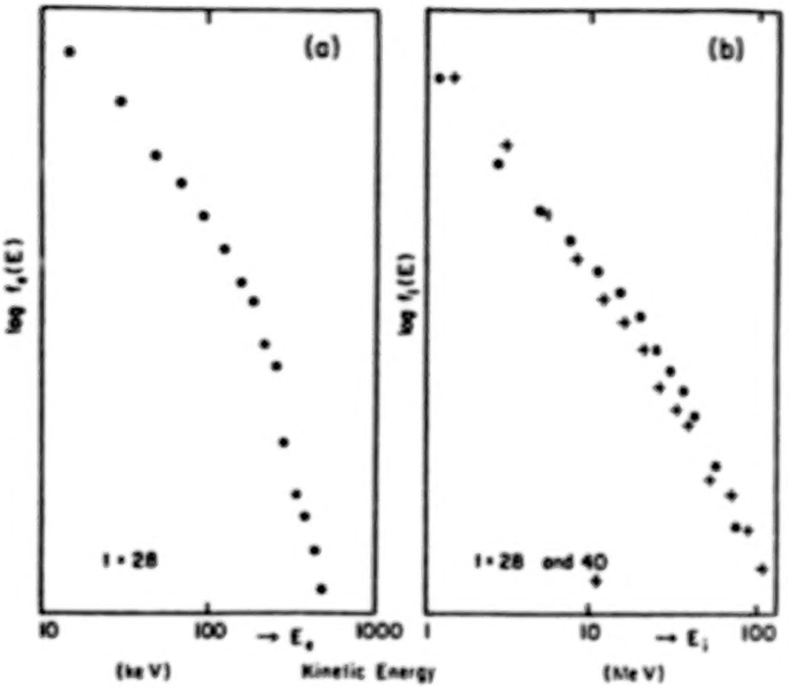

18. (a) Electron energy spectrum just after explosive coalescence. (b) Proton energy spectrum just after (t=28) and later explosive Coalescence (t=40).

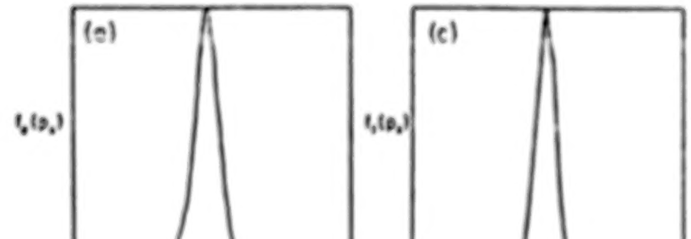

19. Distribution functions for electrons and protons in the case of multiple-current loop interactions.

7 (a) shows the temporal development of plasma kinetic energy (the electron pressure energy) during the coalescence. Also shown in Fig. 7 (b) is the time history of the integrated reconnected magnetic flux through the X-point (case shown in Fig. 5(a) in Bhattacharjee, et al., 1983) Note that a slight amount of oscillations of reconnected flux can be seen around the straight line. Again we can see the oscillatory behavior with double sub-peak structure in both time histories, though it is less prominent compared with that of the explosive coalescence case presented in the previous subsection. The period of oscillation is about 5 times the Alfven transit time.

The obtained time history resulting from the simulation is explained as follows. In the case of slower reconnection, the two plasma blobs do not pass through each other but are pushed back by the pressure of the magnetic field compressed between the two loops. This motion is repeated resulting in the damping oscillation shown in Fig. 7 (a). The amplitude of the oscillation in this case is less prominent compared with the previous case.

The observed plasma kinetic energy oscillation exhibit a structure quite similar to the microwave time profile of the November 26, 1982 flare as shown in Fig. 17(a). The source size of the November 26 flare is about 10 times larger than that of the June 7 flare. We therefore estimate the calculated period of the oscillation to be $5 \times 4 \times 10 = 200$ sec, assuming that the Alfven velocity is about the same for both cases. This period is close to the observed period of about 6 minutes. Note also that in this case the flow velocity is much below the Alfven velocity in agreement with the observational fact that the 40 km/s colliding velocity of the lower loop is much smaller than the Alfven velocity of $\sim 10^3$ km/s.

The results obtained from computer simulations of the coalescence instability of two current loops are in good agreement with observations of two widely differing flares. The key characteristics which are well explained are the simultaneous accelerations of both electrons and ions, and the double sub-peak structure in quasi-periodic pulses. The double sub-peak structure is more pronounced when the currents in the two loops are sufficient for the explosive coalescence to occur. This case corresponds to the June 7, 1980 flare. When the currents are insufficient for the fast coalescence, the double sub-peak structure is less pronounced. This case corresponds to the November 26, 1982 flare. In addition, we have the observation suggesting the collision of the two microwave sources for the November 26, 1982 event.

4. Conclusions and Discussion

In the preceding chapters we have shown fundamental characteristics of current loop coalescence plasma dynamics and compared them with solar flare observations. The current loop coalescence has been successful in explaining several important natures of the impulsive phase as follows: (1) the sudden explosive development in time profiles, (2) simultaneous acceleration of electrons and protons up to several times their rest mass energy, (3) plasma heating due to adiabatic compression up to several times 10 K, and (4) quasi-periodic pulses of microwave, x-ray and γ-ray radiations and also double-peak structure in each pulse. With regard to (2), it is noteworthy that the enegy spectrum of accelerated electrons is almost consistent with observations. Further, we have revealed that the energy release due to the coalescence can be very explosive or relatively gradual depending upon various physical conditions, the key parameters of which are plasma ratio, colliding velocity (current localization and peakness condition), and B_P / B_T. Thus this model is applicable both to very "impulsive flares" and to "gradual flares", as is shown in Chapter 3. Probably in impulsive flares such as the June 7, 1980 flare small current loops develop and interact with each other in the lower corona, while in gradual flares such as November 26, 1982 flare, large current loops whose to reaches several 10 km in its height, develop and interact with each other, whose current distribution might be comparable with the distance of the two loops.

So far, we have argued that the quasi-periodicity is one of the most important signatures of the two current loop coalescence, because of its ideal situation. However, the quasi-periodic pulsation is not a common phenomenon for the majority of flares. In particular, the beautiful regularity such as seen in the June 7, 1980 flare has been rarely observed. Therefore one might claim that the current loop coalescence in not a basic mechanism of solar flares, even though in some specific flares it plays a role. On the contrary, we believe that the coalescence is an elementary process commonly occurring in the impulsive phase of solar flares.

In Chapter 2 we have presented the result of a computational simulation of multiple interaction of many current filaments in addition to that of two current loop interaction. The multiple coalescence exhibits many bursts that are more irregular than the simple two current loop coalescence. In other words, it is very difficult for us to find any regularity from the resultant time profiles alone. We suggest that this is the case that happens in most flares. As is easily expected, two dominant loops with comparable current with each other may be (rarely) hardly realized in flare-producing active regions where the photospheric magnetic configuration and the photospheric motion are very complicated.

As shown in the previous sections, the current loop coalescence model has been successful in various observed points in the impulsive energy release stage. We have shown the many characteristics of the coalescence dynamics as the element process of current-current interactions which might be basically of fundamental importance for the energy release process. We now discuss the preflare stage in which multiple current-filament structure as shown in Fig. 20 might be generated due to the photospheric shear motions. The H_α observations near the active region imply that before several hours of the onset of the flare there exists photospheric shear motion across the magnetic neutral line as shown in Fig. 20 . The photospheric shear motion can give rise to plasma currents along the potential magnetic field produced by the sunspots near the active region. If the photospheric motions are associated with plasma vortex motion, the current loop structure can be generated in the arcade-like structure as shown in the figure.

As the shear motions proceed, the current density can increase and the current loops might move up, associated with relaxation of magnetic tension. Recent computer simulation (Wu, 1985) suggests in the modeling of arcade-like preflare stage that the current tends to localize by its pinching effect in the low region. Recently, the preflare acceleration in the current sheet moving up across the external potential magnetic field is discussed (Sakai et al., 1985). Furthermore, the recent simulation (Aydemir et al., 1985) of current generation in the current loop with line-typing effect suggests the multi-current filament structure with different helicity as shown in Fig. 21. The multi-current filament system might ascend with increase of the current density as well as current constriction into the low region of the corona. In the low β region the current constriction can be enhanced and each current filament can be well separated. If the current density continues to increase further, such that the condition $B_\rho > B_T$ can be realized, the current loop coalescence can be set up. Of course, as seen in the multi-coalescence simulation, the not-well separated current filaments might coalesce without a large amount of energy release and can grow to high current density filaments before explosive strong energy release. A similar situation can also occur in the braized current filament system in Fig. 21.

Next we discuss the later phase after the current loop coalescence in connection with the observed two Ribbon structure. As discussed above, the flaring region might consist of multiple current loops associated with ascending motions. As shown in the figure, if the current loop coalescence happens to start locally where the condition for the explosive onset can be satisfied in the lower current loops, the sequential flaring might precede firstly to the direction along the magnetic neutral line, as observed in the recent H_α observation (Kurokawa et al., 1985). The reason why the sequential flaring proceeds along the arcade might be due to geometrical structure or the fact that the metastable filaments sit around in the same height in the corona. The flaring loops move up slowly and continue to trigger the current

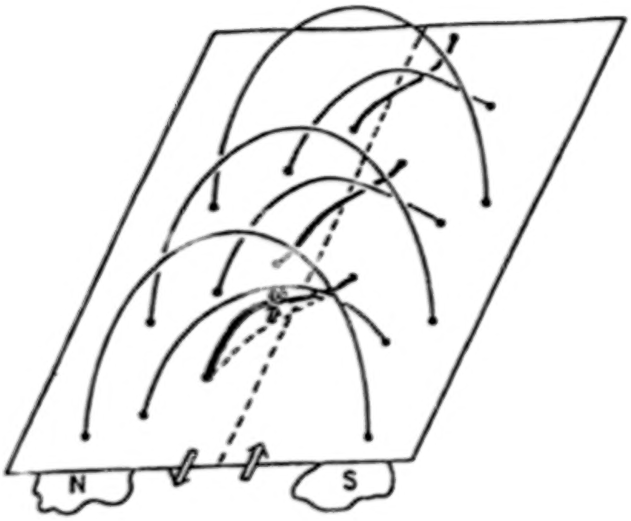

20. Multi-loop coalescence process leads to the two-ribbon flare.

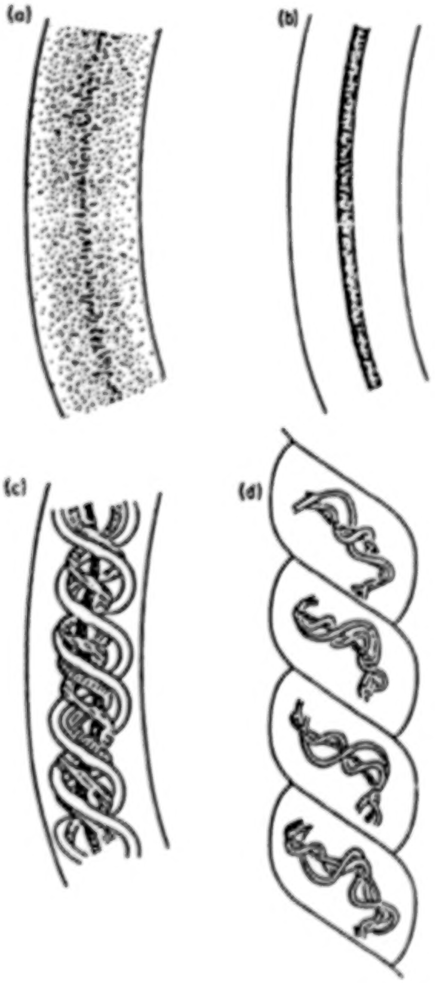

21. Current loop generation process (a) to (d) with line-tying effect.

loop coalescence with upper currect loops. The sequential flaring on the upper loops can be observed in the H_α picture which shows slow expansion motions far from the magnetic neutral line.

We need more investigations about current filament generation in the preflare stage, in connection with the explosive current loop coalescence process.

References

Aydemir, A., Tajima, T., and Sakai, J. 1985, AGU Fall Meeting, 1985.

Bai, T., Hudson, H.S., Pelling, R.M., Lin, R.P., Schwartz, R.A., and von Rosenvirge, T.T. 1983, Ap. J., 267, 433.

Bai, T., and Ramaty, R. 1979, Ap. J., 227, 1872.

Bhattachargee, A., Brunel, F., and Tajima, T. 1983, Phys. Fluids, 26, 3332.

Brunel, F.; Tajima, T., and Dawson, J.M. 1982, Phys. Rev. Lett. 49, 323.

Carreras, B., Rosenbluth, M.N., and Hicks, R. 1981, Phys.Rev. Lett. 46, 1131.

Chow, Y. 1983, Private Communication.

de Jager, C. 1969, in COSPAR Symposium on Solar Flares and Space Science Research, ed. c. de Jager and Z. Svestka (Amsterdam : North Holland) , p.1.

Drake, J.F., and Lee, Y.C. 1977, Phys. Rev. Lett. 39, 453.

Finn, J.M. and Kaw, P.K. 1977, Phys. Fluids 20, 72.

Forrest, D.J. et. al. 1981, 17th Inter. Cosmic Ray Conf. 10, 5.

Forrest, D.J. and Chupp, E.L. 1983, Nature (Letters), 305, 291.

Furth, H.P., Killeen, J., and Rosenbluth, M.N. 1963, Phys. Fluids 6, 1054.

Gold, T., and Hoyle, F. 1960, M.N.R.A.S., 120, 89.

Heyvaerts, J., Priest, E.R., and Rust, D.M. 1977, Ap. J., 216, 123.

Howard, R., and Svestka, Z. 1977, Solar Phys., 54, 65.

Kane, S.R., Kai, K., Kosugi, T., Enome, S., Landecker, P.B., and Mckenzie, D.L. 1983, Ap., J. 271, 376.

Kiplinger, A.L., Dennes, B.R., Frost, K.J., and Orwig, L.E. 1983, Ap. J., 273, 783.

Kurokawa, H. 1985 Private Communication.

Machado, M.E. 1985 Private Communication.

Nakajima, H., Kosugi, T., Kai, K., and Enome, S. 1983, Nature (letters) 305, 292.

Nakajima, H., Tajima, T., Brunel, F., and Sakai, J. 1984, in Proc. Course and Workshop on Plasma Astrophysics (Varenna, Italy, ESA, 1984) p. 193.

Parker, E.N. 1957, J. Geophys. Res. 62, 509.

Petschek, H.E. 1964, in Proc. AAS-NASA Symp. on Physics of Solar Flares (NASA sp-50) p. 425.

Priest, E.R. 1982, Solar Magnetohydrodynamics, (Reidel, Dordrecht).

Pritchett, P.L., and Wu, C.C. 1979, Phys. Fluids, 22, 2140.
Rutherford, P.H. 1973, Phys. Fluids, 16, 1903.
Sagdeev, R.Z., and Shapiro, V.D. 1973, JETP Lett. 17, 279.
Sakai, J., Tajima, T., and Sugihara, R. 1986, Ap. J. (submitted)
Sweet, P.A. 1957, in Electromagnetic Phenomena in Cosmic Physics (Cambridge Univ. Press, London) p. 123.
Sturrock, P.A. ed. 1980, Solar Flares: Monograph from Skylab Solar Workshop II, Colorado Associated University Press.
Sugihara, R., and Midzno, Y. 1979, J. Phys. Soc. Jpn. 47, 1290.
Svestka, Z. 1976, Solar Flares (Dordrecht : Reidel)
Tajima, T., and Sakai, J. 1985, IFSR # 186 and # 197, Institute for Fusion Studies, University of Texas.
Phys. Fluids (submitted)
Tajima, T., Brunel, F., and Sakai, J. 1982, Ap. J. 245, L45.
Tajima, T., Brunel, F., Sakai, J., Vlahos, L., and Kundu, M.R. 1983, IAU Symp. No. 107. p. 197.
Wild, J.P., Smerd, S.F., and Weiss, A.A. 1963, Ann. Rev. Astr. Ap. 1, 291.
Wu, S.T. 1985, Private Communication.

N87
21828
UNCLAS

N87-21828

THERMAL WAVES OR BEAM HEATING IN THE 1980, NOVEMBER 5 FLARE

Dean F. Smith

Berkeley Research Associates
Berkeley, California
and
Department of Astrophysical, Planetary and Atmospheric Sciences
University of Colorado
Boulder, Colorado

ABSTRACT

Observations of the temporal evolution of loop BC in soft X rays in the November 5, 1980 flare are reviewed. Calculations are performed to model this evolution. The most consistent interpretation involving a minimum account of energy is the following. Thermal heating near B gives rise to a conduction front which moves out along the loop uninhibited for about 27 s. Beam heating near C gives rise to a second conduction front which moves in the opposite direction and prevents any energy reaching C by thermal conduction from B. Thus both thermal waves and beam heating are required to explain the observed evolution.

1. INTRODUCTION

Two analyses have been performed for the heating and subsequent evolution of loop BC in the 1980, November 5 flare. The first was a beam heating calculation by Duijveman, Somov and Spektor (1983; hereafter DSS). They showed that beam heating could not explain the observed large increase in density of the loop during the flare which requires continuous energy and/or mass input after the impulsive phase. The second was an investigation of observations supporting a thermal wave interpretation by Rust, Simnett and Smith (1985; hereafter RSS). They used observations of a weak contour from bands 1-3 (3.5-11.5 keV) of the Hard X-ray Imaging Spectrometer (HXIS) to infer the presence of a conduction front moving out from B along loop BC. It was noted in RSS that the electron beam of DSS arrived at point C at about 22:33 UT and thus the contours immediately after this time could be influenced by a beam component.

Our approach is to examine the observations to determine what constraints they place on a model. We employ our flux-corrected transport (FCT) code (Smith and Harmony 1982) to model cases of normal heating and beam heating using the model loop of DSS as described in Section 3. The latest results of the laser-fusion community on heat transport in steep temperature gradients (Smith 1986) are employed in our code. The results presented in Section 4 show that thermal conduction and thermal waves play an important role in all cases, but not as dominant a role as could be inferred from RSS. A discussion of these results and their implications is given in Section 5.

2. OBSERVATIONS

We divide the observations into three phases. The first phase is the preflare phase up to HXIS image 152 or 22:32:29 UT. The second phase is an expansion phase from 22:32:29 to 22:33:16 which coincides with the images used by RSS to infer thermal waves (Figure 1b). The third phase is a slow continuation of this expansion contemporaneous with another expansion from footpoint C which eventually results in their merging from 22:33:16 to 22:34:31. We consider these phases in turn.

The first phase is of interest mainly for determining appropriate initial temperatures and densities in loop BC. The end time of the 4.5 s accumulation interval corresponding to frame 152 is 22:32:29. DSS present in their Table II values for the density and temperature at an earliest time of 22:32:50 averaged over ±1 min at the top of the loop and footpoint C. The problem with this procedure is that the flare had already started for a significant fraction of this interval as is clear from Figure 2 of DSS so that the temperatures are not indicative of the preflare state. Machado (private communication) obtained temperatures over the interval 22:30 to 22:31 and found 12×10^6 K for footpoint C and 13×10^6 K for the top of the loop, but with a lower counting rate. Thus, assuming an isothermal loop at 12×10^6 K is a good approximation. The density of 5×10^9 cm^{-3} for both footpoint C and the top of the loop is almost the same as in DSS as would be expected since the amount of heating included in DSS only leads to a substantial density increase sometime beyond 22:32:50.

The observations of the initial expansion phase are shown in Figure 1. Figure 1a includes bands 1 and 2 (3.5-8 keV) with a single 6.7 counts s^{-1} contour whereas Figure 1b includes bands 1-3 (3.5-11.5 keV) and has 2.2, 4.4, 9, and 18 counts s^{-1} contours. The 4.4 counts s^{-1} contour of Figure 1b should correspond closely with the single 6.7 counts s^{-1} contour of Figure 1a. While there is a rough correspondence, it is clear that the addition of band 3 in Figure 1b results in additional smoothing not present in Figure 1a. This throws doubt on the procedure of including band 3 because the number of counts in band 3 should be small compared to the number in bands 1-2 in a purely thermal model for the $10\text{-}30 \times 10^6$ K temperature range of interest.

A larger problem with a simple thermal wave interpretation of Figure 1b is found by comparing it with Figure 1a. If the weak 2.2 counts s^{-1} contour of Figure 1b was really the result of a thermal wave, then we would expect (Brown et al., 1979; Smith and Harmony, 1982; hereafter SH) that the more intense 6.7 counts s^{-1} contour of Figure 1a should tend to follow the weak contour of Figure 1b. The reason is that a thermal wave is driven by the hot plasma behind it which continues to expand unless there is some very dense cool material like the chromosphere to stop it. There is a complication because the optical depth through the loop varies along the loop, but on purely geometrical grounds, one would expect about 47% as much emission from a pixel at the top of the loop as from one at a footpoint for an isothermal constant density loop near the center of the disk as for the November 5 flare (MacKinnon, Brown and Hayward 1985). Thus at least the 4.4 counts s^{-1} contour of Figure 1b should follow the 2.2 counts s^{-1} contour because the wave only becomes visible some distance along the loop and the expected optical depth variation would be much less than a factor of 2 over significant sections of the tongue of the 2.2 counts s^{-1} contour in the 22:33:16 image.

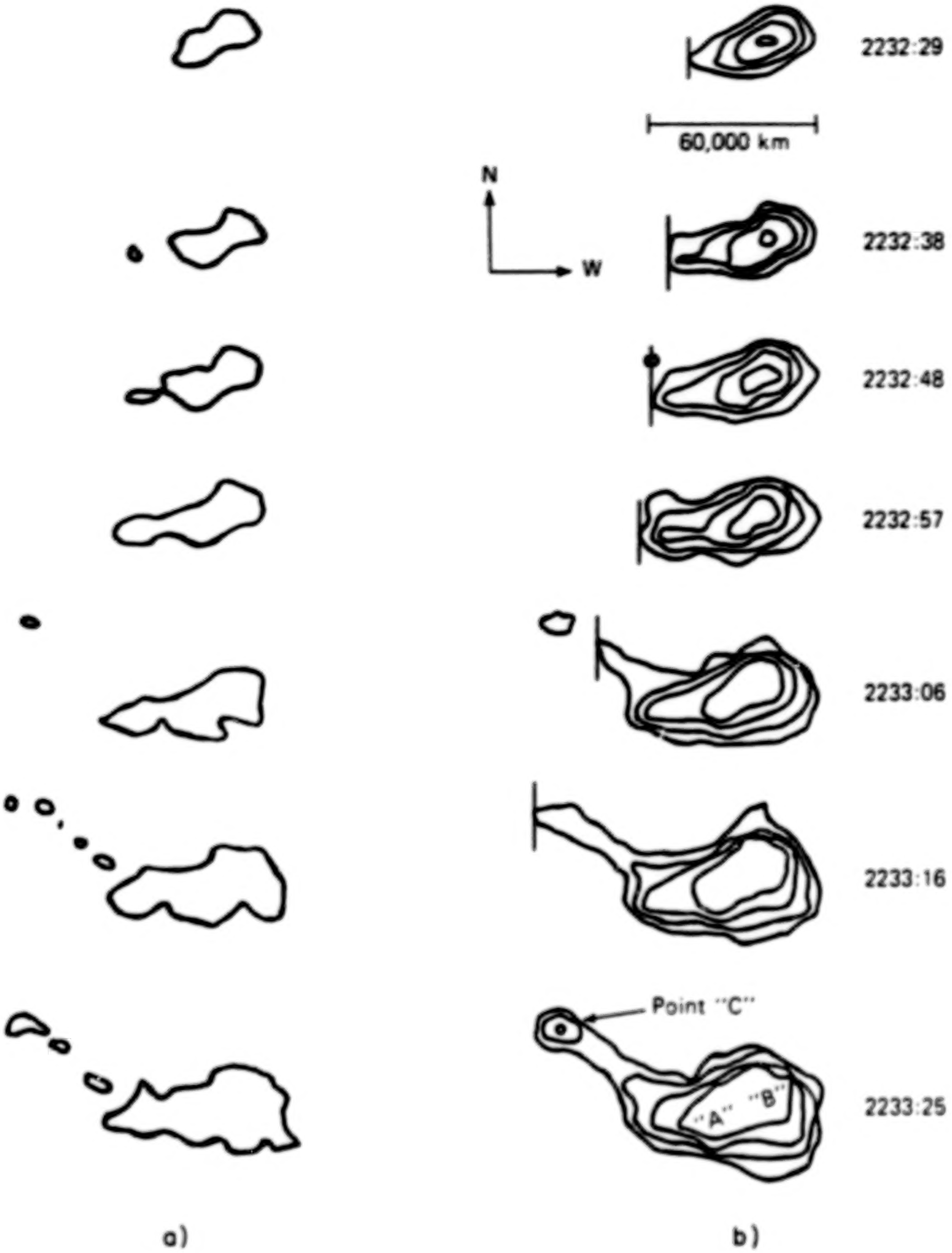

Figure 1. (a) HXIS bands 1 and 2 (3.5-8 keV) at the 6.7 counts pixel^{-1} s^{-1} contour for the times shown at the far right on November 5, 1980. (b) HXIS bands 1-3 (3.5-11.5 keV) at the 2.2, 4.4, 9 and 18 counts pixel^{-1} s^{-1} contours for the same times as (a).

Although there is some indication of the extension of the 4.4 counts s^{-1} contour in this image, it is much less pronounced than would be expected for a pure thermal wave.

Loop BC was there several hours before the flare and continued to exist for several hours after the flare. This implies that whatever caused the X-ray brightening of the loop did not significantly change the gross configuration of the loop and thus it should be sufficient to consider energy transport processes to explain the brightening.

3. MODEL AND METHOD

The model loop used is the same as in Figure 3 of DSS, i.e. a semi-circular loop of radius 35,000 km. The total length of the loop is 10^5 km including an extension into the chromosphere as in SH with an initial coronal density of 5×10^9 cm^{-3} and an initial coronal temperature of 5.1×10^6 K. The loop is divided into 900 cells of length 111.1 km. The equations solved are the same as in SH, and the boundary conditions at the coronal end $x=0$ were

$$v = 0; \quad \frac{\partial T_e}{\partial x} = \frac{\partial T_i}{\partial x} = \frac{\partial \rho}{\partial x} = 0,$$

where v is the velocity, T_e and T_i are the electron and ion temperatures, respectively, and ρ is the total mass density.

The boundary conditions at $x = 10^5$ km were

$$\frac{\partial \rho}{\partial x} = \frac{\partial v}{\partial x} = \frac{\partial T_e}{\partial x} = \frac{\partial T_i}{\partial x} = 0.$$

Ionization equilibrium is assumed to calculate the radiative losses as discussed in SH.

The heat flux Q was calculated in the manner appropriate for steep gradients in which the fast electrons have mean free paths much larger than the temperature scale height (Smith 1986). This has the effect of reducing the heat flux relative to the classical Spitzer-Harm value without anomalous effects such as ion-acoustic waves. Treating the physics adequately leads to the reduction automatically and there is no enhanced electron-ion coupling ($C_{te} = C_{ti} = 0$ in the terminology of SH).

The source term S is taken in one of the two following forms. For thermal heating

$$S = \frac{F(t)}{(2\pi)^{\frac{1}{2}}\sigma(t)} \exp\left[-x^2/2\sigma^2(t)\right], \tag{1}$$

where

$$F(t) = \frac{t}{t_o} J \quad (t < 0.1 \text{ s}),$$

$$F(t) = J \qquad (t \geq 0.1 \text{ s}),$$

where $t_o = 0.1$ s, and $\mathcal{J}$ is the energy input. For beam heating S is of the form (Emslie 1978)

$$S = K\Lambda n(\delta-2)G(t)E_c^{\delta-2} \int_{E*}^{\infty} (E_o^{-(\delta+1)} dE_o)/[1- \frac{3K\Lambda N(x,t)}{E_o^2}]^{2/3} , \qquad (2)$$

where the beam flux distribution (electrons cm^{-2} s^{-1} per unit E_o) is of the form

$$F(E_o,t) = (\delta-2) \frac{G(t)}{E_c^2} \left(\frac{E_o}{E_c}\right)^{-\delta} , \quad E_o \geqslant E_c ; \qquad (3)$$

$K = 2\pi e^4$, Λ is the Coulomb logarithm, n is the density, N(x,t) is the transversed particle column depth, E_c is the cutoff energy, δ is the spectral index and $E* = \max(E_c, (3K\Lambda N)^{1/2})$. Here G(t) is given by

$$G(t) = \frac{t}{t_o} F \quad (t < 0.1 \text{ s}),$$

$$G(t) = F \quad (t > 0.1 \text{ s}),$$

where F is the energy flux of the beam in ergs cm^{-2} s^{-1}.

For even integer values of δ, the integral in equation (2) is analytic and the results for $\delta = 4$, which is the only value that will be used here, are given in Nagai and Emslie (1984). Equation (2) gives the result for a directed beam. It is a straightforward matter to derive the result for an isotropic beam, but we do not present it because the minimum E_c to propagate a significant amount of energy to footpoint C with a directed beam over the 10^5 km loop with $n = 5\times10^9$ cm^{-3} is 20 keV. It would be significantly higher in the case of an isotropic beam.

The X-ray emission due to both the beam and the heated plasma were calculated at 4 and 8 keV corresponding to energies in bands 1 and 2 of HXIS using standard equations (see, e.g., Emslie 1980; Emslie and Vlahos 1980). For the emission from the beam the results for photon energies $\epsilon < E_c$ must be used. The results in photons cm^{-2} s^{-1} erg^{-1} cm^{-1} refer to a 1 cm thick slab of source. To obtain the total emission we would have to integrate over the line of sight through the loop. This step is beyond the scope of this paper, but it needs to be kept in mind in interpreting the results.

4. RESULTS

The results shown in Figures 2-5 can be divided into the results for thermal heating and emission and the results for beam heating and emission. We consider these in turn. The initial σ used for thermal heating was 3500 km. In Figure 2 the solid lines show a typical conduction front moving out along the loop with a speed ~5 c_s, where c_s is the ion-sound speed. The highest temperature of ~30×10^6 K is about the temperature DSS deduced for the top of the loop averaging over ±1 min around 22:32:50. The speed of the

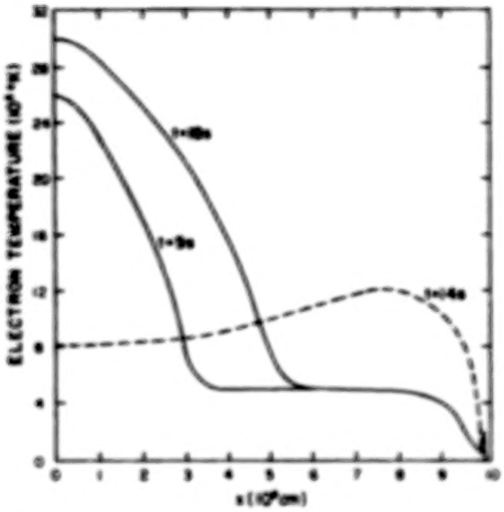

Figure 2. The electron temperature versus distance along the loop for thermal heating with an input of 11.4 erg cm^{-3} s^{-1} for two times (solid lines) and beam heating with an energy flux of 10^{10} erg cm^{-2} s^{-1} (dashed line) which corresponds exactly to the level of thermal heating.

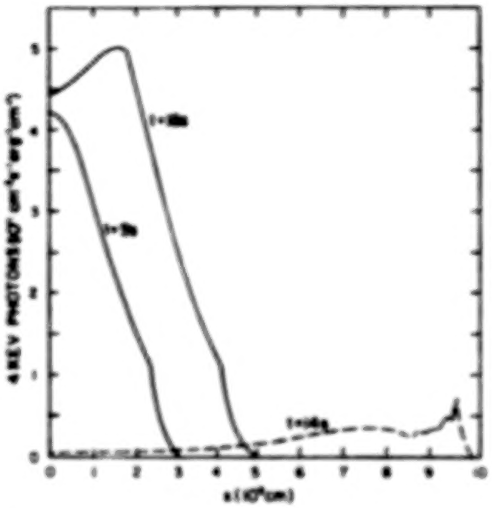

Figure 3. The X-ray emission per unit length (dI/dx) at 4 keV at the source versus distance for thermal heating (solid lines) and beam heating (dashed lines). Only the X-ray emission due to heating is shown for the beam.

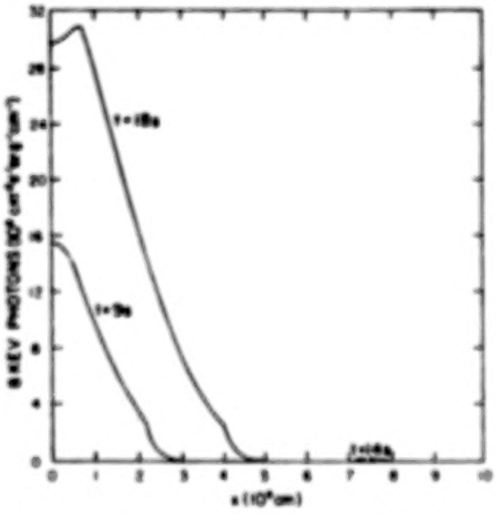

Figure 4. The X-ray emission per unit length (dI/dx) at 8 keV at the source versus distance for thermal heating (solid lines) and beam heating (dashed lines). Only the X-ray emission due to heating is shown for the beam.

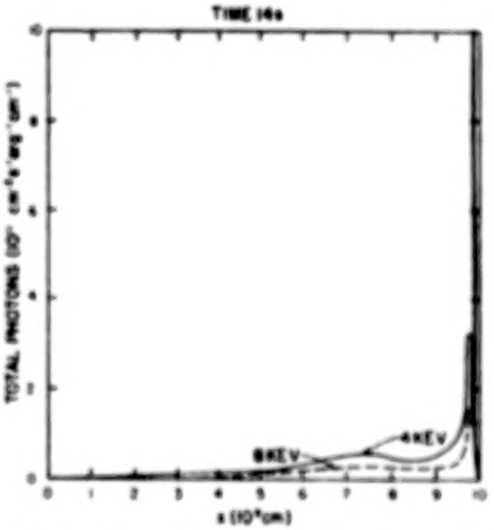

Figure 5. The total X-ray emission per unit length at the source versus distance for a beam. The 4 keV emission (solid line) has a peak off the scale at 24.8×10^{11} photons cm^{-2} s^{-1} erg^{-1} cm^{-1} and the 8 keV emission (dashed line) has a peak off the scale at 12.4×10^{11} photons cm^{-2} s^{-1} erg^{-1} cm^{-1}.

front is $\sim 2.2\times 10^8$ cm s^{-1} which means that, without anything to stop it, the front would run into footpoint C in about 45 s.

However, a conduction front will only continue to move forward if the temperature of the plasma ahead of the front is lower than the temperature of the plasma behind the front. We know that a beam was impacting footpoint C from 22:32:50-22:33:20 because of the impulsive 16-30 keV signature (DSS) which leads to the brightenings in Figure 1a,b at 22:33:06 and some time beyond. This leads to heating as shown by the dashed line in Figure 2 which at $t = 14$ s would correspond approximately to the 22:33:06 image in Figure 1. This heating would prevent any energy from conduction reaching footpoint C until long after (> 1 minute) beam heating had stopped since it is very unlikely that temperatures higher than those due to beam heating would be produced by a conduction front so far from the region of energy input without producing temperatures near $x = 0$ much higher than those observed. Because of computer time limitations, we were not able to show this explicitly. It should also be noted that the times in Figures 2-4 are referenced to the start times of two independent calculations, one for thermal heating (solid lines) and one for beam heating (dashed line). Again, because of computer time limitations we made no attempt to heat near $x = 0$ and sometime later turn on a beam in one computation. Still, a fairly complete scenario for this flare can be made from the results presented.

The thermal heating X-ray results in Figures 3-4 show a front moving out which would be consistent with Figure 1a,b from 22:32:29 to 22:32:57. Because the heating near $x = 0$ causes a slight density depression and the X-ray emission is proportional to n^2, the X-ray emission at 18 s has a peak away from $x = 0$. It is doubtful that this 10% variation could be detected with present spatial resolution.

The beam used in the beam heating results had $E_c = 20$ keV, $F = 10^{10}$ ergs cm^{-2} s^{-1}, and $\delta = 4$. The flux comes from DSS and δ from Dennis (private communication). This leads, using (Emslie 1978)

$$E = E_o\left[1 - \frac{3K\Lambda N}{E_o^2}\right]^{1/2}, \tag{4}$$

to the expectation that the maximum energy deposition will occur at $N = E_c^2/3K\Lambda = 3.5\times 10^{19}$ cm^{-2} for $\Lambda = 28$ which is at $x = 70{,}000$ km. We see in Figure 2 that the maximum heating has occurred at 76,000 km at 14 s because some of the material in the flux tube has moved to larger x due to the heating by this time. The beam thermal X-ray signature in Figures 3-4 is quite small relative to the signature due to thermal heating.

In Figure 5 we have plotted the total X-ray signature of the beam including the nonthermal X-rays. In fact one can see by comparison of Figure 5 with Figures 3-4 that most of the emission is nonthermal emission. The physical reason is that the beam deposits energy over a large fraction of the loop so that the heating in one region does not raise the temperature a large amount over another region as is clear from Figure 2. Consequently the thermal emission is small. The nonthermal emission has a first peak around 73,000 km where the beam is depositing most of its energy. Intuitively one might guess that this is also the place from which the maximum emission dI/dx would occur (see, e.g., Brown and McClymont 1975). The reason that this is not the case is that the photon energies are substantially below E_c and n rises steeply in the chromosphere. dI/dx is proportional to n/α^2, where $\alpha = 3KAN/E_c^2$, and the n factor increases much more rapidly than α^2 well beyond the place of maximum energy deposition.

Thus the beam X-ray emission should be concentrated near the footpoints, but will still be substantial to about 30,000 km above the footpoint. It should be kept in mind that the quantity plotted, dI/dx, must be integrated over the line of sight to obtain I. Nevertheless, there appears to be an order of magnitude discrepancy between the X-ray emission of the beam and the thermal X-ray emission (Figures 3-4 and Figure 5) with the same energy flux into both. The reason is that the beam energy is deposited over a relatively large area, keeping the thermal contribution small. We are investigating the effect of increasing the beam flux. DSS already concluded that the injected beam energy should be increased to obtain more evaporated material and, since they did not take into account scattering of beam electrons, their energy transfer was unrealistically efficient. Within the uncertainty of not having the results for higher beam fluxes, we feel that we have sufficient results to make a qualitatively, but not quantitatively, consistent scenario for this flare.

5. DISCUSSION

The results presented indicate the simplest manner of explaining the observations of Figure 1 with a minimum amount of injected energy. The observations from 22:32:29 to 22:32:57 can be explained by heating above footpoint B and the progressive expansion of a conduction front. An energy flux of 10^{10} erg cm^{-2} s^{-1} leads to temperatures and X-ray emission levels (Figures 2-4) consistent with the observations. The footpoint present at 22:33:06 can only be explained by a beam which was known to turn on about 22:32:50. A conduction front consistent with the observations from 22:32:29 to 22:32:57 could not have reached footpoint C at this time. Hence one cannot use the edge of the 2.2 counts s^{-1} contour to infer the position of a conduction front beyond 22:32:57 because of the contribution of the beam, a possibility already noted in RSS.

Thus, the velocity inferred on the basis of the 2.2 counts s^{-1} contour in RSS is too high. It is still less than the velocity obtained in Section 4 from the numerical results which is probably unrealistically high because the initial temperature is a factor 2 too low. Another effect which could be important in slowing the conduction front is the beam heating although it would not be important until after 22:32:48.

The observations from 22:33:06 to 22:33:25 can be explained by a combination of nonthermal X-rays from a beam, beam heating and the interaction of the conduction fronts from thermal heating and beam heating. Most of the extension of the 2.2 counts s^{-1} contour at 22:33:16 is due to beam heating and nonthermal X-rays. By 22:33:25 a conduction front is starting to move up from footpoint C which is consistent with the 6.7 counts s^{-1} contour and which could be made more pronounced in the numerical results by more beam heating. DSS noted that the amount of beam energy was uncertain by a factor ~4. Energy from thermal heating would then never be able to flow to footpoint C within the times in Figure 1 since the conduction front due to beam heating would prevent the conduction front from B from traveling much beyond the center of loop BC. It is also possible to see, using equation (4), that energy in the 16-30 keV range as seen in Figure 2 of DSS for 30 s requires the injection of greater than 30 keV electrons. Beam heating could continue beyond 22:33:20 by the injection of lower energy electrons which would give no hard (16-30 keV) X-ray signature.

Thus, the most consistent interpretation of the observations in Figure 1 involves a combination of thermal waves and beam heating.

The author is grateful to Drs. Brian Dennis, Gordon Emslie, Alan Kiplinger, Marcos Machado and David Rust for helpful discussions. This work was supported by NASA contract NASW-3603 and NSF grant ATM-8314511.

REFERENCES

Brown, J. C., and McClymont, A. N. 1975, Solar Phys., 41, 135.
Brown, J. C., Melrose, D. B., and Spicer, D. S. 1979, Ap.J., 228, 592.
Duijveman, A., Somov, B. V., and Spektor, A. R. 1983, Solar Phys., 88, 257.
Emslie, A. G. 1978, Ap.J., 224, 241.
Emslie, A. G. 1980, Ap.J., 235, 1055.
Emslie, A. G., and Vlahos, L. 1980, Ap.J., 242, 359.
MacKinnon, A. L., Brown, J. C., and Hayward, J. 1985, Solar Phys., 99, 231.
Nagai, F., and Emslie, A. G. 1984, Ap.J., 279, 896.
Rust, D. M., Simnett, G. M., and Smith, D. F 1985, Ap.J., 288, 401.
Smith, D. F. 1986, Ap.J., in press.
Smith, D. F., and Harmony, D. W. 1982, Ap.J., 252, 800.

N87
21829
UNCLAS

N87-21829

A DOUBLE LAYER MODEL FOR SOLAR X-RAY AND MICROWAVE PULSATIONS

K. F. Tapping

Herzberg Institute of Astrophysics
Ottawa, K1A OR6, Canada

Abstract

The wide range of wavelengths over which quasi-periodic pulsations have been observed suggests that the mechanism causing them acts upon the supply of high energy electrons driving the emission processes. A model is described which is based upon the radial shrinkage of a magnetic flux tube. The concentration of the current, along with the reduction in the number of available charge carriers, can give rise to a condition where the current demand exceeds the capacity of the thermal electrons. Driven by the large inductance of the external current circuit, an instability takes place in the tube throat, resulting in the formation of a potential double layer, which then accelerates electrons and ions to MeV energies. The double layer can be unstable, collapsing and reforming repeatedly. The resulting pulsed particle beams give rise to pulsating emissions which are observed at radio and X-ray wavelengths.

1. Introduction

Most of the models for the quasi-periodic pulsations which are often observed at radio and X-ray wavelengths are based upon the modulation of synchrotron radiation by MHD wave modes in magnetic flux tubes, or by relaxation processes in wave/electron beam coupling. A summary of the observational data and models is given by Krüger (1979). The implicit assumptions embodied in these models is that the high energy electrons and mechanical disturbances required to drive the process are externally supplied by the flare.

However pulsations have been observed in the absence of flares (e.g. Kobrin et al., 1978; Kaufmann et al., 1980; Strauss et al., 1980; Gaizauskas and Tapping, 1980; papers by Kaufmann et al. included in these proceedings). In such cases modelling is more difficult. In addition to explaining the characteristic time-scales of the events, it is also necessary to identify the acceleration mechanism supplying the high energy electrons and how it is driven.

The wide frequency range over which the pulsations have been simultaneously observed, ranging from radio wavelengths to X-rays, implies that rather than modulation of the emissive process, for example by a time-varying magnetic field, it is more probably the variation of the supply of high energy electrons driving the various radiative processes that causes the pulsations. This may be due to a relaxation instability in the particle beams themselves, or by production of a pulsed electron beam by the accelerator. In this latter case the acceleration mechanism has to be highly efficient, accelerating the electrons from thermal to

PRECEDING PAGE BLANK NOT FILMED

relativistic velocities in time-scales of the order of seconds or less. Direct acceleration by field-aligned electric fields are the most viable ways of achieving this. The short time-scales indicate that the acceleration zone is spatially small, not larger than about 10^4 km.

One candidate is the potential double layer. They have been extensively used in models for the acceleration of auroral electrons in the Earth's magnetosphere. They have also been used in at least one flare model (Alfvén and Carlquist, 1967, Hasan and Ter Haar, 1978). The formation, maintenance and dynamics of double layers have been discussed extensively (Block (1978); Torvén (1979); Torvén and Lindberg (1980-two references); Swift (1981); Davey (1983)).

Double layers are highly efficient electron accelerators, producing mono-energetic electron beams having small pitch angles. There is evidence that double layers exist in the laboratory and in the Earth,s magnetosphere; however there is as yet little evidence that such structures form in the solar atmosphere. This may be because of the difficulty in identifying structures of such small spatial extent.

2. The Model

Evolutionary forces in solar active regions cause the overlying chromospheric and coronal magnetic fields to depart from simple, potential configurations, leading to the generation of electric currents. The current carriers are the ambient thermal electrons and ions. The complex magnetic structures contain sheared and curved magnetic field lines, giving rise to some motion of the current carriers across the field, from one loop structure to another. Therefore to at least some extent, the active region is a complex current circuit containing many interactive elements. Changes in one part of the region may modify the current system and so affect conditions in distant areas.

The formulation of model which is truly descriptive of the active region processes is very difficult if not impossible, yet the taking of one element of the region in isolation may not be realistic. This is particularly the case with double layers, where the formation criteria and the subsequent stability of the layer are defined by the external current circuit.

Consider the case of a magnetic flux tube forming part of an active region. It is firmly anchored at the ends by its connections to other structures, but is free to expand or contract in its middle section. It is always in pressure equilibrium with the surrounding magnetoplasma. Evolution of the active region leads to an increase of the current carried by the tube, causing it to contract radially.

As the cross-sectional area of the tube decreases, the current density is further enhanced. The variation in strength of the longitudinal magnetic field strength along the tube leads to mirroring of electrons at the tube throat, particularly at the centre, where the field is strongest. Since the mean free path of the electrons is much larger than the dimensions of the trap, the current is carried only by electrons lying in the loss cones.

Finally, the number of available charge carriers becomes inadequate to carry the current. However the large self-inductance of the external current circuit forces the current to be maintained. The continuity of the current is achieved by the formation of a potential double layer in the throat. The layer's field-aligned electric field accelerates electrons into the loss-cones at MeV energies. These maintain the current at the required value. If the rate of energy supply to the double layer is less than the energy dissipation rate, the layer will collapse and reform, producing a pulsed beam of high energy electrons. The pulsations are due to the time-variation of the electron beam driving the various emission processes.

(1) Radial Contraction of a Magnetic Flux Tube

Consider the case of an infinitely long, thin, straight magnetic flux tube. It carries a current driven by an external source. The current density is assumed to be uniform across the tube cross-section. The ends of the tube are fixed but the rest of the tube is free to move. It is in pressure equilibrium with the external plasma. Initially it assumed to be a uniform cylinger of radius R_0, containing a longitudinal magnetic field of strength B_0. The configuration is shown in Figure (1). All changes in the quantities dictating the tube structure are assumed to take much longer than any of the characteristic time-scales of the tube. In the force-free case, the tube equilibrium is described by the equations:

$$\mathrm{Curl}\ (\vec{B})\times\vec{B} = 0 \tag{1}$$

$$\mu\vec{j} = \mathrm{Curl}\ (\vec{B}) \tag{2}$$

where μ is the permeability of free space.

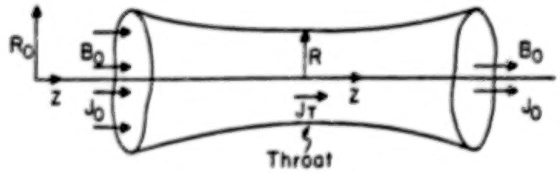

Figure 1: The Collapsing Flux Tube.

In the axisymmetric case these equations become:

$$B_Z . \partial B_Z/\partial r + B_\phi . \partial B_\phi/\partial r + B_\phi^2/r = 0 \tag{3}$$

$$j_Z = \mu/r\ \partial(rB_\phi)/\partial r \tag{4}$$

where r, ϕ, Z represent the usual cylindrical coordinate frame.

If the current density is assumed to be uniform across the tube cross-section then j_Z can be replaced by

$$j_Z = j_o(R_o/R)^2 \qquad (5)$$

where R_o and R are respectively the radius of the tube at the (fixed) ends and R the radius of the tube elsewhere along the length of the tube. The quantity j_o represents the current density at the tube end.

Using (5) and (4), equation (3) may be solved for B_Z as a function of r. At the tube periphery (r=R), there must be pressure equilibrium with the external plasma. Also, since the total longitudinal magnetic flux is conserved:

$$\Pi.R_o^2.B_o = 2\Pi \int_o^R B_Z(r).r.dr \qquad (6)$$

Where B_o = Magnetic field strength in un-perturbed tube.

Solving (6) gives the variation of tube radius as a function of the longitudinal current density, j_o, and can be used to calculate the throat current density (Equation (5)). The radial shrinkage of a tube of radius 10^4 km and an initial magnetic field strength (B_o) of 2.5 mWb.M^{-2} is shown as a function of current density in Figure (2). The maximum limit of the x-scale is equivalent to tube twist pitch of about unity.

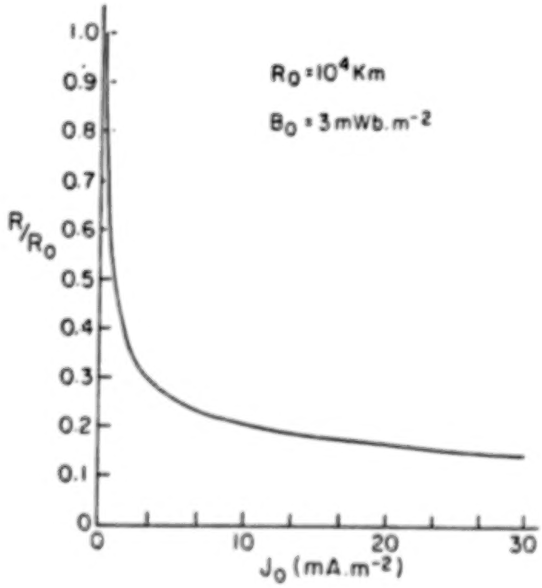

Figure 2: The Relative Change in Tube Radius as a Function of Current Density for a Tube of Radius 10,000 km.

(ii) The Formation of the Double Layer

As the current density increases, a point is reached where there are insufficient available charge carriers to carry the required current. If the charge carriers initially have an isotropic pitch angle distribution, the fraction lying the loss cones is given by:

$$\eta = 1 - (1 - B_o/B_Z)^{\frac{1}{2}} \qquad (7)$$

Only electrons lying in the loss-cones can contribute to the carrying of the current, so using equation (7), the maximum allowable current density in the throat is:

$$j_{max} = N.u_T.e.[1 - (1 - B_0/B_Z)^{\frac{1}{2}}] \qquad (8)$$

Where N = Number density of thermal electrons;
u_T = Mean thermal velocity of electrons;
e = Electronic charge

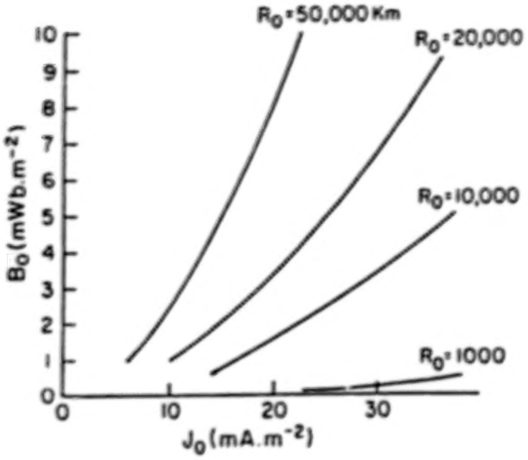

Figure 3: The Values of and Satisfying the Double Layer Formation Criteria for Various Tube Radii.

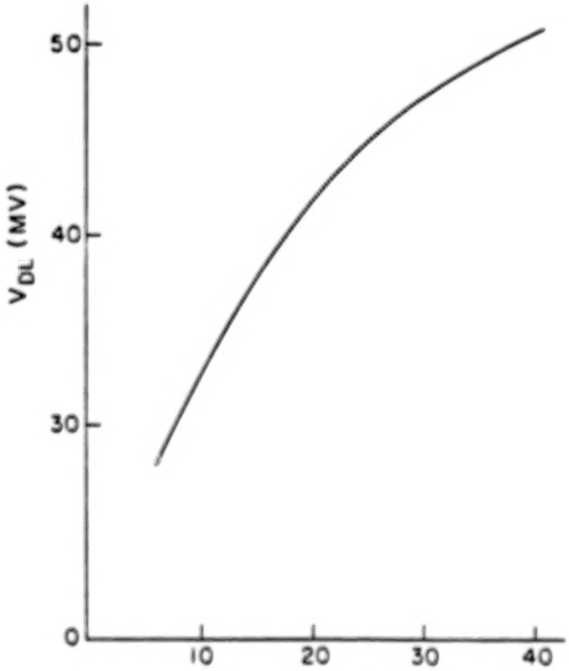

Figure 4: The Potential Difference Across the Double Layer as a Function of Current Density.

When the current density exceeds this value, the thermal particles cannot carry the current unless more electrons are scattered into the loss-cones. Since the mean free path is large, collisions will not do this. A plasma instability is required. The large self-inductance of the global electrical circuit prevents disruption of the current flow over short timescales; this factor provides the driving force for any instability leading to the scattering of more current carriers into the loss-cones. Such scattering implies the presence of a field-aligned electric field and a fall of the plasma density in the throat of the tube. The field-aligned potential difference accelerates enough electrons into the loss-cones for the current to be maintained. The density in the region of the electric field falls and the current becomes space charge limited. The curves shown in Figure (3) indicate the values of initial magnetic field strength (B) and current density (j) for tubes of various radii. Any conditions lying to the right of the appropriate curve satisfy the instability threshold criterion.

(iii) The Acceleration of Electrons

The value of the potential difference required to inject the extra electrons into the loss-cones may be calculated using Poisson's equation. The one-dimensional case is sufficient here. The relationship between the current density and potential drop across the layer is easily calculated using Poisson's equation in one dimension. The "cold plasma" approximation (Langmuir, 1929) gives the relation:

$$V_{DL} = \left(\frac{m.j_o^2(R/R_o)^4.d^4}{\varepsilon_o^2.e} \right)^{1/3} \tag{9}$$

where d = Thickness of the layer,
e = electron charge,
m = electron mass,
R_o = initial tube radius,
R = current throat radius,
ε_o = permittivity of free space.

The thickness scale d, of the layer is a function of the geometry of the flux tube. It is of the order of the distance between the point where the instability criterion is met and the tube throat. In this calculation d is assumed to be 1 km. The electrons passing through the layer would be accelerated to an energy of Vdl eV. The potential drop across a layer of thickness 1 km, when the condition for the formation of the double layer is just satisfied, is shown in Figure (4). In this case electrons would be accelerated to energies of the order of 10 MeV. If the current density exceeds the threshold value, the potential difference will be larger.

(iv) The Pulsations

The rate of energy dissipation by the double layer is given by the product of the total current through the double layer and the potential difference across it. A minimum condition for the stability of the double layer is that the rate of energy supply is not less than that value.

The dissipation of the energy of the magnetic field structure is equivalent to the dissipation of the torsional magnetic field component associated with the longitudinal current. The torsional magnetic field propagates to the double layer in the form of torsional (Alfvén) waves, where the magnetic field becomes unfrozen and the tube is free to untwist. It is very unlikely that the maximum torsional magnetic field strength associated with the Alfvén waves will exceed the longitudinal magnetic field strength in the tube, so the absolute maximum rate of energy supply to the double layer without disrupting the flux tube is therefore given roughly by:

$$W_{max} = u_a.B_o{}^2/2\mu \tag{10}$$

Provided that

$$W_{max} \geqslant \Pi.R_T^2.j_T.V_{DL} \tag{11}$$

where u_a = Alfvén speed
R_T = Throat radius
j_T = Throat current density

The stability of the layer will be a function of other criteria. However if the condition in Equation (11) is not satisfied, the layer will collapse as soon as the tube has untwisted in its vicinity so that Equation (11) is not longer satisfied. The layer will then collapse until the adjacent parts of the tube have once more become twisted enough for the layer to reform. The time taken for this would be of the order of an Alfvén transit time along the tube. For a tube carrying a current density of 40 mA per square meter and having a radius of 10,000 km, a double layer sustaining a potential difference of 10^7 volts will dissipate energy at a rate of 10^{20} W. This value assumes that the double layer formation criterion has just been satisfied. For an Alfvén velocity of 2000 km/s and a tube radius 10,000 km - the maximum energy input rate would be about 10^{18} W. In this particular instance the layer would not be stable; it would be subject to a relaxation instability consisting of successive formation and collapse where the mean rate of energy supply is equal to the mean energy dissipation rate. The period of the instability is very small compared with the characteristic time-scales of the active region structures, so they would remain unaffected.

The pulsing double layer will produce pulses of electrons having MeV energies. These maintain the current and drive the X-ray and radio emission processes.

(v) The X-ray and Radio Emission

The production of X-rays is by free-free (bremsstrahlung) emission. Having small pitch angles, the electrons are potentially capable of penetrating to low levels in the solar atmosphere before being subject to mirroring. At these heights the beams are collisionally damped by the dense, thermal plasma, producing X-ray emission.

At meter wavelengths there are a variety of wave/particle interactions which can result in extraction of energy from the particle beam and the growth of plasma waves, which then contribute to radio emission. However plasma waves are probably not important for microwave emission, because the high densities required would damp the waves. This would lead to the conversion of the beam energies into heat. Electromagnetic radiation by the gyro-synchrotron mechanism would probably be more important at centimeter wavelengths. Electrons having small pitch angles are not subject to gyro-magnetic radiation losses, they must be scattered in pitch angle. There are beam/plasma instabilities which will achieve this. Once scattered the electrons will produce gyro-magnetic radiation.

(vi) The Radiated Flux

The spectrum of the radiation is difficult to estimate. At meter wavelengths the radiation will be a mix of plasma and gyro-synchrotron emission; at microwave (centimeter) wavelengths, gyro-synchrotron emission will be predominant; the X-rays are produced by free-free damping of the high energy particles by the dense thermal plasma at lower heights above the photosphere. The total emission as a function of frequency is hard to calculate. If the emission is assumed to be uniformly distributed with frequency it is possible to estimate the flux density at the Earth. A double layer of dissipation 10^{20} W driving emission processes producing a uniform flux density over the wavelength range 1 A to infinity, the flux density at the Earth would be about 10 solar flux units. The pulsations observed by Gaizauskas and Tapping (1980) had a flux density of about 2 sfu at 2.8 cm wavelength.

3. Discussion

The high repetition rates of quasi-periodic pulsations imply small spatial sizes for the sources. Since pulsations have been observed which have a large instantaneous bandwidth, more than one emission mechanism is probably involved. This in turn suggests that the modulation mechanism is most likely to involve the supply of high energy electrons driving the various processes than the processes themselves. There are few acceleration mechanisms that are suspected to take place under solar conditions which can produce relativistic electrons from the thermal population in about a second.

The energetic electrons driving the gyro-synchrotron emission are damped primarily due to radiative energy losses. The damping time may be many seconds long, perhaps longer than the repetition period of the pulses. However the successive formation and collapse of the double layer in the flux tube would ensure that the tube contains torsional Alfvén waves. These will strongly modulate the gyro-synchrotron emission with the same period as the pulsing of the electron beam (Tapping, 1983). The pulsations at microwave and X-ray wavelengths would therefore occur at the same rate but not necessarily in synchronism. The pulse shapes would not necessarily be the same.

The pulsations observed during flares probably form just one way in which the energy release drives external phenomena. There is an abundance of available energy, accelerated electrons and evidence for magnetohydrodynamic disturbances. This is not the case for the pulsations observed in the absence of flares. In this latter case the fundamental problem is the electron acceleration process, and the way in which the slow evolution of the active region can, if the magnetic fields form the primary energy reservoir, lead to localized magnetic reconnection.

Acknowledgements

I would like to thank G. Atkinson for his suggestions and comments, and J. Ricketts and S. Dewar for their help in preparing this paper.

References

Alfvén, H., Carlquist, P.; Solar Physics, Vol. 1, 220, 1967.

Block, L.P.; Astrophys. and Space Sci., Vol. 85, 59, 1978.

Davey, K.R.; Astrophys. and Space Sci., Vol. 95, 47, 1983.

Gaizauskas, V., Tapping, K.F.; Astrophys. J., Vol. 241, 804, 1980.

Hasan, S.S., Ter Haar, D.; Astrophys. and Space Sci., Vol. 56, 89, 1978.

Kaufmann, P., Strauss, F.M., Raffaelli, J.C., Opher, R.; "Solar-Terrestrial Pred. Proc.", R.F. Donnelly (ed.), Vol. 3, 115, C-115, U.S. Dept. of Commerce, Boulder, Colorado, 1980.

Kobrin, M.M., Korshunov, A.I., Arbuzov, S.I., Pakhomov, V.V., Fridman,V.M., Tikhomirov, Yu.V.; Solar Physics, Vol. 56, 359, 1978.

Krüger, A.; "Introduction to Solar Radio Astronomy and Radio Physics", "Geophysics and Astrohysics Monographs", publ. Reidel, 1979.

Langmuir, I.; Phys. Rve., Vol. 33, 954, 1929.

Strauss, F.M., Kaufmann, P., Opher, R.; Solar Physics, Vol. 67, 83, 1980

Swift, W.; J. Geophys. Res., Vol. 80, 2096, 1975.

Tapping, K.F.; Solar Physics, Vol. 87, 177, 1983.

Torvén, S.; "Wave Instabilities in Space Plasmas", Palmadesso and Papadoulos (eds), 109, publ. Reidel, 1979.

Torvén, S., Lindberg, L.; "Electron and Plasma Physics", Royal Institute of Technology, Stockholm, Sweden, TRITA-EPP-80-02.

Torvén, S., Lindberg, L.; J. Phys., Vol. 13, 2285, 1980.

N87
21830
UNCLAS

N87-21830

THEORETICAL STUDIES ON RAPID FLUCTUATIONS IN SOLAR FLARES

Loukas Vlahos

Department of Physics
University of Thessaloniki
54006 Thessaloniki, Greece

Abstract

Rapid fluctuations in the emission of solar bursts may have many different origins e.g. the acceleration process can have a pulsating structure, the propagation of energetic electrons and ions can be interrupted from plasma instabilities and finally the electromagnetic radiation produced by the interaction of electrostatic and electromagnetic waves may have a pulsating behavior in time. In two separate studies (Vlahos, Sharma, and Papadopoulos, 1983; Vlahos and Rowland, 1984) we analysed the contitions for rapid fluctuations in solar flare driven emission.

1. Time evolution of a beam-plasma system

A possible interpretation of the solar hard X-ray bursts is that a relativly large flux of non-thermal electrons accelerated near the energy release site of a solar flare, stream along the magnetic field lines toward the chromosphere. The interaction of the non-thermal electrons with the ions in the upper chromosphere produces, via collisional Bremsstrahlung, photons with energies from 20 Kev to several Mev. The energetic electrons are unstable to the growth of plasma waves. In the linear regime , plasma waves with phase velocity $\omega_e/k_b < v_b$ will grow with a rate

PRECEDING PAGE BLANK NOT FILMED

$$\gamma_L = \frac{n_b}{n_0} (v_b/\Delta v_b)^2 \omega_e \cos^2\gamma \qquad (1)$$

where v_b is the beam velocity, ω_e is the plasma frequency, n_b, n_0 are the beam and ambient densities, Δv_b is the beam spread around the beam velocity and γ the angle between the wave vector and the external magnetic field. As the beam driven waves reach a threshold value e.g. $W_{th}/n_0T_e = [v_e/v_b]^2$ the dispersion characteristics of the medium change dramatically and lead to the formation of solitons. The long wavelength high frequency waves are localised in space, producing soliton type formations in the wave energy and cavities in the ion density. The local ion density is propotional to the plasma wave energy (Papadopoulos, 1975) e.g.

$$\frac{\delta n}{n_0} =- [W_1^1/(2n_0T_e)] \qquad (2)$$

where W_1^1 is the energy density of the beam exited waves. The localization in space of the plasma waves causes a fast transfer of wave energy out of resonance with the beam electrons and into resonance with the low energy tail of the Maxwellian distribution. The rate with which the waves are transfered away from resonance with the beam is

$$\gamma_{NL} = (m/M)^{1/2} \{W_1^1/n_0T_e\}^{1/2} \omega_e \qquad (3)$$

for $(W_1^1/n_0T_e) > (v_e/v_b)^2$. The net result from the soliton formation is: (1) the transfer of energy from the beam driven waves to non-resonant plasma waves (W_2^1) with low phase velocity and (2) the excitation of ion-density fluctuations. As long as $(W_2^1/n_0T_e) = \delta n/n_0$ the ion fluctuations are undamped. The non-linear frequency shift, due to W_2^1, for the low frequency waves is $-kc_s$, so we obtain an essentially stationary non-linear ion pertrubation. When W_2^1 is absorbed by Landau damping on the electrons, this non-linear frequency shift disapears, and the ion fluctuations are converted to normal linear modes (ion acoustic waves) of the plasma and can then damped.

The evolution of a beam-plasma system then follows three stages: (1) the linear growth of beam driven waves with rate γ_L. (2) Once the wave energy passes a threshold value, discussed above, a fast transfer of plasma waves to lower phase velocity waves occurs. (3) Ion density cavities are also formed once $(W_1^1 / n_0 T_e)$ is above $(v_e/v_b)^2$. When $W_2^1 < W_s$ the non-resonant waves cannot support the cavitons and the "cavitons radiate" ion density fluctuations. The ion density fluctuations scatter the high frequency waves to lower phase velocityies with a rate

$$\alpha_{NL} = (W_s/n_0 T_e)(\lambda_s/\lambda_{De})^2 \omega_e \qquad (4)$$

where $\lambda_s = 10\lambda_D$ and λ_{De} is the electron Debye length. The time dependent evolution of the beam driven waves can also be described by the folowing phenomenological system of rate equations

$$\frac{dW_1^1}{dt} = \gamma_L W_1^1 - \gamma_{NL} W_2^1 \,\theta(W_1^1 - W_2^1) - \alpha_{NL} W_1^1 \,\theta(W_s - W_2^1) \qquad (5)$$

$$\frac{dW_2^1}{dt} = \gamma_{NL} W_2^1 \,\theta(W_1^1 - W_{th}) - \nu_L W_2^1 - a_{NL} W_2 \theta(W_s - W_2^1) \qquad (6)$$

$$\frac{dW_s}{dt} = \gamma_{NL} W_2^1 \,\theta(W_1^1 - W_{th}) - \nu_1 W_s \theta(W_s - W_2^1) \qquad (7)$$

where ν_L is the damping of the Langmuir waves in the tail, ν_1 is the damping of the ion density fluctuations and θ is a step function (see more discussion on egs(5)-(7) in Vlahos and Rowland, 1984). We solved eqs(5)-(7) numerically and the results are ploted in Fig.(1).

2. Stochastic three wave interaction

Electron beams, formed during the impulsive acceleration phase of a flare, stream continuously toward the chromosphere. Since the magnetic field increases slowly in the direction of propagation a fraction of the beam electrons precipitate while the remainder became part of the stably

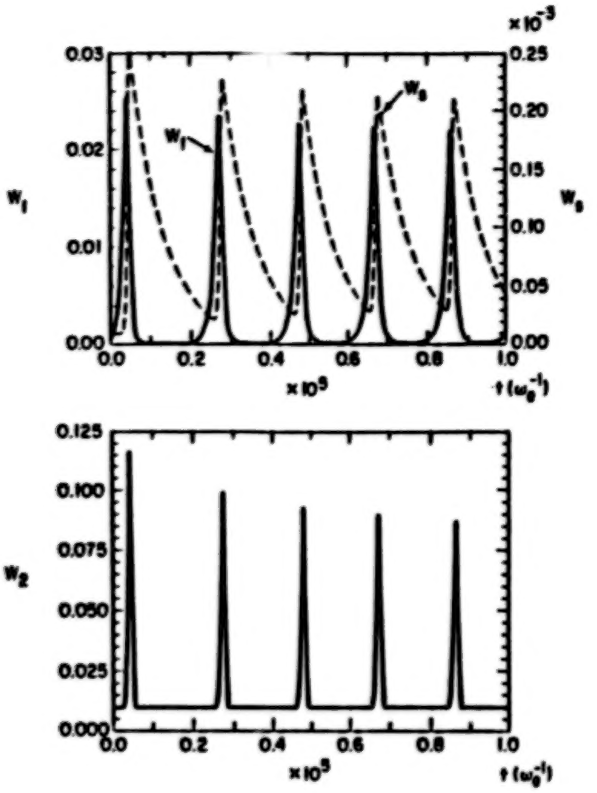

Figure 1: The rate equations are solved numerically using $n_b/n_0=10^{-2}$, $W_1^1(t=0)=5*10^{-5}$, $W_2^1(t=0)=W_s(t=0)=10^{-5}$, $v_b/v_e=10$. (a) The temporal evolution of the resonant high frequency waves and the acoustic wave (b) the temporal evolution of the non-resonant waves. The individual pulse have a duration ≅ μsec to msec, dependig on the beam strength.

trapped component. For a plasma with cyclotron frequency (Ω_e) larger than the plasma frequency (ω_e), the presence of the beam can amplify waves in both , lower and upper hubrid brances. The beam exited electrostatic waves are convectivly amplified and propagate toward the cutoff region where their energy piles up in a narrow wave packet with bandwith $\delta\omega_{UH}$.

Coherent upconversion of the beam amplified electrostatic waves to electromagnetic waves produce an intrinsically stochastic emission component. For a coherent interaction we average the basic three wave coupling equations over space, retaining however their dynamic character. We thus have a zero-dimension but dynamic model. The energy input is steady and represents the rate at which electrostatic waves convert into the interaction volume. The three wave equations for the real amplitude(a_j) and phase are

$$\frac{d\alpha_1}{dt}=\gamma_1\alpha_1-\Lambda_1\alpha_2\alpha_3\cos\phi \qquad (8)$$

$$\frac{d\alpha_2}{dt}=\gamma_2\alpha_2-\Lambda_1\alpha_3\alpha_1\cos\phi \qquad (9)$$

$$\frac{d\alpha_3}{dt}=\gamma_3\alpha_3+\Lambda_2\alpha_1\alpha_2\cos\phi \qquad (10)$$

$$\frac{d\phi}{dt}=-\delta\omega_{UH}+(\Lambda_2\alpha_1\alpha_2/\alpha_3-\Lambda_1\alpha_1\alpha_3/\alpha_2-\Lambda_1\alpha_2\alpha_3/\alpha_1)\sin\phi \qquad (11)$$

where Λ_1,Λ_2 are the coupling coefficients and γ_j are the linear growth (or damping) of the wave.

The evolution of the electromagnetic wave is shown in Fig.(2).

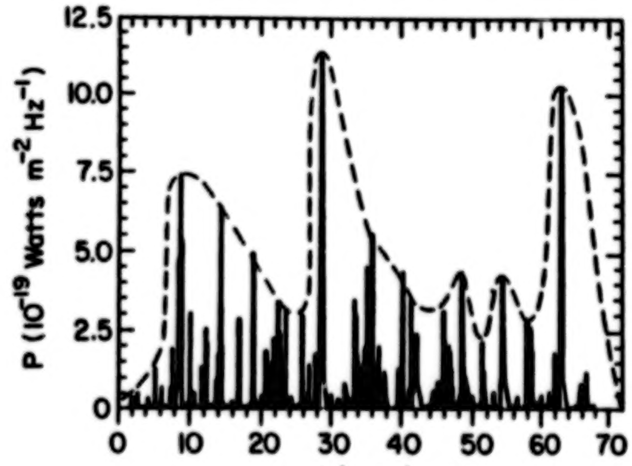

Figure 2: The time evolution of the electromagnetic wave resulting from the dynamic interaction of two electrostatic waves near the cutoff region. The individual pulses have a duration < 1msec. The dotted line represents the response of an instrument with resolution >10 msec.

References

Papadopoulos,K, 1975, Phys. Fluids, 18,1769
Vlahos,L., and Rowland,H.L., 1984, Astr. & Astroph.,139,263
Vlahos,L., Sharma, R.R., and Papadopoulos, K.,1983, Ap.J,275,374

N87
21831
UNCLAS

N87-21831

A JAPANESE PLAN:
LARGE RADIO HELIOGRAPH IN THE SOLAR MAX #22

Shinzo Enome

Toyokawa Observatory
Nagoya University
Toyokawa 442, Japan

Abstract

An outline as of February, 1986 is briefly described of a Japanese plan to construct a large radio heliograph in the next solar maximum. The principal performance specifications of the heliograph are 10 arsec by 10 arcsec x SEC(Zenith Distance) spatial resolution, 1 arc degree by 1 arc degree field of view, 1-sec temporal resolution, and six hour coverage of observing time. It will be operated at 17 GHz with possible other frequency of 35GHz.

1. Motivation

In the solar activity cycle #22 as many as ten examples or so are obtained of simultaneous high-resolution observations by X-ray telescopes on board SMM or HINOTORI and large radio telescopes such as VLA or WSRT. Results obtained from these examples are diverse, and they are unfortunately not associated with an intense flare. It is evidently premature to draw any definite conclusion from these poor samples on the physics in solar flares.

One of fundamental objectives in observations of high energy phenomena in solar flares will be to obtain quite good number of samples on simultaneous observations in X-rays and microwaves with high spatial and temporal resolutions enough for studies on such critical issues as thermal/non-themal, foot-point/loop-top arguments and conduction front problems etc. It is also important to observe preflare activities, which will give us clues to locate such points as of energy build-up, of particle acceleration and/or of energy release. For these and other purposes we have a plan to construct a large radio heliograph in Japan in the next solar maximum, which will be expected around 1991, which, if realized, hopefully operated simultaeously with X-ray telescopes on board a Japanese satellite Solar-A currently scheduled to be launched in August, 1991.

2. Performance Goals

During post several years we had now and then oppotunities among radio astronomers in Japan to discuss the feasibilities to have a large radio heliograph in the solar maximum #22 and its general performance such as what are the most important necessary conditions it has to satisfy. It turned out that the heliograph requires to have full Sun images and to be dedicated to solar observations. These requirements emerged from considerations of the facts that either VLA or WSRT was limited in observation time alocated for the Sun, and restricted in the filed of view they can map in a single observation, which both believed directly related to poor sample of solar flares. The following goals agreed a few years ago after critical discussions based on both aspects of technical feasibility studies and scientific output considerations.

Field of View As mentioned earlier, the field to be mapped is as large as 1 arc degree times 1 arc degree or larger according to hour angle and declination to cover full Sun image. This allows us to observe any bursts which give rise to during the antennas are pointed to the Sun. It also gives us rather uniform sample of solar flare events with respect to time, and we will be free from laborious but sometime fruitless work of flare prediction. The size of element antenna is automatically determined by this parameter, if the operating frequency is given.

Spatial Resolution It is clearly evident that greater resolution is always desirable, but at the same time the resolution is limited by the area of the site available to the radio astronomers. The latter point is very severe particularly in Japan. There is one and only way to relax this severe constraint, which is to choose a higher frequency of observations. This, however, brings us other aspects of physics involved, which will be discussed later in Polarization and Frequency. The resolution chosen is 10 arcsec times 10 arcsec in the favorable condition and 5 arcsec in one dimension (E-W), taking the above and other restrictions into consideration.

Temporal Resolution It is evidenced in this cycle that high energy phenomena showed very rapid fluctuations as fast as tens msec in hard X-rays and 1 sec or possibly less in gamma-rays. Our choice is 1 sec for normal mode, in which the heliograph is operated as long as 6 hours of observations, and 50 msec for fast mode or burst mode for some limited time of observations, which will be bounded by the fast recording device available. A possible physical resasoning of the desirable temporal resolution will be given by the ratio of the spatial resolution over the velocity of electrons relevant to microwave emissions, which will be given by 7000 km / 100,000 km/sec (20 keV), and it is equal to 70 msec.

Polarization and Frequency It is rather easily acceptable that the heliograph is capable to measure both right- and left-handed circular polarizations, since the circular polarization observations are key parameters to estimate magnetic fields of solar flares in acceleration and/or energy release regions. The choice of frequency, on the other hand, requires some considerations on what physical quantities are to be obtained. Microwave spectra of bursts usually show a peak at some frequency around 10 GHz. This spectral peak, which sometimes shifts to a higher or lower frequency, is believed to be due to saturation of radiation in lower frequency side, whereas upper side is due to optically thin gyro-synchrotron emission. The spectral peak frequency is primary function of magnetic field vector and electron energy distribution. It is, therefore, necessary in ideal situation to determine spectral peak value across each burst source, and/or spectral index in optically thin part. The primary frequency of the heliograph is chosen to be 17 GHz, where most of burst source will be optically thin, but for very energetic flares sources will be possibly optically thick. The secondary frequency, if possible, will be either higher or lower than this. Our choice, based on the above consideration, is 35 GHz for the secondary frequency, since our emphasis is put on high energy phenomena in solar flares. It is, however, still difficult to estimate its feasibility, as the cost of 35-GHz amplifiers strongly depends on state-of-the-art.

Time Coverage With conventional equatorial mounting or microcomputer-controlled altitude-azimuth mounting system, antennas will usually cover observation time of 6 hours a day or 3 hours before and after CMP around 0^{o} declination.

Sensitivity The sensitivity of the heliograph is limited by several factors, among which major contributions will be radiometer system noise, confusion due to side lobes and to atmospheric effects. The goal for the overall sensitivity or dynamic range of image is 1/100 or 100:1. Each factor should be, therefore, much smaller than the total value in the sense of the sensitivity. As far as the contribution from the radiometers is concerned the requirement is overcome either for intense bursts in snapshots or weak active regions in synthesis maps as will be explained later. For other contributions they will also be discussed in the later sections.

3. Conceptual Design

Array Configuration and Number of Antennas A tee array configuration is chosen for the heliograph, since the simple application of Fast Fourier Transform is possible to obtain images from complex correlations or visibility functions or, in other words, there is no step to perform time-consuming gridding procedure, which will give us much less burden in computer time in the flood of data to process such as an image in a sec even in normal mode. Further discussion on array configuration will be given later in Image Formation and in Aperture Synthesis. Basic idea to determine number of antennas is given by the number of independent pixels in the field of view. If we take the fundamental grating lobe interval as 35 arcmin or 98 lambda with 10 arcsec angular resolution, the number of pixels will be 44,000. This means that more than 400 by 200 element element antenna tee array will be necessary to form a complete map of independent pixels. When there is some symmetry in source structure or when structure is simple, entire pixels are not independent, and we will not need so many number of antennas. This is expressed in other way as a simple image can be recovered from incomplete samples in UV plane, where a sort of interpolation in done in UV plane or in image plane. One straight-forward way to solve incomplete sampling problem in UV plane is as follows: a tee array is formed of double tees. One is a dense array of 64 x 32 antennas with a fundamental base line interval of 90 lambda or so, and the other is a sparse array of 64 x 32 with a larger fundamental interval of 6 times that of dense array or 540 lambda. Total number of element antennas will be 174 instead of 192, if a single antenna represents each role for the sparse and the dense array at duplicated positions. The fundamental grating lobe interval of the sparse array is about 6 arcmin, which well covers the size of most of intense active regions. With the dense array we can have a complete map of quiet Sun with 1 arcmin resolution, from which we can estimate accurate beam positions both for dense and sparse arrays, taking into account of redundancy of antenna configuration. If we have a single burst source whose brightness at maximum is much higher than that of the quiet Sun, the image obtained with the sparse array represents a high-resolution image of the burst source, and its position is shown in the low-resolution image from the dense array.

Image Formation and Phase Calibration Most popular method is CLEAN to restore an image from a so-called dirty map, which is Fourier transform of incomplete UV plane data. It is, therefore, a kind of interpolation performed in image plane. This procedure will be a powerful tool in the case of the heliograph to recover images from dirty maps of double tee array configuration, which will be snapshots. If this configuration is adopted, there will be ample redundancy in antenna configuration, which may be used for calibration of complex gain, or amplitude and phase, of each antenna, where the Sun is employed as an only calibrator source because of the small antenna size. This method has been extensively used in the 17-GHz interferometer at Nobeyama Solar Radio Observatory. With the calibrated complex antenna gain, we can correct distorted maps to obtain high-quality images with a high-dynamic range.

Atmospheric Effects Successful operations of 5-Element 10-Meter Diameter mm-Wave Synthesis Radio Telescope at Nobeyama have revealed that atmospheric scintillation is serious even at 22 GHz at arcsec resolution. It is operated with 10 sec integration time, therefore, there are no data available on atmospheric scintillation spectra in the range faster than 10 sec, in which the heliograph will be operated. When atmospheric scintillation effects are serious, very frequent calibrations of complex antenna gain have to be conducted using the redundancy antenna configuration.

Aperture Synthesis In normal mode of observations snapshots of the Sun are obtained, which are as mentioned earlier synthesized from incomplete UV plane samples. As the dynamic range of image is not expected to be high for these snap-shots, we can not well see small or weak active regions or other fine structures in or above quiet area. In order to observe those low-brightness structures with intense background radiation of quiet Sun, rather complete coverage of UV plane will be necessary. Appreciable improvement of UV coverage is expected for 15 to 30 minutes accumulation of UV data in favorable conditions as simulated in preliminary analyses.

Alternative Choice: Array Configuration, Self-Calibration So far we have described image formation in the heliograph system based on the double tee array configuration. There is, however, an alternative to handle this problem in a more progressive way, which is to employ the self-calibration developed for VLA and MERLIN and extensively used for both, and also applied recently to radio maps observed by the mm-Wave Synthesis Radio Telescope at Nobeyama. If we adopt this self-calibration method for image formation and antenna calibration, we will not need redundancy in array configuration, which implies there is a possiblity to reduce the number of antennas of the heliograph. In this case array configuration will not be of grating type but for example randomly spaced tee. Risky points associated with the self-calibration method are first, there is no stable general software is developed for extended source structures, which are mostly the case for solar bursts with possible simple or complex sources and the disk of quiet Sun, and it is a time-consuming procedure for a large mass of image data, which means we will need extensive computer time or an ultra-fast super-computer to process these data. The problem to be solved will be, therefore, what is a proper balance between one part of cost and manpower spent for the antenna system and the other part spent for the computer system with an assumption of a limited total cost for the entire heliograph system.

4. Concluding Remarks

An artist impression of the radio heliograph is illustrated in the Figure.

System Design Preliminary studies have been started and are in progress on system design of the heliograph, involving several firms such as specialized in electronics, computer systems, small antenna systems, etc. The system design includes element antennas and mounting, frontend and IF receivers, the local oscillator system, the correlator system, cable systems, control and data-processing computer systems etc. Results of the studies will be reported separately, after certain step and proper reviews are cleared.

Some of cosmic radio astronomers show strong interest in this plan to employ the heliograph as a radio Schmidt camera to find new radio objects or to survey time-varying peculiar radio sources. In that case we will have to install very low-noise receivers with a wide bandwidth.

This plan is promoted by radio astronomers at Tokyo Astronomical Observatory, University of Tokyo, at the Research Institute of Atmospherics, Nagoya University, and the Department of Physics, Nagoya University. Vigorous efforts are undertaken to obtain fund for this plan. In this respect we will welcome supports from scientists in every aspect and comments, suggestions, criticism etc, as well as international supports.

Acknowledgements This article is a short summary of works, studies, and discussions of a large number of scientists, engineers and technicians on the radio heliograph plan, to whom I acknowledge their significant contributions.

大型太陽電波写真儀

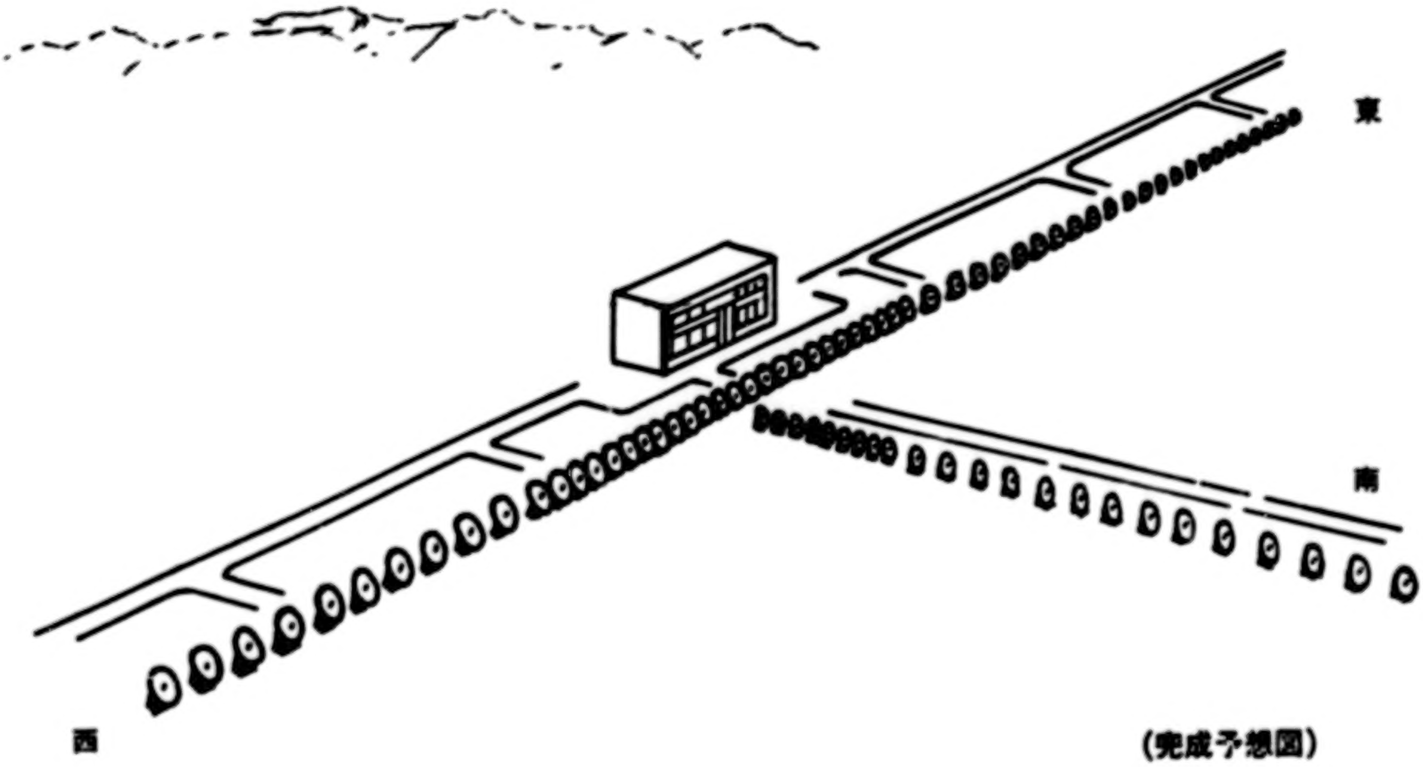

(完成予想図)

装置の概要

全長	600m（東西） 300m（南北）
アンテナ総数	~200基（口径１m赤道儀）
観測波長	短センチ波帯
空間分解能	10秒角×10秒角 ５秒角（東西方向）
時間分解能	１秒
偏波	左右円偏波
前置増幅器総数	~200
相関器総数	~20,000

太陽電波研究者グループ

(昭和57年９月)

N87
21832
UNCLAS

N87-21832

THE HESP PROJECT

K. Kai

Tokyo Astronomical Observatory
University of Tokyo
Mitaka, Tokyo 181, Japan

ABSTRACT. A project for space observations of solar flares for the comming solar maximum phase is briefly described. The main objective is to make a comprehensive study of high energy phenomena of flares through simultaneous imagings in both hard and soft X-rays. The project will be performed with collaboration from US scientists.

The HESP (High Energy Solar Physics) WG of ISAS (Insitute of Space and Astronautical Sciences) has extensively discussed future aspects of space observations of high energy phenomena of solar flares based on successuful results of the Hinotori mission, and proposed a comprehensive research program for the next solar maximum, called the HESP (SOLAR-A) project. Meanwhile in Februrary 1985 a joint discussion with US scientists was made at ISAS about the scientific objectives the collaboration between US and Japan scientists. The collaboration will cover not only hardwares but also softwares and data analyses.

The objective of the HESP project is to make a comprehensive study of both high energy phenomena of flares and quiet structures including pre-flare states, which have been left uncovered by SMM and Hinotori. For such a study simutaneous imagings with better resolutions in space and time in a wide range of energy will be extremely important. Therefore, we consider a hard X-ray telescope in 10 - 100 keV and a soft X-ray telescope to be the main instruments.

Hard X-Ray Telescope(HXT)

The fundamental requirements for HXT are as follows.

(1) Simultaneous imagings over a wide range of energy. In particular flare images at enrgies higher than 30 keV are essentially important to

separate nonthermal components from thermal components. Images taken at above 50 keV would not be poluted by thermal components. Simultaneous imagings at 3 - 4 different energies between 10 and 100 keV are needed.

(2) High resolution. In order to know, for instance, whether successive spikes of impulsive flares occur in a single loop or successively adjacent loops, or whether the whole part of a loop or only its foot points brighten, the spatial resolution should be better than that of the SXT and the temporal resolution should be as short as 1 s.

(3) Wide field of view. The whole Sun coverage is desirable to catch trasient flare phenomena, because we cannot predict to our present knowledge in which region flares occur.

(4) Accuracy of absolute position determination. It is crucial to compare HXR images with those of Hα, microwaves,and magnetograms. The accuracy of absolute position determination of HXR images should be better than 2' - 3'.

A spin-stabilized satellite is not suited for a soft X-ray telescope from a view point of loss of signal, and therefore a non-spinning satellite is desirable. As a result a HXR telescope of a rotating modulation collimeter type such as SXT cannot be adopted. Instead, a HXR telescope of a multi-grid synthesis type has been proposed by Kosugi. It is somewhat analoguous to a radio interferometer of a multi-correlator type. It consists of a number of modulation collimeters (MC) with various pitches and orientations. Each MC consists of a pair of grids installed in parallel (perpendicular to the optical axis) with a separation of ~ 1 m. The response patterns for a point source are triangle. The repetition rate of the response patterns in the sky depends on both the pitch of grids and the separation. The repetition rate corresponding to the largest pitch is chosen to be ~ 2', since HXR flare images rarely extend over areas of 2' x 2'. It is noted, however, that the field of view of HXT covers the whole Sun. We consider that ~ 100 MC's are necessary to obtain flare images of complex structure. The final number and configuration of MC's will be determined by trade-off between technical feasibility and scientific demand.

It is troublesome to prepare a separate detector for each of MC's. Instead, we use a photomultiplier as position-sensitive detectors. Thence the total number of photomultipliers can be reduced to less than 10.

Soft X-Ray Telescope

High resolution observations in soft X-rays is also crucial for understanding of not only high energy phenomena of flares but also pre-flare conditions and large scale quiet stuctures of the Sun. The fundamental requirements for a soft X-ray telescope is high resolutions in space and time. Magnetic field structure in flaring region and its change before, during and after flares can be investigated only with spatial resolution of down to a few arc seconds and temporal resolution of as short as 1 s. In addition simultaneous imagings at different wavelengths are also of special interest.

The soft X-ray telescope is one of important items of the Japan-US collaboration. The optical system and detector will be provided from US scientists and the data processor from Japanese scientists.

Other Instruments

In addition to hard and soft X-ray telescopes, X-γ ray continuum spectrometers, a Bragg crystal spectrometer, and a solar intensity monitor are candidates for supporting instruments. Which instruments are to be aboard will be decided after the design of the two telescopes has been fixed.

Satellite

The satellite will be launched by a M-3S-II roket on a near circular orbit of $\sim$600 km altitude. The total weight allowed for scientific payload will be limitted to $\sim$140 kg.

N87
21833
UNCLAS

N87-21833

THE PROPOSED NRAO MILLIMETER ARRAY AND ITS USE FOR SOLAR STUDIES

Mukul R. Kundu

Astronomy Program
University of Maryland
College Park, Maryland 20742, USA

ABSTRACT

In this report we give a brief summary of the proposed NRAO Millimeter Array discussed at a workshop held in Green Bank, W. Va., September 30-October 2, 1985. We also provide a brief description of the solar studies that can be made with such an array.

THE ARRAY

A millimeter array consisting of two arrays to cover the range of desired resolutions and fields of view was proposed:
(1) A large array of ~ 21 movable antennas of ~ 10 m diameter and a small array of ~ 21 antennas of ~ 4 m diameter which are mounted on a structure ~ 29 m in size in a multi-telescope (M-T) configuration with ~ 50% filling factor and 25 m resolution. Figure 1 schematically illustrates the major options being discussed for configuration of the two arrays. The antennas in both arrays will operate in both aperture synthesis mode and single antenna mode. Figure 2 summarizes the observing modes that will be used to cover all resolutions from the $56''\lambda_{mm}$ beam size of the 4 m antennas down to the resolution of the largest arrays of the 10 m antennas. Single dish observing in total power/beam switching mode covers the largest two size scales, the M-T in aperture synthesis mode covers the next step of a factor of 2.5 in resolution, and the large array configuration $\geq$ 90 m covers all higher resolutions (Hjellming 1985). Mapping by mosaicing is also intended, which involves the combination of 4 m and 10 m data to observe the fields of view of the 4 m antennas with the resolution of the 10 m antennas or array of 10 m antennas. The main reason for two arrays with antennas of two different sizes is to allow imaging of a wide range of spatial scales with reasonable surface brightness sensitivity. The collecting area of the array will be between 1000 and 2000 m^2, and it will operate at 9, 3, 2 and 1 mm, and submillimeter wavelengths, for both continuum and spectral line observations. The VLA-Y or the randomized circle for the large array is believed to be the most suitable configuration.

PRECEDING PAGE BLANK NOT FILMED

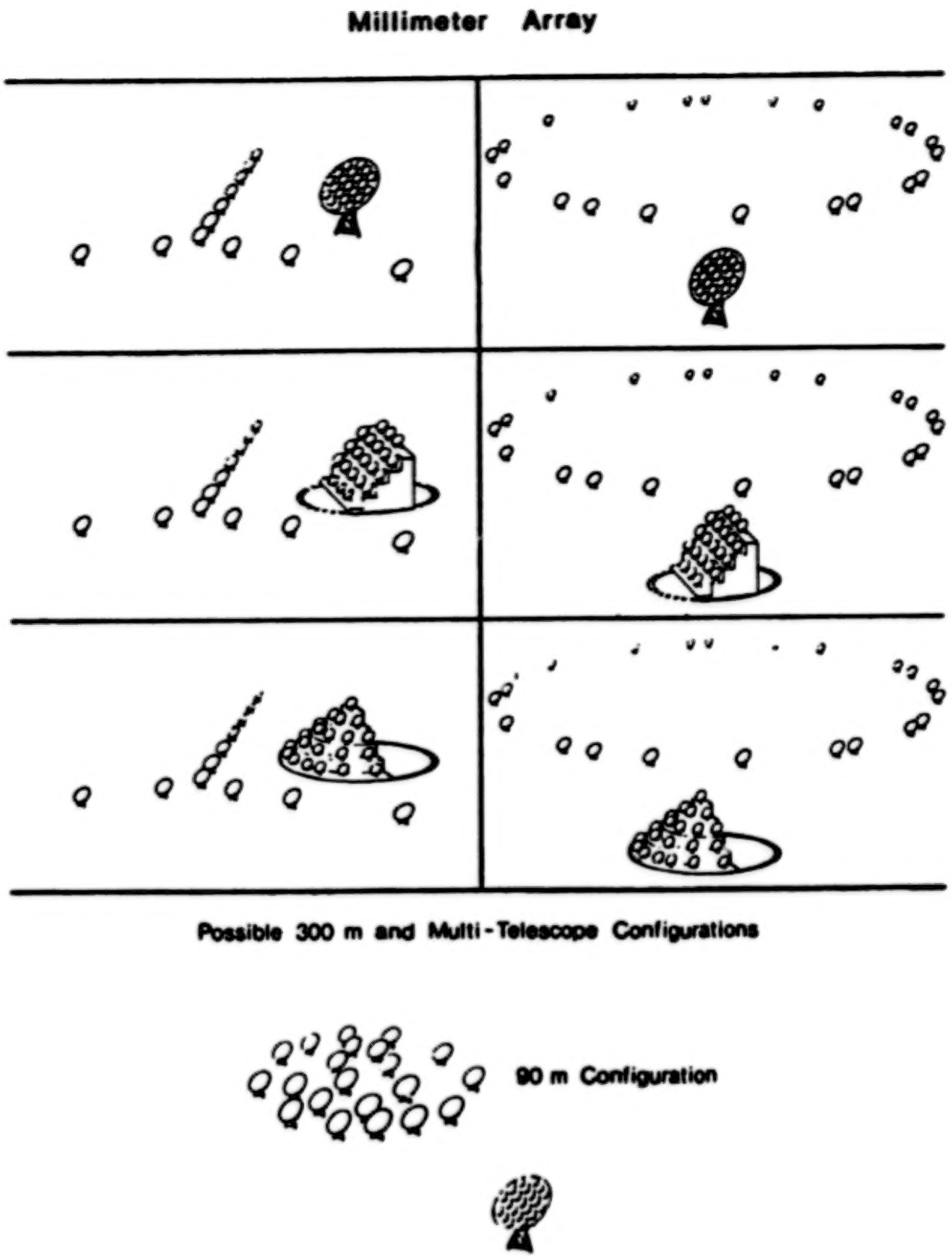
Millimeter Array
Possible 300 m and Multi-Telescope Configurations
90 m Configuration

Fig. 1. Various Millimeter Array configurations (see text).

Millimeter Array Imaging/Mosaicking Problem

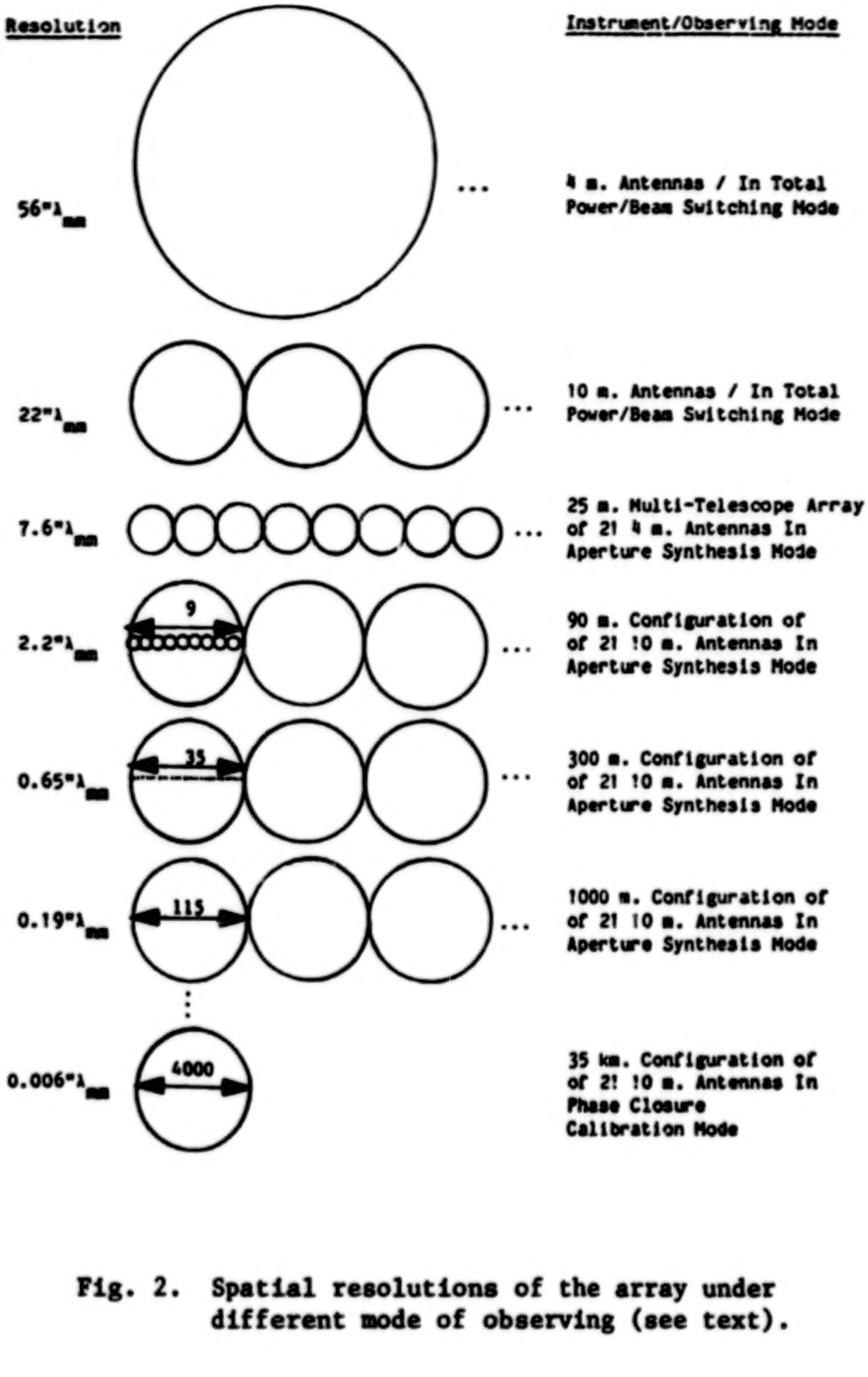
Resolution
Instrument/Observing Mode
$56''\lambda_{mm}$
4 m. Antennas / In Total Power/Beam Switching Mode
$22''\lambda_{mm}$
10 m. Antennas / In Total Power/Beam Switching Mode
$7.6''\lambda_{mm}$
25 m. Multi-Telescope Array of 21 4 m. Antennas In Aperture Synthesis Mode
$2.2''\lambda_{mm}$
9
90 m. Configuration of of 21 10 m. Antennas In Aperture Synthesis Mode
$0.65''\lambda_{mm}$
35
300 m. Configuration of of 21 10 m. Antennas In Aperture Synthesis Mode
$0.19''\lambda_{mm}$
115
1000 m. Configuration of of 21 10 m. Antennas In Aperture Synthesis Mode
$0.006''\lambda_{mm}$
4000
35 km. Configuration of of 21 10 m. Antennas In Phase Closure Calibration Mode

Fig. 2. Spatial resolutions of the array under different mode of observing (see text).

SOLAR STUDIES

I. FLARES

(a) Gamma ray-mm wavelength flares

One important solar problem that can be studied with a mm wave array is that of gamma ray-mm wave flares. In gamma ray-mm wave flares, recent evidence (from Solar Maximum Mission and mm wave observations) has demonstrated that electrons and protons are accelerated almost simultaneously to very high energies. In particular, electrons attain energies of 10 to 100 MeV within one or two seconds of flare onset, and emit both mm waves and continuum gamma rays of high intensity. This continuum radiation is accompanied by nuclear gamma ray lines at energies less than ~ 10 MeV due to protons, and neutrons are sometimes detected at Earth (e.g. Chupp 1984).

At the present time there is no widely accepted explanation for this very rapid acceleration. Some argue that there must be a "first phase" process because of the very short time scale, possibly involving electric fields in double layers. Others argue that shock acceleration can act on short enough time scales (e.g. Decker and Vlahos 1985).

In the radio range, the special characteristic of gamma ray-mm wave flares is that the flux density increases with frequency. Figure 3 shows the spectra of several flares (Kaufman et al. 1985).

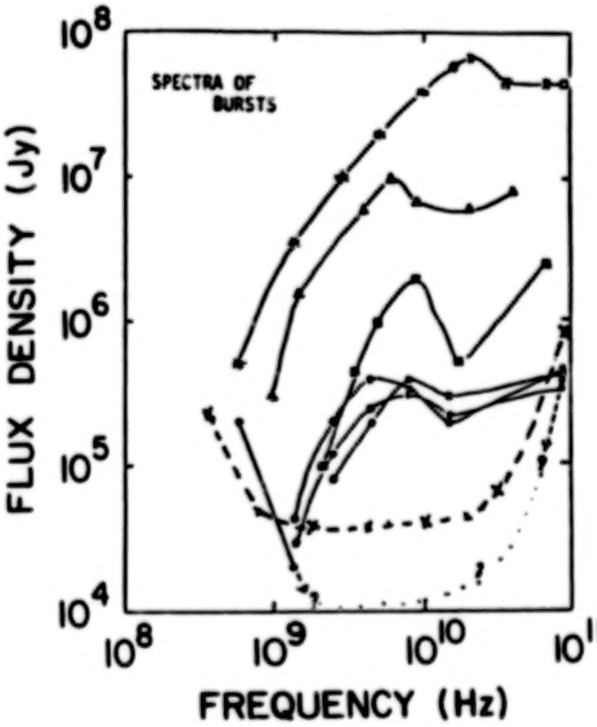

Fig. 3. Flux density spectra of millimeter bursts associated with Gamma ray flares (Kaufman et al. 1985).

Observations at mm waves are obviously of great interest: there have been no spatially resolved studies in either mm waves or gamma rays. Since there are no instruments being designed with arcsec resolution in the energy range > 10 MeV, the mm wave array is probably the next best thing for understanding these very energetic solar flares. In order to study properly the problem of electron and proton acceleration in gamma ray-millimeter flares, one must have $\lesssim 0.1$ sec time resolution and $\lesssim 1''$ spatial resolution, and measure circular polarization with ~ 1% accuracy. Mapping of wide fields by mosaicing is obviously necessary.

(b) Penetration of electron beams into the lower atmosphere

In many flares, brightenings occur in Hα, EUV and even white light simultaneously with hard X-ray bursts. There is a controversy over the cause of these brightenings, whether due to electrons, protons, or an ion acoustic conduction front. Each method has problems: it is uncertain whether electrons are able to penetrate deeply enough into the dense atmosphere; we do not know how to accelerate an adequate number of protons in the required 1 s; and heat conduction by an ion acoustic front may be too slow (Dulk et al. 1986).

Observations of mm waves can help answer these questions because they originate in the relevant region of the atmosphere, namely the low chromosphere, in contrast to cm waves which originate in the lower corona. If the mm wave emission in some flares is due to thermal bremsstrahlung from the heated plasma, it is relatively easy to relate radio wave brightness to the density-temperature structure in the heated region. The relative timing of mm wave vs. cm wave bursts should help distinguish among the possible causes.

II. MAPPING OF SOLAR ACTIVE REGIONS, SOLAR FILAMENTS AND PROMINENCES

Mm wave emission from active regions is due to free-free bremsstrahlung, and is partially polarized due to the difference between x-mode and o-mode emissivities. It therefore gives information about the magnetic field strength and topology in the low chromosphere, whereas most magnetogram data apply to the photosphere. Changes in magnetic field topology, pre- to post-flare, should be much larger in the chromosphere than the photosphere, and hence much more evident at mm wavelengths (Kundu and McCullough 1972a; Kundu and McCullough 1972b).

Since filaments are optically thick, their brightness temperature should equal the electron temperature determined at optical wavelengths. However, the radio observations indicate that the observed brightness temperature T_b of a filament increases with wavelength. It is believed that this is due to radiation from the transition sheath where T_e increases from 6000 K at the filament to about 10^6 K, the temperature of the surrounding corona. The variation of $T_b(\lambda)$ can provide information on the temperature and density structure of the transition sheath. This is important since the temperature gradient determines the amount of thermal energy conducted into the filament from the corona. Rao and Kundu (1977) studied this problem by considering a model in which the conductive flux from the corona balances the energy radiated away by the transition sheath. They found that best fit to observations is obtaned when almost all of the conductive flux is dissipated in the transition sheath. The observations used by Rao and Kundu were obtained using single dish telescopes with a few arc minute resolution. Obviously there is a need for high spatial resolution observations in both mm and cm domains to determine more precisely the radio spectrum of the filament transition sheath and then address the question of thermal conduction into the filament.

Most centimeter and millimeter observations show that the radio and optical filaments are of very similar size. On the other hand, observations made between 3.5 mm and 11 cm wavelengths (e.g. Kundu and McCullough, 1972a; Kundu et al, 1978) have demonstrated that the radio filaments are sometimes much larger than their optical counterparts. The considerably larger size of the radio filament as compared to the optical filament suggests that the immediate environment of a filament differs from that of the undisturbed corona. This is consistent with white light coronal measurements which show that Hα filaments are sometimes surrounded by low density regions (coronal cavities) with weaker emission than the ambient corona. These low density regions lead to a broadening of the optical Hα filament at radio wavelengths. The radio filament appears as a temperature depression because it is optically thick at radio frequencies and is cooler than the quiet Sun. A high resolution study in both cm and mm domains of the radio structure and spectra of filaments should permit us to understand the physics of coronal cavities.

For these studies, it is necessary to image a field of about 1 arc min with a resolution of about 1 arc sec at 1 mm. This is feasible with a 3 x 3 mosaic, or by under-illuminating the 10 m dishes. Quasi-simultaneous observations at 1, 3 and 9 mm including circular polarization measurements are required.

III. MAPPING OF THE QUIET SUN: QUIET REGIONS AND CORONAL HOLES

At 36 GHz, recent Japanese results (Kosugi et al. 1985), using the Nobeyama 45 m millimeter telescope, demonstrate that coronal holes are brighter than quiet regions (Fig. 4a), contrary to what is observed at almost all other frequencies (e.g. 10 and 98 GHz). Similar results were reported earlier (Fig. 4b) by Kundu and McCullough (1972a) and Efanov et al (1980), although this highly unexpected result was not properly understood, because of the manner the results were presented (namely, contour maps versus spectacular photographic representation). The cause of the anomalous brightening is unknown: it is possibly related to a lower gradient of density and temperature in the transition region of coronal holes compared to average quiet regions, or to a wider temperature plateau in the upper chromosphere. Maps with arc sec resolution are desirable to determine whether the brightness difference is related to fine structures or widespread emission, and to compare brightness distributions at the solar limb where the emission scale height is only about 1".

ORIGINAL PAGE IS
OF POOR QUALITY

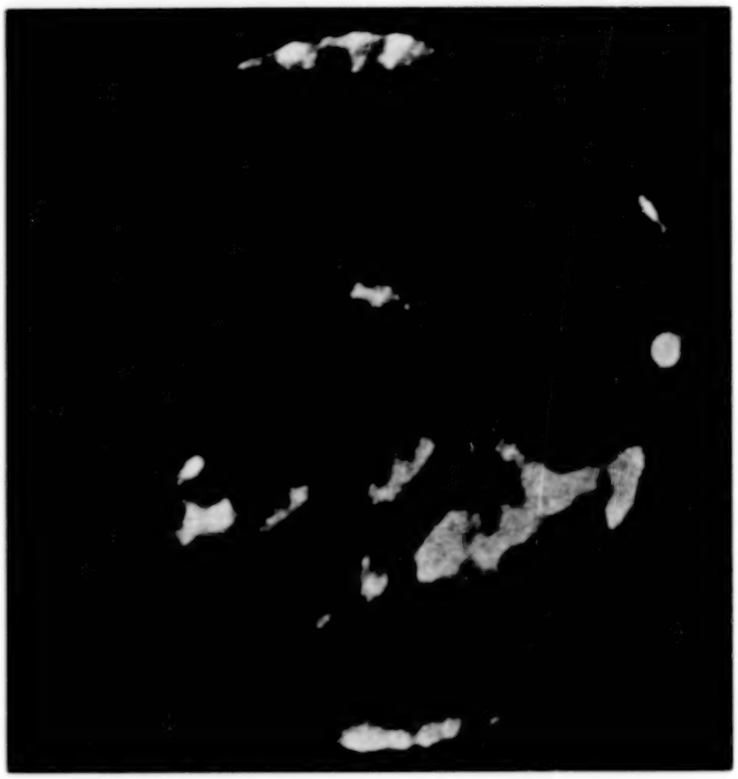

Fig. 4a. Polar cap brightening associated with coronal holes observed on July 19, 1984 at 36 GHz by Kosugi et al (1985) using the Nobeyama 45 m milli-meter telescope with 46" resolution

Fig. 4b. Brightening in the polar region (marked "P") observed on February 26, 1971 by Kundu and McCullough (1972a) at 33 GHz with a resolution of 1.'6.

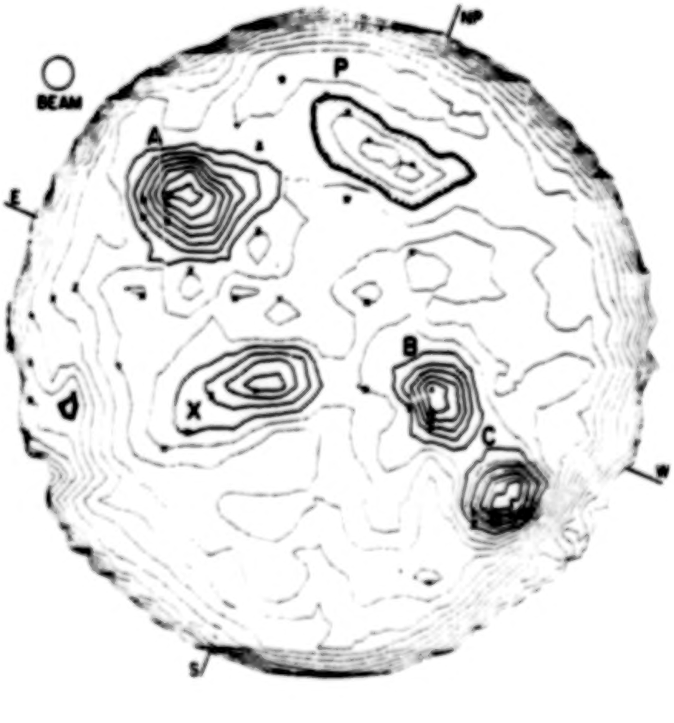

Other studies include the thermal phase of flares, coronal heating, and oscillations (both radial and torsional) and pulsations.

ACKNOWLEDGEMENT

This paper is largely based upon the Working Group Report on the Sun and Stars (Dulk et al. 1986) presented at the NRAO Mm Array workshop. Partial support for this work was obtained from NASA grant NGR 21-002-199 and NASA contract NAG 5511.

REFERENCES

Chupp, E.L., 1984, Ann. Rev. Astr. Ap. **22**, 359.
Decker, R.B., and Vlahos, L., 1985, "Prompt Acceleration of Ions By Oblique Turbulent Shocks in Solar Flares", International Cosmic Ray Conference, La Jolla.
Dulk, G.A., Gary, D.E., Hjellming, R.M., and Kundu, M.R., 1986, "Report of the Working Group on the Sun and Stars", Proc. NRAO Millimeter Array Workshop, in press.
Efanov, V.A., Moiseev, I.G., Nesterov, N.S., and Stewart, R.T., 1980, "Radio Physics of the Sun" (ed. M.R. Kundu and T.E. Gergely, D. Reidel), p. 141.
Hjellming, R.M., 1985, NRAO Millimeter Array Memo No. **34**.
Kaufman, P. et al., 1985, Private communication.
Kosugi, T., Ishiguro, M. and Shibasaki, K., 1985, Publ. Astron. Soc. Japan, in press.
Kundu, M.R. and McCullough, T.P., 1972a, Solar Phys. **24**, 133.
Kundu, M.R. and McCullough, T.P., 1972b, Solar Phys. **27**, 182.
Kundu, M.R., Fürst, E., Hirth, W. and Butz, M., 1978, Astron. Astrophys. **62**, 431.
Rao, A.P. and Kundu, M.R., 1977, Solar Phys. **55**, 161.
Sprangle, P. and Vlahos, L., 1983, Ap. J., **273**, L95.

BIBLIOGRAPHIC DATA SHEET

1. Report No. NASA CP-2449	**2. Government Accession No.**	**3. Recipient's Catalog No.**

4. Title and Subtitle Rapid Fluctuations in Solar Flares	**5. Report Date** March 1987 **6. Performing Organization Code** 602.6
7. Author(s) Brian R. Dennis, Larry E. Orwig, and Alan L. Kiplinger,* Editors	**8. Performing Organization Report No.** 87B0102
9. Performing Organization Name and Address Goddard Space Flight Center Greenbelt, Maryland 20771	**10. Work Unit No.** **11. Contract or Grant No.**
12. Sponsoring Agency Name and Address National Aeronautics and Space Administration Washington, D. C. 20546	**13. Type of Report and Period Covered** Conference Publication **14. Sponsoring Agency Code**

15. Supplementary Notes

*Kiplinger—Systems Applied Sciences Corporation-Technologies, Landover, Maryland

16. Abstract

Papers resulting from a workshop on the Rapid Fluctuations in Solar Flares held at the Ramada Hotel in Lanham, Maryland from September 30 to October 4, 1985. The papers are divided into five sections: X-rays, radio and microwaves, thermal response, plasma physics, and future plans. Variations on time scales generally shorter than 10 s are presented along with possible theoretical interpretations.

17. Key Words (Selected by Author(s)) Solar Flare X-rays Radio	**18. Distribution Statement** Unclassified - Unlimited Subject Category 92

19. Security Classif. (of this report) Unclassified	**20. Security Classif. (of this page)** Unclassified	**21. No. of Pages** 496	**22. Price*** A21

*For sale by the National Technical Information Service, Springfield, Virginia 22161

GSFC 25-44 (10/77)

This publication was printed at the UNICOR Print Plant,
Federal Correctional Institution, Ray Brook, NY

END

DATE

FILMED

JUL 7 1987